

ADA 278808

UNITED STATES AIR FORCE
SUMMER FACULTY RESEARCH PROGRAM
1988
PROGRAM TECHNICAL REPORT
UNIVERSAL ENERGY SYSTEMS, INC.
VOLUME III OF IV

Program Director, UES
Rodney C. Darrah

Program Manager, AFOSR
Lt. Col. Claude Cavender

Program Administrator, UES
Susan K. Espy

Submitted to
Air Force Office of Scientific Research
Bolling Air Force Base
Washington, DC

December 1988



94-12297

DISCONTINUED EXPECTED 3

94-12297 081

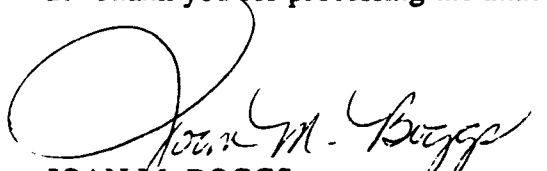
*Rtn to Foretla
Tech Rpt -
7/7/11 1/4 Noo ang*

MEMORANDUM FOR DTIC (Acquisition)
(Attn: Pat Mauby)

SUBJECT: Distribution of USAF (AFOSR Summer Research Program (Air Force Laboratories) and Universal Energy Systems, Inc., and the Research Initiation Program

FROM: AFOSR/XPT
Joan M. Boggs
110 Duncan Avenue, Suite B115
Bolling AFB DC 20332-0001

1. All of the books forwarded to DTIC on the subjects above should be considered Approved for Public Release, distribution is unlimited (Distribution Statement A).
2. Thank you for processing the attached information.


JOAN M. BOGGS
Chief, Technical Information Division

*USAF Graduate Student Research
Program (1988)
8 Technical Reports Enclosed*

TABLE OF CONTENTS

<u>SECTION</u>	<u>PAGE</u>
Preface	i
List Of Participants	ii
Participant Laboratory Assignment	xxviii
Research Reports	xxxii

Accession For	
NTIS GPO#1	<input checked="" type="checkbox"/>
DTIC RM	<input type="checkbox"/>
Unannounced	<input type="checkbox"/>
Justified	
By _____	
Distribution _____	
Availability Codes	
Dist	Avail. and/or Special
A-1	

PREFACE

The United States Air Force Summer Faculty Research Program (USAF-SFRP) is designed to introduce university, college, and technical institute faculty members to Air Force research. This is accomplished by the faculty members being selected on a nationally advertised competitive basis for a ten-week assignment during the summer intersession period to perform research at Air Force laboratories/centers. Each assignment is in a subject area and at an Air Force facility mutually agreed upon by the faculty members and the Air Force. In addition to compensation, travel and cost of living allowances are also paid. The USAF-SFRP is sponsored by the Air Force Office of Scientific Research, Air Force Systems Command, United States Air Force, and is conducted by Universal Energy Systems, Inc.

The specific objectives of the 1988 USAF-SFRP are:

- (1) To provide a productive means for U. S. Faculty Members to participate in research at Air Force Laboratories/Centers;
- (2) To stimulate continuing professional association among the Faculty and their professional peers in the Air Force;
- (3) To further the research objectives of the United States Air Force;
- (4) To enhance the research productivity and capabilities of the Faculty especially as these relate to Air Force technical interests.

During the summer of 1988, 153-faculty members participated. These researchers were assigned to 23 USAF laboratories/centers across the country. This four volume document is a compilation of the final reports written by the assigned faculty members about their summer research efforts.

LIST OF 1988 PARTICIPANTS

NAME/ADDRESS

DEGREE, SPECIALTY, LABORATORY ASSIGNED

Dr. Ibrahim A. Ahmad
Professor and Director
Division of Statistics
Dept. of Math Sciences
Northern Illinois University
DeKalb, IL 60115
(815) 753-6739

Degree: Ph.D., Statistics, 1975
Specialty: Statistics and Operations
Research
Assigned: Armament Laboratory

Dr. Robert J. Arenz
Professor
Dept. of Mechanical Engineering
Gonzaga University
Spokane, WA 99258
(509) 328-4220

Degree: Ph.D., Aeronautical Eng., 1964
Specialty: Solid Mech.
Assigned: Materials Laboratory

Dr. Lucia M. Babcock
Assistant Professor
Dept. of Chemistry
Louisiana State University
Choppin Hall
Baton Rouge, LA 70803
(504) 388-3239

Degree: Ph.D., Chemistry, 1978
Specialty: Gas Phase Ion-Molecule Chem.
Assigned: Air Force Geophysics Lab.

Dr. Praphulla K. Bajpai
Professor
Dept. of Biology
University of Dayton
300 College Park
Dayton, OH 45469
(513) 229-3029

Degree: Ph.D., Animal Physiology, 1965
Specialty: Physiology and Biomaterials
Assigned: Harry G. Armstrong Aerospace
Medical Research Laboratory

Dr. Stephen D. Baker
Professor
Dept. of Physics
Rice University
Houston, TX 77251-1892
(713) 527-8101

Degree: Ph.D., Physics, 1963
Specialty: Nuclear Physics
Assigned: Air Force Geophysics Lab.

Dr. Pradip M. Bakshi
Research Professor
Dept. of Physics
Boston College
Chestnut Hill, MA 02167
(617) 552-3585

Degree: Ph.D., Theoretical Physics,
1962
Specialty: Quantum Theory
Assigned: Air Force Geophysics Lab.

NAME/ADDRESS

DEGREE, SPECIALTY, LABORATORY ASSIGNED

Dr. Shankar S. Bale
Professor
Dept. of Science and Math
Saint Paul's University
Lawrenceville, VA 23868
(804) 848-3111

Degree: Ph.D., Genetics, 1971
Specialty: Toxicology-Cytogenetics
Assigned: Harry G. Armstrong Aerospace
Medical Research Laboratory

Mr. Beryl L. Barber
Assistant Professor
Dept. of Electronics Eng.
Oregon Institute of Technology
3201 Campus Drive
Klamath Falls, OR 97601-8801
(503) 882-6890

Degree: MSEE, Electrical Eng., 1961
Specialty: RF/Microwave Components
Assigned: Rome Air Development Center

Dr. Bryan R. Becker
Assistant Professor
Dept. of Aerospace Engineering
University of Missouri
600 West Mechanic
Independence, MO 64050-1799
(816) 276-1279

Degree: Ph.D., Eng. Science, 1979
Specialty: Computational Fluid Dynamics
Assigned: Aero Propulsion Laboratory

Dr. Reuben Benumof
Professor
Dept. of Applied Sciences
College of Staten Island
130 Stuyvesant Pl.
Staten Island, NY 10301
(718) 390-7973

Degree: Ph.D., Physics, 1945
Specialty: Semiconductor Physics
Assigned: Air Force Geophysics Lab.

Mr. George N. Bratton
Associate Professor
Dept. of Math and Comp. Science
Austin State Peay State Univ.
P O Box 8343
Clarksville, TN 37044
(615) 648-7834

Degree: Ed.D., Mathematics Ed., 1977
Specialty: Statistics
Assigned: Electronics Systems Division

Dr. Dan R. Bruss
Assistant Professor
Dept. of Physical Sciences
Albany College of Pharmacy
106 New Scotland Avenue
Albany, NY 12208
(518) 445-7225

Degree: Ph.D., Chemistry, 1985
Specialty: Physical Organic Chemistry
Assigned: Frank J. Seiler Research Lab.

NAME/ADDRESS

DEGREE, SPECIALTY, LABORATORY ASSIGNED

Dr. Ronald Bulbulian
Associate Professor
Dept. of Health, Physical
Education and Recreation
University of Kentucky
Seaton 100
Lexington, KY 40506
(606) 257-7904

Degree: Ph.D., Physiology, 1980
Specialty: Exercise Physiology
Assigned: School of Aerospace Medicine

Dr. Charles M. Bump
Assistant Professor
Dept. of Chemistry
Hampton University
P O Box 6483
Hampton, VA 23668
(804) 727-5330

Degree: Ph.D. Organic Chemistry, 1979
Specialty: Organic Synthesis
Assigned: Frank J. Seiler Research Lab.

Dr. John A. Burke, Jr.
Professor
Dept. of Chemistry
Trinity University
715 Stadium Drive
San Antonio, TX 78284
(512) 736-7316

Degree: Ph.D., Chemistry, 1963
Specialty: Inorganic Compounds
Assigned: School of Aerospace Medicine

Mr. Mike Burlakoff
Assistant Professor
Dept. of Computer Science
Southwest Missouri State Univ.
901 S. National
Springfield, MO 65804
(417) 836-5930

Degree: MS., Math, Computer Sci., 1965
Specialty: Computer Science
Assigned: Avionics Laboratory

Dr. Larry W. Byrd
Assistant Professor
Dept. of Mechanical Engineering
Arkansas State University
P O Box 1080
State University, AR 72467-1080
(501) 972-3421

Degree: Ph.D., Mechanical Eng., 1984
Specialty: Mechanical Engineering
Assigned: Flight Dynamics Laboratory

Dr. Clarence Calder
Associate Professor
Dept. of Mechanical Engineering
Oregon State University
Corvallis, OR 97331
(503) 754-2427

Degree: Ph.D., Mechanical Eng., 1969
Specialty: Stress Wave Propagation
Assigned: Astronautics Laboratory

NAME/ADDRESS

DEGREE, SPECIALTY, LABORATORY ASSIGNED

Dr. Richard T. Carlin
Assistant Professor
Dept. of Chemistry
Polytechnic University
333 Jay St.
Brooklyn, NY 11201
(718) 260-3339

Degree: Ph.D., Chemistry, 1983
Specialty: Inorganic Chemistry
Assigned: Frank J. Seiler Research Lab.

Dr. Gene O. Carlisle
Professor
Dept. of Chemistry and Physics
West Texas State University
Canyon, TX 79016
(806) 656-2282

Degree: Ph.D., Inorganic Chem., 1969
Specialty: Coordination Chemistry
Assigned: Materials Laboratory

Dr. Patricia Carlson
Professor
Dept. of Humanities
Rose-Hulman Institute of Tech.
5500 Wabash
Terre Haute, IN 47803
(812) 877-1511

Degree: Ph.D., Language & Lit., 1973
Specialty: Document Design
Assigned: Human Resources Laboratory:
Logistics & Human Factors Div.

Dr. David R. Cecil
Professor
Dept. of Mathematics
Texas A&I University
Campus Box 172
Kingsville, TX 78363
(512) 592-1839

Degree: Ph.D., Mathematics, 1962
Specialty: Algebra (Finite Fields)
Assigned: Wilford Hall Medical Center

Dr. Wayne A. Charlie
Associate Professor
Dept. of Civil Engineering
Colorado State University
Fort Collins, CO 80523
(303) 491-8584

Degree: Ph.D., Civil Engineering, 1975
Specialty: Geotechnical Engineering
Assigned: Engineering & Services Center

Dr. Steven C. Chiesa
Assistant Professor
Dept. of Civil Engineering
Santa Clara University
Santa Clara, CA 95053
(408) 554-4697

Degree: Ph.D., Civil Eng., 1982
Specialty: Biological Waste Treatment
Assigned: Occupational and Environment
Health Laboratory

NAME/ADDRESS

DEGREE, SPECIALTY, LABORATORY ASSIGNED

Dr. Karen C. Chou
Associate Professor
Dept. of Civil Engineering
Syracuse University
Syracuse, NY 13244-1190
(315) 423-3314

Degree: Ph.D., Structural Eng., 1983
Specialty: Structural Engineering
Assigned: Flight Dynamics Laboratory

Dr. Phillip A. Christiansen
Associate Professor
Dept. of Chemistry
Clarkson University
Potsdam, NY 13676
(315) 268-4099

Degree: Ph.D., Physical Chem., 1978
Specialty: Physical Chemistry
Assigned: Astronautics Laboratory

Dr. Keith A. Christianson
Assistant Professor
Dept. of Electrical Engineering
University of Maine
Orono, ME 04469
(207) 581-2244

Degree: Ph.D., Materials Science and
Engineering, 1985
Specialty: Electronic Materials
Assigned: Rome Air Development Center

Dr. Mingking K. Chyu
Assistant Professor
Dept. of Mechanical Eng.
Carnegie Mellon University
Pittsburgh, PA 15213
(412) 268-3658

Degree: Ph.D., Heat Transfer, 1986
Specialty: Heat Transfer
Assigned: Aero Propulsion Laboratory

Dr. Jerry D. Clark
Assistant Professor
Dept. of Physics
Wright State University
248 Fawcett Hall
Dayton, OH 45435
(513) 426-3917

Degree: Ph.D., Physics, 1982
Specialty: Atomic Physics
Assigned: Aero Propulsion Laboratory

Dr. Lane Clark
Assistant Professor
Dept. of Mathematics
University of New Mexico
Albuquerque, NM 87106
(505) 277-2104

Degree: Ph.D., Mathematics, 1980
Specialty: Graph Theory
Assigned: Weapons Laboratory

NAME/ADDRESS

DEGREE, SPECIALTY, LABORATORY ASSIGNED

Dr. Donald F. Collins
Faculty in Physics
Dept. of Physics
Warren Wilson College
Swannanoa, NC 28778
(704) 298-3325

Degree: Ph.D., Physics, 1970
Specialty: Optics, Image Processing
Assigned: Air Force Geophysics Lab.

Dr. Susan T. Collins
Assistant Professor
Dept. of Chemistry
California State University
18111 Nordhoff Street
Northridge, CA 91330
(818) 885-3367

Degree: Ph.D., Physical Chem., 1981
Specialty: Matrix Isolation Spectroscopy
Assigned: Astronautics Laboratory

Dr. Charles D. Covington
Assistant Professor
Dept. of Electrical Engineering
University of Arkansas
Bell Engineering Center 3217
Fayetteville, AR 72701
(501) 575-6583

Degree: Ph.D., Electrical Eng., 1984
Specialty: Digital Signal Processing
Assigned: Harry G. Armstrong Aerospace
Medical Research Laboratory

Dr. Parvis Dadras
Professor
Dept. of Mech. Systems Eng.
Wright State University
Dayton, OH 45435
(513) 873-2944

Degree: Ph.D., Mechanical Eng., 1972
Specialty: Mechanics of Materials
Assigned: Materials Laboratory

Dr. John F. Dalphin
Professor
Dept. of Computer Science
Towson State University
Baltimore, MD 21204
(301) 321-3701

Degree: Ph.D., Mathematics, 1973
Specialty: Computer Science
Assigned: Electronics Systems Division

Mr. Darin S. DeForest
Research Associate
Dept. of Computer Science
Arizona State University
Tempe, AZ 85287
(602) 965-3664

Degree: B.Sc., Computer Science, 1984
Specialty: Programming Language Design
Assigned: Rome Air Development Center

NAME/ADDRESS

Dr. David H. DeHeer
Associate Professor
Dept. of Biology
Calvin College
3201 Burton Street, S.E.
Grand Rapids, MI 49506
(616) 957-6083

Dr. Eustace L. Dereniak
Associate Professor
Dept. of Optical Science
University of Arizona
528 N. Martin
Tucson, AZ 85719
(602) 621-1019

Prof. Paul T. Dingman
Assistant Professor
Dept. of Electronics Eng. Tech.
Oregon Institute of Technology
3201 Campus Drive
Klamath Falls, OR 97601-8801
(503) 882-6890

Dr. David A. Dolson
Assistant Professor
Dept. of Chemistry
Murray State University
Murray, KY 42071
(502) 762-4490

Dr. Hugh K. Donaghy
Assistant Professor
Dept. of Computer Science
Rochester Inst. of Technology
1 Lomb-Memorial Drive
Rochester, NY 14623
(716) 475-2994

Dr. Stephen J. Dow
Assistant Professor
Dept. of Math and Statistics
Univ. of Alabama in Huntsville
Huntsville, AL 35899
(205) 895-6252

DEGREE, SPECIALTY, LABORATORY ASSIGNED

Degree: Ph.D., Molecular Biology, 1972
Specialty: Molecular Biology
Assigned: Engineering & Services Center

Degree: Ph.D., Optics, 1976
Specialty: Infrared Physics
Assigned: Arnold Engineering
Development Center

Degree: MSEE., Electrical Eng., 1974
Specialty: Digital, Microprocessors
Assigned: Rome Air Development Center

Degree: Ph.D., Physical Chem., 1981
Specialty: Laser Spectroscopy
Assigned: Weapons Laboratory

Degree: Ph.D., Philosophy, 1972
Specialty: Natural Language Processing
Assigned: Rome Air Development Center

Degree: Ph.D., Mathematics, 1982
Specialty: Discrete Mathematics
Assigned: Armament Laboratory

NAME/ADDRESS

DEGREE, SPECIALTY, LABORATORY ASSIGNED

Dr. Derek Dunn-Rankin
Assistant Professor
Dept. of Mechanical Engineering
University of California
616 Engineering
Irvine, CA 92717
(714) 854-0460

Degree: Ph.D., Mechanical Eng., 1985
Specialty: Laser Diagnostics (combustion)
Assigned: Aero Propulsion Laboratory

Dr. Deanna S. Durnford
Assistant Professor
Dept. of Agric. & Chem. Eng.
Colorado State University
Ft. Collins, CO 80523
(303) 491-5252

Degree: Ph.D., Civil Eng., 1982
Specialty: Groundwater
Assigned: Engineering & Services Center

Dr. Suren N. Dwivedi
Associate Professor
Dept. of Mechanical Eng.
University of North Carolina
Charlotte, NC 28223
(704) 547-2303

Degree: Ph.D., Engineering, 1976
Specialty: Material Processing
Assigned: Materials Laboratory

Dr. Wayne A. Eckerle
Associate Professor
Dept. of Mech. & Ind. Eng.
Clarkson University
Potsdam, NY 13676
(315) 268-2203

Degree: Ph.D., Fluid Mech., 1985
Specialty: Experimental Fluid Mechanics
Assigned: Aero Propulsion Laboratory

Dr. J. Kevin Ford
Assistant Professor
Dept. of Psychology
Michigan State University
East Lansing, MI 48824
(517) 353-5006

Degree: Ph.D., Philosophy, 1983
Specialty: Industrial/Organ. Psychology
Assigned: Human Resources Laboratory:
Training Systems

Prof. Michael E. Frantz
Assistant Professor
Dept. of Math and Physics
University of LaVerne
1950 Third Street
LaVerne, CA 91750
(714) 593-3511

Degree: M.S., Mathematics, 1978
Specialty: Partial Differential Equations
Assigned: Air Force Geophysics Lab.

NAME/ADDRESS

DEGREE, SPECIALTY, LABORATORY ASSIGNED

Dr. Barry K. Fussell
Assistant Professor
Dept. of Mechanical Engineering
University of New Hampshire
Kingsbury Hall
Durham, NH 03824
(603) 862-1352

Degree: Ph.D., Mechanical Eng., 1987
Specialty: Systems Modeling & Controls
Assigned: Materials Laboratory

Dr. Hugh. P. Garraway, III
Associate Professor
Dept. of Computer Science
Univ. of Southern Mississippi
Box 5106
Hattiesburg, MS 39406
(601) 266-4949

Degree: Ph.D., Instruc. Tech., 1980
Specialty: Computer Based Learning
Assigned: Human Resources Laboratory:
Training Systems

Dr. Christopher P. Godfrey
Assistant Professor
Dept. of Computer Science
Missouri Western State College
4525 Downs Drive
St. Joseph, MO 64507
(816) 271-4372

Degree: Ph.D., Physics, 1982
Specialty: High Energy Astrophysics
Assigned: Air Force Geophysics Lab.

Dr. Barry P. Goettl
Assistant Professor
Dept. of Psychology
Clemson University
108 Brackett Hall
Clemson, SC 29634-1511
(803) 656-2831

Degree: Ph.D., Psychology, 1987
Specialty: Engineering Psychology
Assigned: Harry G. Armstrong Aerospace
Medical Research Laboratory

Dr. Gerald W. Grams
Professor
School of Geophysical Sciences
Georgia Tech.
Atlanta, GA 30332
(404) 894-3628

Degree: Ph.D., Meteorology, 1966
Specialty: Atmospheric Physics
Assigned: Avionics Laboratory

Dr. Edward K. Greenwald
Assistant Professor
Engineering Professional Dev.
Univ. of Wisconsin-Madison
432 N. Lake Street
Madison, WI 53706
(608) 262-0573

Degree: Ph.D., Physics, 1967
Specialty: Electrical Engineering
Assigned: Engineering & Services Center

NAME/ADDRESS

DEGREE, SPECIALTY, LABORATORY ASSIGNED

Prof. William M. Grissom
Assistant Professor
Dept. of Physics
Morehouse College
830 Westview Dr., S.W.
Atlanta, GA 30314
(404) 681-2800

Degree: M.S.E., Mechanical Eng., 1978
Specialty: Combustion Diagnostics
Assigned: Arnold Engineering
Development Center

Dr. David A. Grossie
Assistant Professor
Dept. of Chemistry
Wright State University
Dayton, OH 45435
(513) 873-2210

Degree: Ph.D., Chemistry, 1982
Specialty: X-ray Crystallography
Assigned: Materials Laboratory

Dr. Vijay K. Gupta
Professor
Dept. of Chemistry
Central State University
Wilberforce, OH 45384
(513) 376-6423

Degree: Ph.D., Chemistry, 1969
Specialty: Physical Chemistry
Assigned: Materials Laboratory

Dr. Awatef Hamed
Dept. of Aerospace Eng.
University of Cincinnati
Mail Location 70
Cincinnati, OH 45221
(513) 475-5630

Degree: Ph.D., Engineering, 1972
Specialty: Engineering
Assigned: Flight Dynamics Laboratory

Dr. Albert A. Heaney
Professor
Dept. of Electrical Eng.
California State University
Shaw & Cedar Avenues
Fresno, CA 93740-0094
(209) 294-4823

Degree: Ph.D., Electrical Eng., 1972
Specialty: Computer Engineering
Assigned: Eastern Space Missile Center

Dr. David Hemmendinger
Assistant Professor
Dept. of Compt. Sci. & Eng.
Wright State University
Research Bldg.
317 Research Blvd.
Kettering, OH 45420
(513) 259-1345

Degree: Ph.D., Philosophy, 1973
Specialty: Logic Programming
Assigned: Avionics Laboratory

NAME/ADDRESS

Dr. Bennye S. Henderson
Associate Professor
Dept. of Biology
Jackson State University
1325 Lynch Street
Jackson, MS 39217
(601) 968-2586

Dr. Darrell E.P. Hoy
Assistant Professor
Dept. of Mechanical Eng.
Tennessee Technological Univ.
Box 5014
Cookeville, TN 38505
(615) 372-3732

Dr. Manuel A. Huerta
Professor
Dept. of Physics
University of Miami
P O Box 248046
Coral Gables, FL 33124
(305) 284-2323

Dr. Randolph B. Huff
Professor
Dept. of Chemistry
Presbyterian College
Clinton, SC 29325
(803) 833-2820

Dr. Neil J. Hutzler
Associate Professor
Dept. of Civil Engineering
Michigan Tech. University
Houghton, MI 49931
(906) 487-2194

Dr. Douglas E. Jackson
Professor
Dept. of Math Sciences
Eastern New Mexico University
Portales, NM 88130
(505) 562-2367

DEGREE, SPECIALTY, LABORATORY ASSIGNED

Degree: Ph.D., Physiology, 1979
Specialty: Physiology
Assigned: School of Aerospace Medicine

Degree: M.S.E., Mechanical Eng., 1985
Specialty: Ballistic Impact Shocks
Assigned: Arnold Engineering
Development Center

Degree: Ph.D., Physics, 1970
Specialty: Plasma Physics
Assigned: Armament Laboratory

Degree: Ph.D., Inorganic Chem., 1969
Specialty: Physical-Inorganic Chemistry
Assigned: Occupational and Environment
Health Laboratory

Degree: Ph.D., Environmental Eng.,
1978
Specialty: Environmental Engineering
Assigned: Engineering & Services Center

Degree: Ph.D., Mathematics, 1969
Specialty: Math/Statistical Information
Assigned: Human Resources Laboratory:
Manpower & Personnel Division

NAME/ADDRESS

DEGREE, SPECIALTY, LABORATORY ASSIGNED

Dr. Oleg G. Jakubowicz
Assistant Professor
Dept. of Elect. & Compt. Eng.
State University of New York
238 Bell Hall
Buffalo, NY 14260
(716) 636-2406

Degree: Ph.D., Physics, 1984
Specialty: Neural Nets
Assigned: Rome Air Development Center

Dr. Manjit S. Jawa
Professor
Dept. of Mathematics
Fayetteville State University
Fayetteville, NC 28301
(919) 486-1675

Degree: Ph.D., Applied Math., 1967
Specialty: Applied Mathematics
Assigned: Arnold Engineering
Development Center

Dr. David W. Jensen
Assistant Professor
Dept. of Aerospace Eng.
Pennsylvania State University
233N Hammond Bldg.
University Park, PA 16802
(814) 863-1077

Degree: Ph.D., Structures Tech., 1986
Specialty: Advanced Composite Materials
Assigned: Astronautics Laboratory

Dr. Eric R. Johnson
Associate Professor
Dept. of Chemistry
Ball State University
Muncie, IN 47306
(317) 285-8078

Degree: Ph.D., Biochemistry, 1974
Specialty: Protein Biochemistry
Assigned: School of Aerospace Medicine

Dr. William M. Jordan
Assistant Professor
Dept. of Mech. & Indus. Eng.
Louisiana Tech. University
P O Box 10348
Ruston, LA 71272
(318) 257-4304

Degree: Ph.D., Intersdisciplinary
Eng., 1985
Specialty: Composite Materials
Assigned: Weapons Laboratory

Dr. Mohammad A. Karim
Assistant Professor
Dept. of Electrical Eng.
University of Dayton
KL-2410
Dayton, OH 45469
(513) 229-3611

Degree: Ph.D., Electrical Eng., 1982
Specialty: Electro-Optics
Assigned: Avionics Laboratory

NAME/ADDRESS

DEGREE, SPECIALTY, LABORATORY ASSIGNED

Dr. Arkady Kheyfets
Assistant Professor
Dept. of Mathematics
North Carolina State Univ.
Box 8205
Raleigh, NC 27695-8205
(919) 737-3265

Degree: Ph.D., Physics, 1986
Specialty: Mathematical Physics
Assigned: Weapons Laboratory

Prof. Daisy W. Kimble
Assistant Professor
Dept. of Chemistry
Southern University
P O Box 11487
Baton Rouge, LA 70813
(504) 771-3734

Degree: M.S., Analytical Chem., 1986
Specialty: Analytical Chemistry
Assigned: School of Aerospace Medicine

Dr. Yulian B. Kin
Associate Professor
Dept. of Engineering
Purdue University Calumet
Potter Building
Hammond, IN 46323
(219) 989-2684

Degree: Ph.D., Fatigue Stress Analysis
1971
Specialty: Stress Analysis
Assigned: Flight Dynamics Laboratory

Dr. Samuel P. Kozaitis
Assistant Professor
Dept. of Electrical Eng.
Florida Institute of Tech.
Melbourne, FL 32901-6988
(305) 768-8000

Degree: Ph.D., Electrical Eng, 1986
Specialty: Optics, Computer Architecture
Assigned: Rome Air Development Center

Dr. Janet U. Kozyra
Assistant Research Scientist
University of Michigan
Space Physics Research Lab.
2455 Hayward
Ann Arbor, MI 48109-2143
(313) 747-3550

Degree: Ph.D., Atmospheric Sci., 1986
Specialty: Space Physics
Assigned: Air Force Geophysics Lab.

Dr. Charles E. Lance
Assistant Professor
Dept. of Psychology
University of Georgia
Athens, GA 30602
(404) 542-3053

Degree: Ph.D., Psychology, 1985
Specialty: Industrial/Organizational Psy.
Assigned: Human Resources Laboratory:
Manpower & Personnel Division

NAME/ADDRESS

DEGREE, SPECIALTY, LABORATORY ASSIGNED

Dr. Thomas L. Landers
Assistant Professor
Dept. of Industrial Engineering
University of Arkansas
4176 Bell Engineering Ctr.
Fayetteville, AR 72703
(501) 575-6042

Degree: Ph.D., Industrial Eng., 1985
Specialty: Reliability & Maintainability
Assigned: Human Resources Laboratory:
Logistics & Human Factors Div.

Prof. Anastas Lazaridis
Assistant Professor
Dept. of Mechanical Eng.
Widener University
Chester, PA 19013
(215) 499-4487

Degree: Sc.D., Thermal Fluids, 1969
Specialty: Ablation, Solar Energy
Assigned: Armament Laboratory

Dr. L. James Lee
Associate Professor
Dept. of Chemical Eng.
The Ohio State University
140 W. 19th Avenue
Columbus, OH 43210
(614) 292-2408

Degree: Ph.D., Chemical Eng., 1979
Specialty: Polymer & Composite Processing
Assigned: Materials Laboratory

Dr. Robert Y. Li
Assistant Professor
Dept. of Electrical Eng.
University of Nebraska
Lincoln, NE 68588
(402) 472-5892

Degree: Ph.D., Electrical Eng., 1981
Specialty: Image Processing
Assigned: Avionics Laboratory

Dr. Irving Lipschitz
Associate Professor
Dept. of Chemistry
University of Lowell
1 University Lane
Lowell, MA 01854
(617) 452-5000

Degree: Ph.D., Physical Chem., 1965
Specialty: Vibrational Spectroscopy
Assigned: Air Force Geophysics Lab.

Dr. Harold G. Longbotham
Visiting Assistant Professor
Dept. of Electrical Eng.
Univ. of Texas - San Antonio
San Antonio, TX 78285
(512) 691-5518

Degree: Ph.D., Electrical Eng., 1985
Specialty: Nonlinear Digital Filtering
Assigned: School of Aerospace Medicine

NAME/ADDRESS

DEGREE, SPECIALTY, LABORATORY ASSIGNED

Dr. David A. Ludwig
Assistant Professor
Dept. of Mathematics
Univ. of North Carolina
at Greensboro
Greensboro, NC 27412
(919) 334-5836

Degree: Ph.D., Biostatistics, 1982
Specialty: Biostatistics, Exp. Design
Assigned: School of Aerospace Medicine

Dr. Douglas A. Mandra
Associate Professor
Dept. of Psychology
Francis Marion College
P O Box 7500
Florence, SC 29501
(803) 661-1378

Degree: Ph.D., Psychology, 1974
Specialty: Experimental Psychology
Assigned: Human Resources Laboratory:
Operations Training Division

Dr. Robert E. Masingale, Sr.
Professor
Dept. of Chemistry
Jarvis Christian College
Hawkins, TX 75765
(214) 769-2174

Degree: Ph.D., Organic Chemistry, 1968
Specialty: Organic & Analytical Chemistry
Assigned: Harry G. Armstrong Aerospace
Medical Research Laboratory

Dr. John P. McHugh
Assistant Professor
Dept. of Mechanical Eng.
University of New Hampshire
133 Kingsbury
Durham, NH 03824
(603) 862-1899

Degree: Ph.D., Applied Mechanics, 1986
Specialty: Fluid Mechanics
Assigned: Air Force Geophysics Lab.

Dr. Michael L. McKee
Associate Professor
Dept. of Chemistry
Auburn University
Auburn, AL 36849-5312
(205) 826-4043

Degree: Ph.D., Chemical Physics, 1977
Specialty: Molecular Orbital Theory
Assigned: Frank J. Seiler Research Lab.

Dr. Thomas T. Meek
Associate Professor
Dept. of Materials Sci. & Eng.
University of Tennessee
434 Dougherty Engineering Bldg.
Knoxville, TN 37966-2200
(615) 970-0940

Degree: Ph.D., Ceramic Eng., 1977
Specialty: Ceramic Processing
Assigned: Materials Laboratory

NAME/ADDRESS

DEGREE, SPECIALTY, LABORATORY ASSIGNED

Dr. Tammy J. Melton
Assistant Professor
Dept. of Chemistry
St. Norbert College
DePere, WI 54115
(414) 337-3206

Degree: Ph.D., Inorganic Chem., 1986
Specialty: Inorganic Synthesis
Assigned: Frank J. Seiler Research Lab.

Dr. Carolyn W. Meyers
Assistant Professor
Dept. of Mechanical Eng.
Georgia Inst. of Technology
School of Mechanical Eng.
Atlanta, GA 30332
(404) 894-3264

Degree: Ph.D., Physical Metallurgy,
1984
Specialty: Microstructure
Assigned: Engineering & Services Center

Dr. David W. Mikolaitis
Assistant Professor
Dept. of Engineering Sciences
University of Florida
231 Aero
Gainesville, FL 32611
(904) 392-0961

Degree: Ph.D., Theoretical & Applied
Mechanics, 1981
Specialty: Applied Math
Assigned: Armament Laboratory

Dr. Kwang S. Min
Professor
Dept. of Physics
East Texas State University
Commerce, TX 75428
(214) 885-5483

Degree: Ph.D., Physics, 1962
Specialty: Signal Processing
Assigned: Armament Laboratory

Dr. Joseph J. Molitoris
Professor
Dept. of Physics
Muhlenberg College
Allentown, PA 18104
(215) 821-3413

Degree: Ph.D., Physics, 1985
Specialty: Nuclear Physics
Assigned: Armament Laboratory

Mr. Augustus Morris
Instructor
Dept. of Manufacturing Eng.
Central State University
Wilberforce, OH 45384
(513) 376-6435

Degree: B.S., Biomedical Eng., 1981
Specialty: Biomedical Engineering
Assigned: Flight Dynamics Laboratory

NAME/ADDRESS**DEGREE, SPECIALTY, LABORATORY ASSIGNED**

Dr. William P. Mounfield
Assistant Professor
Dept. of Mechanical Eng.
Louisiana State University
R2513-A CEBA Bldg.
Baton Rouge, LA 70803-6413
(504) 388-6488

Degree: Ph.D., Mechanical Eng., 1985
Specialty: Automatic Controls
Assigned: Engineering & Services Center

Dr. Nanda L. Mukherjee
Associate Professor
Dept. of Chemical Eng.
Tuskegee University
Tuskegee, AL 36088
(205) 727-8050

Degree: Ph.D., Chemical Eng., 1967
Specialty: Kinetics
Assigned: Flight Dynamics Laboratory

Dr. Richard S. Myers
Professor
Dept. of Physical Sciences
Delta State University
P O Box 3255
Cleveland, OH 38733
(601) 846-4482

Degree: Ph.D., Physical Chem., 1968
Specialty: Experimental Physical Chem.
Assigned: Engineering & Services Center

Dr. Himanshoo V. Navangul
Professor
Dept. of Chemistry and
Physical Science
North Carolina Wesleyan College
Wesleyan Station
Rocky Mount, NC 27804
(919) 977-7171

Degree: Ph.D., Physical Chem., 1967
Specialty: Molecular Spectroscopy
Assigned: Air Force Geophysics Lab.

Dr. Mark A. Norris
Assistant Professor
Dept. of Mechanics
Virginia Polytechnic Inst.
and State University
227 Norris Hall
Blacksburg, VA 24061
(703) 961-4576

Degree: Ph.D., Eng. Mechanics, 1986
Specialty: Structural Dynamics & Controls
Assigned: Astronautics Laboratory

Dr. Mufit H. Ozden
Associate Professor
Dept. of Systems Analysis
Miami University
2303 Kreger Hall
Oxford, OH 45056
(513) 529-5937

Degree: Ph.D. Eng. Systems, 1975
Specialty: Operations Research
Assigned: Human Resources Laboratory:
Logistics & Human Factors Div.

NAME/ADDRESS

DEGREE, SPECIALTY, LABORATORY ASSIGNED

Prof. Martin A. Patt
Associate Professor
Dept. of Electrical Eng.
University of Lowell
1 University Ave.
Lowell, MA 01854
(617) 452-5000

Degree: M.S., Electrical Eng., 1964
Specialty: Computer Applications
Assigned: Air Force Geophysics Lab.

Dr. David G. Payne
Assistant Professor
Dept. of Psychology
SUNY Binghamton
Binghamton, NY 13901
(607) 777-4610

Degree: Ph.D., Cognitive Psy., 1984
Specialty: Human Memory
Assigned: Harry G. Armstrong Aerospace
Medical Research Laboratory

Dr. William Z. Plachy
Professor
Dept. of Chemistry & Biochem.
San Francisco State University
San Francisco, CA 94132
(415) 338-1436

Degree: Ph.D., Physical Chem., 1967
Specialty: Physical Chemistry
Assigned: School of Aerospace Medicine

Dr. Patricia L. Plummer
Professor
Dept. of Physics & Chemistry
Columbia Univ. of Missouri
Columbia, NC 65211
(314) 882-3053

Degree: Ph.D., Chemical Physics, 1964
Specialty: Quantum Chemistry
Assigned: Frank J. Seiler Research Lab.

Dr. Leonard E. Porter
Professor
Dept. of Physics & Astronomy
University of Montana
Missoula, MT 59812
(406) 243-6223

Degree: Ph.D., Nuclear Physics, 1965
Specialty: Nuclear Physics
Assigned: Weapons Laboratory

Dr. Ramalingam Radhakrishnan
Assistant Professor
Dept. of Civil Engineering
Prairie View A&M University
Prairie View, TX 77084
(409) 857-2418

Degree: Ph.D, Structure Eng., 1974
Specialty: Structures
Assigned: Engineering & Services Center

NAME/ADDRESS**DEGREE, SPECIALTY, LABORATORY ASSIGNED**

Dr. Periasamy K. Rajan
Professor
Dept. of Electrical Eng.
Tennessee Tech. University
Box 5004
Cookeville, TN 38505
(615) 372-3308

Degree: Ph.D., Electrical Eng., 1975
Specialty: Digital Signal Processing
Assigned: Avionics Laboratory

Dr. Panapakkam A. Ramamoorthy
Associate Professor
Dept. of Elect. & Computer Eng.
University of Cincinnati
M.L. #30
Cincinnati, OH 45220
(513) 475-4247

Degree: Ph.D., Digital Signal
Processing, 1977
Specialty: Optical Memory
Assigned: Avionics Laboratory

Dr. Dharam S. Rana
Associate Professor
Dept. of Management & Marketing
Jackson State University
1400 J.R. Lynch
Jackson, MS 39217
(601) 968-2534

Degree: Ph.D., Statistics, 1976
Specialty: Quantitative Techniques
Assigned: Human Resources Laboratory:
Manpower & Personnel Division

Dr. Sunita S. Rana
Instructor
Dept. of Computer Science
Jackson State University
1400 Lynch Street
Jackson, MS 39217
(601) 968-2105

Degree: Ph.D., Biology, 1969
Specialty: Computer Science
Assigned: Human Resources Laboratory:
Training Systems

Dr. Hal C. Reed
Associate Professor
Dept. of Biology
Oral Roberts University
7777 S. Lewis
Tulsa, OK 74171
(918) 495-6945

Degree: Ph.D., Entomology, 1982
Specialty: Insect Behavior
Assigned: School of Aerospace Medicine

Dr. Michael D. Rice
Associate Professor
Dept. of Computer Science
George Mason University
4400 University Dr.
Fairfax, VA 22030
(703) 323-3884

Degree: Ph.D., Mathematics, 1973
Specialty: Computer Science/Math
Assigned: Weapons Laboratory

NAME/ADDRESS

DEGREE, SPECIALTY, LABORATORY ASSIGNED

Dr. Mateen M. Rizki
Assistant Professor
Dept. of Computer Science
Wright State University
410 Fawcett Hall
Dayton, OH 45435
(513) 873-2394

Degree: Ph.D., Computer Science, 1985
Specialty: Modeling and Simulation
Assigned: Avionics Laboratory

Dr. Thomas R. Rogge
Professor
Dept. of Eng. Science & Math
Iowa State University
3015 Black Eng.
Ames, IA 50010
(515) 294-2956

Degree: Ph.D., Applied Math, 1964
Specialty: Finite Element Analysis
Assigned: School of Aerospace Medicine

Dr. Joe M. Ross
Assistant Professor
Dept. of Chemistry
Central State University
Wilberforce, OH 45384
(513) 376-6214

Degree: Ph.D., Molecular Bio., 1977
Specialty: Biochemistry of Macromolecules
Assigned: School of Aerospace Medicine

Dr. Joseph E. Saliba
Assistant Professor
Dept. of Civil & Engr. Mechanics
University of Dayton
300 College Park
Dayton, OH 45469
(513) 229-3847

Degree: Ph.D., Solid Mechanics, 1983
Specialty: Engineering Mechanics
Assigned: Harry G. Armstrong Aerospace
Medical Research Laboratory

Dr. Dhiraj K. Sardar
Assistant Professor
Dept. of Physics
University of Texas
Div. of Earth & Physical Sci.
San Antonio, TX 78285-0663
(512) 691-5462

Degree: Ph.D., Physics, 1980
Specialty: Materials Science & Lasers
Assigned: School of Aerospace Medicine

Prof. Sonia H. Sawtelle
Teaching Associate
Dept. of Education
Univ. of Texas - San Antonio
San Antonio, TX 78285
(512) 691-4412

Degree: MS., Exercise Physiology, 1975
Specialty: Exercise Physiology
Assigned: School of Aerospace Medicine

NAME/ADDRESS

DEGREE, SPECIALTY, LABORATORY ASSIGNED

Dr. Paul O. Scheie
Professor
Dept. of Physics
Texas Lutheran College
1000 West Court
Seguin, TX 78155
(512) 379-4161

Degree: Ph.D., Biophysics, 1965
Specialty: Electrophysiology
Assigned: School of Aerospace Medicine

Dr. James L. Schmutz
Professor
Dept. of Chemistry
Central Wesleyan College
1 Wesleyan Drive
Central, SC 29630
(803) 639-2453

Degree: Ph.D., Chemistry, 1976
Specialty: Inorganic Polymers
Assigned: Frank J. Seiler Research Lab.

Dr. Jodye I. Selco
Assistant Professor
Dept. of Chemistry
University of Redlands
P O Box 3080
Redlands, CA 92373-0999
(714) 793-2121

Degree: Ph.D., Chemical Physics, 1983
Specialty: Spectroscopy, Kinetics
Assigned: Astronautics Laboratory

Dr. Shawky E. Shamma
Professor
Dept. of Math/Statistics
University of West Florida
Pensacola, FL 32514
(904) 474-2281

Degree: Ph.D., Applied Math, 1969
Specialty: Applied Mathematics
Assigned: Armament Laboratory

Dr. Rameshwar P. Sharma
Associate Professor
Dept. of Mechanical Engineering
Western Michigan University
2065 Kahrman Hall
Kalamazoo, MI 49008
(616) 383-1408

Degree: Ph.D., Mechanical Eng., 1978
Specialty: Fluid Mechanics
Assigned: Astronautics Laboratory

Dr. Larry R. Sherman
Professor
Dept. of Chemistry
University of Akron
Akron, OH 44325-0001
(216) 375-7333

Degree: Ph.D., Analytical Chem., 1969
Specialty: Organotin Chemistry
Assigned: Occupational and Environment
Health Laboratory

NAME/ADDRESS

DEGREE, SPECIALTY, LABORATORY ASSIGNED

Dr. James A. Sherwood
Assistant Professor
Dept. of Mechanical Eng.
University of New Hampshire
Kingsbury Hall
Durham, NH 03824
(603) 862-2624

Degree: Ph.D., Aerospace Eng., 1987
Specialty: Solid Mechanics
Assigned: Flight Dynamics Laboratory

Dr. Sanford S. Singer
Professor
Dept. of Chemistry
University of Dayton
300 College Park
Dayton, OH 45469
(513) 229-2833

Degree: Ph.D., Biological Chem., 1967
Specialty: Enzymology
Assigned: Harry G. Armstrong Aerospace
Medical Research Laboratory

Dr. Trilochan Singh
Professor
Dept. of Mechanical Eng.
Wayne State University
Detroit, MI 48202
(313) 577-3845

Degree: Ph.D., Mechanical Eng., 1970
Specialty: Chemical Combustion
Assigned: Astronautics Laboratory

Dr. Jorge L. Sintes
Chairman
Dept. of Preventive Dentistry
and Community Health
Meharry Medical College
1005 D.B. Todd Blvd.
Nashville, TN 37208
(615) 327-6185

Degree: Ph.D., Nutrition, 1978
Specialty: Dentistry
Assigned: Wilford Hall Medical Center

Dr. Kenneth M. Sobel
Associate Professor
Dept. of Electrical Engineering
The City College of New York
138th St. & Convent Ave.
New York, NY 10031
(212) 690-4241

Degree: Ph.D., Electrical Eng., 1980
Specialty: Eigenstructure
Assigned: Flight Dynamics Laboratory

Dr. Jonathan M. Spector
Assistant Professor
CSIS
Jacksonville State University
Pelham Road
Jacksonville, AL 36265
(205) 231-5718

Degree: Ph.D., Philosophy, 1978
Specialty: Logic
Assigned: Human Resources Laboratory:
Training Systems Division

NAME/ADDRESS

DEGREE, SPECIALTY, LABORATORY ASSIGNED

Dr. Gary R. Stevens
Assistant Professor
Dept. of Statistics
Oklahoma State University
301 MS
Stillwater, OK 74078
(405) 624-5684

Degree: Ph.D., Statistics, 1986
Specialty: Stochastic Processes
Assigned: Occupational and Environment
Health Laboratory

Dr. Patrick J. Sweeney
Asst. Dean of Engineering
University of Dayton
300 College Park, KL201
Dayton, OH 45469
(513) 229-2736

Degree: Ph.D., Mechanical Eng., 1977
Specialty: Computer Modeling
Assigned: Flight Dynamics Laboratory

Dr. Michael Sydor
Professor
Dept. of Physics
University of Minnesota
Duluth, MN 55812
(218) 726-7205

Degree: Ph.D., Physics, 1965
Specialty: Optics, Material Science
Assigned: Materials Laboratory

Dr. Douglas G. Talley
Assistant Professor
Dept. of Mechanical Eng.
University of Michigan
313 Automotive Lab
Ann Arbor, MI 48109-2121
(313) 936-0429

Degree: Ph.D., Mechanical Eng., 1978
Specialty: Combustion
Assigned: Aero Propulsion Laboratory

Dr. David J. Townsend
Associate Professor
Dept. of Psychology
Montclair State College
Upper Montclair, NJ 07042
(201) 893-7222

Degree: Ph.D., Cognitive Psy., 1982
Specialty: Cognitive Science
Assigned: Rome Air Development Center

Dr. Donald R. Ucci
Associate Professor
Dept. of Elect. & Computer Eng.
Illinois Inst. of Technology
3300 S. Federal
Chicago, IL 60616
(312) 567-3405

Degree: Ph.D., Electrical Eng., 1986
Specialty: Adaptive Arrays
Assigned: Rome Air Development Center

NAME/ADDRESS

DEGREE, SPECIALTY, LABORATORY ASSIGNED

Dr. Ahmad D. Vakili
Associate Professor
Dept. of AE/ME
Univ. of Tennessee Space Inst.
Tullahoma, TN 37388
(615) 455-0631

Degree: Ph.D., Aerospace Eng., 1978
Specialty: Unsteady Flows
Assigned: Arnold Engineering
Development Center

Dr. Richard S. Valpey
Assistant Professor
Dept. of Chemistry
Wilberforce University
Wilberforce, OH 45384
(513) 376-2911

Degree: Ph.D., Organic Chemistry, 1983
Specialty: Organic Synthesis
Assigned: Materials Laboratory

Dr. Peter J. Walsh
Professor
Dept. of Physics
Fairleigh Dickinson University
Teaneck, NJ 07666
(201) 692-2493

Degree: Ph.D., Physics, 1960
Specialty: Superconductivity
Assigned: Rome Air Development Center

Dr. Kenneth L. Walter
Associate Professor
Dept. of Chemical Engineering
Prairie View A&M University
Prairie View, TX 77446
(409) 857-2827

Degree: Ph.D., Chemical Eng., 1972
Specialty: Chemical Engineering Process
Assigned: Rome Air Development Center

Dr. Gwo-Ching Wang
Associate Professor
Dept. of Physics
Rensselaer Polytechnic Inst.
Troy, NY 12180-3590
(518) 276-8387

Degree: Ph.D., Materials Science, 1978
Specialty: Surface Sciences
Assigned: Rome Air Development Center

Dr. Andrew P. Whipple
Associate Professor
Dept. of Biology
Taylor University
Upland, IN 46989
(317) 998-5333

Degree: Ph.D., Biology, 1979
Specialty: Cell Biology
Assigned: Harry G. Armstrong Aerospace
Medical Research Laboratory

NAME/ADDRESS

Prof. Sharon T. Williams
Instructor
Dept. of Chemistry
Southern University
Baton Rouge, LA 70813-2074
(504) 771-3990

Dr. Lawrence A. Witt
Assistant Professor
Dept. of Psychology
Western Illinois University
Macomb, IL 61455
(309) 298-1593

Dr. Frank A. Witzmann
Assistant Professor
Dept. of Biology
IUPUI - Columbus
4601 Central Avenue
Columbus, IN 47203
(812) 372-8266

Dr. William E. Wolfe
Associate Professor
Dept. of Civil Engineering
Ohio State University
2070 Neil Avenue
Columbus, OH 43210
(614) 292-0790

Dr. John R. Wright
Professor
Dept. of Chem., Physical Sci.
Southeast Oklahoma State Univ.
Box 4181, Station A, SEOSU
Durant, OK 74701
(405) 924-0121

Prof. Wafa E. Yazigi
Instructor
Dept. of Mathematics
Columbia Basin College
2600 N. 20th
Pasco, WA 99301
(509) 547-0511

DEGREE, SPECIALTY, LABORATORY ASSIGNED

Degree: M.S., Biochemistry, 1981
Specialty: General Chemistry
Assigned: School of Aerospace Medicine

Degree: Ph.D., Psychology, 1985
Specialty: Industrial/Organ. Psychology
Assigned: Human Resources Laboratory:
Operations Training Division

Degree: Ph.D., Biology, 1981
Specialty: Protein Analysis
Assigned: Harry G. Armstrong Aerospace
Medical Research Laboratory

Degree: Ph.D., Engineering, 1979
Specialty: Geotechnical Engineering
Assigned: Flight Dynamics Laboratory

Degree: Ph.D., Chemistry, 1971
Specialty: Biochemistry
Assigned: School of Aerospace Medicine

Degree: M.S., Aeronautical Eng., 1986
Specialty: Solid Mechanics
Assigned: Armament Laboratory

NAME/ADDRESS

Dr. Lawrence F. Young
Associate Professor
Dept. of QA/IS, CBA
University of Cincinnati
ML 30
Cincinnati, OH 45220
(513) 475-7169

Dr. Robert K. Young
Professor
Dept. of Psychology
University of Texas
Mezes 330, Psychology Dept.
Austin, TX 78713
(512) 471-9228

Dr. Juin S. Yu
Professor
Dept. of Mechanical Eng.
West Virginia Tech.
Montgomery, WV 25136
(304) 442-3248

DEGREE, SPECIALTY, LABORATORY ASSIGNED

Degree: D.Sc., Industrial Eng., 1978
Specialty: Industrial Engineering
Assigned: Human Resources Laboratory:
Logistics & Human Factors Div.

Degree: Ph.D., Exp. Psychology, 1954
Specialty: Experimental Psychology
Assigned: Human Resources Laboratory:
Manpower & Personnel Division

Degree: Ph.D., Mechanical Eng., 1964
Specialty: Thermofluid Transport
Assigned: Aero Propulsion Laboratory

PARTICIPANT LABORATORY ASSIGNMENT

C. PARTICIPANT LABORATORY ASSIGNMENT (Page 1)

1988 USAF/UES SUMMER FACULTY RESEARCH PROGRAM

AERO PROPULSION LABORATORY (AFWAL/APL)
(Wright-Patterson Air Force Base)

- | | |
|----------------------|---------------------|
| 1. Bryan Becker | 5. Wayne Eckerle |
| 2. Mingking Chyu | 6. David Mikolaitis |
| 3. Jerry Clark | 7. Douglas Talley |
| 4. Derek Dunn-Rankin | 8. Juin Yu |

ARMAMENT LABORATORY (AD)
(Eglin Air Force Base)

- | | |
|----------------------|---------------------|
| 1. Ibrahim Ahmad | 5. Kwang Min |
| 2. Stephen Dow | 6. Joseph Molitoris |
| 3. Manuel Huerta | 7. Shawky Shamma |
| 4. Anastas Lazaridis | 8. Wafa Yazigi |

HARRY G. ARMSTRONG AEROSPACE MEDICAL RESEARCH LABORATORY (AAMRL)
(Wright-Patterson AFB)

- | | |
|----------------------|--------------------|
| 1. Praphulla Bajpai | 6. David Payne |
| 2. Shankar Bale | 7. Joseph Saliba |
| 3. Charles Covington | 8. Sanford Singer |
| 4. Barry Goettl | 9. Andrew Whipple |
| 5. Robert Masingale | 10. Frank Witzmann |

ARNOLD ENGINEERING DEVELOPMENT CENTER (AEDC)
(Arnold Air Force Base)

- | | |
|---------------------|-----------------|
| 1. Eustace Dereniak | 4. Manjit Jawa |
| 2. William Grissom | 5. Ahmad Vakili |
| 3. Darrell Hoy | |

ASTRONAUTICS LABORATORY (AL)
(Edwards Air Force Base)

- | | |
|-------------------------|---------------------|
| 1. Clarence Calder | 5. Mark Norris |
| 2. Phillip Christiansen | 6. Jodye Selco |
| 3. Susan Collins | 7. Rameshwar Sharma |
| 4. David Jensen | 8. Trilochan Singh |

AVIONICS LABORATORY (AFWAL/AL)
(Wright-Patterson Air Force Base)

- | | |
|-----------------------|---------------------------|
| 1. Mike Burlakoff | 5. Robert Li |
| 2. Gerald Grams | 6. Periasamy Rajan |
| 3. David Hemmendinger | 7. Panapakkam Ramamoorthy |
| 4. Mohammad Karim | 8. Mateen Rizki |

EASTERN SPACE AND MISSILE CENTER (ESMC)
(Patrick Air Force Base)

- | |
|------------------|
| 1. Albert Heaney |
|------------------|

C. PARTICIPANT LABORATORY ASSIGNMENT (Page 2)

ELECTRONIC SYSTEMS DIVISION (ESD)

(Hanscom Air Force Base)

1. George Bratton
2. John Dalphin

ENGINEERING AND SERVICES CENTER (ESC)

(Tyndall Air Force Base)

- | | |
|---------------------|-----------------------------|
| 1. Wayne Charlie | 5. Neil Hutzler |
| 2. David DeHeer | 6. William Mounfield |
| 3. Deanna Durnford | 7. Richard Myers |
| 4. Edward Greenwald | 8. Ramalingam Radhakrishnan |

FLIGHT DYNAMICS LABORATORY (FDL)

(Wright-Patterson Air Force Base)

- | | |
|--------------------|--------------------|
| 1. Larry Byrd | 6. Nanda Mukherjee |
| 2. Karen Chou | 7. James Sherwood |
| 3. Awatef Hamed | 8. Kenneth Sobel |
| 4. Yulian Kin | 9. Patrick Sweeney |
| 5. Augustus Morris | 10. William Wolfe |

FRANK J. SEILER RESEARCH LABORATORY (FJSRL)

(USAF Academy)

- | | |
|-------------------|---------------------|
| 1. Dan Bruss | 5. Tammy Melton |
| 2. Charles Bump | 6. Patricia Plummer |
| 3. Richard Carlin | 7. James Schmutz |
| 4. Michael McKee | |

GEOPHYSICS LABORATORY (AFGL)

(Hanscom Air Force Base)

- | | |
|-------------------|------------------------|
| 1. Lucia Babcock | 7. Christopher Godfrey |
| 2. Stephen Baker | 8. Janet Kozyra |
| 3. Pradip Bakshi | 9. Irving Lipschitz |
| 4. Reuben Benumof | 10. John McHugh |
| 5. Donald Collins | 11. Himanshoo Navangul |
| 6. Michael Frantz | 12. Martin Patt |

HUMAN RESOURCES LABORATORY (HRL)

(Brooks, Williams, and Wright-Patterson Air Force Bases)

- | | |
|---------------------|----------------------|
| 1. Patricia Carlson | 8. Mufit Ozden |
| 2. Kevin Ford | 9. Dharam Rana |
| 3. Hugh Garraway | 10. Sunita Rana |
| 4. Douglas Jackson | 11. Jonathan Spector |
| 5. Charles Lance | 12. Lawrence Witt |
| 6. Thomas Landers | 13. Lawrence Young |
| 7. Douglas Mandra | 14. Robert Young |

C. PARTICIPANT LABORATORY ASSIGNMENT (Page 3)

MATERIALS LABORATORY (ML)

(Wright-Patterson Air Force Base)

- | | |
|------------------|--------------------|
| 1. Robert Arenz | 7. Vijay Gupta |
| 2. Gene Carlisle | 8. L. James Lee |
| 3. Parvis Dadras | 9. Thomas Meek |
| 4. Suren Dwivedi | 10. Carolyn Meyers |
| 5. Barry Fussell | 11. Michael Sydor |
| 6. David Grossie | 12. Richard Valpey |

OCCUPATIONAL AND ENVIRONMENTAL HEALTH LABORATORY (OEHL)

(Brooks Air Force Base)

- | | |
|------------------|------------------|
| 1. Steven Chiesa | 3. Larry Sherman |
| 2. Randolph Huff | 4. Gary Stevens |

ROME AIR DEVELOPMENT CENTER (RADC)

(Griffiss Air Force Base)

- | | |
|-----------------------|--------------------|
| 1. Beryl Barber | 7. Samuel Kozaitis |
| 2. Keith Christianson | 8. David Townsend |
| 3. Darin DeForest | 9. Donald Ucci |
| 4. Paul Dingman | 10. Peter Walsh |
| 5. Hugh Donaghy | 11. Kenneth Walter |
| 6. Oleg Jakubowicz | 12. Gwo-Ching Wang |

SCHOOL OF AEROSPACE MEDICINE (SAM)

(Brooks Air Force Base)

- | | |
|----------------------|---------------------|
| 1. Ronald Bulbulian | 9. Hal Reed |
| 2. John Burke | 10. Thomas Rogge |
| 3. Benny Henderson | 11. Joe Ross |
| 4. Eric Johnson | 12. Dhiraj Sardar |
| 5. Daisy Kimble | 13. Sonia Sawtelle |
| 6. Harold Longbotham | 14. Paul Scheie |
| 7. David Ludwig | 15. Sharon Williams |
| 8. William Plachy | 16. John Wright |

WEAPONS LABORATORY (WL)

(Kirtland Air Force Base)

- | | |
|-------------------|--------------------|
| 1. Lane Clark | 4. Arkady Kheyfets |
| 2. David Dolson | 5. Leonard Porter |
| 3. William Jordan | 6. Michael Rice |

WILFORD HALL MEDICAL CENTER (WHMC)

(Lackland Air Force Base)

1. David Cecil
2. Jorge Sintes

RESEARCH REPORTS

RESEARCH REPORTS
1988 SUMMER FACULTY RESEARCH PROGRAM

<u>Technical Report Number</u>	<u>Title</u>	<u>Professor</u>
Volume I		
Armament Laboratory		
1	Measuring Systems Effectiveness and Systems Availability of Hardened Targets Subject to a Variety of Weapons	Dr. Ibrahim Ahmad
2	Model Drawing Algorithms for a Matching Problem	Dr. Stephen Dow
3	Two Dimensional Simulation of Railgun Plasma Armatures	Dr. Manuel Huerta
4	Modeling Reactive Fragments	Dr. Anastas Lazaridis
5	Target-Aerosol Discrimination Techniques for Active Optical Proximity Sensors	Dr. Kwang Min
6	The Dynamics of Projectile Impact	Dr. Joseph Molitoris
7	ARIMA Modeling of Residuals in AD/KR TDOP Models	Dr. Shawky Shamma
8	Stress Analysis for a Fin Stabilized Projectile	Dr. Wafa Yazigi
Arnold Engineering Development Center		
9	Infrared Charge Transfer Device Characterization	Dr. Eustace Dereniak
10	Liquid Film Cooling In Rocket Engines	Dr. William Grissom
11	Diffuser Failure Investigation/Non-Interference Stress Measurement System Algorithms Study	Dr. Darrell Hoy
12	Solid Rocket Motor Plume Analysis Through Emission Computerized Tomography	Dr. Manjit Jawa
13	Skin Friction Measurement Using Surface Mounted Hot Films	Dr. Ahmad Vakili

Astronautics Laboratory

- | | | |
|----|---|--------------------------|
| 14 | Study of Embedded Sensors in Graphite-Epoxy Composites | Dr. Clarence Calder |
| 15 | Core Polarization in Lithium and Aluminum | Dr. Phillip Christiansen |
| 16 | The Photochemistry of μ^3 -(η -Diethylacetylene)-Decacarbonyltriosmium in Solid Argon | Dr. Susan Collins |
| 17 | Composite-Embedded Fiber-Optic Strain Sensors | Dr. David Jensen |
| 18 | Observer Design for the AFAL Grid Structure Using Low-frequency Accelerometer Data | Dr. Mark Norris |
| 19 | Photochemistry of Azulene Solutions and a Novel Photochemical Nitration Process | Dr. Jodye Selco |
| 20 | Injection System and Spray Characteristics | Dr. Rameshwar Sharma |
| 21 | Chemical Kinetic Mechanisms for $\text{CH}_4/\text{NO}_2/\text{O}_2$ Flames | Dr. Trilochan Singh |

Eastern Space and Missile Center

- | | | |
|----|---|-------------------|
| 22 | Generic Requirements for a CAE/CAD/CAM System | Dr. Albert Heaney |
|----|---|-------------------|

Electronics Systems Division

- | | | |
|----|--|--------------------|
| 23 | Alaskan HF Test Data Analysis | Dr. George Bratton |
| 24 | Stage 1 Analysis of Alaskan High Frequency Radio Network | Dr. John Dalphin |

Engineering and Services Center

- | | | |
|----|---|----------------------|
| 25 | High Intensity Stress Wave Propagation in Partially Saturated Sand | Dr. Wayne Charlie |
| 26 | Individualization of Human Tissue by the Serologic Identification of Erythrocyte Antigens | Dr. David DeHeer |
| 27 | Estimation of Jet Fuel Contamination in Soils | Dr. Deanna Durnford |
| 28 | Cogeneration Assessment on Military Bases | Dr. Edward Greenwald |

- | | | |
|----|--|------------------------------|
| 29 | Soil Vapor Extraction of Volatile Organic Chemicals | Dr. Neil Hutzler |
| 30 | A Preliminary Investigation of Neural Networks for the Air Force Engineering and Services Center | Dr. William Mounfield |
| 31 | Rapid Measurements of Adsorption and Desorption of Volatile Organic Compounds | Dr. Richard Myers |
| 32 | Prefabricated Hypar Structural System Cost Comparison with Box and Arch Structures | Dr. Ramalingam Radhakrishnan |

Volume II

Frank J. Seiler Research Laboratory

- | | | |
|----|--|----------------------|
| 33 | Thermal Decomposition Kinetic Studies of NTO by High Performance Liquid Chromatography | Dr. Dan Bruss |
| 34 | Preparation and Properties of Nitronium Tetrachloroaluminate | Dr. Charles Bump |
| 35 | Homogeneous Ziegler-Natta Catalysis in Lewis Acid Molten Salts | Dr. Richard Carlin |
| 36 | A MCSCF Study of the Rearrangement of Nitromethane to Methyl Nitrite | Dr. Michael McKee |
| 37 | The Effects of Sodium Chloride on Room Temperature Molten Salts | Dr. Tammy Melton |
| 38 | AB Initio and Chemical Dynamics Study of Energetic Materials | Dr. Patricia Plummer |
| 39 | Separators for Molten Salt Batteries | Dr. James Schmutz |

Geophysics Laboratory

- | | | |
|----|---|--------------------|
| 40 | Radiative Association In Ion-Molecule Reactions: Reactions of Some Carbon Cations | Dr. Lucia Babcock |
| 41 | Upward Continuation of Gravity Data With Error Estimates | Dr. Stephen Baker |
| 42 | Impulse Approximation Formalism for Atom Molecule Collisions | Dr. Pradip Bakshi |
| 43 | Total Dose Effect on Soft Error Rate for Dynamic MOS Memory Cells | Dr. Reuben Benumof |

44	Digital Photometric Calibration of and Analysis with Video Imagers in the Ultraviolet	Dr. Donald Collins
45	A Model for Intensified Frontogenesis Over a Modified Mountain Ridge	Dr. Michael Frantz
46	Gamma and X Radiation from Solar Flares	Dr. Christopher Godfrey
47	Theoretical and Observational Studies of Geomagnetic Storm-Related Ion and Electron Heating in the Subauroral Region	Dr. Janet Kozyra
48	Update of the Hitran Database	Dr. Irving Lipschitz
49	Spectral Domain Decomposition	Dr. John McHugh
50	On the Possible Inclusion of "Heavy" Molecules in the HITRAN Database	Dr. Himanshu Navangul
51	Software Tools for Processing Large Lidar Data Streams	Dr. Martin Patt
Rome Air Development Center		
52	Noise Calculations in a RADAR Receiver	Dr. Beryl Barber
53	Stability of Au/W/GaAs and Au/Pt/Ti/GaAs Schottky Barrier Height: A Preliminary Study	Dr. Keith Christianson
54	Parallel Runtime System For Lucid	Dr. Darin DeForest
55	Pre-Sort Processor Phase Distortion Evaluation	Dr. Paul Dingman
56	A PROLOG Natural Language Front End to an ERIC Object Oriented Database	Dr. Hugh Donaghy
57	No Report Submitted at this Time	Dr. Oleg Jakubowicz
58	Design of an Optical Correlator Testbed and Optical Co-Processor	Dr. Samuel Kozaitis
59	Characteristics of Dialog in a Noisy Channel for Performing a Time- Oriented Task	Dr. David Townsend
60	The Effects of Nonlinearities of High Speed Analog-to-Digital Converters on Digital Beamforming Arrays	Dr. Donald Ucci

61	Studies in Microwave Superconductors	Dr. Peter Walsh
62	Chemical Vapor Deposition of Titanium Compounds with an Atomic Layer Epitaxy System	Dr. Kenneth Walter
63	Surface Effects on the High Temperature Superconducting YBaCuO Thin Films grown by RF Sputtering	Dr. Gwo-Ching Wang
Weapons Laboratory		
64	Realization of Sublayer Relative Shielding Order in Electromagnetic Topology	Dr. Lane Clark
65	Diode Laser Probe of Vibrational Energy Transfer Kinetics in Sulfur Monoxide	Dr. David Dolson
66	Evaluating How Laser Irradiation Damages Loaded Composite Materials	Dr. William Jordan
67	Relativistic Effects in GPS Time Transfer	Dr. Arkady Kheifets
68	Stopping Power and Penetration Physics	Dr. Leonard Porter
69	Performance Models for Parallel Algorithms	Dr. Michael Rice
Volume III		
Air Force Wright Aeronautical Laboratories		
Aero Propulsion Laboratory		
70	Computation of the Flow Field and Heat Transfer in a Rectangular Passage with a Turbulator	Dr. Bryan Becker
71	Use of Laser Light Visualization Techniques on Studies of Film Cooling Flow And Flow Over Cavities	Dr. Mingking Chyu
72	Experimental Study of Electronic Excitation of Xenon by Electron Impact	Dr. Jerry Clark
73	Cars Thermometry in Droplet-Laden Flows	Dr. Derek Dunn-Rankin

- | | | |
|----|---|----------------------|
| 74 | Measurement of the Velocity Field and Heat Transfer Coefficients Associated with a Rectangular Wall Jet | Dr. Wayne Eckerle |
| 75 | Lifted Jet Diffusion Flames | Dr. David Mikolaitis |
| 76 | Interpretation of a Lifted Turbulent Diffusion Flame as a Problem in Stratified Combustion | Dr. Douglas Talley |
| 77 | Diffusion and Convection in the Condenser of a Gas-Loaded Heat Pipe | Dr. Juin Yu |

Avionics Laboratory

- | | | |
|----|---|----------------------------|
| 78 | Ada Compiler Evaluation Capability | Dr. Mike Burlakoff |
| 79 | A Study of Sky Backgrounds and Sub-Visual Cirrus at the Megalidar Site and a Proposed Turbulence Monitoring Facility for Wright-Patterson AFB | Dr. Gerald Grams |
| 80 | Formal Verification of VHDL Specifications | Dr. David Hemmendinger |
| 81 | Low Voltage Broadband Beam Steering Devices Using Liquid Crystals | Dr. Mohammad Karim |
| 82 | Model-based Target Recognition Using Laser Radar Imagery | Dr. Robert Li |
| 83 | Signal Processing for ESM Receivers | Dr. Periasamy Rajan |
| 84 | Neural Networks and their Applications in Digital Receiver Design | Dr. Panapakkam Ramamoorthy |
| 85 | Applications of Evolutionary Learning Strategies to Pattern Recognition Tasks | Dr. Mateen Rizki |

Flight Dynamics Laboratory

- | | | |
|----|---|------------------|
| 86 | Heat Flux Prediction for Nucleate Boiling in Liquid Metal Heat Pipes | Dr. Larry Byrd |
| 87 | Reliability Study of Nonlinear Structural Response under Reversible Cyclic Loading Processes | Dr. Karen Chou |
| 88 | Survey and Assessment of Validation Data Base for Shockwave Boundary Layer Interaction in Supersonic Inlets | Dr. Awatef Hamed |

89	Failures of F-16 Transparencies Analysis and Failure Prevention Recommendations	Dr. Yulian Kin
90	Visual Capabilities on a Robot Aided Aircraft Refueler Prototype	Mr. Augustus Morris
91	Reaction Kinetic of Halon 1301 Suppression of Fire Explosion in an Aircraft Fuel Tank	Dr. Nanda Mukherjee
92	Development of an Aircraft Tire- Wheel Interface Model for Flange/Beadseat Contact Loads	Dr. James Sherwood
93	Robust Eigenstructure Assignment for Flight Control Design	Dr. Kenneth Sobel
94	A Computer Model for Air-to-Air Combat (Force on Force) Assessment	Dr. Patrick Sweeney
95	Damage in Graphite/Epoxy Plates Subjected to Low Velocity Impact	Dr. William Wolfe
Materials Laboratory		
96	Analysis Methods for Nonlinear Mechanical Behavior of Glassy Polymers	Dr. Robert Arenz
97	Laser Hardened Materials Via Magnetically Aligned Polypeptide- Phthalocyanines	Dr. Gene Carlisle
98	Joining of Carbon-Carbon Composite Materials	Dr. Parviz Dadras
99	Rapid Simulation for Experimental Validation of H Section Forging Using Finisher Punch	Dr. Suren Dwivedi
100	QPA Control of the End Milling Process	Dr. Barry Fussell
101	Single-Crystal Diffraction Analysis of Compounds with Potential Nonlinear Optical Properties	Dr. David Grossie
102	Effect of Various Metals on the Thermal Degradation of a Chlorotrifluorethylene Based Fluid	Dr. Vijay Gupta

- | | | |
|-----|---|--------------------|
| 103 | Characterization of Heat Transfer and Reaction in the Autoclave Curing of Graphite/Epoxy Composites by Scaling Analysis | Dr. L. James Lee |
| 104 | A Study of the Melting of the Plagioclase Feldspars in a Microwave Field | Dr. Thomas Meek |
| 105 | Reaction Zone Characteristics of Titanium Aluminide Composites | Dr. Carolyn Meyers |
| 106 | Photoreflectance Measurements of Unintentional Impurities in Undoped Gallium Arsinide | Dr. Michael Sydor |
| 107 | The Synthesis of 2-Formyl Pyridoimidazoles | Dr. Richard Valpey |

Volume IV

Human Systems Division Laboratories

Harry G. Armstrong Aerospace Medical Research Laboratory

- | | | |
|-----|--|-----------------------|
| 108 | Ceramic Composites for Studying Bone Ingrowth and Remodeling | Dr. Praphulla Bajpai |
| 109 | In Vitro Cytotoxic Effects of Perfluorodecanoic Acid on Human Peripheral Blood Lymphocytes | Dr. Shankar Bale |
| 110 | Auditory Modeling | Dr. Charles Covington |
| 111 | Cognitive Demands of Tracking Strategies as Assessed by the Optimum-Maximum Procedure | Dr. Barry Goettl |
| 112 | Evaluation of an Extraction Procedure for the Analysis of Serum Steroids | Dr. Robert Masingale |
| 113 | Performance in a Visual Monitoring Task with Serial and Simultaneous Display Formats | Dr. David Payne |
| 114 | A Nonlinear Lumped Parameter Model for the Seated Humans | Dr. Joseph Saliba |
| 115 | In Vitro Modeling of Perfluoro-N-Decanoate Effects on Enzymes of Fatty Acid Metabolism | Dr. Sanford Singer |
| 116 | Perfluorodecanoic Acid Efflux from Cultured Primary Rat Hepatocytes | Dr. Andrew Whipple |

117	Determination of Perfluoro-N-Decanoic Acid Toxicity in Vitro and in Vivo Via Two-Dimensional Polyacrylamide Gel Electrophoresis	Dr. Frank Witzmann
Human Resources Laboratory		
118	Hypertext and Intelligent Interfaces for Text Retrieval	Dr. Patricia Carlson
119	Linking Training Evaluation to Training Needs Assessment: Development of a Conceptual Model	Dr. J. Kevin Ford
120	A Concept for an Intelligent Tool to Facilitate the Development of Qualitative Process Models in Novice Programmers	Dr. Hugh Garraway
121	A Tool for Studying the Effect of Range Restriction on Correlation Coefficient Estimation	Dr. Douglas Jackson
122	Evaluation of a Methodology for Estimating Cross-AFS Transferability of Skills	Dr. Charles Lance
123	An Expert System Approach for Reliability Data Analysis	Dr. Thomas Landers
124	No Report Submitted at this Time	Dr. Douglas Mandra
125	Graphical Programming of Simulation Models in an Object-Oriented Environment	Dr. Mufit Ozden
126	A Study of Interaction Between Job Properties and Personal Characteristics in the New PACE System	Dr. Dharam Rana
127	An Intelligent Tutor for the IBM System/360 Assembly Language: BIGBLUE	Dr. Sunita Rana
128	Preliminary Design Considerations for an Advanced Instructional Design Advisor	Dr. Jonathan Spector
129	Effectiveness of Contract Monitors In An Air Force Human Resources Laboratory: Prediction and Measurement	Dr. Lawrence Witt

130	Computer Support of Creativity in Unified Life Cycle Engineering	Dr. Lawrence Young
131	The Relationship Between Inspection Time and Intelligence	Dr. Robert Young
Occupational and Environmental Health Laboratory 132	Solvent Extraction of Boron From Wastewater	Dr. Steven Chiesa
133	Extention of the Detection Limits of Arsenic and Selenium in Solid Samples by ICP/AES Utilizing Preconcentration Techniques	Dr. Randolph Huff
134	Determination of Asbestos Fibers in Environmental Samples Using Scanning Electron Microscopy and Energy Dispersive X-ray Analyses (SEM-EDXA)	Dr. Larry Sherman
135	Analysis of Contaminated Ground Water Using Kriging Methods	Dr. Gary Stevens
School of Aerospace Medicine 136	Blood Flow Distribution In The Non-Working Forearm During Exercise	Dr. Ronald Bulbulian
137	Photophysics and Photochemistry of Transition Metal Complexes of 8-Quinolinamine Schiff Bases	Dr. John Burke
138	Immunocytochemical Localization of Vasoactive Intestinal Peptide, Neuropeptide Y and Arginine Vasopressin within the Supra-chiasmatic Nuclei of the Rat	Dr. Bennye Henderson
139	Development of Improved Assays for Cholesterol and Major Lipoprotein Fractions	Dr. Eric Johnson
140	Plasma Catecholamine Assays by High Performance Liquid Chromatography	Dr. Daisy Kimble
141	Application of Nonlinear Filters to VEP Data	Dr. Harold Longbotham
142	Extensions of Several Difference Score Approaches for the Analysis of Time Ordered Repeated Measures	Dr. David Ludwig

143	Spin Label Studies of Oxygen in Biological Systems	Dr. William Plachy
144	The Stinging Wasps (Hymenopter: Vespidae) of South Texas	Dr. Hal Reed
145	Modeling of Blood Flow in the Systemic Human Arterial Tree	Dr. Thomas Rogge
146	The Separation of HDL2 and HDL3 Using the Technique of Ultra-centrifugation	Dr. Joe Ross
147	An Experimental Design to Demonstrate the Dispersion Effects of Salt Water on OPTICAL PULSES	Dr. Dhiraj Sardar
148	Literature Search on Nutrition and the Relation to Tactical Air Command Pilots, G-Tolerance and Energy Output	Dr. Sonia Sawtelle
149	A Small Inert-Gas Generator	Dr. Paul Scheie
150	High Performance Liquid Chromatography (HPLC) Determination of High Energy Phosphate Pool	Dr. Sharon Williams
151	Chemiluminescent Probes Based on Luminol and Luminol Derivatives	Dr. John Wright
Wilford Hall Medical Center		
152	PC - Mainframe Interface for Data Entry	Dr. David Cecil
153	Oral Health	Dr. Jorge Sintes

1889s

1988 USAF-UES SUMMER FACULTY RESEARCH PROGRAM/
GRADUATE STUDENT SUMMER SUPPORT PROGRAM

Sponsored by the
AIR FORCE OFFICE OF SCIENTIFIC RESEARCH

Conducted by the
Universal Energy Systems, Inc.

FINAL REPORT

COMPUTATION OF THE FLOW FIELD
AND HEAT TRANSFER IN A RECTANGULAR PASSAGE
WITH A TURBULATOR

Prepared by:	Bryan R. Becker, Ph.D., P.E.
Academic Rank:	Assistant Professor
Department and	Department of Mechanical and Aerospace Engineering
University:	University of Missouri-Columbia
Research Location:	USAFWAL/POTC Wright-Patterson AFB, OH 45433
USAF Researcher:	Richard B. Rivir, Ph.D.
Date:	12 August 1988
Contract No:	F49620-87-R-0004

COMPUTATION OF THE FLOW FIELD AND HEAT
TRANSFER IN A RECTANGULAR PASSAGE
WITH A TURBULATOR

by

Bryan R. Becker, Ph.D., P.E.

ABSTRACT

A detailed numerical study of the aerothermal mechanics within a short straight section of a turbine blade internal cooling passage with a single turbulator is described. The two dimensional, transient, Reynolds averaged Navier Stokes, continuity and energy equations are iterated to a steady state solution using the MacCormack explicit predictor-corrector algorithm. Turbulence closure is achieved through the use of the Baldwin-Lomax algebraic two layer eddy viscosity model.

Axial distributions of local skin friction coefficient, local Stanton number and local Nusselt number are given. Profiles of velocity and temperature are presented as well as contours of streamfunction and temperature which display complex details of the flow structure. It was found that the widely used Reynolds Analogy greatly underpredicts the heat transfer rate as given by a direct calculation using Fourier's law. Finally, the numerical results are found to compare favorably to the experimental results published by Han et al (1986).

ACKNOWLEDGMENTS

I wish to thank the Air Force Systems Command, the Air Force Office of Scientific Research and the Air Force Wright Aeronautical Laboratories, Aero Propulsion Laboratory for their sponsorship of this research. Universal Energy Systems must be mentioned for their concern and help to me in all administrative aspects of this program.

I wish to especially thank Dr. Richard B. Rivir, not only for his excellent technical guidance and insight, but also for his encouragement, support and friendship throughout my assignment. Dr. Rivir made this summer a rewarding, stimulating and enriching experience by sharing with me his insight into the physics of fluids and the methods of experimental fluid dynamicists. His continued inspiration and encouragement throughout the past year was instrumental in my establishment of a research program in the field of gas turbine aerothermal phenomena.

The concern and encouragement of Mr. William A. Troha was greatly appreciated. I would also like to thank Dr. Joseph S. Shang, Dr. Donald P. Rizzetta and Mr. Jerry Trummer for their help in overcoming many technical problems. Dr. Rizzetta spent many long hours explaining to me the MacCormack predictor-corrector numerical technique, application of consistent boundary conditions and methods of grid generation and computer graphics. Finally, I would like to thank Lt. Col. Jack D. Mattingly for his support.

I. INTRODUCTION

Advanced gas turbine engines will be designed for higher thermal efficiency and specific thrust which will necessitate higher operating speeds, temperatures, and pressures. As a consequence, the heat loads on the turbine blades will increase, which can result in both high metal temperatures and thermal stress concentrations due to severe thermal gradients. To reduce these effects, cooling air is extracted from the compressor and is routed through small rectangular cooling passages within the turbine blades.

As shown in Figure 1, the cooling air enters the root of each turbine blade and flows through complex, serpentine passages until it exits through the blade's surface into the cavity surrounding the turbine rotor-stator. Since the pressure drop, and thus the mass flowrate, along these cooling passages is limited by the pressure differential between the compressor and the turbine stage, methods other than increased coolant flow, such as the introduction of turbulators, must be used to enhance the heat transfer. These turbulators or turbulence promoters, which consist of ribs protruding from the walls of the internal cooling passages, increase the turbulence level within the cooling air flow and thus augment the rate of energy transfer from the turbine blade through the cooling passage wall and into the cooling air flow. Thus, the resulting coolant flows contain many complex phenomena which are not adequately included in the current heat transfer design of turbine blades. The detailed modeling of these flows is essential to the accurate prediction of the distribution of the local heat transfer coefficient along the cooling passages. Such prediction is necessary to achieve a thermal design of these components which incorporates efficient cooling and thereby alleviates the effects of the increased heat load.

My research interests are in the area of computational fluid dynamics and heat transfer. During my more than 10 years at the Oak Ridge National Laboratory, I used both finite difference and finite element techniques to analyze numerous thermal science

problems which arose as a result of the Nation's nuclear/power production effort administered by the Department of Energy (DOE).

These problems involved the modeling of the physical processes of laminar and turbulent flow, heat transfer and thermodynamics. In particular, as part of the DOE gas centrifuge uranium enrichment program, I developed two Navier Stokes models of the rotating flow field within the gas centrifuge: one using a Newton's method; the other, an approximate factorization scheme.

This background contributed to my being assigned to the Components Branch of the Aeropropulsion Laboratory, Air Force Wright Aeronautical Laboratories during both the 1987 and 1988 SFRP research periods.

II. OBJECTIVES OF THE RESEARCH EFFORT

There have been numerous experimental and analytical studies of the flow field and heat transfer within straight rectangular ducts which simulate the flow within the internal cooling passages inside a turbine blade. However, there remains work to be done in the detailed modeling of the heat transfer and fluid flow processes very near the fluid-solid interface. This paper reports on a two dimensional modeling effort which begins to address this need.

During my tenure as a Summer Research Fellow in the 1987 Summer Faculty Research Program (SFRP), I began modeling of the fluid flow and heat transfer in a straight rectangular passage with a single turbulence promoter. This work was completed and a technical paper was written during the Spring 1988 term with funding by the 1987 Mini Grant Program. This paper, "A Numerical Simulation of the Flow Field and Heat Transfer in a Rectangular Duct with a Turbulator Using a Predictor-Corrector Algorithm," (AIAA-88-2903), was presented at the AIAA/ASME/SAE/ASEE 24th Joint Propulsion Conference, July 11-13, 1988 in Boston, MA [1]. A copy of this AIAA paper is attached to this 1988 SFRP Final Report as an Appendix.

This first objective of this 1988 SFRP research effort was to modify the numerical model developed last summer by incorporating true symmetry boundary conditions at the upper boundary of the computational mesh:

$$\frac{\partial \phi}{\partial y} = 0 \quad (1)$$

for all dependent variables ϕ . The resulting numerical model was then iterated to a well converged steady state solution.

The second objective was to develop a post processor program to read and analyze the converged solution. After reading the solution from an online data file, this post processor first calculates the L2-Norm of the error in the solution. It then generates a plot data set which contains the information necessary to plot nondimensional velocity and temperature profiles. It then calculates the axial distributions of the local skin friction, local Stanton Number (via both Reynold's Analogy and Fourier's

Law), as well as the local Nusselt Number scaled by McAdams-Dittus-Boelter correlation for fully developed Nusselt Number in rectangular ducts. Following these calculations, the post processor appends the experimental data reported by J. C. Han et al [2] and then generates data sets for plotting all of the above mentioned quantities as a function of distance along the duct. This program then integrates both the calculated and the experimental Nusselt numbers to determine axial average values of these quantities. Finally, the post processor integrates the velocity distribution throughout the computational mesh so as to evaluate the streamfunction. It then writes a third plot data set containing the information necessary for plotting contours of streamfunction and nondimensional temperature.

The third and final objective of the 1988 SFRP research period was to begin work on a numerical model of a rectangular passage with four turbulators. The computational grid shown in Figures 2 and 3 was generated for this model. Figure 2 shows the entire computational domain containing an entrance region, four turbulators, and a downstream region. Figure 3 shows details of the first ten rib heights of the mesh. It can be seen that the grid is very fine near the lower boundary and in the vicinity of the top of the rib. The MacCormack Predictor-Corrector algorithm was modified to account for the boundaries of the four turbulator surfaces. Every effort was made to accurately model the exact conditions reported by Han et al [2]. At the close of the 1988 SFRP research period this model is still in the "development and check-out" phase. It is intended that this work will be continued at my university with funding from the Research Initiative Mini Grant Program.

III. DISCUSSION OF RESULTS GENERATED BY THE IMPROVED SINGLE TURBULATOR MODEL

As stated in Section II, the first objective of this summer's research was to improve the single turbulator model which was developed during the 1987 SFRP research period. This improved model was then iterated to a well converged solution which was analyzed by the post processor developed during this 1988 SFRP research period. The computational mesh used in the single turbulator model is shown in Figure 4.

A. Convergence

Iteration towards the improved solution was begun by using the earlier solution as an initial condition. The previous solution was achieved after 100,000 iterations and then an additional 100,000 iterations were performed with the improved single turbulator model. The convergence of the predictor-corrector algorithm is measured by the L-2 norm of the change in the normalized global solution vector. Typically, in the iteration to a converged steady state solution, the value of this norm will drop 3 orders of magnitude from the initial conditions and then oscillate about this reduced value, indicating that convergence has been achieved [3]. In the earlier simulation, the value of this norm decreased from 7.137 at the outset to 0.002662 after 50,000 iterations and oscillated near that value for the next 50,000 iterations. After the symmetry boundary condition was improved, the solution was restarted and the norm dropped to less than 0.0008 within the first 50,000 iterations and continued to oscillate just below that value for the final 50,000 iterations. This behavior is typical of convergence to the steady state solution.

B. Streamfunction Contours

Streamfunction contours over the entire computational domain are shown in Figure 5. As shown in this figure, counterclockwise vortices are present both upstream and downstream of the turbulator rib. Reattachment of the large separated flow behind the

turbulator occurs approximately nine to ten rib heights downstream of the rib. Figure 6 shows the size of the counterrotating vortex upstream of the rib. Figure 7 gives detail of the flow structure atop the turbulator and shows the presence of a long thin counterrotating vortex centered over the rib. Detail of the large counterclockwise recirculation behind the turbulator is shown in Figure 8. The dividing streamline departs from the rib near the top corner. The small bubble located at the point where the rib rejoins the horizontal surface indicates the presence of a small clockwise rotating vortex at that juncture which is shown in Figure 9.

C. Temperature Contours

The flow field temperature distribution is shown in Figure 10. Upstream of the turbulator, very little mixing is occurring as indicated by the concentration of temperature contours near the horizontal surface. The bulk of the approaching fluid is slightly warmer than the free stream value, T_∞ , as indicated by the uppermost contour which attaches at the front corner of the rib. This slight warming is due to heat conduction from the hot isothermal wall. Downstream of the rib, the turbulent mixing of the fluid has greatly diffused the thermal energy upward, well beyond the first rib height. The thickness of this warm air region grows downstream of the turbulator. Just behind the rib, the temperature distribution shown in Figure 11, reflects the effects of the complex flow structure which exists there.

D. Velocity and Temperature Profiles

Figures 12 through 15 present profiles of u/u_∞ and T/T_∞ plotted against Y/Y_{MAX} at 9 streamwise locations, X/H , where H is the rib height. The profiles at $X/H = 0.0$ represent the specified inflow boundary conditions.

At $X/H = 3.0$ and 4.0 , the profiles display the development of the momentum and thermal boundary layers. At $X/H = 4.0$, the horizontal velocity is negative near the solid wall which indicates the presence of the upstream recirculation zone shown in Figure 6.

The locations, $X/H = 5.0, 5.5,$ and $6.0,$ are at the front top corner, midline and back top corner of the rib, respectively. At $X/H = 5.0,$ the horizontal velocity has increased dramatically near the solid wall as the flow accelerates over the rib which results in a corresponding decrease in flow field temperature since the total energy of the flow must be preserved. By $X/H = 5.5,$ the flow has begun to decelerate with a corresponding increase in temperature. At $X/H = 6.0$ these trends continue.

The streamwise locations, $X/H = 7.0$ and $10.0,$ are located at the back bottom corner of the rib and at the midline of the large recirculation bubble which exists downwind of the rib. The temperature profiles show that the turbulent mixing behind the rib has greatly diffused the energy from the hot solid wall to form a warm air region which extends more than 1.0 rib height vertically from the solid wall. The horizontal velocity profile is typical of a recirculation zone with a negative upstream flow near the wall changing to a positive downstream flow higher in the flow field.

The profiles at $X/H = 20.0,$ demonstrate that both the momentum and thermal boundary layers are reestablished downstream of the recirculation bubble. However, comparison of these profiles to those upstream of the turbulence promoter, show that the downstream boundary layers are much thicker and well mixed, illustrating the effects of the intense turbulent mixing caused by the flow over the turbulence promoter.

E. Skin Friction and Stanton Number

The axial distribution of the local skin friction, shown in Figure 16, was calculated from the following equation:

$$c'_f = \frac{\tau_{wall}}{\frac{1}{2}\rho_\infty u_\infty^2} = \frac{\mu \left(\frac{\partial u}{\partial y} \right)_{y=0}}{\frac{1}{2}\rho_\infty u_\infty^2} \quad (2)$$

The normal derivative of the horizontal velocity was evaluated at the wall using a second order accurate three point difference expression. The viscosity was determined as a function of temperature at the wall. As shown in Figure 16, the skin friction achieves a maximum at approximately $X/H = 5.0$ which corresponds to the very steep velocity gradient near the wall as the flow

accelerates over the rib. As mentioned earlier, this reduces the temperature of the fluid near the wall which results in a steep thermal gradient there and the high heat transfer rate displayed in Figures 17 and 18.

The axial distribution of the local Stanton Number, given in Figure 17, was evaluated from the following equation using two different methods:

$$St = \frac{Q_{wall}}{c_p \rho_\infty u_\infty (T_{wall} - T_\infty)} \quad (3)$$

In the first method, the Reynolds Analogy was used, in which the heat transfer rate is related to the skin friction as follows:

$$\text{Stanton Number} = \frac{1}{2} c_f' \quad (4)$$

This method is widely used in turbomachinery calculations but these calculations greatly underpredict the heat transfer rates measured experimentally.

In the second method, Fourier's Conduction Law was used to evaluate the heat transfer rate at the wall, Q_{wall} , which appears in Equation (3):

$$Q_{wall} = -K \left(\frac{\partial T}{\partial y} \right)_{y=0} \quad (5)$$

In this calculation, the normal derivative of temperature at the wall was calculated in a manner similar to that used for the normal derivative of the horizontal velocity discussed above and the thermal conductivity was evaluated as a function of temperature at the wall.

In the convection heat transfer process, the energy is first transferred by conduction from the solid wall to the fluid particles adjacent to the wall. These fluid particles are then transported away from the solid wall by the bulk mixing of the fluid which results in the diffusion of energy from the solid wall. The basis for the Reynolds Analogy is the assumption that the same mechanism is responsible for the exchange of both heat and momentum. This assumption disregards the details of the energy transfer process at the solid wall-fluid interface. As shown in

Figure 17, the direct calculation of the heat transfer rates via Fourier's Law predicts heat transfer rates which can be as great as 3 times that given by the Reynolds Analogy. This discrepancy can be explained by the fact that the Reynolds Analogy is derived for laminar or fully turbulent flows over a flat plate with laminar and turbulent Prandtl number, $Pr = Pr_t = 1.0$. Thus, the Reynolds Analogy is not applicable to flows with recirculation zones and flow reversals which cause the normal gradient of velocity to differ greatly from the normal gradient of temperature.

F. Comparison of Numerical to Experimental Results

In an effort to validate the numerical algorithm, the numerical results were compared to the experimental results published by Han et al [2]. In the work by Han et al, parametric studies of the heat transfer and friction characteristics in rectangular channels with turbulators were performed. The parameters of the test case which is most similar to the numerical simulation are as follows:

$$Re_D = 60,000$$

$$\text{channel width/channel height} = 4$$

$$\text{rib angle of attack} = 90^\circ$$

$$\text{rib pitch/rib height} = 20$$

For this test case, Han et al report that reattachment occurs about two rib heights downstream from separation. As discussed earlier, the numerical results predict reattachment nine to ten rib heights downstream of the rib. This great disparity is a result of the difference in rib shapes. As shown in Figure 18, the experimental rib is square in cross section and much smaller than the "flatten sin curve" used in the numerical model. The gentle slope of the rib in the numerical solution permits the flow downstream of the rib to straighten more gently, thus preserving its horizontal momentum and lengthening the recirculation zone.

In Figure 18, the calculated axial distribution of the Nusselt Number is compared to experimental results reported by Han et al [2]. In the calculation of the Nusselt Number the heat transfer at the wall was evaluated by using Equation (5).

In the comparison of the numerical results to the experimental

results, it is necessary to take into account the difference in resolution: the experimental results are given as nine data points while the calculated distribution contains 100 data points. Thus, the experimental results represent the local average Nusselt Number distribution which is much smoother than the detailed pointwise distribution given by the numerical calculation.

In spite of this difference in resolution, both the numerical and experimental results show similar trends. Both exhibit high heat transfer near the upstream corner of the rib with minimum heat transfer just behind the downstream edge of the turbulator. Both distributions show the heat transfer first increasing and then decreasing as X/D increases downstream of the turbulator.

The average values of these distributions were determined by integrating along the axis of the rectangular channel. The average of the calculated Nusselt Number was found to be 1.5123 while the average of the experimental Nusselt Number was found to be 2.3028. Thus the average calculated Nusselt Number is approximately 34% lower than the average experimental Nusselt Number.

This difference can be attributed to several factors. Again, the rib shape has a profound effect on the flow field and hence the heat transfer. The experimental data includes 3-d effects which are not present in the numerical model. The Baldwin-Lomax turbulence model may not be adequate to predict the turbulence effects in the recirculation zone. Another important factor may be the difference in free stream velocity. Han et al report an average free stream velocity of approximately 70.0 ft/sec while the corresponding value used in the numerical prediction was 270.0 ft/sec. The Reynolds number based on hydraulic diameter in both cases was 60,000. However, since the numerical model is 2-d, the channel width in the simulation is arbitrary and was chosen to be four times the channel height since that was the highest aspect ratio reported by Han et al. Finally, the experimental test set up included several ribs along the duct while the numerical model contained only a single rib. Han et al [2] report that the heat transfer results do not settle into a periodic pattern until the flow has gone over the first three ribs.

Several of these possible causes of error will be eliminated in the four turbulator model. Obviously the number of ribs is greater than the three required to establish the periodic results reported from the experiment. The free stream velocity will be set equal to that reported by Han et al. Also the turbulator size, geometry, pitch and angle of attack will duplicate the experimental conditions. This work will be continued at the University of Missouri with funding from the Research Initiation Mini Grant Program.

G. Conclusions

In conclusion, the flow field and heat transfer along a turbine blade internal cooling passage was numerically simulated using a two dimensional geometry. Attention was focused on the flow along a short straight section of a rectangular passage with a single transverse mounted turbulator protruding from its floor.

In contrast to the work done by earlier investigators, this study was performed using a computational mesh which had very high resolution. There were 100 grid lines in the horizontal (axial) direction clustered around the turbulator and 60 grid lines in the vertical direction with 44 within the first rib height which was well within the turbulent boundary layer. This high resolution mesh revealed considerable detail of the flow field and heat transfer near the turbulator.

The calculation revealed a flow structure near the turbulator which is more complex than is ordinarily expected for such a simple passage/turbulator geometry and has a pronounced effect upon the heat transfer as shown in Figures 17 and 18. This significant insight indicates that further study is needed into the effects of turbulator geometry and spacing (or pitch) as a means of heat transfer enhancement. Furthermore, this calculation revealed a considerable difference between the heat transfer rate calculated by using the Reynolds Analogy and that given by a direct calculation using Fourier's law. This discrepancy results from the complex flow structure near the turbulator which causes the normal gradient of velocity to differ greatly from the normal gradient of

temperature. Similar flow structures exist throughout many turbomachinery components, and therefore, corresponding heat transfer effects may occur in those components which would also be inadequately predicted by the Reynolds Analogy. This significant insight may lead to remedies for the underprediction of heat transfer rates in many turbomachinery calculations.

Finally, the numerical results were found to compare favorably with reported experimental results. Both sets of results display similar trends. Comparison of the axially averaged Nusselt Number shows 34% error which is reasonable considering the difference in rib geometry, number of ribs, and free stream velocity as well as the absence of 3-d effects in the numerical model.

IV. RECOMMENDATIONS

As outlined in Section II of this report, work has begun on a four turbulator model and as discussed in the conclusions of Section III, this model will remove many of the causes of discrepancy between the numerical results and the experimental results. It is recommended that this modeling effort be completed and the algorithm validated by comparison with experimental results. After this has been done several parametric studies can be performed.

First, a grid resolution study will be done by producing a converged solution using a course mesh formed by omitting every other grid line shown in Figures 2 and 3. This converged solution will then be interpolated to the fine mesh of Figures 2 and 3. Iteration will then be restarted. Thus, the grid dependence of the solution can be determined. Also, this should produce an efficient solution strategy since part of the iteration will be done using only a quarter of the total grid points.

Second, using the refined mesh, parametric studies of the effects of Reynolds Number and rib pitch can be done and compared to the experimental results.

Third, the ribbed surface could be reflected about the duct line of symmetry and the effects of top and bottom rib alignment studied.

Fourth, various turbulence models could be incorporated in the algorithm and these effects upon flow field structure and heat transfer ascertained.

Finally, this work should eventually progress towards a full 3-d Navier Stokes solution which could then include effects of rib angle of attack and duct rotation.

REFERENCES

1. Becker, Bryan R. and Richard B. Rivir, "A Numerical Simulation of the Flow Field and Heat Transfer in a Rectangular Duct with a Turbulator Using a Predictor-Corrector Algorithm," AIAA-88-2903, AIAA/ASME/SAE/ASEE 24th Joint Propulsion Conference, Boston, MA, 1988.
2. Han, J. C., J. S. Park and M. Y. Ibrahim, "Measurement of Heat Transfer and Pressure Drop in Rectangular Channels with Turbulence Promoters," NASA Contractor Report 4015, 1986.
3. Personal communication with Dr. Donald P. Rizzetta, Flight Dynamics Laboratory, Wright Patterson AFB, Ohio, 1987.

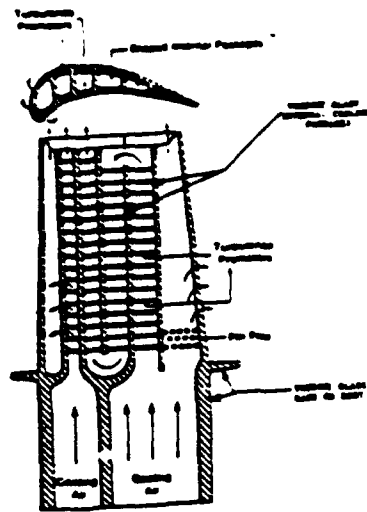


Figure 1. Schematic diagram (top) view of a turbulator blade.

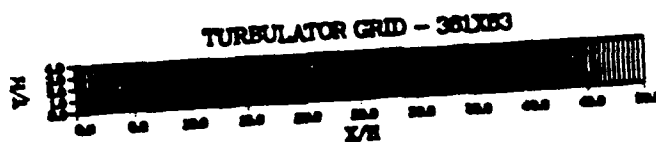


Figure 2. Computational domain for the four turbulator model.

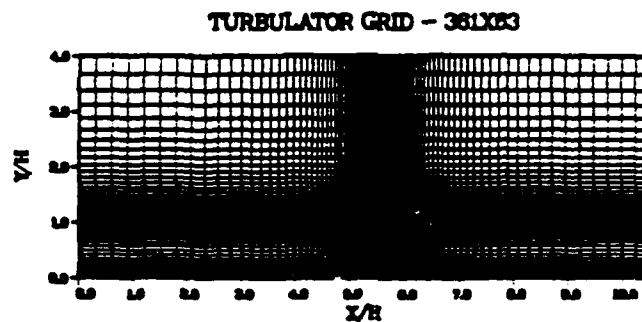


Figure 3. Detail of the computational domain near the first turbulator of the four turbulator model.

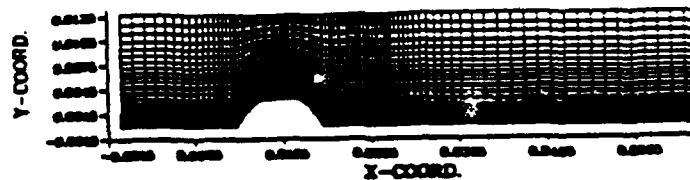


Figure 4. The 180 by 60, (X,Y), computational mesh used in the single turbulator model.

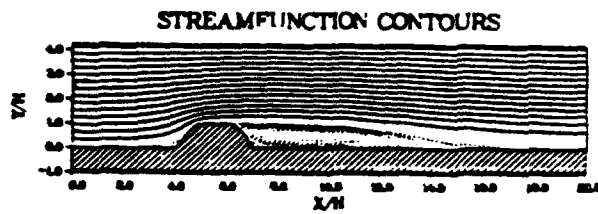


Figure 5. Calculated streamfunction contours. Counterclockwise rotation is indicated by dashed streamlines.

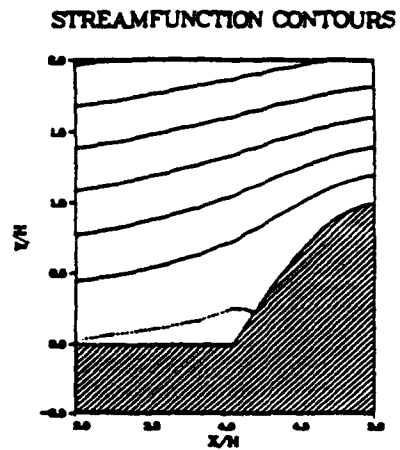


Figure 6. Detail of the streamfunction contours upstream of the turbine. Counterclockwise rotation is indicated by the dividing streamline which appears as a dashed line.

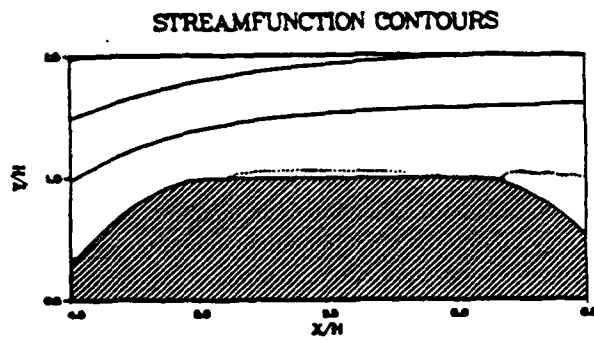


Figure 7. Detail of the streamfunction contours atop the turbine. Counterclockwise rotation is indicated by the dividing streamline which appears as a dashed line.

STREAMFUNCTION CONTOURS

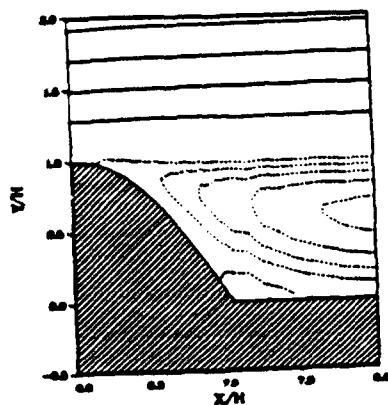


Figure 8. Detail of the streamfunction contours downstream of the turbulator. Counterclockwise rotation is indicated by dashed streamlines.

STREAMFUNCTION CONTOURS

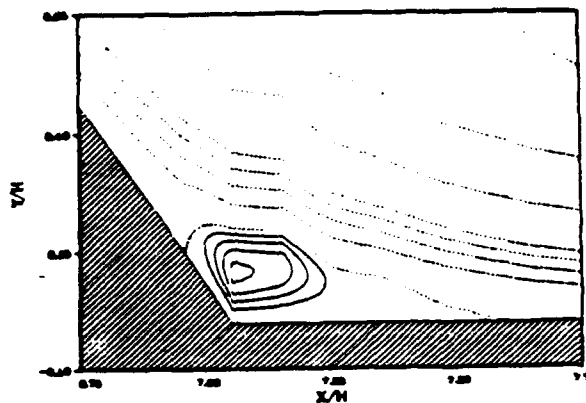


Figure 9. Streamfunction contours near the hub of the turbulator. The clockwise rotating vortex is indicated by the solid streamlines.

TEMPERATURE CONTOURS

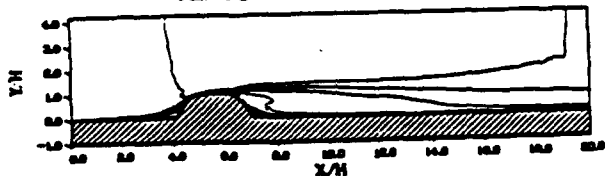


Figure 10. Calculated temperature contours.

TEMPERATURE CONTOURS

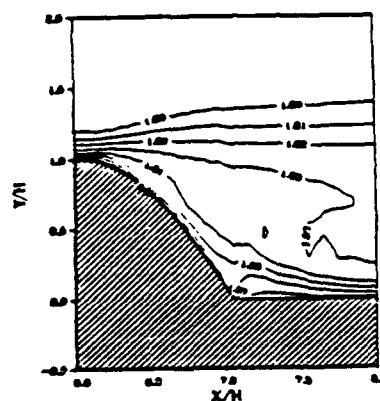


Figure 11. Detail of the temperature distribution downstream of the turbulator. Values of T/T are indicated.

VELOCITY PROFILES UPSTREAM OF RIB

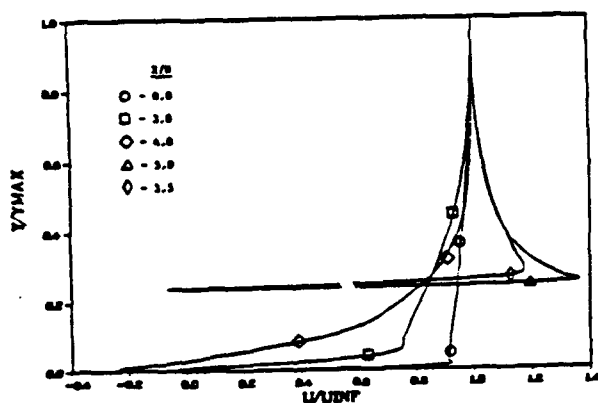


Figure 12. Calculated velocity profiles, upstream of the turbulator.

VELOCITY PROFILES DOWNSTREAM OF RIB

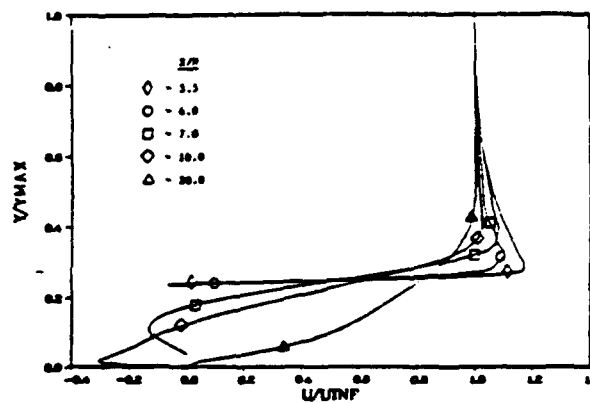


Figure 13. Calculated velocity profiles, downstream of the turbulator.

TEMPERATURE PROFILES UPSTREAM OF RIB

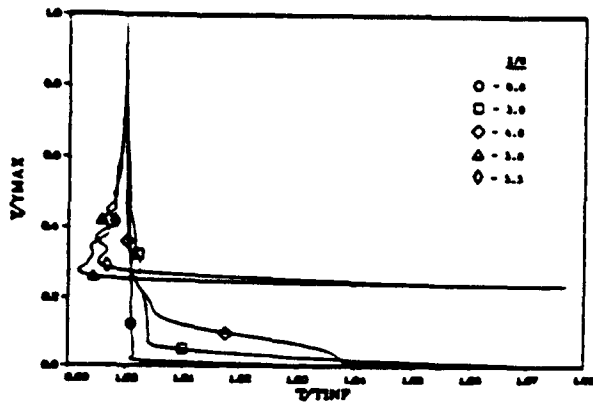


Figure 14. Calculated temperature profiles, upstream of the turbulator.

TEMPERATURE PROFILES DOWNSTREAM OF RIB

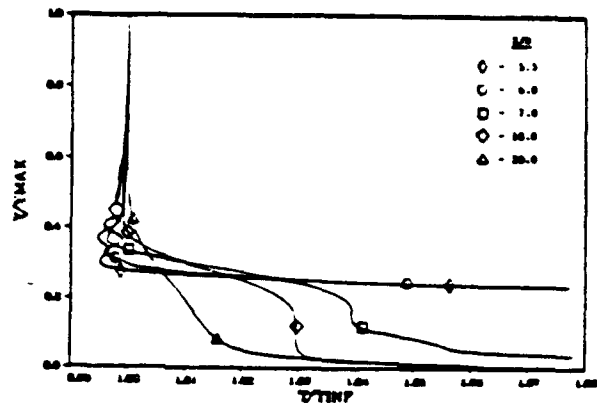


Figure 15. Calculated temperature profiles, downstream of the turbulator.

LOCAL SKIN FRICTION

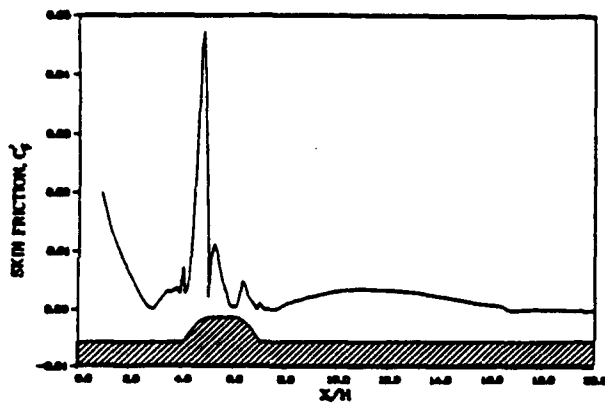


Figure 16. Calculated axial distribution of local skin friction coefficient.

LOCAL HEAT TRANSFER RATE

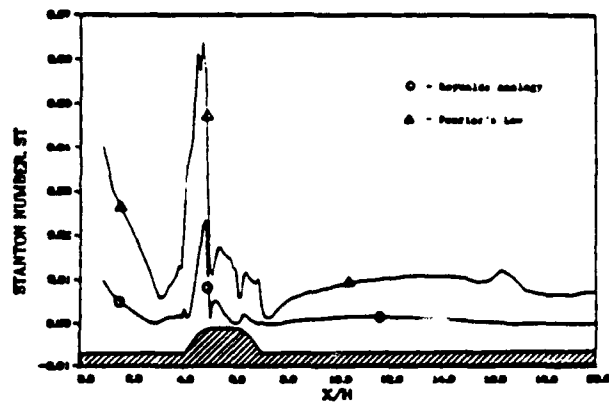


Figure 17. Calculated axial distribution of local Stanton Number.

NUSSELT NUMBER VERSUS X/D

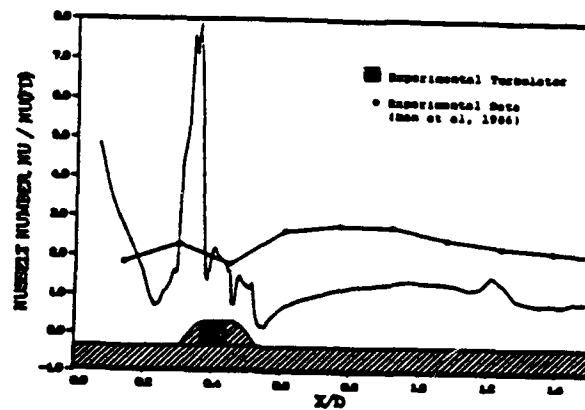


Figure 18. Calculated axial distribution of local Nusselt Number.

APPENDIX AVAILABLE FROM AUTHOR
OR UES UPON REQUEST

1988 USAF-UES SUMMER FACULTY RESEARCH PROGRAM
GRADUATE STUDENT RESEARCH PROGRAM

Sponsored by the
Air Force Office of Scientific Research
Conducted by
Universal Energy Systems, Inc.

FINAL REPORT

Use of Laser Light Visualization Technique on Studies
of Film Cooling Flow and Flow Over Cavities

Prepared By:	Mingking K. Chyu
Academic Rank:	Assistant Professor
Department and University:	Dept. of Mechanical Engineering Carnegie Mellon University
Research Location:	Air Force Wright Aeronautical Laboratories POTC, Dayton, OH 45433
USAF Researcher:	Dr. Richard B. Rivir
Date:	30 September 1988
Contract No.	F49620-88-C-0053

USE OF LASER SHEET LIGHT VISUALIZATION TECHNIQUE ON STUDIES OF
FILM COOLING FLOW AND FLOW OVER CAVITIES

M. K. Chyu

Dept. of Mechanical Engineering
Carnegie Mellon University
Pittsburgh, PA 15213

R. B. Rivir

AFWAL/POTC
Wright Patterson Air Force Base
Dayton, OH 45433

ABSTRACT

Flow visualization studies on characteristics of film cooling flow and cavity flow are performed using the technique of laser sheet light illumination with $TiCl_4$ seedings. Primary efforts focus on the detailed structures of film cooling injection and cavity induced free shear layer. The high Reynolds number flow existing in the present film cooling system produces distinctly different coherent structures compared to the low Reynolds number cases reported earlier by Rivir et al. This is, in part, caused by the lift-off effects which induce the injection structures leaning more to those of a free shear layer than to a wall layer. For the cavity flow, development of the separated shear layer is largely determined by the value of the cavity aspect ratio, W/H . The shear layer reattaches on the cavity floor when $W/H \geq 8$. For cavities with $W/H < 8$, current observation clearly shows that part of the shear layer diverts back inside the cavity. Nevertheless, the proportion of this diversion diminishes as the value of W/H decreases. The present flow characteristics support the results of local mass transfer data obtained in a separate study.

Acknowledgements

The first author (MKC) of this report is grateful to Air Force Systems Command, Air Force Office of Scientific Research, Universal Energy System and AFWAL/POTC for the appointment of Summer Faculty Research Fellowship.

In addition, he expresses his special appreciation to Dr. Richard B. Rivir at AFWAL/POTC for his collaboration in this project and personal friendship. Dr. Rivir has provided this project with incisive ideas, valuable and helpful suggestions.

Thanks to Mr. Jim Heil for his assistance in fabrication of test apparatus, Mr. Benjamin Sakar for his help in running the experiments, Dr. Larry Goss for setting up the laser optics, and Dr. W.M. Roquemore for his enthusiastic support.

I. INTRODUCTION

Convection transport is known to be the most common mode existing in gas turbines. This is specially true in a blade cooling system. Current methods for cooling of a turbine blade or vane include film cooling, jet impingements, internal cooling passages and pin-fin pedestals. All of these are dominated by turbulent, forced-convection, wherein heat transfer is the ultimate concern. To fully understand the thermal behavior in such a convection-dominated system, it requires sufficient knowledge of the associated flow characteristics. Nevertheless, in many heat transfer studies, information on the flow aspect is not known a priori. Hence, separate efforts are often directed to flow investigation. These often involve measurements of mean flow fields, pressures and turbulence and flow visualizations. Flow information provides a basis for the description of the corresponding heat transfer behavior. This is always the case for a complex system but its complexity inhibits detailed understanding.

The present study describes a state-of-the-art flow visualization technique by which detailed structures of two flow systems are investigated. The two systems are flows associated with film cooling and inside rectangular cavities. Hydrodynamically, the film cooling flow involves the complexity of a jet injection from a hole or a slot to a generally turbulent mainstream. In reality, this is further complicated by multiple-temperature problems, as temperatures of the injection, the mainstream and the surface to be cooled differ markedly. The cavity flow is considered to be a bench-mark case for flow with separation. It possesses the special features of flow in an blade internal cooling passage roughened by transverse ribs. Besides, cavity flow exists in dump combustors of a gas turbine.

The first author of this report (MKC), a AFOSR-UES summer faculty researcher, is experienced in performing research in heat transfer and fluid mechanics. Cooling of turbine components is one of his primary research areas. His recent contribution includes studies of blade cooling with internal passages, pin-fins in pedestal and

heat transfer near a blade tip. The present project is directly related to his research background and has provided him with extensive scopes in future research. Knowledge gained from this project and possible future follow-ups will provide valuable information for advanced gas turbine developments.

II. OBJECTIVES OF RESEARCH EFFORTS

The objectives of this research are two-fold. The first objective is to investigate the structures of film cooling flow using the laser sheet light technique. Particular interest lies in investigating the effects of Reynolds number on the large scale vortex motion in the flow. Results obtained from this study, in association with those with relatively low Reynolds numbers, will provide a reference basis for further studies with different injection-to-mainstream density ratios. The second objective is to assess the present flow visualization technique applied to flow systems having significant turbulent mixing. Characteristics of flow over rectangular cavities are thoroughly studied for this assessment. The behavior of the free shear layer separated at the cavity upstream corner and the flow inside a cavity are of utmost concern.

III. FLOW VISUALIZATION TECHNIQUE

Present flow visualization is performed using the technique of laser sheet lighting with TiCl_4 seedings. The general setup of this technique requires two fluid (air) systems; one contains water vapor and the other carries TiCl_4 seedings. As these two fluids meet, the water vapor and TiCl_4 reacts virtually instantaneously and produces TiO_2 and HCl particles, each about 1 micron diameter in size. Besides the very fast reaction rate, such a chemical reaction requires a mixing of reactants to the molecular levels. Hence, the traces of product particles will reflect the details of flow streaks. This can be visualized by illuminating a laser sheet light on the flow domain and taking a 35 mm photo at the same instant. In this study, a YAG laser pulsed at 10 nano seconds provides the illumination, and laser is

triggered by the camera shutter. Photos shown in this paper are taken with a camera setting at 1/250 sec shutter speed and $f = 4$.

Compared to other flow visualization techniques, e.g. using smoke or hydrogen bubbles, the unique advantage of the present method is its unique capability of revealing detailed turbulence structures. At AFWAL, several recent in-house studies on investigation of combustion flames (Roquemore et al., 1986; Chen et al., 1986) and film cooling flows (Rivir et al., 1987) have demonstrated such a capability.

IV. EXPERIMENTAL APPARATUS AND TEST CONDITIONS

The forced air flow is supplied by a centrifugal blower equipped with a 5 HP motor. The blower has a 254 mm diameter circular exit. Attached to the blower exit is a 508 mm long conversion section, made of sheet metal and containing honeycomb flow straighteners inside. The other end of conversion section is connected to the test section inlet. The test section is a plexiglas channel having a 89 mm square cross section and approximately 1.22 m long. Downstream of the test section, flow passes through a flexible, discharging duct and then exhausts outside the building. Flow velocity is varied by changing the opening size of bleeding holes located around the conversion section.

Figure 1 shows a schematic view of the present film cooling flow study. On one of the channel walls, an injection hole is made by drilling a 12.7 mm diameter hole with a 30 degree inclination relative to the mainstream. The center of the injection hole is located about 305 mm downstream of the channel inlet. The injection is first induced by a dry-air compressor, then flows through a rotameter, a $TiCl_4$ seeder and a plenum attached to the channel outside, and finally, through the injection hole, discharges to the mainstream. Details of the seeder flow system has been discussed in an earlier work by River et al. (1987). The mainstream mean velocity varies between 48.2 m/sec and 64.4 m/sec. Reynolds number based on these two velocities and the injection hole diameter are 3.9×10^4 and 5.2×10^4 , respectively. Boundary layer thickness of these two Reynolds number measured at 25 mm

ahead of the injection hole is about 23 mm and 18 mm, respectfully. Thus, the ratio of boundary layer thickness to the injection hole diameter is in the order of 1.5 to 2. The injection Reynolds number, based on the hole diameter and the injection mean velocity, varies between 4.19×10^3 and 1.06×10^4 . The injection-to-mainstream mass flux ratios lie between approximately 0.07 and 0.27.

The cavity flow experiment uses the same test channel without injection hole and plenum. Figure 2 shows a schematic sketch of flow over a rectangular cavity. A cavity is produced by placing two wood blocks one upstream and the other downstream of the designated cavity location. The cavity upstream (backward-facing) wall is fixed at 152 mm downstream of the channel inlet. The streamwise location of cavity downstream (forward-facing) wall is adjustable, which gives different values of cavity aspect ratio. The cavity aspect ratio is defined as the ratio of cavity width (W) and depth (H), and, in the present study, the value of W/H varies between 1 and 10. The TiCl_4 seeded flow is bled out of a hole at the upper corner of the cavity upstream wall. Using this arrangement, traces of the TiO_2 particles will reveal structures of the separated shear layer initiated at this corner. The Reynolds number investigated, based on mainstream velocity and cavity depth, is 1.06×10^5 . At the cavity upstream top-corner where the separation starts, the boundary layer displays a nearly $1/6$ power-law, fully turbulent profile. The boundary layer thickness is approximately 12 mm, about one-half the cavity depth.

V. RESULTS AND DISCUSSION

Film Cooling Flow

This part of the study serves as an extension of an earlier work done by Rivir et al. (1987). The main difference is that the Reynolds numbers of the present study, in both mainstream and injection, are much higher. In the previous study, the mainstream Reynolds number varies from 500 to 2000, and 150 to 4.7×10^3 for the injection. This gives a wider range of injection-to-mainstream mass flux ratio (0.3 to 3.0) than the present one. One important

phenomenon observed in the previous study is the nearly stable hairpin like structures in the boundary layer. Details of the hairpin structures have been viewed from different angles and spanwise locations. At very low mainstream Reynolds numbers and with a thin approaching boundary layer, these hairpins tend to roll up forming a periodic sheet at the interface between the main flow and injection. The hairpins incline at approximately 56-degree relative to the direction of mainstream.

Due to the page limitation on this report, majority of the photos taken have to be excluded. Figure 3 shows a sample results with mainstream Reynolds number equal to 3.9×10^4 . The figure includes three photos representing a sequential variation of injection-to-mainstream mass flux ratio. Comparing with the observation reported by Rivir et al. (1987), the photos have clearly shown the effects of high freestream Reynolds numbers. The turbulence scales are in general smaller, as expected for higher Reynolds number flow. The boundary layer structure is less coherent, especially in regions further downstream of approximately 5 diameters from the injection hole. The previously reported, periodic sheet near the interface between the injection and mainstream becomes rather random and obscure. This is especially true for cases with high injection rates, as shown in Figures 3(c).

Near the wall, the hairpin like roll up phenomenon as reported under the situations of low Reynolds number and thin approaching boundary layer is nonexistent. This is, in part, due to the strong separation occurring at the discontinuity of the trailing edge of the injection hole. In addition to mass flux ratio, such a separation is greatly influenced by the momentum ratio between the mainstream and injection. As shown in Figure 3, all the injections lift off and virtually never attach to the wall. Thus, the jet, in fact, bears the nature of a free shear layer rather than a wall layer.

The large eddy structures in a free shear layer are considered to be associated with the so-called "vortex-pairing" mechanism (Brown and Roshko, 1974). In pairing, adjacent vortices rotate about each other under their mutually induced velocity field. As the rotation

progresses they blend into a single vortex of large scale. At low mass flux ratios, the vortex pairing appears to be the characteristic near the injection hole. Downstream, the coalesced vortices give away to a small-scaled chaotic motion. For large injection ratios, the vortex-pairing type structure is indistinct, at least immediately adjacent to the injection hole. In this region, the strong lift off effects make the injection simulate the model of cylinder in a cross flow. The coherent structures in the near wake of a cylinder, or a bluff body, are eddies produced in a relatively constant, regular manner and, except for some dispersion, are not subject to pairing and any strong interaction. In some cases, the present photos show that pairing and amalgamating motion resumes when the injection flow is deflected to a certain extent and just begins to flow parallel to the mainstream direction. The injection lift off, or a too-large injection Reynolds number, is considered to be undesirable for the purpose of film cooling. First of all, the coolant fails to protect the surface with a direct contact. In addition, the large-scale vortex motions which dominate the turbulent transports are suppressed. The effect of injection lift off is less significant for cases with high mainstream Reynolds number, the large momentum of the main flow forces the injectant stay close to the wall.

Cavity Flow

The typical flow pattern over a cavity consists of three regimes: (1) an outer core flow, (2) a shear layer or mixing region, and (3) a recirculating flow inside a cavity. The outer core flow represents the flow region essentially uninfluenced by the presence of the cavity. It can be part of the wall layer for external flow or the mainstream core regime for channel flow. The second regime is initiated by separation, which occurs at the top edge of the cavity upstream wall and produces a shear layer between the outer flow and recirculating regime within the cavity. Depending mainly on the magnitude of the cavity aspect ratio (W/H), the separated shear layer either bridges the cavity completely and impinges partially on the upper portion of the cavity downstream wall or it reattaches on the cavity bottom

floor. As the free shear layer bears strong mixing effects, its behavior dominates the transport phenomena in a cavity.

Figure 4 shows the sample photos of shear layer development and flow inside cavities for aspect ratios (W/H). Based on the present results, the shear layer reattachment on the cavity floor occurs when $W/H \geq 8$, as the TiO_2 traces are completely confined in the front portion of a cavity. This agrees favorably with other studies reported earlier (Yamamoto et al., 1979; Sinha et al., 1981). The reattachment, in the literature, is taken to mean the localized zone where separated shear layer meets another layer or a bounding wall. In this case, the separated layer usually envelops a region of low velocity, reversed flow. Hence, at reattachment, two flows of opposing direction exist. The hypothetical streamline which separates the reversing fluid particles from those that flow in the direction of mainstream immediately after leaving the reattachment, is known as the dividing streamline. Thus, a reattachment point is defined as the point where the dividing streamline meets another separated layer or surface. Near the reattachment point, high turbulence intensity exists which is largely contributed by the separated shear layer in the region.

For a cavity with $W/H < 8$, the entire cavity is filled with TiO_2 particles. This implies that the shear layer does not reattach on the cavity floor. Instead, the shear layer impinges the top corner of the downstream wall, and the flow divides into two parts. One diverts back to the cavity inside which enhances the recirculation in the cavity, and the other proceeds further on the surface downstream of the cavity. As W/H decreases, the part of shear layer diverted back to the cavity also decreases. In the limiting case, when $W/H = 1$, the present study shows that the shear layer skims pass the cavity nearly completely, and the recirculation inside the cavity is primarily caused by the mainstream shear. In this case, the shear layer is thin and the large-scaled vortex interaction is non-existent. The shear layer grows thicker as the cavity width increases, and its structure shows the characteristic of vortex pairing and amalgamation. Such a large-scaled vortex interaction is expected to elevate the turbulent transport in the

cavity overall, particularly in the region near the cavity downstream wall where the developed shear layer impinges on the surface.

Flow information gained from the present study can provide a reference basis for examining results pertaining to other transport processes, such as heat or mass transfer. Figure 5 show the distributions of local mass transfer coefficients on cavity surfaces. These are results obtained from an earlier study by Chyu and Goldstein (1986). St , the Stanton number, represents the dimensionless mass transfer coefficient. St_0 is the Stanton number on a flat plate without cavity present. The value of St/St_0 gives a measure of heat transfer variation with a cavity and without. The mass transfer results clearly reflect the effects of free shear layer and the characteristics of cavity flow as observed in the present study. Note that the mass transfer on the surface downstream of a cavity is also strongly affected by the shear layer developments. For $W/H \geq 4$, with a highly turbulent shear layer attaching on the surface, the mass transfer shows a transition boundary layer behavior, as a peak mass transfer exists slightly downstream of the corner.

VI. CONCLUSION

Flow characteristics in both film cooling flow and cavity flow are visualized using the laser sheet light/ $TiCl_4$ technique. The method provides detailed information on turbulence structures as well as the general mean flow characteristics. For film cooling, the present results have shown a significant difference in organized motions of turbulence from those with lower Reynolds numbers. The turbulence scales are generally smaller. Meanwhile, the phenomenon of hairpin roll-up, typically observed in a turbulent wall layer, is obscure or even non-existent. This, in part, is produced by the lift-off effects as the injection rate increases. Without a direct wall-attachment, flow downstream of an injection bears the nature of a free shear layer, rather than a wall boundary layer. For the cavity flow, the present flow visualization shows that the reattachment on a cavity floor occurs when $W/H \geq 8$. For $2 \leq W/H < 8$, the separated free shear layer divides into two parts as it

impinges on the cavity downstream wall. For $W/H = 1$, the narrowest cavity investigated, the shear layer skims past the cavity completely. The large-scale, organized vortex motion becomes more significant as the width of a cavity suffices the development of shear layer. The flow information obtained provides a viable basis for examining mass transfer results from a separate study.

VII. RECOMMENDATIONS

The present study has demonstrated that the laser sheet light technique is very effective for investigation of flow characteristics, specially for the details of turbulence structures. The technique can be used for studies of many film cooling phenomena which are currently not understood but critical to developments of turbine blade cooling. One of the areas that needs to be addressed is the effects of fluid density ratio between the injection and mainstream. In an actual gas turbine, due to the marked temperature difference, the density of coolant is about 4 times greater than that of the mainstream. Nearly all the research efforts up to date have virtually excluded this effect, and data resulted from these studies may be inaccurate for actual turbine designs.

The suggested follow-up work should include detailed investigations of both flow and heat transfer characteristics with density ratios simulating actual turbine conditions. Heat transfer is the primary concern in film cooling and needs to be studied in parallel to the flow investigation. As a continuing effort from the summer faculty program, systematic research addressing the aforementioned aspects is being proposed to UES for an initiation grant. In the proposed study, the dense film cooling injection uses air cooled extensively by liquid nitrogen, and the mainstream is air maintained near room temperature. This innovative arrangement not only provides the density ratios desired but also is experimentally manageable. The flow visualization will use the laser sheet light technique described in the present study. In heat transfer aspect of the study, film cooling effectiveness and heat transfer coefficients are to be measured using a state-of-the-art infrared themographic system. The system will be provided

by the principal investigator's home institution, Carnegie Mellon University, as the cost-sharing toward this research.

REFERENCES

- Brown, G.L., Roshko, A., 1974, "On Density Effects and Large Structure in Turbulent Mixing Layers," J. Fluid Mechanics, Vol. 64, pp. 775-816.
- Chyu, M.K. and Goldstein, R.J., 1986, "Local Mass Transfer in Rectangular Cavities with Turbulent Separated Flow," Proc. 8th Int. Heat Transfer Conf., San Francisco, Vol. 3, pp. 1065-1070.
- Chen, L.T. and Roquemore, W.M., 1986, "Visualization of Jet Flames," Combustion Flames, Vol. 66, pp. 81-86.
- Rivir, R.B., Roquemore, W.M. and McCarthy, J.W., 1987, "Visualization of Film Cooling Flows Using Laser Sheet Light," AIAA-87-1914.
- Roquemore, W.M., Tankin, R.S., Chiu, H.H. and Lottes, S.A., 1986, "A Study of A Bluff-Body Combustor Using Laser Sheet Lighting," Experiments in Fluids, Vol. 4, pp. 205-210
- Sinha, S.N., Gupta, A.K. and Oberai, M.M., 1981, "Laminar Separation Flow Over Backsteps and Cavities, Part II - Cavities" AIAA J, Vol. 20, pp. 370-375.
- Yamamoto, H., Seki, N. and Fukusako, S., 1979, "Forced Convection Heat Transfer on Bottom Surface of A cavity," J. Heat Transfer, Vol. 101, pp. 475-479.

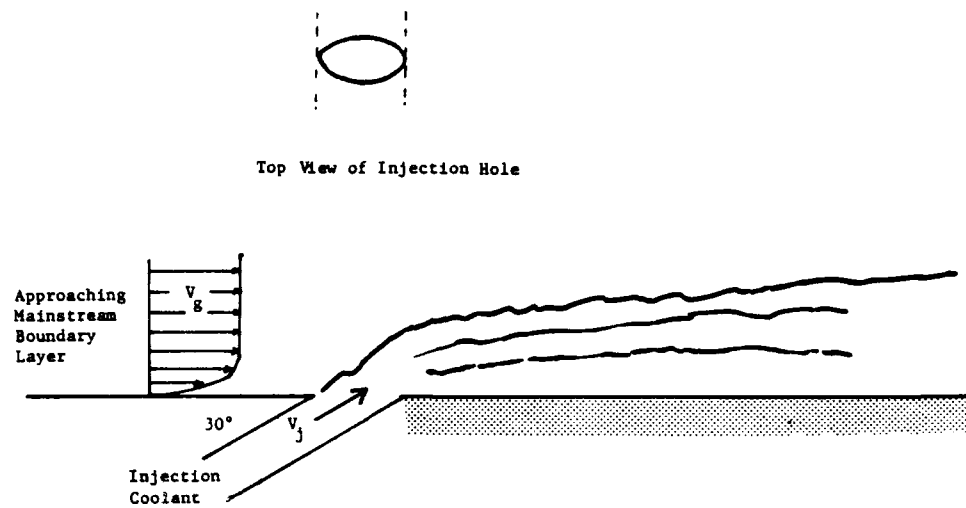


FIGURE 1 FILM COOLING WITH 30° INJECTION

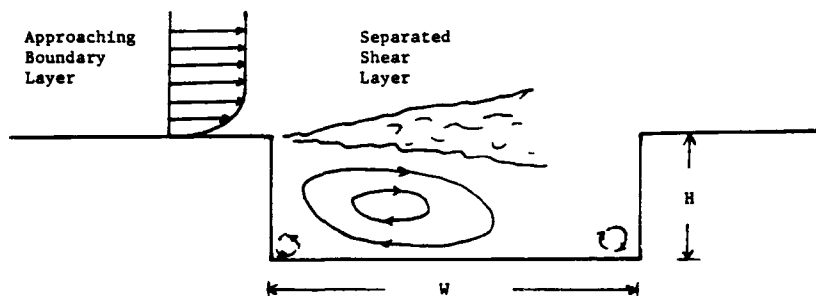
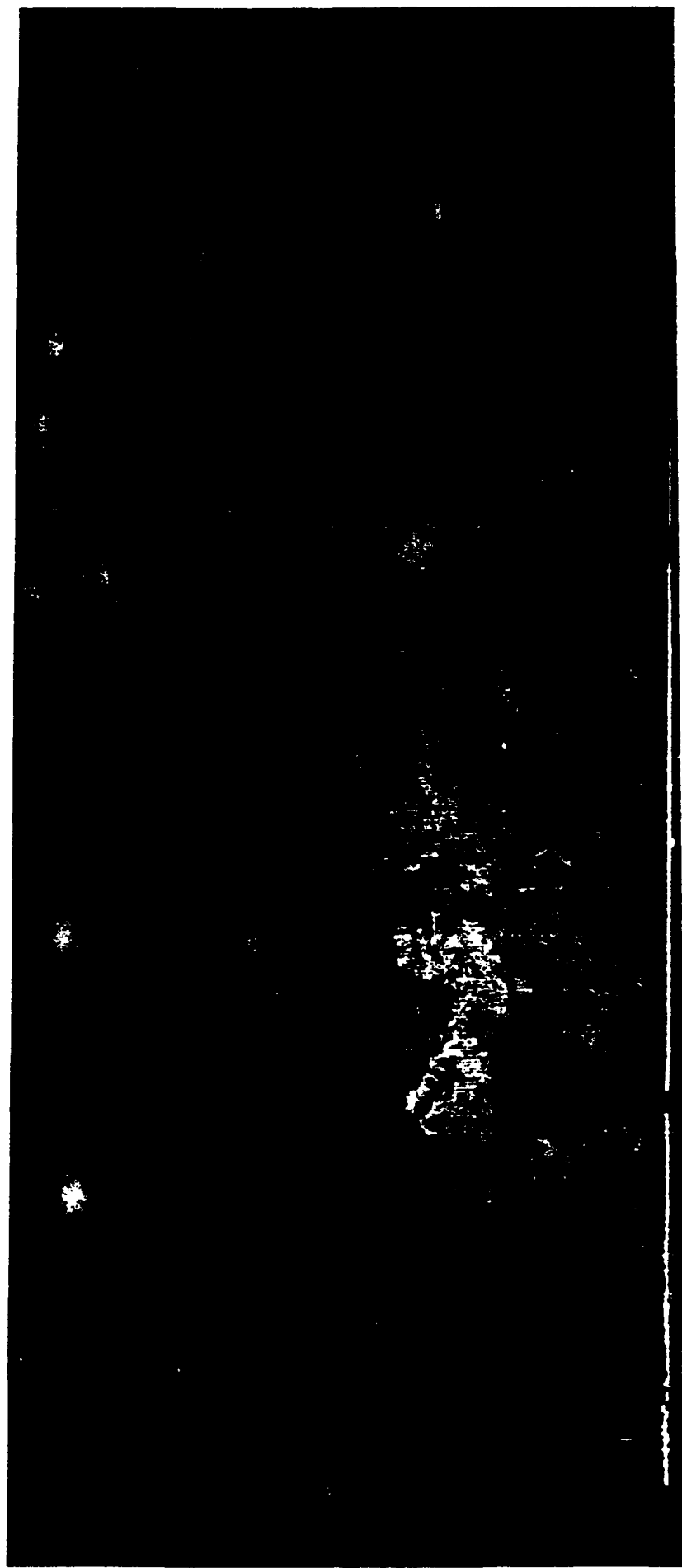


FIGURE 2 FLOW OVER A RECTANGULAR CAVITY

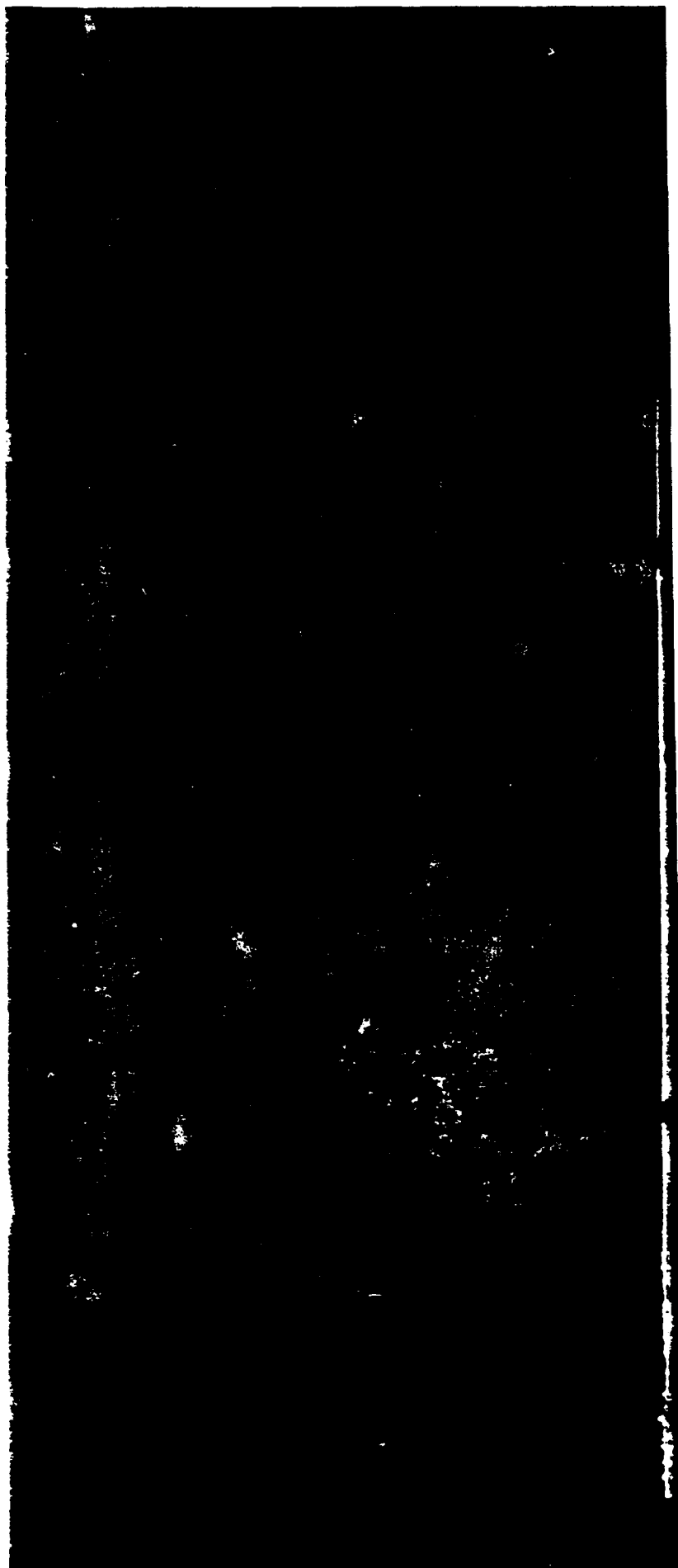


(a) $V_j/V_g = 0.11$

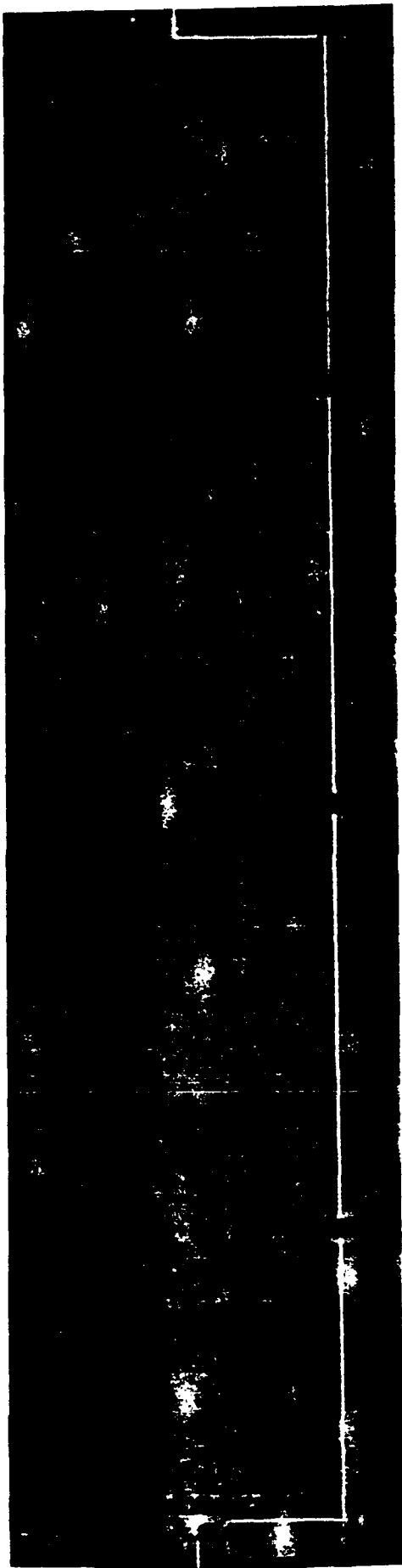
FIGURE 3 PHOTOS OF FILM COOLING FLOW; $Re = 3.9 \times 10^4$



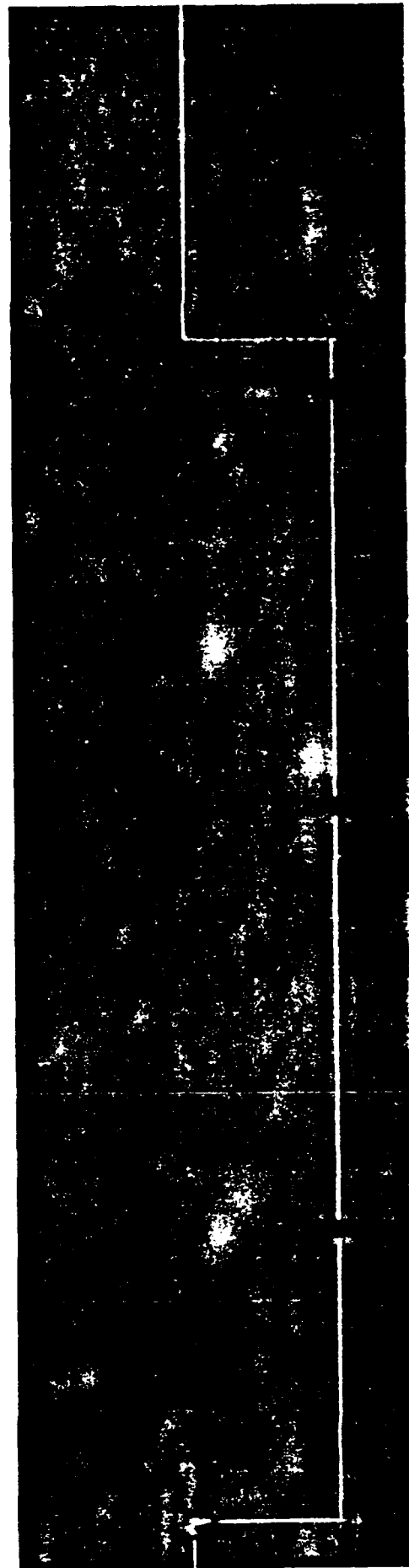
(c) $V_j / V_g = 0.16$



(b) $V_j / V_g = 0.13$

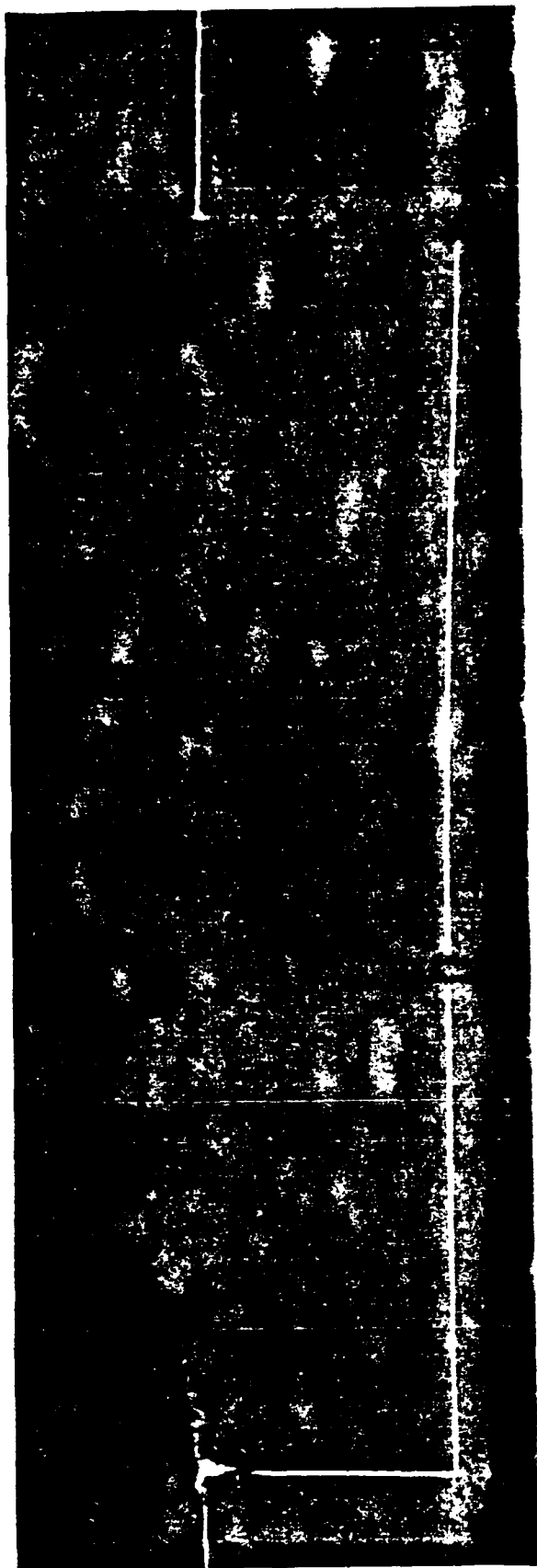


$w/H = 10$

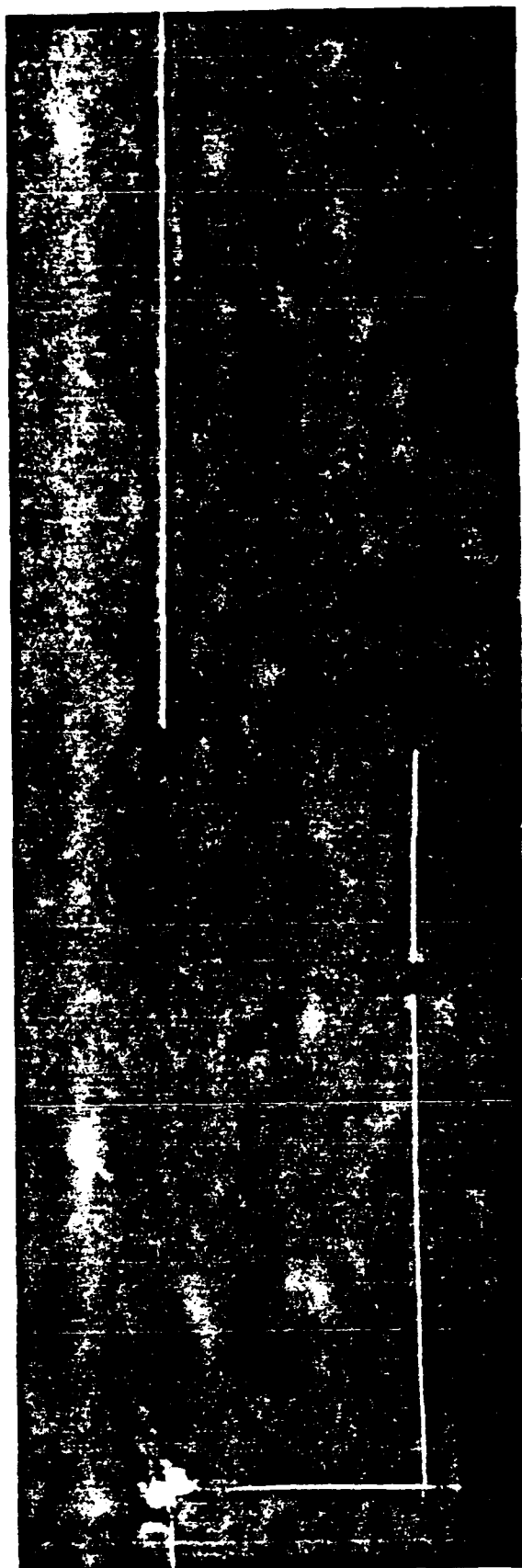


$w/H = 8$

FIGURE 4 PHOTOS OF CAVITY FLOW, $Re = 1.06 \times 10^5$



$W/H = 5$



$W/H = 3$

FIGURE 4 (Cont.)

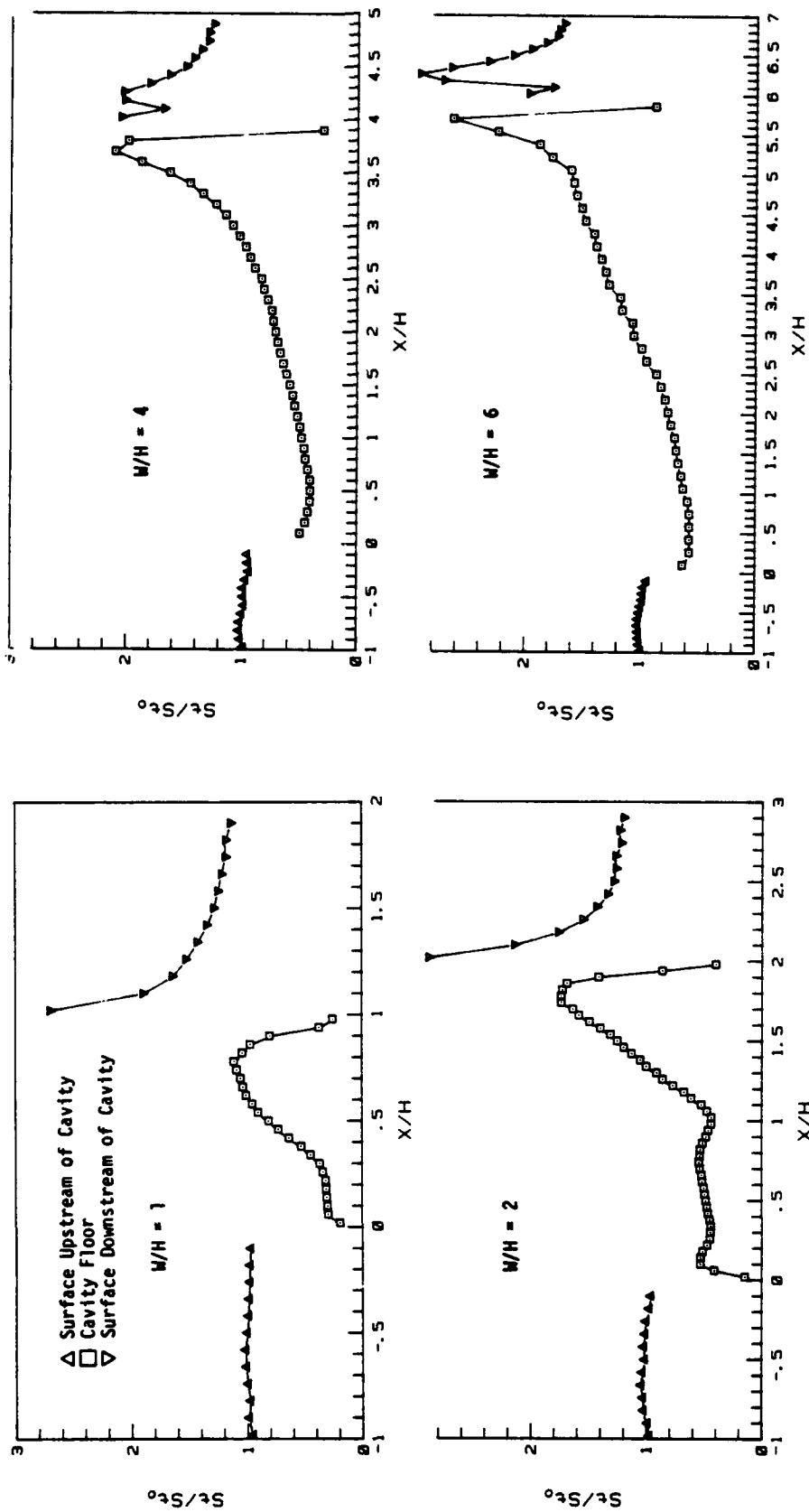


FIGURE 5 LOCAL MASS TRANSFER IN RECTANGULAR CAVITIES

1988 USAF-UES SUMMER FACULTY RESEARCH PROGRAM

Sponsored by the

AIR FORCE OFFICE OF SCIENTIFIC RESEARCH

Conducted by the

Universal Energy Systems, Inc.

Final Report

Experimental Study of Electronic Excitation of Xenon by Electron
Impact

Prepared by:	Jerry D. Clark, Ph.D.
Academic rank:	Assistant Professor
Department and	Physics Department
University:	Wright State University
Research Location:	Aero Propulsion Laboratory Wright Patterson Air Force Base Dayton Oh
USAF Researcher :	Charles DeJoseph
Date:	Sept 26, 1988
Contract No:	F49620-87-R-0004

Experimental Study of Electronic Excitation of Xenon by Electron Impact

by

Jerry Clark

ABSTRACT

Preliminary 5d optical excitation functions of atomic xenon have been measured from the onset to 100 eV. Particular interest has centered on the technique of fourier transform spectroscopy for the determination of these cross sections. Cross sections of the 5d[3/2] level for the lines at 2.026 microns and 1.73 microns were measured to be $1.89 \cdot 10^{-17} \text{ cm}^2$ and $7.17 \cdot 10^{-18} \text{ cm}^2$ respectively at 50 eV electron energy. Interesting structure has been observed in the excitation function the 2.026 micron line below 10 eV and between 10 and 50 eV. Acquisition of spectra for the determination of optical cross sections is discussed.

Acknowledgement

The author would like to express his gratitude to the Air Force and Universal Energy Systems for the administration and sponsorship of thisvaluable program. The helpfulness and friendliness of the personnel at UES and Aero Propulsion Laboratory made this summer a real pleasure.

The rewarding research experience I had this summer is in no small part due to the collaboration with Charles DeJoseph. Others always willing to help also deserve a mention including Bruce Wolfe and Bob Knight. A special thanks to Dr. Alan Garscadden for the opportunity to work within his group.

I. INTRODUCTION

Xenon the largest of the stable rare gases is an important constituent in many laser systems due the high relative energy content in the excited states and their high reactivity. One such laser system is the lasing of neutral xenon lines lying in the wavelength range between 1 and 5 microns. Many of these transitions correspond to transmission windows of the atmosphere. These lasing lines which originate on the 5d levels and terminate on the 6p levels are known to have extremely high gains. Recent reports by Russian scientists¹⁻² indicating high energy laser pulses from a high pressure mixture of argon and xenon excited by electron impact have stimulated the Air Force to refocus on the xenon atomic laser. The ability to model a laser plasma is advantageous in determining optimal operating parameters for a laser system. To do this basic atomic data on the probability of excitation to a particular state by electron impact is vital. This probability or cross section is dependent on the electron energy and a plot of the cross section versus electron energy is called an excitation function. Many studies³⁻⁵ have been made of optical excitation functions in xenon but few have been made for the upper laser level transitions the 5d levels due to the difficult experimental problems in the infrared region.

II. RESEARCH OBJECTIVES

The goal of this project was two fold. First to measure the optical excitation function for the 5d levels in neutral and xenon. Second, to demonstrate the feasibility of utilizing fourier transform spectrometry to acquire optical excitation functions.

The optical excitation function or optical cross section is obtain by exciting a known sample of gas with a flux of electrons of defined energy and measuring the radiance from the excitation region. Consider an electron beam of cross sectional area A and current I the photon flux from the interaction region of length Δx is given by:

$$F_{ij} = N \Delta x Q_{ij} I/e$$

Here F_{ij} is the photon flux from transition i to j and Q_{ij} is the optical cross section. N is the gas density and e is the charge on the electron. The radiance from the transition which can be measured by a

calibrated spectrophotometer is given by:

$$R_{ij} = F_{ij} \frac{hc}{\lambda} \frac{1}{4\pi \Sigma} \frac{1}{\Delta\lambda}$$

Here Σ is the surface area of the emitting region and $\Delta\lambda$ is the doppler broadened linewidth given by:

$$\Delta\lambda = \left[\frac{8kT \ln(2)}{mc^2} \right]^{1/2}$$

Therefore by measuring the gas pressure, the electron current, the beam geometry and the transition radiance the optical cross section for that level may be determined. The following is a discussion of the summers effort to assemble an experiment to perform this measurement.

III. EXPERIMENT

The apparatus used in these studies involves three basic components: (1) an evacuated collision chamber, (2) an electron gun to provide a flux of electrons into the field free collision region, (3) the necessary electronics to detect and record the radiation emitted from the excited atoms. The techniques applied for acquisition of the data will be discussed later. Below we will describe the details of the construction and parameters of the apparatus used.

The vacuum chamber or collision chamber was a stainless steel six way cross with four eight inch "conflat" flanges and two six inch "conflat" flanges. The chamber was pumped using a model TPU 270 Balzers turbo molecular pumping stand. This pump had a rated pumping speed of 270 liters per second in air and we could reach a base pressure in the mid 10^{-8} range without baking. The pump was attached to one of the eight inch ports with a manually controlled gate valve between the chamber and pump. The vacuum pressure was determined using a Baird Alpert Nude gage with a series 270 Granville Phillips controller attached to one of the eight ports of the vacuum chamber. The other appendages to the chamber were for the electron gun, viewing ports, gas pressure measurement, and gas inlet. The viewing ports consisted of sapphire windows one 4 inches in diameter and the other 1 inches in diameter mounted on ports 180 degrees apart. The large window was for viewing the collision region by the detection electronics while the smaller was used only for alignment and visual inspection. The sample gas was inserted into the interaction region by a capillary array used to form an atomic beam or by flooding the chamber through a mini conflat flange in the chamber. The array was mounted on a long quarter inch

stainless tube and was inserted into the vacuum chamber from the port directly above the pump such that the gas flow was into the pump throat. The gas pressure was measured by means of MKS capacitance manometers one 1 torr head (220-BHS) mounted on a "mini-conflat" flange directly on the collision chamber and the other a 10 torr head (315-BHS) mounted on the high pressure side of the capillary array.

The gas pressure was measured both as a background pressure in the collision chamber and as a backing pressure for the capillary array. The exact pressure in the interaction region due to the flow of the atomic beam is still a large question mark, yet flowing the gas allowed us to maintain a higher atomic number density in the interaction region. We believe this pressure may be calibrated if one can seal the chamber and obtain an optical cross section measurement under a stagnant pressure condition or flow a gas under identical conditions with known cross section such that a pressure calibration may be made. In the first case we could not seal the chamber without "killing" the electron gun probably due to outgassing of materials detrimental to the cathode. We did not try to solve this problem until the last week of the summer when we placed into the vacuum system a small getter pump of unknown specifications and history (previously used). This still failed to allow us to completely close the gate valve yet it looked promising. Perhaps baking the system and a new getter pump might allow this measurement. The second calibration technique was not applied since we were not aware of any strong well known transitions in other simple gas systems which would maintain similar flow conditions.

ELECTRON GUN

In the initial phases of this experiment calculations of expected signal for various experimental parameters indicated that the lines of interest would be just detectable with the a 1 micro amp. beam and a 1 mm. spot size. These parameters were the maximum rating for a commercially available gun from Kimball Physics Inc. Therefore this gun was chosen for the initial studies and was the prime reason for the choice of the vacuum chamber discussed above due to the near perfect dimensions for interfacing the Kimball gun. In testing the gun we readily obtained the 1 micro amp. beam current under vacuum or very low gas pressure conditions. The first test of the system used a helium test gas since it appeared to be a well studied system, has some

reasonably bright visible transitions which are needed for alignment purposes, and has a very strong transition in the near IR close to our wavelengths of interest. It was found that when helium was inserted to a background pressure of a few tenths of a millitorr the collected current reduced significantly (less than 0.5 micro amp). In addition the beam was virtually unobservable visually or with the spectrophotometer due to the weak emissions. Under ideal conditions the beam could be observed and appeared to have close to it's quoted spot size of 1 mm^2 . This gun was considered to be limited in the beam current and we opted for a more robust design.

The next gun we tried was a gun constructed in house and was used previously in similar experiments by Steven³ and Walker⁴. This gun has a 1 cm diameter cathode and according to previous reports was producing beam currents in excess of 1 milliamp. which is a significant jump from the Kimball gun. This gun was of a five grid design and along with a faraday collection cup was housed in an approximately 3 inch diameter by 4 inch length cylindrical copper can with a slits on the side for radiation emission and a small hole on top for insertion of the capillary array. In tests with this gun we were able to obtain beam currents of a couple of hundred microamps and saw visible emissions from the interaction region in both helium and neon. Observation with the spectrophotometer indicated weak but observable signal from the collision region but with a relatively large background signal from the cathode. For these reasons and alternate design was considered.

The last gun constructed was a modification of the gun used by Steven and Walker. The electron gun was constructed using a five grid design. The first grid or cathode was biased to a negative potential which provides the accelerating voltage for the electron beam. The next two grids provide for current control and focusing properties. The electron gun control electronics provided the second grid(anode) with a constant +12 volts referenced to the cathode while the third grid could be biased in two modes. It could be biased with respect to ground thereby having a variable potential when the cathode was swept or could be connected to ± 15 volt supply referenced to the cathode. Both of these bias modes were used, unfortunately not enough time existed this summer to do a critical study of the electron gun and its various bias modes for optimal performance. The fourth grid was again at the cathode

potential and the fifth was grounded which provided the final acceleration.

This gun differed from Walker's in that the cylindrical copper radiation shield was cut down just to house the gun. The faraday cup and interaction region were outside the radiation shield which we believe provides better pumping when using the capillary array allowing a significant (even if unknown) pressure in the interaction region while maintaining the electron gun at a lower background pressure. In addition the shield was cooled by wrapping copper tubing about the radiation shield and flowing cool water while the cathode was on. This gun had a significant reduction in the background emissions from the previous design probably due to the gun being set back farther from the interaction region. The cooling seemed to do little in terms of the background emissions yet seemed to help reduce quenching of the cathode by impurities. The faraday cup was of cylindrical stainless steel covered with a fine mesh on one end which was transparent to the electrons and at ground potential but shielded the interaction region from the collector cup at the other end which was biased between 0 and +40 volts with respect to ground suppressing secondary electrons.

LIGHT DETECTION SYSTEM

The excitation emitted from the interaction region was collected and focused onto a Bomem DA3 spectrophotometer. The collection mirror was a four inch diameter spherical mirror with a 60 cm focal length. The collimated light directed by two plane mirrors to a four inch diameter off axis parabolic mirror with a focal length of 32.5 cm which focused the signal on the circular aperture (3.5 mm) of the spectrophotometer. The spectrophotometer was a fourier transform system of a classical Michelson design. The spectral coverage is limited by the detector and beam splitter and ranged in most of these experiments between 4000 cm^{-1} to 13000 cm^{-1} . The detector used predominantly was an InSb detector at 77 K with a cold filter to limit the spectral coverage, the approximate Noise equivalent power (NEP) was $6 \cdot 10^{-13}\text{ W/Hz}^{1/2}$. The beam splitter was made of fused silica and was the limiting component at 4000 cm^{-1} . The dominate noise component was detector noise even at highest preamp gain. A measurement of the noise voltage from the Bomem detector electronics using a SRS 510 lockin verified our noise calculations considering the quoted noise current from the detector.

DATA ACQUISITION

One of the stated goals of this study was to demonstrate the usefulness or multiplex advantage of the fourier transform spectrometer to the conventional optical filtering and synchronous detection. This involves acquisition of the spectral emissions from the source over the bandwidth of the spectrophotometer at a particular electron voltage, current and sample pressure. Additional spectra can then be acquired with varying electron voltage such that a tabulation of relative signal versus electron voltage can be performed. This would represent the relative excitation function for each observed spectral line. If the spectrophotometer was calibrated such that it measured absolute radiance the tabulation can represent the optical excitation function or the optical cross section as a function of electron energy. This technique is powerful if one can detect several lines of interest and make use of the multiplex advantage. However in our early experiments this summer very little signal was observed particularly from the 5d levels of interest. Not until the last couple of weeks of this summer were reasonable spectra observed.

The spectra in figures 1 and 2 represent the best data taken this summer where the spectra in figure 1 was obtained at a pressure of 1.4 mtorr with the chamber flooded. This data presents the best opportunity for acquiring optical cross sections. The spectra in figure 2 represents our typical best spectra and was taken using the capillary array to enhance the pressure in the interaction region. Each of these data sets were acquired at an electron voltage 50 volts and currents over 1 milliamp. Also of note is that the intensity scale in each of these figures is calibrated in Watts/cm²/sterradian/cm⁻¹.

The calibration of the spectra is performed by knowing the instrumental response function of the spectrometer. This is determined by observing a blackbody radiator of known temperature and comparing the observed spectral response to that of a theoretical blackbody. This was accomplished using an Infrared Industries blackbody source at 1000⁰C and using the calibration calculations of the spectrophotometer software. Calibration checks for the system were made by collecting blackbody spectra at other temperatures and calibrating with the instrument response function determined at 1000⁰C these were then compared to theoretical blackbody functions with excellent agreement.

Optical cross sections may be determined from this data by measuring the integral intensity ($R \Delta\lambda$) of a line of interest and using

$$R \cdot \Delta\lambda = 1.726 \cdot 10^{-2} \cdot Q_{ij} (\text{cm}^{-2}) \cdot P(\text{mtorr}) \cdot I(\mu\text{A}) \cdot \sigma(\text{cm}^{-1})$$

Here geometrical considerations of interaction region dimensions and collection optics have been incorporated into the constant in front. Two 5d lines can be seen in the spectra in figure 1 for which the optical cross section may be determined the 2.026 micron line and the 1.73 micron line. Both of these lines originate from the same upper level the $5d[3/2]_1$ state. The cross section for each state at 50 volts was determined at a pressure of 1.4 mtorr and is given below.

$$Q(2.026) = 1.89 \cdot 10^{-17} \text{ cm}^{-2}$$

$$Q(1.73) = 7.17 \cdot 10^{-18} \text{ cm}^{-2}$$

As mentioned earlier the above represents data taken at only one electron voltage obtained in the last week of the summer. Previous data samples had limited success in observing the 5d lines. Therefore an alternative was taken since we had an optical bandpass filter which was centered over the 2.026 μm line which originates on a 5d level. The alternative technique involves filtering out all radiation except that from the line of interest, modulating the electron beam and synchronously detecting the radiation. This allows for an increase in the signal to noise for that transition. In this experiment the Bomem spectrophotometer was used as an optical mount for the filter and detector. This allowed the detector with the cold filter to be used, the filter bandpass to be measured with the spectrometer and the same optics and apertures to be used. The electron beam was modulated at 100 Hz by switching the voltage to the cathode which was set by a Kepco power opamp supply referenced by 10 bit D/A from the lockin amplifier. The lockin synchronously detected the signal from the detector and output the result to a HP 9400 computer which controlled the experiment. The computer collected three samples over one time constant which was set at 100 seconds. The computer also sampled the current from the gun such that the signal could be normalized to changes in beam current. The computer swept the electron beam voltage by changing the the value on D/A in increments of 1 volt or 5 volts. Three time constants were

allowed before sampling on changes of the beam voltage. Figures 3 through 5 represent the results of this study. Figure 3 is a plot of rms signal (volts) from the detector divided by rms current (amps) from the electron beam versus electron energy in volts. The error bars represent the statistical standard deviations for the number of measurements made at that accelerating voltage. This curve represents the relative excitation function for the 2.026 micron line at a pressure of 1.4 millitorr. This pressure was obtained by flooding the chamber (not through the capillary array) however with very little throttle of the pump. Figure 4 represents a similar data at 0.8 millitorr with acceleration voltage from 0 to 50 volts. Comparison of this data indicates reasonable agreement with an onset at approximately 12 volts and a peak in the excitation function at about 50 volts. The shape of the excitation function is very similar to the only other known measurement of the excitation function by Borozdin and Smirnov⁶ for this line.

An interesting feature of the excitation function is the large signal/current below 10 volts. It is unclear whether this is real or an artifact of the ratio of two small values, the signal and the current. However it is consistently observed as can be seen in figures 3 and 4. Figure 5 shows the signal component of the data taken at 1.4 millitorr and there is evidence of a small increase in the signal below 10 volts. It should be pointed out however that the noise components the detector signal was measured to be approximately 8 mvolts/ $\sqrt{\text{Hz}}$ while the detected signal is well less than 1 mvolt. If this signal is real it might represent a two step excitation probably from the metastable states of xenon. This could have a significant effect on populating the 5d levels if the excitation cross sections from the metastable levels are large.

The data in figures 3 and 4 also show significant structure between 10 and 50 volts. The cause of this structure is not known by this investigator and needs further study. It may be due again to two step processes or cascading from higher levels at these electron energies.

The relative excitation functions could be converted to optical excitation functions if the system response is calibrated. The calibration procedure involved measuring the optical response of the narrow band filter and is shown in figure 6, assume that at the spectrometer response is the same shape as when scanned and use the

blackbody as a standard source. A calibration was then accomplished with the optical cross section determined by

$$Q(\text{cm}^{-2}) = \frac{1.042 \cdot 10^{-13}}{\text{Gain} \cdot P(\text{mtorr})} \cdot \frac{V(\text{volts})}{I_{\text{rms}}(\text{amps})} \quad @ \ 2.026 \ \mu\text{m}$$

This can be compared to the results obtained with the fourier transform method at 50 volts excitation energy. From the data in figures 3 and 4 the optical cross sections are:

$$\text{at } 1.4 \text{ mtorr } Q = 1.99 \cdot 10^{-17} \text{ cm}^2 \text{ at } 50 \text{ volts}$$

$$\text{at } 0.8 \text{ mtorr } Q = 1.52 \cdot 10^{-17} \text{ cm}^2 \text{ at } 50 \text{ volts}$$

These values compare extremely well to the values determined above but are an order of magnitude larger than the peak in the excitation function published by Borozdin. It should also be noted however that Filipovc et al⁷ using electron loss scattering techniques have measured a integral cross sections for the 5d[3/2] level at 30 volts of $8.88 \cdot 10^{-17} \text{ cm}^2$.

IV. RECOMMENDATIONS

Although the optical cross sections determined this summer are reasonable, they represent preliminary results. To completely detail these measurements in the xenon system and to extend the technique to other levels and atomic systems will require additional study. I have enumerated several areas below which I believe can enhance the overall effort.

- 1) Study the pressure and current effects on the optical cross section. Although we took efforts to stay in a linear range in signal versus pressure, previous studys indicate significant variation of excitation functions with pressure. Therefore a detailed study with variation in pressure and electron current should be undertaken.
- 2) Evaluation of the electron gun is important. Much of the work this summer involved finding an electron gun which will produce signals capable of being detected. The electronics which controlled the gun was not well documented or well understood and a detailed study of the operational parameters of the gun is essential. In addition, the gun was not stabilized for constant electron current. This is of particular importance when taking a long integration with the fourier transform spectrometer. A design for the stabilization was made this summer but was not implemented. I believe this should be done.

3) I believe we have demonstrated a powerful technique for the determination of optical cross sections with the fourier transform spectrometer. This work could be extended in several ways. First the measurement of optical cross sections for other levels is currently present as can be seen from the many transitions in figure 2. This work could also be extended toward shorter wavelengths with other detectors or to longer wavelengths with a different beam splitter. A CaFl beam splitter is definitely recommended such that the possibility of observing transitions of the 5d levels at longer wavelength exists. Second, the technique can be easily applied to other atomic systems as spectra was observed in helium, neon and argon this summer.

4) Finally a critical look should to be made of the results of these measurements. Several questions come up such as: What is going on below 10 volts of electron energy?; What is the role of cascading in the measured excitation functions?; and What is the effect of the measured cross sections on the xenon laser system?. The answers to the questions are not obvious and will require a great deal more study.

References

1. F.V. Bunkin et al, "High-Power laser of 270-liter active volume utilizing infrared transitions in Xenon", Sov. J. Quantum Electronics 16, 576-577, April 1986.
2. N.G. Basov et al, "Possibility of construction of a pulse-periodic large- volume electron beam-controlled laser utilizing infrared transitions in Xenon atom and characterized by a specific output of $0.5-1 \text{ W/cm}^3$, Sov. J. Quantum Electronics, 16, p. 1008-1009, Aug. 1986.
3. Mark D. Stephen, "Measurements on Electron Impact Excitation Functions of Xenon Transitions", Master's Thesis, Air Force Institute of Technology, WPAFB, Ohio (1979)
4. Keith G. Walker, "Electronic Excitation of Atomic Xenon by Electron Impact", Final Report 1983 USAF-SCEEE Summer Faculty Research Program
5. Max L. Lake, "Experimental Measurements of Cumulative Excitation and Ionization in Atomic and Molecular Gases", Technical Report AFAPL-TR-77-84
6. V.S. Borozdin and Yu. M. Smirnov, "Research of the excitation of xenon by electron impact in the IR region of the spectrum", Trudy Moskovskogo Energeticheskogo instituta, Prikladnaya, Fizicheskaya Optika Vol 350, 1978, p 91-93.
7. D. Filipovic et al, "Electron-impact excitation of xenon at incident energies between 15 and 80 eV", Physical Rev. A , 37, p. 356-364, 1988.

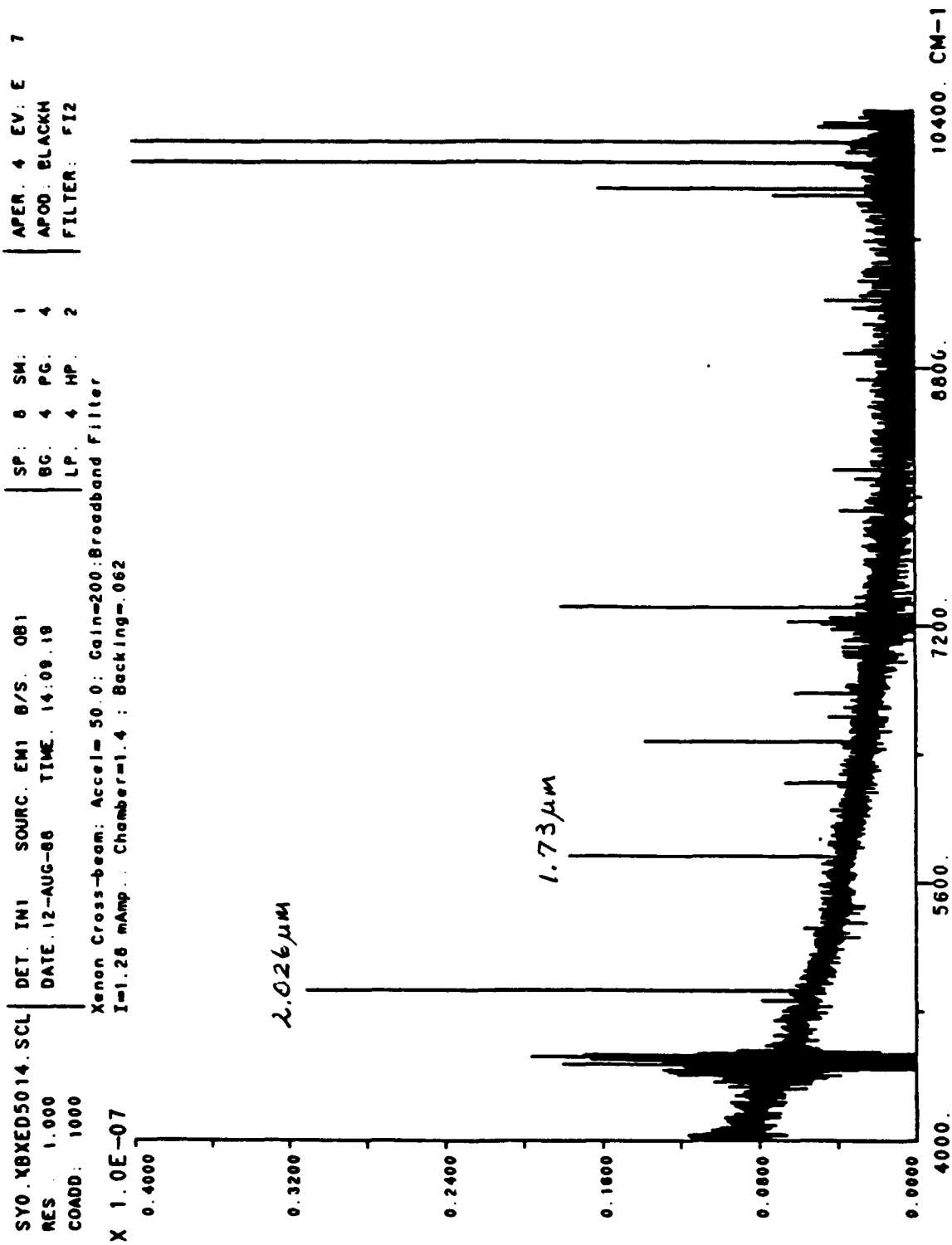


Figure 1

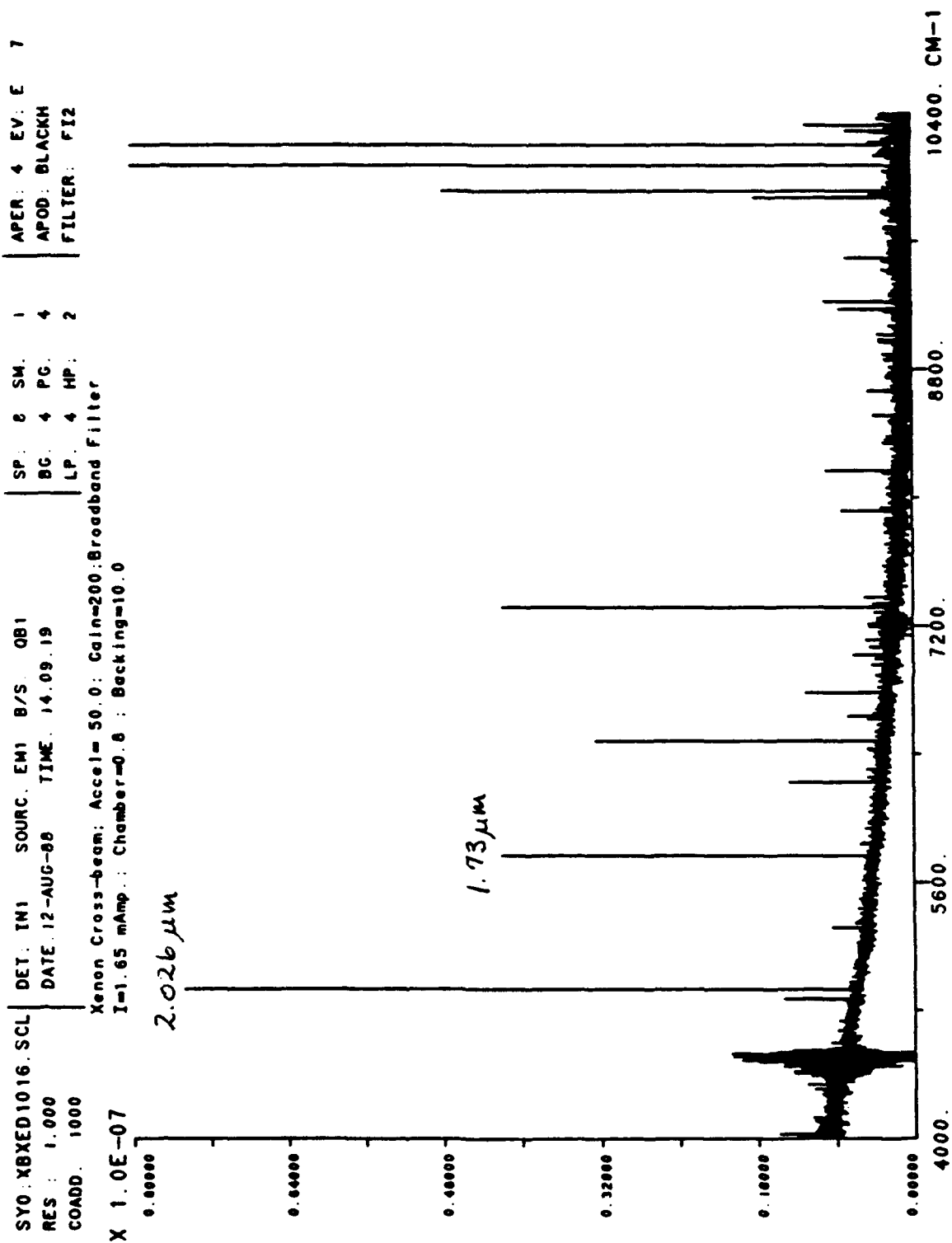
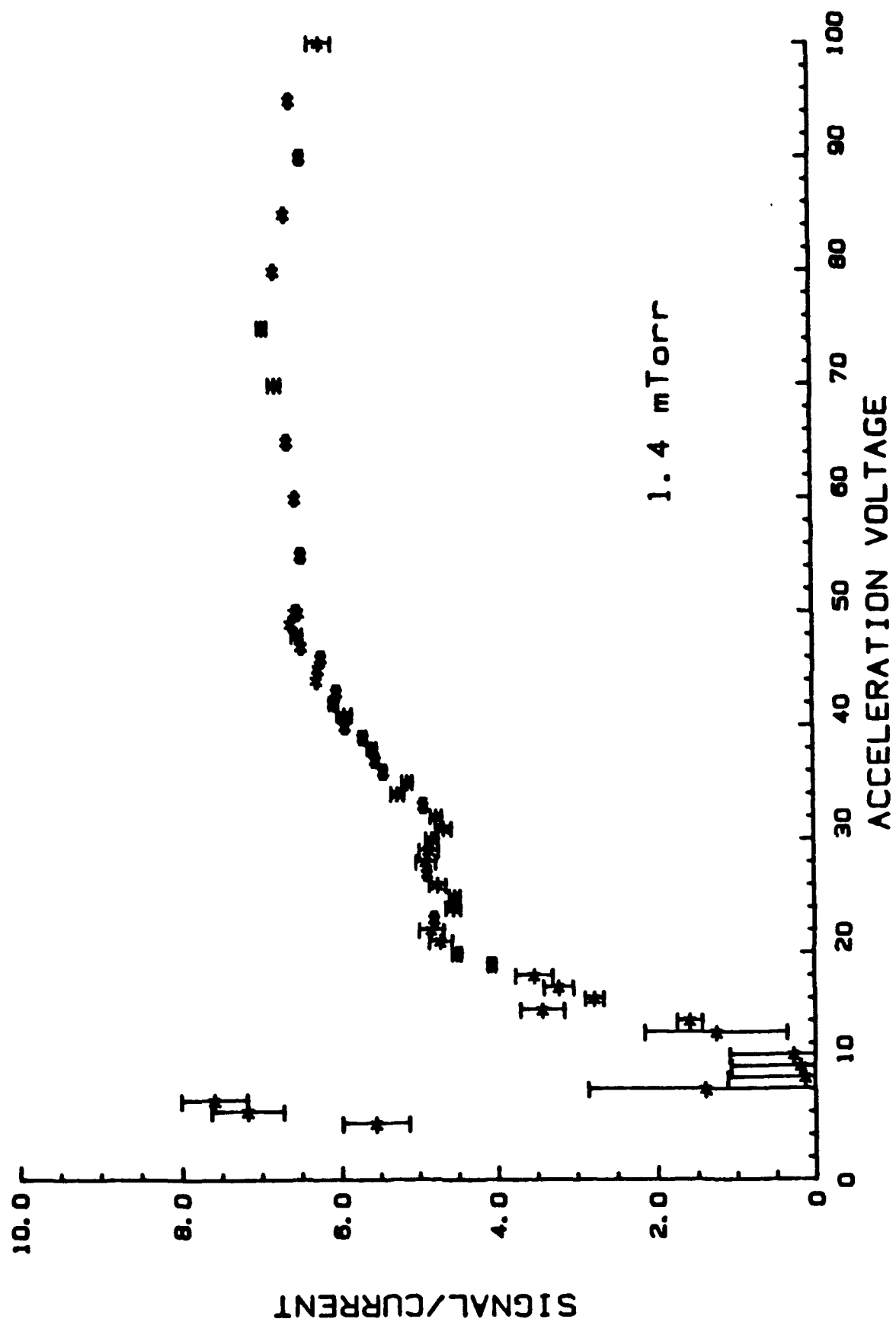
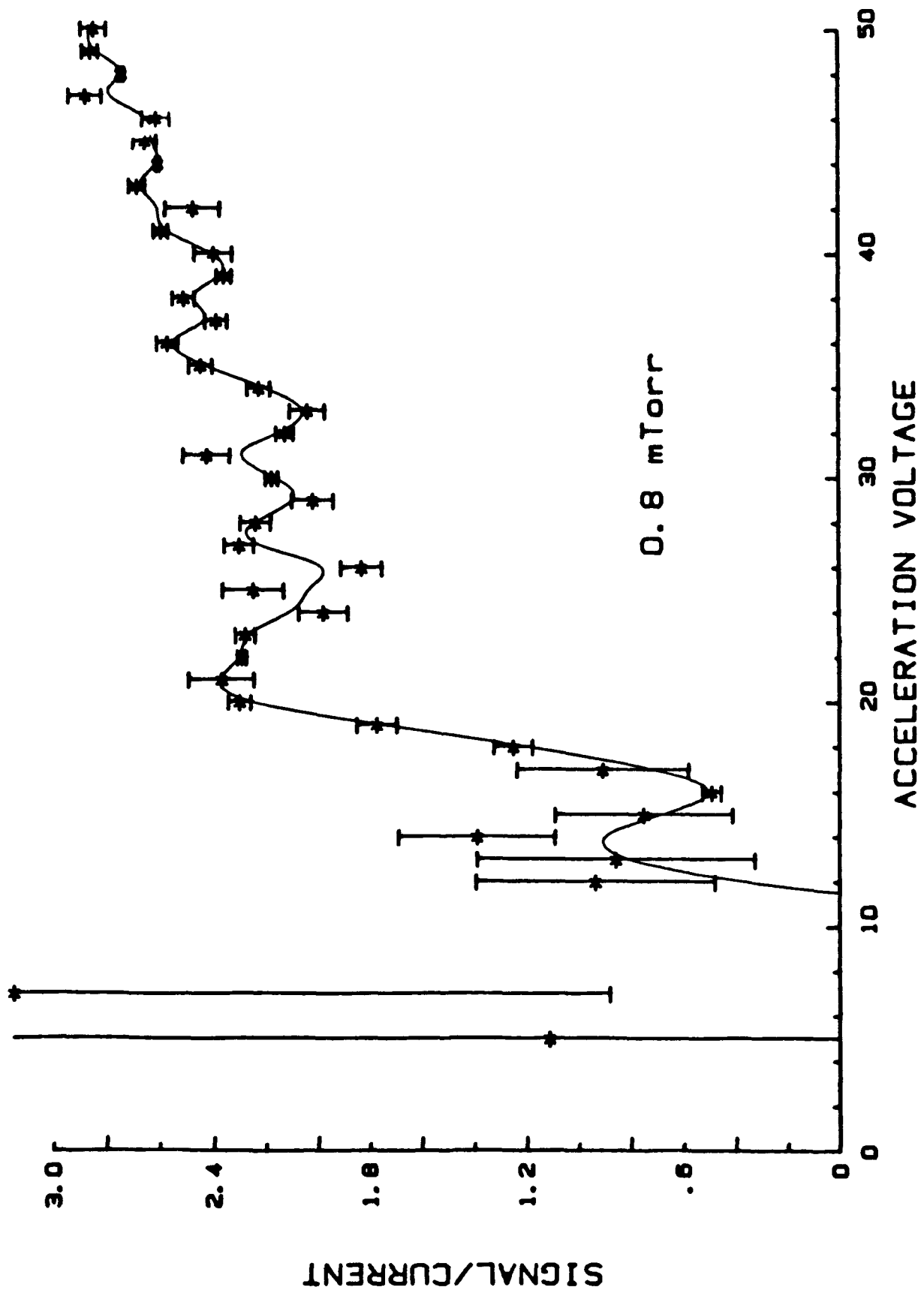


Figure 2



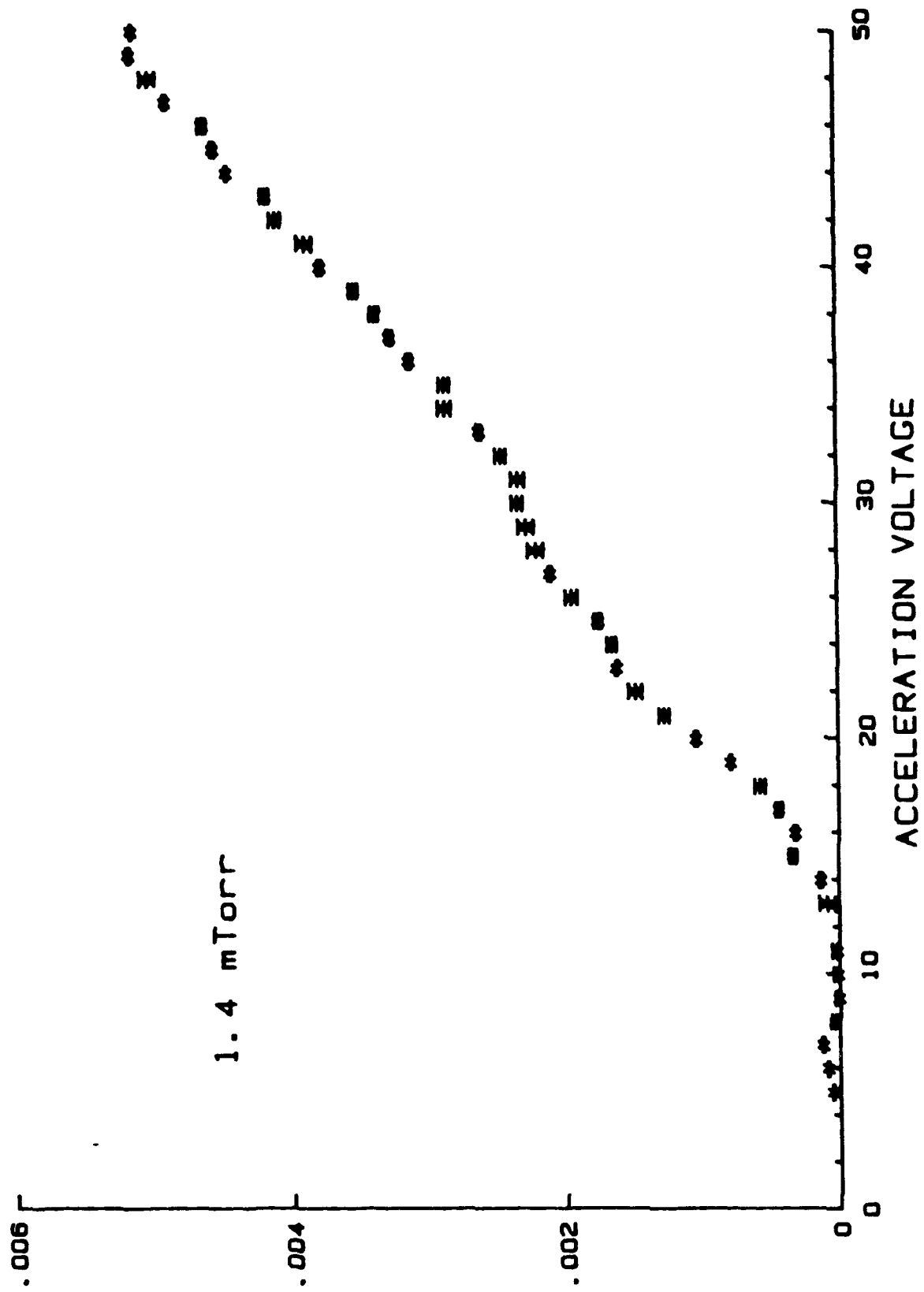
72-17

Figure 3



72-18

Figure 4.



7VNGIS

72-19

Figure 5

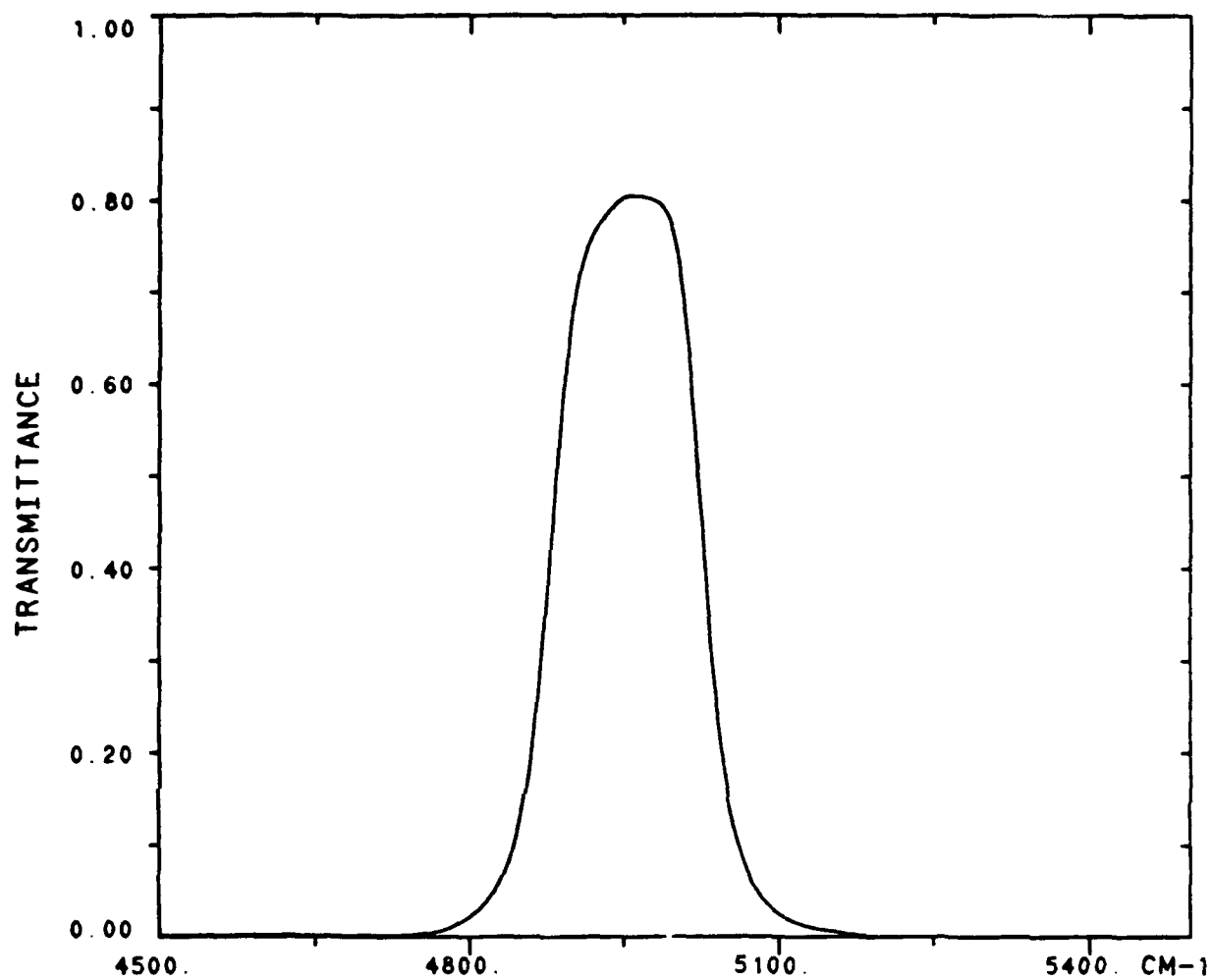


Figure 6
72-20

**1988 USAF-UES SUMMER FACULTY RESEARCH PROGRAM/
GRADUATE STUDENT RESEARCH PROGRAM**

**Sponsored by the
AIR FORCE OFFICE OF SCIENTIFIC RESEARCH**

**Conducted by the
Universal Energy Systems, Inc.**

FINAL REPORT

CARS THERMOMETRY IN DROPLET-LADEN FLOWS

Prepared by: Derek Dunn-Rankin
Academic Rank: Assistant Professor
Department and Department of Mechanical Engineering
University: University of California, Irvine
Research Location: AFWAL/POSF
 Wright-Patterson AFB
 Dayton, OH 45433
USAF Researcher: Dr. Tom Jackson
Date: September 10, 1988
Contract No: F49620-87-R-0004

CARS THERMOMETRY IN DROPLET-LADEN FLOWS

by

Derek Dunn-Rankin

ABSTRACT

The ultimate objective of this research is to measure simultaneously, and non-intrusively, all of the parameters important in gas turbine combustion. These parameters include droplet size, droplet velocity, gas velocity, gas temperature, and major gas phase species concentration. In support of this ultimate objective, the present research examines the potential for coherent anti-Stokes Raman scattering (CARS) to provide reliable temperature measurements in the presence of liquid droplets. The droplets cause a dielectric breakdown by focussing the CARS laser beams. This breakdown produces a plasma that can disrupt or obscure the CARS signal. Specifically, we examine the influence of laser induced breakdown on the CARS signal, and we determine the importance of droplet position relative to the sample volume, and the importance of droplet concentration, on the reliability of CARS temperature measurements in droplet-laden flows. In addition, we propose a reliable data reduction procedure to minimize the disruptive influence of laser induced breakdown on CARS temperatures.

I. INTRODUCTION

Proper characterization of spray combustion flows requires spatially resolved maps of droplet size, droplet velocity, droplet composition, gas velocity, gas species concentration, and gas temperature. In addition, it is important to determine these properties without disturbing the flow-field. The Aero Propulsion Laboratory at WPAFB has developed and employed several non-intrusive optical diagnostic techniques for this purpose (Roquemore et al., 1986). However, non-intrusive temperature measurements in liquid spray flames have not been reported. Our eventual goal is to provide these temperature measurements, simultaneous with measurements of the flow field and the droplet field, by combining coherent anti-Stokes Raman scattering (CARS) thermometry with phase-Doppler interferometry. Toward this goal, the present work concentrates on resolving difficulties of CARS thermometry in droplet laden flows.

My research has examined two-phase combustng flows for many years, primarily utilizing non-intrusive optical diagnostics. Previously, these diagnostics have been limited to particle sizers and particle velocimeters. Recently, however, I have become interested in spectroscopic interrogation of two-phase flow. Spectroscopy provides a new avenue for examining temperature, and species concentration in combustng flows. Similarly, the Aero-Propulsion Laboratory at Wright-Patterson AFB is beginning to use spectroscopic techniques for two-phase flow investigations. Our parallel interests, combined with the technically advanced expertise of the Aero-Propulsion Laboratory, makes my collaboration at Wright-Patterson particularly fruitful.

II. OBJECTIVES OF THE RESEARCH EFFORT

The ultimate objective of this research is to measure simultaneously, and non-intrusively, all of the parameters important in gas turbine combustion. These parameters include droplet size, droplet velocity, gas velocity, gas temperature, and gas species concentrations. In support of this ultimate objective, the present research examines the potential for CARS to provide reliable gas temperature measurements in droplet-laden flows.

There are three specific objectives in the study: (1) determine the influence of

droplet induced breakdown on the CARS spectrum, and how that influence affects the temperature fit of the experimental spectrum, (2) explore software tests to extract valid CARS temperature measurements from spectra affected by breakdown events, and (3) determine the droplet number density where droplet breakdown has significant effects.

III. BACKGROUND—CARS in Particle Laden Environments

CARS is a non-linear spectroscopic technique for measuring the energy spectrum from an ensemble of molecules. Through quantum mechanics, the energy spectrum is a predictable function of temperature. CARS thermometry determines temperature by comparing the measured energy spectrum to calculated spectra using temperature as the fitting parameter. Because CARS thermometry relies on spectral fitting, disruption of the measured energy spectrum by scattered light has potentially serious consequences for the accuracy of the temperature measurements.

One source of scattered light is laser induced breakdown (LIB) caused by particles in the flow. Laser breakdown occurs in clean air at standard temperature and pressure at a laser energy density of approximately 10^{12} W/cm² for a wavelength of 532 nm. This energy is slightly above the energy density found in typical CARS systems. However, large particles in the sample volume reduce the breakdown threshold energy density by 1–2 orders of magnitude, and consequently, any large particle in the CARS interaction volume produces a breakdown. Beiting (1985), Lucht (1988), and Noda et al. (1987) showed significant breakdown, and disruption of CARS signals with solid particles (1–100 μ m) present.

The plasma generated by laser breakdown affects the CARS signal in several ways: (1) the bright plasma discharge produces a background signal that obscures the CARS signal; (2) the non-resonant CARS signal generated in the plasma competes with the resonant CARS signal, making analysis of the spectrum difficult; (3) the plasma prevents CARS generation by absorbing laser radiation. Lucht (1988) reported difficulties with (1), and Beiting (1985) reported difficulties with (2). Although (3) has been reported in high density plasmas, it has not been significant for plasmas generated during CARS measurements in particle laden combustion systems.

IV. EXPERIMENTS

The experiments combine a thoroughly tested CARS system with 3 different droplet generators. This combination provides a well-controlled environment to investigate the effect of droplet induced breakdown on CARS temperature measurements in a sprays.

The CARS system uses the second harmonic (532 nm) of a pulsed Nd:YAG laser (Spectra-Physics DCR-2) as its primary photon source. Part of the 532 nm light pumps a Rhodamine 590 dye laser oscillator to generate a broadband (150 cm^{-1}) Stokes laser beam peaked at 607 nm. The peak of the dye laser output is concentration tuned to probe the N_2 Q-branch. The remaining 532 nm beam is split into a pair of pump beams. A 500 mm focal length lens combines the two pump beams and the one Stokes beam in an interaction volume approximately 2 mm long and $500\text{ }\mu\text{m}$ in diameter. Dispersing prisms separate the CARS signal beam from the pump beams, and focusing optics converge the CARS energy onto the face of an optical fiber. The fiber transmits the CARS signal to a spectrometer. A Tracor Northern TN-1710 DARSS linear array detector collects the spectrum and passes it to a ModComp computer for analysis. Additional details of the CARS system have been reported by Switzer and Goss (1982).

We use three well-characterized droplet sources in the study: a drop-on-demand piezoelectric generator, a pressure atomizer, and a capillary breakup droplet stream generator. We mount the droplet generators on a three dimensional translation stage to place the droplets or spray at different positions relative to the CARS focal volume. All of the measurements use water as the droplet fluid, and the droplets travel perpendicular to the laser beam direction.

The drop-on-demand generator is synchronized to the 10 Hz laser firing to place a single droplet in the CARS sample volume during each measurement. The pressure atomizer is a Delavan, 45°, 0.5 gal/hr nozzle. We operate this nozzle at 3 pressures (30 psi, 40 psi, and 50 psi) to produce different droplet size distributions and number densities. The capillary breakup droplet stream generator is similar to the commercially available Bergland-Liu droplet generator (TSI Incorporated). The generator produces a stream of mono-sized droplets. We used this droplet generator both at room temperature and in heated air. A small propane/air

burner provides high temperature (800 K) gas via a heat pipe and the single droplet stream does not affect the gas temperature significantly.

Each experiment consists of 400 single shot CARS measurements. For each shot the reduced data contains the following: (1) the temperature fit to the experimental CARS spectrum, (2) the peak amplitude of the CARS signal, (3) the average of 10 baseline pixels representative of the on-axis background intensity seen by the spectrometer, and (4) the intensity of the laser breakdown recorded by a PIN diode viewing the event 90° from the laser beam direction. In this work, the signal to noise ratio (SNR) is defined $SNR = (\text{peak-baseline})/\text{baseline}$.

V. RESULTS AND DISCUSSION

The results include CARS temperature measurements in the following droplet environments:

- (a) single drops from the drop-on-demand generator in room temperature air at different locations along the CARS laser beam axis
- (b) single drops from the capillary breakup drop generator in heated air at different locations along the CARS laser beam axis
- (c) a spray of fluid drops from the pressure atomizer in room temperature air centered above the CARS focus; different atomizing pressure and different heights above the focus provide different droplet size and number density conditions

Figure 1 demonstrates the effect of droplet breakdown on CARS measurements by comparing a room temperature CARS spectrum without droplet breakdown to a CARS spectrum with droplet breakdown. The breakdown reduces the peak amplitude of the CARS signal, and increases the baseline amplitude. This combination substantially degrades the SNR of the measurement, making temperature fitting difficult. Figure 2 shows the temperature fits for the two spectra of Figure 1. Without breakdown, the CARS fit is accurate, and produces a temperature close to room temperature. With breakdown, however, the CARS fitting routine tries to accommodate the lifted baseline and reduced peak by adding a hot band to the calculated spectrum. Adding a hot band produces a very high, incorrect temperature.

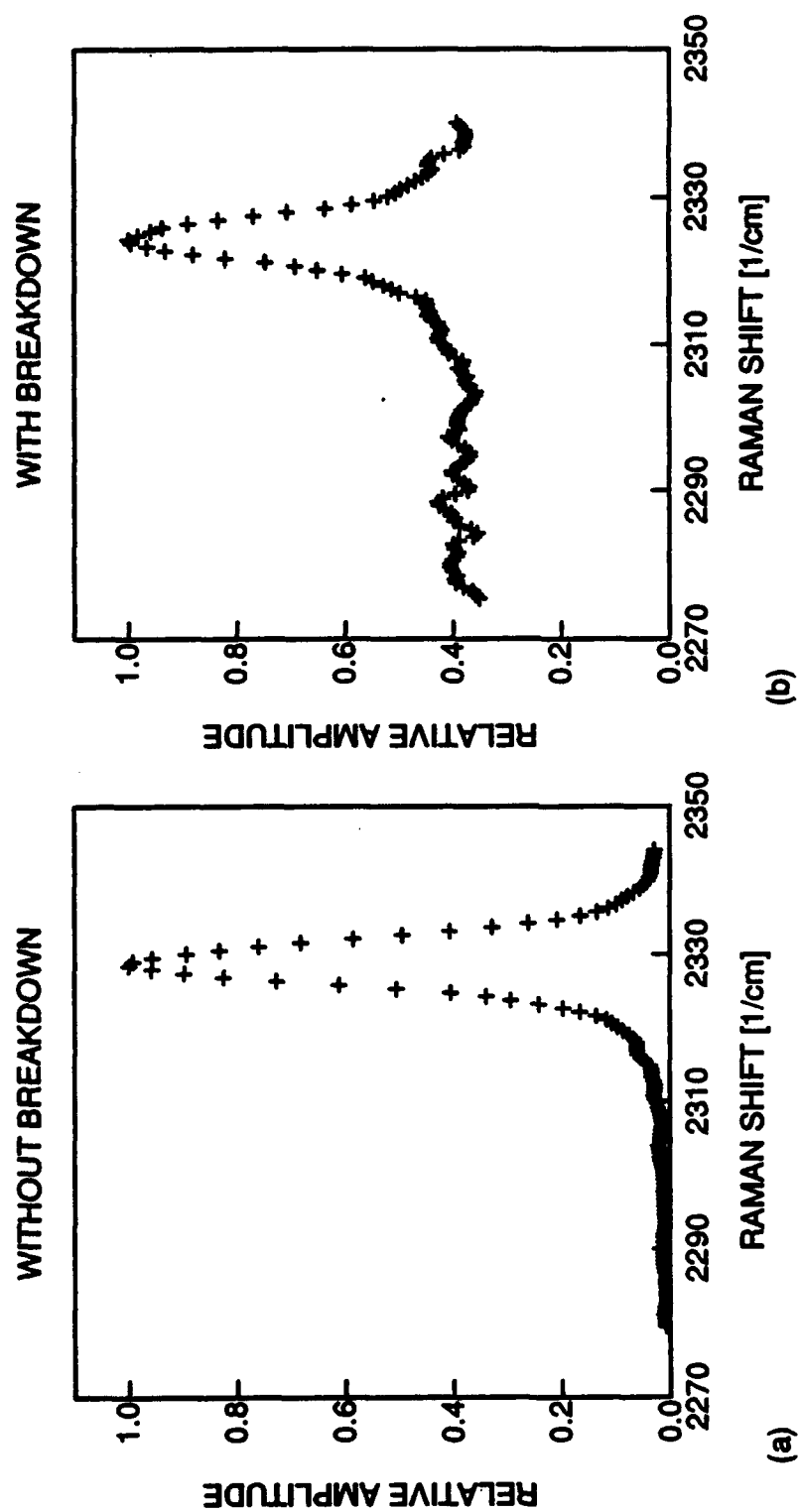


Figure 1. Comparison between CARS spectra without (a) and with (b) plasma noise from droplet breakdown.

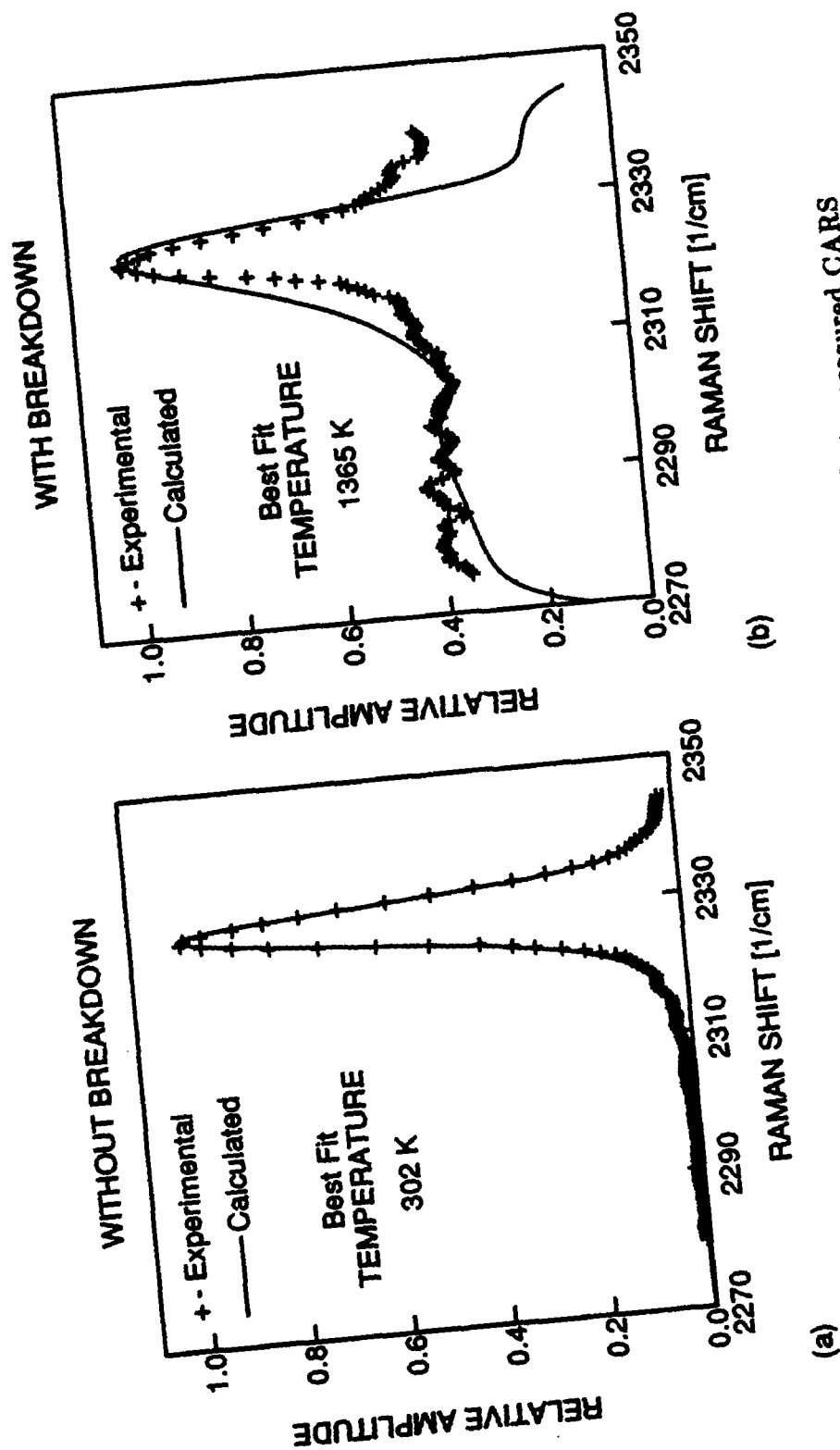


Figure 2. Effect of plasma noise on the temperature fit to measured CARS spectra of Figure 1.

Figure 3 shows the average CARS temperature as a function of signal to noise ratio. Three cases are shown in the figure: single drops in heated air, with the drops falling through the focus of the CARS interaction volume; single drops in room temperature air, with the drops falling through the focus of the CARS interaction volume; and a spray in room temperature air, with the spray centered above the CARS interaction volume. The drop-free temperature range is centered about the average CARS temperature with no droplets present. The range includes ± 1 standard deviation of the drop-free temperatures. All of the curves show an incorrectly high temperature for low SNR, and an accurate temperature for high SNR. The cutoff between low and high SNR is approximately 20.

The results shown in Figure 3 indicate that reliable average temperature measurements can be obtained by utilizing only CARS spectra with high signal to noise ratio. Unfortunately, however, even with a high SNR (> 30), the root mean square (RMS) temperature with droplets present is larger than the droplet-free RMS temperature. To improve our measurements of RMS temperature, we eliminate the influence of dielectric breakdown noise before we attempt a temperature fit. If the baseline lift is caused by plasma enhanced non-resonant background, as suggested by Beiting (1985), then we must subtract a normalized non-resonant background. If the baseline lift is caused by stray light from plasma recombination, then we must subtract a normalized breakdown noise spectrum.

Figure 4 compares a normalized non-resonant spectrum to a normalized breakdown noise spectrum. The noise spectrum is taken with the dye laser beam blocked to prevent CARS generation. The non-resonant spectrum is spectrally narrower than the noise spectrum. Figure 5 shows that the breakdown noise spectrum matches very closely the baseline structure of a CARS spectrum influenced by droplet breakdown. For our experiments, therefore, the dominant source of baseline lift comes from breakdown noise rather than from an enhanced non-resonant CARS contribution. This dominance may depend on droplet composition and on the gas environment. For example, hydrocarbons have large non-resonant susceptibilities (Farrow et al., 1987) which may increase the non-resonant contribution, and as noted earlier, Beiting (1985) found a dominant non-resonant contribution when breakdown was caused by irradiation of solid flyash particles.

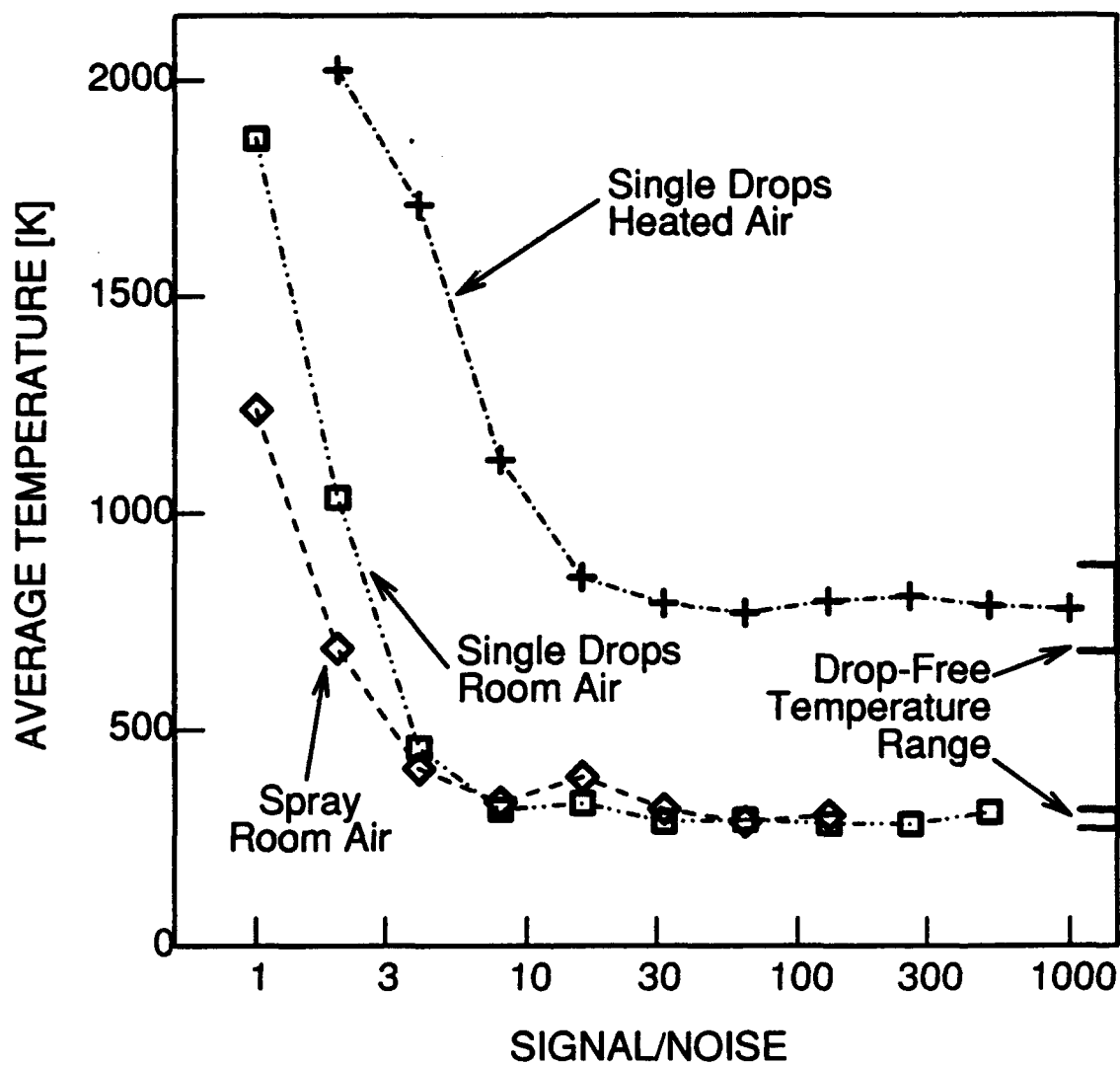


Figure 3. Sensitivity of average temperature fit to the signal to noise ratio of the measured CARS spectrum. The drop-free temperature range represents ± 1 standard deviation of temperature measurements with no drops present.

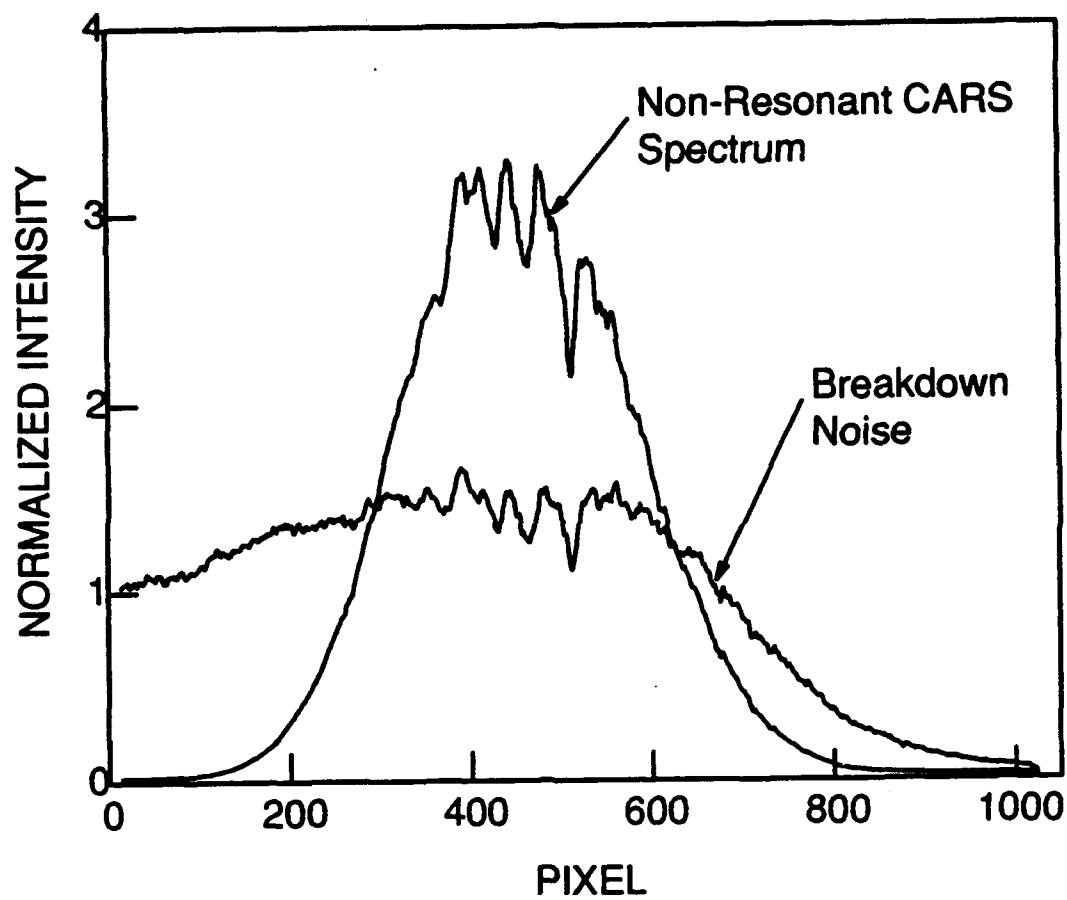


Figure 4. Comparison of non-resonant CARS spectrum to spectral noise produced by droplet breakdown.

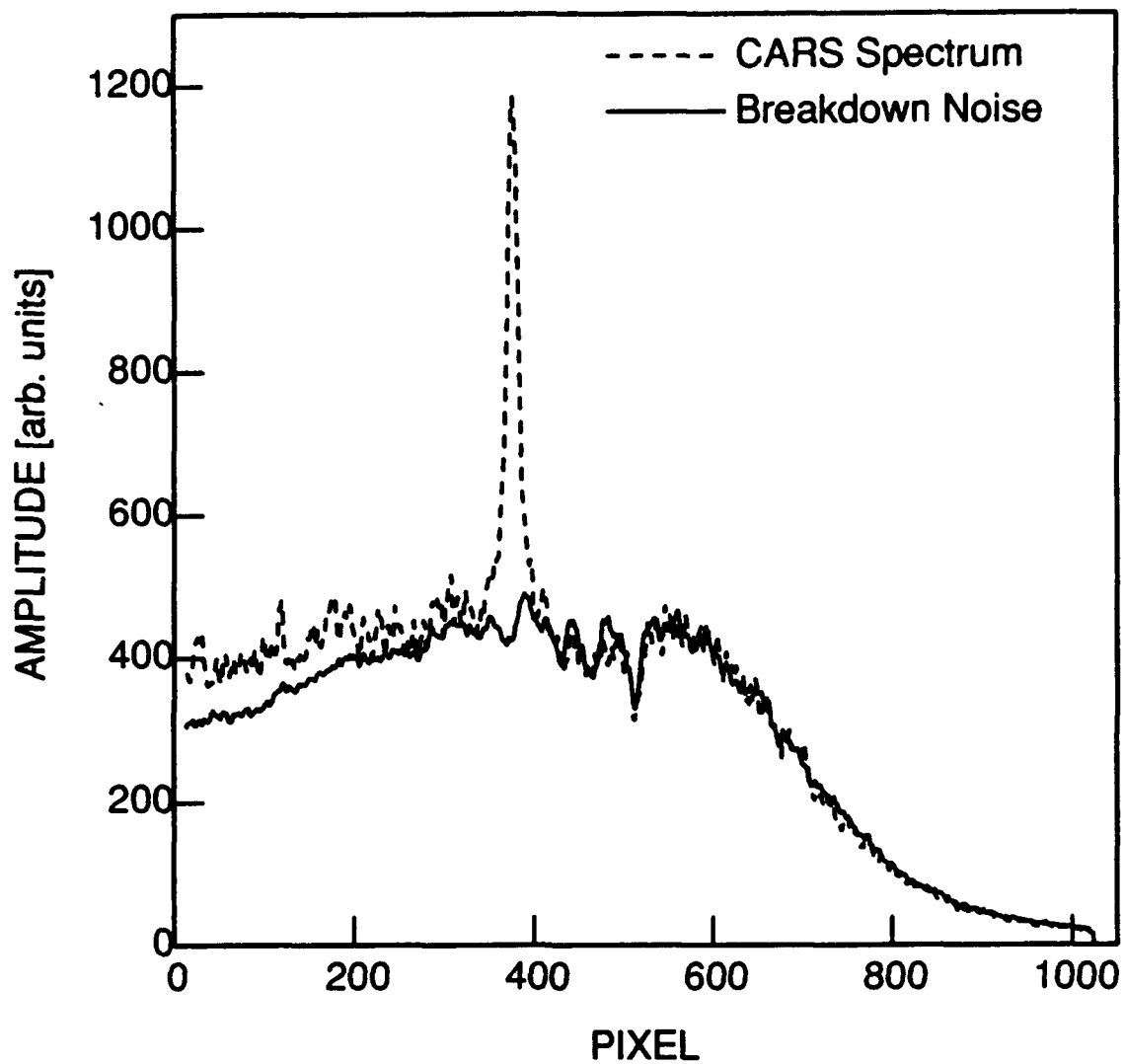


Figure 5. Comparison of CARS spectrum with droplet breakdown and the noise spectrum of the breakdown alone. This comparison shows that most of the noise in the CARS measurements results from droplet breakdown noise.

Based on the results shown in Figure 5, we correct our experimental spectra for breakdown noise by subtracting a normalized breakdown spectrum from the raw data before we attempt a temperature fit. Figure 6 compares the temperature fit between an uncorrected and a corrected room temperature CARS spectrum. While the corrected temperature is a little high, it is within the temperature uncertainty typical of low temperature CARS measurements. Figure 7 compares the variation of temperature with SNR for corrected and uncorrected spectra. The figure shows results from measurements in a room temperature spray. The corrected spectra produce acceptable average temperatures for $\text{SNR} > 3$, while the uncorrected temperature is not acceptable until $\text{SNR} > 20$. More importantly, however, Figure 8 compares the temperature distribution for uncorrected, corrected and drop-free spectra. The figure shows results from a room temperature spray. The temperature distribution for corrected spectra ($\text{SNR} > 30$) matches the drop-free temperature distribution. These results indicate that background subtraction, in combination with SNR conditional measurements, can provide accurate mean and RMS temperatures in droplet-laden flows.

Figure 9 shows the fraction of CARS measurements that result in a valid temperature as a function of axial droplet position relative to the CARS focus. For this figure, the fraction is the number of temperatures within ± 1 standard deviation of the drop-free temperature divided by the number of measurements containing a noticeable breakdown event. Both the room air experiments and the heated air experiments indicate that the valid fraction is relatively insensitive to axial droplet position when the droplet is within 2 mm of the CARS focus. With droplets in the near-focus region, we obtain valid temperatures in 30–40% of the measurements. The droplets travel across the narrow dimension of the CARS sample volume. Valid measurements occur when droplets breakdown at the vertical edges of the sample volume because the collection optics spatially discriminate between the CARS signal and the plasma discharge. A similar discrimination does not occur with droplets at the axial edges of the sample volume because the collection optics are nearly on-axis and therefore insensitive to variations in axial position. Our results suggest that a droplet breakdown will disrupt the CARS measurement if it is along the beam axis and in the primary CARS interaction volume.

From the above information and Poisson statistics we can estimate the upper

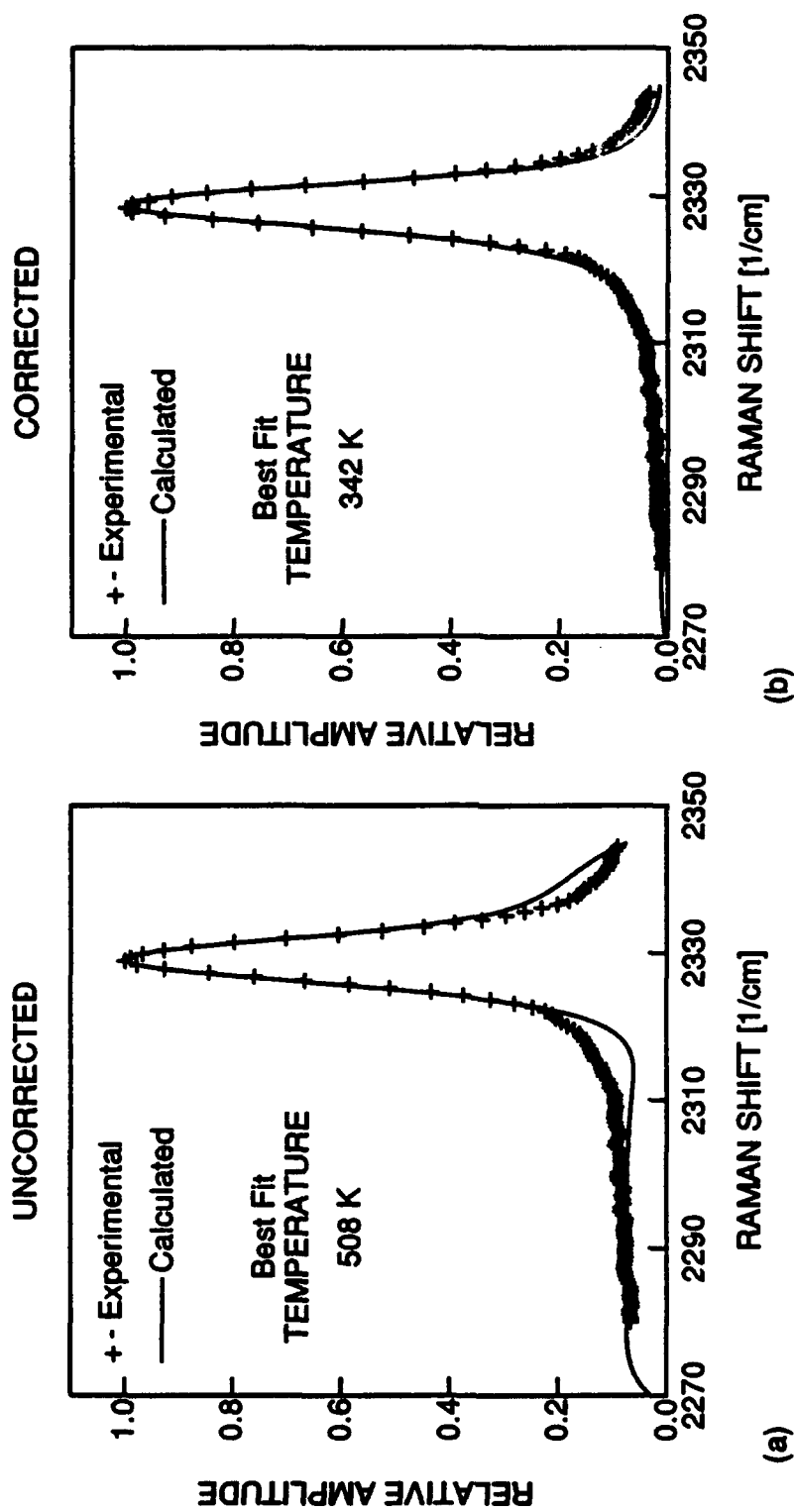


Figure 6. Comparison of temperature fit for CARS spectra uncorrected (a) and corrected (b) for plasma breakdown.

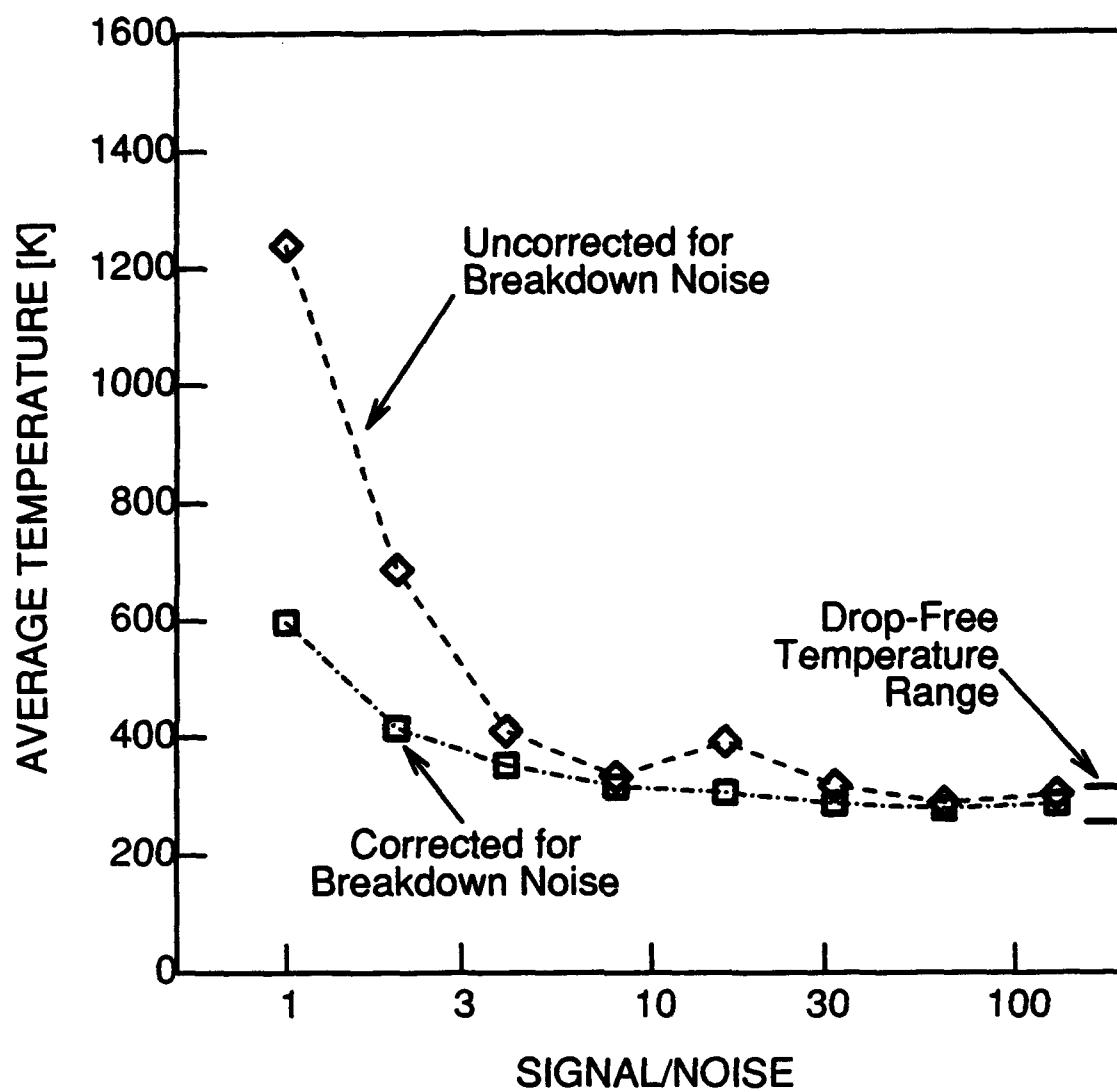


Figure 7. Correcting the CARS spectra for breakdown noise decreases the sensitivity of average temperature to the signal to noise ratio of the CARS signal.

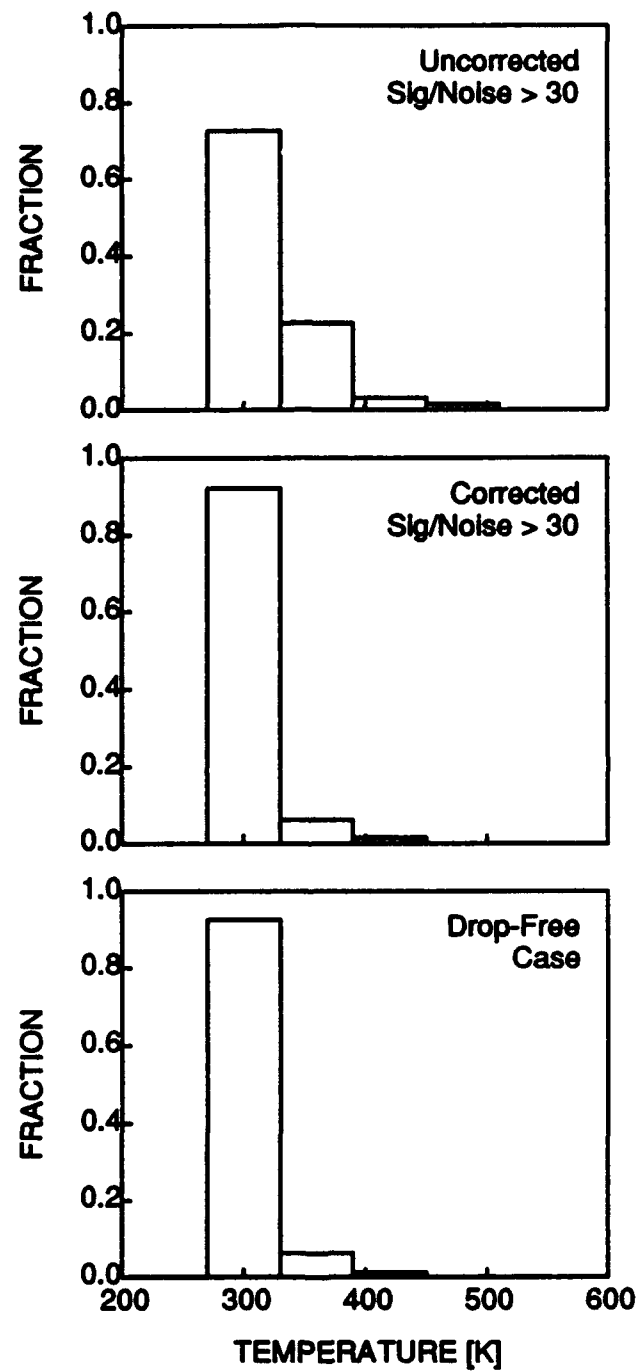


Figure 8. Correcting the CARS spectra for breakdown noise allows accurate measurement of the temperature distribution in the presence of droplets.

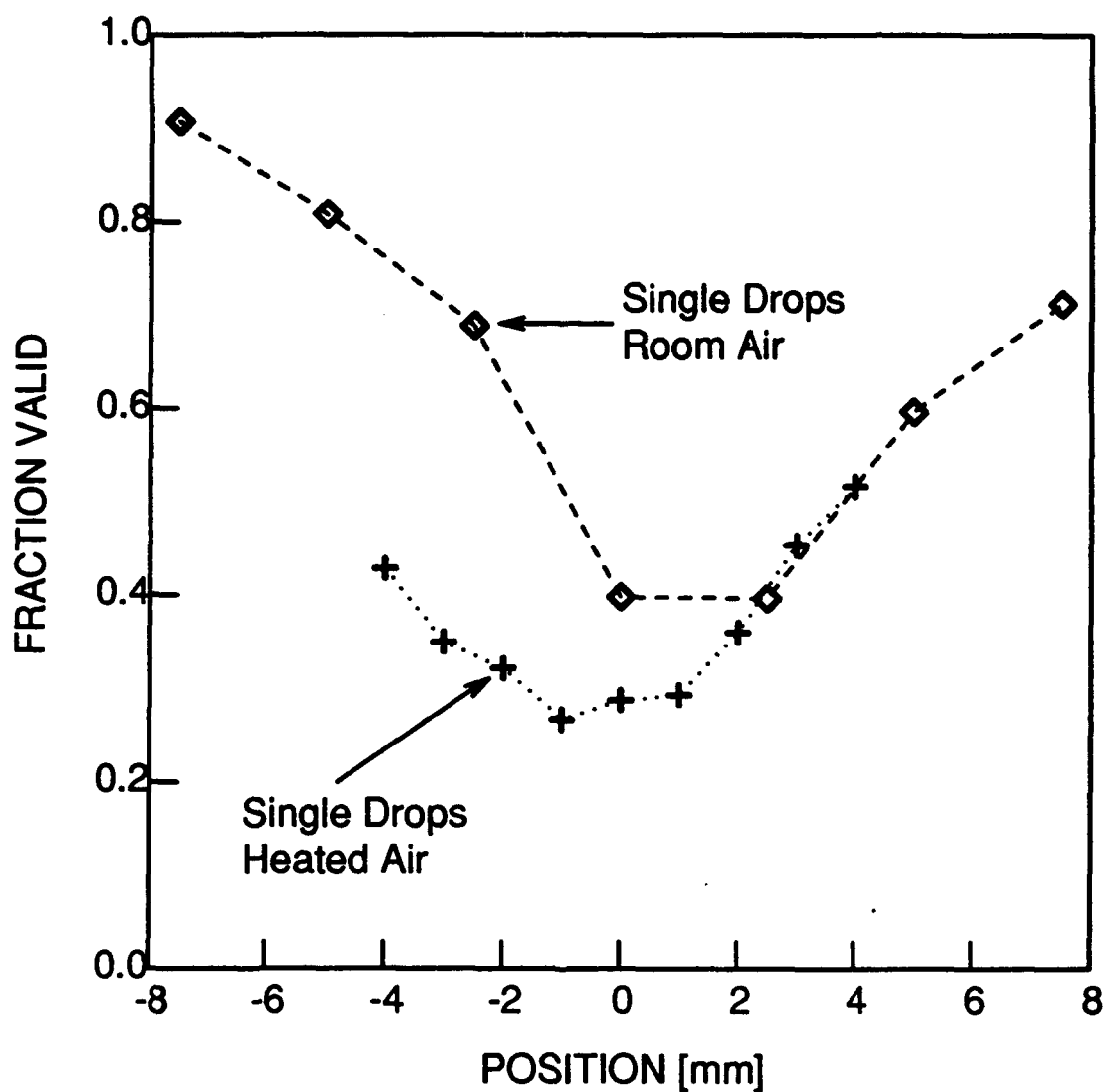


Figure 9. Fraction of CARS measurements that result in valid temperatures as a function of droplet position relative to the CARS focus. Positive is in the direction of laser propagation.

bound on particle number density that will result in 40% valid temperature measurements. The number of particles in the CARS sample volume can be described with a Poisson distribution. The mean of the Poisson distribution is the product of the particle number density N and the probe volume V . Our CARS system has $V = 1 \text{ mm}^3$. For $N = 1000 \text{ particles/cc}$, a particle will be present in the sample volume in 60% of the measurements. From this calculation, we expect that 1000 particles/cc is the number density limit for 40% valid temperature measurements. Figure 10 shows the fraction of valid measurements as a function of particle number density from our CARS temperature measurements in a water spray. The solid line is a least squares cubic fit to the data. The experiments suggest 2500 particles/cc as the number density producing 40% valid measurements. The difference between our estimate and the measurement may be due to an error in our estimate of the CARS sample volume size. It is also possible that the difference is due to a droplet size effect. The number density measurement in the spray includes particles that are too small to contribute to breakdown problems.

Our experiments suggest the following conclusions:

- Droplets that breakdown near the center of the CARS interaction volume influence the CARS signal by decreasing the peak signal intensity, and by raising the background intensity. There is little evidence of noise due to the plasma enhanced non-resonant CARS signal that has been observed in similar experiments using solid particles rather than droplets to produce LIB.
- LIB leads to inaccurate temperatures because the CARS fitting routine tries to fit the elevated background by enhancing the first nitrogen hot band. Subtracting a background spectrum characteristic of LIB improves the temperature fit substantially.
- Background subtracted CARS spectra with high signal to noise ratio provide accurate mean and RMS temperatures in droplet laden flows.
- The LIB process is a single droplet event. For 40% valid temperatures with our CARS sample volume requires a particle number density less than 2500 particles/cc.

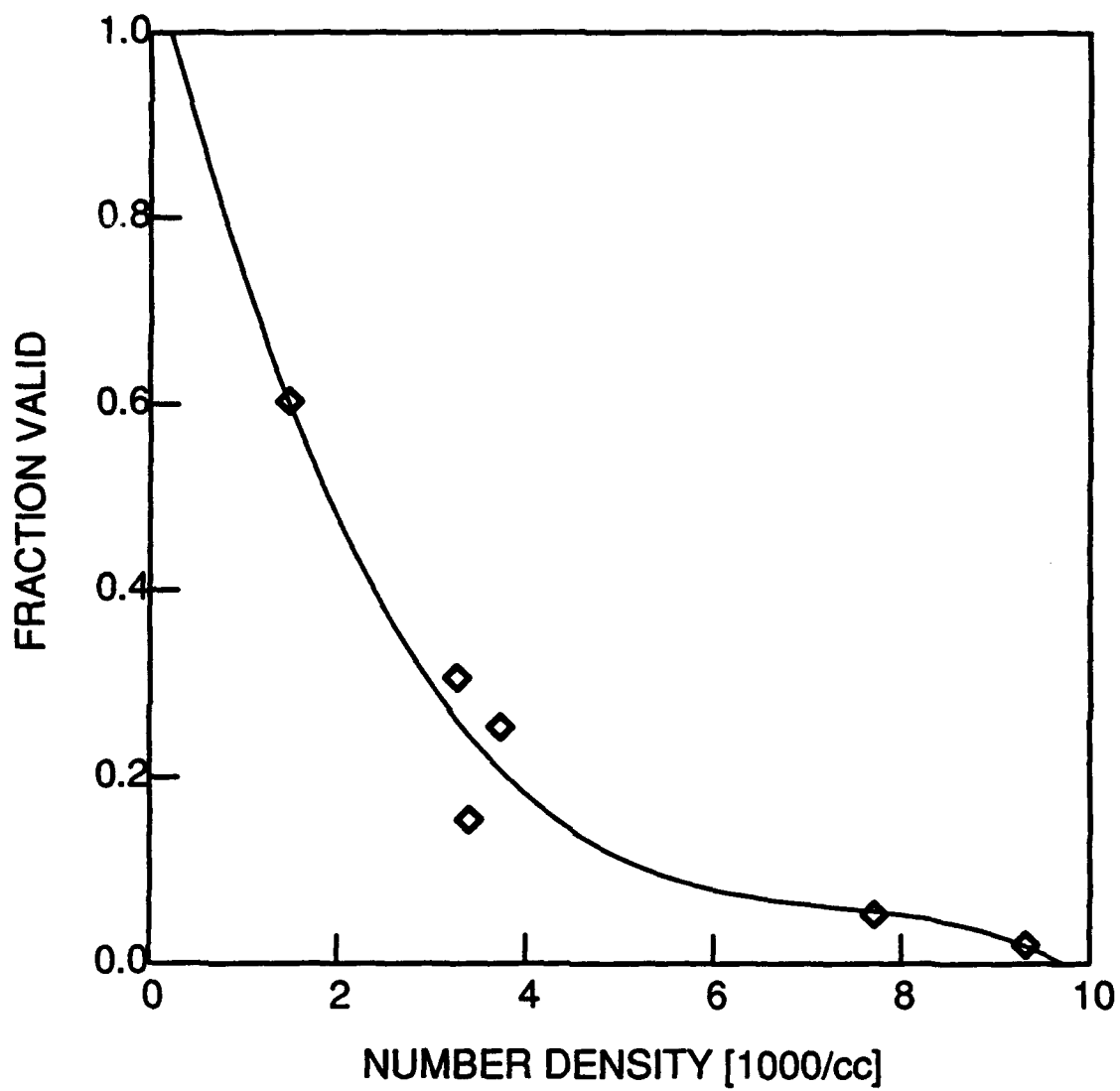


Figure 10. Fraction of CARS measurements that result in valid temperatures as a function of droplet number density in a spray.

VI. RECOMMENDATIONS

The results of this research suggest the following methods to minimize the effect of breakdown on CARS temperature measurements:

- (1) Reduce laser power: reducing laser power decreases the volume in which there is sufficient energy to generate breakdown. Unfortunately reducing laser power also reduces the CARS signal. It is possible to compensate for the decrease in CARS signal with an increased interaction volume at the expense of degraded spatial resolution.
- (2) Minimize optics field of view: restricting the optics field of view ensures that breakdown events outside the CARS interaction volume will not affect the CARS signal.
- (3) Reduce detector gate time: the entire CARS signal is collected in less than 10 ns, while the plasma recombination occurs on the microsecond time scale. Gating the detector in a narrow time window around the CARS laser pulse will reduce the breakdown noise. Reducing the detector gate time will not reduce the non-resonant contribution to the noise, but our results indicate little non-resonant contribution.
- (4) Software corrections and conditional sampling: CARS spectra that have been affected by breakdown noise can be improved by subtracting a normalized background characteristic of the breakdown. In addition, conditional sampling the measurements to include only spectra with high signal to noise ratio allows accurate temperature measurements in droplet laden flows.

REFERENCES

- Beiting, E.J. (1985) "Coherent Interference in Multiplex CARS Measurements: Nonresonant Susceptibility Enhancement due to Laser Breakdown," Applied Optics, **24**, 18, 3010.
- Farrow, R.L., Lucht, R.P., and Rahn, L.A. (1987) "Measurements of the Nonresonant Third-Order Susceptibilities of Gases using Coherent Anti-Stokes Raman Spectroscopy," Journal of the Optical Society of America B, **4**, 1241.
- Lucht, R.P. (1988) "Coherent Anti-Stokes Raman Scattering Measurements in Coal-Particle-Laden Flames," Paper WSS/CI 88-61, Western States Section/The Combustion Institute Meeting, Provo, Utah, March 21-22.
- Noda, M., Gierulski, A., Marowsky, G. (1987) "CARS-Studies of Coal and Coal-Water-Mixture Combustion," Paper 7C-109, Joint Meeting of the Western States and Japanese Sections/The Combustion Institute, Honolulu, Hawaii, November 22-25.
- Roquemore, W.M., Bradley, R.P., Jackson, T.A., Kizirnis, S.W., Goss, L.P., Switzer, G.L., Trump, D.D., Sarka, B., Ballal, D.R., Lightman, A.J., Yaney, P.P., and Chen, T.H. (1986) "Development of Laser Diagnostics for Combustion Research," Invited paper of the Central States Section/The Combustion Institute Spring Meeting, NASA Lewis Research Center, May 5-6.
- Switzer, G.L. and Goss, L.P. (1982) "A Hardened CARS System for Temperature and Species Concentration Measurements in Practical Combustion Environments," Temperature: Its Measurement and Control in Science and Industry—Vol 5, edited by J.F. Schooley, 583.

1988 USAF-UES SUMMER FACULTY RESEARCH PROGRAM/
GRADUATE STUDENT RESEARCH PROGRAM

Sponsored by the
AIR FORCE OFFICE OF SCIENTIFIC RESEARCH

Conducted by the
Universal Energy Systems, Inc.

FINAL REPORT

Measurement of the Velocity Field and Heat Transfer
Coefficients Associated with a Rectangular Wall Jet

Prepared by:	Wayne A. Eckerle, Ph.D.
Academic Rank:	Associate Professor
Department and	Mechanical and Industrial Engineering Department
University:	Clarkson University
Research Location:	AeroPropulsion Laboratory Wright Patterson AFB Dayton, Ohio 45433
USAF Researcher	Dr. R. B. Rivir
Date:	September 28, 1988
Contract No.:	F49620-87-R-0004

Measurement of the Velocity Field and Heat Transfer Coefficients
Associated with a Rectangular Wall Jet

by

Wayne A. Eckerle

ABSTRACT

The effect of high free-stream turbulence on heat transfer was experimentally investigated. High turbulence and large length scales simulating gas turbine engine conditions were produced with a wall jet. A 7cm x 48cm rectangular nozzle created the jet. The rectangular geometry reduced the edge effects observed in previous tests with a circular wall jet. All three components of mean and fluctuating velocities were acquired with a three-component Laser Doppler Velocimeter(LDV). Profiles were acquired at the jet centerline at eight streamwise locations. Supply conditions were controlled to provide a maximum velocity in the profiles of 37 m/s. Free-stream turbulence varied from 10% to 20% at these locations. Heat transfer coefficients on the flat wall were acquired at six locations for free-stream velocities ranging from 56 m/s to 10 m/s. Because of the extensive effort required to set up the LDV system and a malfunction of the laser during the program, reduction and correlation of these data is in progress. Some preliminary analysis is presented in this report. A complete summary of the results will be presented at the American Physical Society's Fluid Dynamics Meeting, November 20-22, 1988.

ACKNOWLEDGEMENTS

I wish to gratefully acknowledge the support provided by the Air Force Systems Command, the Air Force Office of Scientific Research, and Universal Energy Systems, Inc.

A special acknowledgement is due Dr. R. B. Rivir for his cooperation during the project. His help with getting the experimental setup in place and coordinating support work was essential to completing this project. I learned from our technical discussions, and his graciousness made my stay very enjoyable. I thank Mr. W. John Schmoll for his assistance with setting up the LDV system and acquiring the data. Without John's expertise and helpfulness, this experiment could not have been accomplished within the time constraints of this program.

The friendly and helpful atmosphere in the Components Branch of the Turbine Engine Division is truly special. Without their support and cooperation, this work could not have been accomplished.

I. INTRODUCTION

An important aspect of improving the performance of advanced gas turbine engines is to increase engine operating temperatures. Development of new materials to handle the increased heat loads is critical to reaching significant performance enhancement. However, some components, in particular the turbine, will require convective cooling to survive. Since cooling flow is bled from the compressor, coolant flow must be minimized to maximize engine efficiency. Proper coolant levels are difficult to determine, however, because of a lack of accurate heat transfer prediction methods for the highly turbulent flow passing out of the combustor into the turbine.

Part of the Aero Propulsion Laboratory's program to develop advanced gas turbine engines involves providing information on heat transfer in highly turbulent flows. One effort involves using the aggressive flow characteristics of a wall jet. A wall jet simulates the high turbulence levels and large length scales of the flow exiting the combustor. A schematic of the test configuration is shown in Figure 1. The experiment consists of a jet, created by a 20.3 cm diameter ASME nozzle, attached to a 61 cm wide flat plate. The plate is made up of two sections. A removable 1.5 m unheated starting length can be positioned upstream of a 3 m long instrumented surface. The unheated starting length contains holes near the plate trailing edge for injecting a coolant film simulative turbine blade surface cooling. The instrumented plate was designed to create a constant heat flux surface for heat transfer measurements. The surface was instrumented with thermocouples for calculating heat transfer coefficients and measuring film effectiveness. This model was initially built and checked out by Han¹ and later modified by MacMullin² and Jumper³ for their investigations.

MacMullin's study determined the convective heat transfer coefficient as a function of axial turbulence intensity, integral length scale, and Reynolds number. The length scale was

a linear function of distance downstream of the nozzle and was not intentionally varied during this study. Centerline turbulence intensity above the wall jet boundary layer varied as a function of axial distance along the plate and was largely independent of nozzle velocity. Accordingly, turbulence intensity and length scale were fixed by location on the plate. The Reynolds number was varied by adjusting the nozzle exit jet velocity. Measurements were taken over a range of Reynolds number for three different turbulence levels with and without the 1.6 m unheated starting length. A coolant film was not investigated during these tests.

The relationship between Stanton number and Reynolds number is presented in Figure 2. At a constant Reynolds number, heat transfer from the plate increased with increasing turbulence levels. The Stanton numbers for the 7% turbulence level were 2 to 11% higher than Blair's⁴ 6% results. The data at the higher turbulence levels were almost parallel to that of Moffat⁵ despite being an order of magnitude greater in Reynolds number. Thus, the results compare favorably with other data in the literature. An even more significant aspect of these results, however, is the comparison with full scale engine data. MacMullin's results are expressed as Nusselt numbers in Figure 3 for comparison with the ATEGG engine results. The APL data is nearly identical to the suction surface measurements. The 16% APL results are also close to the ATEGG high Reynolds number results on the pressure surface. The key implication of these results, then, are that the wall jet simulates the relationship between heat transfer and Reynolds number as a function of turbulence level for flow conditions coming from a combustor. Design guidelines for cooling turbine components, then, can be developed from experimental results with the wall jet.

Jumper³ directed a program to measure film effectiveness in highly turbulent flow with the wall jet. The single row of 30-deg slant-hole injectors located near the downstream end of the unheated starting length were used to introduce the coolant film. The major

conclusions of this work are that high turbulence levels in the wall jet did not significantly affect the blowing rate for optimum cooling effectiveness but had a significant deleterious effect on cooling effectiveness. This reduced effectiveness is clearly shown in Figure 4. Beyond approximately 22 cooling hole diameters downstream of the injection point, no film effectiveness was measured with the wall jet. Han⁶ measured cooling effectiveness of 15% at 40 diameters downstream of the injection location with free-stream turbulence of 5%. This persistence of the coolant film to many diameters downstream of the injection location has been applied to designs used in highly turbulent flows resulting in an over prediction of cooling effectiveness downstream of the injection site. The importance of properly including the effects of high turbulence in design analysis for cooling turbine components is evident in this comparison.

The above results have significant implications for properly calculating heat transfer and sizing coolant levels for surfaces exposed to highly turbulent flows. Therefore, this project was undertaken to provide more information relating the heat transfer to the momentum properties of the flow field. In the previous studies, a wall jet was created with a round nozzle. A problem with this configuration is that the flow field is not uniform in the lateral direction along the flat plate. An indication of the nonuniformity in the lateral direction are MacMullin's heat transfer coefficient distributions, some of which are shown in Figure 5. Consequently, edge effects are difficult to isolate. A more two-dimensional flow was created for these tests by replacing the round nozzle with a 6.7 by 48.3 cm rectangular nozzle. In addition, velocity profiles were acquired with a three-component LDV system instead of single hot wires as previously used. Thus, all three velocity components were acquired simultaneously so that Reynolds stresses, which have a significant impact on heat transfer, can be calculated. Also, an LDV is nonintrusive and more accurate in highly turbulent flows (Refs. 7 and 8).

II. OBJECTIVES OF THE RESEARCH EFFORT

This study was conducted to provide a detailed data set for correlating the heat transfer coefficients measured in highly turbulent flows with the associated momentum transfer. The same wall jet configuration was used except that the circular nozzle was replaced with a rectangular nozzle. The specific objectives were:

1. Set up a three-component LDV system on a narrow traverseable table.
2. Set up the wall jet experimental configuration.
3. Acquire all three components of mean and fluctuating velocities at the wall jet centerline. Initially, acquire data with the circular nozzle for comparison with previous hot wire data. Subsequently, acquire data with the rectangular nozzle at several streamwise locations.
4. Acquire heat transfer coefficients on the flat wall with and without the unheated starting length.
5. Correlate the LDV data with the heat transfer results.

III. EXPERIMENTAL APPARATUS

The major portion of this effort was devoted to getting the LDV system aligned on the narrow optic table that fits into a traversing system. Though a preliminary layout was established prior to setting up the system, the final configuration could only be established through trial and error since the actual mirror and lense adjustment ranges could only be estimated. A diagram of the final LDV layout is shown in Figure 6. The LDV system was powered by an Argon-Ion laser. The laser beam was separated into three colors (blue, green and violet) with each color split into two beams. The system contained two optical legs. One leg contained sending optics for the green and blue beams and receiving optics for the violet beams, while a second leg contained the sending optics for the violet beams and the receiving optics for the green and blue beams. Velocity data, then, were acquired in

backscatter. For each color, a reference beam was frequency-shifted by 40 MHz in order to discriminate forward and reverse flows in each of the velocity components.

Because of the high temperatures and dusty environment in the test cell, the extensive initial alignment was accomplished in the control room. Once the components were positioned on the table, the system was aligned, and a limited amount of calibration data were acquired to provide familiarization with the data acquisition system.

The weight and sensitivity of some of the LDV components precluded moving the table out to the test cell with the LDV system intact. Consequently, the system was dismantled prior to mounting the optic table into the traverser. Realignment of the system with the table mounted in the traverser was then accomplished. Calibration tests with a spinning thread and a calibration jet were conducted. Data acquired with the spinning thread agreed with the calculated thread velocities. However, attempts to acquire data with the calibration jet were unsuccessful for several reasons. One problem was that the system did not stay aligned when the table was traversed across the calibration jet. Fine adjustment to achieve beam crossing was required several times during a typical day.

The second problem was more severe. The maximum power of the laser beam was only 0.5 watts. Consequently, the signal-to-noise level of the violet beam was too low to acquire accurate data. Tap settings in the laser power supply were adjusted to increase the laser operating range. However, the laser tube failed after only several minutes of operation. In order to repair the laser, the laser head was removed from the LDV system and a new tube was installed. After repositioning the laser head in the LDV layout, the system had to again be aligned. During this realignment, a loose mirror mount that may have been causing the system to lose its alignment was discovered. Calibration tests with the realigned system and the retubed laser were successful. The system maintained its alignment, and the increased power with the new tube was enough to allow accurate data to be collected on all

three channels of the LDV system. Because of these problems, the entire process to establish a working LDV system required seven weeks of this ten-week effort.

The flat plate test section was the same as that used by MacMullin. The unheated starting length was positioned upstream of the constant heat flux section. The wall boards shown in Figure 1 were not used in these tests since the rectangular nozzle reduced edge effects.

IV. EXPERIMENTAL RESULTS

The last three weeks of this effort were devoted to acquiring data with the LDV system and measuring heat transfer coefficients. Three velocity profiles were acquired with the circular ASME nozzle. The streamwise mean and fluctuating velocities for one of the profiles are compared with MacMullin's hot wire data in Figures 7 and 8, respectively. The fluctuating velocities agree quite well except near the edge of the jet. In this region with quite high local turbulence, the hot wire underpredicts the turbulence level as expected from the theoretical analysis^{7,8}. The mean velocity distributions are in reasonable agreement. Near the flat plate, the velocities measured with the hot wire are higher. This difference may be due to the side boards that were not installed for these tests. By constraining the flow near the flat plate, the flow velocity should be higher. The good agreement of the fluctuating velocities indicates that the LDV signals were not being significantly affected by noise or vibration in the test cell.

Centerline traverses were acquired at eight streamwise locations with the rectangular nozzle. Six of the profiles were acquired at thermocouple locations on the constant heat flux portion of the flat plate. The other two were acquired at positions over the unheated starting length corresponding to thermocouple positions if the unheated starting length were removed. While most of this data could not be analyzed before writing this report, mean and fluctuating velocity distributions are shown in Figures 9-12 for the profile acquired nearest the

nozzle ($X/H=7.81$) and the most downstream profile ($X/H=52.95$) where H is the nozzle height of 6.67 cm. The velocities are normalized by the maximum velocity in the profile. The maximum velocity for all eight profiles is near 37 m/s. These data show the development of the jet as it moved downstream along the plate. U , V and W are the mean velocities in the axial, vertical and transverse direction, respectively. The primed lower case symbols represent the corresponding fluctuating velocities. The streamwise mean velocity gradient at the wall decreased in the flow direction. The mean vertical and transverse velocities were small and remained relatively constant along the plate. The vertical fluctuating velocity distribution changed little along the flat plate while the streamwise and transverse components increased along the plate. Both u' and w' increased significantly near the floor in the upstream profile to values near those of the downstream profile. The large values of these fluctuating velocities near the plate may be a strong contributing factor to the large heat transfer measured with this configuration.

Heat transfer coefficients were measured on the constant flux surface at the six locations corresponding to those where velocity profiles were acquired. To determine the effect of Reynolds number on heat transfer, coefficients were measured for velocities of 10 to 56 m/s. The coefficients are expressed as Stanton numbers and plotted in terms of Reynolds number in Figure 13. The data have the same slope but fall slightly above the 16 percent turbulence results of MacMullin shown in Figure 2. These heat transfer results should be similar since turbulence levels corresponding to coefficients measured in this test were at the 16-20 percent level. The difference between the data sets may be due to the different length scales of the two experiments. Length scales were not measured during this project. A key implication of the comparison in Figure 13 is that the test conducted this summer generated a good heat transfer data set. These data will be correlated with the LDV data to understand the flow mechanisms associated with the high heat transfer

coefficients.

V. CONCLUSIONS

During this 10-week program a three-component LDV system was set up and calibrated. A wall jet configuration was used to create flow conditions on a flat plate similar to jet engine conditions from a heat transfer standpoint. Centerline velocity profiles were acquired with the LDV system along with heat transfer coefficients. The unheated starting length was in place for these tests. Because of problems with setting up the LDV system, only three weeks could be devoted to data acquisition. Reduction and analysis of the data is in progress. The general features of the wall jet were established with velocity distributions. Heat transfer data are similar to the results of MacMullin. The implication of these results is that a good data set was acquired, and correlation of the heat transfer results with the LDV data should identify the flow mechanisms associated with the high heat transfer.

VI. RECOMMENDATIONS

In order to put together a complete data set with the rectangular nozzle, the following data needs to be taken:

1. Measure integral length scales at the same locations that LDV data were acquired.
2. Remove the unheated starting length and measure heat transfer coefficients at locations corresponding to where LDV data were acquired. These coefficients will provide heat transfer information in regions with lower turbulence. LDV data were acquired with turbulence intensities down to 10%.
3. Introduce film cooling and measure film effectiveness with the rectangular nozzle. Use the LDV system to establish details of how the film reacts as it mixes with the wall jet.

The tests conducted in this program and recommended above are applicable to regions

without a significant pressure gradient. A wall jet could also be used to investigate heat transfer in highly turbulent flow with a pressure gradient. For example, at the junction of the turbine cascade and the engine casing, the adverse pressure gradient created by the cascade causes the flow to separate from the casing surface. The amount of coolant required to cool this region is not known. An obstacle, such as a cylinder, could be mounted on the flat plate to create a large separation. LDV, heat transfer, and film effectiveness measurements could then be acquired to develop guidelines for cooling this region of the engine.

LIST OF REFERENCES

1. Han, J., "Effect of High Free-Stream Turbulence from a Free Jet on Flat Plate Turbulent Boundary Layer Flow and Heat Transfer", 1985 USAF-UES Summer Faculty Research Program, Contract No. F49620-85-C-0013, August 30, 1985.
2. MacMullin, R., "Effects of Free-Stream Turbulence from a Circular Wall Jet on Flat Plate Heat Transfer and Boundary Layer Flow", MS Thesis, AFIT/GA/AA/86D-10, School of Engineering, Air Force Institute of Technology, Wright-Patterson AFB, OH, December, 1986.
3. Jumper, G. W., "Film Cooling Effectiveness on a Flat Plate in High Free-Stream Turbulence Using a Single Row of 30-deg Slant-hole Injectors", MS Thesis, AFIT/GAE/AA/87D-7, School of Engineering, Air Force Institute of Technology, Wright-Patterson AFB, OH, December, 1987.
4. Blair, M. F., "Influence of Free-Stream Turbulence on Turbulent Boundary Layer Heat Transfer And Mean Profile Development, Parts I and II", Trans. ASME, Journal of Heat Transfer, Vol. 105, pp. 33-47, February, 1983.
5. Moffat, R. and Maciejewski, P. K., "Heat Transfer with Very High Free-Stream Turbulence", NASA Grant NAG3-522, Proceedings of the 1985 Turbine Hot Section Technology Conference, NASA Conference Publication 2405, pp. 203-215, October 22, 1985.
6. Han, J. C. and Mehendale, A. B., "Film Cooling and Heat Transfer with Steam Injection Through Inclined Circular Holes", AVCO Lycoming Division, Contract N-832132-E, May, 1985.
7. Hussein, H. J., George, W. K. and Capp, S. P., "Comparison Between Hot-Wire and Burst-Mode LDA Velocity Measurements in a Fully-Developed Turbulent Jet", in press, AIAA, 1988.
8. Tutu, N. K. and Chevray, R., "Cross-Wire Anemometry in High Intensity Turbulence", J. Fluid Mech., Vol. 71, Part 4, pp. 785-800, 1975.

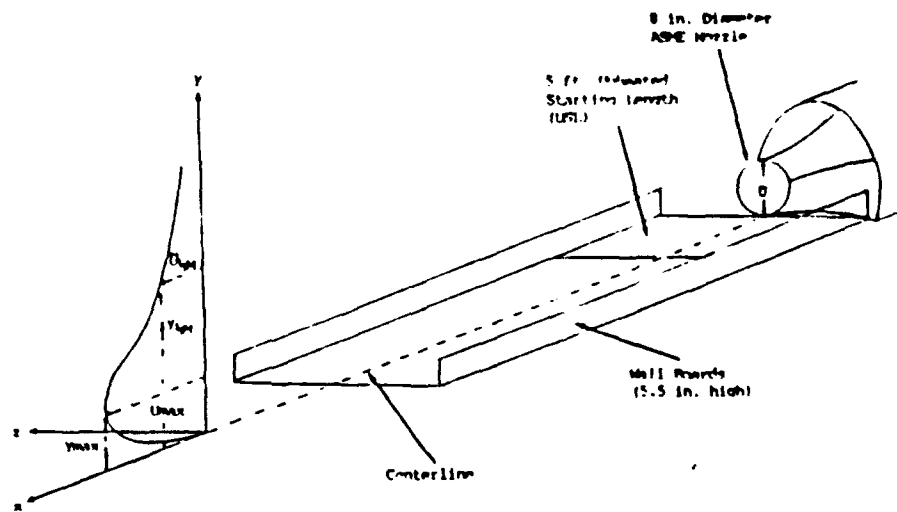


Figure 1. APL Wall Jet Configuration

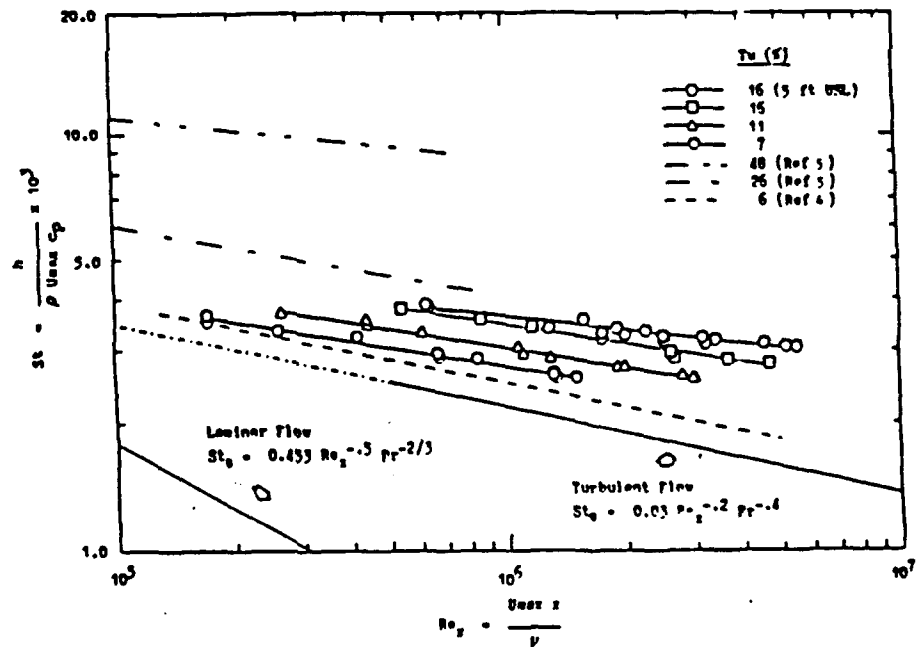


Figure 2. MacMillan's Heat Transfer Data

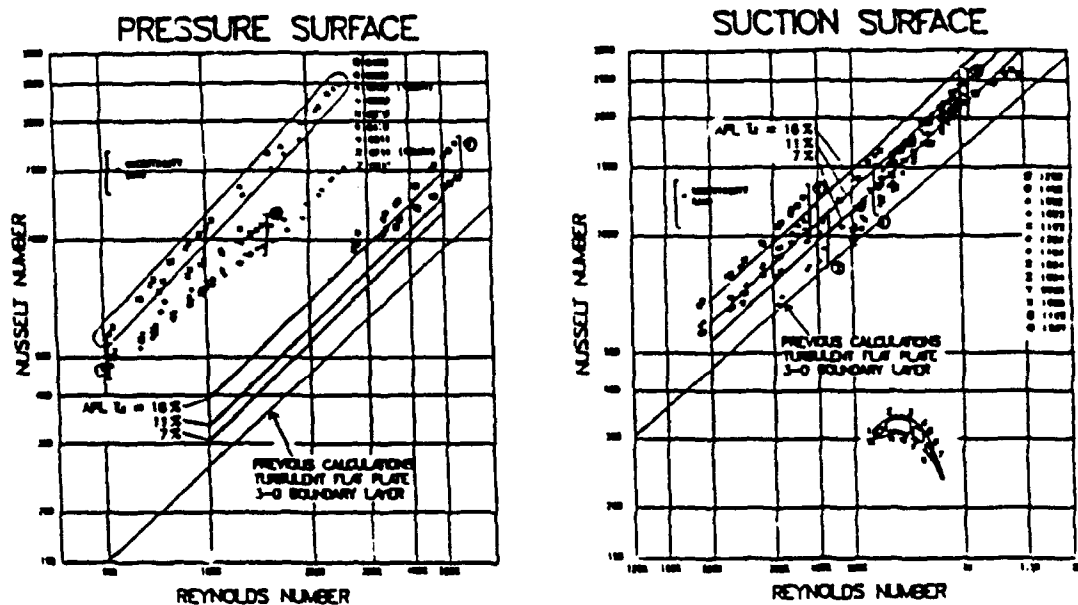


Figure 3. Comparison of MacHullin's Wall Jet Data with ATECG Data

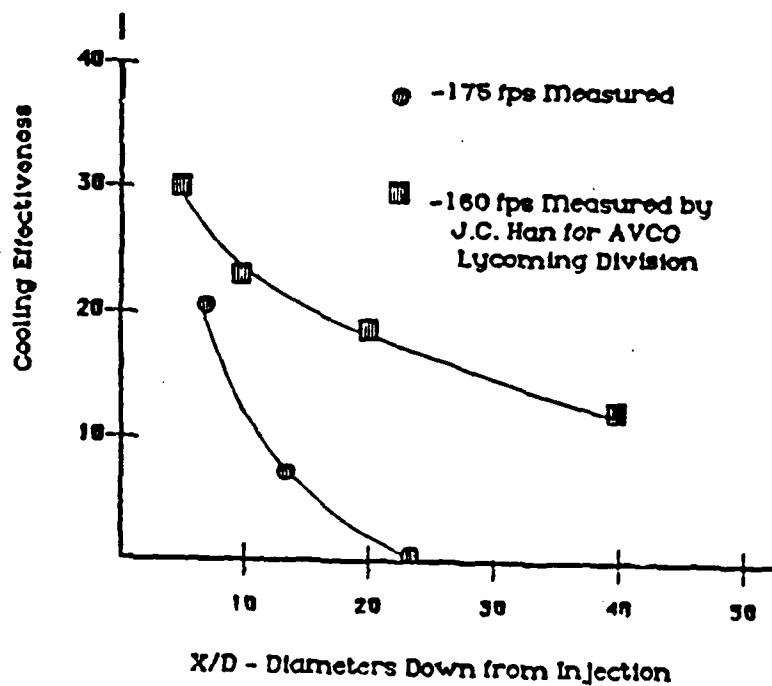
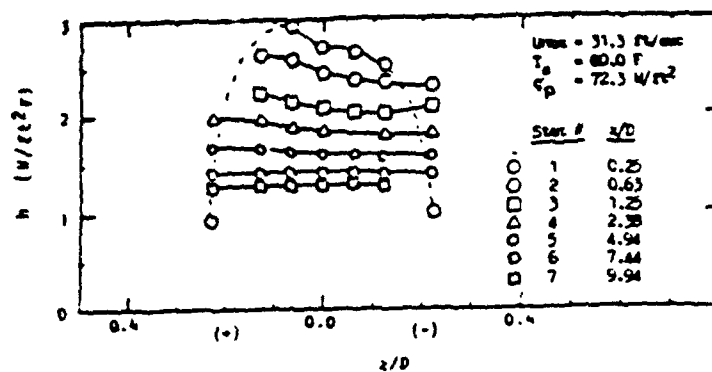
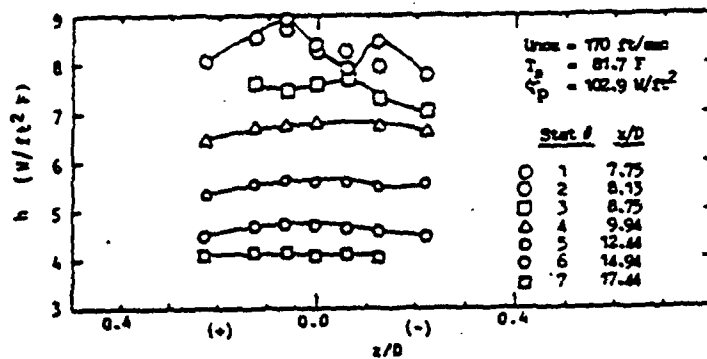


Figure 4. Comparison of Jumper's Film Effectiveness with Han's Results at Lower FST



Without Unheated Starting Length



With Unheated Starting Length

Figure 5. Heat Transfer Coefficient Distribution with Circular Wall Jet

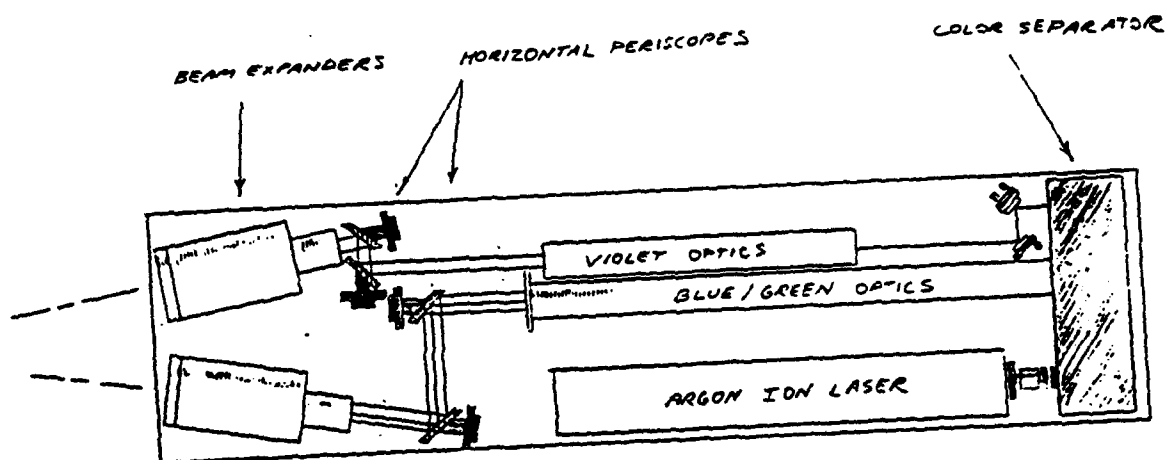


Figure 6. Layout of Three-Component LDV System on 0.6m x 2.5m Traversible Table.

COMPARISON OF HOT WIRE AND LDV TURBULENCE INTENSITIES.
ASME NOZZLE $X/D=9.8$

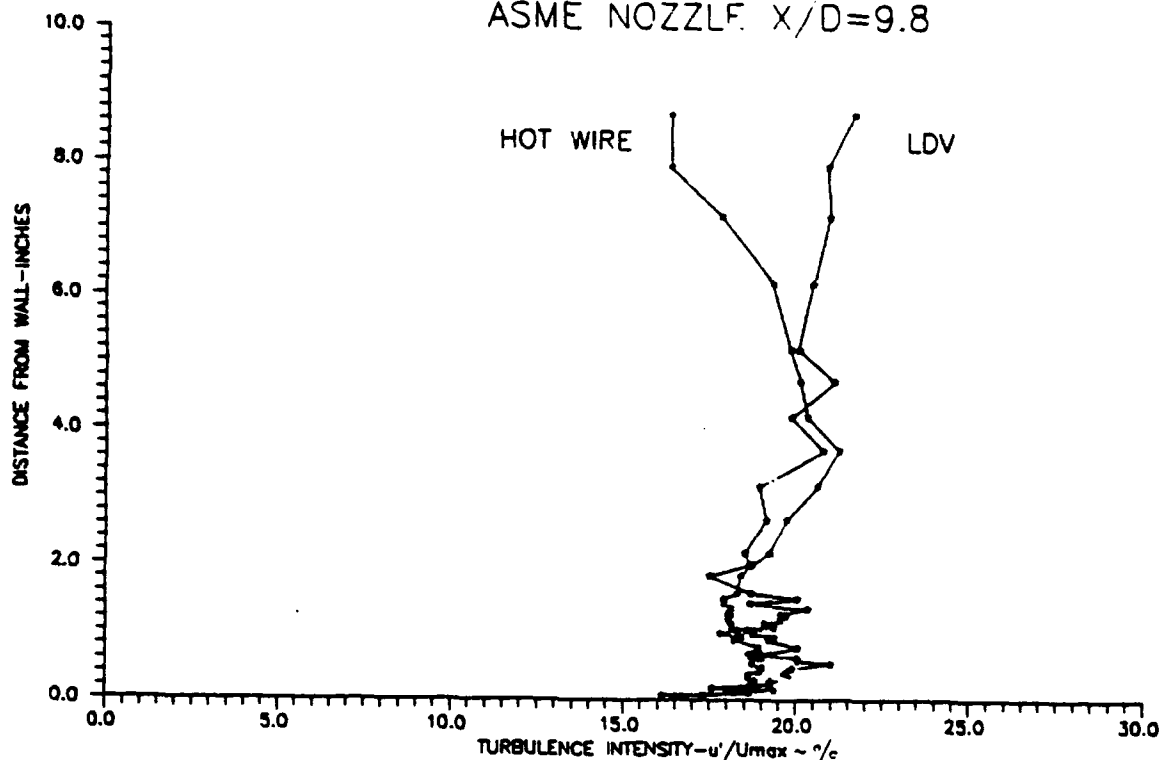


Figure 7. Comparison of Streamwise Turbulence Intensities

COMPARISON OF HOT WIRE AND LDV MEAN VELOCITIES
ASME NOZZLE $X/D=9.8$

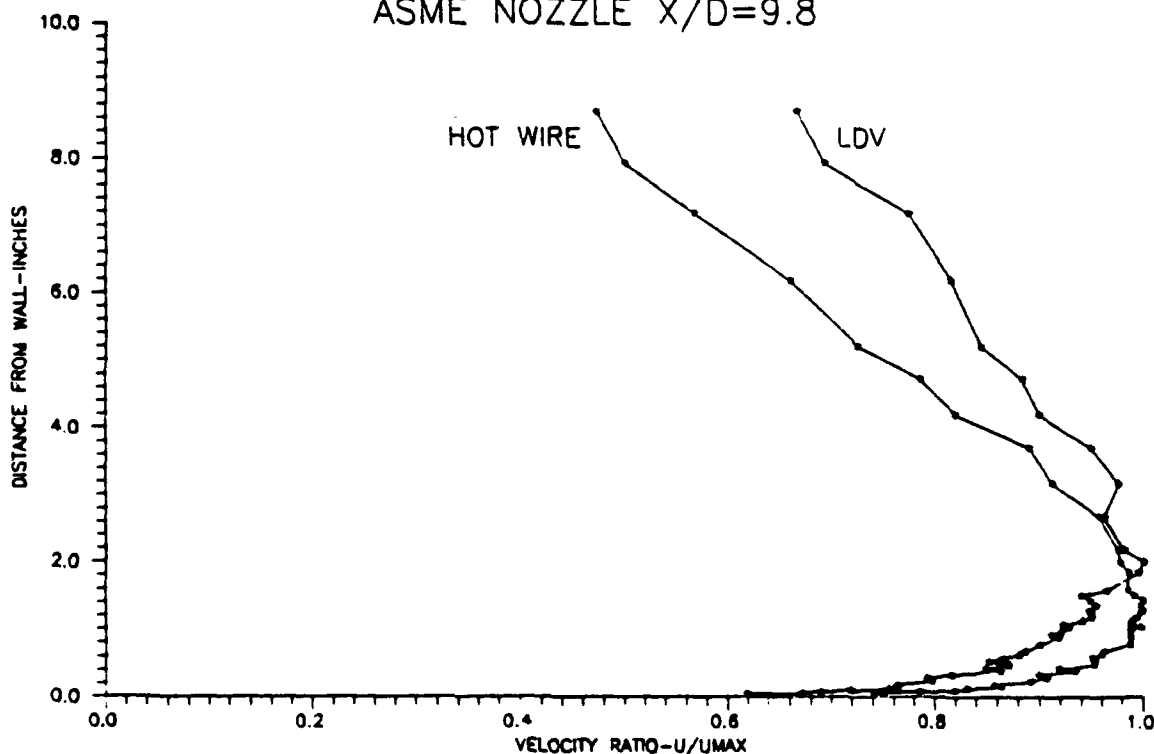


Figure 8. Comparison of Streamwise Mean Velocities

MEAN VELOCITIES WITH RECTANGULAR NOZZLE $X/H=7.81$

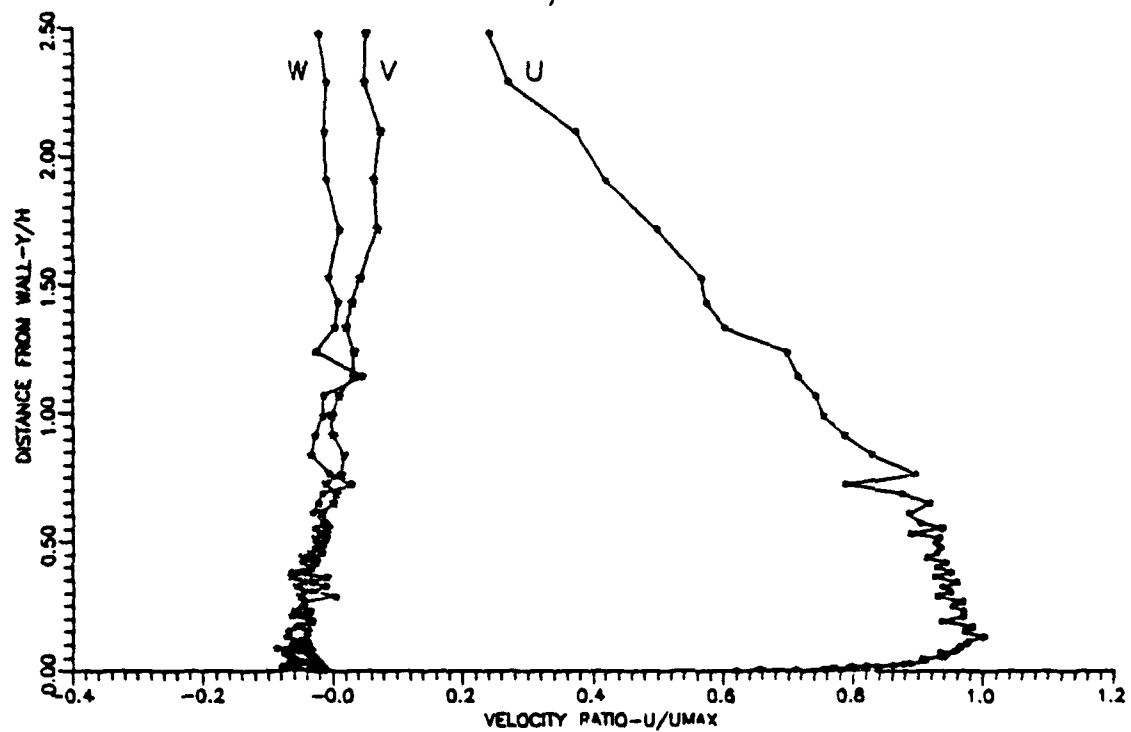


Figure 9. Mean Velocities at Upstream Location

FLUCTUATING VELOCITIES WITH RECTANGULAR NOZZLE $X/H=7.81$

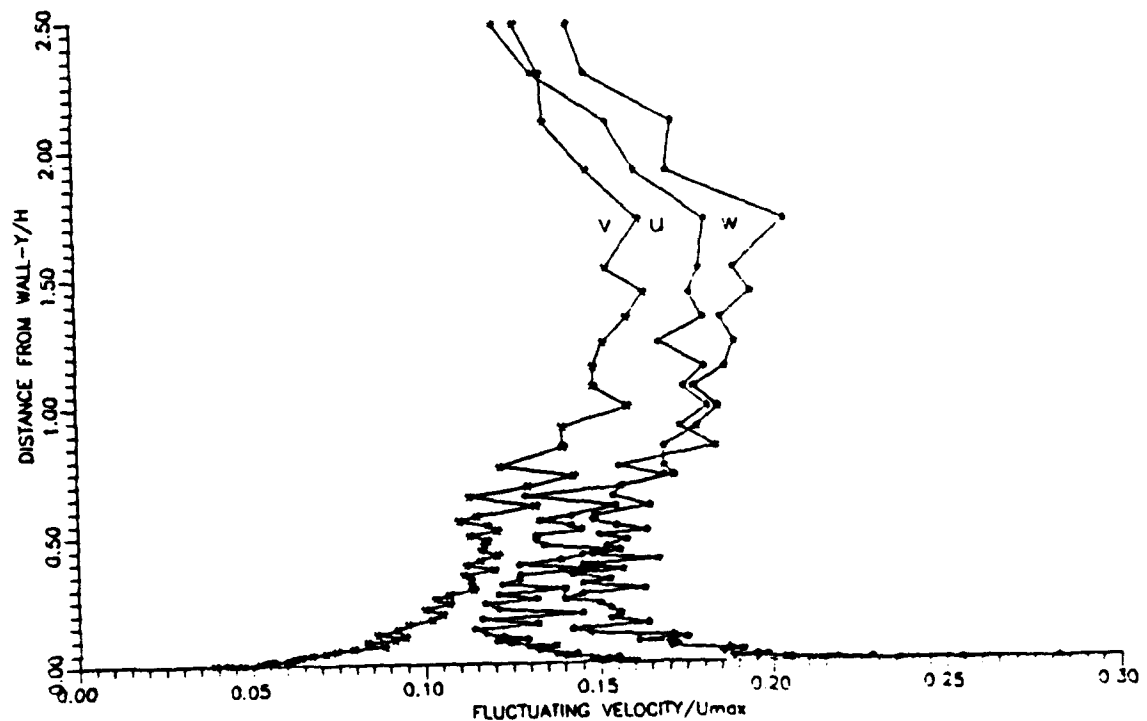
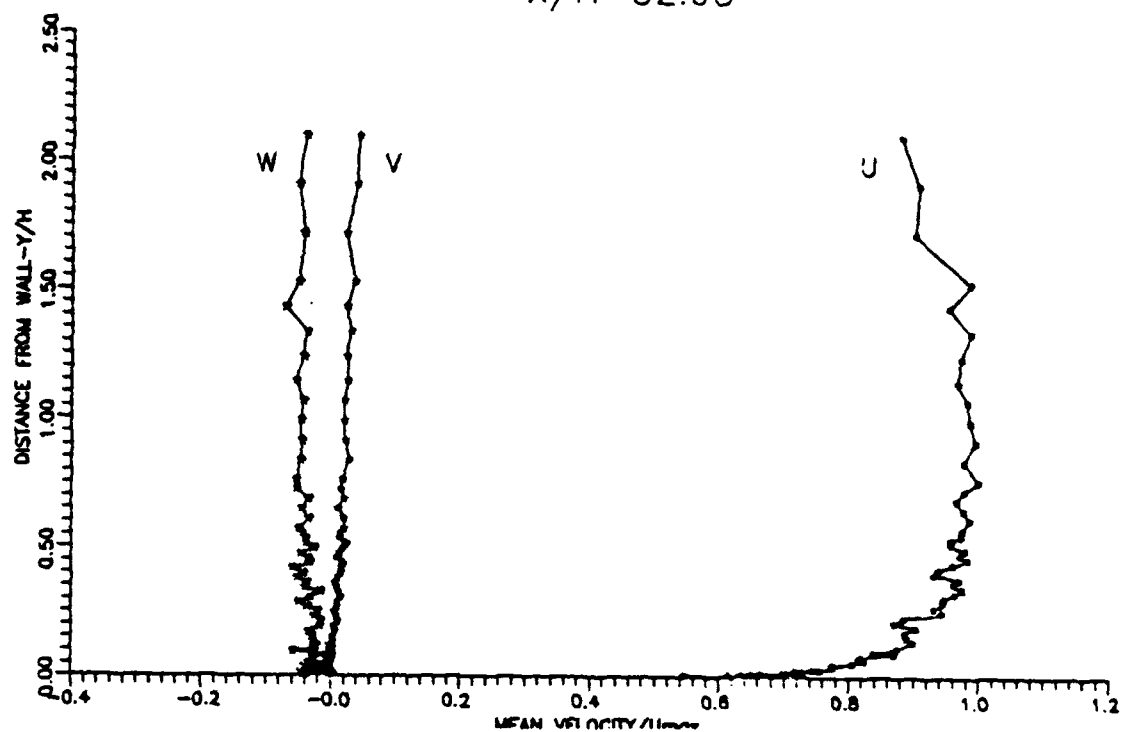


Figure 10. Fluctuating Velocities at Upstream Location

MEAN VELOCITIES WITH RECTANGULAR NOZZLE $X/H=52.95$



FLUCTUATING VELOCITIES WITH RECTANGULAR NOZZLE $X/H=52.95$

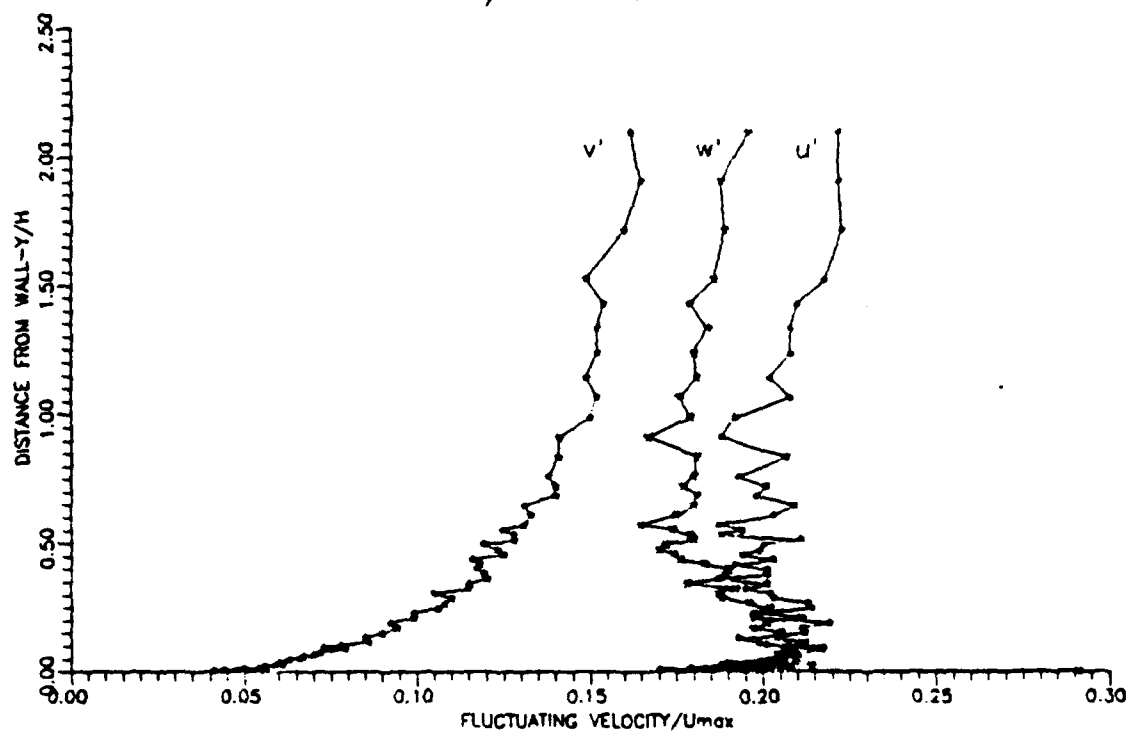


Figure 12. Fluctuating Velocities at Downstream Location

Heat Transfer Data with Unheated Starting Length

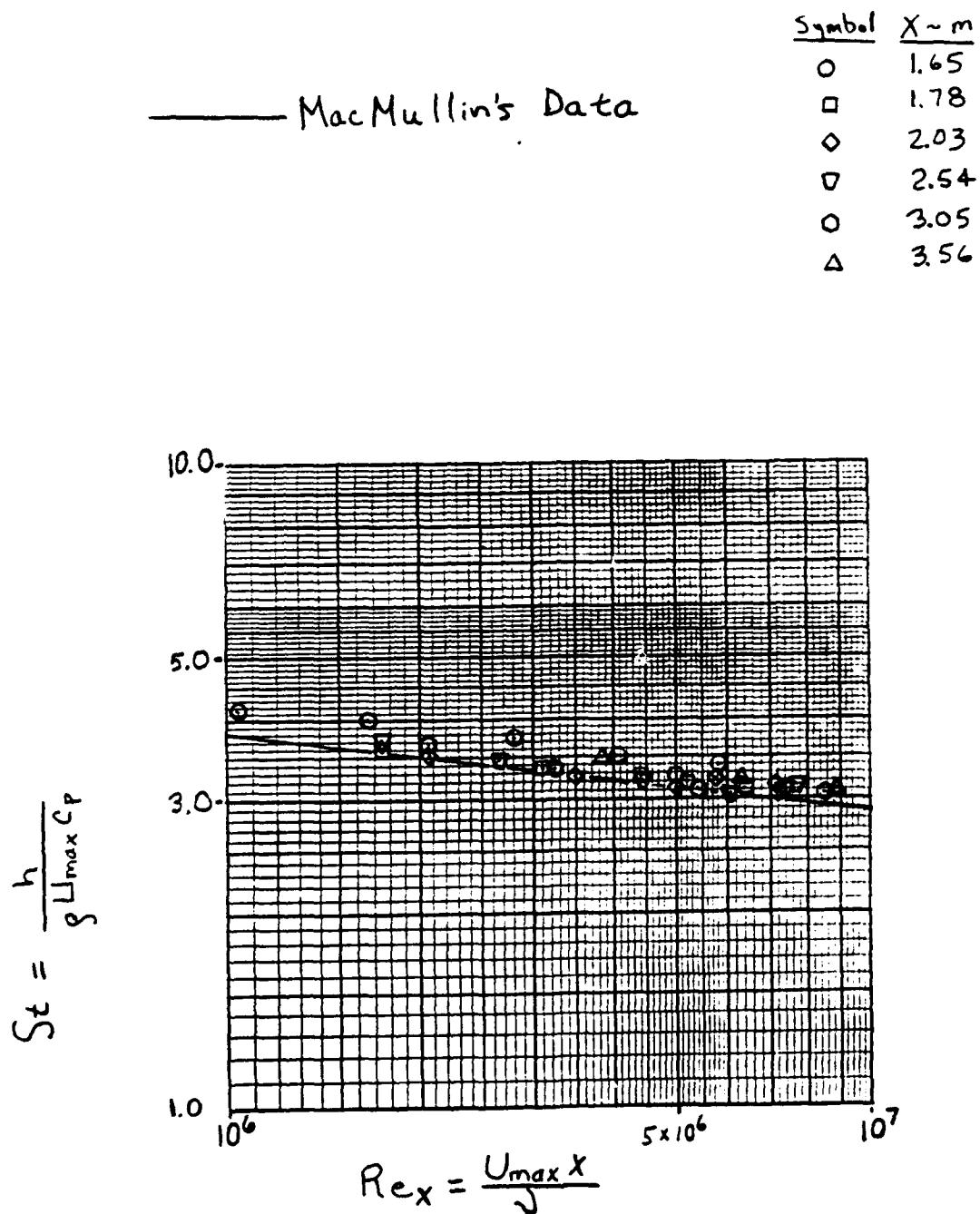


Figure 13. Comparison of Heat Transfer Coefficients

1988 USAF-UES SUMMER FACULTY RESEARCH PROGRAM

Sponsored by the
AIR FORCE OFFICE OF SCIENTIFIC RESEARCH

Conducted by the
Universal Energy Systems, Inc.

FINAL REPORT

Prepared by:	David W. Mikolaitis
Academic Rank:	Associate Professor
Department and	Department of Aerospace Engineering, Mechanics, and Engineering Science
University:	University of Florida
Research Location:	AFWAL/POSF Wright-Patterson AFB, Ohio 45433
USAF Researcher:	W. M. Roquemore
Date:	July 26, 1988
Contract Number:	F49620-87-R-0004

Lifted Jet Diffusion Flames

by

David W. Mikolaitis

ABSTRACT

The larger problem of flame extinction due to strong turbulence intensity has been investigated through the study of the lifted turbulent diffusion flame. Existing extinction criteria were evaluated and the need for a better extinction criterion was identified. A new extinction criterion based on laminar flame theory has been developed and implementation into a numerical fluid dynamics code (GENMDX) has been started. Specific problems in laminar flame theory have been identified whose solution will result in an extinction theory without adjustable constants. Further work is needed to validate the theory.

Acknowledgements

I wish to thank the Air Force Systems Command and the Air Force Office of Scientific Research for sponsoring this research. I am especially grateful to Dr. Arje Nachman of the Air Force Office of Scientific Research for encouraging me to apply for this program. Universal Energy Systems must also be commended on their smooth and efficient administration of the research program.

The fruitfulness and enjoyment of my summer at AFWAL/POSF was made possible by the wonderful people that I met here. I am especially grateful to Dr. W. M. (Mel) Roquemore for giving me the proper balance of guidance and freedom. The exchange of ideas with Dr. Geoffrey Sturgess of Pratt and Whitney is gratefully acknowledged. The special help of Curtis Reeves was of invaluable aid in completing the computational aspects of my work. Experimental work conducted by Dr. T. H. Chen and co-workers at Systems Research Laboratories (a Division of Arvin/ Calspan) was essential to the study. The stimulating discussions with my fellow visitors, Prof. Doug Tally of the University of Michigan , Prof. L-D. Chen of the University of Iowa, and Jeff Riley of Cornell University, made the summer a truly enriching experience.

I. INTRODUCTION

The study of the lifted turbulent diffusion flame is important both technologically and scientifically. It is an excellent example problem for the study of fundamental processes in combustion. In addition it can be found in practice from gas turbine combustors to natural gas well fires. In spite of the fact that the control of lifted turbulent diffusion flames is a very important problem in many engineering applications, the physical mechanisms involved in the flame are not well understood, even qualitatively. The fundamental mechanism by which the flame is stabilized downstream of the fuel supply is currently a matter of great controversy in the combustion community.

The Fuels Branch of the Fuels and Lubrication Division of the Wright Aeronautical Laboratory (AFWAL/POSF) at Wright-Paterson Air Force Base is very concerned with trying to understand the physical mechanisms by which jet diffusion flames become turbulent, lift off from the burner, and eventually blow out as the rate of fuel flow is increased. The expertise at AFWAL/POSF is heavily weighted toward the experimental, specifically in the design and implementation of new diagnostic techniques that have been of invaluable aid in understanding these flames.

My research interests have been in laminar flame theory which can be applied to develop micromechanical models of turbulent combustion. This type of theoretical viewpoint nicely compliments the in-house capabilities of AFWAL/POSF.

II. OBJECTIVES OF THE RESEARCH EFFORT

Two very distinct models of the lifted diffusion flame have been proposed in the combustion literature. One school of thought holds that the central jet of fuel mixes with the ambient air before the flame is reached and so the lifted flame is essentially a propagating premixed flame (for example, see the work of Vanquickenborne and van Tigglen [1]). Alternatively, a second model has been proposed where it is argued that the fuel and air do not have sufficient time to mix before they burn and hence the nature of the lifted flame is like a diffusion flame as in Peters and Williams[2].

Knowing the answer to this question is of interest in a much wider context than just understanding the lifted jet diffusion flame. It is the first step in answering some of the most commonly asked questions in combustion: "For a given flow condition does a flame exist? If so, where?"

Predicting where a flame is in a turbulent flow field is not an easy or routine exercise. Unfortunately, it is also the single most important piece of information in the design of combustion devices such as the gas turbine combustor. The development of criteria determining whether or not a flame can exist in a given flow field and for locating the flame if it does exist would be a very useful contribution and greatly enhance the usefulness of computational fluid dynamics (CFD) codes as a design tool for jet engines.

III.

a.

It is assumed that mixtures that lie outside the limits of flammability cannot support combustion, a reasonable working assumption although not entirely correct. Many mixtures normally considered to be non-flammable will burn in the presence of a continuous ignition source and this ignition source can be supplied through the burning of adjacent mixtures within the limits of flammability. It seems unlikely that an analysis based on this simple flammability criteria will be in serious qualitative error, however.

It is also assumed that local flow conditions can also extinguish the flame. The development of a fluid mechanical extinction criterion and its implementation is the main focus of the summer research effort.

An extinction parameter of the form

$$\frac{1.887D}{(S_L + k(\epsilon\nu)^{1/4}) (\nu^3/\epsilon)^{1/4}}$$

is derived in Lockwood and Megahead [3] based on the dimensional argument that if the characteristic mixing time of a Kolmogorov eddy is shorter than the characteristic chemical time of that same eddy the flame will extinguish. Extinction is assumed if the parameter becomes bigger than one. In this parameter S_L is the laminar flame speed, D is the diffusion coefficient (molecular), ν is the kinematic viscosity (molecular), ϵ is the dissipation rate of the turbulence kinetic energy, and k is an $O(1)$ constant where $O(1)$ means on the order of magnitude of 1. In Lockwood and Megahead it is felt that the characteristic reaction time is shortened

due to the presence of turbulence and hence a "correction" to the laminar burning velocity is sought. Their "correction" term is derived on the assumption that the eddy rotates as a solid body with all viscous action taking place in a thin zone at the boundary of the eddy. From this a radial pressure gradient is uncovered which is supposed to generate a radially inward velocity. This physical picture is inconsistent with the notion that the eddy size is on the Kolmogorov length scale. If the eddy size is on the Kolmogorov length scale, then the proper viscous length scale for the eddy is the eddy size itself and not some very much smaller scale.

Even if we accept Lockwood and Megahead's physical model of the Kolmogorov eddy, the derived pressure difference does not induce a radial velocity as is claimed. The derived pressure difference merely provides the necessary central force to keep the fluid elements on the periphery of the vortex in their "orbital" motion about the axis. After all, it is derived from a solid body rotation model that has no radial velocity.

It is argued in Lockwood and Megahead that when the extinction parameter is greater than 1 the flame cannot exist because the mixing time has become shorter than the chemical time. That the flame is extinguished if the mixing time is very short compared to the chemical time seems likely. In this event the bringing together of two vortices comprised individually of cold reactants and hot products would simply result in a tepid, diluted mixture that is most likely non-flammable. It is also clear that if the mixing time is very long, the hot eddy can act as an ignition source for the cold reactants and a flame will propagate through them. A critical ratio of mixing time to reaction time must therefore exist. It is not at all clear why the critical ratio should be 1, however.

In addition, this extinction criterion is highly sensitive to the value of the unknown constant k as is easily shown. The extinction parameter is a monotonically increasing function of the dissipation rate ϵ and is bounded from above by the quantity $1.887D / kv$. This upper bound can also be written as $1.887/(Sc)k$ where Sc is the molecular Schmidt number. A schematic of the variation of the extinction parameter with dissipation rate is given in Figure 1. If k is greater than $1.887/(Sc)$ the extinction parameter can never be greater than 1 and hence extinction is never predicted. As a practical example, dilute mixtures of propane and air have a Schmidt number of approximately 1.5 and hence if k is greater than 1.26 the stability parameter could never predict extinction. In Lockwood and Megahed comparisons between their theory and experiment are taken for methane/air and ethylene/air mixtures and not for heavier fuels where higher Schmidt numbers are anticipated. If propane is used as the fuel, their results suggest that k should be around 1.34 and so their theory would predict that propane/air flames could never be extinguished by turbulence no matter how strong. This flies in the face of experience.

For these reasons a more useful criterion for flame extinction is sought that does not contain unknown constants and does not predict that some flames can never be extinguished. A mechanistic approach from laminar flame theory was attempted and preliminary work was completed to implement the resulting fluid mechanical flame extinction criterion into a numerical fluid mechanics code called GENMIX.

b.

It is well known that both premixed and diffusion flames can only tolerate a finite amount of flame stretch, S , where the flame stretch is defined by

$$S = \frac{\delta}{S_L} \frac{d \ln A}{dt}$$

Here δ is the flame thickness (reaction zone plus preheat zone), which can be approximated by the diffusion length scale, l , given by

$$l = \frac{\lambda}{\rho C_p S_L}$$

and A is the Lagrangian flame area. C_p is the specific heat, ρ is the density, and λ is the heat conduction coefficient.

In flows dominated by a single velocity gradient, the flame stretch reduces to the more familiar Karlovitz number, K , given by

$$K = \frac{\delta}{S_L} \frac{du}{dx}$$

where $\frac{du}{dx}$ is the characteristic velocity gradient in the flow. A characteristic velocity gradient based on the Kolmogorov scale turbulence structure is the Kolmogorov velocity scale divided by the Kolmogorov length scale and is given by

$$\frac{(\epsilon v)^{1/4}}{(v^3/\epsilon)^{1/4}} = \sqrt{\epsilon}/v.$$

The resulting Karlovitz number, which we will call the microscale Karlovitz number, is

$$K = \frac{\lambda \sqrt{\epsilon}/v}{S_L^2 \rho C_p} = \frac{1}{Pr} \frac{v^2}{S_L^2}$$

where v is the Kolmogorov velocity and Pr is the Prandtl number of the fluid. A critical value of the microscale Karlovitz number as a function of the local equivalence ratio, transport properties (i.e., Lewis number) and reactant temperature should exist and flames will not be sustained when the local microscale Karlovitz number exceeds the critical value. Theoretical analyses of laminar flamelets in non-uniform flow fields (see Chapter 10 in Williams [4] for a fairly complete discussion) may be of some use in calculating the critical microscale Karlovitz numbers in practical applications. In these analyses it has been assumed that the chemical kinetics can be represented by a one-step irreversible reaction with Arrhenius reaction rate and large activation energy and very simple transport models are employed. There has been some recent work along these lines where the large activation energy assumption is relaxed [5-6]. It is expected that the critical microscale Karlovitz numbers will be $O(1)$ and so for preliminary calculations it might be useful to set the critical microscale Karlovitz number to 1.

Another method of determining the critical microscale Karlovitz number is through experiments with counterflow premixed flames. Some experiments of this type have already been done ([7-11], for example).

This extinction criterion can be very easily implemented into numerical codes for calculating turbulent flows. One such code is the well known GENMIX code of Spalding [12]. A version of this code that had been successfully implemented on an IBM mainframe computer was graciously supplied by L-D. Chen of the University of Iowa. The Fortran source code has now been suitably altered so that it now has been successfully implemented on both IBM style and Macintosh personal computers.

IV. RECOMMENDATIONS

a.

There are theoretical analyses that may be of great usefulness in theoretically predicting critical values of the microscale Karlovitz number for premixed flames as a function of equivalence ratio, reactant temperature, transport properties, heat release, etc. [4-6]. If it is found that these highly idealized analyses can give legitimate quantitative predictions of the critical microscale Karlovitz numbers, then the extinction criterion developed here will be self-contained and can be directly implemented into computational codes.

b.

This type of analysis may also be applicable for diffusion flames as well. Of course, the concept of a local laminar flame speed as it is commonly understood makes no sense for a diffusion flame and this parameter appears in the definition of the microscale Karlovitz number. An effective laminar flame speed can be constructed, however. If we take a fluid element from each side of the diffusion flame and mix them in stoichiometric proportions then the resulting mixture has a characteristic laminar flame speed. This "flame speed" is undoubtedly related to the local volumetric rate of chemical reaction. Unfortunately, the state of theoretical knowledge about the extinction of diffusion flames is not nearly as complete as it is for premixed flames. The current state-of-the-art restricts the Lewis numbers of all reactants to be exactly 1 [12]. In premixed flame theory small deviations of the Lewis number away from one have been shown to lead to large qualitative changes in flame behavior. While there is no guarantee that the same will hold for diffusion flames, it is important that cases where the Lewis numbers are not 1 be analyzed. This is especially important in the analysis of hydrogen/air diffusion flames where the Lewis number is much smaller than 1.

It is also crucial that the proposed extinction criterion be implemented into an actual turbulent flow code and the results compared to experiment. The full implementation of the extinction criterion into the GENMDX code has not been completed as of yet and must be done. Once this is done the results of a series of calculations predicting the lift off heights of various lifted turbulent jet diffusion flames can be compared to a corresponding series of experiments.

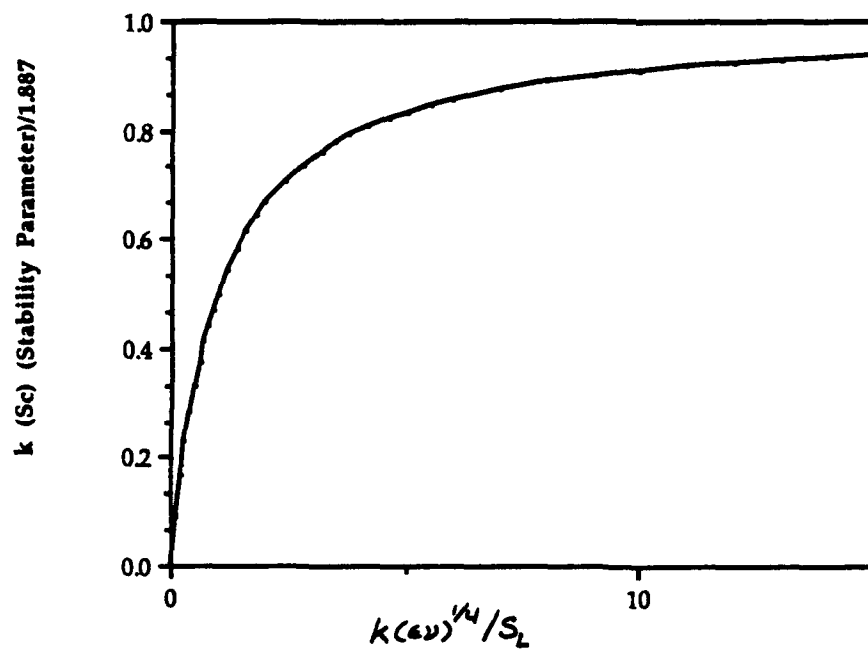


FIGURE 1
Extinction Parameter vs.
turbulence intensity

REFERENCES

- [1] Vanquickenborne, L. and van Tiggelen, A., "The Stabilization Mechanism of Lifted Diffusion Flames," Combustion and Flame, v. 10, 1966, pp. 59 - 69.
- [2] Peters, N. and Williams, F. A., "Liftoff Characteristics of Turbulent Jet Diffusion Flames," AIAA Journal, v. 21, 1983, pp. 423 - 429.
- [3] Lockwood, F. C. and Megahed, I. E. A., "Extinction in Turbulent Reacting Flows," Combustion Science and Technology, v. 19, 1978, pp. 77 - 80.
- [4] Williams, F. A., Combustion Theory, 2nd Edition, Menlo Park, California, Benjamin/Cummings, 1985.
- [5] Mikolaitis, D., "Strained Laminar Premixed Flames," Combustion Science and Technology, v. 53, 1988, pp. 23 - 31.
- [6] Mikolaitis, D., "On the abrupt extinction of premixed flames with Lewis numbers less than one," To appear in Combustion Science and Technology, 1988.
- [7] Law, C. K., Ishizuka, S., and Mizomoto, M., 18th Symposium (International) on Combustion, Pittsburgh, Pennsylvania, The Combustion Institute, 1981.
- [8] Ishizuka, S., Miyasaka, K., and Law, C. K., "Effects of Heat Loss, Preferential Diffusion, Flame Stretch on Flame-Front Instability and Extinction of Propane/Air mixtures," Combustion and Flame, v. 45, 1982, pp. 293 - 308.
- [9] Ishizuka, S. and Law, C. K., 19th Symposium (International) on Combustion, Pittsburgh, Pennsylvania, The Combustion Institute, 1982.
- [10] Tsuji, H. and Yamaoka, I., 19th Symposium (International) on Combustion, Pittsburgh, Pennsylvania, The Combustion Institute, 1982.
- [11] Sato, J., 19th Symposium (International) on Combustion, Pittsburgh, Pennsylvania, The Combustion Institute, 1982.

- [12] Spalding, D. B., GENMIX - A General Computer Program for Two-Dimensional Parabolic Phenomena, Oxford, Pergamon Press, 1977.
- [13] Linan, A., "The Asymptotic Structure of Counterflow Diffusion Flames for Large Activation Energies," Acta Astronautica, v. 1, 1974, pp. 1007 - 1039.

1988 USAF-UES SUMMER FACULTY RESEARCH PROGRAM/
GRADUATE STUDENT RESEARCH PROGRAM

Sponsored by the
AIR FORCE OF SCIENTIFIC RESEARCH

Conducted by the
Universal Energy Systems, Inc.

FINAL REPORT

Prepared by: Douglas G. Talley
Academic Rank: Assistant Professor
Department: Mechanical Engineering and
Applied Mechanics
University: The University of Michigan
Research Location: AFWAL/POSF
Wright-Patterson AFB
Dayton, Ohio 45433-6563
USAF Researcher: W. M. Roquemore
Date: July 22, 1988
Contract No.: F49620-87-R-0004

Interpretation of a Lifted Turbulent Diffusion Flame as
a Problem in Stratified Combustion

by

Douglas G. Talley

ABSTRACT

The lifted turbulent diffusion flame has been examined theoretically. Interpretation as a stratified flame partially reconciles conflicting ideas about how the flame becomes stabilized in space by recognizing that the fundamental stability mechanism probably changes as the flame evolves from the just-lifted to the near-blowout condition. Although fundamental understanding of the stratified combustion processes is currently very limited, a model has been proposed for parabolic flows which incorporates the best existing knowledge about stratified combustion and about turbulent combustion. It allows simultaneous calculation of the lifted flame height and the hot and cold flows which should be valuable for engineering purposes.

Acknowledgements

The author is indebted to the Air Force Systems Command, the Air Force Office of Scientific Research, and Universal Energy Systems for sponsorship of this research. The congenial atmosphere along with the free and creative thinking which is encouraged at the Aero Propulsion Laboratory made this a truly rewarding experience. The author would like to especially thank his sponsor, Dr. Mel Roquemoire, and the staff at Systems Research Laboratories, especially Dr. Tzong Chen. He is also grateful to his colleagues Dr. David Mikolaitis and Dr. Lea Chen for many stimulating discussions.

I. INTRODUCTION:

If a jet of fuel is injected into a stagnant environment containing oxidizer and ignited, a diffusion flame will be established. As the jet velocity is increased, the flame will become turbulent and can lift above the burner rim, stabilizing at a mean position in space against the bulk flow. When this happens, some amount of premixing between the fuel and oxidant can occur in the cold flow prior to reaching the flame. If the jet velocity is further increased, the flame will eventually extinguish, or blow out. The mechanism by which a lifted turbulent diffusion flame becomes stabilized in space is currently not well understood.

The Fuels Branch of the Fuels and Lubricants Division of the Aero Propulsion Laboratory at Wright-Patterson Air Force Base has been studying diffusion flames for sometime, and has recently expanded its effort to include lifted turbulent diffusion flames. These flames possess many similarities to the flames which exist in gas turbine combustion.

My own research interests lie in the area of combustion in stratified fuel/air mixtures, or mixtures which contain intermediate amounts of mixing compared with premixed flames and diffusion flames. A lifted turbulent diffusion flame is one example of a flame in which intermediate amounts of mix-

ing probably have to be taken into account. My previous research on bluff body flame stability in stratified fuel/air mixtures and on the propagation of weakly stratified flames helped lay the foundation for this summer's research under the SFRP program.

II. OBJECTIVES OF THE RESEARCH EFFORT:

Currently, the stabilization mechanism of lifted turbulent diffusion flames is the subject of considerable controversy. In one view^{1,2}, the amount of premixing of fuel and air upstream of the flame is sufficient for the front to be essentially premixed and propagate against the mean flow as a turbulent premixed flame. In another³, the upstream gas does not have enough time to mix significantly, implying the flame is essentially a diffusion flame whose location depends on whether the turbulent scalar dissipation is too great to allow the flame to exist. The amount of premixing which actually exists upstream of the flame is therefore seen to be an important factor. The research goals were initially formulated as follows:

a. Experimentally investigate lifted turbulent propane/air diffusion flames using two dimensional Rayleigh scattering and LDV techniques to assess the degree of premixing and the velocity field in the vicinity of the flame front over a series of conditions ranging from - lifted to near blowout.

b. Develop a theoretical framework within which to view the leading flame front as a stratified flame. Explore how to incorporate this in a form useful for practical applications.

It turned out that laboratory time could not be obtained for taking the Rayleigh/LDV data, due to a heavy laboratory workload having more pressing commitments elsewhere. A few high-speed movies were taken, but these revealed nothing new. Therefore only the theoretical aspects of this project could be accomplished. This resulted in a new interpretation of a lifted turbulent diffusion flame as a stratified flame.

III. THEORETICAL CONSIDERATIONS:

Both the premixed and diffusion flame views of the lifted flame are subject to criticism on different grounds. The stratified view encompass the following points:

a. Any mechanistic explanation must include a mechanism for flame propagation against the bulk flow.

b. The leading flame should probably be treated as a front, not as a collection of segments propagating at the local premixed flame speed.

c. The propagation velocity of the front depends on the gradient of the fuel/air ratio as well as on its local value and other factors.

Some work was performed on general ways of classifying stratified flames. A method of comparing reaction-conserved scalar (RCS) fields with nonreaction conserved scalar (NRCS) fields was felt to hold much promise. Ideally, RCS are not affected by the presence of chemical reactions. In reality they may be influenced by them, even if they are not created or destroyed, due to the effects of reaction on density, differential diffusion, and other processes. However, in many situations these influences may often be small. Under this view, unless the gradients in all RCS are zero, there is a good possibility that the mixture may be stratified. Classification of premixed flames and diffusion flames as well as stratified flames appear to be possible using this method. Under certain circumstances it is useful to refer to RCS as mixture fractions and to NRCS as progress variables.

IV. THE LIFTED TURBULENT DIFFUSION FLAME:

A conceptualization of what an instantaneous view of a lifted turbulent diffusion flame might look like is illustrated in Figure 1. Two conditions are illustrated simultaneously: a just lifted condition and a near blowout condi-

tion. All scalar fields are assumed to be functions of the single mixture fraction Z . The crosshatches indicated regions where the mixture is flammable.

If the flame is just lifted, it will be located near the burner rim as illustrated in the inset to the right. The crosshatched bars again indicate flammability limits. Shown in the inset are what the iso-contours of the mixture fraction and the flame position might instantaneously look like. Due to the dynamics of the turbulence, the flame could in fact occupy any position within the flammable region, but since the flammable region is thin, it will be located in the general vicinity of the stoichiometric contour Z_{st} . A pure diffusion flame with infinite reaction rates would be located on this contour. The flame may propagate at various local speeds normal to its surface, but a downward component must be present on average in order for it to hold its position against the flow.

If the flame is near blowout, it will be located higher up as illustrated in the inset at the left. Here the flammability limits are much broader. The iso-contours of mixture fraction may sometimes be grouped close together, in which case a diffusion-like flame may be present, or they may be spaced widely apart, providing the possibility of a premixed-like flame. Premixed flames would be more likely here

than in the just lifted condition, due to the greater amount of time available for the premixing to occur.

One consequence of this conceptualization, if correct, is that the fundamental stabilization mechanism may change from diffusion-like to premixed-like as the flame approaches blowout. Theories based on premixed turbulent flame speeds may not be too objectionable near blow-out; this may be why they are often able to predict blowout characteristics yet do less satisfactorily in predicting flame heights. It appears that much more work needs to be done to understand the just-lifted stabilization regime.

V. ENGINEERING MODEL:

A rigorous model of the flame stabilization process would require an understanding of the three dimensional propagation of flames in stratified mixtures. This understanding does not exist at present. Nevertheless it is often desirable to have engineering models capable at least of predicting trends.

An attempt has been made to combine existing knowledge about stratified combustion and about turbulent combustion into an engineering model. Many of the assumptions which have been made could be highly questionable; they are in many cases justified largely by the need to make them in order to pro-

ceed. However, the model is easily modified to incorporate improved knowledge of the propagation process as it becomes known. The details of the model are too lengthy to describe within the space limitations of this report; what follows is a brief summary.

Since premixed theories may be adequate for flames near blowout, the model focuses on just-lifted flames. The flame is assumed to essentially be a diffusion flame on the stoichiometric surface, but with a leading edge which contains the physics of a propagation mechanism. The propagation mechanism is assumed to occupy a negligibly small region in space. The flame position is determined by the position where the propagation velocity v_f is equal to the flow velocity. Because of these features, the model is called the propagating laminar diffusion flamelet model. The propagation velocity is assumed to be a function of the scalar dissipation χ and the laminar flame speed S_u of the homogeneous stoichiometric mixture, ie, $v_f = f(\chi, S_u)$. The scalar dissipation is related to the local gradient in mixture fraction through $\chi = 2D|\nabla Z|^2$, where D is the mass diffusivity. Fluid properties are assumed to be given by a fast reaction, equilibrium assumption above the flame, and by a cold flow, frozen assumption below the flame. Turbulence is accounted for by probability density function methods⁴. The model can be inserted into existing parabolic turbulent flow codes.

An important advantage of the model is that the hot and cold flows can be calculated simultaneously along with the flame position. This feature does not depend on a stratification concept; it works independently of the means by which the flame position is specified. The most important disadvantage of the model is that the functional form of $v_f = f(\chi, Su)$ is currently not well known. For the present, this can be compensated in part by substituting empirical relationships based on experimental measurements. Another disadvantage of a more short term nature is that it currently only works in parabolic flows. However, it should be possible to extend it to elliptic flows, and this ought to be explored.

VI. RECOMMENDATIONS:

a. The conceptualization of Figure 1 could be significantly better substantiated by following through with the Rayleigh/LDV experiments originally envisioned as part of this project. The two-dimensional Rayleigh data should provide information on instantaneous flame position as well as gradients in fuel/air ratio similar to that illustrated by the insets to Figure 1. A mapping of lifted flame regimes based on these measurements over conditions ranging from just-lifted to near blowout in propane/air flames would provide new and unique information. LDV measurements near the leading edge of the flame would help to assess propagation velo-

cities. A new CH imaging technique which is currently being implemented at WPAFB would be extremely valuable in better indentifying flame configurations.

b. The engineering model formulated herein should be implemented in a turbulent code for jets. The parabolic GENMIX code⁵ would be a likely candidate. There are a (very) few functional forms for $v_f = f(\chi, Su)$ which have been suggested in the literature^{6,7}, and these should be evaluated by comparing predicted lift off heights with experimental values. This exercise would help suggest alternative forms even if the suggested forms are not successful. It would also be of significant practical value to explore how the model could be implemented elliptic flows.

c. Over the longer term, a great deal of work needs to be performed on the fundamental nature of combustion in stratified mixtures. This remains an all but neglected area in combustion. Both theoretical and experimental work is needed. Over the shorter term, even fairly unsophisticated approaches would be valuable.

REFERENCES

Vanquickenborne, L., and van Tiggelen, A., The Stabilization Mechanism of Lifted Flames, Comb. Fl., 1966, Vol. 10, pp. 59-69.

Kalghatgi, G. T., Lift-off Heights and Visible Lengths of Vertical Turbulent Jet Diffusion Flames in Still Air, Comb. Sci. and Tech., 1984, Vol. 41, pp. 17-29.

Peters, N., and Williams, F. A., Lift-off Characteristics of Jet Diffusion Flames, AIAA Journal, 1983, Vol. 21, pp. 423-429.

Libby, P. A., and Williams, F. A., eds., Turbulent Reacting Flows, Springer-Verlag, 1980.

Spalding, D. B., GENMIX: A General Computer Program for Two-Dimensional Parabolic Phenomema, Pergamon Press, 1977.
Liebman, I., Corry J., and Perlee, H. E., Flame Propagation in Layered Methane-air Systems, Comb. Sci. and Tech., 1970, Vol. 1, pp. 257-267.

Kulkarny, V. A., Shwartz, J., and Fink, S., A Two-Dimensional Flow Model of Laser Supported Combustion Waves, AIAA 16th Fluid and Plasma Dynamics Conference, 1983, paper AIAA-83-1718.

STABILIZATION REGIMES:

NORMALIZED CONSERVED SCALAR FIELD
INSTANTANEOUS PROFILES

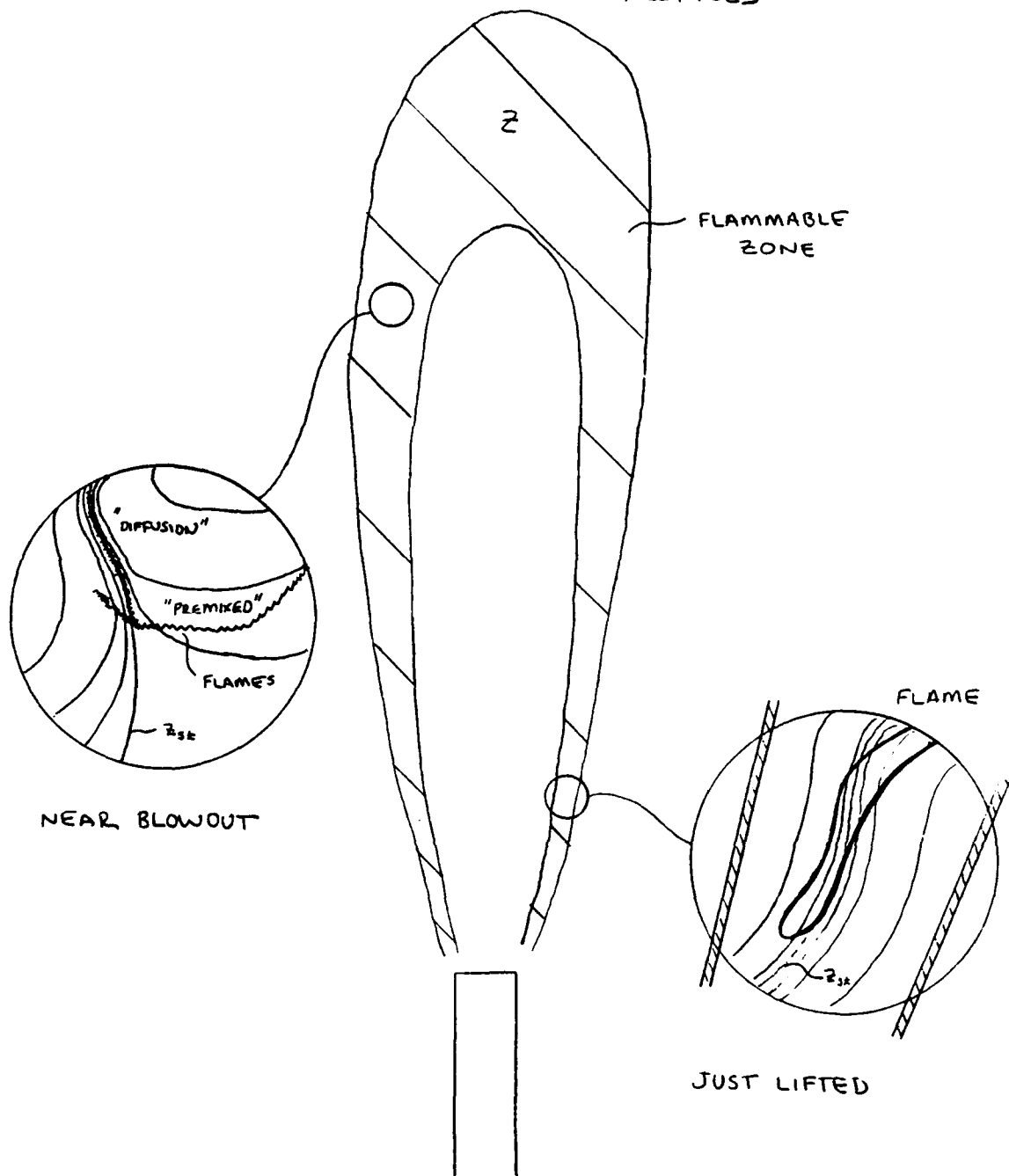


FIGURE 1.
76-14

1988 USAF-UES SUMMER FACULTY RESEARCH PROGRAM/
GRADUATE STUDENT RESEARCH PROGRAM

Sponsored by the
AIR FORCE OFFICE OF SCIENTIFIC RESEARCH
Conducted by the
Universal Energy Systems, Inc.

FINAL REPORT

DIFFUSION AND CONVECTION IN THE CONDENSER
OF A GAS-LOADED HEAT PIPE

Prepared by: Juin S. Yu
Academic Rank: Professor
Department and Mechanical Engineering
university: West Virginia Institute of Technology
Research Location: AFWAL/POOS-3, WPAFB, Ohio 45433
USAF Researcher: Dr. Won Soon Chang
Date: September 1, 1988
Contract No: F49620-87-R-0004

DIFFUSION AND CONVECTION IN THE CONDENSER
OF A GAS-LOADED HEAT PIPE

by
Juin S. Yu

ABSTRACT

This work presents a systematic and self-consistent analysis on the basis of two-dimensional diffusive convection between the vapor and the noncondensable gas for the determination of the rate of heat transport in a gas-loaded heat pipe of circular cross-section. The analysis makes use of the physical conditions that the condenser end plate is insulated and that saturated equilibrium states of the heat transfer fluid exist at the liquid-vapor interface. As a simplification presently used to account for axial heat conduction, the pipe wall is assumed to exist at the local liquid-vapor interface temperature, and the wick structure, the liquid gap (if exists) and the pipe wall are lumped together as a homogeneous region having an effective thermal conductivity. The condenser section of the pipe is allowed to lose heat by either convection or radiation or both. It is shown that the one-dimensional analysis of Edwards and Marcus[1] and the two-dimensional equations of Peterson and Tien[2] represent the lowest levels of approximation of the present formulation.

ACKNOWLEDGEMENTS

This work was performed under the auspices of the Nuclear/Thermal Technology Group of the Aero Propulsion Laboratory, WPAFB. I wish to express my gratitude to the Air Force Systems Command and the Air Force Office of Scientific Research for their financial sponsorship. The sincere help in various forms furnished by the Universal Energy Systems throughout the research period is greatly appreciated.

I am indebted to Dr. E. T. Mahefkey and Dr. W. S. Chang for the assignment and many helpful discussions dealing with the performance of gas-loaded heat pipes. I wish to thank them for their suggestions in specific matters of exposition. Many persons have helped me during the performance of this work. I am particularly grateful to my summer colleagues of the Nuclear/Thermal Technology Group for their friendly assistance.

I. INTRODUCTION:

A gas-loaded heat pipe which contains a fixed quantity of a noncondensable gas in addition to the primary heat transfer fluid is known to have distinctive advantages over conventional heat pipes for startup and thermal control under varying evaporator load conditions[3]. A simplistic picture may be given as follows. As the vapor flow steadily develops in the pipe after the onset of heat transfer, the noncondensable gas is pushed in the flow direction and accumulates in a volume adjacent to the condenser end plate. A portion of the condenser thus becomes inaccessible to the condensing vapor which must then seek to adjust its temperature conditional to of the existing rate of heat transfer. The higher the heat transfer rate the smaller is the inaccessible volume because of static compression due to increased system pressure and the larger is the surface area available for the condensing vapor. A gas-loaded heat pipe thus has an added degree of freedom in comparison with a conventional heat pipe of similar structure in that the latter has a fixed pipe conductance while the former has a conductance which increases with increasing heat transfer rate. One therefore concludes from this observation that a gas-loaded heat pipe can be used for moderating the system temperature subject to variable load conditions.

A complete theory for predicting the performance of gas-loaded heat pipes must simulate closely the process of simultaneous convection and diffusion. My research work over the last several years has been in the area of convective

diffusion in bounded rectilinear flows. Recently, Dr. W. S. Chang and I have submitted for publication a paper dealing with this topic[4]. Also with Dr. Chang, a separate paper[5] is scheduled for presentation at the Annual Fluid Dynamics Meeting of the American Physical Society to be hosted by SUNY Buffalo, Nov. 20-22, 1988. The work described in this report will be submitted at a later date for presentation and publication. It is believed that my work on dispersion is relevant to my assignment at the Nuclear/Thermal Technology Group of the Aero Propulsion Laboratory.

II. OBJECTIVES OF THE RESEARCH EFFORT:

The steady state concentration distribution of the noncondensable gas inside a gas-loaded heat pipe is governed by the intricate balance between convective flow and mass diffusion. For the simplest pipe circular in geometry, a two-dimensional configuration must be employed for its analysis. Simple theories[6-8] ignoring diffusion altogether obviously do not represent the existing physical processes. The one-dimensional diffusion model of Edwards and Marcus[1,9] falls short of being realistic. The two-dimensional formulation for the gas concentration distribution, which to this author's knowledge was first used by Sockol[10] and then by Tien and his students[2,11], is sound in principle. But their attempted methods of solution are somewhat less rigorous than desired and, therefore, their predictions may be of questionable accuracy. The objective of the present effort is to develop a mathe-

matically consistent procedure for solving the steady state two-dimensional problem of simultaneous heat and mass transfer at the presence of diffusion within a gas-loaded heat pipe of circular cross-section.

A series representation which converges in the mean to the true solution has been analytically formulated through the method of separation of variables for the local mole fraction of the noncondensable gas in terms of a transverse mean function. The radially dependent coefficient functions in the series solution can be determined to arbitrary orders. The transverse mean function is coupled to the interface temperature by a set of two simultaneous equations which are established by using the conditions over the condenser section of the pipe wall in relation to its environment. The present general approach reveals that the formulation of Edwards and Marcus[1] and that of Peterson and Tien[2] represent the lowest-order approximations. The equations are highly nonlinear and, therefore, purely numerical methods must be used for their attack. A computer program is being developed for their solution and it is hoped that the present work could be continued at my institution through the support of the AFOSR-UES mini-grant research program.

III. GOVERNING EQUATION FOR STATIONARY STATE IN DIFFUSION:

In a binary system consisting of the working fluid vapor and the noncondensable gas, where thermal, pressure and forced diffusion are ignored, the local molar flux of the gas due to the local concentration gradient is $-D\vec{\nabla}(cx_g)$ and that

due to convective flow is $cx_g \vec{V}$. Here \vec{V} is the gradient operator, c the molar concentration of the mixture, D the diffusion coefficient, x_g the local mole fraction of the noncondensable gas, and \vec{V} the local velocity of flow. Under steady state operating conditions in the absence of internal sources, the net flux of the gas is zero and one has

$$-D\vec{V}(cx_g) + cx_g \vec{V} = 0, \quad (1)$$

which is the diffusion equation relating the flow velocity to the molar concentration. As a commonly accepted legitimate practice for the analysis in diffusing systems, the molar density c of the mixture and the diffusion coefficient D are considered to be average system parameters which are independent of position. With the use of this assumption, equation (1) gives

$$\vec{V} = D\vec{V} \ln x_g, \quad (2)$$

and the mixture continuity equation $\text{grad}(c\vec{V}) = 0$ becomes

$$\nabla^2 \ln x_g = 0, \quad (3)$$

which is the equation governing the stationary state molar concentration distribution of the noncondensable gas.

The coordinate system used for analyzing a cylindrical heat pipe is shown in Figure 1. The heat pipe under consideration has a uniform wick of an inner radius r_i . Introduce the dimensionless coordinates

$$r = R/r_i, \quad z = Z/r_i, \quad (4)$$

and define

$$F(z, r) = \ln x_g(z, r). \quad (5)$$

Then eq. (3) becomes, because of axial symmetry,

$$\frac{1}{r} \frac{\partial}{\partial r} \left(r \frac{\partial F}{\partial r} \right) + \frac{\partial^2 F}{\partial z^2} = 0, \quad (6)$$

and the flow velocity components are given by

$$\text{axial: } v = \frac{D}{r_i} \frac{\partial F}{\partial z}, \quad \text{radial: } u = \frac{D}{r_i} \frac{\partial F}{\partial r}. \quad (7)$$

IV. FORMULATION OF SOLUTION:

We seek a solution to eq. (6) in the form

$$F(z, r) = F_m(z) + \sum_{k=1}^{\infty} f_k(r) \frac{d^k F_m}{dz^k}, \quad (8)$$

where

$$F_m(z) = 2 \int_0^1 F(z, r) r dr, \quad (9)$$

depending exclusively on the axial coordinate z , is the transverse average of $F(z, r)$ over the flow cross-section. It follows that, by integrating eq. (8) over the flow cross-section,

$$\int_0^1 r f_k(r) dr = 0. \quad (10)$$

Also axial symmetry requires that

$$df_k/dr = 0 \quad \text{at} \quad r = 0. \quad (11)$$

Substitution of eq.(9) into eq.(6) gives

$$\sum_{k=1}^{\infty} \frac{d^k F_m}{dz^k} \frac{1}{r} \frac{d}{dr} \left(r \frac{df_k}{dr} \right) + \frac{d^2 F_m}{dz^2} + \sum_{k=1}^{\infty} f_k \frac{d^{k+2} F_m}{dz^{k+2}} = 0. \quad (12)$$

By equating the coefficients of $d^k F_m / dz^k$ in the above equation individually to zero, the following equations are obtained for the radial functions $f_k(r)$:

$$\frac{1}{r} \frac{d}{dr} \left(r \frac{df_k}{dr} \right) + f_{k-2} = 0, \quad k = 1, 2, \dots, \quad (13)$$

with

$$f_0 = 1 \quad \text{and} \quad f_{-1} = 0. \quad (14)$$

Multiplying eq. (6) by $2rdr$ and integrating the resulting equation from $r=0$ to $r=1$, there yields, after making use of the condition given by eq. (10),

$$\left. \frac{\partial F}{\partial r} \right|_{r=1} = - \frac{1}{2} \frac{d^2 F_m}{dz^2}, \quad (15)$$

which is to be used in the next section for establishing the interface relations governing the rate of heat transfer from the condenser to the cooling ambient.

The radial functions $f_k(r)$ for $k \geq 1$ are to be determined from eq. (13) subject to the boundary conditions given by eqs. (10) and (11). The required solutions can be categorically formulated according to whether the order k is odd or even.

To obtain the solutions with odd orders, we start with $k=1$ in eq. (13). We have, by noting $f_{-1}=0$,

$$\frac{d}{dr} \left(r \frac{df_1}{dr} \right) = 0. \quad (16)$$

Integrating eq. (16) from $r=0$ to $r=r$ by using the condition of eq. (11) gives $rdf_1/dr = 0$, or simply $df_1/dr = 0$. Thus f_1 is a constant which can be evaluated by employing eq. (10) to yield the result

$$f_1(r) = 0. \quad (17)$$

Substituting eq. (17) into eq. (13), an equation identical to eq. (16) is obtained for f_3 . Since the boundary conditions to be imposed on f_3 are the same as those on f_1 , the former must also be identically zero. By repeating the same procedure to eq. (13) for the radial functions of successively larger odd orders, the same result follows and it can therefore be readily concluded that

$$f_{2k+1}(r) = 0, \quad k=0,2,\dots \quad (18)$$

Consequently, eq. (8) becomes

$$F(z,r) = F_m(z) + \sum_{k=1}^{\infty} f_{2k}(r) \frac{d^{2k} F_m}{dz^{2k}}. \quad (19)$$

The even-order radial functions are to be determined from eq. (13). Noting that $f_0=1$, one has

$$\frac{d}{dr} \left(r \frac{df_2}{dr} \right) = -r. \quad (20a)$$

Integration of eq. (20a) gives, after making use of eq. (11),

$$df_2/dr = -r/2, \quad (20b)$$

which can be solved to yield the solution

$$f_2(r) = -r^2/4 + C_2, \quad (20c)$$

where C_2 is a constant of integration. Use of eq. (10) gives

$C_2 = 1/8$ and we have the explicit result

$$f_2(r) = -(r^2 - 1/2)/4. \quad (20d)$$

Now by using eq. (20d) in eq. (13) and by going through the same algebra as above, we can easily get $f_4(r)$ which can in turn be used to obtain $f_6(r)$. It is apparent that radial functions of progressively higher even orders can be similarly determined.

Simple calculations show that a radial function having an index $2k$ ($k=0,1,2,\dots$) is a polynomial in even powers of the radial coordinate r with the highest power being $2k$. This property allows the derivation of a set of recursive relations by which radial functions of successively higher even orders can be determined purely on an algebraic basis without separately integrating the individual equations as described in the last paragraph. We write

$$f_{2k} = \sum_{j=0}^k a_j^{(2k)} r^{2j} \quad \text{for } k = 1, 2, \dots \quad (21)$$

Then, by using eq. (21) for f_{2k-2} on the right-hand side, eq. (13) becomes

$$\frac{d}{dr} \left(r \frac{df_{2k}}{dr} \right) = - \sum_{j=1}^k a_{j-1}^{(2k-2)} r^{2j-1}. \quad (22)$$

Integration with the use of eq. (11) yields

$$\frac{df_{2k}}{dr} = - \sum_{j=1}^k a_{j-1}^{(2k-2)} \frac{1}{2j} r^{2j-1}, \quad (23)$$

which, upon integration, gives

$$f_{2k} = - \sum_{j=1}^k a_{j-1}^{(2k-2)} \frac{1}{4j^2} r^{2j} + C_{2k}. \quad (24)$$

The constant of integration can then be determined by requiring eq. (24) to satisfy eq. (19). The result is

$$C_{2k} = \sum_{j=1}^k \frac{a_{j-1}^{(2k-2)}}{4j^2(j+1)} \quad (25)$$

and thus we have

$$f_{2k} = - \sum_{j=1}^k \frac{a_{j-1}^{(2k-2)}}{4j^2} r^{2j} + \sum_{j=1}^k \frac{a_{j-1}^{(2k-2)}}{4j^2(j+1)}, \quad (26)$$

Comparing eq. (26) with eq. (21), we get the recurrence relations for $k \geq 1$,

$$a_0^{(2k)} = \sum_{j=1}^k \frac{a_{j-1}^{(2k-2)}}{4j^2(j+1)}, \quad a_j^{(2k)} = -\frac{a_{j-1}^{(2k-2)}}{4j^2} \quad \text{for } 1 \leq j \leq k, \quad (27)$$

with $a_0^{(0)} = f_0 = 1$. Using these recurrence relations, we get the first few radial functions to have the explicit expressions

$$f_0 = 1, \quad f_2 = -\frac{1}{4}\left(r^2 - \frac{1}{2}\right), \quad f_4 = \frac{1}{32}\left(\frac{1}{2}r^4 - r^2 + \frac{1}{3}\right), \quad (28)$$

$$f_6 = -\frac{1}{128}\left(\frac{1}{18}r^6 - \frac{1}{4}r^4 + \frac{1}{3}r^2 - \frac{7}{72}\right),$$

and functions of higher orders can also be easily determined. Substituting the results of eq. (28) into eq. (19), we have explicitly

$$F(z, r) = F_m(z) - \frac{1}{4} \left(r^2 - \frac{1}{2} \right) \frac{d^2 F_m}{dz^2} + \frac{1}{32} \left(-r^4 - r^2 + \frac{1}{3} \right) \frac{d^4 F_m}{dz^4} - \dots \quad (29)$$

V. GOVERNING EQUATIONS FOR HEAT AND MASS TRANSFER:

The transverse average function $F_m(z)$ which is central to the construction of the solution in the present formulation is related to the liquid-vapor interface conditions. The noncondensable gas is stationary. Therefore the condensing vapor flows radially outward with a velocity u given by eq. (7). As a first approximation, the Wick-wall structure of the pipe is treated as a homogeneous shell having an effective thermal conductivity \bar{k} at a radially uniform temperature (due to its small thickness). Under steady state conditions, an energy balance as shown in Figure 2 over an area element of the condenser by including axial conduction and heat transfer to the ambient by both convection and radiation then gives

$$c D h_{fg} M_v \left. \frac{\partial F}{\partial r} \right|_{r=1} = r_o [h_o (T_i - T_b) + \epsilon \sigma (T_i^4 - T_r^4)] - \frac{\bar{k} A}{2\pi r_i^2} \frac{d^2 T_i}{dz^2}, \quad (30)$$

where T_i = liquid-vapor interface temperature, T_b = bulk temperature of the condenser cooling fluid, T_r = radiation sink temperature, M_v = molecular weight of the vapor, h_{fg} = latent heat of the vapor, h_o = outside heat transfer coefficient of pipe wall, ϵ = emissivity of outer wall surface, σ = Stefan-Boltzmann constant, A = Axial conduction area of shell structure. In terms of the nondimensional quantities

$$\Theta = \frac{T_i - T_b}{T_s - T_b}, \quad H = \frac{h_o}{h_s}, \quad H = \frac{cDh_{fg}M_v}{r_o h_s (T_s - T_b)}, \quad B = \frac{\bar{k}A}{2\pi r_i^2 r_o h_s},$$

$$F_r = \frac{5.67\epsilon}{h_s (T_s - T_b)}, \quad q_b(\Theta) = \left[\frac{T_b + \Theta(T_s - T_b)}{100} \right]^4 - \left(\frac{T_r}{100} \right)^4, \quad (31)$$

where T_s is the temperature of the vapor in the pipe and h_s is the value of h_o at the location where the interface temperature is T_s , eq. (29) becomes, upon using eq. (15) for the term on the left-hand side,

$$-\frac{E}{2} \frac{d^2 F_m}{dz^2} = H\Theta + F_r q_b(\Theta) - \frac{d^2 \Theta}{dz^2}. \quad (32)$$

Assuming saturation equilibrium, then the mole fraction of the noncondensable gas at the liquid-vapor interface is given by

$$x_{gi}(\Theta) = 1 - p_i(\Theta)/p_s \quad (33)$$

where p_i is the saturation pressure of the condensing vapor at the interface temperature Θ and p_s is the pressure of the mixture in the pipe. Brennan and Kroliczek[3] have reported p_i in the form of a polynomial in terms of the saturation temperature for a number of working substances of heat pipe interest. The same interface mole fraction must also be given by eq. (29) at $r = 1$ and one therefore has

$$F_m(z) + \sum_{k=1}^{\infty} f_{2k}(1) \frac{d^{2k} F_m}{dz^{2k}} = \ln x_{gi}(\Theta) \quad (34)$$

where, evaluated at $r=1$ from eqs. (21) and (27),

$$f_2(1) = -1/8, \quad f_4(1) = 1/192, \quad f_6(1) = -1/3072, \quad \text{etc.} \quad (35)$$

Eqs. (32) and (34) together with eq. (33), within the assumption of equilibrium liquid-vapor interface, are the desired equations for finding $F_m(z)$ and $\Theta(z)$. For a condenser with an adiabatic end plate, the pertinent boundary conditions are

$$d\Theta/dz=0, \quad dF_m/dz=0 \quad \text{at } z=0, \quad (36)$$

$$\Theta \rightarrow 1, \quad F_m \rightarrow \infty \quad \text{as } z \rightarrow l \leq l_c, \quad (37)$$

where $l_c = L_c/r_i$ is the nondimensionalized total length of the condenser and l must be so adjusted that the total gas inventory in the pipe is conserved, that is, if N_g is the number of moles of the gas in the pipe, then

$$N_g = 2\pi r_i^3 \int_0^l dz \int_0^1 r x_g(z, r) dr. \quad (38)$$

In the one-dimensional analysis of Edwards and Marcus[1], the concentration of the noncondensable gas is assumed to be radially uniform. Thus $F(z, r) = F_m(z)$ and, from eq. (19), $f_{2k}(r) = 0$ for $k \geq 1$. Combining eqs. (32) and (34) then gives

$$-\frac{E}{2} \frac{d^2}{dz^2} \ln x_{gi}(\Theta) = H\Theta + F_r q_b(\Theta) - B \frac{d^2 \Theta}{dz^2}, \quad (39)$$

which is equivalent to their formulation under the assumption of lumped pipe shell structures.

Peterson and Tien[2] methodically constructed a solution to the two-dimensional governing equation, eq. (6), in the form

$$F(z,r) = F_m(z) - \frac{1}{4}(r^2 - \frac{1}{2}) \frac{d^2 F_m}{dz^2}, \quad (40)$$

which, upon comparison with eq. (29), is immediately seen to be the lowest order approximation to the general solution. To this level of approximation, the condition of saturation equilibrium at the liquid-vapor interface, instead of eq. (34), is specified as

$$F_m(z) - \frac{1}{8} \frac{d^2 F_m}{dz^2} = \ln x_{gi}(\theta), \quad (41)$$

which is coupled to eq. (32) for the approximate solutions of $\theta(z)$ and $F_m(z)$.

RECOMMENDATIONS

The problem to achieve variable conductance in a heat pipe by using a noncondensable gas has been under analysis and development for the last two decades. The need for a thorough understanding of the performance of gas-loaded heat pipes arises from their essential role in providing spacecraft thermal control[12].

The series representation given by eq. (29) which converges in the mean to the true solution is seen to be mathematically rigorous. The series of eq. (33), therefore, converges to the interface equilibrium mole fraction in the same sense, i.e., the larger the number of terms is taken into account in the series the more efficient is the representation. It has been seen that the work of Edwards and Marcus[1] is the result of using the first single term in the

series and that of Peterson and Tien[2] the first two terms. Since the effectiveness of series representations usually depends strongly on the number of terms used in the calculations unless such numbers are sufficiently large, it is unlikely that these low-order approximations can be regarded as uniformly valid throughout the entire interior region of the condenser section of the heat pipe. In particular, the length l (See eq. (38)) needed to comply with gas inventory conservation is highly susceptible to the actual number of terms employed in the approximation if it falls too far short of what is required for uniform convergence. Going beyond the two-term approximation developed by Peterson and Tien, i.e., $k \geq 2$ in eq. (34), therefore, appears to be an immediate necessity in order to further understand the details of the convective diffusion process associated with the mathematical ramifications of the basic solution.

The exact solution, eq. (29), is derived for the first time as a result of the present effort. To determine the condenser heat transfer, a method of solution of the coupled equations, eqs. (32) and (34), subject to the boundary conditions of eqs. (36) and (37) has yet to be developed for $k \geq 2$. A computer program using finite difference is being formulated in an attempt to achieve this objective. With the hope to continue the presently on-going work, a proposal will be submitted for financial sponsorship through the AFOSR-UES mini-grant research program.

REFERENCES

1. Edwards, D.K., and B.D. Marcus, "Heat and Mass Transfer in the Vicinity of the Vapor-Gas Front in a Gas-Loaded Heat Pipe," ASME Journal of Heat Transfer, vol. 94, 1972, pp. 94-101.
2. Peterson, P.F., and C.L. Tien, "Numerical and Analytical Solutions for Two-Dimensional Gas Distribution in Gas-Loaded Heat Pipes," 1988, under review for publication in the ASME Journal of Heat Transfer.
3. Brennan, P.J., and E.J. Kroliczek, Heat Pipe Design Handbook, B & K Engineering, Inc., 1979, vols. I & II.
4. Yu, J.S., and W.S. Chang, "Dispersion of Solute in Wall-Bounded Parallel Shear Flows," 1988, submitted for publication in Journal of Fluid Mechanics.
5. Yu, J.S., and W.S. Chang, "Dispersion Approximation for Mass Transport in Laterally-Bounded Rectilinear Flows," to be presented at the 41st Annual Fluid Dynamics Meeting of the American Physical Society, SUNY Buffalo, New York, November, 1988.
6. Chi, S.W., Heat Pipe Theory and Practice, Hemisphere, 1976.
7. Antoniuk, D., "Generalized Modeling of Steady State and Transient Behavior of Variable Conductance Heat Pipes," AIAA Paper 87-1615.

8. Bobco, R.P., "Variable Conductance Heat Pipes: A First Order Model," Journal of Thermophysics, vol. 1, 1987, pp. 35-42.
9. Shimoji, S., H. Kimura, and T. Matsushita, "Prediction of Evaporator Temperature of a Gas Loaded Heat Pipe by the Diffuse Front Model," 3rd International Heat Pipe Conference, Palo Alto, 1978.
10. Sockol, P.M., "Startup Analysis for a High Temperature Gas-Loaded Heat Pipe," Technical Memorandum NASA TM X-2840, 1973.
11. Hijikata, K., S.J. Chen, and C.L. Tien, "Noncondensable Gas Effect on Condensation in a Two-Phase Closed Thermosyphon," International Journal of Heat and Mass Transfer, vol. 27, 1984, pp. 1319-1325.
12. Kirkpatrick, J.P., and P.J. Brennan, "The Advanced Thermal Control Flight Experiment," Progress in Astronautics and Aeronautics, vol. 35, MIT Press, 1973, pp. 409-430.

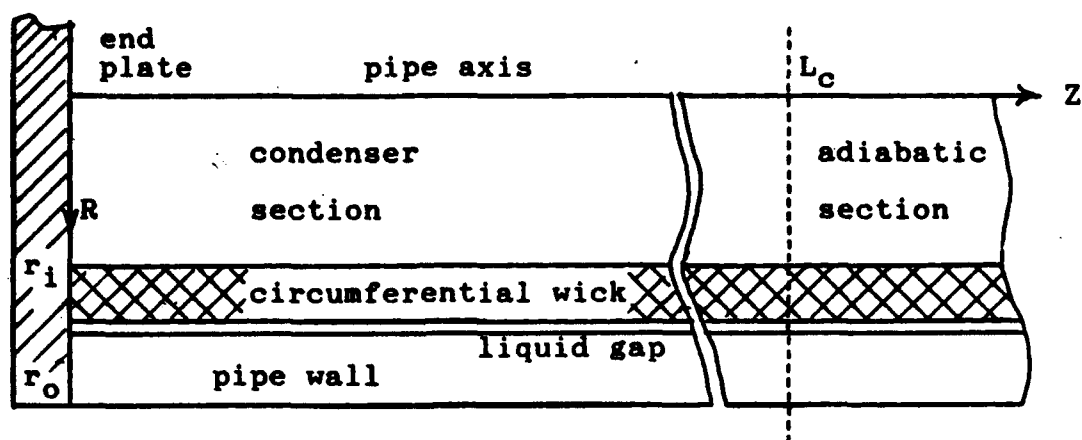


Figure 1. Schematic of basic circular heat pipe showing coordinate system and configurational dimensions; L_c = total length of the condenser section.

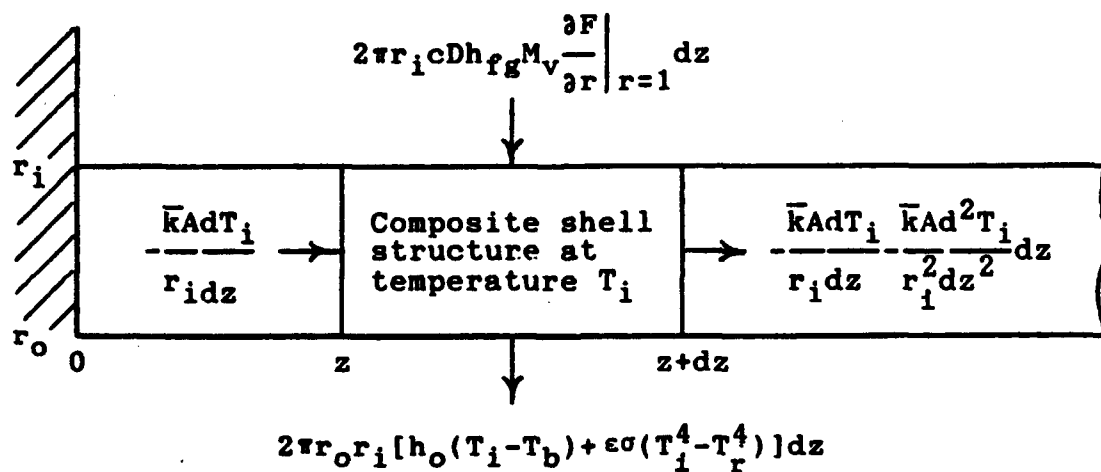


Figure 2. Energy balance for the composite shell structure of the condenser; z and r are dimensionless distances.

1988 USAF-UES SUMMER FACULTY RESEARCH PROGRAM

Sponsored by

AIR FORCE OFFICE OF SCIENTIFIC RESEARCH

Conducted by the

Universal Energy Systems, Inc

FINAL REPORT

Ada Compiler Evaluation Capability

Prepared by:	Mike Burlakoff
Academic Rank:	Assistant Professor
Department & University:	Computer Science Department Southwest Missouri State University Springfield, Mo., 65804
Research Location:	Air Force Avionics Laboratory, AFWAL/AAAF-3, WPAFB, Oh, 45433
USAF Researchers:	Bob Marmelstein, Marc Pitarys
Date of Report:	August 8, 1988
Contract:	F49620-97-R-0004

Ada Compiler Evaluation Capability

by

Mike Burlakoff

ABSTRACT

The initial phase of the Ada Compiler Evaluation Capability (ACEC) test suite and support software is presently being delivered to the Air Force by the Boeing Company ACEC contractor. The system has undergone formal contractor testing with additional Air Force evaluation and testing. The Air Force determined that it would be desirable to provide additional Independent Validation and Verification (IV&V) of this initial delivery. The primary purpose is to verify test results and to determine whether any usability improvements in the products could be made.

Following are the major areas which were investigated: Execution of the test suite and analysis of the results, verification of procedures for use of the test suite, review of statistical support software and review of the major documentation for users of the system.

ACKNOWLEDGEMENTS

I wish to thank the Air Force Systems Command and the Air Force Office of Scientific Research (AFOSR) for sponsorship of this research. LTC Cavender of AFOSR was especially helpful in this sponsorship. Mr. Ray Szymanski of the Avionics Laboratory, System Avionics Division, Systems Evaluation Branch, Logistics Technology Group was responsible for my being assigned to this project and was my administrative point of contact during this period. Universal Energy Systems was always available to answer questions and provide help in the administrative aspects of the program.

The administrative staff at Southwest Missouri State University (SMSU) was also supportive of this work. Dr. Jerry Berlin, Dean of the College of Science and Mathematics endorsed support of this effort. Dr. Bruno Schmidt, Department Head, Computer Science, approved the use of the VAX computer facilities for installing and executing the test suite. John Province of SMSU Computer Services aided in the installation of the test suite.

I could not have achieved many of the results that were achieved in this effort without the excellent technical support throughout this period. Marc Pitarys provided the help that was needed to become familiar with the technical aspects and provided initial support and direction. Bob Marmelstein provided guidance and direction for the areas to be investigated. Their help and encouragement clearly added to the results of this research project.

1. INTRODUCTION:

In 1975 the Department of Defense (DoD) High Order Language Working Group was formed with the goal of establishing a single high order language for use in DoD systems (in particular, in Embedded Computer Systems). Following establishment of technical requirements and international competition, the Ada language as currently defined in (1) was selected. One of the major goals of Ada is to reduce the rapidly increasing costs of software development and maintenance in military systems.

Early in the development process it was realized that the acceptance and benefits derived from a common language could be increased substantially by the development of an integrated system of software development and maintenance tools. The requirements for such an Ada Programming Support Environment (APSE) were stated in the STONEMAN (2) document. STONEMAN identifies the APSE as support for "the development and maintenance of Ada application software throughout its life cycle." (2)

In June 1983 the Ada Joint Program Office (AJPO) proposed the formation of the E&V Task and a tri-service APSE E&V Team, with the Air Force designated as the lead service. In October 1983 the Air Force officially accepted responsibility as the lead service for the E&V Task.

The purpose of the E&V Task is to provide a focal point for addressing the need to provide the capability to assess APSEs and their components and to determine their conformance to applicable standards, such as the Ada Language Standard (1). This will be accomplished by (1) identifying and defining specific technology requirements, (2) developing selected elements of the required technology, (3) encouraging others to develop some elements, and (4) collecting

information describing existing elements. This information will be made available to DoD components, other government agencies, industry and academia (3).

The Ada Compiler Evaluation Capability (ACEC) is one of the technology initiatives of the E&V effort. The E&V team proposed the initial ACEC concept and has made valuable contributions in the guidance and direction of this technology. The Boeing Military Airplanes (BMA) Software and Languages Organization is the contractor responsible for the work.

To provide insight into the process of executing the ACEC and using the analysis tools, the following summary is provided:

Before test problems are translated for execution, ACEC source code is "included" in the test problem. The purpose of the source code is to perform initialization, compute timing, produce output, etc. Some of this code precedes the test problem and some follows it. This process permits new test problems to be easily added to the test suite with no test measurement overhead needed. Following test suite execution, some of the outputs from these "included" programs are: Memory size, minimum and mean of the execution time, counts of how many iterations/repetitions the problems was executed, standard deviation of time measurements, a code (#) which signifies that a specified timing confidence interval was not reached, etc. These outputs can be saved for later processing by ACEC support software for later analysis.

A program called FORMAT reads the above resulting raw data and generates Ada source code consisting of two initialized data array aggregates. One of the aggregates gives the "minimum" execution time, and the other the "space" measurement. (Note that a user does not need to execute FORMAT, but can generate these aggregates manually).

The source code output by FORMAT is then hand edited into a Ada package called MED_DATA.Ada. MED_DATA.Ada contains the formal type declarations, etc. In particular, it contains a two dimensional array type. One of the dimensions ranges is user supplied names of the systems to be analyzed (VAX, IBM, ...). The range of the other dimension is all of the ACEC test names. Therefore, when the user edits in the initialized values into MED_DATA.Ada, a correct Ada program exists. MED_DATA is then compiled, and serves as the input for the ACEC statistical analysis and output program MEDIAN.

II. OBJECTIVES OF THE RESEARCH EFFORT:

The initial phase of the Ada Compiler Evaluation Capability (ACEC) test suite and support software is presently being delivered to the Air Force by the Boeing Company ACEC contractor. The system has undergone formal contractor testing with additional Air Force evaluation and testing. The Air Force determined that it would be desirable to provide additional Independent Validation and Verification (IV&V) of this initial delivery. The primary purpose is to verify test results and to determine whether any usability improvements in the products could be made.

My assignment as a participant in the 1988 Summer Faculty Research Program (SFRP) was to perform the above IV&V of the ACEC. Following were the major areas to be investigated:

- a. Execution of the test suite and verification of results.
- b. Use of contractor supplied tests procedures and scenarios.
- c. Use of statistical analysis support tools to determine correctness and usefulness.
- d. Review and critique of the ACEC User's (4) and Reader's Guides (5).
- e. Analysis of specific test problems which demonstrated incorrect or exceptional results.

III. ACCOMPLISHMENTS AND RESULTS:

a. The ACEC test suite was executed on the AFWAL VAX-11/780 and the Southwest Missouri State University (SMSU) VAX-11/750. The results of both systems were verified that they agreed with the results presented in the Boeing Test Report, dated 27 May 1988.

b. A separate execution of the test suite was performed on the SMSU system to purposely follow the procedures and scenarios provided in the User's Guide. The majority of the procedure worked as specified. Minor comments are listed in (6).

c. Two subsets of the ACEC were repeatedly executed on the SMSU VAX, during various times of the day, using both CPU and Elapsed (clock) time computed measurements. The purpose was to investigate the consistency of these computed times. The results were processed by the ACEC statistical analysis tools. The times were approximately equal. For this system and tests, the CPU times were the most consistent. It should be noted that this was a small subset of tests with a small number of repetitions, and no conclusions should be drawn from this experiment.

d. The statistical analysis tools were used on much of the resulting data and the results were analyzed.

e. The ACEC User's and Reader's Guides were reviewed. The specific comments are listed in (6) and (7). In general, the documents were complete, well written and provided the needed ACEC users and background information. The major recommendations were: (1) Additional summaries to present the extent and coverage of the ACEC test suite, and (2) Additional examples in portions of both manuals.

REFERENCES

1. DoD. Ada Programming Language, ANSI/MIL-STD-1815A. 22 Jan 83.
2. DoD. "Stoneman". Requirements for Ada Programming Support Environments. Feb 80.
3. DoD. Evaluation & Validation (E&V) Plan. Version 4.0. 4 Jun 87.
4. Boeing. ACEC Technical Operating Report. User's Guide. 10 Jun 88.
5. Boeing. ACEC Technical Operating Report. Reader's Guide. 10 Jun 88.
6. Burlakoff, M. ACEC User's Guide Comments. 7 Jul 88.
7. Burlakoff, M. ACEC Reader's Guide Comments. 14 Jul 88.
8. Leavitt, T.C. ACEC Working Paper Number 21. 23 May 88.

The last line of the table gives the System Factor. This is computed by using ... (give an example of how computed). Note that the first system is assigned a value of 1.0 and the computations for the other systems are based on this value. The amount by which the System Factor is greater or less than one provides a measure of how much slower or faster the system is compared to the first system."

c. The Histogram explanation needs to state that the Actual Factor column relates to the Residual Factors listed on the Residual, Problem and Systems Factors table. That is, for each Slot Number, the value under Entries Per Slot refers to the number of Residual Factors for that system or entire data set.

d. It may be helpful to change the title of the "Summary Data for each System" table to something like "Summary Data of Residual Factors for each System".

e. The last summary table should be of interest to most users. It would be helpful if all eight possible outcomes (VALID, CMP_TIME,...) were output in this table. If necessary a code could be used for the titles. This information is probably already computed, so it should only be a matter of finding a way to display the data.

For a user with a non-statistical background, the MEDIAN outputs may appear to be extremely detailed and complex. It may be that the explanations are presented from a statistical viewpoint rather than a compiler evaluator's viewpoint. Following are suggestions which may aid in understanding some of the outputs:

a. Since the Histograms relate to the Problem, System Residual table, the Histograms would be more understandable if they followed that table.

b. The Problem, Systems and Residual Factors table is the basis for much of the statistical analysis. Consider using an explanation page similar to the following format:

"The purpose of this table is to provide a statistical basis for comparison of systems performance. From this data, a user may determine which systems and/or problems performed as expected or much better or worse than expected.

The data given for each problem and system represents Residual Factors. The final column gives Problem Factors for each problem.

A Residual Factor of 1.0 indicates a exact expected performance result. The Residual Factor will be large ... (Use the remainder of the paragraph on page 49 of the Readers Guide along with the explanations of the character indicator fields. Then add the paragraph and equations presented at the beginning of the present explanation on page 49. Then continue the explanation as follows:

The Problem Factor values approach the mean of the problem times, however the values are scaled because System Factor for the first system is arbitrarily chosen to be 1.0.

6. FORMAT RECOMMENDATIONS:

FORMAT outputs a mnemonic ("UNRELIABLE") whenever the desired timing confidence level was not reached (a code "#" in the raw data file). The User's Guide discusses how a user may change this process on page 86. However, it may be preferable for FORMAT to always output all measurements and add a suffix code ("#", etc.) to the values. These would also be input and output by MEDIAN. A user will then have all the raw measurements along with a indicator which flags unusual measurements.

Presently, when a subset of the ACEC is executed, and the results are processed by MED_DATA, the user must manually edit out all test names that are not used. An alternative is for the user to indicate missing tests by the "OTHERS => err_no_data" code. When this is done, MEDIAN outputs a full report, with much of the data as "err_no_data" codes showing null values for the tests which were not run. Recommend that FORMAT contain an option which creates the package declarations, with only the test names that are needed for MED_DATA (e.g. create the complete source file MED_DATA.Ada).

FORMAT presently outputs both time and space measurements. Since only one or the other can be used at one time for statistical analysis, a user must presently manually delete one of them from the FORMAT output. A option should exist so FORMAT would produce only one of the measurements (with default being time).

7. MEDIAN RECOMMENDATIONS:

As stated under FORMAT recommendations, all "raw" measurements should be output by FORMAT and MEDIAN. Unusual measurements should be followed by a suffix error code. Also, since Standard Deviation is an indicator of the degree of timing error, output this value on the Timing Measurements Table.

3. DELIVERY TAPE HELP FILE:

The User's Guide which is supplied with the ACEC is complete and helpful in guiding a user in the use and execution of the ACEC. However, as experience is gained in using the system, improved procedures and techniques may become available, and frequent updates to the User's Guide would be needed. It may be helpful if the delivery tape contained a file such as README.DOC which provided a quick summary of procedures to use the ACEC. This could simply be a summary such as presently provided on pages 15-17 of the User's Guide (updated with improvements in use, etc). One of the more valuable uses of this file could be suggestions and hints on lessons learned from executing the ACEC on specific host and targets.

4. VERSION DESCRIPTION DOCUMENT:

Appendix V, Feature Cross References lists test problems which use a particular Ada Language Reference Manual (LRM) feature. A reader could easily misconstrue this appendix and assume that the tests listed under each of the features were specially constructed to test that feature, where in fact, all that is meant is that the test USES the feature. An appendix which listed all LRM features specifically tested by the ACEC may be quite useful. Consideration should be given on whether the present appendix should be kept.

5. EXPANSION SIZE COMPUTATION:

The test problem expansion size computation is presently initiated in the INCLUDE program, and then "included" in the STOPTIME2 program. This is not a part of the INCLUDE process and should be coded elsewhere. The STOPTIME2 program would be a more appropriate place for this computation.

IV. RECOMMENDATIONS:

1. REVIEW OF TEST FAILURES:

The ACEC Software Test Report, dated 27 May 88, gives a summary of test results. Many of the tests failed for various reasons on several of the hosts (except for the Dec VAX). A standard classification failure mnemonic is listed for the failures. However, in reviewing the test logs at the end of the document, in many cases, reasons for the failures are not given. All test failures should be investigated and problem tests should be corrected.

2. REVIEW OF TEST SUITE COVERAGE AND CORRECTNESS:

The entire test suite should be reviewed to verify that the LRM features listed as comments in the tests are correct. The LRM feature should reflect the major purpose of the test. The LRM features could be used as a guide to verify that the ACEC LRM test coverage is complete. Other categories that should be reviewed for completeness of coverage are other typical ACEC programming example tests (benchmarks) and other embedded computer system applications.

The ACEC is a large and rigorous set of test problems which are designed to measure and compare performance of various hosts and targets which use Ada compiled software. Because of the size and complexity of the test suite, it may be that the performance of some of the tests may not be as intended. Individual test problems should be reviewed for being correct Ada and for testing what was intended to be tested (that is, not being amenable to "unintended optimization"). Where appropriate, any problems of test portability should also be reviewed (8).

1988 USAF - UES SUMMER FACULTY RESEARCH PROGRAM

GRADUATE STUDENT RESEARCH PROGRAM

Sponsored by the

AIR FORCE OFFICE OF SCIENTIFIC RESEARCH

Conducted by the

Universal Energy Systems, Inc.

FINAL REPORT

A STUDY OF SKY BACKGROUNDS AND SUB-VISUAL CIRRUS

AT THE MEGALIDAR SITE

AND

A PROPOSED TURBULENCE MONITORING FACILITY

FOR WRIGHT-PATTERSON AFB

Prepared by:	Dr. Gerald W. Grams
Academic Rank:	Professor
School and	School of Geophysical Sciences
University:	Georgia Institute of Technology
Research Location:	AFWAL/AARI Wright-Patterson AFB Dayton, Ohio 45433
USAF Researcher:	Jan Servaites
Date:	September 30, 1988
Contract Number:	F49620-87-R-0004

A Study of Sky Backgrounds and Sub-Visual Cirrus
at the MEGALIDAR Site and a Proposed
Turbulence Monitoring Facility for Wright-Patterson AFB

by

Gerald W. Grams

ABSTRACT

This project involved the supervision of two Ph. D. graduate students from the School of Geophysical Sciences at Georgia Tech. Both students carried out independent research efforts.

Eric Schmidt performed a series of experiments designed to characterize sky background conditions at the MEGALIDAR site at WPAFB. He also observed subvisual cirrus clouds and smoke layers from forest fires in Yellowstone Park using a portable LIDAR system, ground-based photometers and video imaging devices. These observations are supplemented with meteorological records and satellite images.

Randal Mandock completed a thorough study of the need for characterizing atmospheric turbulence as part of the test and evaluation procedures for new optical sensors. This study resulted in a detailed plan for characterizing atmospheric turbulence at the existing electro-optics sensor test facility operated by AFWAL/AARI.

I. INTRODUCTION:

The principal investigator has been a Professor in Georgia Tech's School of Geophysical Sciences since 1977 and has held a joint appointment in the GTRI (Georgia Tech Research Institute) Electromagnetics Laboratory's Electro-Optics Division since 1985. Since the beginning of his joint appointment, he has sought to promote and actively participate in interdisciplinary projects that combine the resources of GTRI with the interests of faculty members in Georgia Tech's academic units to advance our capabilities in the general area of understanding atmospheric effects on the propagation of electromagnetic waves. As part of that effort, he and Dr. Robert Hyde from GTRI's Electro-Optics Division have worked with AFWAL/AARI to help explore the feasibility of using the 100-inch optical collimator at the Wright-Patterson Air Force Base as the receiver for an atmospheric LIDAR (Light Detection And Ranging) system - capable of measuring atmospheric parameters from the Earth's surface to altitudes in excess of 100 km.

At the present time, through a contract from AFWAL/AARI with Dr. Alan Garrison of GTRI, Georgia Tech has completed a detailed study on the use of the 100-inch facility as a zenith telescope as the receiver for what would be the world's most powerful LIDAR system. The study addressed the various parameters that could be observed with the "MEGALIDAR" system (as it has been called during the past year).

Funding has also been provided for a MEGALIDAR demonstration during the fall of 1988. The test will utilize parts of an operational LIDAR system built by Georgia Tech last year under Air Force contract F0963-85-G-3104; Delivery Order 0013, "IRSTS" Flight Test Support Services (Atmospheric Instrumentation Development Program). The principal investigator on this Summer Fellowship Program had served as technical director of that program. The equipment to be used with the 100-inch collimator as part of the MEGALIDAR demonstration includes a state-of-the-art frequency-doubled Nd:YAG laser to be used as the

transmitter and a computer-controlled data system which incorporates a transient recorder capable of digitizing the LIDAR echoes at 7.5-m range intervals with 12-bit resolution. The demonstration will represent the first use of the 100-inch system as a LIDAR receiver to study temperature and density profiles to altitudes up to 100 km.

Our preliminary plans for work to be carried out under the Summer Faculty Research Program included multi-sensor studies at the MEGALIDAR site to characterize the sky background characteristics under different atmospheric conditions. Data on the amount of radiation that would be collected by the collimator from the overhead sky at different wavelengths due to scattering of sunlight, moonlight, street lights and other illumination sources for different cloud-cover and aerosol conditions are needed for us to complete our models for calculating signal-to-noise ratios for the wide variety of LIDAR experiments that we have proposed for the MEGALIDAR system.

We also had a special interest in initiating studies of the effect of thin subvisual high-altitude cirrus layers on the propagation of infrared radiation in quasi-horizontal directions. This topic was the main reason for funding the previous Georgia Tech efforts in the area of atmospheric instrumentation development to support IRSTS sensor tests. It has also been a long-time research interest of both the principal investigator and one of his Ph. D. students, Eric Schmidt, who had applied for and received one of the UES Summer Graduate Student Fellowships.

Mr. Schmidt already had extensive experience in geophysical research programs - including remote sensing and atmospheric radiation transfer. From 1985 until he returned to graduate school to work on his Ph. D. degree, he worked at Teledyne Brown Engineering in Huntsville where he was involved in the evaluation of the LOWTRAN atmospheric model code by means of correlation and comparison of data from a cold optics radiometer and an infrared spectrometer. He completed work on validation

of ozone extinction coefficients near 9.8 microns and has continued work on an analysis in the 11.2 micron region where nitric acid, freons and aerosol particles may contribute (Schmidt, 1988). He was also involved in on-going work on the validation of models to evaluate atmospheric effects on ground-based laser propagation.

We felt that Mr. Schmidt's background and experience were relevant and necessary for the success of the proposed plan. We also thought that the proposed plan would benefit his academic progress since his research interests included studies of the propagation of infrared radiation through layers of non-spherical particles as a potential topic for his Ph. D. thesis.

Another of the principal investigator's graduate students, Randal Mandock, also participated in the Summer Graduate Student Fellowship Program. Mr. Mandock took on a assignment that we believe could lead to new facilities to make significant improvements in the characterization of the effect of atmospheric turbulence on the performance of some of the new infrared sensors being tested by the Air Force. As Electro-Optical sensors achieve higher and higher resolution, atmospheric effects on the propagation of the electromagnetic energy being detected by the sensor can act to degrade performance. Factors such as scattering by aerosol particles and atmospheric turbulence can significantly affect a sensor's ability to see a target.

Again, we were able to offer an outstanding student for this project. The principal investigator has worked with Mr. Mandock since 1985 as his thesis supervisor for a Masters degree in the Atmospheric Sciences. At that time, we was working on a problem involving the effects of adverse weather on millimeter wave propagation. The database for his study was obtained from a series of experiments conducted near Flatville, Illinois, by research groups from GTRI's Millimeter Wave Division, by NOAA's Wave Propagation Lab from Boulder, Colorado, and by the U.S. Army's Atmospheric Sciences Lab (ASL) from White Sands, New

Mexico. At that time, Randy's work was being carried out as a graduate student in the School of Geophysical Sciences at Georgia Tech with the principal investigator of this Summer Faculty Research Program as his thesis supervisor. His Graduate Research Assistantship was paid by GTRI with funds provided by the U.S. Army Research Office; his thesis committee included scientists from GTRI, NOAA and ASL. This arrangement turned out to be a very successful bridge between the academic and research units on the Georgia Tech campus. In fact, the arrangement was highlighted as a model for graduate education opportunities in several major proposals for Centers of Excellence at Georgia Tech (a \$10 million dollar proposal to the U.S. Army Research Office for a Center of Excellence in Geosciences in 1986 and a \$20 million proposal to NSF for a Center for Atmospheric Propagation and Remote Sensing in 1988).

The hard work and enthusiasm displayed by Mr. Mandock in the above efforts led us to undertake a project that would explore the needs of groups at AFWAL and elsewhere for a facility to characterize atmospheric turbulence during operational tests of advanced Electro-Optical sensor systems. At WPAFB, the Electro-Optics Sensor Evaluation and Analysis Group of the Avionics Laboratory is directly concerned with the potential impact that atmospheric turbulence will have on future sensor systems. The Laser Hardened Materials Technical Area of the Materials Laboratory is interested in understanding the effects of atmospheric turbulence on propagating laser beams. The Communications Technology Group of the Avionics Laboratory needs to know the effect of atmospheric scintillation on optical communication links.

The diverse interests of these and other groups at WPAFB and elsewhere could be addressed by enhancing the capabilities of the existing sensor test range on Wright Field. Our Technical Focal Point for the summer program, Jan Servaites (AFWAL/AARI), is the individual responsible for the operation of the test range. Mr. Mandock worked with him and representatives of the other groups mentioned above to develop a plan for adding a capability for characterizing atmospheric

turbulence during future sensor tests. Mr. Mandock's Ph. D. topic will be in the area of atmospheric turbulence and, as was the case for the project carried out by Eric Schmidt, the summer program will be of direct benefit to the student's academic progress.

II. OBJECTIVES OF THE RESEARCH EFFORT:

A. Sky backgrounds and subvisual cirrus clouds:

In this area, our preliminary goals were to determine the sky background at the MEGALIDAR site under a variety of weather conditions and to detect and parameterize subvisual cirrus clouds. Methods for observing sky background radiance levels involve the use of a variety of radiometric and/or photometric sensors. Subvisual cirrus clouds have been detected by LIDAR systems. However, there has been little progress to date in the detection and characterization of subvisual cirrus using multi-sensor techniques. Our goal was to coordinate photometric observations of the radiation received from the sky with simultaneous satellite data, ground-based camera images and synoptic meteorological data at times when a LIDAR system had detected the presence of subvisual clouds.

B. Turbulence monitoring facility for WPAFB:

At the present time, there is no atmospheric turbulence monitoring facility in the Department of Defense that is able to quantify and monitor the degradation of the performance of electro-optical systems under a wide variety of atmospheric conditions. Only limited results are available on the vertical variability of atmospheric turbulence parameters and no predictive models exist for their horizontal variability during non-neutral conditions. Thus, the availability of a facility of the type that we envision would have research as well as operational value. Our goal was to develop a plan for building up a capability for characterization of atmospheric turbulence at WPAFB based upon facilities for sensor evaluation and testing and that are already in place.

III. RESULTS OF STUDY ON SKY BACKGROUNDS AND SUBVISUAL CIRRUS.

We were extremely pleased with the results of this project. This was an experimental program involving the identification of a number of instruments for carrying out the proposed work, calibration of the instruments, installation of the instruments in a trailer near the MEGALIDAR site, and operation of the instruments under a variety of atmospheric conditions to characterize the sky background conditions at the site.

The second part of our goal, however, was somewhat speculative in that it involved our attempt to observe subvisual cirrus clouds, an atmospheric phenomena that is not well understood (and cannot even be seen by the human eye). These clouds are believed to be geometrically thin (perhaps several hundred meters in vertical extent) but they may extend for tens or hundreds of miles in the horizontal direction. Even though we can not see the clouds in normal upward viewing situations, they could totally obscure an airborne target when viewed in near-horizontal directions from an aircraft. The cloud particles are believed to be ice crystals with dimensions in excess of 10 microns and they are thereby expected to cause significant attenuation of infrared radiation.

As stated earlier, subvisual cirrus have occasionally been detected by LIDAR systems. We also expect that the relatively large particle sizes would cause a significant amount of forward scattering of sunlight and the particles might thereby be detected by careful studies of the sky radiation coming from the direction of the sun.

The results of this study have been detailed by Eric Schmidt in his Final Report for the 1988 USAF - UES Graduate Student Research Program (Schmidt, 1988a). Information on the natural sky background variability was obtained by means of two Pritchard photometers. Video images were recorded simultaneously from two CCD (charge coupled device)

cameras: a solar aureole camera with an occultation disk and an all-sky camera with a field-of-view of 160 degrees. One of the visible photometers was directed upward and the other was set up as a off-vertical system designed to scan the region near the sun to observe the solar aureole (i.e., to measure the variation of intensity of scattered sunlight as a function of angle away from the sun).

The principal investigator provided the LIDAR system used in this program. The MINILIDAR developed recently by the author as a joint project between GTRI and the University of Washington is a portable unit designed for ground-based or airborne LIDAR observations. During the first week of September, the system was transported to WPAFB and installed in the trailer that housed the equipment described in the above paragraph. The LIDAR and the equipment described above were operated simultaneously for a 10-day period during the first two weeks of September. The equipment was operated during both daylight and nighttime conditions, as described in Mr. Schmidt's detailed report.

We were extremely fortunate with respect to the weather-dependent nature of program. Mr. Schmidt had worked closely with Maj. Bob Hughes and his colleagues in the Air Weather Service at WPAFB. He attended weather briefings and arranged to obtain satellite data for the observation time periods. The meteorological conditions and the satellite data are, in fact, regarded as part of the data set that we obtained during the Summer Program. During the time that the experiment was in operation, two fronts passed through the Dayton area. During the second frontal passage, visible high altitude cirrus streaks were observed to move through the area. Camera images verified the presence of the cirrus clouds, as well as their apparent absence. During part of that observation period, in apparently clear skies, a persistent LIDAR echo was observed at an altitude of 12.5 km. The scattering layer was approximately 0.5 km thick and its backscattering cross-section was approximately 12 times that of the molecular backscattering at the same altitude. This subvisual layer was observed for approximately two and a

half hours with high-altitude winds of approximately 50 knots from the west-southwest, thereby indicating the presence of a subvisual cirrus band that was approximately 240 km wide. This solitary finding does agree with our expectations on the conditions that lead to the formation of subvisual cirrus layers. We conclude that subvisual cirrus clouds are associated with frontal systems and that follow-on work should incorporate plans to test and validate models for predicting their onset.

In addition to our success on the subvisual cirrus observations, we had an unexpected "bonus" during the observation period. Shortly after the LIDAR started operating at the site, it detected well-defined scattering layers throughout the first few kilometers above the LIDAR site - often as multiple layers. We have associated these LIDAR echoes with smoke layers from the forest fires in Yellowstone Park. These layers were originally detected on September 8th and they persisted until the onset of heavy rains in the Dayton area on September 12th. We thereby were able to obtain a completely unexpected data set to add to the already extensive set of observations that we obtained for the thin cirrus study. We are now exploring the possibility of using these observations (LIDAR profiles, satellite images, ground-based photometer data, etc.) to test various large-scale atmospheric dispersion models as part of our follow-on work with the data set obtained during the Summer Program.

IV. RESULTS OF STUDY ON A TURBULENCE MONITORING FACILITY:

As discussed earlier, we believe that many state-of-the-art sensor systems may experience degradation in performance due to the effects of atmospheric turbulence. Other projects such as those involving the propagation of coherent laser beams may also benefit by an understanding of the effect of turbulence on the propagation of an electromagnetic beam through the atmosphere. Programs for testing and evaluating new electro-optical sensors will experience an increasing need to document the contributions of atmospheric turbulence to any real or perceived degradation of sensor performance. A need is also perceived for research programs that will help us develop better models for predicting the intensity of turbulence in complex terrain for a wide variety of meteorological conditions.

Details of our approach to this topic are described in Randal Mandock's Final Report for the 1988 USAF - UES Graduate Student Research Program (Mandock, 1988). Mr. Mandock began this project with an effort to evaluate the need for obtaining atmospheric turbulence measurements at the AFWAL sensor testing site. He began by organizing a series of three 2-hour meetings with representatives of different groups (e.g., MLPJ, AAAI, AARI and AAWP) to discuss their needs for documenting the effects of atmospheric turbulence for their applications. He presented a 2-hour seminar "An Introduction to Atmospheric Turbulence" to representatives of MLPJ and AAAI - an audience that was composed of scientists and engineers who believe that atmospheric turbulence does degrade the performance of their equipment. At the end of that seminar, he passed out survey forms on the need for turbulence information and has thereby documented a need for the facility that we are proposing.

Mr. Mandock carried out extensive reviews of the theoretical and experimental progress in the field. As mentioned earlier, he has previous experience in the analysis of data obtained in joint field experiments involving GTRI and NOAA's Wave Propagation Lab (WPL), who

are the recognized leaders in atmospheric turbulence studies. As part of this Summer Program, he made a trip to Boulder to visit with key personnel in WPL to discuss the latest developments in instrumentation for characterizing atmospheric turbulence and also to discuss the specific plans to instrument Wright Field for turbulence measurements. As part of these discussions, he obtained a variety of agreements for technical assistance and for help in fabricating special one-of-a-kind devices that are used by WPL for their atmospheric boundary layer studies.

After reviewing the needs of the research programs at WPAFB and the instruments and measurement techniques that are available for atmospheric turbulence studies, Mr. Mandock has proposed a comprehensive plan, including specific instruments and locations on Wright Field that are best suited for their installation. Complete details are included in his report (Mandock, 1988); the major features of his report are discussed below.

The primary component of the wave propagation test site on Wright Field would be a Tower Triangle featuring 3 meteorological towers instrumented for a variety of measurements at heights of 2, 5 and 10 meters. The purpose of this part of the facility would be to fully document the target end of the beam path during testing of sensors located in Building 620 and to acquire turbulence data which would be used to develop predictive models for the spatial and temporal variation of turbulence structure parameters using gross meteorological parameters. A variety of observations involving horizontal beam paths of up to 1.5 km in length would traverse the triangle and several other instruments would be located within the triangle or at various prespecified distances from it.

Atmospheric turbulence is expected to vary along a slant beam path in both horizontal and vertical directions. In addition to the triangle, we also propose a means of characterizing atmospheric

turbulence along the slant beam path from Building 620 to the target areas on Wright Field. The main features of this facility would include 22 pole- or tower-mounted temperature structure function sensors, a single-axis sodar (acoustic radar) system located 140 meters west of the nominal sensor location in Building 620, a 3-axis sodar located near the Environmental Monitoring and Control System (EMACS) on the AFWAL test range at Wright Field and 2 path-averaged optical wind sensors.

This effort has proven to be a thorough and extensive study. Mr. Mandock's report is very detailed and interested readers are referred to the document. The document lists all instruments needed for the installation, presents the rationale for using each device and includes useful budget information.

V. RECOMMENDATIONS:

Detailed recommendations are found in the final reports prepared by my two students (Schmidt, 1988a; Mandock, 1988). In the near future, we will be submitting two separate proposals for follow-on work to be performed during the coming year. Both projects were highly successful.

Mr. Mandock has completed a very thorough study of the needs for characterizing turbulence at AFWAL's sensor test facility. He has documented needs of the scientific groups that would use the facility. He has explored the equipment and measurement techniques that are available for characterizing turbulence during test and evaluation programs. A plan has been presented for implementing this facility. The plan includes such items as equipment lists with budget information and details on where the equipment should be installed on Wright Field are included in his report.

Mr. Schmidt has obtained data on sky backgrounds at the MEGALIDAR site that are needed for improved simulations of experiments that have been planned for the system. Furthermore, he has observed subvisual cirrus clouds with simultaneous LIDAR profiles, satellite images, ground-based video images and visible photometer observations. He also obtained a "bonus" data set due to the fact that these observations also include the presence of smoke layers from the forest fires in Yellowstone Park. Each of these databases represent topics of significant interest to the scientific community and we expect that several publications will ensue from the analysis of these data sets.

VI. ACKNOWLEDGEMENTS:

I wish to thank the Air Force Avionics Laboratory at Wright-Patterson AFB, the Air Force Systems Command and the Air Force Office of Scientific Research for sponsorship of this research. Universal Energy Systems, Inc., must be mentioned for their concern and help in all administrative and directional aspects of this program.

Special thanks are extended for Jan Servaites who was our technical focal point during this effort. He provided us with the equipment, contacts, and other help necessary to carry out our objectives. I also extend a special note of appreciation to each of my students, Eric Schmidt and Randal Mandock, for their enthusiasm and hard work on this program.

REFERENCES

Grams, G.W., A.K. Garrison, G.G. Gimmestad and E.O. Schmidt, 1988: Effects of Subvisual Cirrus Clouds on Background Sky Radiance at the MEGALIDAR Site. Paper presented at 11th Annual Review Conference on Atmospheric Transmission Models, AFGL, Hanscom Air Force Base, Bedford, Massachusetts (1-3 June 1988).

Mandock, R., 1988: A Proposed Turbulence Monitoring Facility for Wright-Patterson AFB. Final Report, Contract Number F49620-88-C-0053, Universal Energy Systems, Inc., Dayton, Ohio.

Schmidt, E., 1988a: A Study of Sky Backgrounds and Sub-Visual Cirrus. Final Report, Contract Number F49620-88-C-0053, Universal Energy Systems, Inc., Dayton, Ohio.

Schmidt, E., 1988b: High Altitude Cirrus Effects on Spectral Measurements". Proc. 1988 SPIE Technical Symposium, Vol. 924.

**1988 USAF-UES SUMMER FACULTY RESEARCH PROGRAM/
GRADUATE STUDENT RESEARCH PROGRAM**

**Sponsored by the
AIR FORCE OFFICE OF SCIENTIFIC RESEARCH**

**Conducted by the
Universal Energy Systems, Inc.**

FINAL REPORT

Formal Verification of VHDL Specifications

Prepared by:	David Hemmendinger, Ph.D.
Academic Rank:	Assistant Professor
Department and	Computer Science and Engineering
University:	Wright State University
Research Location:	AFWAL/AADE
	Wright-Patterson AFB
	Dayton, Ohio
USAF Researcher:	Dr. John Hines
Date:	9 August 88
Contract No:	F49620-87-R-0004

Formal Verification of VHDL Specifications

by

David Hemmendinger

Abstract

The VHDL (hardware description) language is a powerful tool for the hierarchical specification of computer hardware. Techniques to verify formally that designs meet their specifications would simplify its use by reducing the role of exhaustive simulations. Temporal logic was the first formal verification technique studied in this project, but it subsequently focused on the use of the *assert* statement within VHDL, which permits the designer to state the specification a component is to meet. A major part of the project was devoted to Prolog programs to extract such assertions automatically from low-level VHDL architectures, using the signal attributes provided by VHDL, and to translate these into the form required by a theorem-proving program, LCF. The initial stages of the project indicate that such a theorem-prover has the capacity to verify that a low-level architecture meets a high-level specification stated in VHDL.

Acknowledgements

I wish to thank the Air Force Systems Command and the Air Force Office of Scientific Research for sponsorship of this research. Universal Energy Services is to be commended for their help to me in all the administrative aspects of this program.

I am also happy to acknowledge the role played by many people in making my summer interesting and productive. Dr John Hines provided me with an introduction to the VHDL specification language and with the orientation that helped me to get the project underway. The other members of the group, particularly Darrell Barker, Lt. Jack Ebel, and Lt. Nick Naclerio, were always ready to answer questions, discuss problems, and share their knowledge of VHDL with me. Ben Carroll and Mike West provided aid in using the computer systems, and responded quickly when I needed something fixed or needed access to computer resources. Dr. Frank Brown and Capt. Mike Dukes of the Air Force Institute of Technology were generous in sharing their work on VHDL and verification, and the staff of the AFWAL Technical Library were very helpful in clarifying obscure references and getting the books via interlibrary loan. Finally, I must commend my graduate student assistant, John Van Tassel, for the energy that he put into learning new material and the vigor with which he worked on the prototype programs for the project.

1. Introduction

My proposal for the summer project was to investigate formal verification techniques for the VHDL hardware description language, and to look at temporal logic in particular. While the project has evolved in a slightly different direction from the one anticipated, I consider it to have been worthwhile and potentially very fruitful.

The Microelectronics Section of the Avionics Laboratory of Wright Patterson Air Base is particularly concerned with the refinement and use of the new IEEE_1076 Standard for the hardware description language, VHDL. This language offers powerful tools for the hierarchical specification of computer hardware and for the simulation of these specifications. Its value would be still greater if its designs could be formally verified to meet their specifications, as that would reduce the need to conduct time-consuming simulations.

My research interests have been in concurrent programming, particularly in formal specification and verification of multi-process programs, and in the use of executable formal specifications. Temporal logic plays a major role in the formal analysis of concurrency, and my initial project was to investigate its use in hardware verification.

2. Objectives

The first two phases of the project were

- To investigate the literature on the formal verification of hardware specifications, and on the use of temporal logic in particular.
- To become familiar with the VHDL description language and its simulator.

As a result of what I learned from these phases, I decided to refocus the research effort slightly, and to concentrate on the rich set of features available within VHDL for application to verification, namely, its *assert* statements. This led to the next two phases of the project.

- Develop a prototype program to extract automatically such assertions from a low-level VHDL architectural statement.
- Develop a prototype program to translate such extracted assertions into the syntax of a theorem-prover, Cambridge LCF.

John Van Tassel, the graduate student working with me this summer, has written these prototypes in Prolog. They can translate a significant portion of VHDL, and I believe that their success warrants continuing with the work, as I shall propose to do in a follow-up grant. The work to be done under the grant would be to develop the theorem-prover in order to be able to verify that assert-statements made in high-level VHDL descriptions were satisfied by

the low-level architectural descriptions from which assert-statements were automatically extracted.

3. Existing work on formal verification of hardware specifications

During the first two weeks of the summer project I acquired copies of most of the published work done in the past decade in this area. It falls into three main branches. One is formal verification with theorem-proving tools such as the Boyer-Moore theorem prover, HOL, based on Cambridge LCF, or specialized term-rewriting theorem provers. In recent years these have been used to verify specifications of small chips of up to 30,000 transistors. The reports typically remark that the tools require a considerable amount of intervention by the user, and knowledge of theorem-proving. At present, though, there are major projects at several universities that are using versions of HOL for the verification of moderate-sized chips.

Temporal logic is the second branch. Since a significant portion of hardware verification consists of determining if a design meets timing constraints and avoids race conditions, temporal logic appears useful. Much of the work with temporal logic has been done in connection with the formal semantics and verification of concurrent programs, and there have been several efforts to transfer these tools to the hardware verification domain. One approach is to construct a finite-state machine to model the hardware, and then to prove temporal invariants for all the relevant transitions in the machine [Mishra, 1983; Clarke, 1986]. Another is to treat temporal logic as a programming language in which one can simulate hardware, and then to translate this language into the appropriate formal logic for theorem-proving. [Moszkowski, 1986] uses interval temporal logic', in which the primitive assertions concern properties true over a time interval].

The third, not altogether disjoint from the preceding two, is to use simulation to provide assurance of correct design, although except in simple cases of exhaustive simulation, this does not provide verification. We have chosen not to pursue this route, as the VHDL simulator is already designed to facilitate such modeling, and we are looking at possible tools for extending what it can do in order to make exhaustive simulation unnecessary.

4. VHDL

The VHDL language for hardware description is a large language whose semantics are defined largely in terms of an underlying process model of hardware. This model, in turn, receives its operational definition in terms of the simulator that is to execute VHDL descriptions as programs. Learning the language thus requires using the simulator, and since the

version available at the start of the summer had a number of bugs, at first I concentrated on studying the language manual and existing sample programs. When an improved simulator became available, I began using it.

It turned out that this version, though better, still had a number of defects in it. In part because it was better, though, I was able to execute enough sample VHDL descriptions to begin to learn how the simulator worked. As I continued in this part of the project, I began to investigate some of its features that looked useful for verification, particularly its signal attributes and its 'assert' statement. This turned up a number of further defects in the simulator; many of the signal attributes were not implemented correctly, and the strong type-checking of the language interfered with the use of the 'assert' statement.

As a result, this part of my project consisted largely in testing the simulator and documenting the defects that I found. While not what I had set out to do, this had two virtues. First, the debugging was useful to the group responsible for the development of the simulator, and second, in order to decide whether there were flaws in it, I was led to understand the model of hardware on which the language was based — as usual, one learns more from studying pathological examples than by studying normal ones.

5. Automatic derivation of specifications

Despite the impossibility of actually running simulations that used some of the more interesting features of the VHDL language, I decided at this point that the use of the 'assert' statement and the signal attributes should make it feasible to develop tools for the automatic derivation of specifications and their subsequent verification. In outline, the strategy that my assistant and I chose to pursue was to work out a program to take as input low-level VHDL architectures and to extract from them the assertions that could be made about their timing characteristics. These assertions could be embedded in the VHDL, of course, where they would be automatically true, of course. Given the hierarchical design technique encouraged by VHDL, they could also be carried upward through the layers of design, becoming more complex as more components were added. Eventually the result would be a complex assertion about the high-level entity being designed. At this point, assuming that the designer had written the design with an independent set of assertions about its behavior, the two could be compared. The comparison would require further tools to reduce the two sets of assertions to simpler terms and to verify their equivalence or show that they were not in fact equivalent. If successful the outcome would be a demonstration that the implementation met the high-level specification.

One reason for our choosing to focus on these features of VHDL was that one could expect its users to become accustomed to embedding the appropriate assertions in their designs. Indeed, much of the value of the language would be lost otherwise, since these are a powerful tool that the simulator can use in executing designs. If they are used as both high-level specifications and as automatically derived low-level descriptions, there is a great deal of information available for formal verifications.

6. Extracting assertions from architectures

Anticipating that some facet of our project would involve translating from VHDL to another representation, John Van Tassel had spent the first week of his fellowship writing the context-free (BNF) grammar of VHDL as a Prolog program. Such a program can be readily augmented to become a translation grammar, and this was exactly what we needed. Mr. Van Tassel proceeded to modify his program to produce VHDL 'assert' statements from the typical elements of low-level architectures, such as signal assignments with delays specified. As an example the VHDL statement involving inertial delay:

$$S1 \leftarrow (S2 \text{ and } S3) \text{ after } D$$

means that if S2 and S3 are stable for interval D, then S1 is assigned the value, not (S2 and S3). It yields the following characterization:

$$\text{assert}((\text{not } S2'\text{stable}(D)) \text{ or } (\text{not } S3'\text{stable}(D)) \text{ or } (S1 = (S2'\text{delayed}(D) \text{ and } S3'\text{delayed}(D))))$$

where the *not's* and the *or* are the boolean translation of *if . . . then*. While such expressions rapidly become quite lisp-like in their unreadability, they are not intended to be read, but to be used by the simulator or a theorem-prover.

This part of the project is well-developed; Mr. Van Tassel's program can handle typical low-level architectures, including guarded blocks and case-statements. At the moment we are hampered by not being able to test the program output by letting the VHDL simulator execute it, since the simulator has known bugs in its treatment of precisely the VHDL features that we are using. Once they are fixed, though, we shall be able to simulate the architectures with the automatically added assertions, which will help us to debug our own program. In fact, one side-effect of this program will be that we can further test our understanding of the definition of signal attributes like *S'stable*, *S'quiet*, and *S'delayed*, as well as the timing model of the simulator, since we use these attributes to make assertions that should always be true.

7. Theorem-proving to verify specifications

The last part of this project is just in its nascent state. We recently received the copy of the Cambridge LCF theorem prover that we ordered earlier in the spring. Mr. Van Tassel is now modifying his translation grammar to generate the assertions in the syntax of LCF rather than VHDL. When this program is complete, it will be possible to translate VHDL into propositions to be verified by the theorem prover. Once the translation is complete, we propose to focus on developing the 'theories', or axiom-systems for LCF that will enable it to prove equivalence between specified and derived propositions, or to show their difference.

Using LCF will require three major theories. One is the set of term-rewriting rules required for reducing boolean expressions to canonical form. This is quite standard and should present no problems; there are a variety of normal-form theorems that can be used. A second is the theory required to express temporal rules for the signal attributes. For instance, the attribute, $S' \text{stable}(T)$ is equivalent to the predicate-logic formula

$$(!t) (!\delta) (\delta \leq T \Rightarrow S(t) = S(t+\delta))$$

where $S(t)$ is the value of S at time t and a term like $(!X)$ is universal quantifier, *for all* X . Since this formula has several types; that is, since the quantified variables range over times, while the signal takes values of a different type, this is actually an expression in a higher-order predicate calculus, or the typed lambda-calculus. Theories built in LCF, such as the HOL (higher order logic) developed at Cambridge, are capable of handling such a variety of types.

The third theory to be developed in LCF is the axiom-system required to relate the various signal attributes, including the concatenation of attributes, such as $S' \text{delayed}(T1)' \text{stable}(T2)$, or $S' \text{stable}(T)' \text{event}$. This should not be difficult, although it is an area where we need to be able to work more with the VHDL simulator to check our axioms against the behavior of the simulated specifications. Once we have these axioms developed, it may actually be easier to build them into the lower-level Prolog translation program, to reduce some such attributed signals to simpler expressions as they are constructed. This would also be appropriate for the program that translates into VHDL assertions.

The approach outlined here is probably closest to the *VERIFY* program of H. G. Barrow [Barrow, 1984], a Prolog program to prove specifications equivalent to a set of characterizations derived from an implementation of hardware. Barrow reported success in verifying 18,000-transistor chips, though he acknowledged that some intervention by the user was required. While we do not anticipate being able to eliminate the user from the verification process completely, we hope that by working from the assertion-statements of VHDL, the user

familiar with that language will be able to direct the theorem-proving more effectively. How active a role the user will have to play cannot be determined until we are able to build our prototype verification system. While we could work entirely in Prolog as Barrow did, we prefer at this point to use Prolog for what it seems best-suited: rapid prototyping, and the use of grammars as executable programs to accomplish translations.

8. Recommendations

The summer fellowship project has accomplished several things. We have become acquainted with the literature on formal verification of hardware, including temporal logic and theorem-proving techniques. We have become familiar with VHDL, and once its simulator is fully operable, we are prepared to continue experimenting with the use of those features that seem suitable for verification methods. We have also developed a small prototype of a verification technique that we believe worth pursuing.

Our proposal for further work, supported by a follow-up mini-grant is to continue to develop this prototype to the point that we can determine its utility. This project would have several parts. First, we would continue to work with the VHDL simulator in order to understand VHDL better and to test our translation programs against it. Second, we would complete the programs to translate low-level VHDL architectures into both VHDL with assert-statements added, and to the language of LCF. Third and most important, we would develop the LCF theories necessary to do the verification work. We anticipate that this work could be accomplished within nine months, at which point we could assess the value of our results.

Along with carrying out our own work, we would continue to become familiar with related projects elsewhere. We are trying now to get in touch with H. G. Barrow to see what has become of his *VERIFY* program. We shall also continue to relate our project to the HOL projects at Cambridge and at Calgary, where a newer version of HOL is under development. In particular, I would propose to attend the next Calgary workshop on formal verification of hardware.

References

- H. A. Barrow, "VERIFY: A program for proving correctness of digital hardware designs", *Artificial Intelligence*, vol. 24, 1984, pp. 437-491.
- G. Birtwistle and P. A. Subrahmanyam, *VLSI Specification, Verification, and Synthesis*, Academic Press, New York, 1987.
- D. Borrione, *From HDL Descriptions to Guaranteed Correct Circuit Design*, North-Holland, Amsterdam, 1987.
- E. M. Clarke, E. A. Emerson, and A. P. Sistla, "Automatic verification of finite-state concurrent systems using temporal logic specifications", *ACM Trans. on Programming Languages and Systems*, vol. 8, no. 2, 1986, pp 244-263.
- M. Fujita, H. Tanaka, and T. Moto-oka, "Verification with Prolog and temporal logic", *Computer Hardware Description Languages and Their Applications (Proc. of the 6th Int. Symp. on CHDL's)*, ed. T Uehara and M. Barbacci, North-Holland, Amsterdam, 1983, pp. 103-114.
- A. Galton, ed., *Temporal Logics and Their Applications*, Academic Press, 1987.
- Institute of Electrical and Electronics Engineers, *IEEE Standard VHDL Language Reference Manual*, IEEE Press, New York, 1988.
- G. Milne, and P. A. Subrahmanyam, *Formal Aspects of VLSI Design*, Academic Press, New York, 1987.
- B. Mishra and E. M. Clarke, "Automatic and hierarchical verification of asynchronous circuits using temporal logic", *Technical Report CMU-CS-83-155*, Carnegie-Mellon Univ, Pittsburgh, 1983.
- B. Moszkowski, *Executing Temporal Logic Programs*, Cambridge University Press, 1986.
- T. Uehara, T. Saito, F. Maruyama, and N. Kawato, "DDL verifier and temporal logic", *Computer Hardware Description Languages and Their Applications (Proc. of the 6th Int. Symp. on CHDL's)*, ed. T Uehara and M. Barbacci, North-Holland, Amsterdam, 1983, pp. 91-101.

1988 USAF-UES SUMMER FACULTY RESEARCH PROGRAM/ GRADUATE
STUDENT SUMMER SUPPORT PROGRAM

Sponsored by the
AIR FORCE OFFICE OF SCIENTIFIC RESEARCH

Conducted by the
Universal Energy Systems, Inc.

FINAL REPORT

LOW VOLTAGE BROADBAND BEAM STEERING DEVICES USING LIQUID CRYSTALS

Prepared by: Mohammad A. Karim
Academic Rank: Associate Professor
Department and Department of Electrical Engineering &
 The Center for Electro-Optics
University: The University of Dayton
Research Location: AFWAL/AARI-2
 Wright-Patterson AFB; Dayton; Ohio
USAF Researcher: Dr. Paul F. McManamon
Date: 8 July 1988
Contract Number: F49620-87-R-0004

LOW VOLTAGE BROADBAND BEAM STEERING DEVICES USING LIQUID CRYSTALS

by

Mohammad A. Karim

ABSTRACT

The broadband characteristics of a number of beam steering systems were investigated. It is desirable for the beam steering device to have a large aperture and, at the same time, a fast time response (~ 1 ms) while being controlled with a reasonably small voltage source. The various schemes were examined and judged on the basis of the specifications desirable in the space environment. Two particular concepts were scrutinized to determine if they would be able to deliver a broadband beam steering system. A wollaston prism system in combination with ferro-electric liquid crystal (FLC) layers and an optical phased array system based on nematic liquid crystal (NLC) layer were analyzed. The FLC-based systems are found to be very fast (< 1 ms) but comparatively bulky and sensitive to transmission losses while the NLC based systems are generally very slow (many milliseconds) but comparatively less sensitive to transmission losses. The current quantitative results along with those expected to be generated through a follow-up mini-grant study would be able to dictate the design characteristics of the most optimum broadband beam steering system.

ACKNOWLEDGEMENTS

I wish to thank the Air Force Systems Command and the Air Force Office of Scientific Research for sponsorship of this research. I also wish to acknowledge the work done by Universal Energy Systems, Inc., in administrating this program.

The support and encouragement of many people made my research experience both rewarding and enjoyable. I would especially like to thank Dr. Paul F. McManamon, Lt. L. E. Myers, Ms. C. Heben, and Mr. D. L. Tomlinson for the valuable technical assistances and for providing me with a comfortable working atmosphere. Most importantly, I would like to acknowledge the help provided by Mr. Dan Cook (GSRP Fellow associated with me) in developing the software tools needed to justify our conclusions.

1. INTRODUCTION

Electro-optic beam deflection concept (Karim, 1989) is of growing importance in modern warfare scenario. The effect of electric field on the direction of light propagation can be best utilized to avoid the mechanical inertia that otherwise plagues the electromechanical steering devices. The constraints of a space-borne system, however, rules out the possibility of using electro-optic Pockels (linear) and Kerr (nonlinear) effects for beam steering primarily because of their high voltage requirements.

The Aeronautical Systems Division of the Wright-Patterson AFB and the Naval Weapons Center at China Lake are both currently interested in having a reliable low-voltage beam steering device. In the case of WPAFB, two contractors are presently fabricating nematic liquid crystal (NLC) based beam steering devices suitable for a single wavelength, however, the time response of these devices are expected to be relatively large. The problems associated with the broadband beam steering devices are definitely more cumbersome and, therefore, its design involves more difficult engineering decisions.

One of my current research interests at the University of Dayton has been directed towards exploring the various possibilities of designing and characterizing optical beam transforming systems. The long range goal of the research includes designing optical systems to either transform, shift, or modify an input beam of light. Some of my recent works were geared towards designing high-efficiency optical systems for transforming a Gaussian laser beam into a uniform-intensity laser beam (Karim et. al., 1985), designing systems for the measurement of a micron-sized Gaussian beam radius (Karim, 1985; Karim et. al., 1987a), and designing low-loss refracting systems for transforming a uniform-intensity annular laser beam into an equivalent

uniform-intensity circular beam (Karim. et. al., 1987b). These experiences have served as motivation for the current SFRP work involving the analysis and design of beam deflecting systems whose functional characteristics are controlled, in real-time, by means of either voltage or field.

II. OBJECTIVES OF THE RESEARCH EFFORT

There has been an ever growing interest in achieving rapid large-angle pointing and scanning of large-diameter diffraction-limited laser radar beams. To date, available technology has failed to deliver the perfect beam steering system that meets the required specifications. In the past, experimenters had developed a variety of beam deflection schemes employing mechanical, acoustical, and electro-optic methods. However, to date, development of a real-time optical phased array antenna (Brookner 1985) has not materialized fully, due in great part to the lack of sufficiently small, electrically tunable, optical phase shifters. The recent developments of better and more reliable liquid crystals (nematic and ferro-electric) are indicative of the fact that it may be possible to make practical a true optical analog of a microwave phased array antenna. However, the available nematic liquid crystals (NLC) have neither a large birefringence nor the desirable time response; but trends in the development of "magic" materials have begun to provide incentives for exploring various real-time beam steering concepts. My assignment as a Summer Research Fellow was to perform basic research into the theory and characterizations of deliverable beam steering systems.

The objectives of this research were three-fold: (a) to survey fast liquid crystal like materials; (b) to explore low voltage, large area, broadband beam steering devices meeting the wavelength spread of 0.7 through

1.1 μm , 4.2 through 4.5 μm , and 9.5 through 11.5 μm , a field-of-view of 20 degree cone and time response of less than a millisecond; and (c) to develop software tools to explore the likelihood of processing a broadband beam using systems designed primarily for a single wavelength.

III. BEAM STEERING SYSTEMS

a. FERRO-ELECTRIC LIQUID CRYSTAL BASED BEAM DEFLECTORS

One of the cherished goal is to have a beam steering system that would have a time response of less than a millisecond. This is a formidable challenge since only a 1 μm thick NLC layer will correspond to a time response of 1.063 ns. Thus in order to have the most desirable phased array antenna using NLC, the technology will have to deliver an NLC layer having a thickness less than 1 μm ! On the other hand, if one were to use Pockels cell(s) for deflecting light it would be possible to fabricate a system having ultra-fast response but it would have to make use of very high voltages (\sim kV). For example, corresponding to 632.8 nm wavelength, a 200 resolution element device may require up to 10 kV (Kiefer et. al., 1967). A number of works in the past (Soref and McMahon, 1966; Kulckle et. al., 1966) have indicated that one could produce a high-resolution ultra-fast beam steering system using multiple modules each consisting of a Pockel cell and a Wollaston prism. Despite all advantages, the scheme was not acceptable (Lotspeich, 1968) because of its excessive voltage burden. Incidentally, Pockels cells were used solely to function like halfwave-retarders. Recent advancements have shown that FLCs could also be used for performing the same function as that of Pockels cell but with very little voltage (Patel and Goodby, 1987; Clark et. al., 1985). It is estimated (Jiu-zhi et. al., 1987; Wahl and Jain, 1984; Johnson et. al., 1987) that at elevated temperature FLC switching time is in the order of 5 ns while at room temperature it could be

just about 100 ns. Therefore, one can begin to explore the possibility of designing a high-resolution beam steering system having a very fast response by using multiple modules of an FLC layer and a Wollaston prism. The schematic of one such module is shown in Fig 1 where the incoming light beam is assumed to be incident on the prism at a positive angle of i_{01} .

With a deflection of $2^{m-1} \theta$ in each successive module where m is the number of stage and θ is the deflection in the very first stage, the system can deflect a collimated light beam to each of the 2^m angular positions within the scan range. A geometrical ray analysis (Simon, 1986) would show that the angle of refraction of the emerging ray is given by

$$r_{20} = \sin^{-1} \left[\frac{n_e}{n} \sin \left[\alpha - \sin^{-1} \left[\frac{n_o}{n_e} \sin \left[\alpha - \sin^{-1} \left[\frac{n}{n_o} \sin i_{01} \right] \right] \right] \right] \right]$$

for the ordinary ray while for the extra-ordinary ray it is given by

$$r_{20} = \sin^{-1} \left[\frac{n_o}{n} \sin \left[\alpha - \sin^{-1} \left[\frac{n_e^*}{n_o} \sin \left[\alpha - \sin^{-1} \left[\frac{n}{n_e^*} \sin i_{01} \right] \right] \right] \right] \right]$$

where n , n_o , and n_e are respectively the refractive indices of FLC, ordinary refractive index of the prism, and extra-ordinary refractive index of the prism, α is the split-angle of the prism, and

$$n_e^* = n_e \sqrt{1 - \left(\frac{1}{n_o^2} - \frac{1}{n_e^2} \right) \sin^2 i_{01}}$$

is the effective extra-ordinary refractive index (Simon, 1983) of the birefringent uniaxial crystal. For the case of the negative incident ray, however, the angle of refraction is given by

$$r_{20} = \sin^{-1} \left[\frac{n_e}{n} \sin \left[\sin^{-1} \left[\frac{n_o}{n_e} \sin \left[\frac{\pi}{2} - \alpha + \sin^{-1} \left[\frac{n}{n_o} \sin i_{01} \right] \right] \right] - \alpha \right] \right]$$

for the ordinary wave and

$$r_{20} = \sin^{-1} \left[\frac{n_o}{n} \sin \left[\sin^{-1} \left[\frac{n_e^*}{n_o} \sin \left[\frac{\pi}{2} - \alpha + \sin^{-1} \left[\frac{n}{n_e^*} \sin i_{o1} \right] \right] - \alpha \right] \right] \right]$$

for the extra-ordinary wave. In the case of $n_e > n_o > n$, the angle of deviation is $r_{20} - i_{10}$ and $i_{10} - r_{20}$ respectively for the ordinary and extra-ordinary rays. Again in the case of $n_o > n_e > n$, the angle of deviation is $i_{10} - r_{20}$ and $r_{20} - i_{10}$ respectively for the ordinary and extra-ordinary rays.

The process of beam deflection results in an off-axis beam displacement. Therefore, the beam steering system needs to be properly sized so that the beam remains within the aperture of each of the modules. For an input offset of Ω in any one of the modules, the output offset, Ω' , is given by

$$\Omega' = \frac{\tau \operatorname{cosec} \alpha - \frac{(\tau/2 \cot \alpha - \Omega) \sin(\pi/2 - r_{o1})}{\sin(\pi/2 + r_{o1} - \alpha)}}{\sin(\pi/2 + r_{i2} - \alpha)} \sin(\pi/2 - r_{i2}) - \frac{\tau}{2} \cot \alpha, \text{ +ve } i_{o1}$$

$$\frac{\tau}{2} \cot \alpha - \frac{\tau \operatorname{cosec} \alpha - \frac{\frac{\tau}{2} \cot \alpha + \Omega \sin(\pi/2 + r_{o1})}{\sin(\pi/2 - r_{o1} - \alpha)}}{\sin(\pi/2 - \alpha + r_{i2})} \sin(\pi/2 - r_{i2}), \text{ -ve } i_{o1}$$

where r_{12} is the angle of refraction for the light entering the second half of the prism.

A computer program was written to simulate the design of an FLC based beam deflector. The details of this and the other programs are listed in the report turned in by the GSRP Fellow Dan Cook. Depending on the amount of total scan range (20 degree, for example) and the number of modules, the deflection for each of the modules is determined provided the minimum angle of deflection exceeds $2\lambda/\pi d$ where λ is the wavelength of the incoming light and d is the Gaussian beam diameter. With zero initial incidence angle and beam offset, the split-angle and thickness of the prisms are determined when angular mismatch between the ordinary and extra-ordinary rays is a minimum.

The optimization process results in a system with the least prism-thickness and least angular mismatch. Between successive determination of the module characteristics, the program user could influence the design by opting for a different type of birefringent material. Table I, for example, shows two variations of the beam steering system for the broadband region of 0.7 through 1.1 μm . The total system thickness for the cases are respectively 7.6 and 5.6 cm. Fig 2 shows three dimensional plots of the angular deviations of the steered beams at different scan angles when the wavelength of the inputs are varied over the range of broadband in question. Figs 3 and 4 show the deflection angle errors plotted respectively against the wavelengths (with constant scan angles) and scan angles (with constant wavelengths). It can be seen that as one deviates from the operating wavelength, deflection angle deviation increases with a rate which is larger at a larger scan angle. Again as one deviates from the boresight deflection angle error increases with a rate which is larger at shorter wavelengths.

b. NLC BASED BEAM DEFLECTORS

An electronic phased array is typically made up of a regular arrangement of flat radiating elements each of which is fed with a microwave signal of equal amplitude and matched phase. The beam dwells at the desired target as long as the phases are all maintained in such a way so that the individual signals will result in constructive interference. The beam can be switched to any other target point simply by readjusting the phases of the individual radiators so that the individual beams again all add coherently. An optical analog of such a phased array is realizable by making use of phase shifts introduced in NLC layers. In particular, the flat type of an NLC array consists of individual elements with each element having a tunable but constant phase. However, while it is possible to have a light-weight

steering system, the responses are relatively slow due to the thickness of the NLC layer. Despite its apparent limitation, the technique is attractive since a tremendous amount of effort is being geared to develop promising (i.e., thinner and faster) NLC materials.

In order to use a thinner NLC layer, it will be necessary to look for a material having a larger value of birefringence. But it is often of disastrous consequence because such a requirement forces one to use the nonlinear region of birefringence versus voltage characteristics (Wu et. al., 1984). It is anticipated, however, that the use of a multilayered NLC arrangement may solve a part of this time-response limitation. It should be realized that since the flat element size needs to be comparable to the beam wavelength, it is practically impossible to design a flat NLC type array for the shorter wavelength regime (e.g., 0.7 μm through 1.1 μm). Thus, the flat type NLC array would be restricted in use to only longer wavelengths. The design process involves, first, determining the smallest allowable size for the elements, and then determining the maximum phase change necessary for the array elements which in turn would determine the NLC thickness, time response and voltage characteristics of the system.

For a flat type NLC beam steering system having N elements each having a phase change of $\Delta\phi$, the far-field intensity of the output is found to be:

$$I = \left(\frac{a'b}{x}\right)^2 \frac{\sin^2\left(\frac{\pi b \sin\psi}{\lambda}\right)}{\left(\frac{\pi b \sin\psi}{\lambda}\right)^2} \frac{\sin^2\left(\frac{N}{2}\left(\frac{2\pi}{\lambda} d \sin\psi + \Delta\phi\right)\right)}{\sin^2\left(\frac{1}{2}\left(\frac{2\pi}{\lambda} d \sin\psi + \Delta\phi\right)\right)}$$

where a' is a constant, b is the width of the individual element, x is the distance between the system and the target, d is the center-to-center distance between the neighboring elements, and ψ is the scan angle.

Fig 5 shows plots of angular deflections for different values of phase delay while Figs 6 and 7 show the intensity variations respectively for different values of the scan angle and phase offsets. Fig 8 shows two cases of intensity plots as the scan angle is changed at different wavelengths.

IV. RECOMMENDATIONS

a. Before the design characteristics of the FLC based system is finally specified, a few more aspects need to be considered. They are:

- (i) The actual refractive index characteristics of the FLC material at all wavelengths under consideration must have to be built into the FLC-based system analysis and design process. In our present work, the lack of published FLC data forces us to assume that FLC index of refraction is invariant.
- (ii) Preliminary calculations made during the work is indicative of the fact that the prisms could be properly trained to eliminate most of the pointing inaccuracies. Proper training could lead to devices that would miss the target located at a distance of 100 miles by no more than a few centimeters.
- (iii) Realistic transmission characteristics of the available electrodes like that of indium tin oxide, and uniaxial prism materials need to be identified for proper evaluation of the system efficiencies.

b. The performance of the NLC-based systems needs to incorporate beam obscuration effects, thermal effects, nonlinear birefringence effects and NLC melting effects into the analysis tool developed during this study.

c. To make an exhaustive comparison of all possible beam steering schemes, the designer should explore a few of the more well-understood concepts such as magneto-optic, acousto-optic, and thermal phase grating. The relatively less understood multiple quantum well (MQW) structure concept may provide a viable, and possibly the most promising, solution to the demands of beam steering complexities. Before opting for the most desirable beam steering system, the aforementioned concepts need to be properly evaluated. A mini-grant proposal will include these topics for the follow-up research.

V. REFERENCES

Brookner, E., "Phased-array radars", Sci. Am., February 1985, p. 94.

Clark, N. A., Lagerwull, S. T., and Wahl, J., "Modulators, Linear Arrays, and Matrix Arrays Using Ferro-electric Liquid Crystals", Proc. SID., Vol. 26, 1985, p. 133.

Jenkins, F. A., and White, H. E., Fundamentals of Optics (4th Ed), Newyork, NY. McGraw Hill Book Co., 1976.

Jiu-zhi, X., Handschy, M. A., and Clark, N. A., "Electro-optic response during switching of ferro-electric liquid crystal cell with uniform director orientation", Ferroelectrics, Vol. 73, 1987, p. 305.

Johnson, K. M., Handschy, M. A., and Pagano-Stauffer, L. A., "Optical computing and image processing with ferro-electric liquid crystals", Opt. Engn., Vol. 26, 1987, p. 385.

Karim, M. A., Electro-Optical Devices and Systems, Boston, Massachusetts, PWS-KENT Pub. Co., 1989.

Karim, M. A., Hanafi, A. M., Hussain, F., Mustafa, S., Samberid, Z., and Zain, N. M., "Realization of a uniform circular source using a two-dimensional binary filter", Opt. Lett., Vol. 10, 1985, p. 470.

Karim, M. A., "Measurement of Gaussian beam diameter using Ronchi rulings", Elect. Lett., Vol. 21, 1985, p. 427.

Karim, M. A., Awwal, A. A. S., Nasiruddin, A. M., Basit, A., Vedak, D. S., Smith, C. C., and Miller, G. D., "Gaussian laser-beam-diameter measurement using sinusoidal and triangular rulings", Opt. Lett., Vol. 12, 1987, p. 93.

Karim, M. A., Cherri, A. K., Awwal, A. A. S., and Basit, A., "Refracting system for annular laser beam transformation", Appl. Opt., Vol. 26, 1987, p. 2446.

Kiefer, J. F., Lotspeich, J. F., Brown, W. P., Jr., and Senf, H. R., "Performance characteristics of an electrooptic light beam deflector", IEEE J. Quant. Electr., Vol. QE-3, 1967, p. 261.

Kulckle, W., Kosanke, K., Max, E., Habegger, M. A., Harris, T. J., and Fleisher, H., "Digital light deflectors", Appl. Opt., Vol. 5, 1966, p. 1657.

Lotspeich, J. F., "Electrooptic light-beam deflection", IEEE Spectrum, February 1968, p. 45.

Simon, M. C., "Ray tracing formulas for monoaxial optical components", Appl. Opt., Vol. 22, 1983, p. 354.

Simon, M. C., "Wollaston prism with large split angle", Appl. Opt., Vol. 25, 1986, p. 369.

Soref, R. A., and McMahon, D. H., "Optical design of Wollaston-prism digital light deflection", Appl. Opt., Vol. 5, 1966, p. 425.

Wahi, J., and Jain, S. C., "Bistable electro-optic switching of a ferroelectric liquid crystal (HOBACPC)", Ferroelectrics, Vol. 59, 1984, p. 161.

Wu, S. T., Efron, U., and Hess, L. D., "Birefringence measurements of liquid crystals", Appl. Opt., Vol. 23, 1984, p. 3911.

Table I. FLC based 16-stage Wollaston prism beam steering device at 1.06 μ m.

Stage #	Thickness (mm)	Split Angle (degrees)	Type	Thickness (mm)	Split Angle (degrees)	Type
1	2	0.02064	Quartz	2	0.02064	Quartz
2	2	0.04127	Quartz	2	0.04127	Quartz
3	2	0.08254	Quartz	2	0.08254	Quartz
4	2	0.16509	Quartz	2	0.16509	Quartz
5	2	0.33018	Quartz	2	0.33108	Quartz
6	2	0.66035	Quartz	2	0.66035	Quartz
7	2	1.32053	Quartz	2	1.32053	Quartz
8	2.075	2.70926	Quartz	2.021	2.70926	Quartz
9	4.1523	5.26842	Quartz	4.0445	5.26842	Quartz
10	2	0.57593	Calcite	8.107	10.4506	Quartz
11	2	1.15177	Calcite	2	1.15177	Calcite
12	2	2.30286	Calcite	2	2.30286	Calcite
13	2.348	2.98839	NaN03	3.43	4.60419	Calcite
14	4.683	5.9671	NaN03	6.85	9.18839	Calcite
15	9.237	11.8568	NaN03	13.57	18.2191	Calcite
16	13.913	23.136	NaN03	20.21	35.2474	Calcite

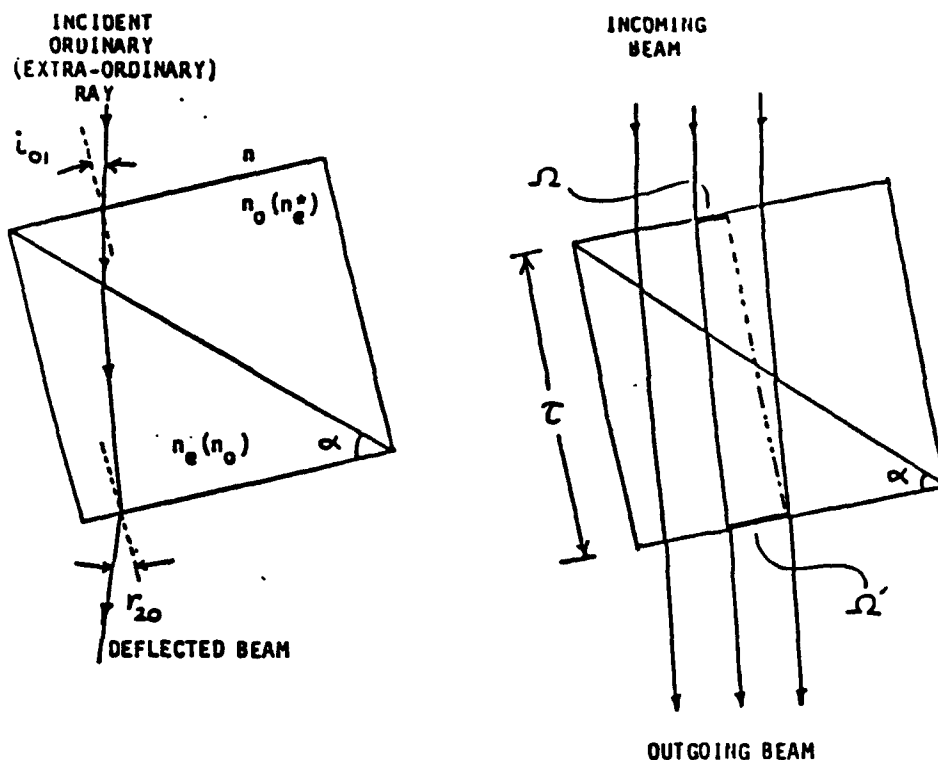


Figure 1. A single module of an FLC based wollaston prism steering device.

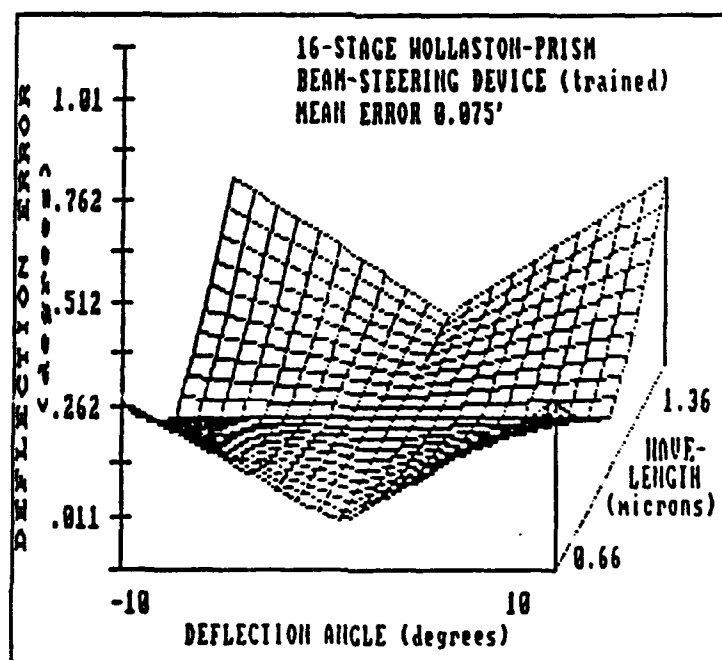


Figure 2. Angular deviations of the steered beam at different wavelengths and scan angles using an FLC based device.

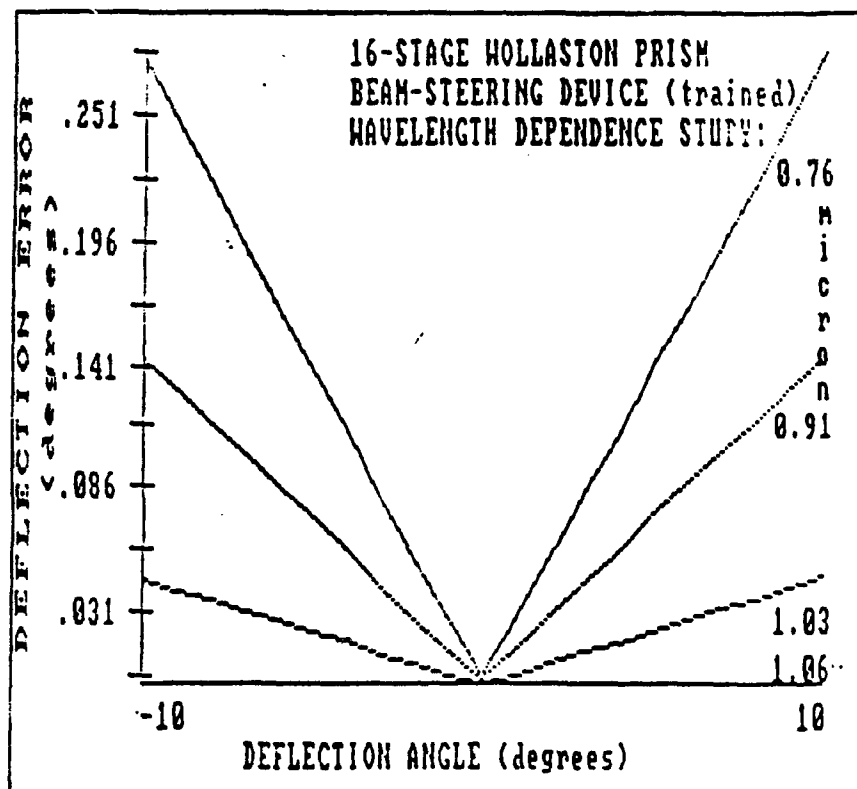
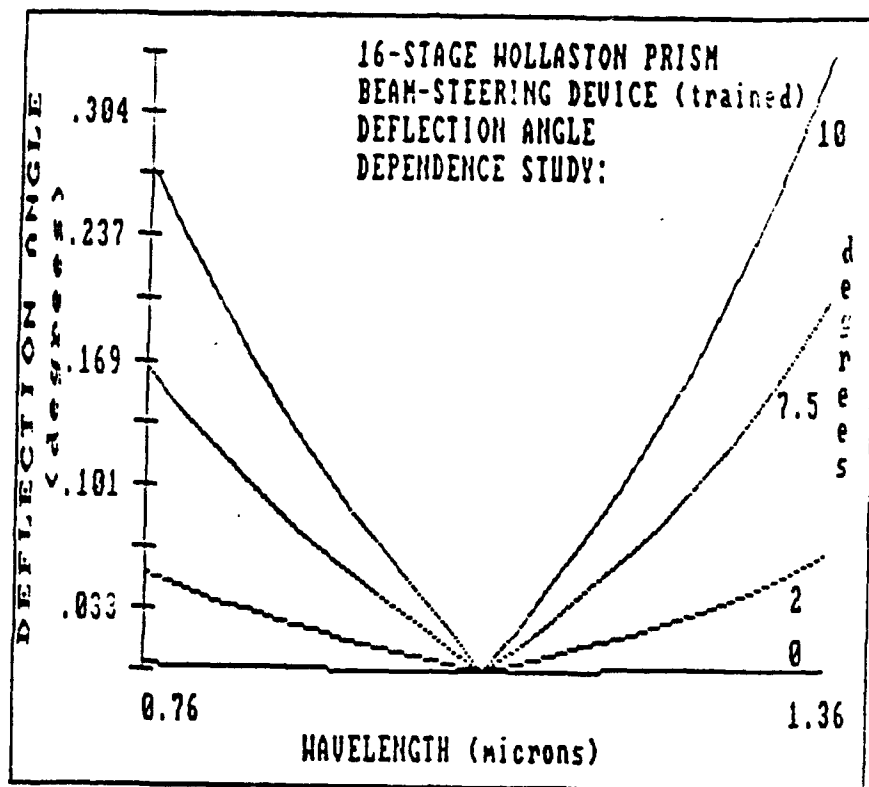


Figure 3-4. Deflection angle error versus (a) wavelength (at constant scan angles); and (b) scan angle (at constant wavelength) using an FLC based system.

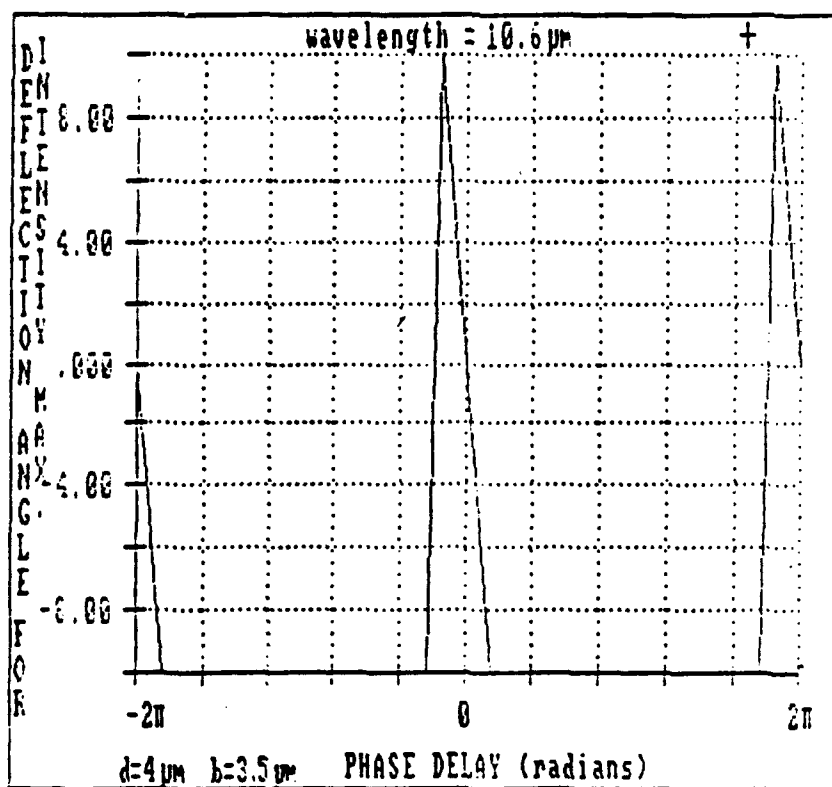
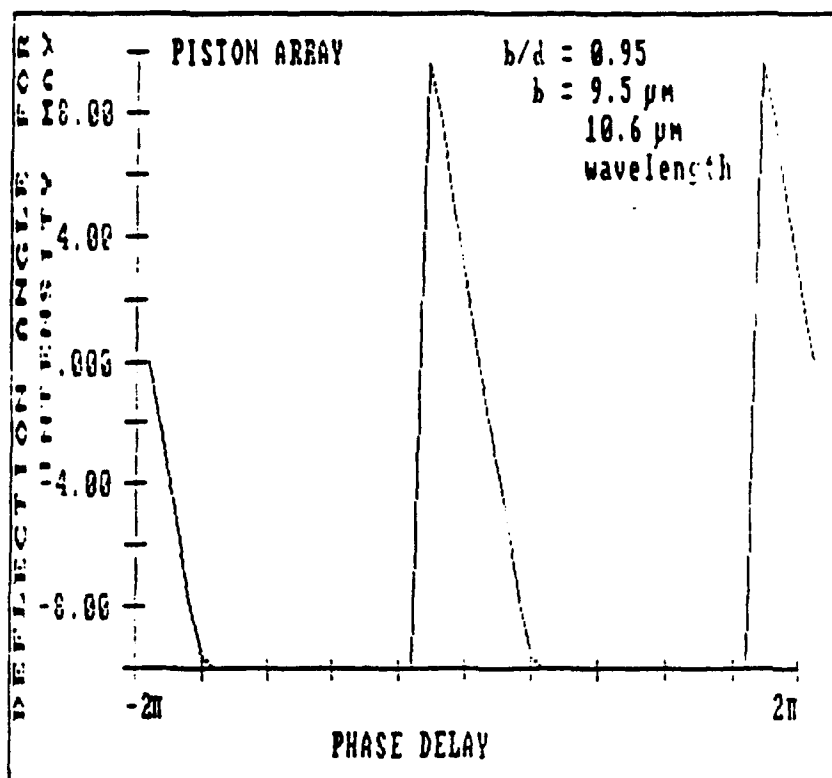


Figure 5. Angular deflection versus phase delay characteristics.

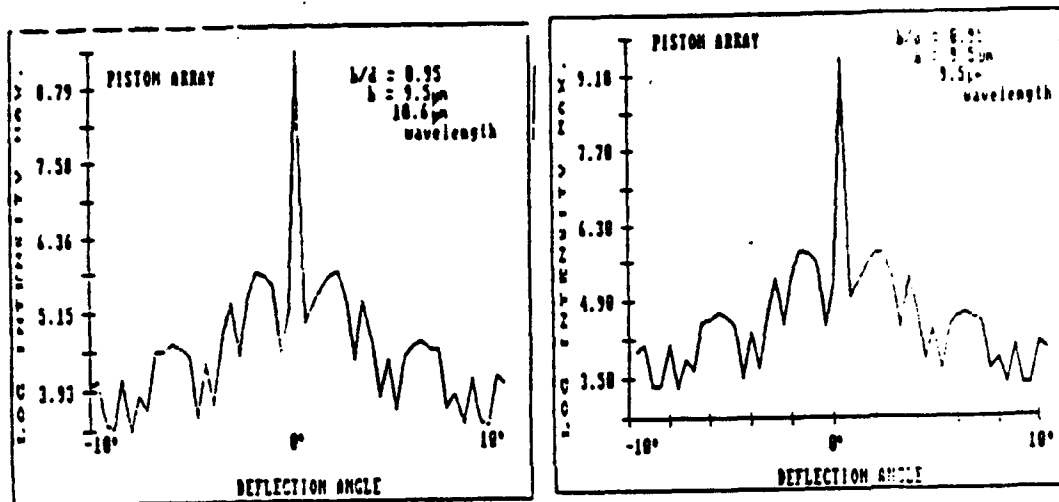


Figure 6. Intensity versus scan angle characteristics.

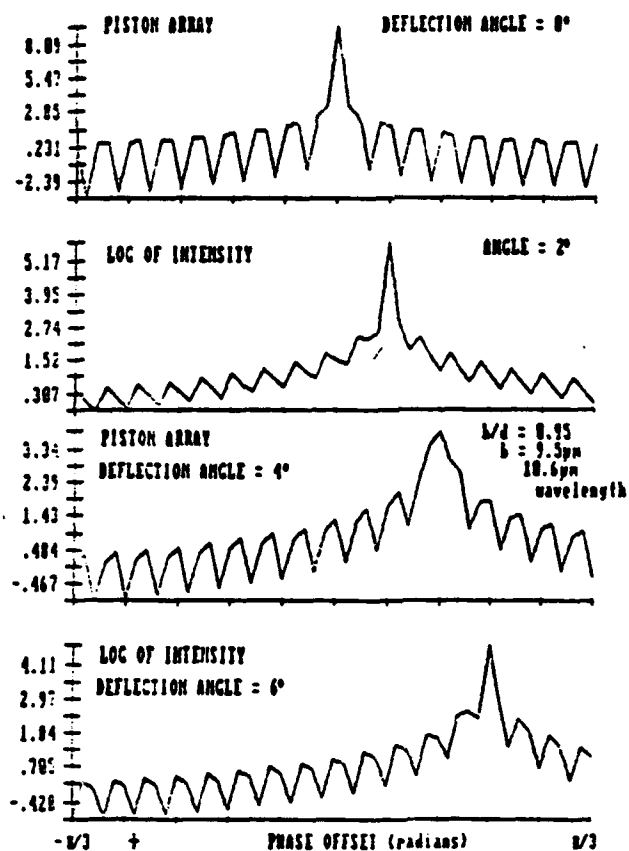


Figure 7. Intensity versus phase offset characteristics at different deflection angles.

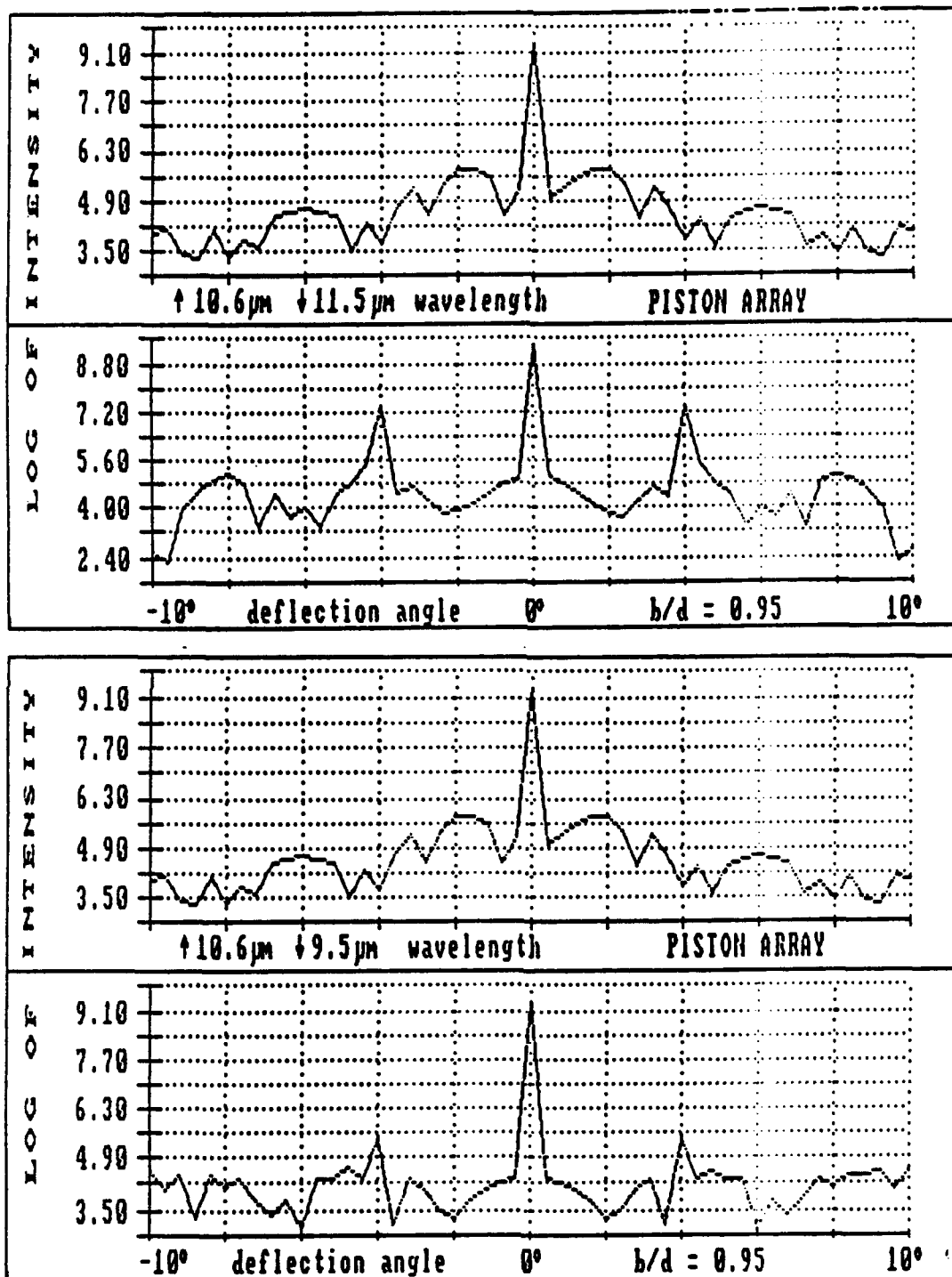


Figure 8. Intensity versus scan angle at different wavelengths.

1988 USAF-UES SUMMER FACULTY RESEARCH PROGRAM
GRADUATE STUDENT RESEARCH PROGRAM

Sponsored by the
AIR FORCE OFFICE OF SCIENTIFIC RESEARCH

Conducted by the
Universal Energy Systems, Inc.

FINAL REPORT

Prepared by : Robert Y. Li, Ph. D. / Yuhong Yu Li
Academic Rank: Assistant Professor / Graduate Student
Department and Electrical Engineering / Computer Science
University: University of Nebraska, Lincoln
Research Location: AFWAL/AARA
Wright-Patterson AFB
Dayton, OH 45433-6543
USAF Researcher: James D. Leonard
Date: August 15, 1988
Contract No: F49620-87-R-0004 / F49620-88-C-0053

Prof. Robert Li, and graduate student Yuhong Li

Model-based Target Recognition Using Laser Radar Imagery

Abstract

Autonomous target recognition can be assisted by using CO₂ laser radar data which contains 3-D information of the scene viewed from the sensor. Using efficient image processing algorithms such as the Hough transform, the orientations and dimensions of the target can be calculated. This information then can be used by a model-based recognition system to identify the target. The identification is based on an inference procedure which tests hypotheses using the available evidence from the sensory data.

Acknowledgements

We wish to thank the Air Force Systems Command and the Air Force Office of Scientific Research for sponsorship of this research. The Target Recognition Technology Branch (AARA) and Universal Energy Systems must be mentioned for their concern and help to us in all administrative and directional aspects of this program.

James D. Leonard provided us with great support; his suggestions, comments, and help are very useful and inspiring. Daniel C. Kinser, Jeffrey A. Barnes and Sgt. Edwin Quillin assisted us in using the computing facility of the laboratory. Mike Bryant helped us with the PC's software and hardware. Their help was a key to our smooth work progress. We want to thank them all.

I. Introduction

The Air Force mission includes the functions of interdiction, close air support, and defense suppression. Autonomous operation of detection, classification, and location of tactical targets should offer significant increase in its tactical air to ground mission capability. CO₂ laser imaging sensors are being explored as a useful tool for these operations, because they offer a unique 3-D target sensing capability to future Air Force systems.

Although the laser sensor hardware has been built, much effort remains to be done on the development of recognition algorithms for automatic target acquisition, and on obtaining an accurate evaluation of the algorithm design. In this research effort, LADAR imagery was obtained from the LTV multi-modal CO₂ laser radar which has the following data types: relative range, Doppler, IR, visual, carrier intensity, and vibration[1]. Among these data, range data offer significant advantage because they preserve the 3-D geometry of the scene viewed from the sensor[2,3]. It is important to use fast and reliable algorithms to extract these geometric features, because speed is a critical factor in a real-time operation. To integrate these features into a decision process, they should be used as input evidence to a hypothesis management system. Using this system, the hypotheses about the nature of the target are tested and evidence is analyzed to support or discredit those hypotheses.

Our research interests are in the area of multi-sensor fusion and artificial intelligence. Dr. R. Y. Li has had extensive experience in working with laser radar images and automatic target recognition while he was with the Lockheed Palo Alto Research Laboratory. At the University of Nebraska, he currently is working on an expert system project for the United States Geological Society (USGS).

II. Objective of the Research Effort

The overall objective of our research is to demonstrate the performance of automatic target classification algorithms using CO₂ laser sensor data. More specifically, the goals are to develop efficient algorithms that can accurately extract geometric features from the target's range measurements, and to develop a hypothesis management system that can identify the target category based on these geometric features. In short, we plan to study the methodology of building a model-based target recognition system and to develop the tools needed for building such a system.

III. Approach

The approach of this project can be summarized by the five tasks listed below. They are further described in details in the following three sections.

1. Conversion to Absolute Range: Convert a portion of a relative range scene into absolute range. Doppler imagery is used to help solve the ambiguity problem.
2. Generation of XYZ maps: After absolute range is obtained, the (x,y,z) coordinates of each pixel in the range data are computed. The computation is based on the geometry of the sensor orientation relative to the sensed scene. Motion effect is also taken into effect.
3. Surface extraction: By computing the magnitude of the vertical and downtrack displacement between adjacent pixels, the existence of horizontal, left-facing vertical, and right-facing vertical pixels can be detected. This segmentation process improves the performance of subsequent feature analysis.
4. 3-D Hough transform: Most potential targets consist of planar or nearly planar surfaces. Instead of using local patch fitting, the 3-D Hough transform is used to find the orientations and dimensions of these surfaces.
5. Hypothesis management systems: Geometric information extracted from the scene will not be useful for the recognition purpose unless they can be matched with a description of the target, such as the tank. An inference procedure was built so that the hypothesis can be evaluated based on the evidence obtained by the previous image processing techniques. A LISP program was written to implement the procedure.

IV. Preprocessing

The first three tasks mentioned in the last section can be considered as the preprocessing step for the feature extraction effort. They are discussed in the following three subsections.

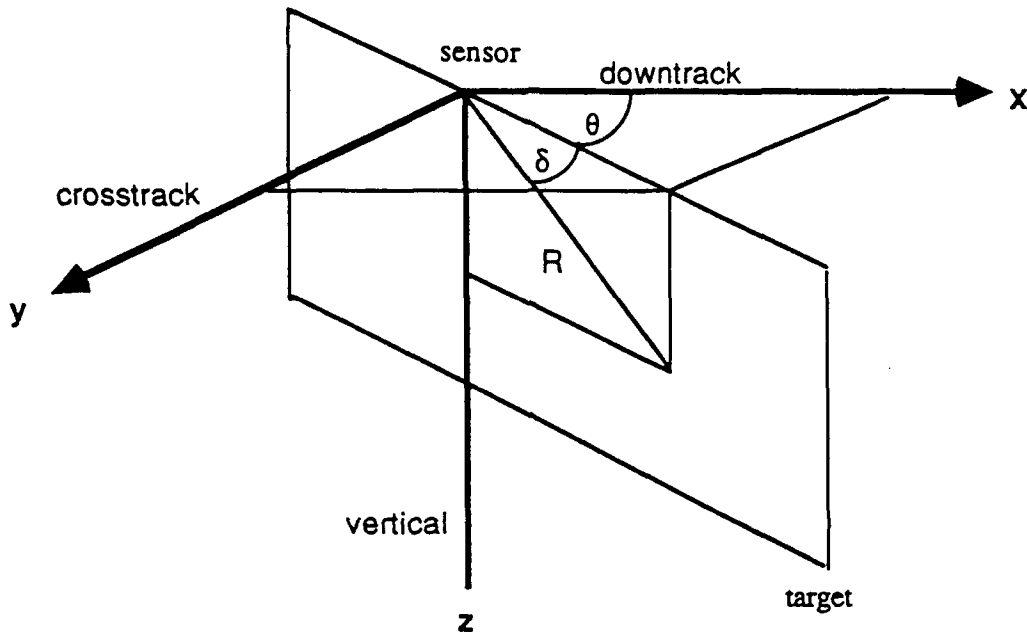
A. Conversion to Absolute Range

The LTV image data set includes relative range images with 15 meter range ambiguity. Since most military targets are smaller than 15 meters, the relative range data covers most targets in one ambiguity level. However, because of low oblique angles, the ground plane around the target is usually covered by 3 to 4 ambiguity levels. To concentrate the analysis on the target, our first step is to segment a section of the relative range image around the target as well as the corresponding part of the Doppler image. Then, this subimage is converted from relative range to absolute range.

The conversion begins by first median-filtering the range and the Doppler data to remove noise using a 3 x 3 window around each pixel. For cases where the window contains range data from two different ambiguity levels, 256 is added to the low values before sorting the nine intensity values in the window. After the median-filtering, the relative range values are examined column-wise from the bottom of the image to the top. Crossing of ambiguity levels is detected by noting large differences between two adjacent pixels, and the range value of each pixel is adjusted accordingly. Because a target obstructs the ground behind it, this conversion from relative range to absolute range often results in ambiguity errors in the image columns above the target. This is corrected by first using the Doppler image as a mask to determine the boundary between the target and the erroneous pixels in a given column. Then in a left to right search, the columns which are in error are detected and corrected using the leftmost pixel of the search as a reference value. Figure 1 shows a tank in a relative range image, the filtered relative range image, the filtered Doppler mask, and the converted absolute range image. Figure 2 shows a fuel truck in a similar set of images. By comparing the original range image and the median-filtered range image, it can be seen that the salt-and-pepper noise no longer exists. The converted absolute range image shows that the range values change gradually and smoothly from pixel to pixel, and the range ambiguity is removed.

B. Generation of xyz maps

The range data should be converted to a sensor-based Cartesian coordinate system (x,y,z) using the known sensor gimbal angles. The coordinate transformation can be described by the following figure and equations:



$$\text{downtrack } x = R \cos \delta \cos \theta$$

$$\text{crosstrack } y = R \cos \delta \sin \theta$$

$$\text{vertical } z = R \sin \delta$$

where δ is the depression angle and θ is the azimuth angle.

The distance and depression angle from the sensor to the center of the image frame and that of the major target are available from the header information. The angular resolution is also available, and is usually either 0.29 milliradians or 0.19 milliradians. They are used in the calculation of the xyz values.

The CO₂ laser radar scans vertically bottom to top with the first scan on the left and the last scan on the right at 10,000 pixels per second. For the 256 x 256 images, each frame takes 6.5 seconds to record. When targets are moving, the range measurement of the target is either elongated or shortened due to the time gap between recordings of different points on the same target. For example, a target moving at 5 mph moves 2.2 meters in 1 second and can cause considerable range discrepancy. For most cases, the Doppler data showed that the target was moving at very slow velocity. However, for some other cases, the target's velocity was at 5 mph or more. We decided to include a correction routine for the downtrack direction because velocity in that direction can be calculated from the Doppler data. The Doppler data is quantized in 0.09752 meter per second per level. The correction assumes that the target is moving at a constant velocity based on the Doppler value at each pixel. The time gap between a pixel and the reference point is calculated dividing the number of pixels scanned between the two points by 10,000 pixels/second.

The xyz values generated in this step are subsequently used for surface extraction and Hough transformation calculations. They are stored in an ASCII file for later use. To see that the xyz values are basically correct, we plotted the perspective view of a target using the xyz values with MATLAB (a matrix-based mathematics software). Figure 3 shows the plot of an M-60 tank with its pixels extracted using a Doppler mask. Although some noise still exists, it can be seen that the lower section, which is the hull and the tracks, is box-like. The upper section shows the existence of a turret with part of the gun-barrel in front.

C. Surface Extraction

Two very useful preprocessing operations were used. The first preprocessing operation tests for vertical displacement between two adjacent downrange pixels to separate vertical pixels from horizontal pixels. The second preprocessing operation then separates these candidate vertical pixels into left and right facing vertical pixels.

The vertical test uses a 3 x 3 convolution mask which is applied to the Z components of all the pixels in the image. The pixels are treated as a spatial array in which each row is at a constant depression angle and each column is at a constant azimuth angle. The convolution operation is given by:

$$SLP = \begin{bmatrix} 1 & 1 & 1 \\ 0 & 0 & 0 \\ -1 & -1 & -1 \end{bmatrix} \text{ (Z value)}$$

If the convolution is applied to row n , the difference in Z value between row $n+1$ (smaller depression angle) and row $n-1$ (larger depression angle) will be positive for any rising slope. The SLP value is normalized over distance and multiplied by a scaling factor. The result of this convolution at each pixel is then compared to a set of threshold values to isolate horizontal surfaces and vertical surfaces.

The second operation classifies the resulting vertical surfaces as left or right facing surfaces. The operation uses another 3×3 convolution mask which is applied to the X component (downtrack) of all of the vertical pixels derived from the first operation. The second convolution mask is given by

$$F = \begin{bmatrix} 1 & 0 & -1 \\ 1 & 0 & -1 \\ 1 & 0 & -1 \end{bmatrix} \text{ (X value)}$$

The results of applying this mask at column n of the image will be positive for left-facing surface since the downtrack value at column $n-1$ (to the left of n) is larger than the downtrack values at column $n+1$ which is to the right of column n . For surfaces that are perpendicular to the sensor's line of sight, F will be close to zero. The results of using these operators are shown in Figure 4. Different gray levels are assigned to highlight the horizontal surface, the left vertical surface, and the right vertical surface.

V. 3-D Hough Transform

The Hough transform is usually used for curve or line detection in a 2-D intensity image. Because each pixel is individually transformed, the Hough technique is relatively unaffected by gaps and noise in the curve[4]. The idea can be extended to 3-D data to detect and measure planar surfaces. A plane in the 3-D space can be described by the following equation:

$$\cos \delta \cdot \cos \theta \cdot x + \cos \delta \cdot \sin \theta \cdot y + \sin \delta \cdot z = D$$

where θ , δ and D are pan angle, tilt angle and normal distance.

To detect a plane, we check for any peak in the accumulator of these three parameters (θ , δ , D). When θ , δ , and D extend over a large range, the calculation can be very time-consuming. However, since most surfaces are either vertical or horizontal, the Hough transform for 3-D space can be simplified. For vertical surfaces, because the tilt angle is zero, the equation reduces to:

$$\cos \theta \cdot x + \sin \theta \cdot y = D$$

and for horizontal surfaces, because the tilt angle is 90 degree, the equation reduces to :

$$z = D$$

These simplifications reduce calculation time greatly, yet still produce reasonably good results.

Our first goal in applying the Hough transform to the data is to estimate target orientation by detecting a dominating vertical surface in the target. This is done by locating the peak in the (θ , D) accumulators using the xy values of each pixel. We initially included all the pixels of the image in calculating votes for each accumulator. Two target types, the M-60 tank and the fuel truck, were used. Because neither the M-60 tank nor the fuel truck consisted of large vertical flat surfaces, this approach did not give good results. We then tried to use only the target pixels extracted with the Doppler mask. Still, no clear peak was

found to give us the correct target orientation. We then reasoned that most vehicles had either a flat top or a large deck, and the portion below that flat horizontal surface was more box-like. Therefore, vertical pixels below the major flat surface are more suitable for the calculation of target orientation. Using this approach, correct orientation angles were obtained for most targets under our consideration.

After target orientation is determined, geometric features such as height, width, and length of the target and the percent of pixels above the target deck can be calculated. These features are to be used as the inputs to a model-based inference net. These dimensions were computed by counting the valid intervals within the Hough space along the proper orientation. The specific steps involved in estimating the orientation and the dimensions of a target are summarized below:

- (1) With the Doppler data as a mask, segment the target's major horizontal surface using the Hough transform.
- (2) Using only vertical pixels below the major horizontal surface, and using only angles from -90 to 90 degrees in the Hough space, find the target orientation.
- (3) With the angles fixed, find the target dimensions by counting valid intervals of the normal distance along these angles.
- (4) Calculate percentage of pixels above and below the major horizontal surface (which is the deck in the case of the tank).

Figure 5 shows the M-60 tank of Figure 1 projected to show horizontal intervals, left-facing vertical intervals, and right-facing vertical intervals as calculated by the Hough transform. The left-facing intervals are at a 60 degree norm and the right-facing intervals are at a -30 degree norm, and each interval is one meter wide. The multiple layers displayed by different intensities assigned to the intervals show how the pixels are allocated in the Hough accumulators. For illustrative purpose, one meter wide intervals were used in the figure to limit the number of layers that are displayed. In calculating actual target dimensions, 0.25 meter intervals are used.

Table 1 lists the results of computing target orientation and dimensions for the targets in the following LTV data sets: LTV-3013, LTV-3015, LTV-3324, LTV-3334, LTV-3335, and LTV-3347. Figure 6 shows the top-down views of these targets. The Hough transform results appear quite consistent with the angular orientations of these top-down

views. Those measurements on height, length, width, and the percent of pixels above the deck are used as evidential inputs to the hypothesis management system which is described next.

VI. Hypothesis Management System

As stated in the introduction, a well-developed recognition strategy should contain two components. The first is a processor for reducing the vast amount of low-level sensory data to a manageable number of symbolic entities. The second is a process for generating high-level hypothesis from these symbolic entries.

Our image analysis of the range data produces certain descriptions of the target such as the target dimensions and the percent of pixels above the deck. These descriptions are then processed by a model-based inference procedure. Figure 7 shows such an inference net for the hypothesis that "the target is a tank." The recognition model is essentially a rule-based decision network. Given certain assumptions, a priori probabilities, and conditional probabilities, the a posteriori probability is then computed for each node based on Bayes' rule outlined below:

$$P(H/E) = P(E/H) * P(H) / P(E)$$

where $P(H)$ = a priori probability that hypothesis H is true

$P(E)$ = a priori probability of the evidence

$P(E/H)$ = conditional probability that if hypothesis H is true then evidence E exists

$P(H/E)$ = a posteriori probability that H is true in light of evidence E

Using Figure 7 as an example, H_2 is the hypothesis that the target's overall dimensions are correct, and E_2 is the evidence that the target's length is correct. If we estimate that the frequency of obtaining the correct overall dimension is 3 out of 10 in a given scenario, then $P(H_2) = 0.3$. Normally, $P(E_2/H_2)$ is one. If $P(E_2)$ is available, then the posterior probability $P(H_2/E_2)$ can be computed by using Bayes' rule. In the model-building process, these a priori probabilities associated with each node must be first known or estimated. Then LS and LN where

LS = measure of support for hypothesis if E is present

LN = measure of discredit for hypothesis if E is missing

are calculated for each nodes. Essentially, $LS = P(H/E)$ and $LN = P(\sim H/\sim E)$ where $\sim H$ means that H is not true.

New information is added to the certainty factors of the evidence nodes and $P(E)$ is adjusted using the following equations:

$$\begin{aligned} P'(E) &= P(E) + (1 - P(E)) \cdot CF / 5 & CF > 0 \\ P'(E) &= P(E) + P(E) \cdot CF / 5 & CF \leq 0 \end{aligned}$$

These changes in $p(E_2)$ yield new values for $p(H_2)$, which are calculated by using Bayes' rule and the values of LS and LN . In this example, H_2 is the hypothesis that "all three measured dimensions are correct for the target". These probabilities are propagated up the inference network using an "AND" relationship such that the new probability of H_2 is determined by the minimum value obtained from the three dimensional measurements. This probability propagation is performed throughout the entire system. Finally, the probability at the root is calculated and a CF value is generated for the hypothesis H_1 . The approach taken here is very similar to the hypothesis testing procedures developed in the PROSPECTOR expert system[5].

The inference procedure is implemented in LISP running on an IBM AT compatible PC. Instructions for entering the data and inspecting the parameters computed for the model can be found in the appendix along with the program listing. The model has been extended to accommodate multiple hypotheses. For instance, after installing several top level hypotheses, the program can estimate the probabilities of each hypothesis and choose the one most likely to be true.

We tested the program with our image analysis results in Table 1 using a battlefield scenario in which equal numbers of tanks, APC's, 2-1/2-ton trucks, and fuel trucks exist. Their dimensions are available from the Jane's Report. The results showed that all tanks except the one from LTV-3015 scene were identified as tanks and both fuel trucks were identified as fuel trucks. In all the cases, the "percent of pixels" was the major feature that separated the vehicle types. Admittedly, this is not truly a robust target recognizer yet. More work needs to be done in this aspect.

VII Recommendations

We feel that the following research areas should be pursued.

1. Extend the analysis to a multiple target scene in which Doppler data is unavailable or the targets are stationary. In this case, potential targets must first be detected as blobs by using spatial filtering techniques. The features can then be extracted for identification purposes. We expect to obtain more geometric features from the range measurements than in our current research effort. Absolute range data should be used if the data become available.
2. During this study, the recognition process only used range and Doppler data. Potentially useful information from infrared and visible data should be explored to set up a synergistic approach. Range data by itself produces good detection results for most scenarios, but the passive data can provide additional target features which will help reject decoys and natural objects with dimensions similar to those of the targets. Multi-sensor fusion using complementary information should improve the accuracy of target detection and recognition.
3. The hypothesis management procedure outlined earlier can serve as a preliminary model to test the concepts of building a sensor-based expert system for automatic target recognition. The procedure can be further expanded to include the concepts of a Bayes network or to incorporate the Dempster-Shafer theory.

References:

1. G. S. Bain and W. K. Cunningham, "Multifunction Laser Radar," Technical Report, LTV Aerospace and Defense Co., May 1986.
2. R. Y. Li, C. M. Bjorklund and R. S. Loe, "Matching of Planar Surfaces for 3-D Terminal Homing," *Proceedings of NAECON conference*, Dayton, Ohio, June 1983.
3. P. Besl and R. Jain, "Range Image Understanding," *Proceedings of Conference of Computer Vision and Pattern Recognition*, June 1985.
4. R. Y. Li, "Range Image Processing for Object Recognition," *Proceedings of the 30th Midwest Symposium on Circuits and System*, Syracuse, N. Y., Aug., 1987.
5. A. Watman, *A Guide to Expert System*, pp. 55-60, Addison Wesley Publishing Co., Dec., 1985.

Table 1 Extracted Target Features

	LTV-3013	LTV-3015	LTV-3324	LTV-3334	LTV-3347	LTV3335
Target Type	M-60 tank ¹	M-60 tank	M-60 tank	M-60 tank	fuel truck ²	fuel truck
Analysis Result						
Angle, deg ³	60	10	10	-70	20	-70
Distance, meter	314	307	880	300	300	371
Width, meter	4.0	5.0	3.75	3.5	3.75	3.0
Length, meter	6.5	5.25	5.0	6.0	12.0	12.0
Height, meter	3.0	3.5	3.5	3.0	3.25	3.25
% pixel above deck	29.8	46.1	30.5	33.3	6.4	3.8
Total no. of target pixels	1940	1365	466	1255	1551	1448

Note: 1. M-60 tank is 3.6 meter wide, 6.9 meter long and 3.2 meter high

2. Fuel truck is 2.46 meter wide, 12 meter long and 2.64 meter high

3. Perpendicular angle to the dominating vertical surface extracted by the Hough transform



Figure 1. LTV 3013 Tank Scene, Clockwise from Left, Bottom: Original Relative Range Image, Median Filtered Relative Range Image, Converted Absolute Range Image, and Median Filtered Relative Range Image



Figure 2. LTV 3347 Fuel Truck Scene, Clockwise from Left, Bottom: Original Relative Range Image, Median Filtered Relative Range Image, Converted Absolute Range Image, and Median Filtered Relative Range Image

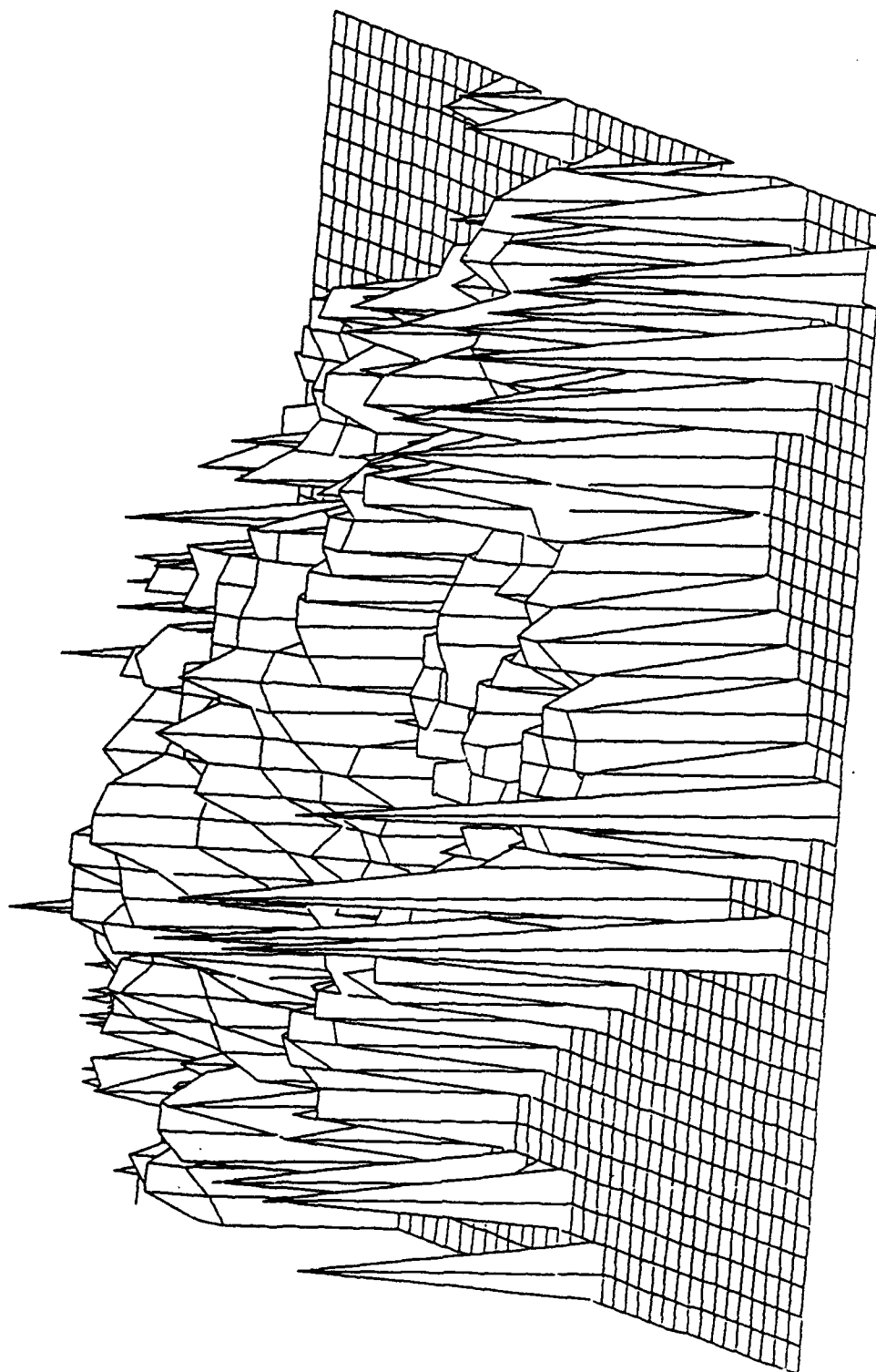


Figure 3. Perspective View of the Tank Scene of LTV-3013



Figure 4. Targets with Surface Extracted



Figure 5. Hough Transform Results Shown by Layers of Different Intensity for Representing Pixels in Different Accumulators



Figure 6. Projection of Targets to Horizontal Plane, Clockwise from Left Bottom:
LTV-3013, LTV-3015, LTV-3334, LTV-3335, LTV-3347 and LTV-3324

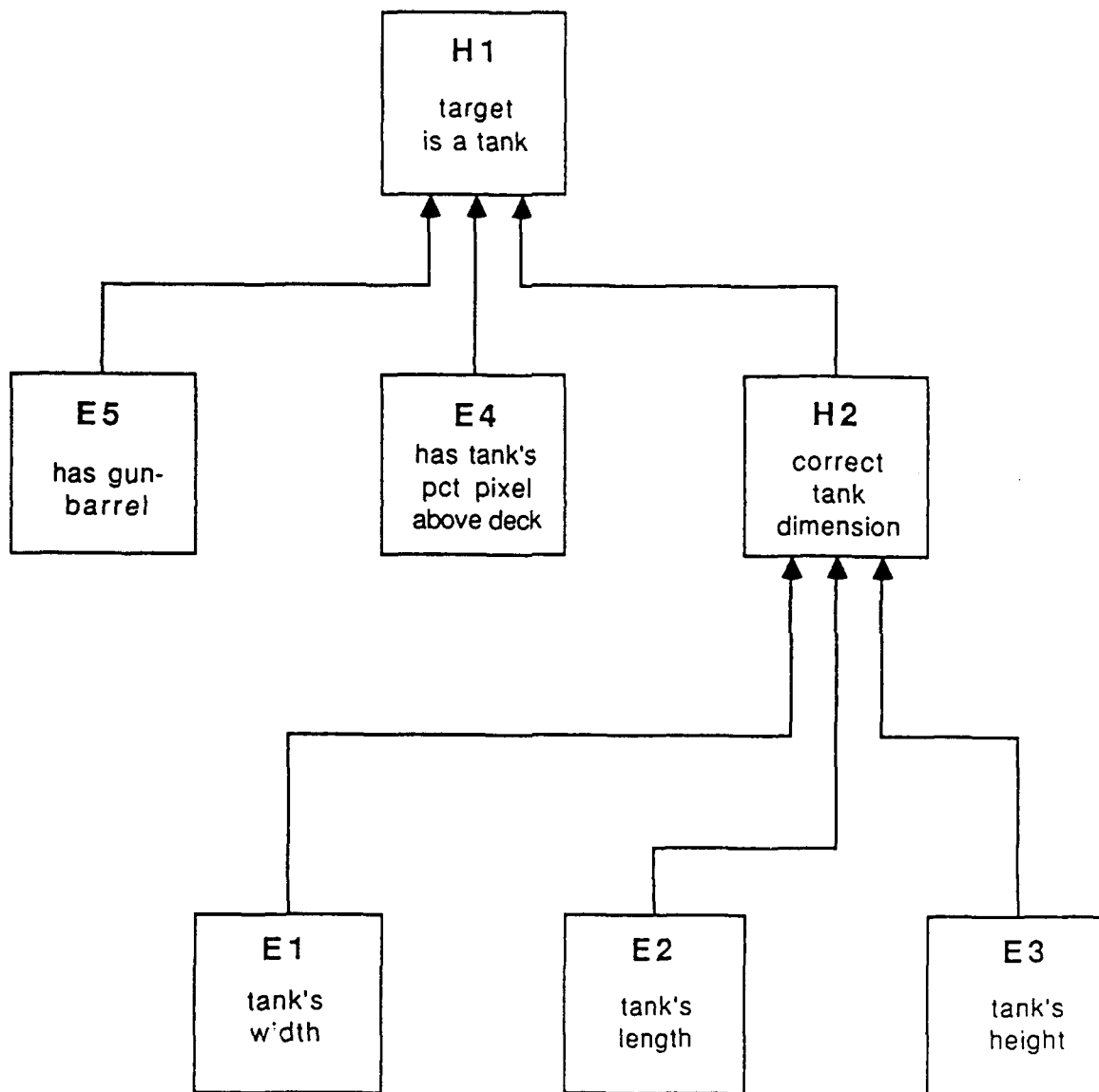


Figure 7. Inference Net for Identifying a Tank

1988 USAF-UES SUMMER FACULTY RESEARCH PROGRAM/
GRADUATE STUDENT RESEARCH PROGRAM

Sponsored by the
AIR FORCE OFFICE OF SCIENTIFIC RESEARCH

Conducted by the
Universal Energy Systems, Inc

FINAL REPORT

SIGNAL PROCESSING FOR ESM RECEIVERS

Prepared by:	Periasamy K. Rajan, Ph.D.
Academic Rank:	Professor
Department and	Electrical Engineering Department
University:	Tennessee Technological University
	Cookeville, Tennessee
Research Location:	Avionics Lab, AFWAL/AAWP-1
	Wright-Patterson Air Force Base
	Dayton, OH 45433
USAF Researcher:	Dr. James B. Y. Tsui
Date:	September 12, 1988
Contract No.:	F49620-87-R-0004

SIGNAL PROCESSING FOR ESM RECEIVERS

by

Periasamy K. Rajan

ABSTRACT

Receivers for electronic support measures(ESM) have some demanding signal processing requirements. A number of parameters of the received signal has to be determined in real time. In this research a study of the various receivers was carried out. The digital instantaneous frequency measurement (DIFM) receiver was analysed. The sensitivity functions of the calculated frequencies to the errors in the measurement of the correlation lags in DIFM receivers were derived for the two frequency case. Further, a new formulation of the equations that avoid the use of the correlation value at zero lag was developed. Finally, a setup for the acquisition of real data in digital form was tested.

Acknowledgements

I wish to thank the Air Force Systems Command and the Air Force Office of Scientific Research for sponsorship of this research. Dr. Jim Tsui of the Avionics Lab was very enthusiastic in sharing necessary details and discussing the various problems associated with this research. I am very thankful for his help and support in carrying out this research. Ed Grissom, my graduate student, contributed significantly to this research by developing necessary software. The members of the AAWP-1 Group of the Avionics Lab provided a very congenial atmosphere, and offered their assistance whenever I needed. Special mention must be made of the assistance provided by J. Caschera, R.L. Davis, N. Pequignot, Dr. R.B. Sanderson and G.H. Schrick. The assistance provided by Rudy Shaw, Paul Hadorn and F.B. Loucks IV is also acknowledged. Universal Energy Systems must be mentioned for their excellent management of this program.

Finally I wish to thank my wife Visalakshi and son Rajkumar for their understanding of my absence from home during the summer to carry out the research reported here.

I. INTRODUCTION

Electronic surveillance is an important facet of electronic warfare (EW)[1]. In electronic surveillance a major task is to detect and identify radio frequency signals present in space. These signals originate from communication, radar, and airborne navigation equipments located in military installations, aircrafts and other hardware. The identification of the sources of the radiowaves is essential for taking proper countermeasures that minimize hostile threats and maximize the effectiveness of one's own weapons. The basic functions that an electronic surveillance system is required to perform are the following:

- 1) Detect the presence of one or more RF signals present in an environment
- 2) Determine the following parameters pertaining to the received signal:
 - i) Number and types of signals present
 - ii) Frequency of each signal
 - iii) Direction of arrival of each signal (DOA)
 - iv) Amplitude of each signal
 - v) Pulsewidth (PW) and pulse repetition interval (PRI)
 - vi) Time of arrival (TOA)
- 3) Sort the signal parameters and assign them to proper signals
- 4) Identify the emitters on the basis of the signal parameters and the existing knowledge base
- 5) Update the knowledge base.

The early surveillance receivers were designed to perform only some of these functions and to a limited extent only. Even the currently available receivers [1] can handle only a single signal at a given time. They operate on analog or hybrid mode, exhibit low accuracies and cannot be used to detect simultaneous signals. On the other hand, with the improvements in transmitter and warfare technology, the receivers are required to operate under severe conditions. Current technology of the radars permit them to send signals with hopping and/or continuously varying frequencies (chirp signals). With increased number of installations and equipments, more dense signal environment is encountered by the receivers. Further, in order to improve their effectiveness and increase the success rate of countermeasures, the surveillance radars are required to perform the above functions in real time, requiring response times to be of the order of a millisecond or less. All these requirements place extraordinary demands on the design of surveillance receivers.

Current techniques and technology of receivers are incapable of meeting the above demands. As pointed out elsewhere ESM data processing presents one of the most complex time critical real time problems of current technology. Hence, research on various aspects of the receiver design is being pursued by many researchers around the world. As this is a problem of crucial importance to Air Force, the Avionics

Laboratory of the Wright Aeronautical Laboratories at Wright-Patterson Air Force Base, Ohio, is conducting intensive research in this area.

My field of research has been digital signal processing for the past ten years. I have expertise in the analysis and design of digital filters and other digital signal processing systems. As the advanced receivers will need to use digital signal processing techniques, research on signal processing algorithms and their implementation for ESM receivers is an appropriate and challenging project. This led to my assignment to the ESM Group of the Avionics Laboratory. Here I conducted research on some aspects of the above signal processing problem for ESM receivers during my tenure as a Summer Faculty Research Fellow. In the following sections, the results of these investigations will be discussed.

II OBJECTIVES OF THE RESEARCH EFFORT

After a discussion with Dr. James B.Y. Tsui, my USAF Research Colleague, the following objectives were arrived at:

1. Carry out a critical study of the ESM receivers and their signal processing techniques.
2. Analyse the algorithms used in DIFM receivers with a view to enhance their performance.
3. Perform a preliminary testing on a scheme to acquire the signal in digital form and determine its spectrum.

III. ESM RECEIVERS

There are basically three types of receivers that can be used for ESM applications. They are: i) analog receivers, ii) analog/digital (hybrid) receivers, and iii) digital receivers. We will next briefly discuss each of these receivers.

i) Analog Receivers:

In this type of receivers, the received signal is processed completely in analog domain. Crystal receivers, superhetro receivers, channelized receivers, and instantaneous frequency measurement (IFM) receivers fall into this category. Out of these four types, crystal receivers could be used only to detect the existence of signals and not to determine their frequencies. Superhetro receivers are very slow and complex. Channelized receivers have poor resolution. This leaves the IFM receiver as the most commonly used receiver for ESM applications. In IFM receivers, the received signal is correlated with a delayed version of the input signal. The correlator output will be a function of the frequency of the input wave. Thus the frequency of the received signal can be determined from this correlator output. The receiver circuit is simple and the accuracy of the frequency determination is quite satisfactory. The major problem associated with this receiver is that the input wave should not contain more than one sinewave. If the input signal

contains more than one sine wave or a varying frequency wave then the frequency determined by this receiver will be completely erroneous.

2) Analog/Digital Hybrid Receivers [2,3]

In order to overcome the above mentioned difficulties, an improved analog receiver has been proposed. In this receiver, part of the processing is done in analog form and the remaining processing is carried out in digital form. Digital instantaneous frequency measurement (DIFM) receivers fall in this category. In this receiver, the correlation lags are obtained using analog circuits as discussed in analog IFM receivers. The correlation values are digitized using A/D converters and these are then processed using digital techniques to determine the frequencies and other parameters.

The research conducted so far show that this receiver has the potential to deal with simultaneous signals. That is, the frequencies of two or more signals simultaneously present in the received signal can be determined using this receiver. The research has also indicated that the receiver has a dynamic range problem. When the received signal has a strong signal and a weak signal simultaneously, the frequency of the weak signal cannot be determined accurately. In this case the frequency determined for the strong signal also can be in error. In order to overcome this problem limiting

amplifiers may be used, however this introduces additional harmonics causing more problems. Further, presence of noise in the received signal affects the value of the correlation value at lag zero while having little effect at other lags.

As part of the summer research two investigations relating to the above problem were undertaken. First, the sensitivity of the frequency calculated using the correlation method for the two frequency case with respect to the estimated correlation lags was determined. Second, a new formulation of the equations was obtained so that the use of the correlation at lag zero is avoided. These two topics will be discussed in the following sections in detail.

3) Digital Receivers [4]

In view of the advancements that have taken place in digital technology and the digital signal processing techniques, it may be expected that the design of an all digital receiver will be feasible in the near future. In this receiver, the wave from the antenna will be digitized directly and the digitized signal will be processed using the various digital signal processing techniques. In view of the variety of signal processing possible when the signal is available in digital form, we will be able to extract all the necessary parameters. However the main problem faced in the design of digital receivers is the speed. Even though the digital technology has produced extra high speed devices, they are

still not fast enough to deal with radar signals in the gigahertz frequency range. The presently available A/D converters can operate to a maximum of 250 MHz frequency with 8 bits. By combining these converters in parallel one may go to 1 GHz conversion rate. However this is not enough. Further, for ESM applications the processing needs to be carried in real time. This means all the necessary calculations need to be carried out within one pulse repetition interval. Thus the successful design of digital receivers require further research in the development of improved algorithms which require fewer number of simple calculations and improved technology which produces faster A/D converters and arithmetic chips. In Section V, the result of an experiment carried out in acquiring real data in digital form and its processing will be discussed.

IV. SENSITIVITY CALCULATIONS FOR DIGITAL IFM RECEIVERS

In a digital IFM receiver, the signal from an antenna is input to an analog discriminator whose output consists of correlations at different lags. These correlation values are digitized using A/D converters. These digital data are processed using digital processors or computers to determine the frequencies of the sinewaves present in the received signal. A brief description of the calculation procedure is given below. The discussion is restricted to the two signal case. That is, we assume that the signal consists of only

two sinewaves and possibly some white noise. Let

$$f(t) = A \exp(jw_1 t) + B \exp(jw_2 t) \quad \text{..(1)}$$

where A and B are the complex amplitudes of the sinewaves. Then the correlation at lag nT is given by

$$\begin{aligned} R(nT) &= E\{f(t)F(t+nT)\} \\ &= P_1 \exp(jw_1 nT) + P_2 \exp(jw_2 nT) \end{aligned} \quad \text{..(2)}$$

Thus,

$$\begin{aligned} R(0) &= P_1 + P_2 \\ R(T) &= P_1 \exp(jw_1 T) + P_2 \exp(jw_2 T) \\ R(2T) &= P_1 \exp(jw_1 2T) + P_2 \exp(jw_2 2T) \\ R(-T) &= [R(T)]^* \\ R(-2T) &= [R(2T)]^* \end{aligned} \quad \text{..(3)}$$

As shown by Pisarenko[5], when the signal has only two complex exponentials, the correlation lags should satisfy the following condition:

$$R(nT) + c_1 R((n-1)T) + c_2 R((n-2)T) = 0 \quad \text{..(4)}$$

where

$$\begin{aligned} c_1 &= - \exp(jw_1 T) - \exp(jw_2 T) \\ c_2 &= \exp(jw_1 T) \exp(jw_2 T) \end{aligned} \quad \text{..(5)}$$

and n is a real number.

In order to determine the two frequencies w_1 and w_2 we need to determine c_1 and c_2 . To determine c_1 and c_2 we may set up two equations as follows: Letting $n=1$ and $n=2$ respectively in Eqn. (4) we get the following two equations:

$$R(0) c_1 + R(-T) c_2 = - R(T) \quad \text{..(6)}$$

$$R(T) c_1 + R(0) c_2 = - R(2T) \quad \text{..(7)}$$

As we know the values of $R(0)$, $R(T)$, $R(-T)$, and $R(2T)$ as the outputs of the discriminators, we can determine c_1 and c_2 and hence the values of w_1 and w_2 . If no noise is present and if the correlation lags are determined without any error, the frequencies can be determined accurately. However, in any received signal there will be some noise and this will affect calculated values. If the noise is assumed to be white, then the error will be only in the zero lag term and a technique to avoid the zero lag term in setting up the above equations will be discussed in the next section. In addition to the noise in the received signal, other sources of error exist. In the discriminators, square law devices are used to carry out the multiplication. It is possible that deviations from square law response to be present in the diodes used for this purpose. Further sources of errors are phase shifters and calibration. As a result of these errors in correlation lags, the calculated frequencies will be in error. It will then be useful to determine the sensitivity of the frequencies to the various correlation lags. Hence in the following we derive expressions for the sensitivities of the frequencies with respect to the various correlation lags.

Procedure of Determining the Sensitivity

The relations of R to C and C to w are given by Equations (4,5). Using Equation (4) we find change in c as a result of change in R. Using Equation (5) we find change in w as a result of change in c. Then combining the above two equations we find expressions relating the change in w as a result of change in R. It is to be noted that R and c are complex quantities. The sensitivity expressions thus obtained are given next.

Notations

$$R(0) = R_0$$

$$R(T) = R_{1r} + j R_{1i}$$

$$R(2T) = R_{2r} + j R_{2i}$$

$$Q_1 = 4 w_1 P_1 \sin^2((w_1 - w_2)T/2)$$

$$Q_2 = 4 w_2 P_2 \sin^2((w_2 - w_1)T/2)$$

$$S_{\frac{w}{R}} = \frac{\Delta w/w}{\Delta R/R}$$

Sensitivity Functions For w_1 :

$$S_{\frac{w_1}{R_0}} = (P_1 + P_2) \sin((w_1 - w_2)T/2) / Q_1$$

$$S_{\frac{w_1}{R_{1r}}} = -(P_1 \cos(w_1 T) + P_2 \cos(w_2 T)) 2 \sin(w_1 T) / Q_1$$

$$S_{R_{11}}^{w_1} = (P_1 \sin(w_1 T) + P_2 \sin(w_2 T))(2 \cos(w_1 T) - 2 \sin(w_2 T))/Q_1$$

$$S_{R_{2r}}^{w_1} = (P_1 \cos(2w_1 T) + P_2 \cos(2w_2 T)) \sin(w_1 T + w_2 T)/Q_1$$

$$S_{R_{2i}}^{w_1} = -(P_1 \sin(2w_1 T) + P_2 \sin(2w_2 T)) \cos(w_1 T + w_2 T)/Q_1$$

Sensitivity functions for w_2 are obtained by interchanging 1 and 2 in the above expressions.

From the above expressions it may be noted that the sensitivity increases as the two frequencies become closer. These formulae clearly show that if two closely spaced frequencies are to be resolved accurately, then the correlation lags must be determined very accurately. Using these equations we can find the accuracy to which the correlation lags need to be determined for a desired accuracy of the frequencies and the desired range of frequencies.

V. Error Due To Noise And Techniques For Its Avoidance

As mentioned earlier, presence of white noise in the received signal contributes an error in the correlation value at zero lag as

$$R(0) = P_1 + P_2 + \text{noise power.} \quad \dots(8)$$

As pointed out earlier, an error in $R(0)$ will introduce an error in the calculated frequency. This has been observed by

previous researchers and some solutions were offered [5,6]. Pisarenko's suggestion involves the determination of noise power as the least eigenvalue of the correlation matrix and subtracting it from the $R(0)$ term. The determination of eigenvalues requires complicated arithmetical operations and hence is not attractive for realtime processing. Further, errors in the determination of the other correlation lags will give rise to erroneous noise power. Kay suggested two procedures. The first technique involves a trial and error approach for the determination of the noise power. This approach is not feasible for real time applications. In the second approach, the equations are set up by choosing a suitably larger value of n in Equation (4) such that $R(0)$ is avoided. For the two frequency case, for example, we may choose $n=3$ and $n=4$ as

$$R(2T) c_1 + R(T) c_2 = - R(3T) \quad \text{..(10)}$$

$$R(3T) c_1 + R(2T) c_2 = - R(4T) \quad \text{..(11)}$$

It may be noted that this formulation requires four lag values $R(T)$, $R(2T)$, $R(3T)$ and $R(4T)$ for setting up two equations for the solution of two frequencies. Thus, this technique requires more hardware and hence is not attractive.

An Alternative Formulation

In order to avoid the use $R(0)$, we suggest the use of $R(T/2)$ and $R(3T/2)$ as follows:

$$R(-T/2) c_1 + R(-3T/2) c_2 = - R(T/2) \quad \text{..(12)}$$

$$R(T/2) c_1 + R(-T/2) c_2 = - R(3T/2) \quad \text{..(13)}$$

This set of equations are valid because these are obtained by letting $n = 1/2$ and $n = 3/2$ respectively in Equation (4). Here we do not need $R(0)$ and further we need only two correlation lags. Further we may establish the following interesting property:

$$c_1 = \frac{-R(T/2)R(T/2) + R(3T/2)R(-3T/2)}{R(-T/2)R(-T/2) - R(T/2) R(-3T/2)} \quad \text{..(14)}$$

$$c_2 = \frac{-R(-T/2)R(3T/2) + R(T/2)R(T/2)}{R(-T/2)R(-T/2) - R(T/2)R(-3T/2)} \quad \text{..(15)}$$

As the numerator of c_2 is the complex conjugate of its denominator, the magnitude of c_2 is equal to unity. This ensures that the roots of the characteristic equation of the system producing the wave are on the unit circle thus giving rise to pure sinewaves rather than damped sinewaves.

VI. TESTS ON A DIGITAL RADAR DATA ACQUISITION SETUP

The last part of this summer's effort was concerned with the acquisition of the antenna signal in digital form and determining the spectrum of the wave using digital spectrum estimation techniques. In this project my graduate student participated heavily and he has included a detailed description of the arrangement, equipment used, the software

developed, and the results obtained in his report[7]. So in order to avoid duplication, only a very brief discussion is presented in this report.

As the frequency of an RF signal lies usually in the range of 2 GHz to 18 GHz, it is not possible to digitize the data using any presently available A/D converters directly. In the laboratory a Hewlett-Packard digital scope was available which could digitize a signal at 1 Ghz sampling rate. This scope used four A/D 8-bit flash converters in parallel each operating at 250 MHz. Therefore a down converter was used to bring down the frequency of the received signal to 0 to 250 MHz band. A H-P Micro-computer was used to initiate the tuning of the down converter, initiate the A/D conversion and transfer the data from the scope to the computer. The data received was then analysed using the periodogram spectral estimation procedure. The testing went on successfully and for the first time the actual signal emitted by a radar was available for analysis. For a more detailed discussion of the results one may refer to [7].

VII. RECOMMENDATIONS

The results of the research carried out during the summer were outlined in the previous sections. They have shown three potential areas for further research.

1. In Section IV error analysis was carried out on the Prony method for the two frequency case. In ESM applications, one is often interested in signals having more than two frequency components. Hence sensitivity studies for higher order Prony method need to be carried out.

2. In Section V a new formulation of the Prony equations without using $R(0)$ term was presented for the two frequency case. This may be extended to higher order cases. Further a sensitivity analysis of this formulation is warranted.

3. The setup for digital data acquisition discussed in Section VI has brought forth many research problems. First one may look into the development of a setup of digital signal processing hardware and signal processing algorithms such that the frequency and other parameter evaluations are carried out in real time. The applicability of the general signal processor developed recently by IBM for the Avionics Laboratory needs to be investigated. A second potential research area is the application of the actual data obtained using the digital data acquisition scheme to identify certain special characteristics of the emitters transmitting these signals. In other words, a pattern analysis scheme may be setup to fingerprint the emitters from the received data. This is a very important objective in ESM applications.

REFERENCES

1. Grant, P.M., and J.H. Collins, "Introduction to electronic warfare," IEE Proc., Vol. 129, Pt. F, No. 3, June 1982, pp. 113-132.
2. East, P.W., "Design techniques and performance of digital IFM," IEE Proc., Vol. 129, Pt. F, No. 3, June 1982, pp. 154-163.
3. Lee, J.P.Y., "Detection of complex and simultaneous signals using an instantaneous frequency measurement receiver," IEE Proc., Vol. 132, Pt. F, No. 4, July 1985, pp. 267-274.
4. Tsui, James B.Y., Digital microwave Receivers - Theory And Concept, Artech Publishing House, to be published.
5. Pisarenko, V.F., "The retrieval of harmonics from a covariance function," Geophys. J. Roy. Astron. Soc., Vol. 33, 1973, pp. 347-366.
6. Kay, Steven M., "Noise compensation for autoregressive spectral estimates," IEEE Trans. Acoust., Speech, Signal Processing, Vol. ASSP-28, No. 3, June 1980, pp. 292-303.
7. Grissom, Edward, "Acquisition of digital radar data for use on the improved ISPX Software", Summer Faculty Research Program/Graduate Student Research Program Final Report, 1988.

1988 USAF-UES SUMMER FACULTY RESEARCH PROGRAM

Sponsored by the

AIR FORCE OFFICE OF SCIENTIFIC RESEARCH

Conducted by the Universal Energy Systems, Inc.

FINAL REPORT

Prepared by: P.A. Ramamoorthy, Ph.D.

Academic Rank: Associate Professor

Department: Electrical and Computer Engineering

University: University of Cincinnati

Research Location: Wright Patterson Avionics Lab
Dayton, Ohio

USAF Monitor: Dr. Jim Tsui

Date: Sept. 15, 1988

Contract No: F49620-85-C-0013

NEURAL NETWORKS AND THEIR APPLICATIONS IN DIGITAL RECEIVER DESIGN

P.A. Ramamoorthy
University of Cincinnati,
Dept. of Electrical & Computer Engg., M.S.#30
Cincinnati, Ohio 45221
(513) 475 4247

October 4, 1988

Abstract

Recently there is tremendous interest in Artificial neural network models for applications such as pattern recognition and function minimization or optimization. These networks are modeled based on our present understanding of the biological nervous systems and seem to achieve good performance via dense interconnection of simple computation elements. In this report, we present a simple review of some neural network architectures, their potentials and problems. It has to be emphasized here that in most of the articles that are available in the open literature, neural networks are touted as solution or "cure-all" for all problems, without consideration to the real gains as compared to existing conventional techniques. Therefore, in this report we take a critical and hopefully unbiased look at the neural networks and point out what the real innovations or potentials are and where they are simply used to map known algorithms/techniques into network form (old wine in the new bottle syndrome). More importantly we discuss how neural networks can be applied to digital receiver design and arrive at some innovative approaches to solving that problem.

1 Introduction

Neural networks (or artificial neural networks) get their name from their resemblance to biological nervous systems where computations are carried out via dense interconnection of simple computational elements working in parallel. This is in contrast to Von-Neuman or stored program control computers (most computers in use today fall under this category) where the instructions are executed sequentially by a single, but much powerful, (central) processing unit. It is shown through few examples and claims have been made by interpolations or conjunctures that such a

Acknowledgements

I wish to thank the Air Force Systems Command and the Air Force Office of Scientific Research for sponsorship of this research. Universal Energy Systems must be mentioned for their concern and help to me and to my graduate students in all administrative and directional aspects of this program.

My experience was rewarding and enriching because of many different influences. Dr. Jim Tsui provided me with support, encouragement, and a truly enjoyable working atmosphere. He provided me an opportunity to learn some of the technical problems that need to be solved and study some innovative approaches in solving some of them.

I would like to acknowledge here the warm welcome provided by the various members of AFWAL/AAWP section.

parallel architecture is better than the current best systems and achieve performance comparable to human beings.

In this report we take a critical look at neural networks and describe some of the known models. The work here originated due to a desire to find new approaches to solving some of the problems in the receiver design for passive listening, which is one of the primary functions of the Electronic Warfare division, Air Force Avionics Laboratory, Wright-Patterson AFB. As we show in later sections, there seems to be some areas where neural networks can play an important role and offer solutions which are much better than existing techniques. Thus it is a more revolutionary than evolutionary design approach.

2 Neural Networks

In Figure 1, we illustrate the basic concept, that of a node, used in all types of neural networks. There we find N inputs that are weighted by N different weights, summed and passed through a non-linear function to produce an output. Thus, a neural network may be described in terms of the inputs (numbering N , which can be binary, or real or complex), outputs (same possibility as inputs), interconnections (mostly dense) from each input to each output and sometimes or in certain models feedback as well, the type of non-linearity being used, the weights and the way the weights are obtained. A neural network specialist, who has had training/career in neuro-physiology, etc., may describe such networks and their attributes using terminologies such as neuron, synapse, weight or efficacy, pre- and post-synaptic signals and levels of activity, lateral and conditional inhibition, firing of neurons, habituation and extinction, learning mechanism and learning rate and so on. Those who are trained in mathematics, computer science or electrical and computer engineering (as is the author) and specially the latter, may prefer to view them simply as non-linear networks with possible feedbacks that will produce some set of outputs (that are finite and reproducible) for a given set of inputs and initial conditions. Then, we may consider the problem of obtaining the weights of a neural network as similar to linear network design or approximation given the input/output (I/O) relationship. In the case of linear time-invariant networks, this I/O relationship is often best described in the frequency domain (transfer function, etc.). However, for non-linear neural networks, we cannot talk about transfer function, frequency response and so

on. Thus, the neural network design has to be carried out in the I/O domain. In contrast to earlier works in classical non-linear system or control design where researchers concentrated in mathematical means to describe/design such systems (and hence were limited to very simple systems because of the complexities involved) a different approach which the authors would term heuristic, has been taken by neural network researchers and such approach seems to have paid off. In this approach, basically a set of input patterns, the corresponding output patterns or sometimes a grading input or performance score (in lieu of output patterns) that tells how well the network is doing or no output patterns are used along with procedures similar to conjugate gradient approach to obtain the values of the weights in the network. This procedure is called training or learning and the three variations in the available data mentioned above lead to what are known as supervised training, graded training and unsupervised learning (or self-organization). If the training data are adequate (approaching a universal set), then the network should (hopefully) behave as anticipated for inputs not included in the training set. If the weights are changed or updated when the network is in use or operation, then the neural network may be considered to have continuous learning ability.

In the next few pages, we describe some of the specific neural network models, their capabilities and shortcomings. Since this portion is a review with a critical assessment of the potentials, we use materials/information from existing literature and references are made to such articles as appropriate. We first start with adaptive linear network example [1] Though it is not really a neural network, it is one of the original networks whose principles are used in neural network design and from our perspective it will be used to point out certain shortcomings or hurdles that we face (and we will face) in designing neural networks. Before we proceed further, we point out that linear adaptive networks are also called as adaptive linear neuron (ADALINE for short) and multiple or many ADALINES as MADALINES, though it is not clear whether the "neuron terminology" has been in use from the beginning or whether it is a recent phenomena.

2.1 Adaptive Linear Networks

The structure of an adaptive linear network is shown in Fig 2. Here, we assume that each input pattern consists of N elements (total of M patterns) and one desired output y (real valued, for input pattern and weights real) for each pattern. A varia-

tion of this network, which is quite commonly used in adaptive signal processing for adaptive equalizers for high-speed digital modems, adaptive echo cancelers for long distance telephone circuits and satellite channel is shown in Fig. 3 [2]. A common approach to obtain the weights (adaptation for electrical engineers and learning for neurophysiologist) is the least squares adaptation algorithm, also known as LMS algorithm. This algorithm based on a gradient approach minimizes the sum of the squares of the errors over the training set, where the error is defined as the difference between the desired response and the actual output. Denoting by $W_n = [w_{1n}, w_{2n}, \dots, w_{Nn}]$ the present value of the weight vector, X_n the present input vector, ϵ_n the present error (i.e., the difference between the desired response \hat{y}_n and the actual output y_n) and T for transpose of a vector or matrix, we have:

$$\epsilon_n = \hat{y}_n - y_n = \hat{y}_n - W_n^T X_n = \hat{y}_n - x_n^T W_n \quad (1)$$

$$\frac{\delta \epsilon_n^2}{\delta W_n} = -2\epsilon_n x_n \quad (2)$$

and the weights are modified as

$$W_{n+1} = W_n + k\epsilon_n x_n \quad (3)$$

where k is a positive constant. Equation (3) can also be written in a self-normalizing form as

$$W_{n+1} = W_n + \frac{\alpha}{\|x_n\|^2} \epsilon_n x_n \quad (4)$$

where α is another constant. It can be shown that for stability

$$2 > \alpha > 0$$

and

$$\delta \epsilon_n = \delta(y_n - W_n^T x_n) = -\alpha \epsilon_n \quad (5)$$

Therefore, the error is reduced by a factor α as the weights are adapted. Hence one will be tempted to use higher value for α (high learning rate) to make the convergence faster. However, even in the case of linear adaptive networks, (for example Fig. 3, for which case the error surface is quadratic or there is one and only one minima

that is global), higher α leads to oscillations. On the other hand, smaller α (slower learning rate) makes the convergence much slower and number of iterations needed for the convergence can be in the order of thousands and more. This problem is more severe in the case of neural networks as is illustrated by a simple Exclusive-OR network training shown in Fig. 4. Of course researchers are looking into new learning algorithms but we must remember that not much progress even for the simple linear adaptive filter case has been made after nearly a decade of research. Statements such as "the learning that we go through as human being is also a very slow process" are being made but it is a not solace for someone who wants things done or moving fast. Thus one has to be aware of the slow convergence and be prepared to scan through and experiment with available learning techniques. On the positive side, there are problems where training could be done off-line where excessing learning time may not be a problem if we gain in "on-line" performance.

2.2 Single-layer and Multi-layer Perceptron Networks

We now describe a network know as perceptron since it is one of the earlier Neural Network models. Also they seem to be suitable for digital receiver design problem as we show later. Fig. 1a with the hard-limiter is a simple example of this category where we have M inputs and 1 bipolar output (+1 or -1). Thus, this network can be thought of as a classifier network with output +1 corresponding to some class A and output -1 corresponding to some other class B, which are separated by a hyperplane defined by the weights $[w_0, w_1, \dots, w_{N-1}]$ (when $N=2$ this becomes a line and $N=3$ leads to a surface in the 3-D plane). Of course, we can add more nodes as shown in Fig 5a to group the inputs into more than 2 classes (the hard-limiter output will be 0 or 1 with one and only one output on for any set of inputs). In this Fig. we have one layer of inputs (that can take continuous or binary values), and one layer of outputs (derived from weighted sum of all input and thresholding). Such a network is also known as single layer perceptron which received good amount of attention in the 1960's. However, Minsky showed in 1968 [3] that single layer perceptron cannot learn even a simple EX-OR problem shown in Fig. 4. This made the interest in Neural Networks to wane away for a while. However, during early 1980's, it was realized that the short coming can be eliminated by going for what is known as multi-layer perceptron networks. Fig. 4 in fact shows a two layer network that could be trained on the EX-OR problem. In Fig. 5b we show a more general 3-layer network. It can

be shown that a 3-layer perceptron can form arbitrary complex decision regions to classify one class from another, though the mapping or training is not that simple (see [4] for further discussing).

Given a large I/O set corresponding to various classes, a multi-layer perceptron can be trained by a conjugate gradient approach similar to the LMS method discussed before. However, we run into problem since only the inputs and the outputs are known and we have no idea about the intermediate-layer (called hidden layer) outputs. Also, there is no mathematical approach to find exactly the number of nodes needed for each hidden layer. They have to be chosen by heuristics or trial and error. A commonly used method to train multi-layer perceptron networks is that of back-propagation of the outputs to the hidden layers so that the weights can be adjusted [5]. Hence, researchers tend to name multi-layer perceptrons as back-propagation networks which in the authors' opinion is a misnomer as the name refers to a training technique (which perhaps could be used for any other network as well).

We illustrate another important concept through Fig. 6. There we find a neural network with two inputs. However, by using specific operators such as squarer etc. we produce 3 more signals that along with the two original inputs form the 5 inputs of a single-layer, one node perceptron network. The boundary that could be obtained to distinguish between two different classes is shown in Fig. 6b and is elliptical [6]. This illustrates an important point that proper nonlinearities must be used in the network to arrive at an acceptable solution and thus requires some "domain-knowledge" about the problem to be solved. This observation should be contrasted with statements (from some neural-hardware marketeers) such as "any problem can be solved by throwing in few more neural networks; the network will learn by itself or the person training the Neural Network need not be knowledgeable in the particular application field".

In summary, perceptrons which are basically feed-forward networks could be used as classifiers with complex decision regions. They will be highly suitable in situations where all or at least most of the training could be completed off-line. In such a case, the parallel architecture will produce the classifier output in a very short time. Present wisdom in NN community is that the network could be realized as an analog network with all the nodes operating in parallel though it is not possible in foreseeable future to fabricate such an analog network. Thus we would like to quantify the complexity by the number of different operations needed, whether the

implementation is sequential or parallel, so that a meaningful comparison with other classification techniques can be made. It should be mentioned here that a three-layer network has been used by the authors to implement a medical diagnostic system (which otherwise would be implemented as an expert system in LISP) resulting in a tremendous improvement in speed [7].

2.3 Hopfield Network

The Hopfield network is a good example of a network that can be used as content addressable memory or associative memory (recall of a total pattern or information based on partial or noisy information) or to solve optimization problems [8]. The Hopfield net is normally used with binary (bipolar in actual implementation) inputs. It is a network with feedback, describable by the state-equation

$$\frac{d}{dt} \begin{bmatrix} x_1(t) \\ x_2(t) \\ \vdots \\ x_N(t) \end{bmatrix} = \begin{bmatrix} \cdot \\ \cdot \\ \cdot \\ \cdot \\ \cdot \end{bmatrix} W_{ij} \begin{bmatrix} \hat{x}_1(t) \\ \hat{x}_2(t) \\ \vdots \\ \hat{x}_N(t) \end{bmatrix} + \begin{bmatrix} I_1 \\ I_2 \\ \vdots \\ I_N \end{bmatrix} \quad (6)$$

$$\begin{bmatrix} \hat{x}_1(t) \\ \hat{x}_2(t) \\ \vdots \\ \hat{x}_N(t) \end{bmatrix} = f_h \begin{bmatrix} x_1(t) \\ x_2(t) \\ \vdots \\ x_N(t) \end{bmatrix} \quad (7)$$

where $X(t) = [x_1(t), x_2(t), \dots]^T$ is the output of the network at time t , I is the bias or input vector (could be impulsive, applied at $t=0$ and removed or constantly present), w_{ij} are the weights and f_h is a hard limiter. To be used as an associative memory, where we may like to store M patterns Y_j ($j=1$ to M), (each pattern is a vector consisting of N bipolar elements), we choose

$$\begin{aligned} I &= [0, 0, \dots, 0]^T \\ w_{ij} &= \begin{cases} \sum_{k=1}^M y_k^i y_k^j & i \neq j; 1 \leq i, j \leq N \\ 0 & i = j \end{cases} \\ X(0) &= Y_{in} \end{aligned} \quad (8)$$

where y_k^i is the i th element of pattern Y_k and Y_{in} is the input data used as a cue to the network. When the network converges, X represents the output of the CAM and

it will be one of the stored patterns (Y_j that are stored as w_{ij}) closest (in a Hamming distance sense) to the given input pattern.

Hopfield network used as CAM has major limitations. The number of stored vectors must be less than $0.15N$. Further it may converge to a spurious pattern. Also, it has been shown that instead of an iterative process as suggested above, the closest neighbor selection process could be completed in a single step involving matrix to vector multiplication and selection of the element having the minimum value in the resulting vector. The index of that element then gives the closest store vector [9]. Thus even though the Hopfield net has been used for optimization (function minimization) problems [10], it is not very clear whether there is any real gain from the use of this particular network as compared to other classical techniques.

It can be shown that the Hopfield net minimizes an energy function (it reaches a local minima)

$$E = -\frac{1}{2} \sum_{i=1}^N \sum_{j=1}^N w_{ij} x_i x_j - \sum_{i=1}^N x_i I_i \quad (9)$$

it is possible to achieve global minimum by combining simulated canceling approach with the Hopfield net [11].

2.4 Cohen-Grossberg family of models

We next describe a general class of neural networks of which Hopfield model is a special case. These class of networks can be described by a set of dynamic equations given by

$$\frac{dx(t)}{dt} = -A(t)x(t) + Bg[x(t)] + I \quad (10)$$

where $x(t) = [x_1(t), x_2(t), \dots, x_N(t)]^B$, $A(t)$ & B are $N \times N$ matrices, $I = [I_1, I_2, \dots, I_N]^T$ is a constant (or impulsive) external input to the network and $g[x(t)] = [g_1(x_1(t)), g_2(x_2(t)), \dots, g_N(x_N(t))]^T$ with $g_i(t)$, a differentiable function. Though, we can talk of $x_n(t)$ as mean some potential of the i th neuron etc., from an electrical engineering perspective, we have a nonlinear network described by a state-space model. Though equation 10 describes a general time-varying nonlinear net, neural network researchers have considered certain special cases of the above equation, perhaps to make the network manageable (from the stability point of view). For example Allon Guez et al [12, 13] have considered the model where A is a diagonal matrix with a_i (i th diagonal entry) positive and show that such a model will be asymptotically stable for

$x = x^e \in R^N$ iff

$$Ax^e - Bg(x^e) = I \quad (11)$$

$$K_i \doteq B_{ii} \left[\frac{\delta g_i(x_i)}{\delta x_i} \right]_{x_i=x_i^e} - a_i < 0 ; i = 1, 2, \dots, N \quad (12)$$

$$\sum_{j=1, j \neq i}^N \left| \left[T_{ij} \frac{\delta g_j(x_j)}{\delta x_j} \right]_{x_j=x_j^e} \right| - |K_i| < 0 \quad (13)$$

Earlier, Grossberg proposed a much simpler version of (10) called avalanche model [14, 15] governed by the following equations :

$$\frac{dx_i}{dt} = C \left(-ax_i + b [I_i^1 + I_i^2 - T]^+ \right) ; a, b > 0 \quad (14)$$

where

$$I_i^1 = \sum_{j=1}^N w_{ij} x_j = w_i x ; I_i^2 = \sum_{j=1}^N z_{ij} I_j = z_i I$$

$$C(u) = \begin{cases} u & \text{if } u > 0 \\ cu & \text{if } u \leq 0 \end{cases} \quad 0 < c < 1 \quad (15)$$

$$[u]^+ = \begin{cases} u & \text{if } u > 0 \\ 0 & \text{if } u \leq 0 \end{cases}$$

$$w_{ii} = 0 ; 0 \leq w_{ij} \leq 1$$

$$\frac{dT}{dt} = \alpha (S - T) + \beta \frac{dS}{dt} ; s = \sum_{i=1}^N x_i$$

If one looks carefully at these equations, especially the non-linearity used, and the restrictions on the coefficients, it becomes clear that they have been arrived so as to make the network stable, perhaps from the physical considerations (such as neural output should decay to zero or reach a stable saturation level or so on). As stated before Hopfield net is a special case of (10) where $A \equiv 0$ $B_{ii} = 0$, $B_{ij} = w_{ij}$.

From our perspective, Grossberg family of models can serve as an associative memory with information stored in the many local minima (or stable equilibrium points x^e) of the system. To properly use such systems, we then need to define the number of equilibria points ($x_1^e, x_2^e, \dots, x_M^e$ capacity) and determine whether a solution

for A & B to satisfy (11) to (13) can be obtained (which itself is not guaranteed). If a solution is possible, we also have to make sure that there are no other equilibria points than the ones prescribed. If these conditions are satisfied, we may apply the given input as I to the network and let it come to a stable point corresponding to the information we are seeking.

3 Digital Receiver Design

In this section, we discuss the possible application of neural networks to digital RF receiver design. We start with a definition of the RF receiver.

3.1 Problem Definition

In the RF receiver for the passive listening, the electro-magnetic spectrum is scanned to identify signals that may be present. These signals (assumed to be a maximum of four) may be continuous wave signals or gated (pulse) CW signals or other variations (chirp signal etc.). The job of the receiver is to accept these signals as inputs and produce as output (in real-time) data corresponding to: 1) the number of independent signals, 2) the amplitude of each signal, 3) the frequency, 4) the time of arrival, 5) the time duration and 6) angle of arrival. It has to be noted that the received signal will invariably contain noise (most frequently used model: additive white Gaussian model) and the estimator has to be as robust as possible.

There are different techniques to find the 6 parameters listed above. For example, the number, frequency and amplitude can be estimated using spectral estimation (hence most of the recent high resolution spectral estimation techniques based on limited data can be applied). The angle of arrival can be estimated using (a minimum) of two sensors and methods similar to spectral estimation applied to spatial data. The time of arrival and the time duration can be estimated using techniques suitable for time-varying signal analysis such as Wigner distribution.

The estimation of the 6 parameters can be carried out using analog implementation or digital implementation. Though digital implementation can be more robust, high speed components (such as A/D converters) necessary to process such high speed signals are not available. A clever scheme based on residue number system [16] has been proposed to find one frequency [17]. The multiple frequency case can be implemented using redundant residue number scheme and neural networks. In the

following sections, we describe in some detail how neural networks can be applied to various problems.

3.2 Neural Net in the Pairing Problem

Consider a single frequency f , which has been measured by two IFM correlators with delay times τ_1, τ_2 where

$$F_1 = \frac{1}{\tau_1} \text{ and } F_2 = \frac{2}{\tau_2} \quad (16)$$

are prime to each other and can be less than f . Let the two correlator outputs be α_1 and α_2 respectively where

$$\alpha_i = [f]_{\text{mod } F_i}; \quad i = 1, 2 \quad (17)$$

where mod stands for modulo or residue (remainder) of f with respect to F_i . This relationship can also be written as

$$f = \alpha_1 + k_1 F_1 = \alpha_2 + k_2 F_2 \quad (18)$$

where K_1 and K_2 are two (unknown) integers and given α_1, α_2 , possibly with some error, we would like to find f ($0 \leq f \leq F_1 F_2$). The well known procedure is to use more correlators (F_3, F_4, F_5) where the extra information will be used not to increase the measurement range but to provide capability to detect or correct errors. A different approach is used by W.S. McCormick et al [17] by choosing F_1 where the choice of $F_1 = (4q + 1)p_1$, $F_2 = (4q + 1)p_2$ (p_1 and p_2 are relative prime) is made so that any errors in α_1, α_2 of magnitude of q or less can be corrected. The frequency measurement range F_r is given by

$$F_r = (4q + 1)p_1 p_2 = \frac{F_1 F_2}{4q + 1} \quad (19)$$

instead of $F_1 F_2$ if F_1 and F_2 were relatively prime. Given α_1 and α_2 , k_1 and k_2 hence f is obtained by solving for unique k_1, k_2 that satisfies

$$|(\alpha_1 - \alpha_2) + (k_1 F_1 - k_2 F_2)| < 2q + 1 \quad (20)$$

If we have three IFM correlators, it will lead to two inequalities similar to the one given above and for N IFM correlators, $N-1$ inequalities. In ref [17], the authors suggest that these inequalities can be solved by exhaustive search or table look up. For example, in the two variable case, assuming $q=1$, $F_1 = 10$, ($p_1 = 2$), $F_2 =$

15, ($p_2 = 3$) and $F_r = 30$, for a given α_1, α_2 inequality (20) has to be tested for $0 \leq k_1 < p_2$ and $0 \leq k_2 < p_1$ to find the unique value of k_1, k_2 . This leads to a sequential process requiring $p_1 p_2$ multiplications and equal number of additions, subtractions and comparisons or a parallel ROM based approach would require 1k-bit of memory. A one-hidden layer perceptron that can do this job is shown in Fig. 7. An analog network can be used for actual implementation of this perceptron network leading to a parallel implementation. This simple example illustrates the application of one-layer perceptron.

3.3 High Resolution Beamforming & AoA Estimation using two sensors

Here we outline the use of neural networks for high resolution beamforming/AoA estimation using only two sensors. In regular weighted sum beam forming, two sensors give us one degree of freedom (DoF) which can be used to null or cancel one interference and at the same time preserve the gain in the look direction. Since we use a linear network the DoF cannot be increased unless we increase the number of sensors involved. However, by using a non-linear neural network such as a perceptron, for a given number of sensors, we can obtain more DoF by simply increasing the number of internal nodes and training the network properly. Because of the non-linearities present in the network, we cannot reduce it to an equivalent network with less DoF as will be the case with linear beamforming network. A similar argument can be made for the AoA estimation, where a 2 input (2 sensors), large number of hidden layer nodes and 180 output node (to cover 180° AoA with a resolution of 1°) perceptron network can be trained to identify the direction of arrival. Such a network may also indicate the existence of more than one signal. Both concepts are illustrated in Fig 8. This will be an interesting problem from the EW division viewpoint since we can obtain good resolution using just two sensors. The tasks to be looked into are: how to train such networks, the numbers of internal nodes needed and how to make the network adaptive. All these problems will be studied through Research Initiation Program.

3.4 Perceptron/Grossberg Network in Frequency Estimation

A perceptron network could be trained to identify the frequencies of signals that may be present in a given signal. Parameters that have to be chosen properly are: the number of inputs, the number of hidden layer and output nodes, the time-

averaging on input distances (or window size), the type of non-linearity to be used and so on. This will make an interesting problem, since it can make use of the data (obtained through non-linearity transformation) that we may not have used before.

A perceptron network may be provide better performance as compared to Prony's method in noisy situations. Letting y_n ($n=0$ to $N-1$) be the actual measured data, x_n the weighted sum of a complex exponentials and e_n the additive white noise, the Prony algorithm calculates the coefficients of a polynomial $A(z) = \sum_{i=0}^p a_i z^{p-i}$, ($a_0 = 1$) (whose roots are complex frequencies) by minimizing

$$\sum_{n=p}^{N-1} \epsilon_n^2 \quad (21)$$

where

$$\epsilon_n = \sum_{m=0}^p a_m e_{n-m}; \quad n = p, \dots, N-1 \quad (22)$$

instead of $\sum \epsilon_n^2$, since it leads to a difficult non-linear least squares problem. However, since a neural network that will be trained before-hand with synthetic data, it is possible to train it to minimize $\sum_{n=p}^{N-1} \epsilon_n^2$. Thus we may be able to avoid the problems associated with Prony method. Of course, this has to be shown through extensive simulations.

Grossberg network also seems to ideal for frequency estimation as it appears we can map the frequency range and resolution needed ($f_k = \frac{2\pi}{N} \cdot k$; $k=0$ to $N-1$) by choosing the matrices A, B, I (Equations 10 to 13) and the non-linear mapping properly to provide the N.M (M= number of different sinusoids) stable solutions needed without making the size of the matrices very large. We feel that we can restrict the size of the matrices to be $M \times M$ and let the non-linear mapping provide the resolution needed. Thus a small network might be able to do the job. It remains to be seen it can be achieved. The question of "how to start the network" using collected sensory data also has to be addressed as part of the design.

3.5 Neural Nets in Pisarenko Harmonic Decomposition(PHD)

In PHD, given a noisy process, as

$$y_n = x_n + e_n = - \sum_{m=1}^{2p} a_m x_{n-m} + e_n \quad (23)$$

where p denotes the number (unknown) of sinusoids present and a_n is related to the frequencies of the sinusoids, we obtain the value of p by solving for the smallest eigenvalue and its associated vector of

$$R_{yy,m} = \sigma_{e,m}^2 A_m \quad (24)$$

where

$$R_{yy,m} = \begin{bmatrix} R_{yy}(0) & R_{yy}(-1) & \dots & y_{yy}(-2m) \\ R_{yy}(1) & - & & \\ \vdots & - & & \\ \vdots & - & & \\ \vdots & - & & R_{yy}(0) \end{bmatrix} \quad (25)$$

For $m = 0, 1, 2$ etc., until $\sigma_{e,m}^2 = \sigma_{e,m+1}^2$. The value of m thus obtained gives p , the number of sinusoids present and also σ_e^2 , the variance of the noise signal e_n . Thus the procedure is by definition a recursive procedure. It appears we may be able to train a neural network (Fig. 5b) that will output σ_e^2 as well as a_m ($m = 1$ to p). Such a network can be trained to provide the correct order or their corresponding coefficients or directly the frequency values. To make this network work, one needs to study the types of non-linearities needed and so on.

4 Conclusion

A review of neural networks from the Electrical Engg. view point is given in this paper. We have taken a balanced view to highlight the potentials and drawbacks of such networks. We also point out how these networks can be used in the RF receiver design. The methods suggested seem to be superior to existing classical techniques and hence merit further investigation.

References

- [1] B. Widrow and M.E. Hoff, Jr., "Adaptive Switching Circuits", in the IRE WESCON Conv. Rec. pt. 4, 1960, pp. 96-104
- [2] B. Widrow and S. D. Stearns, *Adaptive Signal Processing* Englewood Cliffs, NJ; Prentice-Hall, 1985
- [3] M. L. Minsky and S.A. Papert, *Perceptrons*, The M.I.T. Press, 1969.
- [4] R.P. Lippman, "An Introduction to Computing With Neural Nets," IEEE ASSP Magazine, pp. 4-22, April 1987.

- [5] D.E. Rumelhart, G.E. Hinton, and R.J. Williams, "Learning Internal Representations by Error Propagation," in D.E. Rumelhart and J.L. McClelland (Eds.), *Parallel Distributed Processing: Explorations in the Microstructure of Cognition. Vol. 1: Foundations*. M.I.T. Press, 1986.
- [6] B. Widrow, R.G. Winter and R.A. Baxter, "Layered Neural Nets for Pattern Recognition," *IEEE Trans. ASSP*, Vol. 36, No. 7, pp 1109-1119, July 1988.
- [7] T.P. Kudrycki, "Neural Network Implementation of a Medical Diagnosis Expert System," Master of Science thesis, University of Cincinnati, Sept. 1988.
- [8] J.J. Hopfield, "Neural Networks and Physical Systems with Emergent Collective Computational Abilities," *Proc. Natl. Acad. Sci. U.S.A.*, Vol. 79, pp. 2554-2558, April 1982.
- [9] B.L. Montgomery and B.V.K. Vijaya Kumar, "Evaluation of the Use of Hopfield Neural Network model as a Nearest-Neighbor algorithm," *Applied Optics* Vol. 25, No. 20, pp. 3759-3766, 15 October 1986.
- [10] M. Takeda and J.W. Goodman, "Neural Networks for Computation: Number Representations and Programming Complexity," *Applied Optics*, Vol. 25, No. 18, pp. 3033-3046, 15 Sept. 1986.
- [11] B.C. Levy and M.D. Adams, "Global Optimization with Stochastic Neural Networks," *IEEE First Intl. Conf. on Neural Networks*, San Diego, CA, June 21-24, 1987.
- [12] A.Guez, J.L. Elbert and M. Kam, "Neural Network Architecture for Control," *IEEE Control Systems Magazine*, pp. 22-25, April 1988.
- [13] A. Guez, V. Protopopescu, and J. Barhen, "On the Stability, Storage Capacity and Design of Nonlinear Continuous Neural Networks," *IEEE Trans. Systems, Man and Cybernetics*, Vol. 18, No. 1, pp. 80-87, Jan./Feb. 1988.
- [14] S. Grossberg, "Embedding Fields: Underlying Philosophy, Mathematics and applications to Psychology, Physiology and Autonomy," *J. Cybern.* Vol. 1, No. 28, 1971.
- [15] R. Hecht-Nielsen, "Nearest Match Filter Classification of Spatiotemporal Patterns," *Applied Optics*, Vol. 26, No. 10, pp. 1892-1899, 15 May 1987.
- [16] F.J. Taylor, "Residue Arithmetic: A tutorial with example," *IEEE Computer Magazine*, April 1984.
- [17] W.S. McCormick, J.B.Y. Tsui and V.L. Banne, "A noise Insensitive Solution to a Simultaneous Congruence Problem in real-time Spectral Estimation," to be published.

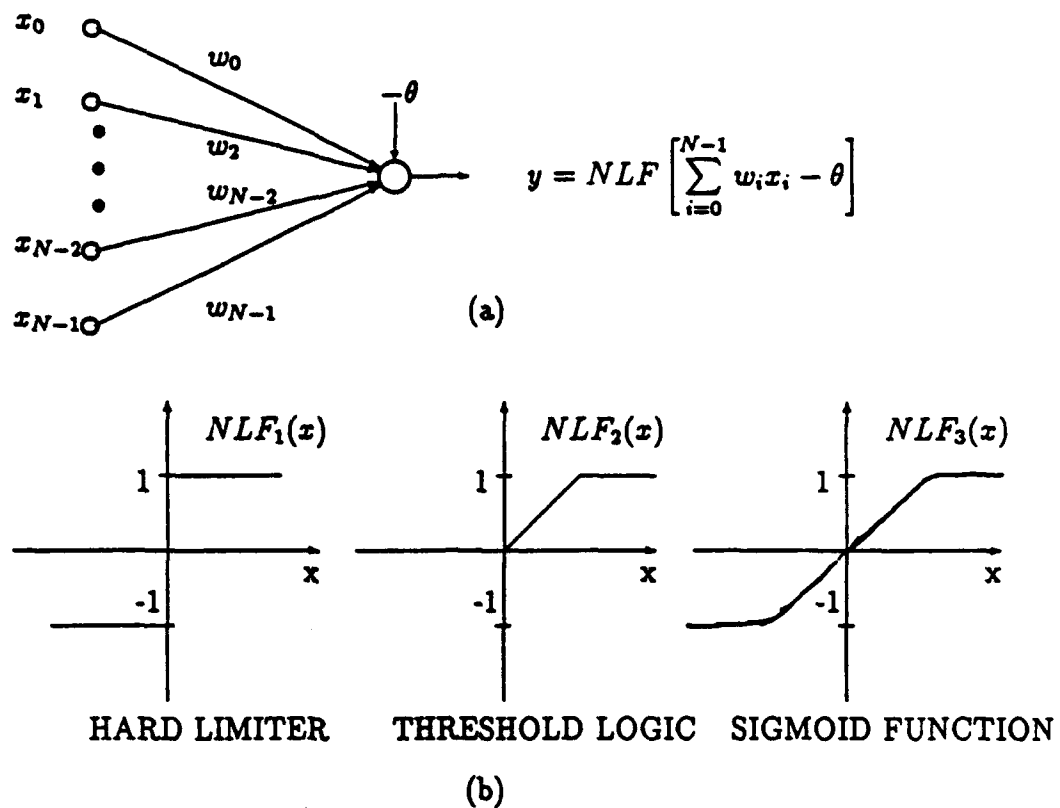


Fig. 1 a) One general node or computational element of a neural network
b) Three different nonlinearities.

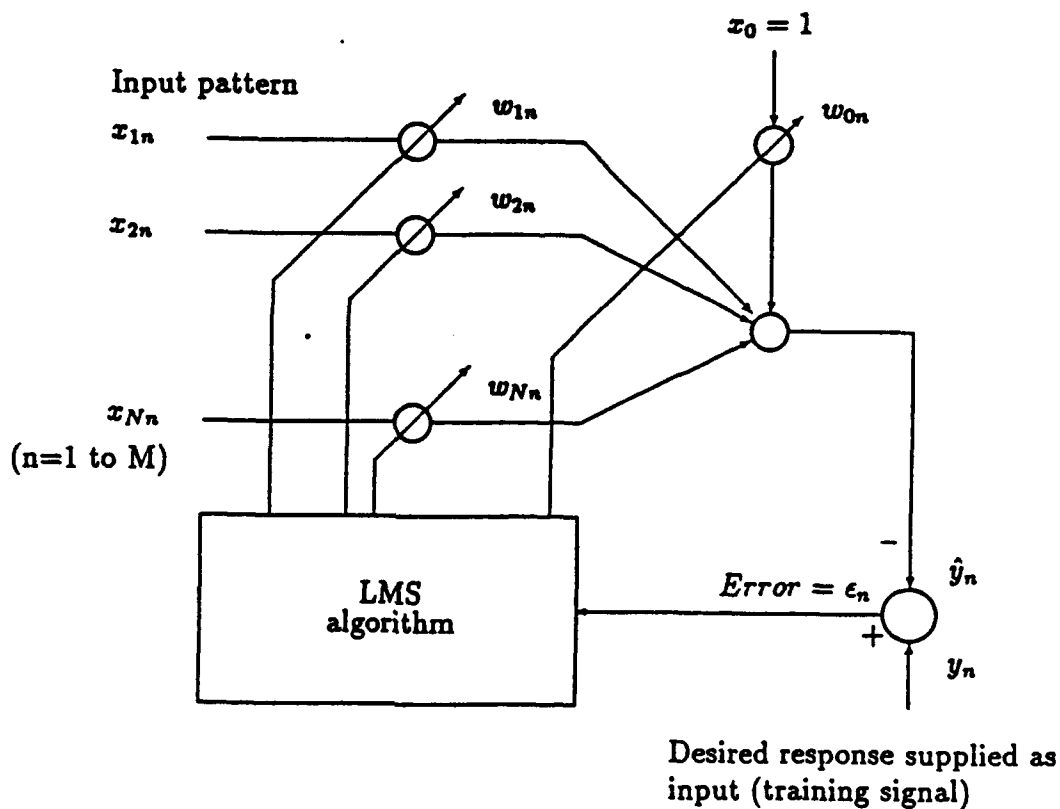


Fig. 2 An adaptive linear network based on LMS algorithm for adaptation of weights

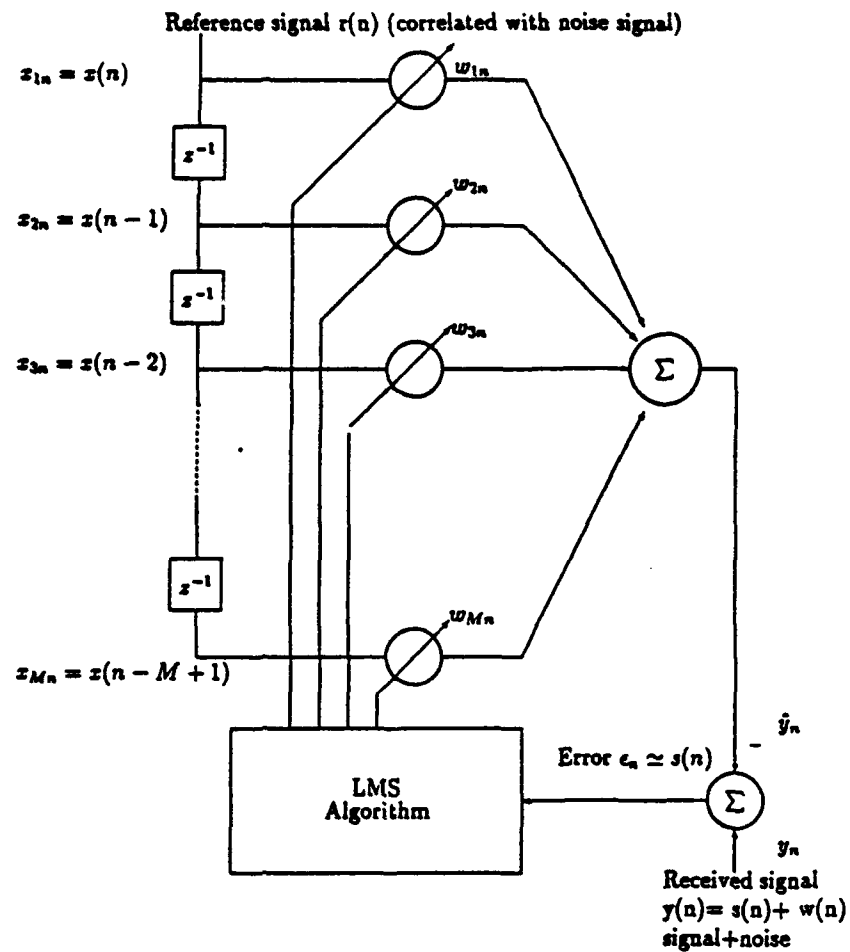
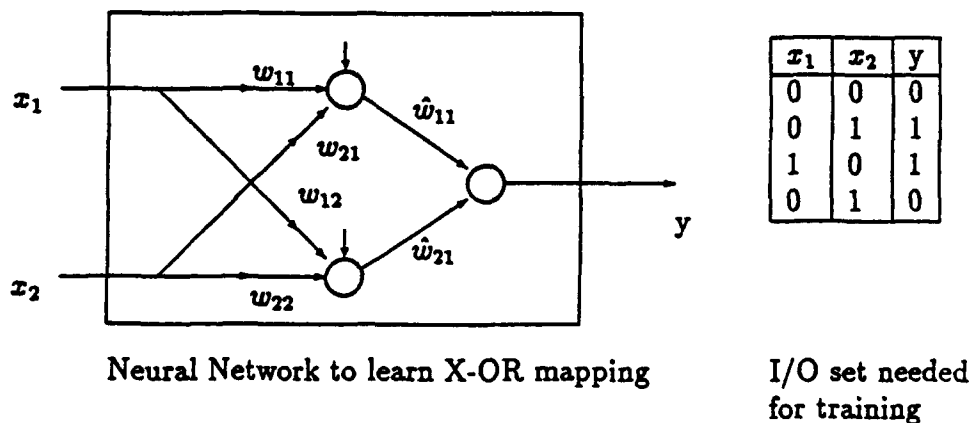


Fig. 3 An adaptive signal processing network configured as noise canceller



Neural Network to learn X-OR mapping

I/O set needed for training

Fig. 4 A simple neural net to learn X-OR mapping. Even for such a small problem (2 input variables, 1 output variables all binary and only 4 set of I/O), 1000's of repeated applications and adjustment is needed.

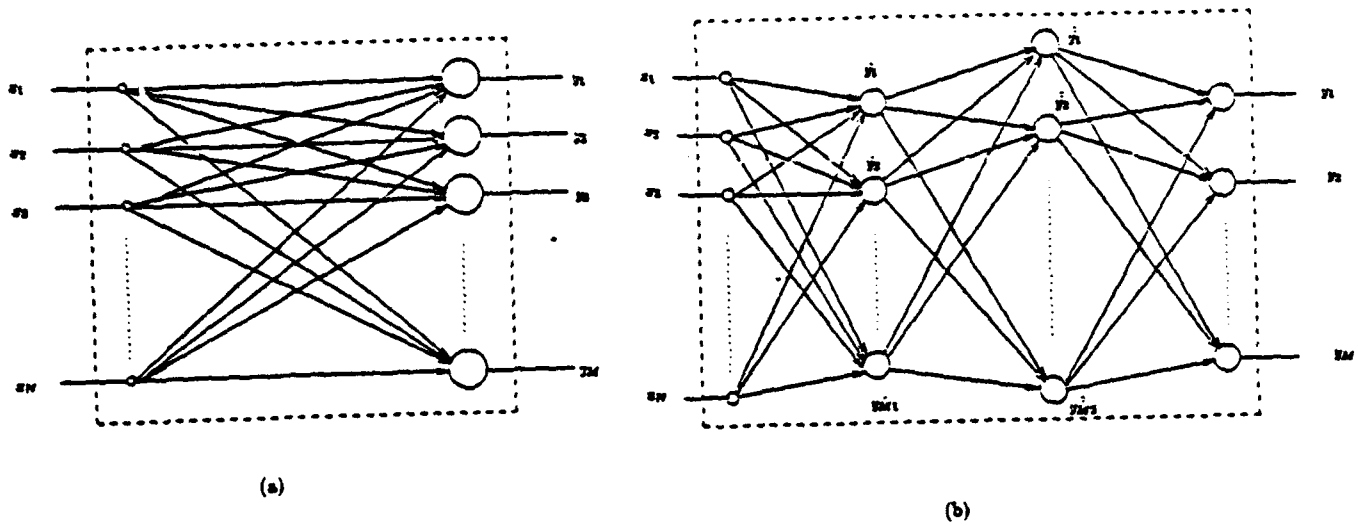


Fig. 5 (a) Single-layer perceptron neural network
(b) Three-layer perceptron neural network

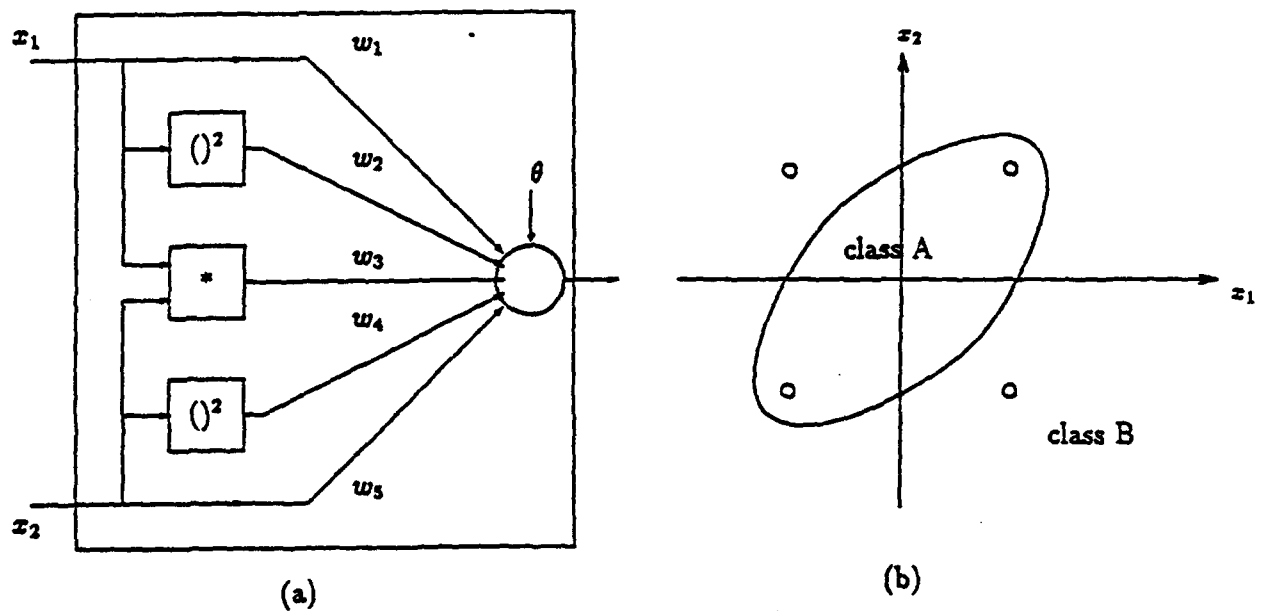


Fig. 6 (a) A neuron with inputs mapped through nonlinearities
(b) The resulting elliptical boundary for classification

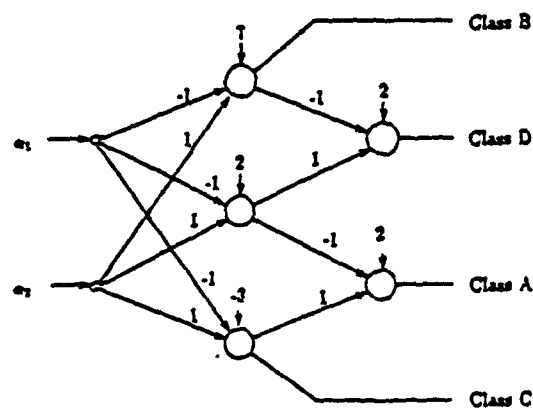


Fig. 7 Perceptrons for parallel implementation of equation (20)

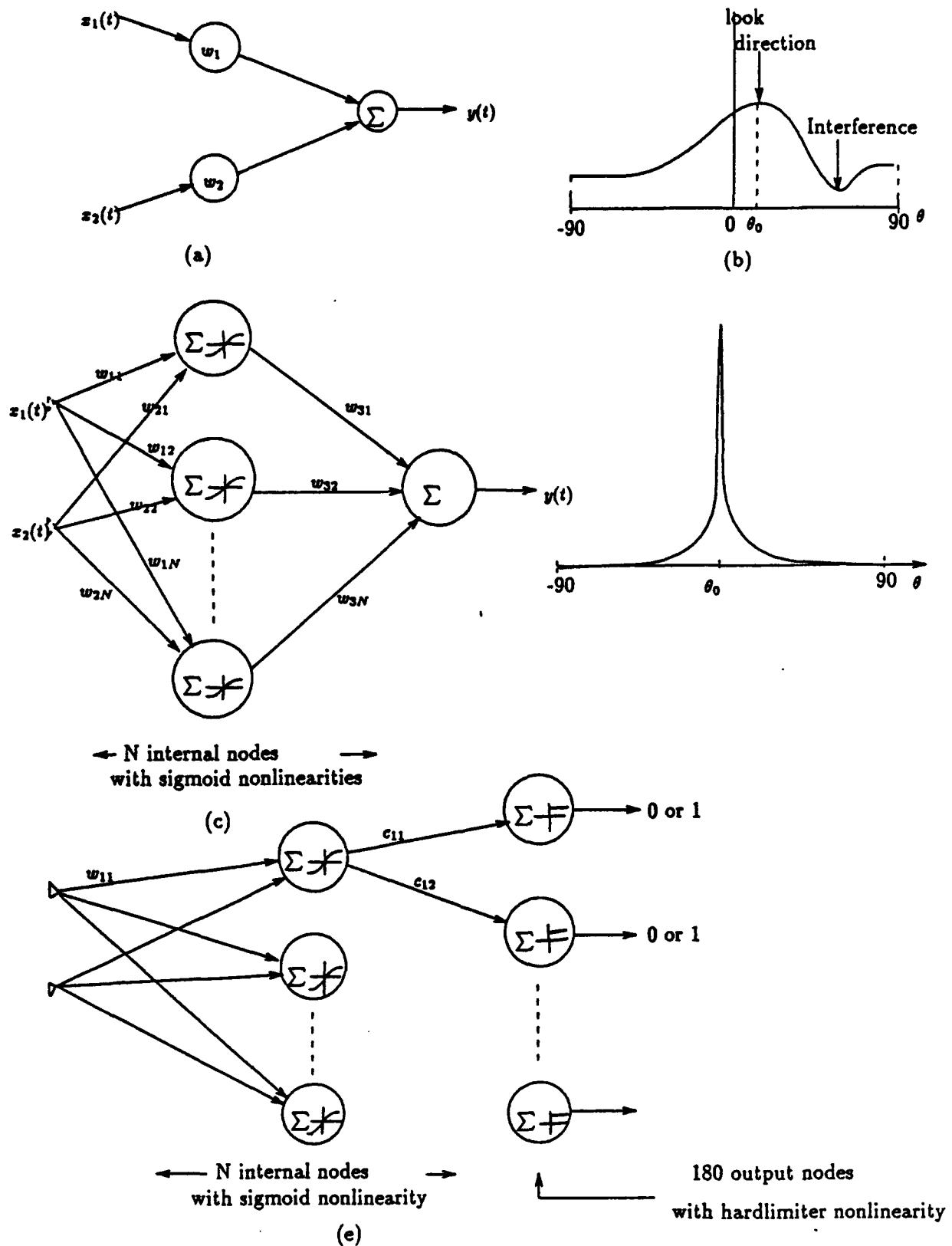


Fig. 8 Use of Neural nets in beamforming and AoA estimation. (a) Linear beamforming network using 2 sensors. (b) Its spatial response. (c),(d) BFN using NN concepts, and (e) AoA estimation using neural networks.

1988 USAF-UES SUMMER FACULTY RESEARCH PROGRAM /
GRADUATE STUDENT SUMMER SUPPORT PROGRAM

Sponsored by the
AIR FORCE OFFICE OF SCIENTIFIC RESEARCH

Conducted by the
Universal Energy Systems, Inc.

FINAL REPORT

APPLICATIONS OF EVOLUTIONARY LEARNING STRATEGIES
TO PATTERN RECOGNITION TASKS

Prepared by: Mateen M. Rizki, Ph.D.
Louis A. Tamburino, Ph.D.
William VanValkenburgh
and Michael Zmuda

Academic Rank: Assistant Professor

Department and Computer Science Department

University: Wright State University

Research Location: AFWAL/AAAT-3
Wright-Patterson AFB
Dayton, Ohio 45433

USAF Researcher: Louis Tamburino, Ph.D.

Date: August 24, 1988

Contract No.: F49620-87-R-0004

APPLICATIONS OF EVOLUTIONARY LEARNING STRATEGIES

TO PATTERN RECOGNITION TASKS

by

Mateen M. Rizki
Louis A. Tamburino
William VanValkenburgh
Michael Zmuda

ABSTRACT

A software environment was developed to study learning strategies applied to tasks in image processing. This environment facilitates the systematic exploration of evolutionary learning processes and embedded adaptive control mechanisms that modify both feature extraction and image classification tasks. The feature detectors were constructed as Hit or Miss templates based on principles of mathematical morphology. This representation provided a suitable substrate for the gradual changes introduced by evolutionary learning algorithms. The software package was used to conduct experiments on a two-class character recognition problem. These preliminary experiments illustrate the importance of incorporating adaptive learning mechanisms in image processing systems.

ACKNOWLEDGEMENTS

I would like to thank the Air Force Systems Command and the Air Force Office of Science Research for the opportunity to participate in a research project at Wright-Patterson Air Force Base. I am also grateful to Universal Energy Systems for their efficient administration of my Fellowship at the Air Force Base.

I especially appreciate the efforts of Dr. Louis Tamburino who accepted my collaboration in his Image Calculus Research Program and provided a stimulating research environment for this study. I am also thankful to Richard Jones and Edward Gliatti for their help with many aspects of this research effort.

I. INTRODUCTION:

The Advanced Systems Research Group in the Avionics Laboratory at Wright-Patterson Air Force Base has initiated the Image Calculus Program to design software systems capable of learning effective search strategies. The focus of this multi-year project is the application of learning strategies to problems in image processing and pattern recognition. The ultimate goal of this program is to develop a software environment that automates the process of engineering models of complex search spaces.

My research interests involve the application of evolutionary processes to problem solving. I have experience in software design and testing, including the development of a software environment for exploring evolutionary processes. This work incorporates genetic algorithms to model multiple layers of biological organization. My assignment as a Summer Fellow was based on my knowledge of the operation of genetic algorithms embedded in evolutionary systems and the applications of these genetic algorithms to search strategies.

The graduate student from Wright State University selected to participate in this project, Mr. Michael Zmuda, has experience with software development and interactive graphics.

II. OBJECTIVES OF THE RESEARCH EFFORT:

The Image Calculus Program was conceived as a bridge between conventional image processing techniques and rigid artificial intelligence approaches to problem solving. Using adaptive control coupled with evolutionary learning strategies, image processing primitives can be developed that perform both feature extraction and image classification tasks.

In discussions with Dr. Tamburino, USAF Researcher, I agreed to collaborate on the design and implementation of a prototype software tool to investigate the automatic generation of Hit or Miss templates for recognition of binary images using evolutionary learning techniques. This tool was designed in a modular fashion to facilitate upgrades and enhancements that will be required as the Image Calculus Program progresses.

Realizing that the scope of this project exceeded the allotted ten weeks of my stay at the Air Force Base, we decided to lay the software foundation for the first learning experiments in the Image Calculus Program. The goal for the ten-week period was to formulate a collection of specific modules including an image management data base, an interactive image editing tool, a skeleton model for learning, a dynamic trace facility for the model, and a basic analysis package.

Recently, an Adaptive Vision Technology Laboratory has been opened at

Wright State University in anticipation of the continued collaboration between myself and Dr. Tamburino. Funding from the Mini Grant Program will be used to conduct additional learning experiments and enhance the software modules. The long-range goal is to define a learning system capable of manipulating 512 x 512 gray level images.

III. DESCRIPTION OF RESEARCH ACCOMPLISHMENTS:

An overview of the Image Calculus Program is given in Figure 1. The package forms a closed loop learning environment consisting of a classical pattern recognition system that detects features in images and then assigns each image to a specific class. The novel elements of this approach are the learning and evaluation subsystems that dynamically train the pattern recognition system to perform the assigned classification task.

The feature detector subsystem is based on principles of mathematical morphology (Serra, 1982). In our prototype system, morphological analysis is limited to erosion operations that utilize structuring elements to evaluate binary images. Image erosion is the systematic removal of points from the input image as it is compared to the structuring element, or second image. The structuring element is a collection of points that serves as a template that is translated across

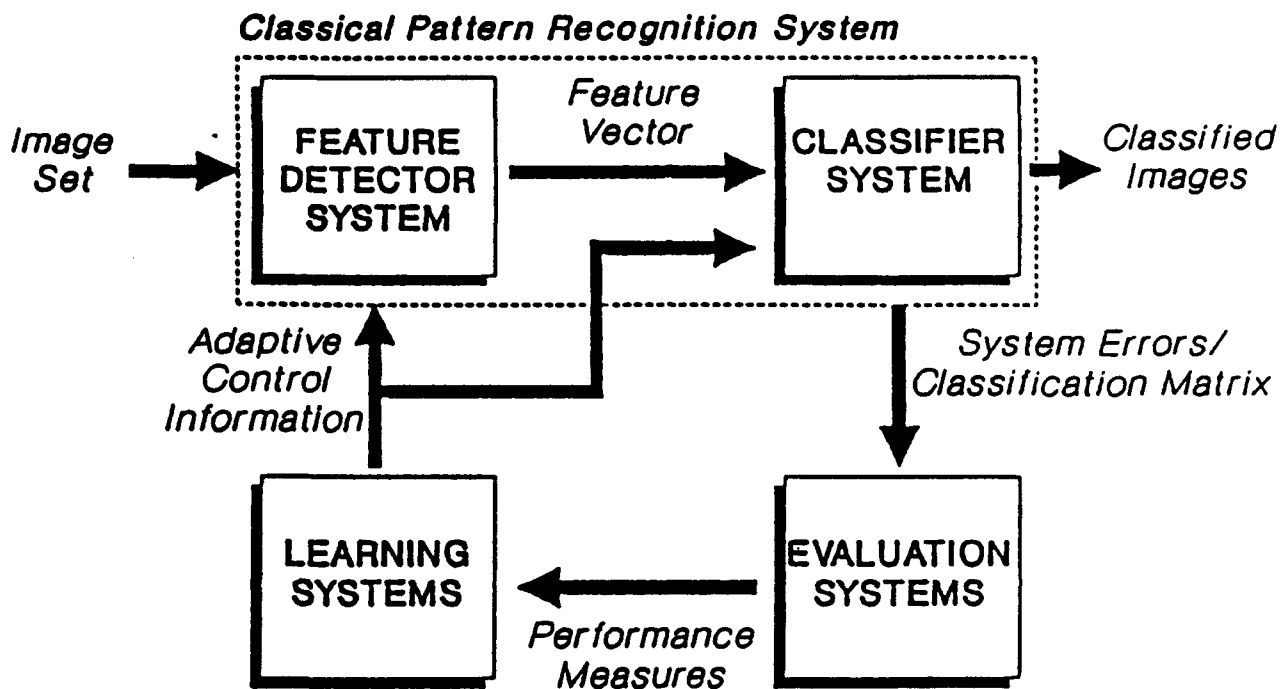


Figure 1. Major components of the Image Calculus Program that form the basis of a closed loop learning environment. Diagram modified from the Image Calculus Program of Dr. Louis Tamburino.

the surface of the input image. Each coincidence between the template and the image is marked as a single point in a third, or resultant, image. The marked point is a distinguished point in the structuring element, and the ultimate result of eroding an image by a specific structuring element is the production of a smaller collection of points in a resultant image. If a detector defined by a structuring element produces a non-null resultant image after an erosion, then the input image contains the feature embodied by the detector. When a structuring element is applied to a set of input images, the collection of binary responses forms a feature vector that is fed to the classification system.

Since our preliminary experiments were limited to two-class identification problems, it was not necessary to develop software for the classification system at this stage. When the system is expanded to handle multi-class problems, it will be necessary to implement a classification subsystem that identifies specific image classes. We propose to use a neural network that will weight the response vectors of a population of detectors to perform this function.

The learning and evaluation subsystems in our first series of experiments concentrated on mechanisms for developing structuring elements capable of discriminating among uppercase letters of the English alphabet. The overall approach to finding a structuring element that discriminates a single class of letters from all others is based on an evolutionary learning process. For example, to discriminate the

letter A from the letters B-Z, a candidate structuring element was generated, and if the structuring element detected all the A's in the training set, it was considered a viable element. The performance rating of each viable element was inversely proportional to its responses to the letters B-Z. The top performers were maintained in a rank-ordered set that could be used to form logical composites. If two members of the set produce errors on different images, then the logical AND of their response vectors can be formed to eliminate the errors.

A guided random search strategy was employed to produce structuring elements. This process consisted of generating random points to add to a structuring element. As each point was generated, a local evaluation was used to identify non-viable points. After a predetermined number of points were tested, the generated structuring element was compared to the population of top performers. If the new structuring element's performance surpassed the performance of the individual with the minimum performance in the population, the worst performer was discarded.

Our preliminary results showed that generating Hit or Miss templates for character recognition is easily handled by our system when the number of classes is small. As the number of classes increases, class interference grows rapidly and greatly increases the difficulty of the classification problem. We noted that image detection using only foreground points is too restrictive so background points were also included in the structuring elements.

There is a tradeoff between employing structuring elements capable of extremely fine levels of discrimination and structuring elements that embody broad characteristics of a class of objects. Our experiments used training sets with 4-8 letters as representatives of a class. With such small sets representing a class, the level of discrimination of a structuring element can become extremely discriminating by including many points. Since our goal was to capture invariant properties of the uppercase letters, we sought less dense structuring elements.

The software was developed on Zenith-248 microcomputers in the Pascal programming language. As planned, we implemented a set of software modules that form the basis for future learning experiments. The basic software components are outlined in Figure 2. The record manager maintains a detailed experimental log that permits the reconstruction of any previous experiment. It also maintains a link between the input information and output information of individual experiments. The image manager contains two sub-units: an image selection program and an interactive image editor program. Using the selection program, random collections of images can be drawn from different classes of objects to form training sets and test sets for experiments. The editor can then be used to modify images in a training or test set. In addition, the editor provides a mechanism for defining new images that can be selected for future experiments. The production system manager is used to establish parameters for an experiment. It also includes a dynamic trace facility that is used to stop the execution of a model at any time

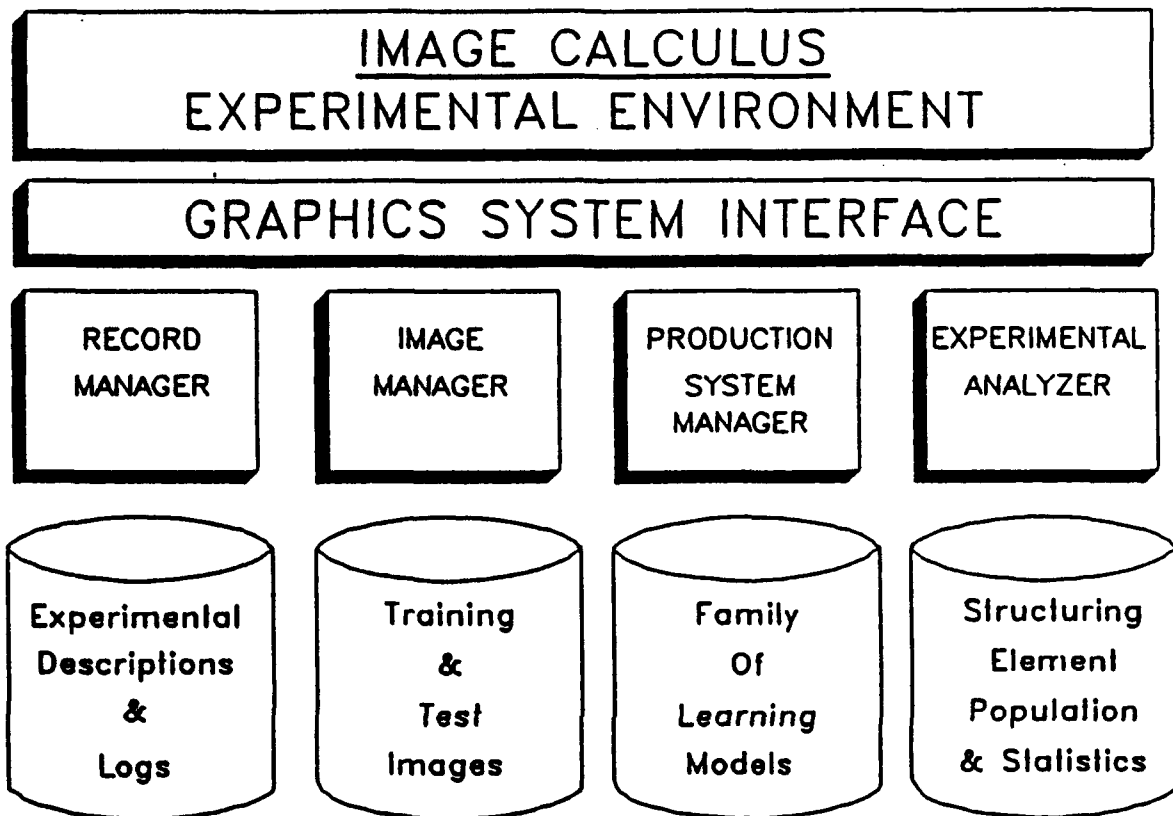


Figure 2. Software subsystems of the Image Calculus experimental environment. The lower bins represent files stored on external devices. The blocks represent specific program modules.

so that individual structuring elements and images can be viewed and manipulated graphically. The experimental analyzer provides a graphical tool for viewing populations of structuring elements and entire image sets. It captures global measures on the populations and allows statistical analysis of experimental results.

The entire software system is joined into a functional unit through a graphics interface that provides pathways and support to all of the sub-units.

IV. RECOMMENDATIONS:

a. Preliminary studies with the Image Calculus software package indicate that this tool is a valuable vehicle for the investigation of learning strategies in the context of image processing. A number of experiments remain to be completed to fully exploit the existing software. Among these is an experiment to generate a full set of non-cooperating character detectors for the letters A-Z. Since similar studies have been done using other software approaches (Kamentsky and Liu, 1963; Liu, 1964; Stentiford, 1985), this experiment will establish the relative merits of our software system. In addition, this examination will serve as a performance base line for evaluation of future software modifications.

b. The image management software is of sufficient sophistication to

permit the construction and analysis of shape data. Therefore, image sets consisting of real world objects will be examined to establish the utility of this program. In this study, shape classification as well as property classification will be investigated.

c. With some modifications, the software can be used to conduct experiments on multi-class recognition problems. To begin this work, the classification system will be designed and implemented. Also, additional computational power will be acquired to conduct recognition studies on larger images.

d. To automate the process of pattern recognition, adaptive control mechanisms must be included in the learning system. This will be done by incorporating genetic algorithms (Holland, 1975) in the learning module. The effects of various genetic operators including mutation, crossover, and inversion will be investigated to determine the quality and speed of structuring element generation. Combinations of these genetic operators will also be considered to determine the optimum mixture of strategies.

REFERENCES

Holland, John H., Adaptation in Natural and Artificial Systems. The University of Michigan Press, Ann Arbor, 1975.

Kamentsky, L. A., and Liu, C. N., "Computer-Automated Design of Multifont Print Recognition Logic," IBM J. Res. Devel., 1963, Vol. 7, pp. 2-13.

Liu, C. N., "A Programmed Algorithm for Designing Multifont Character Recognition Logics," IEEE Trans. Comput., 1964, Vol. C-13, pp. 586-593.

Serra, J., Image Analysis and Mathematical Morphology. Academic Press Inc., London, 1982.

Stentiford, F. W. M., "Automatic Feature Design for Optical Character Recognition Using an Evolutionary Search Procedure," IEEE Trans. PAMI, 1985, Vol. PAMI-7, pp. 349-355.

1988 USAF-UES SUMMER FACULTY RESEARCH PROGRAM/
GRADUATE STUDENT RESEARCH PROGRAM

Sponsored by the
AIR FORCE OFFICE OF SCIENTIFIC RESEARCH

Conducted by the
Universal Energy Systems, Inc.

FINAL REPORT

Heat Flux Prediction for Nucleate Boiling
in Liquid Metal Heat Pipes

Prepared by:	Larry W. Byrd
Academic Rank:	Assistant Professor
Department and	Department of Engineering
University:	Arkansas State University
Research Location:	AFWAL/FDL
	Structural Division/Structural Integrity Branch
	Loads and Criteria Group
USAF Researcher:	Cristopher L. Clay
Date:	August 22, 1988
Contract No.:	F49620-87-R-0004

Heat Flux Prediction for Nucleate Boiling
in Liquid Metal Heat Pipes

by

Larry W. Byrd

ABSTRACT

Suggested methods for calculating the boiling limit for heat pipes give heat fluxes lower than those found experimentally. A better understanding of this limit is needed. The vapor pressure curve for sodium was used to check a method presented by Chi [1] for temperature between 500-1300°C. This method used an approximation of the Clausius-Clapeyron equation to calculate the boiling limit. Chi's method gave much larger values for the heat flux for certain wick geometries and operating conditions. Preliminary work on a conceptual model incorporating partial dryout of the wick simultaneously with boiling was also initiated.

Acknowledgments

I wish to thank the Air Force Systems Command and the Air Force Office of Scientific Research for sponsorship of this research. Universal Energy Systems helped explain Air Force goals in sponsoring the Summer Faculty Research Program as well as general orientation. Personnel at the Flight Dynamics Laboratory were supportive and helpful.

Mr. Charles May and Mr. Mike Pajak provided assistance in locating reference material and orientation to the base. Dr. Don Paul also added his insight to the problem. I have enjoyed my stay at Wright-Patterson AFB and consider myself extremely fortunate to be employed doing something I find so rewarding.

I. INTRODUCTION:

Aircraft leading edges, spacecraft nose caps, and surfaces under laser attack must dissipate large amounts of energy rapidly to prevent thermal damage. Heat pipes offer a possibility for reliable lightweight protection. The Structural Division of the Flight Dynamics Laboratory is currently investigating the maximum energy transfer rates for reusable high temperature heat pipes. However, suggested equations predicting a burnout heat flux have been found to be in considerable disagreement with experimental data. A better understanding of the heat transfer limitations is essential to the safe use of heat pipes.

Interest in heat transfer and thermodynamics contributed to my assignment to the Loads and Criteria Group of the Structural Integrity Branch. Previous work includes a study of transient thermal stresses in gun tubes, freezing flow in pipes and direct-contact, two-phase heat transfer between immiscible liquids.

II. OBJECTIVES OF THE RESEARCH EFFORT:

The objective of my summer research program was to theoretically model liquid metal heat pipes. A method to predict the maximum heat flux for a given wick geometry and operating parameters was desired. Due to the time constraints of the research program, the objective was narrowed to the study of the quasi-static boiling limit and conceptualization of a one-dimensional transient model incorporating partial wick dryout with simultaneous boiling.

III. QUASI-STATIC BOILING LIMIT

The following assumptions were made in order to estimate the radial heat flux necessary for incipient boiling:

- i) The heat flux is slowly increased and assumed to be uniform over the evaporator surface.
- ii) The heat transfer through the wick is primarily by conduction. Thus, the model is more appropriate for liquid metal heat pipes.
- iii) The vapor in bubbles nucleating at the wall is saturated and at the same temperature as the wall and adjacent superheated liquid.
- iv) The liquid and vapor at the inner wick surface are at the same temperature with the vapor being saturated and the liquid superheated.
- v) The liquid/vapor interfaces formed at the wall and the inner wick surface are spherical.
- vi) The liquid mass flow rate through the wick is small enough that the radial pressure drop can be neglected when compared to the vapor core pressure.
- vii) The wick structure can be modeled as though it had a uniform pore radius r_p .
- viii) Nucleation begins at the tube wall, not the interior of the wick.

Mathematical Formulation

Figures 1 and 2 show the geometry used for a cylindrical heat pipe and the liquid/vapor interfaces involved in the model. At the wick interface, the liquid evaporates with vapor moving into the vapor core. Vapor bubbles will also form at the wall at small nucleation sites. The evaporation occurring at the wick interface is similar to

that from the capillary tube shown in Figure 3. At static equilibrium, the pressure difference is given by the LaPlace-Young equation [2] as:

$$P_v - P_l = \frac{2\sigma}{r} = \frac{2\sigma \cos \theta}{r_p} \quad (1)$$

During operation of the heat pipe, there is a radial pressure drop in the liquid associated with the mass flow due to evaporation. This mass flow, \dot{m} , is related to the heat transfer rate, Q , by:

$$\dot{m} \approx Q / h_{fg} \quad (2)$$

The lower liquid pressure results in a larger curvature which is equivalent to a smaller radius of curvature for the interface. This increases the interface area where evaporation occurs. For a perfectly wetting fluid, the minimum value for θ is zero. Thus, at the maximum heat flux for a static interface, the radius of curvature is equal to the capillary radius and the interfacial area is at its maximum value of $2\pi r_p^2$. If the heat flux is increased further, the interface moves into the wick and dryout occurs. It was assumed in the quasi-static model that dryout did not occur.

Returning to Figure 2, the liquid pressure at the wick interface is:

$$P_{li} = P_v - \frac{2\sigma_i}{r_p} \quad (3)$$

P_v is the saturation pressure corresponding to the vapor core

temperature, σ_i is the surface tension evaluated at the vapor temperature and r_p is the mean pore radius in the wick. Similarly, the vapor pressure in the bubble forming at the wall, P_B , is given by:

$$P_B = P_{lw} - \frac{2\sigma_w}{r_n} \quad (4)$$

P_{lw} is the liquid pressure at the wall, σ_w is the surface tension evaluated at the wall temperature and r_n the mean nucleation radius. Typically, the wick is thin and mass flow rates are small enough that $P_i \approx P_{lw}$. Equations (3) and (4) can then be combined to give:

$$P_B = P_i + 2 \left(\frac{\sigma_w}{r_n} - \frac{\sigma_i}{r_p} \right) \quad (5)$$

The vapor pressure curve for sodium [3] is approximated* as:

$$\log_{10}(P_{sat}) = A - \frac{B}{T_{sat}} - C \log_{10}(T_{sat}) \quad (6)$$

Where P_{sat} is in atmospheres and T_{sat} in degrees Kelvin, A, B, and C are constants. The surface tension given in Dunn & Reay [4, pg. 272] can be approximated as:

$$\sigma = A_i T + B_i \quad (7)$$

*The value of B was changed to 5520 to better fit the data presented in Dunn & Reay over the temperature range of 500-1300°C.

Substituting (6) and (7) into (5) gives the following equation for T_w , the fluid temperature at the wall.

$$A - \frac{B}{T_w} - \log_{10} [T_w (A_2 + B_2 T_w)] = 0 \quad (8)$$

where $A_1 = \frac{1}{a} \left(P_{iw} + \frac{2B_1}{r_n} \right)$; $B_2 = \frac{2A_1}{a r_n}$; $a = 101781$

The constants in this equation depend on the thermophysical properties of the working fluid, the mean pore radius, and mean nucleation radius. T_w is substituted into the one dimensional radial heat conduction equation which gives:

$$Q/A = \frac{k_e \Delta T}{r_w \ln(r_w/r_i)} = \frac{k_e \Delta T}{t_e} \quad (9)$$

Several equations for k_e , the equivalent thermal conductivity for the liquid-saturated wick, have been presented for different wick geometries. One was taken from Dunn & Reay [9, pg. 100].

$$k_e = \left(\frac{\beta - \epsilon'}{\beta + \epsilon'} \right) k_l \quad (10a)$$

$$\beta = \frac{1 + k_w/k_l}{1 - k_w/k_l} \quad (10b)$$

k_w is the thermal conductivity of the wick material, k_l is the thermal conductivity of the liquid, and ϵ' is volume fraction of the solid in the wick. Thus, the additional parameters affecting the heat flux include r_i , r_w , k_e . Equation (8) was solved using a Regula-falsi iteration.

Chi [1, pg. 89] used a similar approach except he used an approximation of the Clausius-Clayeyron equation shown below to relate P_B to T_w .

$$\left. \frac{dP}{dT} \right|_{sat} = \frac{h_{fg}}{T_{sat}(\bar{v}_g - \bar{v}_f)} \approx \frac{\rho_v h_{fg}}{T_{sat}} \quad (11)$$

v_g and v_f are the specific volume of saturated vapor and liquid for a given T_{sat} and ρ_v , the vapor density. Chi assumed the right hand side of equation (11) was constant for small changes in T which leads to the following equation for the incipient boiling heat flux:

$$Q/A = \frac{2k_e T_w \sigma}{h_{fg} \rho_v r_w \ln(r_w/r_i)} \left(\frac{1}{r_n} - \frac{1}{r_p} \right) \quad (12)$$

In both approaches, any vapor bubbles that leave the wall should not recondense and collapse before leaving the wick if the bubble radius is smaller than the mean pore radius. It was initially believed the bubbles would become trapped in the wick resulting in heat pipe failure. Further research has indicated that vapor may escape resulting in stable nucleate boiling with much higher heat fluxes.

IV. ONE DIMENSIONAL TRANSIENT MODEL COMBINING WICK DRYOUT AND BOILING

The actual boiling limit of a heat pipe depends on several factors. These include the ability of the vapor to escape the wick, the importance of convective heat transfer, and whether the wick remains saturated with liquid. In pool boiling, large increases in the heat flux can be obtained with relatively small increases in liquid superheat once stable nucleate boiling has been established. This is due to the increased liquid agitation near the surface. In a wick

structure, surface tension effects may cause an early release of vapor bubbles thus affecting this liquid agitation. The effect of partial wick dryout depends on whether the liquid level drops uniformly in the wick or vapor channels form at different points in the wick. Thus the size distribution and length of flow channels in the wick may be important.

A conceptual model that could address these questions is shown in Figure 4. It consists of a set of parallel capillary tubes whose axis lie perpendicular to a heated plate. The physics involved with evaporation and flow through the wick can be modeled at different levels of complexity using a much simpler geometry than actually found in a heat pipe. The relative importance of different parameters may be determined and then applied to a more realistic physical model. An example would be to include small holes in the capillary tube walls which would create interconnecting passageways for fluid flow. The simple geometry also allows greater control of parameters in experimental correlation of the theory to actual heat pipes.

V. RESULTS AND DISCUSSION

If gravity is neglected, Daily & Harleman [4] use Darcy's law to relate the mass flow rate to the radial pressure drop.

$$\dot{m}_2 = \int_0^r (2\pi r l_e) \frac{K_0}{\mu} \left(\frac{dP}{dr} \right) \quad (13)$$

Relating the mass flow rate to the heat flux, separating variables and integrating gives:

$$\frac{Q}{h_{fg}} \approx \rho_l (2\pi r l_e) \frac{k_c}{\mu_l} \left(\frac{dP}{dr} \right) \rightarrow \int_{P_i}^{P_w} dP \equiv \Delta P_l = \int_{r_i}^{r_w} \frac{\mu_l Q dr}{\rho_l (2\pi r l_e) k_c h_{fg}}$$

$$\rightarrow \Delta P_l = \left[\frac{Q l_e \left(\frac{r_w}{r_i} \right)}{2\pi l_e} \right] \left(\frac{\mu_l}{h_{fg} \rho_l k_c} \right) = \frac{\mu_l k_e \Delta T}{h_{fg} \rho_l k_c} \quad (14)$$

For the wick studied,

$$\Delta P_l = \frac{(0.00024 \text{ N s/m}^2) (48 \text{ Nm/sm}^2 \text{ K}) (85^\circ \text{K})}{4.37(10^6) \left(\frac{\text{N m}}{\text{kg}} \right) (828.1 \text{ kg/m}^3) 6(10^{-4}) \text{ m}^2} = 45.1 P_a \approx 0.007 \text{ psi}$$

The Reynolds number based on the mean pore diameter is approximately .09, justifying the use of Darcy's law. This pressure drop could be easily incorporated into the model by substituting equation (14) into equation (5), but it was neglected.

Equation (9) shows that increasing the equivalent conductivity will increase the heat flux necessary for incipient boiling. This can be accomplished by increasing k_w through material selection.

Alternatively, k_e increases if ε' decreases and $k_l > k_w$. If $k_l < k_w$, increasing ε' increases k_e . A drawback to the present model is its independence of the fluid flow which is a function of ε' and the wick geometry.

Decreasing the wick thickness will also increase the heat flux by decreasing the thermal resistance to conduction through the liquid

saturated portion of the wick. However, there is a much larger pressure drop for vapor flow through the remainder of the wick.

Darcy's law gives:

$$\frac{\Delta P_{\text{vapor}}}{\Delta P_{\text{liquid}}} = \left(\frac{\rho_g}{\rho_l} \right) \left(\frac{\mu_v}{\mu_l} \right) \approx 20,000 \text{ at } 500^\circ\text{C} \quad (15)$$

Thus, the saturation temperature in the wick interior will be much higher than that in the vapor core region, limiting the heat transfer rate.

The effect of r_n and r_p can be seen qualitatively as shown below:

$$Q/A \propto \Delta T \propto (p_g - p_v) \propto \left(\frac{\sigma_w}{r_n} - \frac{\sigma_i}{r_p} \right) \approx \frac{\sigma_{ave}}{r_n} \left(1 - r_n/r_p \right) \quad (16)$$

Thus decreasing r_n or increasing r_p increases the heat flux. However, if $r_p \gtrsim 10r_n$, further increases cause only small increases in Q/A . In comparison, the capillary and entrainment limits increase with decreasing r_p . The surface tension and latent heat of vaporization decrease with increasing temperature. Thus, the heat flux necessary for boiling would be expected to decrease as T_v increases.

Figure 5 compares the heat flux calculated from equation (8) and (9) to Chi's method as a function of the vapor core temperature. The geometry approximates a leading edge heat pipe using a sintered nickel wick tested by Clark, et al. [6]. Chi's method gives much larger values for the heat flux at lower vapor core temperatures. This occurs where the liquid superheat exceeds $10\text{-}15^\circ\text{C}$ and the approximation to the Clausius-Clapeyron equation breaks down.

Also shown is the burnout heat flux given by Clark. It agrees with the present model if $r_n \approx 16.5 \mu m$ and burnout occurs at the incipient boiling limit. This is not unreasonable because $r_n \approx r_p$. Another possibility offered by Clark was partial dryout of the wick although the pressure drop was substantially lower than the capillary limit. The data was also manipulated to calculate an equivalent conductivity of $48 \text{ w/m}^\circ\text{K}$ for the wick. Equation (10) gives a value of $k_e = 59 \text{ w/m}^\circ\text{K}$ for an error of 23%. This error could arise from reading data from Figure 13 of Clark's report. The outside surface temperature was taken to be 765°C with a calculated 180°C drop through the wall to give a wick ΔT of 86°C . The conductivity would also be lower if there was a small amount of vapor trapped in the wick. If k_e was set equal to $48 \text{ w/m}^\circ\text{K}$, the calculated nucleation radius is $15.8 \mu m$ only 4.4% smaller. These calculated values fall in the range of $.0254$ to $25.4 \mu m$ referenced by Chi [1, pg. 92].

Figure 6 shows the expected response for increasing r_p/r_n . The heat flux decreases rapidly as r_p approaches r_n and is insensitive to changes in r_p for $r_p/r_n > 10$. The possibility of hot spots increases if $r_p \approx r_n$. In any real wick, the pore radii are not uniform. Because small changes in r_p can cause large changes in the incipient boiling heat flux, localized regions of vapor may appear.

VI. RECOMMENDATIONS

More work is necessary to form and update a data base of heat pipe literature. As a start, a computer search of several data sources has been left with Mr. Chris Clay of the Flight Dynamics Laboratory. The

experience of people such as Dr. Jerry Beam of the Aero Propulsion Laboratory should also be better utilized. Finally, evaporative and boiling heat transfer in a single capillary tube should be theoretically and experimentally studied so the results can be incorporated into the conceptual model proposed in section IV.

Nomenclature

Constants:

$A = 6.67176$, $B = 5520$, $C = .61344$, $A_1 = -9.1(10^{-5})(N/M^{\circ}K)$,

$B_1 = .22057 (N/M)$

English Variables:

dp/dr - radial pressure drop in the wick (Pa/m)

h_{fg} - latent heat of vaporization (J/kg)

k_e - equivalent thermal conductivity in the liquid saturated wick ($W/m^{\circ}K$)

k_l, k_w - thermal conductivity of liquid and wick material respectively ($W/m^{\circ}K$)

K_o - wick permeability (m^2)

ℓ_e - evaporator length (m)

\dot{m} - mass flow rate (kg/s)

P_B - pressure inside a bubble forming at the wall (Pa)

P_{li}, P_{lw} - liquid pressure at the inner wick surface and at the wall, respectively (Pa)

P_{sat} - saturation pressure (Atm)

P_v - pressure in the vapor core region (Pa)

Q - heat transfer rate (W)

r - radius (m)

r_i, r_w - inner wick surface radius and inside pipe radius,
respectively, (m)

r_n - mean nucleation site radius (m)

r_p - mean pore radius (m)

t_e - equivalent wall thickness (m)

T_{sat} - saturation temperature ($^{\circ}\text{K}$)

T_w - temperature of the inside surface of the heat pipe wall ($^{\circ}\text{K}$)

v_f, v_g - specific volume of saturated liquid and vapor
respectively (m^3/kg)

Greek Variables:

$\Delta P_l, \Delta P_v$ - pressure drop in liquid and vapor respectively (Pa)

$\Delta T - (T_w - T_i)$ ($^{\circ}\text{K}$)

θ - angle between tangent to liquid/vapor interface and solid surface

σ_i, σ_w - liquid surface tension evaluated at the wick interface and
wall respectively (N/m)

ρ_l, ρ_v - liquid and vapor density respectively (kg/m^3)

μ_l, μ_v - liquid and vapor dynamic viscosity (Ns/m^2)

REFERENCES

1. Chi, S.W., Heat Pipe Theory and Practice: A Sourcebook, Hemisphere Publishing Company, 1976.
2. Batchelor, G.K., An Introduction to Fluid Dynamics, Cambridge University Press, New York, New York, 1967.
3. Kirk-Othmer Encyclopedia of Chemical Technology, 2nd ed. Vol. 18, p. 434.

4. Daily, J.W. and D.R.F. Harleman, Fluid Dynamics Addison-Wesley Publishing Company, Inc., Reading, Massachusetts, 1966.
5. Dunn, P.D. and D. A. Reay, Heat Pipes, 1st ed., Pergamon Press Inc., Fairview Park, New York, 1976.
6. Clark. L.T., and G.S. Glenn, "Design Analysis and Testing of Liquid Metal Heat Pipes for Applications to Hypersonic Vehicles" Thermophysics, Plasmadynamics, and Lasers Conference, San Antonio, Texas, June 1988.

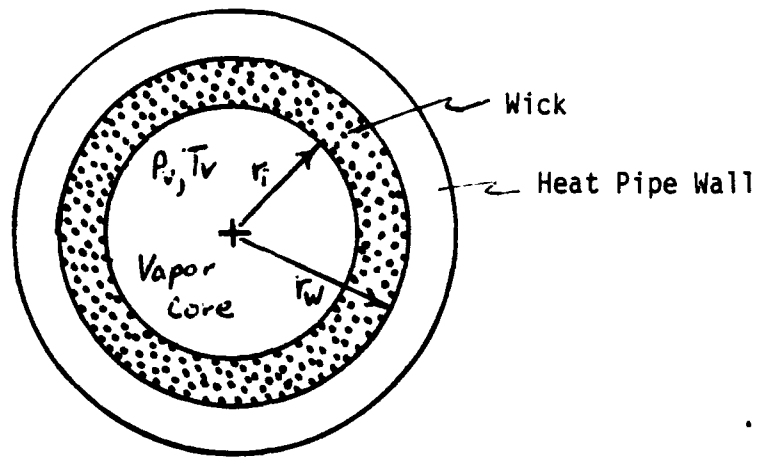


Figure 1 Schematic of Heat Pipe Cross Section

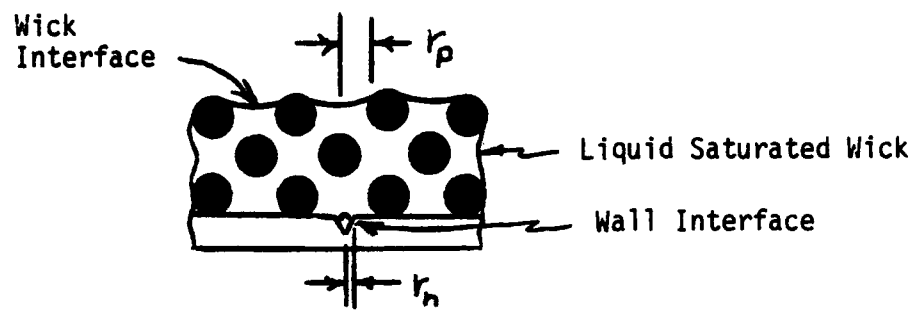


Figure 2 Wick Geometry

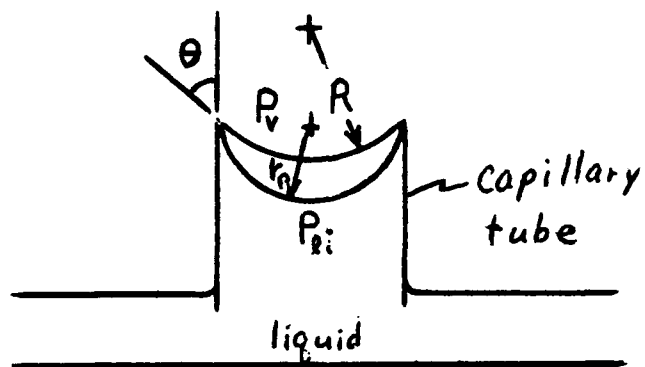


Figure 3 Capillary Interface

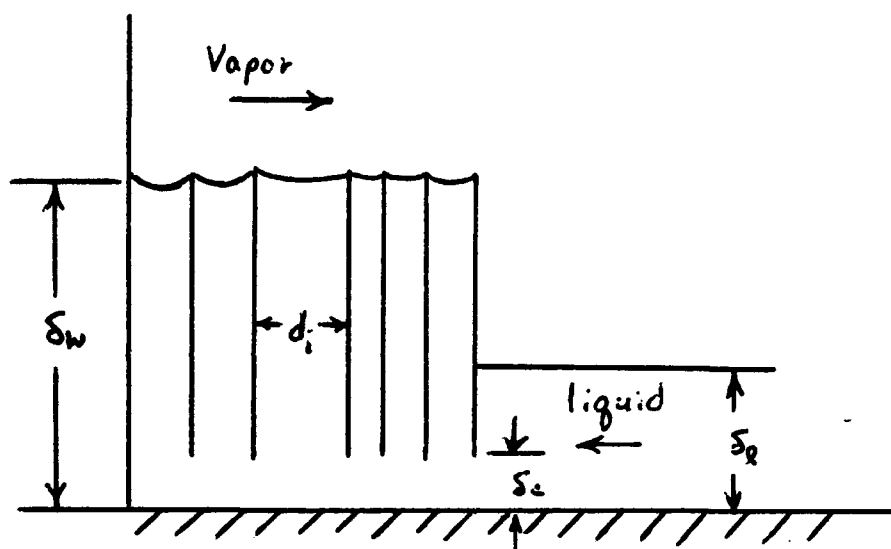


Figure 4 One Dimensional Evaporator Model

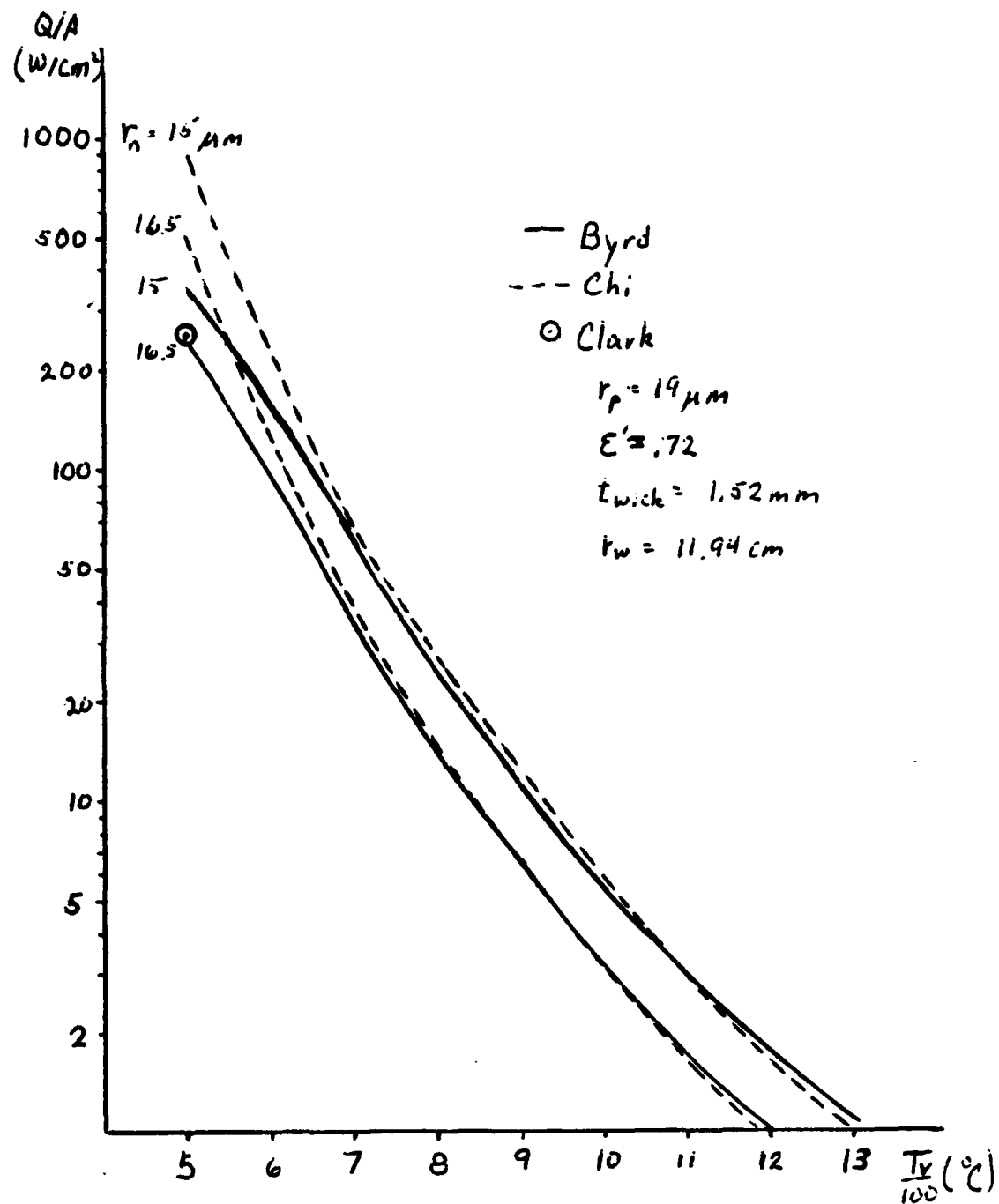


Figure 5 Radial Heat Flux as a Function of T_v

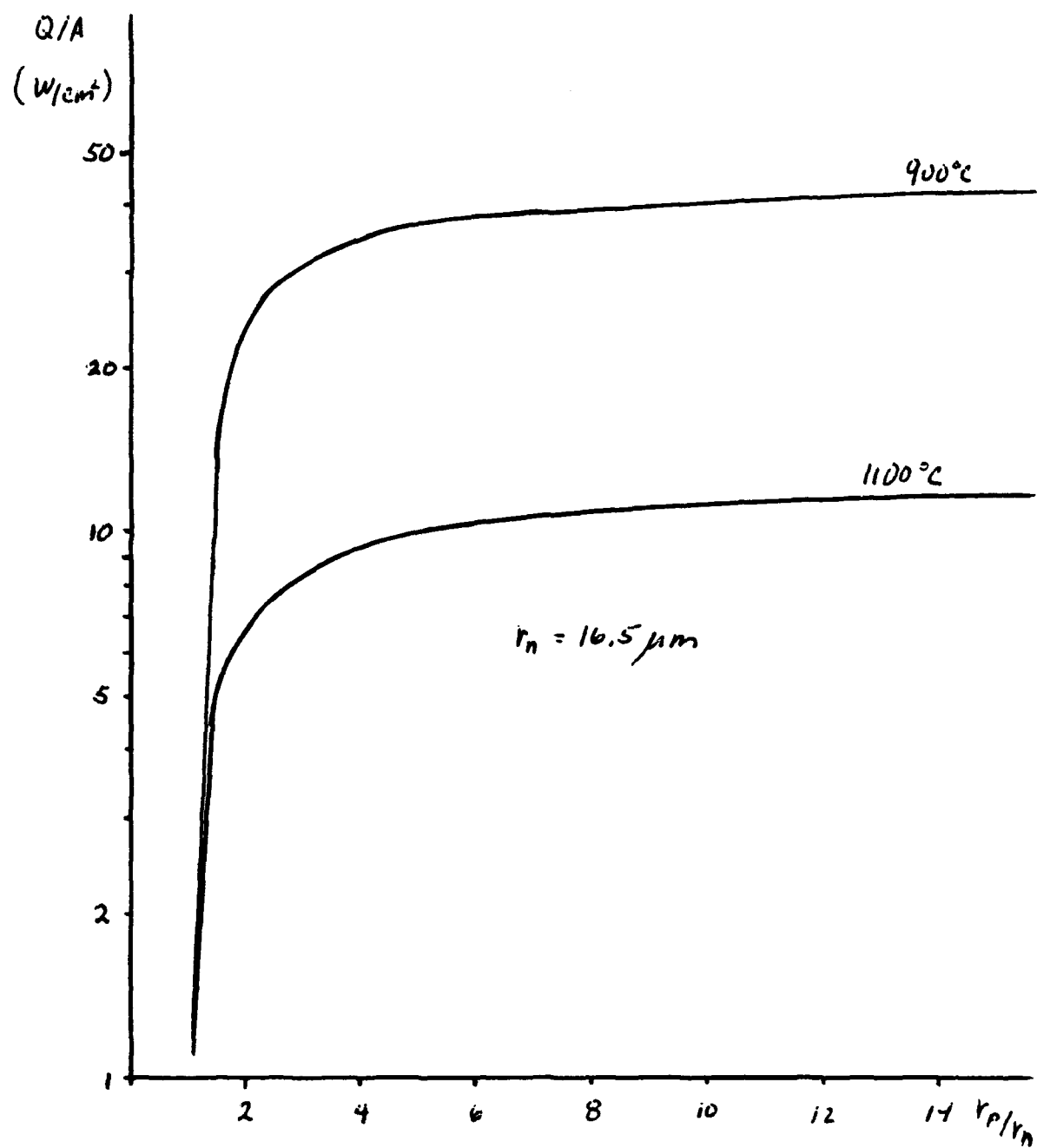


Figure 6 Radial Heat Flux as a Function of Pore Size

1988 USAF-UES SUMMER FACULTY RESEARCH PROGRAM/
GRADUATE STUDENT RESEARCH PROGRAM

Sponsored by the
AIR FORCE OFFICE OF SCIENTIFIC RESEARCH
Conducted by the
Universal Energy System, Inc.

FINAL REPORT

Reliability Study of Nonlinear Structural Response
under Reversible Cyclic Loading Processes

Prepared by:	Karen C. Chou
Academic Rank:	Associate Professor
Department and	Department of Civil Engineering
University:	Syracuse University
Research Location:	AFWAL/FIBEC
	Wright-Patterson AFB, OH 45433
USAF Researcher:	Margery E. Artley
Date:	12 August 1988
Contract No:	F49620-87-R-0004

Reliability Study of Nonlinear Structural Response
under Reversible Cyclic Loading Processes

by

Karen C. Chou

ABSTRACT

Reliability assessment of aircraft components is studied for nonlinear structural response due to stochastic load processes such as thermal and maneuver loads. During the investigation, the material is assumed to have a bilinear load response behavior where the compressive properties are the same as tensile. The load processes may have any form of distributions for load arrivals and magnitudes. A discussion on the reliability analysis procedures are presented in this report.

ACKNOWLEDGEMENT

The author would like to thank the Air Force Office of Scientific Research/AFSC, United States Air Force for providing this opportunity which is administered by the Universal Energy System under the contract F49620-87-R-0004.

This study would not be possible without the support and hospitality from the Fatigue, Fracture and Reliability Group of the Structural Integrity Branch, Structural Division, Flight Dynamics Laboratory, Air Force Wright Aeronautical Laboratories. Special thanks are due to Margery E. Artley for her fruitful discussion and support.

I. INTRODUCTION :

Structural reliability is a probability based safety assessment of structures. The analysis considers the randomness existing in either the load or the resistance or both. The approach provides a systematic treatment of uncertainty embedded in the structural parameters.

The Fatigue, Fracture and Reliability Group of the Flight Dynamics Laboratory at Wright-Patterson AFB is interested in the reliability assessment of airframes under thermal and maneuver loads. The thermal load is a long duration load with random magnitude and duration, while the maneuver load is a short duration load with random magnitude. Since the material response could go beyond the elastic yield, it is essential to incorporate the nonlinear structural response during the development of reliability model.

The objective of the Fatigue, Fracture and Reliability Group is compatible with the author's research interest. The author's primary interest is in the application of probability and statistics in civil engineering problems and specialized in structural reliability. In the area of nonlinear structural response due to stochastic live load processes, the author has published a number of articles in refereed journals and proceedings. Although the author's focus has been on building live loads, the approach in developing the reliability model for the thermal and maneuver load will be very similar.

II. OBJECTIVES OF THE RESEARCH EFFORT :

Numerous studies have been performed by the U.S. Air Force and other researchers on the structural safety of aircraft. These studies have primarily assumed that the resistance and applied loads are deterministic. In addition, the material is assumed to respond elastically. In the past two decades, studies in other structures (such as buildings, nuclear power plants, off shore structures, etc.) have shown that neither the loads nor the structural properties are known with certainty (e.g., Pier and Cornell, 1973; Kam, Corotis and Rossow, 1983; Kennedy et al., 1980; Wirsching, 1983; Bakht, 1983) during the structures' lifetime. The development of reliability studies in those areas has advanced tremendously in the past decade. It had evolved from just a research interest within a small group of researchers to the implementation of the results to design specifications (ANSI, 1982; AISC, 1987). In aircraft safety studies, the application of probability based concepts has begun to increase. The studies performed thus far were focused on the randomness of material (Lin and Yang, 1983; AL-Sugair and Kiremidjian, 1988).

When analyzing the structural response, it is often assumed that the material follows Hooke's law (linear elastic). However, when the structure is subjected to fatigue under high thermal load, the material can respond in the inelastic region. Thus it is essential to consider nonlinear structural response in the reliability analysis.

During the author's participation as a Summer Faculty Fellow at Wright-Patterson AFB, the author and her research colleague have discussed a few possible areas that reliability analysis is applicable. A

brief description of the research objectives is given below:

1. Modelling of Thermal and Maneuver Loads

U.S. Air Force anticipates that future high speed aircraft will generate a tremendous thermal load. The maneuvers performed during each mission will also provide additional stress on the airframe. Since these loads resemble the building live loads which the author had performed extensive studies, it is possible to perform the reliability analysis on the aircraft once the load models are known.

2. Nonlinear Structural Response due to Stochastic Reversible Cyclic Loading Processes

The nonlinear structural response that the author had studied thus far is restricted for positive loads (one directional loads such as gravity loads). However, loads such as vibration are two directional loads. Thus it is necessary to modify the earlier response process to analyze reversible cyclic loads.

3. Implementation of Probability Based Data Bank for Aircraft Maintenance

Besides the necessity to build structures (including airframes) to have a very small probability of failure, it is also desirable to prolong the aircraft's serviceable lifetime through proper maintenance. The goal of this research area is to assess the condition of aircraft that is in service and to recommend an action such as repair, rehabilitation or replacement. Furthermore, plans are to computerize (i.e. utilize an expert system) the entire decision process so that the aircraft can be monitored continuously and the safety assessment and decision making performed simultaneously.

Among the above 3 objectives, the author chose to investigate the second objective during the SFRP. A discussion of the investigation is presented in the subsequent section.

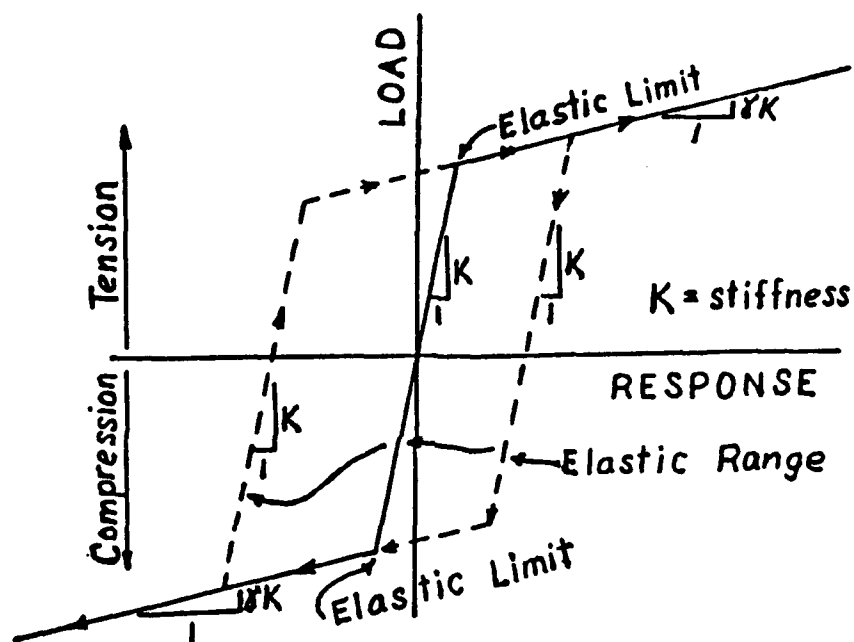


Figure 1. Typical Load-Response Relationship

III. DEVELOPMENT OF NONLINEAR STRUCTURAL RESPONSE DUE TO STOCHASTIC REVERSIBLE CYCLIC LOADS :

It is well known that nonlinear structural response is load history dependent. For a positive load (one directional load) magnitude process, Chou, Corotis and Karr (1985) showed that it is not always necessary to know the load history prior to the first excursion of a predetermined threshold level. They further showed that if one is only interested in the total number of loads exceeding a predetermined syreshold deformation level, the exceedance process depends on the magnitude of the hierarchical peak (maximum load magnitude up to that point in time). However, if one includes the effect of a reversible load, the response will no longer depend on the hierarchical peak alone.

For the purpose of investigation, the material is assumed to have bilinear load-response relationship with the unloading parallel to the initial elastic range and the compressive properties being the same as tensile. A typical load response relationship is shown in Fig. 1. In order to describe the nonlinear structural response due to reversible cyclic loads, a typical reversible cyclic load process along with its corresponding response (shown in Fig. 2) is used. Due to the load reversal, the hierarchical peaks do not necessarily determine all the exceedances. For the typical load process shown in Fig. 2, the response for the first 5 loads is the same as that described in Chou, Corotis and Karr (1985). Due to the load-response relationship assumed, load 6 does not fall onto the unloading path, path b, defined by load 5 but falls onto the nonlinear part of the reverse (compres-

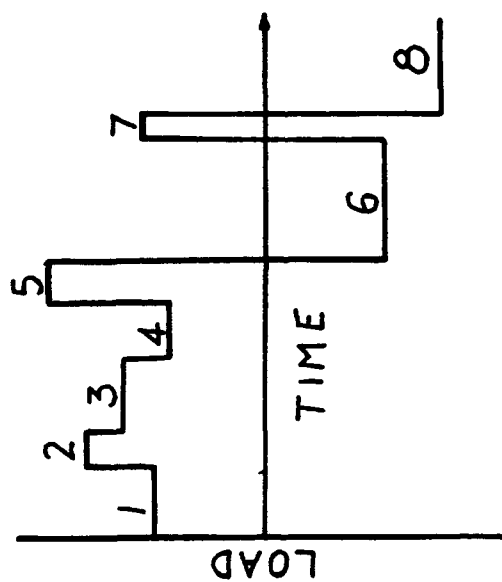
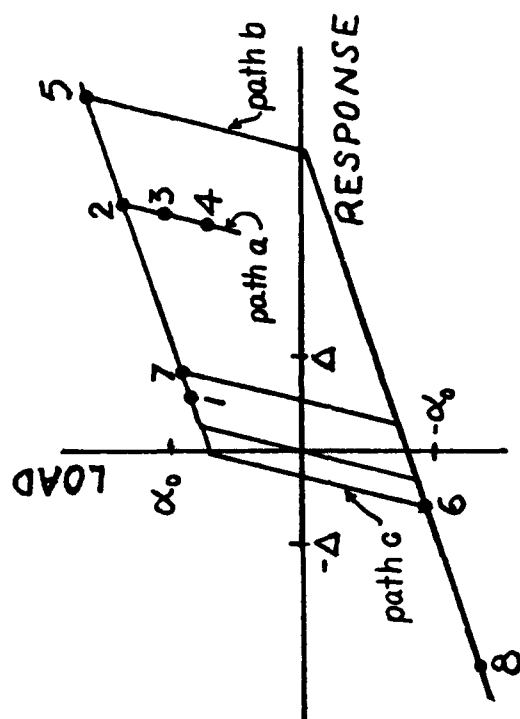


Figure 2. Typical Sustained Load Process and Its Corresponding Nonlinear Response

sive) response portion. Thus load 6, though numerically smaller than load 5, will define a new loading path, path c, for subsequent loads. Because of the reversibility in load and response, load 7 is not considered as an exceedance even though it has a higher numerical load magnitude than load 4 (which is an exceedance). In addition, the response following load 6 is no longer depends on the hierarchical peak, load 5. From this illustration, one can perceive that if one wishes to analyze the number of load exceedances, it may require the knowledge of the entire response process. The mathematics involved will undoubtedly be prohibitively complex. An approach utilizing the Markov chain process appears to be meritorious and is presented herein.

If one is only interested in the number of loads exceeding a predetermined threshold deformation, either on the compressive zone (say $-\Delta$) or on the tensile zone (say Δ) or both, then it is not critical to know the precise response of any load. One only need to know the status of the current load (causing an exceedance or not) in order to predict the status of the future one. For instance, if a load is not an exceedance, how would the subsequent load become one. That is, what magnitude should the second load have in order to become an exceedance while the preceding one is not. To clarify this point, let the load-response space be divided into 7 regions as shown in Fig. 3. If a load response falls into region I, II or V (shaded area in Fig. 4), then there is no exceedance. If a load response falls into any one of the other regions (III, IV, VI or VII (shaded area in Fig. 5)), then there is an exceedance. For example, if a load, say S_i , is not an exceedance, assume its response is in region II, then in order for the subsequent load, S_{i+1} ,

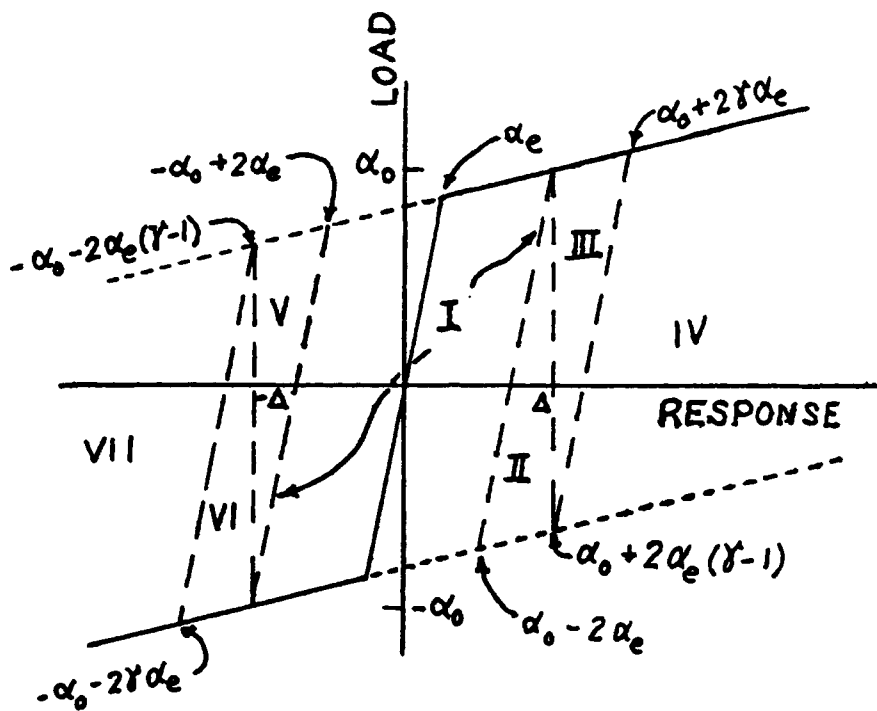


Figure 3. Nonlinear Response States

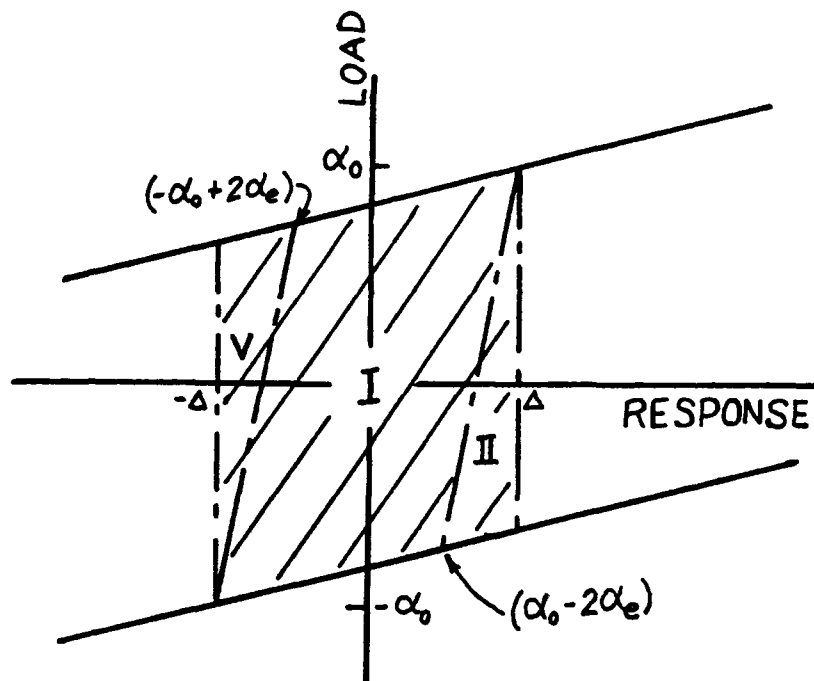


Figure 4. States Where No Load Exceedance Exists

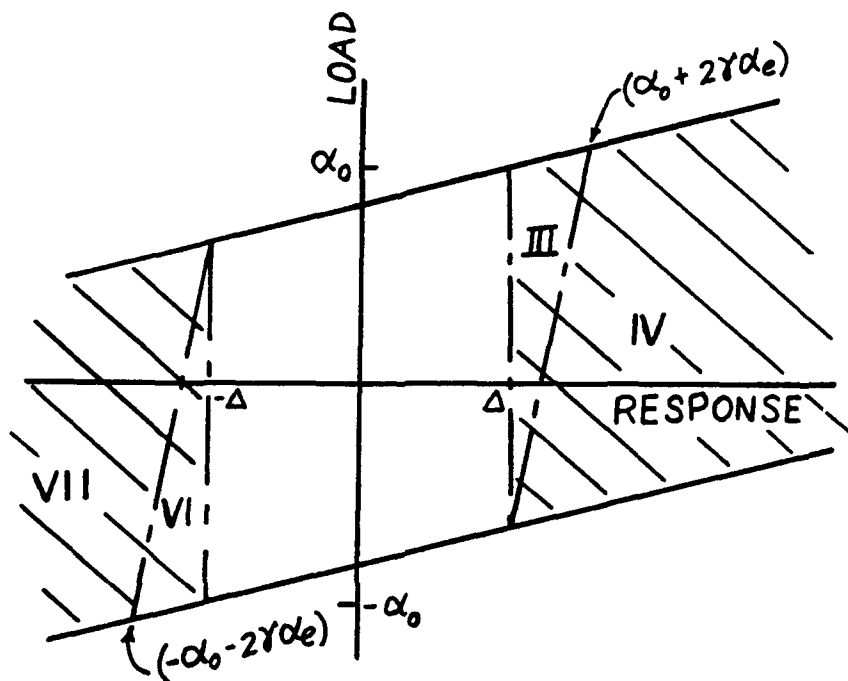


Figure 5. States Where Load Exceedances Exist

to be an exceedance, it must have a response in one of the regions III, IV, VI and VII. The probability that S_{i+1} is an exceedance given that S_i is not is given by

$$\begin{aligned} & \text{Prob } [S_{i+1} \text{ is an exceedance} \mid S_i \text{ is not an exceedance}] \\ &= \text{Prob } [(S_{i+1} \text{ in III} \mid S_i \text{ in II}) \cup (S_{i+1} \text{ in IV} \mid S_i \text{ in II}) \cup \\ & \quad (S_{i+1} \text{ in VI} \mid S_i \text{ in II}) \cup (S_{i+1} \text{ in VII} \mid S_i \text{ in II})] \quad (1) \end{aligned}$$

Consequently one can anticipate that for S_{i+2} to be an exceedance, it would also have to fall into either Region III, IV, VI or VII. However, the transition probability between S_{i+1} and S_{i+2} depends on which region S_{i+1} falls and is independent of the location of S_i . This type of behavior is called the one-step Markov chain process (Cinlar, 1975) since the current state depends only on the immediate preceding state but independent of all previous states.

Once the exceedance process is described by the Markov chain, one can proceed to evaluate the probability of having K exceedances in the lifetime of a structure using probability theory. The procedure can be outlined as follow:

Let N = total number of load arrivals in a lifetime, random value

t = design/service lifetime, deterministic value

K = total number of exceedances in $[0, t]$, random value

S_i = the i-th load in the load process

$[P_{ij}(m)]$ = transition probability matrix that S_m is in region j
given S_{m-1} is in region i

$q_j(m)$ = the marginal probability that S_m is in region j

$[P_{ij}^m(n)]$ = m -th step transition matrix that S_{m+n} is in region j
given that S_n is in region i

To derive the expression for the probability of having K exceedances in the duration $[0, t]$, it is more convenient to derive it via the conditional probability. Consider the situation where the total number of load arrivals in $[0, t]$ is known, say $N = n$. The probability that there are $K = k$ exceedances among these n loads would be a combination of n choosing k at a time which is similar to a binomial distribution. However, the exceedance process here is not stationary. Thus the probability associated with each combination will be different depending on the exact sequence that the exceedances occur. The conditional probability will become

$$\text{Prob}[K=k \mid N=n] = \sum_{i=1}^m p_i \quad (2)$$

where p_i = probability of i -th realization of $\binom{n}{k}$ and m = total number of possible combinations in $\binom{n}{k}$. The unconditional probability will simply be

$$\text{Prob}[K = k] = \sum_{n=k}^{\infty} \text{Prob}[K=k \mid N=n] \text{Prob}[N=n] \quad (3)$$

in which $\text{Prob}[N=n]$ is given by the probability distribution function of the load arrivals. For instance, if the load process is Poisson, then

$$\text{Prob}[N=n] = \frac{(\mu t)^n e^{-\mu t}}{n!} \quad (4)$$

in which μ = arrival rate of the loads.

It is worthy to discuss the calculation for p_i . Since p_i reflects the exact sequence of load exceedances and the exceedance process is nonstationary, i.e.,

$$\text{Prob}[S_i \text{ is an exceedance}] \neq \text{Prob}[S_j \text{ is an exceedance}] ; \text{ for } i \neq j$$

therefore, p_i can be conceptually given by

$$p_i = \sum_{l=1}^n \theta_l \delta(x_l - 1) + \sum_{l=1}^n \beta_l \delta(x_l) \quad (5)$$

in which θ_l = the probability that S_l is an exceedance; β_l = the probability that S_l is not an exceedance; $\delta(\cdot)$ = dirac delta function; and x_l = exceedance indicator where $x_l = 1$ implies that the l -th load is an exceedance and $x_l = 0$ implies that the l -th load is not an exceedance. The probabilities θ_l and β_l can be calculated by

$$\theta_i = q_{III}(i) + q_{IV}(i) + q_{VI}(i) + q_{VII}(i) \quad (6a)$$

$$\beta_i = 1 - \theta_i = q_I(i) + q_{II}(i) + q_V(i) \quad (6b)$$

in which

$$q_j(i) = \sum_{l=1}^7 q_j(l) [P_{lj}^i(i)] \quad (7a)$$

and

$$[P_{lj}^i(i)] = \sum_{k=1}^7 [P_{lk}^{i-1}(i)][P_{kj}(i)] \quad (7b)$$

The transition probabilities depend on the boundaries defining the regions and the states involved during the transition.

IV. RECOMMENDATIONS :

The procedures presented in this report provides a conceptual analysis to the problem of reliability of a structural component subjected to stochastic reversible cyclic loadings with nonlinear material properties. The reliability model discussed here is applicable to a wide range of load processes since no restriction was placed on the probability distribution of the load arrivals nor the load magnitudes. Although the load-response relationship was assumed to be bilinear (most common assumption on material response), one only needs to modify the calculation of the transition probabilities to reflect the general material characteristics. However, it should be noted that the mathematical complexity may increase rapidly with a more complex material curve.

The analysis outlined in the report though conceptually acceptable is not error proof. Numerical verification of the analysis with simulated data is necessary prior to the application of the technique presented here. It is recommended that this study should be pursued through the support of the Mini Grant. In addition, there is a less obvious mathematical complexity in the actual calculation. Recall that the exceedance process is nonstationary. This phenomenon requires the realization of every combination of load exceedances for a given number of load arrivals and exceedances. It has been shown that a direct approach to the enumeration of the load arrivals-exceedances combination can require CPU time in the order of nanoseconds in a VAX 8800 machine (Fleischman and Chou, 1988). An improved algorithm that can reduce the computation time is necessary before the exceedance process presented here can be verified with simulated data.

V. REFERENCES :

- AISC (1987) "Load & Resistance Factor Design Specification for Structural Steel Buildings", American Institute of Steel Construction, Chicago, IL.
- AL-Sugair, F.H. and Kiremidjian, A.S. (1988) "A Stochastic Model for Low-Cycle Elastic-Plastic Fatigue Crack Growth", Probabilistic Methods in Civil Engineering, ASCE, May, pp. 13-16.
- ANSI (1982) "Minimum Design Loads for Buildings and other Structures", ANSI A58.1-1982, American National Standards Institute, New York.
- Bakht, B. (1983) "Statistical Analysis of Timber Bridges", Journal of Structural Engineering, ASCE, Vol. 109, No. 8, pp. 1761-1779.
- Chou, K.C., Corotis, R.B. and Karr, A.F. (1985) "Nonlinear Response to Sustained Load Processes", Journal of Structural Engineering, ASCE, Vol. 111, No.1, pp. 142-157.
- Cinlar, E. (1975), Introduction to Stochastic Processes, Prentice-Hall, New Jersey.
- Fleischman, W.M. and Chou, K.C. (1988) "Computing the Distribution of the Number of Time-Dependent Events", Proceeding of the 36-th International Conference on Mini and Microcomputers and Their Applications, Sant Feliu de Guixols, Spain, June 27-30.
- Kam, T.Y., Corotis, R.B. and Rossow, E.C. (1983) "Reliability of Nonlinear Framed Structures", Journal of Structural Engineering, ASCE, Vol. 109, No. 7, pp. 1585-1601.

- Kennedy, R.P., Cornell, C.A., Campbell, R.D., Perla, H.F. and Kaplan, S. (1980) "Seismic Safety of an Existing Nuclear Power Plant", Nuclear Engineering & Design, Vol. 59, No.2, pp. 315-338.
- Lin, Y.K. and Yang, J.N. (1983) "On Statistical Moments of Fatigue Crack Propagation", Engineering Mechanics, Vol. 18, No.2, pp. 243-256.
- Peir, J-C and Cornell, C.A. (1973) "Spatial and Temporal Variability of Live Loads", Journal of the Structural Division, ASCE, Vol. 99, No. ST5, pp. 903-922.
- Wirsching, P.H. (1983) "Probability Based Fatigue Design Criteria for Offshore Structures", Final Report, API-PRAC Project 81-15, The American Petroleum Institute, Dallas, Texas.

1988 USAF-UES SUMMER FACULTY RESEARCH PROGRAM/
GRADUATE STUDENT RESEARCH PROGRAM

Sponsored by the
AIR FORCE OFFICE OF SCIENTIFIC RESEARCH

Conducted by the
Universal Energy Systems, Inc.

FINAL REPORT

SURVEY AND ASSESSMENT OF VALIDATION DATA BASE
FOR SHOCKWAVE BOUNDARY LAYER INTERACTION IN SUPERSONIC INLETS

Prepared by:	Awatef Hamed
Academic Rank:	Professor
Department and University:	Aerospace Engineering and Engineering Mechanics, University of Cincinnati
Research Location:	Flight Dynamics Laboratory, Aeromechanical Division, Aerodynamics and Airframe Branch, Computational Aerodynamics Group.
USAF Researcher:	Joseph S. Shang
Date:	27 September 1988
Contract No.:	F49620-87-R-0004

SURVEY AND ASSESSMENT OF VALIDATION DATA BASE
FOR SHOCKWAVE BOUNDARY LAYER INTERACTION IN SUPERSONIC INLETS

by

Awatef Hamed

ABSTRACT

The performance of supersonic inlets is strongly affected by the boundary layer development over its internal surfaces. Boundary layer bleed is used to suppress separation and to provide the desired inlet performance. The gain in pressure recovery and stability is accompanied however with a loss in mass flow and an increase in drag which must be minimized by optimizing the amount of bleed and bleed configuration.

The purpose of this work is to review and assess the data base for shock boundary layer interaction, which is pertinent to the flow prediction in supersonic inlets. The effect of bleed in the interaction zone is especially emphasized.

ACKNOWLEDGEMENTS

I would like to express my appreciation for the support and encouragement of Dr. Joseph S. Shang during the course of this work. My experience has been enhanced by his stimulating discussions, and the work atmosphere in the Computational Aerodynamics Group. I also wish to thank the following WPAFB Library Personnel for their help: Elwood White, Ronald Ludquist, Jeanie Stewart, Martha Kline and Judy Jones-Findly. I wish to thank the Air Force Systems Command and the Air Force Office of Scientific Research for their sponsorship of this research.

I. INTRODUCTION

The Flight Dynamics Laboratory, Aero-Mechanical Division will develop the supersonic to hypersonic technology basis, including the propulsion systems. The generation of an experimental validation data base for computational fluid dynamics is essential for the development of inlet flow prediction methodology. Its application to the overall system performance will contribute directly to Forecast II initiative in hypersonic technology.

My research interests in the academic environment have been in airbreathing propulsion and prior to that I have had industrial experience in aircraft engine inlet integration. The work I have done in the experimental investigation and numerical modeling of turbomachinery flow fields and engine stability contributed to my assignment to the Flight Dynamics Laboratory, Aero-Mechanical Division.

II. OBJECTIVES OF THE RESEARCH EFFORT

The performance of mixed compression supersonic inlets should meet the requirements of high total pressure recovery for maximum engine thrust and low distortion at design and off design conditions. It should have tolerance to transient changes in free stream Mach number, angle of incidence and engine corrected flow demand. The inlet bleed system should provide the needed boundary layer control, at reduced bleed drag, since it is the most significant component of inlet drag at cruise Mach number. The optimum bleed configuration meets these requirements by minimizing the bleed mass flow and maximizing the recovered bleed pressure. This requires a clear understanding of the nature of shock turbulent boundary layer interaction and the underlying mechanisms affecting boundary layer separation.

The objective of this work is to survey and assess the existing shock-wave/boundary-layer-interaction data base for validating flow computational efforts in supersonic inlets. The first part of the review concerns mixed compression supersonic inlets and their bleed system performance at design and off-design conditions. Based on the assessment of this data, specific areas related to shock wave/boundary

layer interaction bleed for flow separation control were identified. The last part of the review addresses this phenomena in various two and three dimensional flow configurations.

III. BACKGROUND

One of the problems that faces the designer of a supersonic inlet system is how to provide for the highest possible pressure recovery, at the mass flows required by the engine, within the vehicle imposed integration constraints and, along with the required stability. It is well known that one of the most important operational considerations in the design of a supersonic inlet system is its operational stability. Vehicles whose flight Mach numbers are between 1.0 and approximately 2.0 often have fixed geometry inlets because of the weight penalty and complexity of the variable geometry required to operate in the started mode. When the flight Mach number is about above 2.0, the recovery losses associated with the normal shock upstream of the inlet lip become excessive, and a started inlet requires variable geometry. The terminal shock wave in started inlets is stabilized in the diffusing section upstream of the compressor or fan face in a conventional installation. The closer to the inlet throat the terminal shock is allowed to move, the higher the inlet recovery. However, along with this benefit comes the increased risk of unstating the inlet. When the inlet unstarts and the terminal shock wave is expelled, the mass flow rate and pressure recovery are sharply reduced, the drag increases and a significant transient load is applied to the inlet structure. A large drop in pressure recovery, may cause the engine to stall and flame out [1]. Williams [2] described the complex starting process in mixed compression supersonic inlets.

Unstart can result from an internal disturbance such as a reduction in the inlet airflow requirement or from an external disturbance such as a gust. Bowditch et al. [3] reviewed the test data for 60-40, 40-60 and 20-80 mixed compression inlets to demonstrate the effect of external-internal supersonic area contraction ratio on the unstart limits and distortion. They also discussed the throat bypass system to improve the

stability and vortex generators to control distortion in supersonic inlets internal contraction. Krohn [4] discussed the means for suppressing buzz which is observed on supersonic inlets in subcritical operations. He investigated experimentally boundary layer bleed to prevent the instability which is triggered by the shock induced boundary layer separation on the spike surfaces, and demonstrated that instabilities could be avoided. Hiller et al. [5] used the results obtained from the different inlets tested during the preceding 10 years to demonstrate that the total pressure recovery, boundary layer bleed, and cowl drag have the greatest influence on aircraft range.

Since the performance of supersonic inlets is strongly affected by the boundary layer development over its internal surfaces, boundary layer bleed have been used to suppress separation and to provide good performance [2-7]. The gain in pressure recovery and stability is accompanied however with a loss in mass flow and an increase in drag which must be minimized by optimizing the amount of bleed and bleed configuration. Using the data from different axisymmetric and two-dimensional supersonic inlets designed for flight Mach numbers between 2.5 and 3.5, Bowditch [8] showed that a linear relation exists between the inlet to capture flow ratio, and the wetted to throat area ratio. The same data was correlated by Hiller et al. [5] in terms of the percentage of internal compression, which is often used to classify supersonic inlets. The results indicated a linear increase in the amount of bleed, with internal compression, with 70 percent more bleed required for two dimensional inlets at the same internal compression.

The bleed is accomplished through holes, porous wall sections, slots, and scoops which are distributed at the shock-boundary layer interaction locations along the ramp, cowl and side walls, for two dimensional inlets and cowl and centerbody, for axisymmetric inlets. Seyberg and Koncsek [9], discussed the bleed inlet design procedures, and the selection of bleed geometry. The performance characteristics of scoops, slots, and bleed holds affect the bleed drag and inlet stability. Bleed holes are simple to fabricate, and the hole size, spacing and slant angles can be easily adjusted according to the optimum

local condition. The low slant angle bleed holes, have higher flow coefficient, can operate at higher plenum pressure, and are therefore superior for minimizing bleed drag. In the throat region, 90° holes are used to provide maximum normal shock stability [9]. The determination of inlet contours and bleed systems in inlet design procedures are usually based on independent [10-14] or coupled [15] inviscid flow and boundary layer analyses. The shock/boundary-layer interaction regions are usually handled in a separate analysis [16] which requires empirical or semi-empirical relations [17]. These procedures cannot model the boundary-layer in the region of contained normal shocks [14, 16]. When the shock was strong enough to cause local separation [14, 16], the computations exhibited discrepancies with experimental measurements in started axisymmetric mixed compressor inlets [18-20]. Large flow separation regions might exist in supersonic inlets at high pitch or yaw angles [21]. In addition, the strong expelled shock during subcritical operations could cause boundary layer separation which alternately choke or unchoke the inlet throat [22]. Algorithms developed for the numerical solution of the unsteady Navier Stokes equations in supersonic inlets have also been used to predict steady state [23, 24] and oscillatory flows [25]. These procedures are capable in principle, of modeling strong shock boundary layer interaction and flow separation. However, comparisons with the steady state experimental results in supersonic inlets with boundary layer bleed [26] revealed discrepancies in the prediction of the shock location and velocity profiles.

IV. SUPERSONIC INLET PERFORMANCE

Several studies have been conducted to investigate the performance of supersonic inlets with bleed systems to control the shock-boundary layer interactions. Efforts were focused on total pressure recovery, total pressure distortions at the engine face and stability margins under different operating conditions. The experimental measurements in many of these studies, therefore consisted mainly of the total pressure recovery at the engine face, and the static pressure distribution over

the inner surfaces. Smeltzer and Sorensen [10,11] tested a mixed-compression axisymmetric inlet model with a traveling centerbody, cowl and centerbody bleed, bypass as well as secondary air systems upstream of the engine face and vortex generators downstream of the throat. The bleed slant angle was 20° in the forward regions, 40° in the midblade regions, and 90° in the throat, but the bleed hole diameter was unchanged. They measured the effect of altering the bleed and vortex generator configuration on the inlet performance, at the design inlet Mach number of 2.65. Experimental results were also presented at several inlet Mach numbers ranging between 0.8 and 1.4. The results of the experimental measurements included the static pressure distribution over the inner inlet surfaces and the total pressure distortion over the engine inlet face. Wong and Anderson [28,29] conducted an experimental investigation of a large-scale, two-dimensional mixed compression inlet model with a design Mach number of 3.0, to test its performance at off design transonic Mach numbers between 0.6 and 1.28. Variable features for off-design operation included adjustable ramp height system, and translating cowl. During transonic operation, boundary layer bleed was provided only on the ramp and side wall surfaces, but cowl bleed was eliminated to preclude the possibility of reverse flow through bleed holes. Their results showed the effect of throat boundary layer bleed and vortex generators on the engine inlet total pressure distribution, and boundary layer velocity profile, at different angles of attack and yaw. The inlet performance was found to be insensitive to variations in angle of attack and yaw between 0 and 4° , and vortex generators that proved advantageous at design speed were not significantly effective at transonic speeds.

In addition to the surface pressure distribution, Fukuda, Hingst and Reshotko [30,31] also measured the boundary layers velocity profiles over the cowl and centerbody at selected locations upstream and downstream of the oblique shock boundary layer interaction with bleed. The axisymmetric inlet was tested at $M = 2.5$ and $Re = 8.2 \times 10^6$ /meter in the NASA Lewis 10 ft x 10 ft wind tunnel at subcritical and critical

conditions. Bleed was applied at the first shock wave boundary layer interaction on the cowl and the first and second interactions on the centerbody. By blocking some of the bleed hole rows, it was possible to have the bleed applied across, upstream and downstream of the shock. The inlet was also tested with scoop bleed at the first centerbody shock boundary layer interaction. The boundary layer profiles were investigated before and after each interaction using flattened pitot tubes. The results of the measurements were presented to show the effect of bleed on the evolution of the transformed form factor, H_{tr} , the displacement thickness δ^* and the momentum thickness θ across the interaction regions. It was concluded from the results that, across-the-shock-bleed, should be avoided since H_{tr} decreased with bleed mass flow, then reached a plateau, but δ^* and θ continued to decrease. This was observed at a bleed of 30-40% of the boundary layer mass flow before the shock for normal holes, and at 45-50% for slanted holes.

Hingst and Johnson [18] presented the results of their experimental measurements in an axisymmetric inlet with 60% internal supersonic area contraction designed for Mach 2.5 with boundary layer bleed through rows of normal holes on the cowl and centerbody. The tests were conducted at two Reynolds numbers of 8.2×10^6 and 2.7×10^6 per meter. Static pressure taps were used to obtain the surface pressure and the boundary layer profiles were measured with translating pitot pressure probes, located on both sides of the shock impingements. At the lower Reynolds number, the laminar boundary layer separated at the first centerbody shock interaction, but reattached at the measuring location downstream of the shock. No separation was observed at the higher Reynolds number. Bleed in the aft portion of the centerbody produced reverse flow through the forward holes, resulting in separated boundary layer.

V. BLEED SYSTEM PERFORMANCE

A number of studies on bleed system performance in supersonic inlets were accomplished [10-13, 30-34]. The basis for the analytical development of a bleed system is the incorporation of mass removal in

the regions of boundary layer separation. In order to prevent boundary layer separation, some criteria is used, such as a limit on the value of shape factor or the exponent in the boundary layer velocity profile. Sorensen and Smeltzer [32] maintained an exponent of 3 or greater in the supersonic diffuser and of 7 or greater in the throat. Syberg and Koncsek [13] used the criteria that a shape factor of 1.3 corresponds to a "full" velocity profile, of one seventh power law, while a shape factor between 1.8 and 2 indicates a highly distorted profile close to separation. Fukuda et al. [30] based their evaluation of the bleed system performance on the shape factor, which was determined from the boundary layer profile measurements downstream of the shock-boundary layer interaction-bleed region.

Several factors affect the bleed system performance and consequently the boundary layer development in supersonic inlets, such as the bleed hole geometry, plenum chamber conditions and shock impact location relative to bleed. Slanting the bleed holes, leads to higher bleed pressure recovery, therefore minimizing the momentum drag of the overboard bleed flow. Slant angles of 20° are used in the forward bleed regions, but are increased to 40° in the middle and 90° in the throat region [10, 11, 32]. The trade of bleed mass flow for pressure recovery is necessary in the throat in order to avoid separation at the terminal shock. The effect of hole size on bleed system performance have been investigated by Fukuda et al. [30], who reported no significant effect of the hole size. The conclusions were based on results obtained from bleed through 0.159" and 0.38" diameter holes in the bleed zone. On the other hand, Wong [34] reported significant hole size effects, and recommended hole sizes below the boundary layer thickness for better bleed performance. The plenum pressure also affects the bleed mass flow, since it determines whether or not the flow in the bleed holes is choked. At present, these affects are accounted for empirically in bleed system designs [15]. Flow recirculation through the bleed holes, which might lead to separation, can be prevented if the plenum chamber is compartmented [32]. This also allows higher pressure recovery in each plenum. Syberg and Koncsek [13] concluded from their off-design

performance measurements that high recovery and good boundary layer behavior are obtained, up to the terminal shock followed by flow separation on the centerbody in the subsonic diffuser. This was observed when the inlet designed for $M=3.5$ was tested between $M = 1.7$ and 3.2 . In the same study [13] the measured overall bleed flow rate were about 20% below the predicted values. Similar accuracy of bleed estimates were reported by Sorensen and Smeltzer [32] with the forward, mid and overall cowl bleed 20% below prediction, with better agreement for the centerbody bleed.

It is clear from the preceeding discussion that the measurements are not sufficient to describe the complex flow in the shock/boundary layer interaction regions [35].

The review and assessment of additional experimental investigations of shock-wave/boundary-layer interaction in other flow configurations is therefore included.

VI. SHOCK WAVE/BOUNDARY LAYER INTERACTIONS

Effect of Suction

A number of experimental studies were conducted to investigate the effect of bleed on shock boundary layer interaction, in different geometric configurations [36]. The test arrangements included oblique [37-40], glancing [41], and conical [42] shocks interacting with boundary layers over flat plates [37-41], airfoils [43] and inside cylinders [42]. The bleed through holes [39,41,42], slots [43] or porous wall segments [37,38,40,43] were implemented upstream [37,39,42,43], downstream [39] and across [37-43] the shock. Smits and Wood concluded in their review [46] that experimental investigation of the effect of suction are influenced by surface roughness, and departures from two dimensionality, and that skin friction measurements in most of the studies are inadequate.

When bleed holes or porous wall segments extend across the shock impingement location, sometimes no bleed and even blowing due to flow recirculation inside the bleed chamber, can result upstream of the shock, due to the large surface pressure difference [47]. Blowing [48,

49] and roughness [40, 46, 49, 50] produce somewhat similar influence on the boundary layer velocity profile, that is quite different from the effect of bleed.

Flow Separation

Strong shock boundary layer interactions leading to flow separation have been investigated experimentally in various configurations including two dimensional flows resulting from an oblique shock interacting with a flat plate boundary layer [51, 52], compression corner [53, 54, 55], near normal shocks in transonic flows inside symmetric [56] and nonsymmetric [57] and axisymmetric [65] channels, axisymmetric flow at the junction of a bump with a cylinder [58] and three dimensional shock boundary interaction in different configurations [59-60]. The ratio between the separation length and the undisturbed boundary layer just upstream of the separation was found to exhibit various trends ranging between increasing [61], decreasing [62], and remaining constant [63, 64] with increasing Reynolds number.

Effect of Shock Boundary Layer Interaction on Turbulence

None of the inlet flow experimental investigations, reported any turbulence shear stress, turbulence kinetic energy or other fluctuating velocity measurements which can be used to validate the turbulence models in supersonic inlet flow field computation. It has been shown in external flows, that the turbulence model in the Navier Stokes code, affects the predicted shock location [66, 67], whether or not separation is predicted, and the extent of separation [67-69]. Turbulence measurements in shock boundary layer interactions were reported in a small number of experimental investigations for a normal shock on a flat plate [70], inside a cylinder [71] in a supersonic compression corner [53,54,72-74] and over a cylinder with flare [79].

VII. RECOMMENDATIONS

Experimental data in the form of surface pressure for a number of configurations demonstrates that the boundary layer separation can be

controlled by bleed in the shock wave/boundary layer interaction zone. However, contradictions exist between the results of different investigations, regarding the most effective bleed configuration, for controlling separation. The disagreement is in the bleed location (upstream, downstream or across the shock) and in the bleed hole size. Local bleed flow distribution and turbulence measurements are very scarce in the experiments, which leads to difficulty in using the data for code assessment. In addition, large experimental uncertainties are associated with the data reduction techniques of pitot probes and hot wires data under the shock wave boundary layer interaction conditions.

In view of this, and the lack of experimental data on the efficiency of pressure recovery of unchoked holes, it is recommended that a systematic study be conducted to investigate the flow field in the shock wave/boundary layer/bleed zone. A numerical investigation can provide detailed information on the local bleed flow variation and flow characterization in the interaction zone. This information is essential for the accurate simulation of the plenum conditions and bleed system performance in supersonic inlet computations.

VIII. REFERENCES

1. Sugiyama, Y., Tabakoff, W. and Hamed, A., "J85 Surge Transient Simulation," 8th International Symposium on Air Breathing Engines, AIAA Symposium Volume, June 1987, pp. 568-578.
2. Williams, J., "Aircraft Performance Considerations for Noise Reduction," AGARD LS-67, pp. 12-14.
3. Bowditch, D.N., Coltrin, R.E., Sanders, B.W., Sorensen, N.E. and Wasserbauer, J.F., "Supersonic Cruise Inlets," Aircraft Propulsion, NASA-SP-259, November 1970, pp. 283-312.
4. Krohn, E.O., "Inlet Buzz in Ramjets and Its Suppression," 8th International Symposium on Air Breathing Engines, AIAA Symposium Volume, June 1987, pp. 568-578.
5. Hiller, W.H., Batterton, P.G., Burstadt, P.L. and Szuch, J.R., "Propulsion Systems Technology," Aeronautical Propulsion, NASA SP-381, May 1975, pp. 387-440.

6. Imfeld, W.F., "Development Program for the F-15 Inlet," *Journal of Aircraft*, Vol. 13, No. 4, 1976, pp. 268-291.
7. Rettie, I.H. and Lewis, W.G.E., "Design and Development of an Air Intake for a Supersonic Transport Aircraft," *J. of Aircraft*, Vol. 5, No. 6, 1968, pp. 513-521.
8. Bowditch, D.N., "Some Design Considerations for Supersonic Cruise Mixed-Compression Inlets," AIAA Paper 73-1269, November 1973.
9. Syberg, J. and Koncsek, L., "Bleed System Design Technology for Supersonic Inlets," AIAA Paper No. 72-1138, 1972.
10. Sorensen, N.E., Smeltzer, D.B. and Latham, E.A., "Advanced Supersonic Inlet Technology," *J. Aircraft*, Vol. 10, 1973, pp. 278-282.
11. Smeltzer, D.B., Sorensen, N.E., "Analytical and Experimental Performance of Two Isentropic Mixed Compression Axisymmetric Inlets at Mach Numbers 0.8 to 2.65," NASA TND-7320, June 1973.
12. Sorensen, N.E. and Smeltzer, D.B., "Performance Estimates for a Supersonic Axi-Symmetric Inlet System," *J. Aircraft*, Vol. 9, 1972, pp. 703-706.
13. Syberg, J. and Koncsek, J.L., "Experimental Evaluation of an Analytically Derived Bleed System for a Supersonic Inlet," *J. Aircraft*, Vol. 13, 1976, pp. 792-797.
14. Hingst, W.R. and Towne, C.E., "Comparison of Theoretical and Experimental Boundary Layer Development in a Mach 2.5 Mixed Compression Inlet," NASA TM X-3026, April 1974.
15. Reyhner, T.A. and Hickox, T.E., "Combined Viscous Inviscid Analysis of Supersonic Inlet Flow Fields," *J. Aircraft*, Vol. 9, No. 8, 1972, pp. 589-595.
16. Seebaugh, W.R., Paynter, G.C. and Childs, M.E., "Shock Reflection From a Turbulent Boundary Layer with Mass Bleed," *J. Aircraft*, Vol. 5, No. 5, 1968, pp. 461-467.
17. Pinckney, S.Z., "Semiempirical Method for Predicting Effects of Incident-Reflecting Shocks on the Turbulent Boundary Layers," NASA TN D-3029, 1965.

18. Hingst, W.R. and Johnson, D.F., "Experimental Investigation of Boundary Layers in an Axisymmetric, Mach 2.5 Mixed Compression Inlet," NASA TMX-2903, 1973.
19. Smeltzer, D.B. and Sorensen, N.E., "Investigation of a Nearly Isentropic Mixed-Compression Axisymmetric Inlet System at Mach Numbers 0.6 to 3.2," NASA TN D-4557, 1968.
20. Koncsek, J.L. and Seyberg, J., "Transonic and Supersonic Test of a Mach 2.65 Mixed Compression Axisymmetric Intakes," NASA CR-1977, 1972.
21. Surber, L. and Sedlock, P., "Effects of Airframe-Inlet Integration or Half-Axisymmetric and Two-Dimensional Supersonic Inlet Performance," AIAA Paper 78-960, July 1978.
22. Martin, A.W., Koslin, L.C. and Sidney, D.M., "Dynamic Distortion at the Exit of a Subsonic Diffuser of a Mixed Compression Inlet," NASA CR-1644, December 1970.
23. Knight, D.D., "Calculation of High Speed Inlet Flows Using the Navier-Stokes Equations," Volume I: Description of Results," AFFDL-TR-79-3138, February 1980.
24. Knight, D.D., "Improved Calculation of High Speed Inlet Flows. Part I Numerical Algorithm," AIAA J., Vol. 19, No. 1, January 1981, pp. 34-41, and "Part II: Results," AIAA J., Vol. 19, No. 2, February 1981, pp. 172-179.
25. Newsome, R.W., "Numerical Solutions for Steady and Unsteady Oscillatory Flow About an Axi-Symmetric Inlet," AFWAL-TR-83-3058, AFIT/DS/AA/82-2, April 1985.
26. Carter, T.D. and Spong, E.D., "High Speed Inlet Investigation. Vol. I Description of Program and Results; Vol. II Data Summary," AFFDL-TR-77-105, November 1977.
27. Adamson, T.C. and Messiter, A.F., "Analysis of Two-Dimensional Interactions Between Shock Waves and Boundary Layers," Annual Review of Fluid Mechanics, Vol. 12, 1980, pp. 103-138.

28. Anderson, W.E. and Wong, N.D., "Experimental Investigation of a Large-Scale, Two-Dimensional, Mixed Compression Inlet System- Performance and Design Conditions, $M_\infty = 3.0$," NASA TM-X-2016, 1970.
29. Wong, N.D. and Anderson, W.E., "Experimental Investigation of a Large-Scale, Two-Dimensional, Mixed-Compression Inlet System. Internal Performance and Drag at Transonic Conditions, $M_\infty = 0.6$ to 1.28," NASA TN D-7445.
30. Fukuda, M.K. Hingst, W.G. and Reshotko, E., "Control of Shock Boundary Layer Interactions by Bleed in Mixed Compression Inlets," NASA CR 2595, 1975.
31. Fukuda, M.K., Hingst, W.G. and Reshotko, E., "Bleed Effects on Shock/Boundary-Layer Interactions in Supersonic Mixed Compression Inlets," Journal of Aircraft, Vol. 14, No. 2, February 1977, pp. 151-156.
32. Sorensen, N.E. and Smeltzer, D.B., "Performance Estimates for a Supersonic Axisymmetric Inlet System," J. Aircraft, Vol. 9, No. 10, 1972, pp. 703-706.
33. Smeltzer, D.B. and Sorensen, N.E., "Investigation of a Mixed Compression Axisymmetric Inlet System at Mach Numbers 0.6 to 3.5," NASA TN D-6078, 1970.
34. Wong, W.F., "The Application of Boundary Layer Suction to Suppress Strong Shock-Induced Separation in Supersonic Inlets," AIAA Paper No. 74-1063, October 1974.
35. Delery, J. and Marvin, J.G., "Shock-Wave Boundary Layer Interactions," AGARD-AG-280, February 1986.
36. Delery, J.M., "Shock Wave/Turbulent Boundary Layer Interaction and Its Control," Progress in Aerospace Sciences, Vol. 22, 1985, pp. 209-280.
37. Strike, W.T. and Rippy, J., "Influence of Suction on the Interaction of an Oblique Shock with a Turbulent Boundary Layer at Mach 3," AEDC-TN-61-129, October 1961.

38. Lee, D.B. and Leblanc, R., "Interaction ond de Choc Oblique-Couche Limite sur Paroi avec Aspiration," AGARD-CP-365, "Improvement of Aerodynamic Performance Through Boundary Layer Control and High Lift Systems," Paper 23, Aug. 1984.
39. Hingst, W.R. and Tanji, F.T., "Experimental Investigation of Two-Dimensional Shock-Boundary Layer Interaction with Bleed," AIAA Paper 83-0135, 1973; also NASA TM 83057, 1973.
40. Benhachmi, C., "Shock Wave/Turbulent Boundary Layer Interaction with Continuous Suction," Ph.D. Thesis, Case Western Reserve University, August 1988.
41. Barnhart, P.J., Greber, I. and Hingst, W.R., "Glancing Shock Wave-Turbulent Boundary Layer Interaction with Boundary Layer Suction," AIAA Paper No. 88-0308, January 1988.
42. Seebaugh, W. and Childs, M., "Conical Shock Wave Boundary Layer Interaction Including Suction Effects," Journal of Aircraft, Vol. 7, No. 4, Aug. 1970, pp. 334-340.
43. Thiede, P., Krogmann, P. and Stanewsky, E., "Active and Passive Shock/Boundary Layer Control on Supercritical Airfoils," AGARD-CP-365, Improvement of Aerodynamic Performance Through Boundary Layer Control and High Lift Systems, Paper 24, Feb. 1985.
44. Kuehn, D.M., "Experimental Investigation of the Pressure Rise Required for the Incipient Separation of Turbulent Boundary Layers in Two Dimensional Supersonic Flow," NASA Memo 1-21-59A, February 1959.
45. Seebaugh, W.R., "An Investigation of the Interaction of a Shock Wave and Turbulent Boundary Layers in Axially Symmetric Internal Flow Including the Effects of Mass Bleed," Ph.D. Thesis, University of Washington, 1968.
46. Smits, A.J. and Wood, P.H., "The Response of Turbulent Boundary Layers to Sudden Perturbations," Annual Review of Fluid Mechanics, Vol.17, 1985, pp. 321-358.
47. Lee and Leblanc, "Interaction und de Chock Oblique-Cauché Limite sur Paroi Poreuse avec Aspiration," AGARD CP-365, Paper 23, 1984, Strike and Rippey, AEDC-TN-61-129.

48. Squire, L.C. and Smith, M.G., "Interaction of a Shock Wave with a Turbulent Boundary Layer Disturbed by Injection," Royal Aeronautical Society, May 1980, pp. 85-110.
49. Voisinet, R.L.P., "Combined Influence of Roughness and Mass Transfer on Turbulent Skin Friction at Mach 2.9," AIAA Paper No. 79-0003, January 1979.
50. Berg, D.E., "Surface Roughness Effects on the Hypersonic Turbulent Boundary Layer," Ph.D. Thesis, California Institute of Tech., Pasadena, 1977.
51. LaBalleur, J.C., Delery, J., "Etude experimentale de l'interaction d'une onde de chock plane et d'une couche limite turbulent a $M_\infty = 1.92$," Report ONERA No. 4/7078, Oct. 1970.
52. Law, C.H., "Supersonic Shock Wave Turbulent Boundary Layer Interactions," AIAA Journal, Vol. 14, No. 6, 1976, pp. 730-734.
53. Ardonceau, P.L., "The Structure of Turbulence in a Supersonic Shock-Wave/Boundary-Layer Interaction," AIAA Journal, Vol. 22, No. 9, 1984, pp. 1254-1262.
54. Ardonceau, P., Lee, D.H., de Roquefort, T.L. and Goethals, R., "Turbulence Behavior in a Shock Wave/Boundary Layer Interaction," AGARD-CP-271, Paper 8, 1979.
55. Settles, T.J., Fitzpatrick, T.J., Bogdonoff, S.M., "Detailed Study of Attached and Separated Compression Corner Flowfield in High Number Supersonic Flow," AIAA J., Vol. 17, No. 6, 1979, p. 579-585.
56. Delery, J., "Experimental Investigation of Turbulence Properties in Transonic Shock/Boundary Layer Interaction," AIAA Journal, Vol. 21, No. 2, 1983, pp. 180-185.
57. LaBalleur, J.C. and Blaise, D., "Methode Numerique d'Interaction Visqueux-Non Visqueux pour des Ecoulements Internes Decolles et L'Interaction Couche Limite-Orde de Chock," AGARD CP 280, Transonic and Supersonic Phenomena in Turbomachines, Paper 13, March 1987.
58. Buchalo, W.D. and Johnson, D.A., "An Investigation of Transonic Turbulent Boundary Layer Separation Generated on an Axisymmetric Flow Field," AIAA Paper 79-1479, 1979.

59. Kussoy, M.I., Viegas, J.R. and Horstman, C.C., "Investigation of a Three-Dimensional Shock Wave Separated Turbulent Boundary Layer," AIAA Journal, Vol. 18, No. 12, Dec. 1980, pp. 1477-1484.
60. Benay, R., Pot, T. and Delery, J., "Etudes Fundamentales sur les Interactions orde de Choc-Couche Limite dans un Canal Tridimensional," AGARD CP 280, Paper 1, 1986.
61. Zukoski, E.E., "Turbulent Boundary-Layer Separation in Front of a Forward Facing Step," AIAA Journal, Vol. 5, No. 10, 1967, pp. 1746-1753.
62. Chapman, D.R., Kuehn, D.M., and Larson, H.K., "Investigation of Separated Flows in Supersonic and Subsonic Streams with Emphasis on the Effect of Transition," NASA Report 1356, 1957.
63. Roshko, A. and Thomke, G.J., "Flare-Induced Separation Lengths in Supersonic Turbulent Boundary Layers," AIAA Paper No. 75-6, 1975.
64. Settles, G.S., Bogdonoff, S.M. and Vas, I.E., "Incipient Separation of a Supersonic Turbulent Boundary Layer at Moderate to High Reynolds Numbers," AIAA Paper ;No. 75-7, 1975.
65. Mateer, G.G. and Viegas, J.R., "Mach and Reynolds Number Effects on a Shock-Wave/Boundary-Layer Interaction," AIAA Paper 79-1503, July 1979 and AIAA Journal, Vol. 18, No. 8, 1980, pp. 1016-1018.
66. Coakley, T.J., "Impact of Turbulence Modeling on Numerical Accuracy and Efficiency of Compressible Flow Simulation," NASA-TM-88333, September 1986.
67. LeBalleur, J.C. and Blaise, D., "Methode Numerique d'Interaction Visqueux-non Visqueux pour les Ecoulements Internes Decolles et l'Interaction Couche Limite-Onde de Choc," AGARD-CP-401, Transonic and Supersonic Phenomena in Turbomachines, Paper 13, September 1986.
68. Johnson, D.A., "Prediction of Transonic Separated Flow with an Eddy-Viscosity/Reynolds-Shear-Stress Closure Model," AIAA Paper No. 85-1683, July 1985.
69. Horstman, C.C. and Johnson, D.A., "Prediction of Transonic Separated Flows", AIAA Journal, Vol. 22, No. 7, 1984, pp. 1001-1002.

70. Delery, J.M., "Experimental Investigation of Turbulence Properties in Transonic Shock Boundary Layer Interactions," AIAA Journal, Vol. 21, No. 2, 1983, pp. 180-185.
71. Mateer, G.G., Brosh, A. and Viegas, J.R., "A Normal-Shock Wave Turbulent Boundary-Layer Interaction at Transonic Speeds," AIAA Paper 76-161, Washington, D.C., January 1976.
72. Muck, K.E. and Smits, A.J., "The Behavior of a Compressible Turbulent Boundary Layer Under Incipient Separation," Proceedings of the 4th Turbulence Shear Flow Conference, Karlsruhe, 1983.
73. Hayakawa, K., Smits, A.J. and Bogdonoff, S.M., "Hot Wire Investigation of Unseparated Shock Wave/Turbulent Boundary Layer Interaction," AIAA Paper No. 82-0985, 1982.
74. Hayakawa, K., Muck, K.C., Smits, A.J. and Bogdonoff, S.M., "The Evolution of Turbulence in Shock-Wave/Boundary Layer Interactions," paper presented at 8th Australian Fluid Mechanics Conference, University of Newcastle, N.S.W., Nov. 28-Dec. 2, 1983.
75. Debieve, J.F., Gouin, H. and Gaviglio, J., "Evolution of the Reynolds Stress Tensor in a Shock Wave-Turbulence Interaction," Indian Journal of Technology, Vol. 20, March 1982, pp. 90-97.
76. Brown, J.D., Brown, J.L., Kussoy, M.I., Holt, M. and Horstman, C.C., AIAA Journal, Vol. 26, No. 1, Jan. 1988, pp. 52-56.
77. Settles, G.S., Fitzpatrick, T.J., Bogdonoff, S.M., "Detailed Study of Attached and Separated Compression Corner Flow Fields in High Reynolds Number Supersonic Flow," AIAA Journal, Vol. 17, No. 6, 1979, pp. 579-585.
78. Horstman, C.C. and Rose, W.C., "Hot Wire Anemometry in Transonic Flows," AIAA Journal, Vol. 15, March 1972, pp. 395-401.
79. Hayakawa, K., Smits, A.J., Bogdonoff, S.M., "Turbulence Measurements in a Compressible Reattaching Shear Layer," AIAA Journal, Vol. 22, No. 7, pp. 889-895.

1988 USAF-UES SUMMER FACULTY RESEARCH PROGRAM

Sponsored by the
AIR FORCE OFFICE OF SCIENTIFIC RESEARCH

Conducted by
Universal Energy Systems, Inc.

FINAL REPORT

Prepared by:	Yulian B. Kin, Ph.D.
Academic Rank:	Associate Professor
Department and	Engineering Department
University:	Purdue University Calumet
Research Location:	Flight Dynamics Laboratory
USAF Researcher:	Robert McCarty
Date:	16 August 1988
Contract No:	FY9620-87-R-0004

FAILURES OF F-16 TRANSPARENCIES
ANALYSIS AND FAILURE PREVENTION RECOMMENDATIONS

by

Yulian B. Kin

ABSTRACT

Recently, some F-16 aircraft have experienced damage (cracks and crazes) at the bolt holes of the canopy transparencies. In some units the cracks propagated from the holes to the forward end of the transparency in flight, and this represents a serious problem for the F-16 fleet.

The nature and mechanics of the failures are not fully understood. Therefore, the investigation of the failure mechanics and the recommendations based on that analysis were core endeavors of this research.

ACKNOWLEDGEMENTS

I wish to thank the Air Force Systems Command and the Air Force Office of Scientific Research for sponsorship of this research. Universal Energy Systems must be mentioned for their concern and help to me in all administrative, directional and social aspects during the summer appointment and pre-summer visit.

I am grateful to Mr. Robert McCarty. He provided support, attention, and a comfortable working atmosphere. The help of Mr. Michael Gran was invaluable in quickly overcoming technical roadblocks. I appreciate very much Michael's help with my computer needs. The help of Mr. William Pinnell in sharing experimental data of frameless canopies was also important. Many thanks to Mrs. Evelyn Schutte for help in preparation of this report. Dr. Arnold Mayer's interest in every phase of my summer and possible future projects served as a source of encouragement.

I. INTRODUCTION:

Reports of F-16 transparency failures have been received and have given rise to concern about preventing future failures. Mechanics of these transparency failures are not fully understood, so investigation of the nature of these failures was the starting point of the research.

It was assumed that fatigue causes these failures in some F-16 transparencies and hence, measures to prevent fatigue were also under consideration. The problem was complicated by the fact that no fatigue characteristics of the F-16 transparency material were found.

II. OBJECTIVES OF THE RESEARCH EFFORT:

The immediate objectives of the research were to:

1. Investigate and describe failure mechanics of F-16 transparencies related to the occurrence of bolt hole cracking.

2. Based on the investigated failure modes, propose ways to prevent similar failures in the future.

The long-term objective of the research was to initiate development of technical specifications and requirements for the design, manufacturing, testing and maintenance of canopies. This goal could be achieved on the basis of multiple preliminary tests.

III. FAILURE MECHANICS

The F-16 transparencies are manufactured from flat laminated composites which in general consist of acrylic and polycarbonate structural plies, interlayers and protective surface coatings.

An initially flat laminated sheet is bent to form the final shape of the transparency. After that, the transparency is trimmed and drilled around its periphery, sealed around its edge, and bolted to a metal frame. The assembled canopy is fixed on an aircraft structure. The transparency holes and counterbores for the bolts and bushings are machined independently from frame holes, but with the tolerances to provide interchangeability. However, deviations of the hole pitches in different units still exist. The bushings inserted into the transparency holes are sometimes molded and sometimes machined. Sharp edges and significant eccentricities between the shoulder and outside and inside diameters have been observed for the machined bushings.

Failure analysis was performed on the basis of the reports (1, 2, 3) given to the author by Flight Dynamics Laboratory Engineers, and on the basis of the actual canopies collected by the Flight Dynamics Laboratory at Wright-Patterson Air Force Base. All reports and observations showed many crazes and small cracks occurred in the transparencies near the bolt holes. The reports pointed out that cracks started from bolt holes and propagated to the forward end of the canopies. The ten sketch analysis suggested below is given to explain the reasons for this particular path of crack propagation.

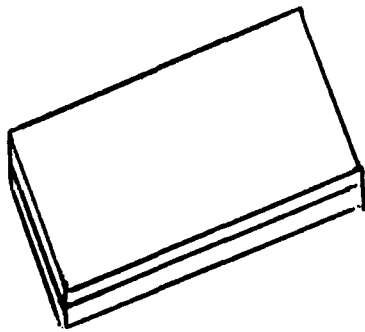


Fig. 1

An initially flat sheet
of transparency composite
material.

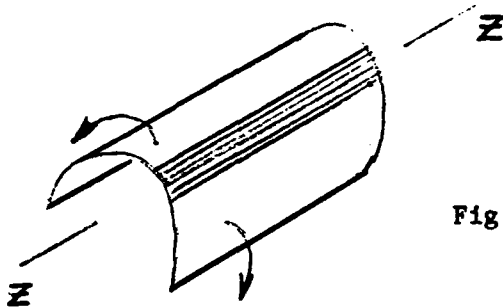


Fig. 2

Transparency forming.
Bending about Z axis.
Creation of residual
stresses. The shaded area
is the most stressed
zone (critical zone).

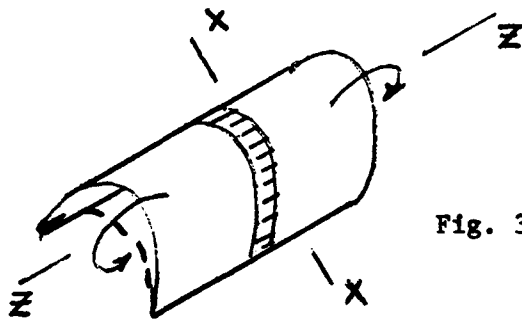


Fig. 3

Transparency forming.
Nonsymmetrical bending
about X axis. The shaded
area is the critical zone.

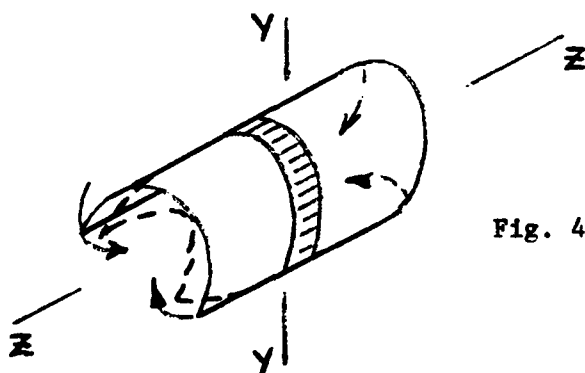


Fig. 4

Transparency forming.
Bending about Y axis.
The shaded area is the
critical zone.

Steps (2), (3) and (4) may occur simultaneously.

Therefore, the final simplified situation is presented on sketch (5).

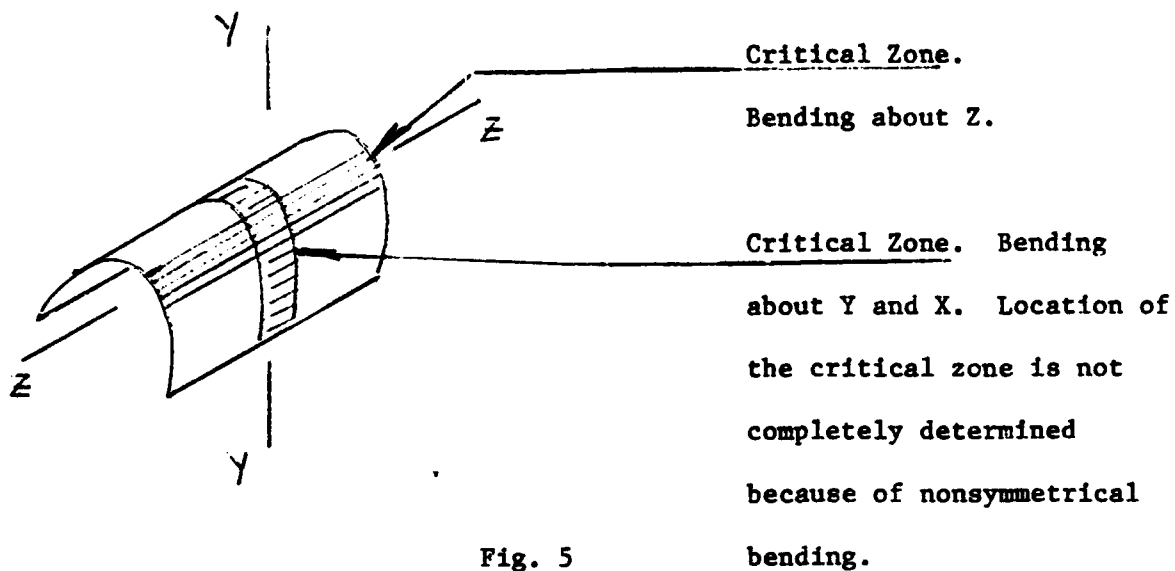


Fig. 5

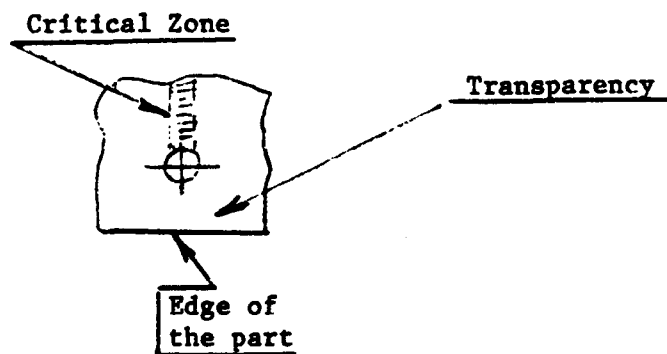
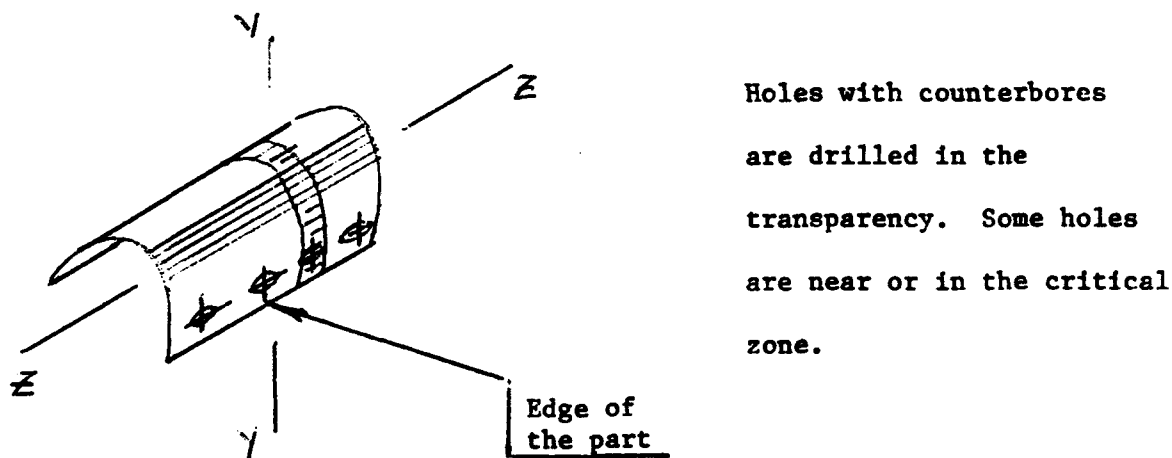


Fig. 6

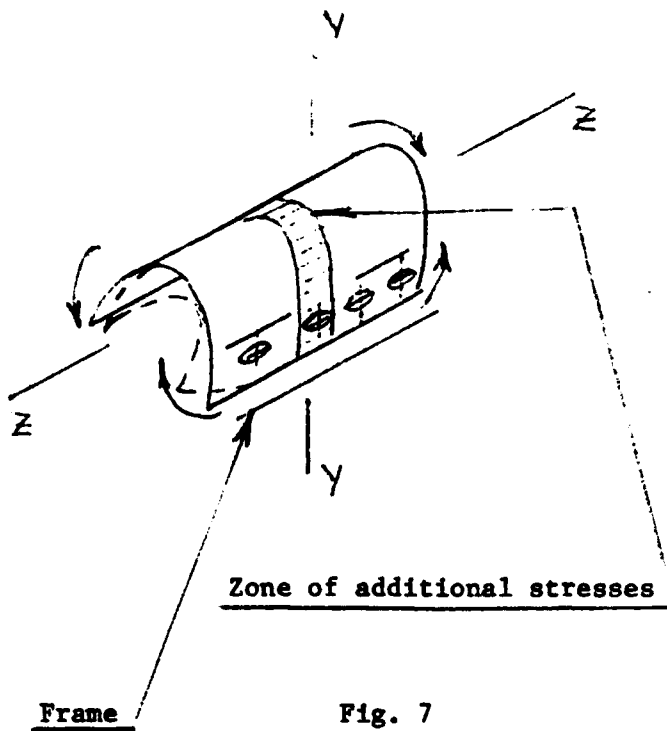


Fig. 7

Formed (Sketch 4)

transparency is installed into the frame. Additional bending about Y.

Combination of the transparency and the frame is

random. The holes already been drilled

independently in the transparency and in the

frame. There is a possibility that new

additional residual stresses are created

because of the deviations in the transparency and

frame shapes and because of the differences between

mating part hole pitches.

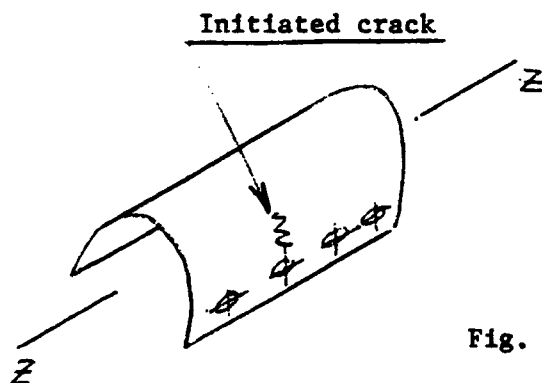


Fig. 8

The hole (for example, #2)

is a stress concentration factor and during bending

(Sketch #7) a microcrack is initiated near the most

critical hole. The

direction of the crack propagation is formed by the holes (1) and (3) equally influencing the initial crack [4].

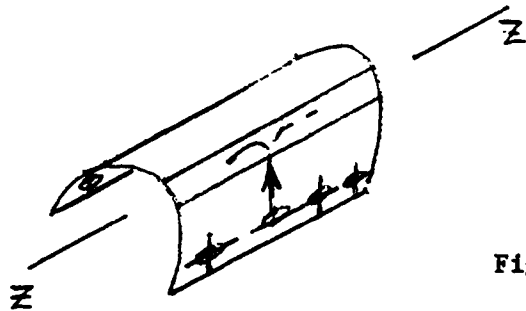


Fig. 9

The crack progresses up to the critical weakened zone and rotates almost 90° .

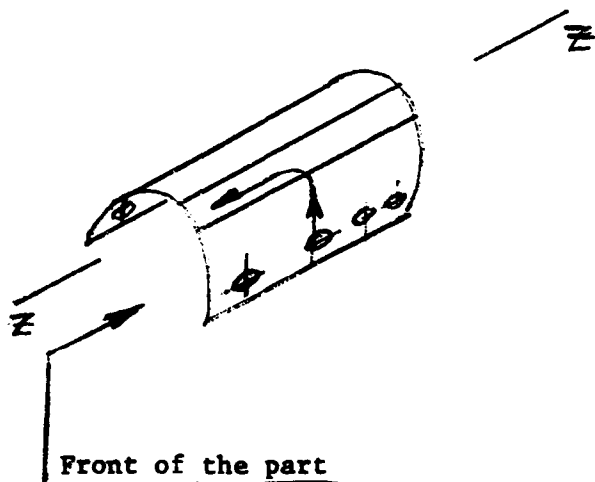


Fig 10.

The crack propagates toward the front. Two reasons for such direction can be assumed: (1) The critical zone was formed closer to the front during non-symmetrical bending about X. The front part of the used canopy was more loaded and therefore, more damaged and weakened than the back part.

It was already mentioned that most cracks in the investigated cases were initiated at or near the bolt holes. From the author's point of view this happens basically because of design or manufacturing imperfections. Some examples are given below.

1. Bushings and counterbores in some cases have sharp edges and therefore, increased stress concentration factors.

2. Taking into account the bushing eccentricity and independent machining of holes in the frame and the transparency, it is easy to create significant additional stresses at critical points (corners) of transparency counterbores during bushing installation. The possible cases are shown in Figure 11.

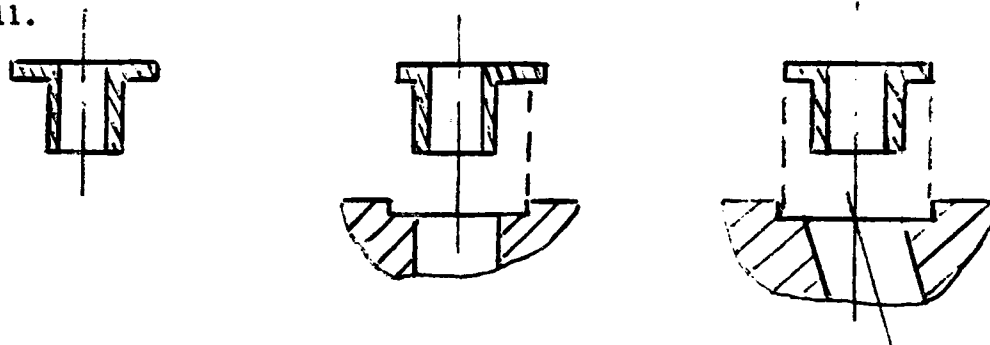


Fig. 11

3. The hole pitches are different in pairs of transparencies and frames. Therefore, there are no clearances between some bolts and bushing hole surfaces. This eventually causes additional stress concentration at the bushing and counterbore corners after the bolts are tightened.

Bolts and bushings have different coefficients of temperature expansion. Because of this, the bushings are pushed by the bolts against the counterbore edges causing crazes and initiating cracks. The situation is aggravated in the presence of forced vibrations.

4. In some designs, a transparency is rigidly fixed on a canopy frame, and hence, subject to all frame motions. This can cause undesirable stresses of unpredictable magnitude, direction, and time within the canopy.

5. According to the Texstar Plastics reports, the most serious damage appeared near the latch hook holes. One could assume that those transparencies were constrained near the hooks when canopies were tightened on the aircraft structure. Vibrations and temperature deformations could then create additional stresses near latch hook holes.

6. There was evidence of frame corrosion which was especially active near the holes. During the corrosion process, hard oxides accumulated in the confined space between frame wall and transparency. They could be embedded into the bushings, damaging their shoulders, or into the transparency, initiating crazes and cracks. Hard oxides could also be considered as additional stress concentration factors. When pressed against the bushing shoulders, they could cause crazes near the counterbore edges.

IV. RECOMMENDATIONS:

a. The creation of residual stresses during manufacturing process is obvious. Magnitudes of the residual stresses and the precise locations of critical zones can be determined by special experiments with strain gages which the author has proposed earlier. The results of these experiments will provide additional conclusions and recommendations for design and manufacturing.

b. In some cases the canopy is replaced because of the multiple crazes or cracks near the holes or because of developing a long crack as shown in [1, 2]. All these cases of failure exhibit fatigue characteristics, and no technology improvements can completely prevent failures due to fatigue and fracture. Therefore, the fatigue potential of the transparency should be known to predict canopy life based on fatigue and fatigue crack propagation. Currently, no fatigue strength characteristics for the F-16 transparency composite exist. Fracture parameters for this material as a whole unit are also unknown. Therefore, it is recommended to investigate fatigue characteristics of the materials used for the aircraft transparencies and develop both long-term and accelerated test methods. An accelerated method can be very useful to control manufacturing processes.

c. Canopies do not have certificates which show their service history. Hence, it is almost impossible to make reliable conclusions, predict the future canopy behavior, and assign maintenance inspection intervals in these cases. Therefore, it is recommended to establish canopy reliability service. To provide it, many different tests should be performed, reliable statistical data collected, and probably special software developed. One of the very important outcomes of this work is the development of a relatively simple service history form. After that, reliable maintenance reports can be made.

It can be added that Flight Dynamics Laboratory has been pursuing this goal for a number of years.

d. A portable device should be used for periodic inspections during canopy operational use and after all manufacturing steps. It was recommended to contact R&J Company which can develop the required device using acoustography method.

REFERENCES

1. Service Report Investigations SR1 375 S/N 0308, F-16 FWD "C" Transparency. Contract No. F-33657-82-C-2034 Texstar Plastics, August 22, 1986.
2. Service Report Investigations SR1 374 S/N 0217, F-16 FWD "C" Transparency, Contract No. F-42600-85-D-4910 Texstar Plastics, August 4, 1986.
3. FIER (M. Kelley,) Examination Report. Wright-Patterson AFB, June 27, 1986.
4. Chudnovsky A., Chaoik., Moet A., Curvilinear Crack Layer Propagation Journal of Materials Science Letter 6 (1987) 1033-1038.

1988 USAF-UES SUMMER FACULTY RESEARCH PROGRAM/
GRADUATE STUDENT RESEARCH PROGRAM

Sponsored by the
AIR FORCE OFFICE OF SCIENTIFIC RESEARCH

Conducted by the
Universal Energy Systems, Inc.

FINAL REPORT

Visual Capabilities on a Robot Aided Aircraft
Refueler Prototype

Prepared by:	Augustus Morris, Jr., Ph.D.
Academic Rank:	Assistant Professor
Department and	Manufacturing Engineering
University:	Central State University
Research Location:	AFWAL/FIEMB Wright Patterson Air Force Base
USAF Researcher:	Mangal Chawla, Ph.D.
Date:	September 30, 1988
Contract No:	F49620-87-R-0004

Visual Capabilities on a Robot Aided Aircraft
Refueler Prototype

by

Augustus Morris, Jr., Ph.D.

ABSTRACT

The Special Projects Group of the Flight Dynamics Laboratory at Wright Patterson Air Force Base is researching robotics as an in-house project. In particular, robotics is being looked at as a means of providing aircraft maintenance during times of chemical warfare. A scaled demonstration system was constructed to maintain a 1/8 scale F-16 aircraft. The present robotic system was capable of pick and place movements under the teach mode. The upgraded version integrates a vision system so that the robot can move to any coordinates within its workspace. The specific task tested was aircraft refueling. Traditional image processing techniques were tried but proved to be too slow for the computer presently used. An ad hoc approach was used to determine the coordinates and orientation of the fuel port so that the robot could successfully locate and insert the fuel nozzle in the refueling port.

Acknowledgements

I wish to thank the Air Force Office of Scientific Research for the sponsorship of this research. Universal Energy Systems need also be recognized for all the support and help I received.

My hands on experience this summer has been very rewarding and I thank Dr. Mangal Chawla for giving me all the help and guidance of a Technical Focal Point. Mr. David J. Perez, the Technical Manager of the Group, has also given me encouragement. The project would never have been possible without the computer support of Mr. Greg Kettell and the technical support of Mr. William Smith. 1st Lt. Sam Hagins and Ms. Patty Schlemmer also made the summer very enjoyable. Overall, I thank the entire staff of the Special Projects Group and Flight Dynamics Laboratory for giving me this unique opportunity to work with them side by side.

I. INTRODUCTION

The field of robotics has exploded in growth in the last decade mainly due to the advent of more powerful microprocessors. It is now possible for many robots to operate fully under microcomputer control. This has brought potential robotic applications within the reach of researchers in many diverse disciplines.

The Special Projects Group of the Flight Dynamics Laboratory have been interested in robotic applications of aircraft turnaround. Two important tasks selected under present consideration are aircraft refueling and rearming. Prior to this summer, the lab had a 1/8 scale model of the F-16 and a gantry frame representative of an airport hanger with a robot hanging down from above. This robotic system had the capabilities of picking and placing objects anywhere within its workspace by means of the teach mode.

This system ;however, had no sensor capabilities. The ability of the robot to examine the environment is prerequisite to any intelligence the robot may have. It was therefore desired to integrate a vision system to the present setup in order to give the robot a sense to "see".

My background is basically in the area of control system modeling of man-machine biomechanical systems. Many

of techniques used for this modeling are also used in the robotics field. The Manufacturing Engineering department of Central State University is striving towards an expertise in robotic manipulators in which I will play a fundamental role. The uniqueness of my university position along with the robotics program of the Flight Dynamics Lab had led to this summer faculty research position.

II. OBJECTIVES OF THE RESEARCH EFFORT

The initial robotic system consisted of a robot arm bolted upside down to an x-y table capable of moving in a plane parallel to the ground. From the position of the robot, the vertical coordinate can be determined. This allowed the robot to pick and place objects anywhere within a rectangular workspace. The major objective of this effort was to integrate a video camera and image processing board to the existing system. This would give the robot the ability to see an object within its workspace and proceed to get the object.

Additional software would need to be developed to support the vision system. This would be the first objective. The fundamental developments would be for calibration of the camera and coordinate transformation

from the camera frame to the world frame. Image processing routines would be developed also to filter out noise and identify objects after segmentation.

Since it was desired for the robotic system to be interactively computer operated, prompts needed to be placed in the software to allow feedback from the computer operator. This would be the second objective.

Throughout the entire development, the third objective would give careful consideration to the speed of the computer and the computational requirements of the software. To increase the computer speed, a Basic language interpreter with a compiler was used for the software development.

III. EQUIPMENT

Some of the equipment needed to complete the objectives were acquired prior to the beginning of the effort. This included a RCA color video camera and the Image Ace II video capture system digitizer. However, the computer used for the existing robot system was not IBM compatible. This type of computer was needed for the digitizer board. Fortunately, the lab was able to borrow an IBM compatible Zenith 241 and a Basic compiler for the

last two thirds of the research period.

Additional work was done on the runway and x-y table of the initial robot system to give the robot a larger workspace and better access to most of the model aircraft.

IV. METHODS

In imaging systems, there are four basic functions. The first function is digitalization of the image for use by the computer. The smallest unit of the digitized image is the pixel. All subsequent procedures of the imaging system directly make use of these pixels.

The next basic function in imaging systems concerns noise reduction or filtering of undesirable artifacts of the image. This occurs usually before the image is digitized. When the image is already digitized, discrete two-dimensional convolution functions are applied to a local pixel area of the image to approximate various filtering functions (3). There are many references in the area of image digital signal processing from the practical to the theoretical (1,2,3,4).

The third basic function of a imaging system is the segmentation of images. This means the image system isolates and labels the object by means of binary images

or other thresholding techniques. Segmentation does not identify objects, but it does show that there are objects and give the coordinates and other statistics to each object (1,4,7).

The last basic function of an imaging system consists of identification of the objects seen on the display. Methods are constantly being developed in this area of image identification (1,5,6). Two fundamental approaches to image identification are template matching and feature space classification.

Template matching generally consists of a library of objects of importance in computer memory. These templates are masked over local areas of the image and a perfect match is sought. However, most methods are not invariant to scale, rotation, and intensity variations.

Feature space identification is the basic alternative to template matching. Features, such as area, texture, and corners are isolated and tabulated for several objects. When an object is identified, each of the object's features are compared against all of the other features of each object. The set of features with the closest match is related to the proper identification of the object.

Well into the development of the principle functions of the imaging systems, it was determined that the present computer system was not fast enough to do the computation

needed for identification. In order to save time an ad-hoc approach was used which was employing the paint command of the Basic language interpreter. This approach selectively fills the screen with a particular color unless it encounters another specified color. For instance , if the paint command starts outside of a circle traced in a certain color, the entire screen would be painted except for the circle and everything inside of the circle. By careful analysis of the image and object, a procedure could be constructed in which the object could be isolated against a contrasting background. Through the statistics of each object, information such as center of area, and orientation could be calculated. The only disadvantage of this technique is that a computer operator must be always present to monitor the images and to adjust the contrast and sync of the digitizer board. This method is not invariant to intensity level.

The software developed, as listed in the appendix, allows an operator to interactively monitor the tasks of the robot. The first procedure the program directs is the calibration of the camera. When this is completed the plane is allowed to enter the hanger. The camera takes a picture of the plane and the computer processes the image. During this process, the fuel port is located in terms of the world frame. The program then instructs the robot to

get the fuel pump and take it to the fuel port. When the refueling is done, the fuel pump is replaced and the robot returns to its initial position. If another plane enters the hangar after the first one leaves, it could be placed anywhere within view of the camera. The process repeats itself with the picture being taken, processed, and the refueling task repeated.

V. RESULTS

The project for the most part was successful. This was despite the delays which slowed the project. The most crucial delay was in getting an IBM compatible computer to drive both the image processing board and the robot. Nearly four weeks went by before the computer was available.

All previous software for the robot was done in Basic language. Since this language is very slow during execution, a Basic compiler was used to increase the execution speed. There were some problems in making the compiler compatible with the existing software. Nearly two weeks of the project was spent finding and correcting these "bugs".

Towards the end of the project time period, the robot itself had problems with the cables which drive the

joints. This occurred during the testing of the entire integration from the video camera to the robot end effector.

Traditional image processing techniques were initially sought for the system. These methods include noise and artifact filtering, binary image thresholding, object segmentation, and calculation of the first and second moments of the objects. The Laplacian Gradient was looked at as an edge detector when the project progressed to the object identification stage. The number of calculations necessary for filtering were so great the computer ran too slow to be appealing for the interactive user. This resulted in the use of the ad hoc method using the "paint" command of the Basic language. This method, when refined, was relatively robust for the same aircraft. However, this method was dependent on the type of plane, and when the technique failed it was usually attributed to noise due to digitization of the image.

The robot was able to reach the location of the fuel port with reasonable accuracy. There was a systematic error between the final position of the end effector and the fuel port. This error was eliminated when compensation for perspective was incorporated. Any remaining error was due to quantization in the digitization process.

VI. RECOMENDATIONS

The project was a good initial effort for the Special Projects Group and myself as far as understanding basic robotic vision systems. Low level image processing was the major emphasis with the higher levels of image processing left for further work. However, any future research in this area should make use of the many computer hardware boards which can perform the basic image processing techniques much faster than conventional software methods. This would relieve the computational burden from the computer and more time could be spent on object identification and obstacle avoidance methods.

As continuing work which will be proposed to the Research Initiation Program, a feature selection approach to object identification through the use of neural networks will be developed and evaluated. Through close communication with the Special Projects Group, every effort will be made to make this project applicable and compatible with their existing in-house robotics project. This will give the Special Projects Group a greater level of sophistication in the area of robotic vision. This base would allow more flexibility in designing experiments and would provide the foundation for any research in obstacle avoidance.

References

1. Ballard, D.H., and C.M. Brown. Computer Vision. Englewood Cliffs, New Jersey, Prentice-Hall, 1982.
2. Baxes, G.A., Digital Image Processing: A Practical Primer. Englewood Cliffs, New Jersey, Prentice-Hall, 1984.
3. Dudgeon, D.E., and R.M. Mersereau, Multidimensional Digital Signal Processing, Englewood Cliffs, New Jersey, Prentice-Hall, 1984.
4. Horn, B.K.P., Robot Vision. Cambridge, Massachusetts, MIT Press, 1986.
5. McCloy, D., and M. Harris. Robotics: An Introduction. New York, New York, Halsted Press, 1986.
6. Nevatia, R., Machine Perception. Englewood Cliffs, New Jersey, Prentice-Hall, 1982.
7. Snyder, W.E., Industrial Robots: Computer Interfacing and Control. Englewood Cliffs, New Jersey, Prentice-Hall, 1985.

APPENDIX MAY BE OBTAINED FROM
UNIVERSAL ENERGY SYSTEMS, INC.
OR FROM THE AUTHOR

1988 USAF-UES SUMMER FACULTY RESEARCH PROGRAM

Sponsored by the
Air Force Office of Scientific Research

Conducted by
Universal Energy Systems, Inc.

FINAL REPORT

Reaction Kinetic of Halon 1301 Suppression of
Fire Explosion in an Aircraft Fuel Tank

Prepared By:	Nanda L. Mukherjee, Ph.D.
Academic Rank:	Professor
Department and University:	Chemical Engineering Tuskegee University
USAF Researcher:	AFWAL/FIES Wright-Patterson AFB, OH 45433
Date:	30 September 1988
Contract No.	F49620-88-C-0053

ABSTRACT

Reaction Kinetic of Halon 1301 Suppression of Fire Explosion in an Aircraft Fuel Tank

By

Nanda L. Mukherjee

A mixture of fuel vapor and air containing more than 10 vol % oxygen in the ullage of a fuel tank will ignite at a temperature of 450-500°C due to ballistic impact and cause fire, flame and explosion. The addition of Halon 1301, monobromotrifluoromethane, compound enhances the ignition temperature as a result of chemical reaction of bromine radicals with active hydrogen radicals of the fuel, thus decreasing intensity of inflammability. The chain reactions mechanism which explains removal of active fuel hydrogen radicals by bromine radicals of Halon 1301 compound is discussed in the report. Reaction kinetic investigations include: (a) specific rate constant equation and calculation of rate constant and (b) active energy calculation. In addition, recommendations have been made for future test runs in order to obtain more useful data required to design an efficient aircraft fuel tank.

ACKNOWLEDGEMENTS

I would like to express my thanks to the Air Force Systems Command and Universal Energy Systems, Inc. for giving me the opportunity to conduct my research at Wright-Patterson Air Force Base as a Summer Faculty Research fellow.

I am also grateful to personnel and specifically to Curtis Fett, John Sparks, and Wallace C. Buzzard of the Survival Enhancement Branch - Flight Dynamics Laboratory, Wright Patterson Air Force Base, for their assistance and cooperation in completing the work.

I. INTRODUCTION

In combat, aircraft are extremely vulnerable to ballistic impact because the fuel tank containing a mixture of fuel vapors and air above the fuel level can easily ignite and causes an explosion. During ignition active oxygen ions strongly and instantaneously react with hydrogen radicals of fuel vapor. This is a highly exothermic reaction which causes a rapid temperature rise with more liquid fuel changing to vapor. This process of hydrogen and oxygen reaction as well as fuel vapor generation continues. This causes overpressure, high flame speed and eventually an explosion.

Halogenated hydrocarbons by means of chemical effect have shown greater power to extinguish flames than have inert diluents - nitrogen and carbon dioxide. The usual way to evaluate the effectiveness of an agent is the degree of flammability of the fuel. The inhibitory of CH_3Br , CCl_4 , CH_2BrCl , CH_3I , CBr_2F_2 and $\text{CBrF}_2\text{CBrF}_2$ on flame propagation in hydrogen - air and hydrocarbon - air mixtures were studied. The study (Day et. al) shows that bromine and iodine compounds are very effective in inhibiting the flame propagation, while chlorine compounds are not so effective.

DuPont Halon 1301 fire extinguishant is monobromotrifluoromethane, CBrF_3 which is the most effective (weight basis) gaseous extinguishing agent available. It is up to three times more effective (DuPont Technical Bulletin B-29E) than carbon dioxide and some other halogenated agents. Halon 1301 extinguishes by a chemical reaction. The halogen compound reacts with the transient combustion products which are responsible for rapid and violent flame propagation. The reaction

terminates the combustion chain reaction and thereby stops the flame propagation. Two different theories explain the extinguishment process, one based on free radical process, the other based on ionic activation of oxygen during combustion.

DuPont has reported Halon 1301 concentrations, vol % for flame extinguishment and inerting of individual fuel compound e.g. methane, n-heptane, propane. The Chemistry and Uses of Fire Retardants has indicated minimum volume percent CF_3Br required to snuff out a flame of n-Heptane as measured by the peak in the flammability curve. The technical report AFFDL-TR-78-66 prepared by Wright-Patterson Laboratory entitled, "Test and Evaluation of Halon 1301 and Nitrogen Inerting Against 23mm HEI Projectiles," has reported the peak combustion pressure changes (figure 1) with Halon concentration. Analysis shows a decrease of pressure with an increase of Halon concentration while the overpressure rise time increases (figure 2). The aircraft fuel tested in this flammability study was JP-4.

What has not yet been investigated is detailed reaction mechanism, kinetics and thermodynamics of Halon 1301 inhibition of flame speed in an aircraft fuel tank. The study would provide information of Halon 1301 reactivity in JP-4/aircraft fuel at ignition temperature and the necessary data to design an efficient fuel tank. The experiment could be conducted in the combined bubbler tank, tank wall simulator (TWS) and bomb sampler systems as shown in figure 3.

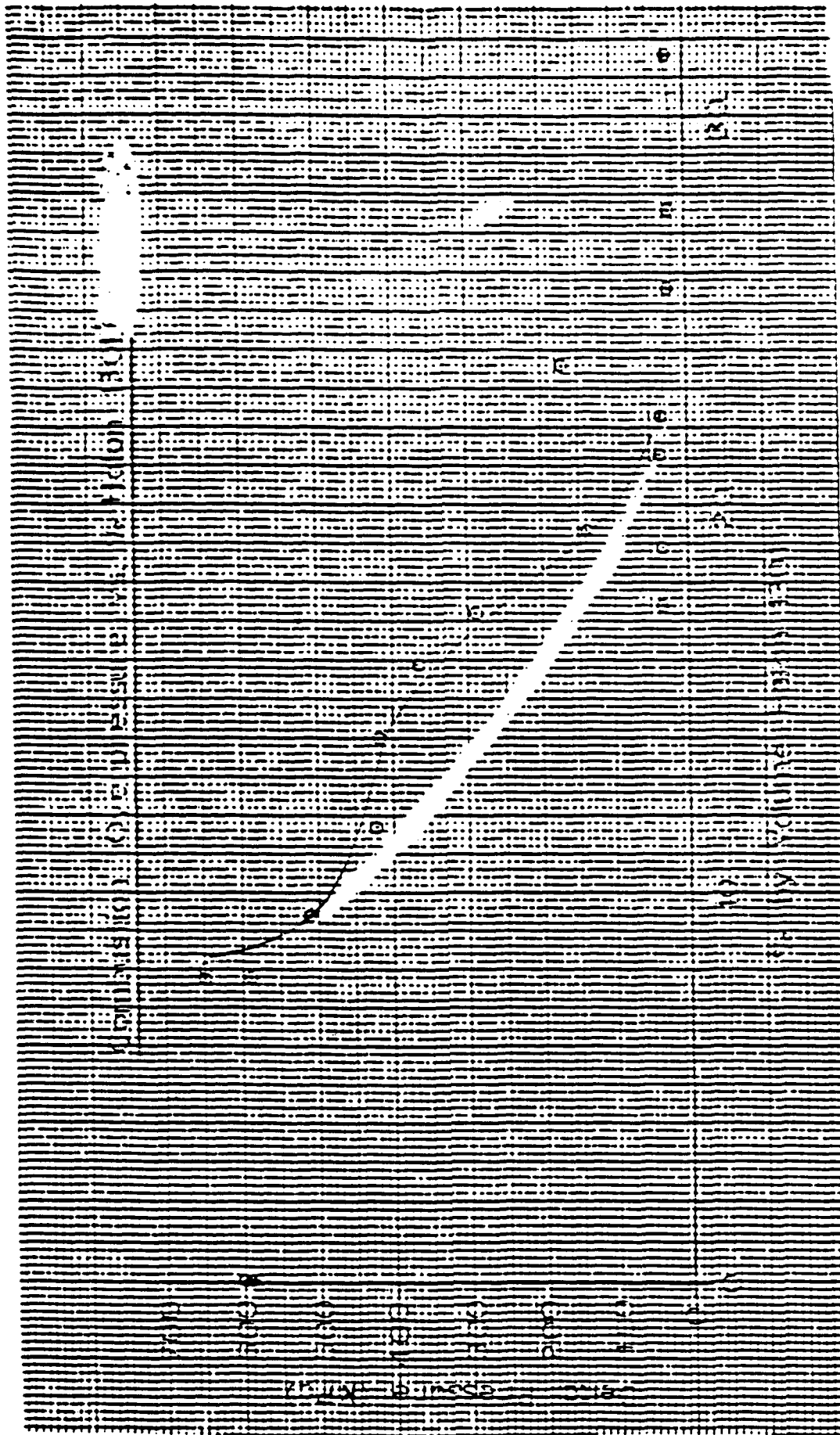


Figure 1.. Combustion Overpressure vs % Halon 1301

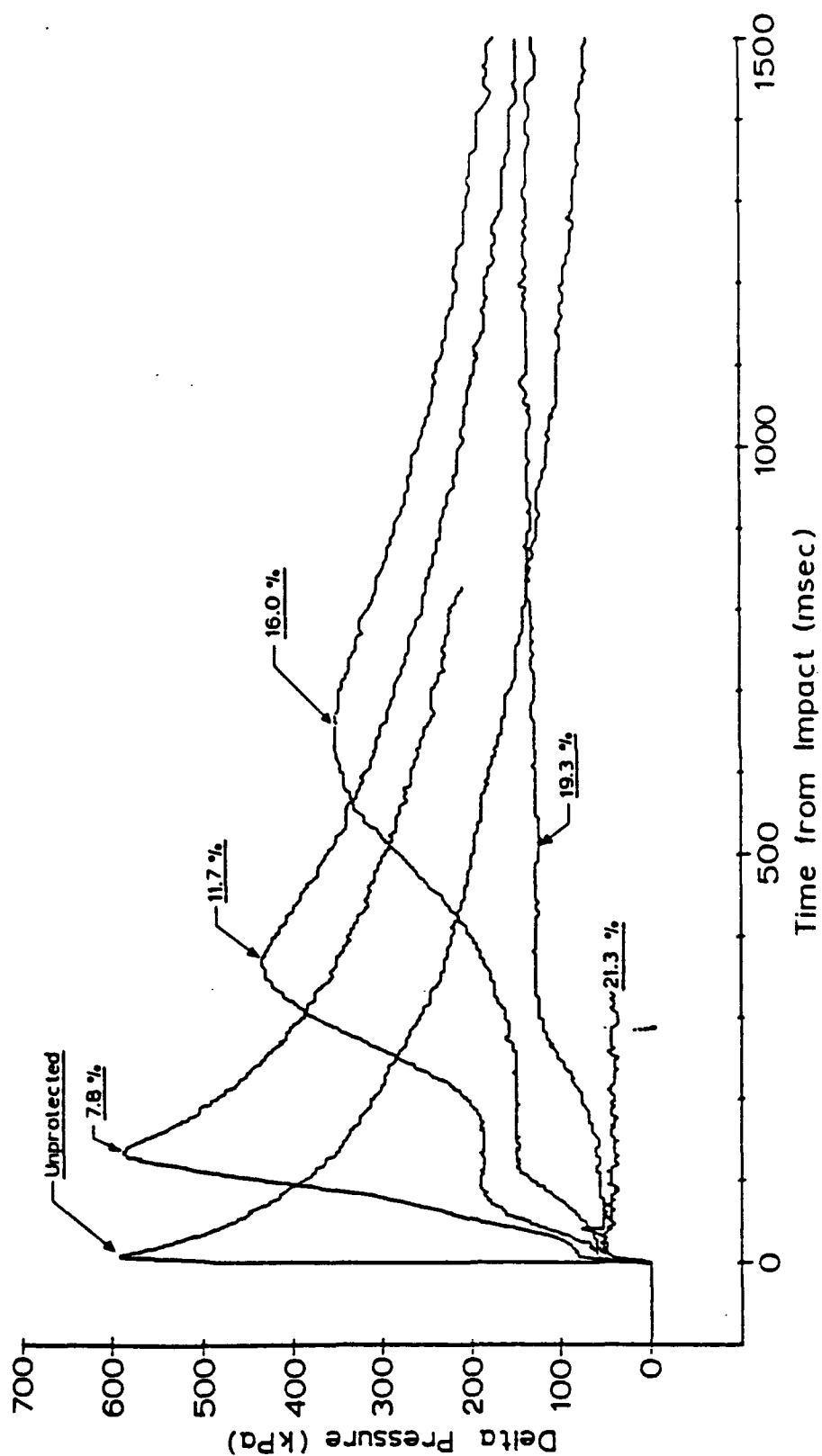


FIGURE 2. OVERPRESSURE RISE TIME WITH HALON 1301 CONCENTRATION

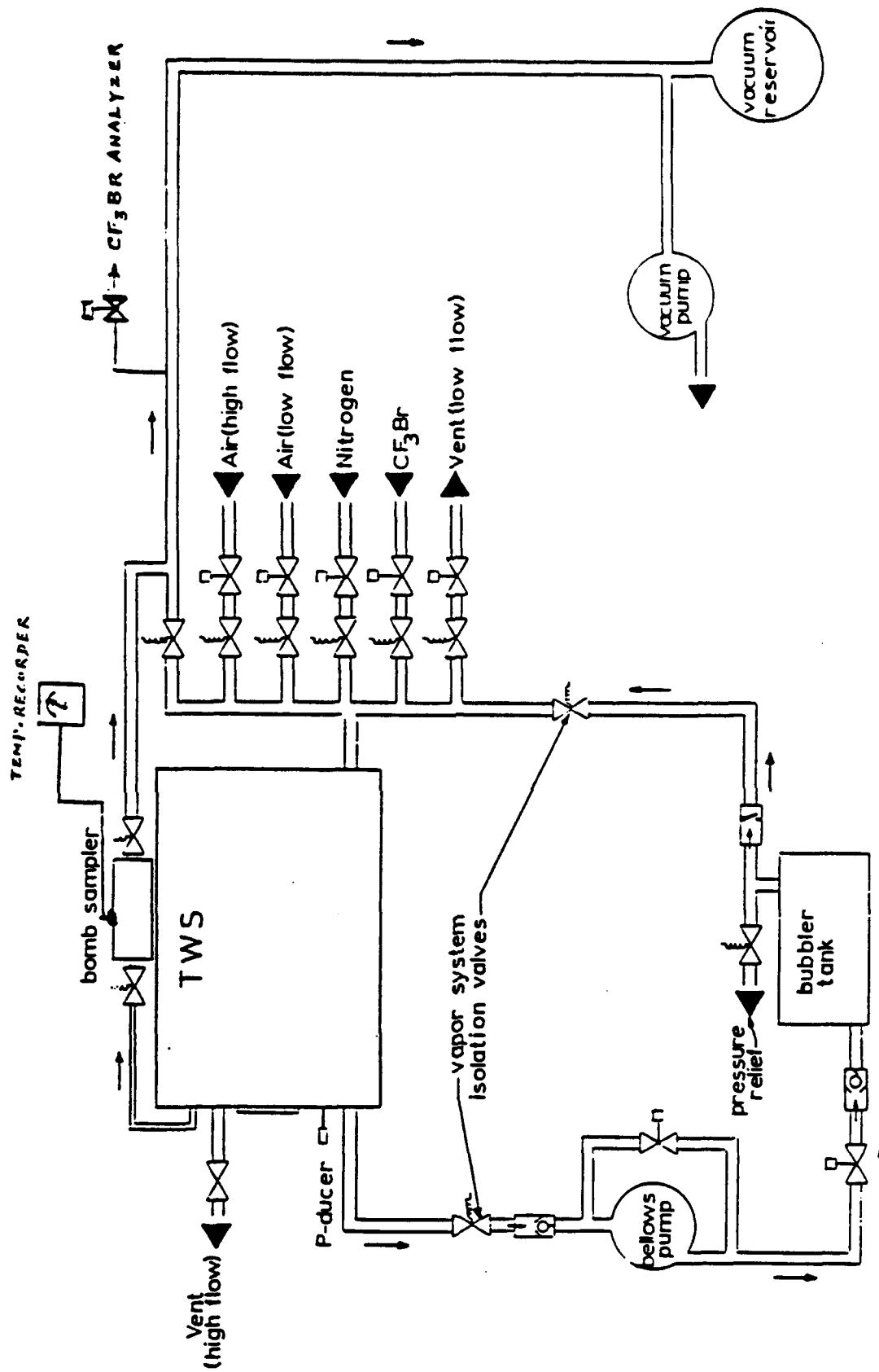


FIGURE 3. HALON 1301 EXPLOSION SUPPRESSION
EXPERIMENTAL SCHEMATIC

II. OBJECTIVES OF THE RESEARCH EFFORT:

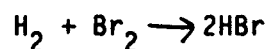
In order to study the effectiveness of Halon 1301 suppression of flame propagation and explosion in an aircraft fuel tank and design efficiently the fuel tank, knowledge of chemical reactions and kinetics are required. So far this has not been accomplished and my work involved the study of (a), (b), (c), and (d) and determining exactly what additional experimental data needs to be recorded during tests. (a) reaction mechanism of Halon 1301 inhibition, (b) overall reaction rate constant equation, (c) calculation of reaction rate constant and (d) active energy equation.

To simplify calculations, all the data have been assumed from Bomb Sampler as shown in figure 3. Experimental data like Halon concentration and temperature corresponding to pressure in the system are not available and so they were assumed.

Some additional work is necessary in order to obtain all the data required. If given the opportunity to continue the work in this laboratory during 1989 Summer Faculty Research Program, I could accomplish the incomplete experimental work. Then the data could be used to achieve kinetic and thermodynamic calculations including process and computer models, with funding from 1989-90 UES Mini-Grant program.

III.

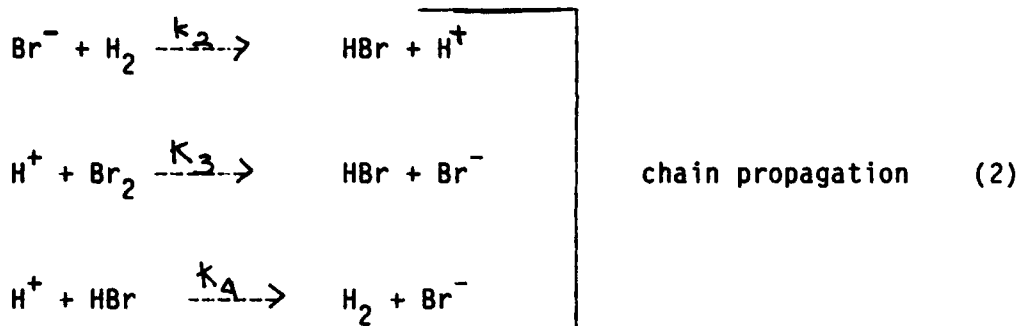
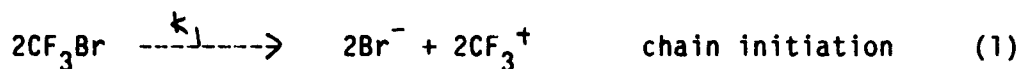
Halon CF_3Br compound liberates Br^\cdot which reacts with active H^\cdot radical of hydrocarbon group to form HBr as in the global reaction:



An increase of the Halon concentration removes more H^\cdot radicals and causes the fuel hydrocarbon radicals to be less active. The result is

the ignition temperature limit is increased which decreases the overpressure. Time rise for the overpressure also increases because of continuing $H_2 - Br_2$ reaction.

The simplified $H_2 - Br_2$ reaction shown, is obtained from a complex chain reaction mechanism. To initiate this chemical reaction, heat is provided during ignition and combustion process. The heat of formation of Br_2 6.71 Kcal/mol of Br_2 is lower than that of hydrogen which is 52 Kcal/mol. This causes the Br_2 to decompose first because H_2 is more stable. Bromine atoms are free radicals which can react with H_2 and a series of chain reactions occur.



The rate of production of HBr does not follow the law of mass action. The experimentally determined (Kenneth) rate law for this reaction is:

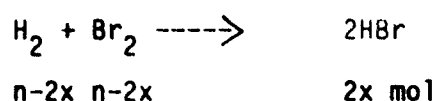
$$\frac{d C_{HBr}}{dt} = \frac{a_1 C_{H_2} C_{Br_2}^{1/2}}{1 + C_{HBr}/(a_2 C_{Br_2})} \quad (4)$$

where a_1 and a_2 are constants at a given temperature:

The equation (4) is comparable to the equation (5) derived from chain reactions equations.

$$\frac{d C_{\text{HBr}}}{dt} = \frac{2K_t C_{\text{H}_2} \sqrt{C_{\text{Br}_2}}}{1 + C_{\text{HBr}} / (10 C_{\text{Br}_2})} \quad (5)$$

Again the specific rate constant equation can be expressed in the form of a total pressure (P) of the system:



$$\text{Total mols} = (n-2x) + (n-2x) + 2x = 2(n-x) \text{ mols}$$

$$C_{\text{H}_2} = P_{\text{H}_2} = P \cdot \frac{n-2x}{2(n-x)}$$

$$C_{\text{Br}_2} = P_{\text{Br}_2} = P \cdot \frac{n-2x}{2(n-x)} \quad [p = \text{partial pressure of the components}]$$

$$C_{\text{HBr}} = P_{\text{HBr}} = P \cdot \frac{2x}{2(n-x)} = \frac{x}{n-x} \cdot P$$

Substituting the values in equation (5), the specific rate constant is calculated:

$$K_p = \frac{\left(\frac{x}{n-x}\right) P \left(1 + \frac{xP}{n-x} / 5P \cdot \frac{n-2x}{n-x}\right)}{P \cdot \frac{n-2x}{n-x} \sqrt{P \cdot \frac{n-2x}{2(n-x)}} \cdot t} = \frac{0.283x(5n-9x)(n-x)^{1/2}}{(n-2x)^{5/2} \cdot P^{1/2} \cdot t} \quad \text{KPA} \cdot \text{mol}^{-1} \cdot \text{sec}^{-1} \quad (6)$$

where: $t = \text{reaction time in secs.}$

The rate of Halon 1301 conversion from the test-data would be used to calculate specific rate constant (Kp) and active energy (E) at the corresponding system pressure.

The data from the Tank Wall Simulator (TWS) and Bomb Sample Systems operated in Wright-Patterson AFB facility by Vehicle Equipment Division,

provide the combustion overpressure (kpa) and the time rise (m sec) during ignition/fire for available Halon 1301 concentration (vol %) in fuel vapor.

It is evident that the Halon 1301 concentration changes as the system overpressure increases. Knowledge of Halon 1301 content and the rate of conversion (mols/litre.sec.) will assist to determine the reaction rate constant (Kp) shown in equation (6). Test data do not report $\text{CF}_3\text{Br}/\text{HBr}$ content at rise time but this could be conveniently determined by gaschromatographic analysis.

Calculation of the reaction rate constant (Kp) from test data:

initial Halon 1301 concentration in fuel gas mixture: 7.8 vol %
 final Halon 1301 content in fuel gas mixture: 4.0 vol % (assume)
 time to attain overpressure: 0.125 sec
 system overpressure: 600 kpa
 system final temperature: 50°C (assume)
 bomb sample system inner volume: 0.262l
 initial vapor mixture pressure: 108kpa
 initial temperature: 38°C

Calculation:

Halon (CF_3Br) content, g. mol initially in bomb sample system:
 volume of CF_3Br = (0.078) (0.262) = 0.0204l

$u/v = p/p$ (Dalton's Law of partial pressure)

$0.0204/0.262 = p/108$, $p = 8.41$ KPa

$p_2 = 15.92$ PSIA, $V_2 = 0.02041$, $T_2 = 311^\circ\text{K}$

$p_1 = 14.70$ PSIA, $V_1 = ?$ $T_1 = 273^\circ\text{K}$

$V_1 = (V_2) \left(\frac{T_1}{T_2} \right) \left(\frac{P_2}{P_1} \right)$ [COMBINED GAS LAWS]

$= (0.0204) \left(\frac{273}{311} \right) \left(\frac{15.92}{14.7} \right) = 0.0196$

1 gm. mol. at NTP $\equiv 22.41$ l

mol of $\text{CF}_3\text{Br} = \frac{0.019}{22.41} = 0.00085$

mol of $\text{Br}_2 = 0.000425$ (n)

Final mols after ignition -

$$v_2 = (0.262) (0.04) = 0.01058, p_2 = 18.184 \text{ PSIA}, T_2 = 323^\circ\text{K}$$

$$v_1 = ?, p_1 = 14.7 \text{ PSIA}, T_1 = 273^\circ\text{C}$$

$$v_1 = (0.0105) \frac{(273)}{323} \frac{(18.184)}{14.7} = 0.0118$$

$$\text{CF}_3\text{Br mols} = 0.0005 \text{ mols, mols of Br}_2 = 0.00025$$

$$\text{mols of Br}_2 \text{ dissociated} = 0.000425 - 0.00025 = 0.000175 (x)$$

Specific rate constant (Kp) -

substituting the values n (initial mols), x (dissociated mols),
P (system overpressure), t (time in secs) in equation (6).

$$= \frac{0.283 (0.000175) (5 \times 0.000425 - 9 \times 0.000175) (0.000425 - 0.000175)^{1/2}}{(0.000425 - 2 \times 0.000175)^{5/2} (600)^{1/2} (0.125)}$$

$$= 2.89 \times 10^{-11} \text{ KPA} \cdot \text{mol}^{-1} \text{sec}^{-1}$$

Reaction rate constant is dependent on temperature and concentration. Increasing temperature and Halon concentration will reduce system overpressure. Specific rate constant is important parameter in Kinetic process to determine the reaction rate as well as to design the fuel tank. Test data of system temperature, pressure, Halon 1301 (vol %) and time period are required to compute the reaction rate constant.

Belles and O'Neal reported the quenching-distance equation to determine the specific rate constant of halogenated extinguishing agent. The following equation is based on the concept that flame quenching is due to destruction of H^+ , O^- and OH^- radicals in the walls.

$$K_a = \frac{-120A \left(\frac{T_R}{T_0}\right)^n + 10 d_1^2 K_f N_f \sum_i \frac{p_i}{D_i^0}}{P d_1^4 K_f N_f N_a \left(\frac{T_0}{T_R}\right)^n \sum_i \frac{p_i}{(D_i^0)^2}} \quad (7)$$

where:

- K_a = Average specific rate constant for reaction of H^+ , O^- and OH^- radical of fuel air mixture with CF_3Br compound, $cm^3 \cdot mol^{-1} \cdot sec^{-1}$.
- A = Fraction of total molecules present in gas phase that must react if flames is to propagate.
- T_R = Mean reaction temperature $^{\circ}K$.
- T_0 = Initial mixture temperature, $0K$.
- d_1 = Distance between parallel plates, cm
- K_f = Average specific rate constant for reaction of H^+ , O^- and OH^- radicals with fuel molecules $cm^3 \cdot mol^{-1} \cdot sec^{-1}$.
- N_f = Number of fuel molecules per unit volume, $mols/cm^3$.
- P_i = Partial pressure of active particles of one kind, atm .
- D_i^0 = Diffusion coefficient for active particles of one kind into unburned gas at atmosphere pressure and initial mixture temperature, cm^2/sec .
- P = Total pressure of mixture, atm .
- N_a = Number of CF_3Br molecules per unit volume, $mols/cm^3$.
- n = Power expressing temperature dependence of diffusion co-efficient, $D \propto T^n$.

The equation (7) involves a number of parameters which are to be obtained by analysis and computation. As a result of this, determination of rate constant by using equation (6) is more convenient and accurate than that obtained from equation (7).

Another characteristic of Halon 1301 reaction is the activation energy, E which explains the heat energy requirement to accomplish the

reaction and this characteristic is temperature dependent. The Arrhenious equation can be effectively used to determine the average reaction rate constant of the chain reactions and breaking system.

$$K = A e^{-E/RT} \quad (8)$$

where K = specific rate constant $m^3/mol^{-1}.sec^{-1}$

A = frequency factor $m^3/mol^{-1}.sec^{-1}$

E = activation energy, Kcal/mol

R = gas constant (0.1986 Kcal/°C.mol)

T = temperature, °K

Activation energy (E) can also be directly calculated (Perry and Chilton) from adjacent pairs of K and T by simultaneously solving two sets of the Arrhenious equation as follows:

$$E = \frac{R \ln (K_2/K_1)}{\frac{1}{T_1} - \frac{1}{T_2}} \quad (9)$$

IV. RECOMMENDATIONS

1(A) The study of the Kinetic reaction of Halon 1301 with hydrocarbon fuel shows that test data of a final temperature (°K) and the Halon concentration (vol %) corresponding to an overpressur (KPa) in the bomb sample system are required to calculate the rate constant (Kp) and the active energy (E) as well as the thermodynamic functions. In order to obtain these data, attach a thermocouple to the bomb sample shell to record system temperature and analyze CF_3Br content of the bomb sample system using gas chromatography (GC) or any standard gas analyzer.

- (B) Perform tests at various ignition/spark temperatures (explosion limit of fuel vapor) and Halon 1301 content. Correlate (a) rate constant and active energy, with temperature at different Halon 1301 initial concentrations, (b) a second set of rate constant and active energy with variable initial Halon concentration at different temperature. This data would enable one to optimize the reaction process.
- (C) Kinetic computer modeling of Halon 1301 inhibition reaction should also be accomplished.
2. Thermodynamic calculations for entropy, thermal co-efficient, specific heat at constant pressure and volume of fuel, air and Halon 1301 vapor mixture are required in order to design the aircraft fuel tank.

REFERENCES

Bamford, C.H., C.F.H. Tipper and R.G. Compton, Kinetics and Chemical Technology, Elsevier, Vol. 23, 1985, p.17.

Belles, F.E. and C. O'Neal, Jr., Effects of Halogenated Extinguishing Agents on Flame Quenching and a Chemical Interpretation of Their Action, Applications of Combustion, p.806.

Day, M.J., D.V. Stamp, K. Thompson and G. Dixon Lewis, Inhibition of Hydrogen - Air and Hydrogen - Nitrous Oxide Flames by Halogen Compounds, Houldsworth School of Applied Science, The University of Leeds, England, p.705.

DuPont Technical Bulletin 29-E, DuPont Halon 1301 Fire Extinguisher, p.

Kenneth K. Kwo, Principles of Combustion, John Wiley and Sons, 1986, p.139-141.

Lyons, J.W., The Chemistry and Uses of Fire Retardents, Wiley-Interscience, 1970, p.15.

Morris, K.B., Principles of Chemical Equilibrium, Reinhold Publishing Corporation, 1965, p.30.

Perry, R.H. and C.H. Chilton, Chemical Engineers' Handbook, McGraw Hill Book Company, Fifth Ed., p.4-16.

1979s

1988 USAF-UES SUMMER FACULTY RESEARCH PROGRAM/

GRADUATE STUDENT RESEARCH PROGRAM

Sponsored by the

AIR FORCE OFFICE OF SCIENTIFIC RESEARCH

Conducted by the

Universal Energy Systems, Inc.

FINAL REPORT

DEVELOPMENT OF AN AIRCRAFT TIRE-WHEEL INTERFACE MODEL

FOR FLANGE/BEADSEAT CONTACT LOADS

Prepared by:	James A. Sherwood, Ph.D.
Academic Rank:	Assistant Professor
Prepared by:	N. Christopher Holmes
Academic Rank:	Graduate Student
Department and University:	Mechanical Engineering University of New Hampshire
Research Location:	AFWAL/FIEMA Wright-Patterson AFB, OH 45433
USAF Researcher:	Monika K. Hilb
Date:	29 Aug 88
Contract No:	F49620-87-R-0004

DEVELOPMENT OF AN AIRCRAFT TIRE-WHEEL INTERFACE MODEL
FOR FLANGE/BEADSEAT CONTACT LOADS

by

James A. Sherwood

N. Christopher Holmes

ABSTRACT

A research program has been initiated to investigate the force distribution at the interface of an aircraft wheel and tire. An F-16 main wheel was instrumented with strain gages at ten critical structural points. Test data were recorded for bolt torque, inflation pressure, vertical static and dynamic load conditions using both radial and bias-ply tires. A detailed three-dimensional finite-element model of the wheel was generated for evaluation via the ADINA finite-element code using the ADINA-IN preprocessor. An analytical technique of using influence coefficients determined from the finite-element analysis was devised to backcalculate the tire-wheel interface load distribution from the experimental data.

ACKNOWLEDGEMENTS

We wish to thank the Landing Gear Systems Group of the AFWAL Flight Dynamics Laboratory and the Air Force Office of Scientific Research for sponsorship of this research. We also wish to thank Universal Energy Systems for their assistance in finding a research topic of mutual interest to the Air Force and us.

Our research experience was enhanced by many individuals. Monika K. Hilb gave us encouragement and enough experimental data to keep us busy for a long, long time. Jon Champion, Mark Boike, Greer McClain and Bob Edwards were helpful in overcoming many computer oriented obstacles. Paul Ulrich and Jack Sperry cleared the administrative roadblocks. The encouragement of Aivars Petersons, Paul Wagner and David Morris was appreciated. We will never forget Kathy Sprowle for making us feel right at home and providing a truly enjoyable work environment.

We would also like to thank B.F. Goodrich for the use of its computing facilities to support this research endeavor.

I. INTRODUCTION

Ever since a tire has been mounted on a wheel, the problem of defining the loads at the tire-wheel interface has existed. Apriori knowledge of this load distribution is required to design new aircraft wheels. For existing wheel designs, well-defined loads are required to investigate the consequences of a change in either tire configuration or mission profile from that which the wheel was originally designed to experience.

In response to a Logistic Need 83003, the Landing Gear Systems Group (LGSg) of the Flight Dynamics Lab at Wright-Patterson Air Force Base is particularly concerned with developing the capability of modelling the structural behavior of aircraft wheels [1] and tires. Currently the LGSg is supporting efforts in the structural modelling of tires [2] and fracture mechanics of wheels [3]. Unfortunately, the boundary conditions at the tire-wheel interface are unknown. Therefore, a tire-wheel interface model is required if a complete and credible finite-element analysis of a wheel-tire assembly is ever to be available, and the fracture behavior of the wheel is to be analytically investigated.

The investigation of tire-wheel interface loads is a research topic that has interested Dr. Sherwood since his employment with B.F. Goodrich in Troy, Ohio. While at B.F. Goodrich, Dr. Sherwood performed stress analyses of new and existing aircraft wheels. If a good tire-wheel interface model was available within the corporation, it would have been

made available to him. Because the development of a tire-wheel interface model was a research task and not a production task, B.F. Goodrich was unable to support its development.

II. OBJECTIVES OF THE RESEARCH EFFORT

With the potentially conflicting requirements of reducing overall aircraft weight while increasing life and reliability, considerable effort has been invested in the development of analytical methods for structural optimization. As a result, the trend in engineering has been to analyze the structural response using finite-element techniques, thus, reducing the dependence upon experimental methods. However, these analytical tools require the designer to possess some apriori knowledge of the load configuration.

Unfortunately, aircraft wheel designers cannot benefit from these structural optimization techniques. This situation is due to a lack of understanding of the tire-wheel interface load distribution. As a consequence, current wheel design is heavily experimentally based and makes limited use of finite-element methods. This dependence upon experimental verification limits the amount of structural information to the number of available strain-gage channels and contradicts the current trend to exploit finite-element methods. Hence, new-wheel design is a time-consuming and costly process.

The reason for the lack of any definitive work on the load distribution at the tire-wheel interface is due to the nonlinear behavior of the tire-wheel interaction. While the wheel is composed of an essentially isotropic homogeneous linear-elastic material undergoing small deformations, the tire is composed of anisotropic inhomogeneous nonlinear materials exhibiting large deformations. Thus, the combination of the wheel and tire yields a highly complex pressure vessel. To further complicate the problem, the tire-wheel contact area is a function of the loading condition under consideration.

Obviously, if a credible model of the tire-wheel interface loads was made available to the aircraft-wheel design engineer, many benefits could be reaped. The process of new wheel design could exploit finite-element techniques, thereby, reducing experimental dependence and the time period required to transition hardware to operational use. This information would be of invaluable assistance in the development of accelerated roll spectra for qualification of the new wheel designs. Additionally, aircraft missions frequently evolve during the life of an aircraft. As a result, aircraft wheel service loads are altered. A reliable analytical tool would aid the engineer in evaluating if and how the structural integrity of the wheel is compromised by the new load spectrum.

An extensive search of the open literature of tire-wheel interface models yielded only one paper by C.H.S. Chen [4]. Chen's two-dimensional model ignored the flexibility of the wheel and contained a

tire constructed of an isotropic material. As a consequence, the model was oversimplified and yielded physically unreasonable results.

Our assignment as participants in the 1988 Summer Faculty Research Program (SFRP) and Graduate Student Research Program (GSRP) was to initiate the development of a credible tire-wheel interface model.

III. MODEL DEVELOPMENT

If instrumentation for measuring pressure loads on the flange and beadseat regions of the wheel were feasible, the development of a tire-wheel interface model would be simple and most likely available. Unfortunately, current instrumentation technology does not permit such measurements. As a consequence, the tire-wheel interface model is being developed using a combination of experimental and analytical contributions.

III.1 Experimental Contribution

An F-16 main wheel [5] and a T-38 main wheel have each been tested for various load conditions. These load conditions include bolt torque, inflation pressure, static vertical, static combined, straight roll, yawed roll and cambered roll. On each wheel, the resulting strains in ten critical locations were recorded using uniaxial strain gages. The F-16 main-wheel strain response was evaluated for both radial and bias-

ply tires. The T-38 main wheel strain response was investigated only for a bias-ply tire.

III.2 Analytical Contribution

III.2.A Finite-Element Model

A finite-element model of the F-16 main wheel was constructed in detail using 20-noded brick elements. This model is shown in Figures 1 through 4. Modelling all of the details of the wheel was a time-consuming and tedious process. However, since the research goal is to match strain-gage measurements as closely as possible, too coarse a mesh could compromise the finite-element calculations.

For the bolt torque and inflation pressure loads, the analyses will take advantage of the wheel's circumferential symmetry. For these conditions, the wheel and loads exhibit five planes of symmetry. Hence, to minimize cpu time, only a 36° wedge of the wheel is necessary. However, for all other loads, the wheel load is not axisymmetric. Hence, a 180° model of the wheel is necessary. If upon further investigation, it is discovered that the wheel also experiences a circumferential torque, then a 360° finite-element model of the wheel will be required.

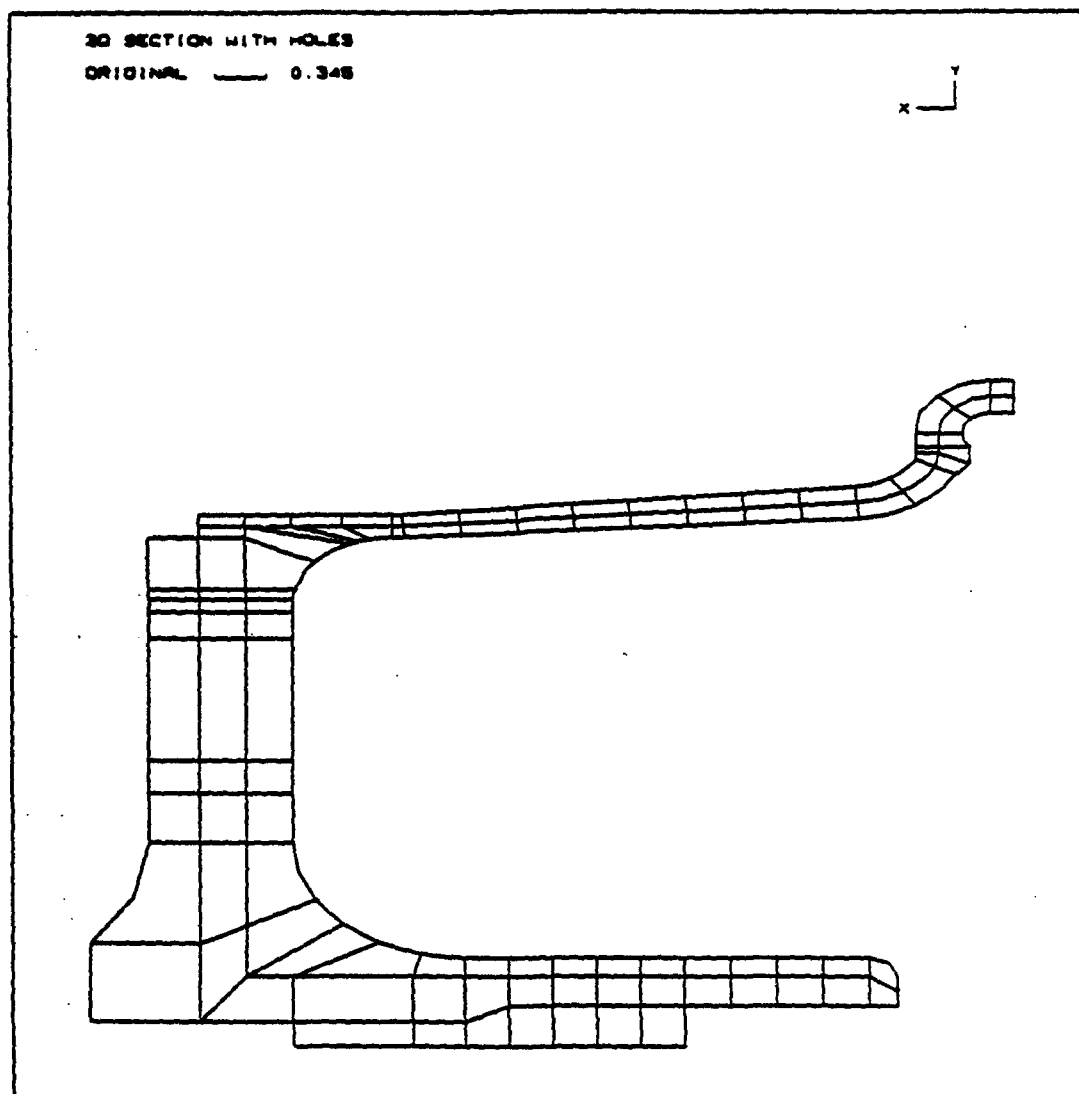


**Figure 1. Typical Cross Section of F-16 Main-Wheel
Inboard-Half Finite-Element Model**

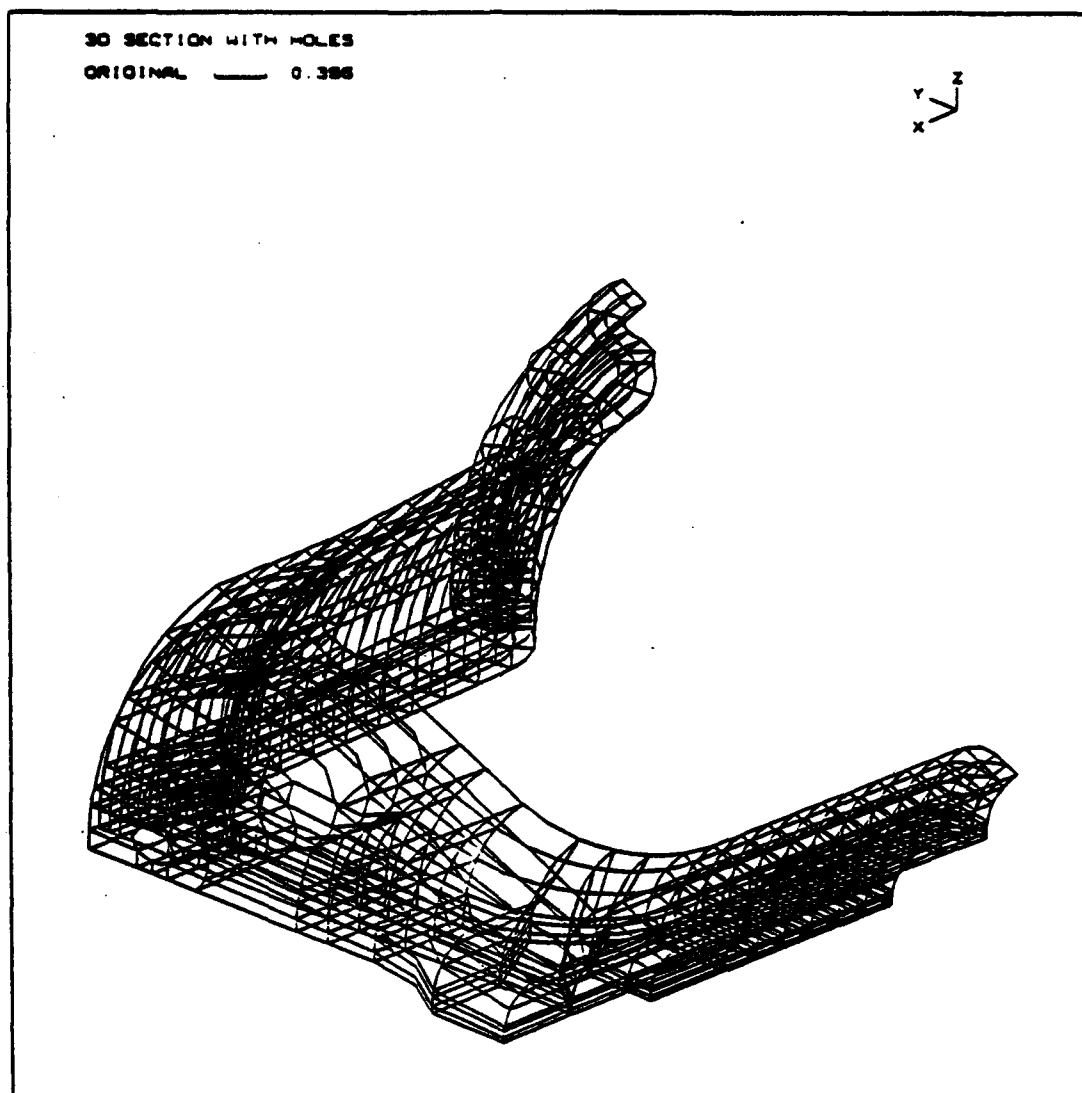


**Figure 2. Typical 3-D Wedge of F-16 Main-Wheel
Inboard-Half Finite-Element Model**

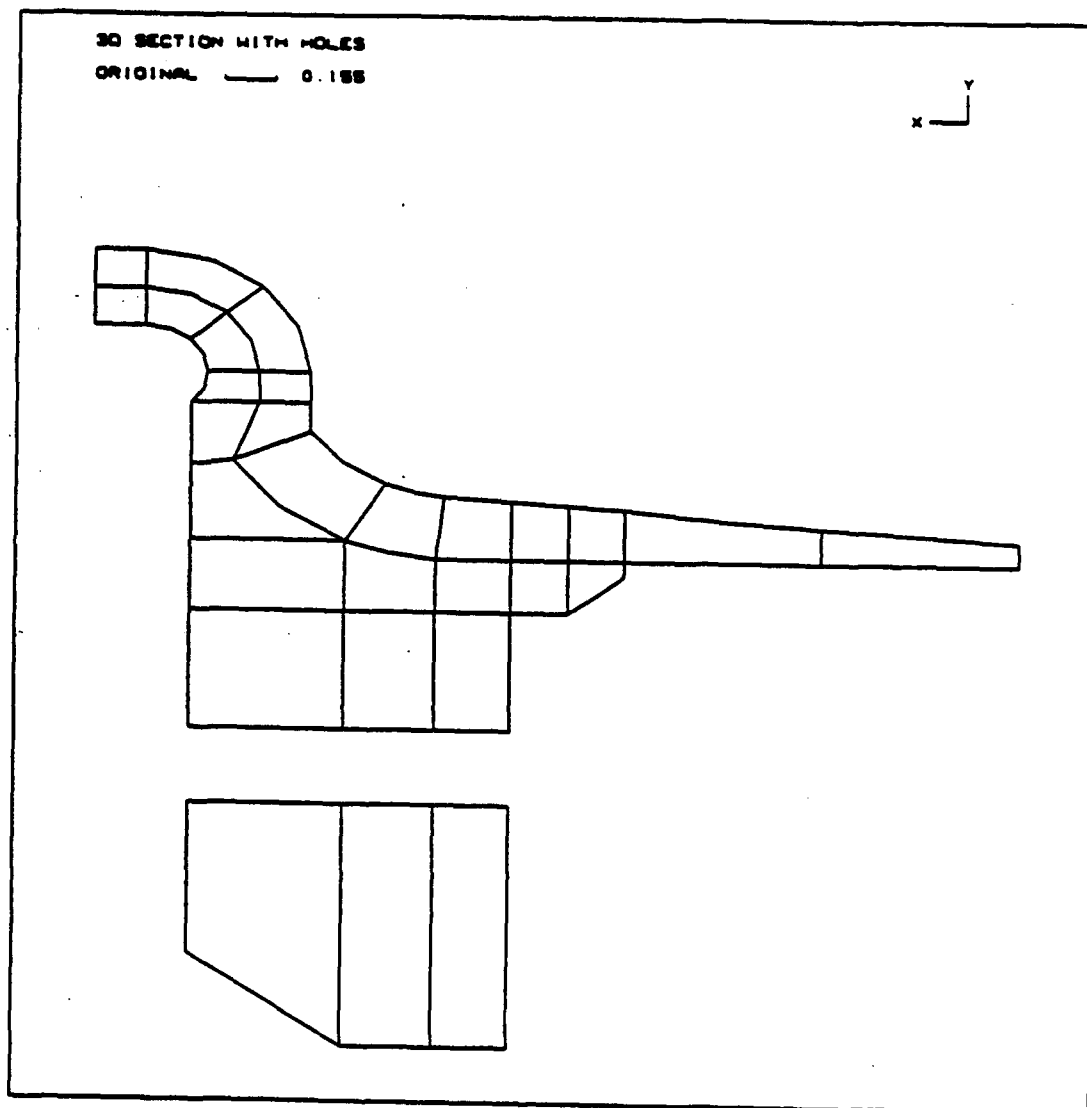


**Figure 3. Typical Cross Section of F-16 Main-Wheel
Outboard-Half Finite-Element Model**

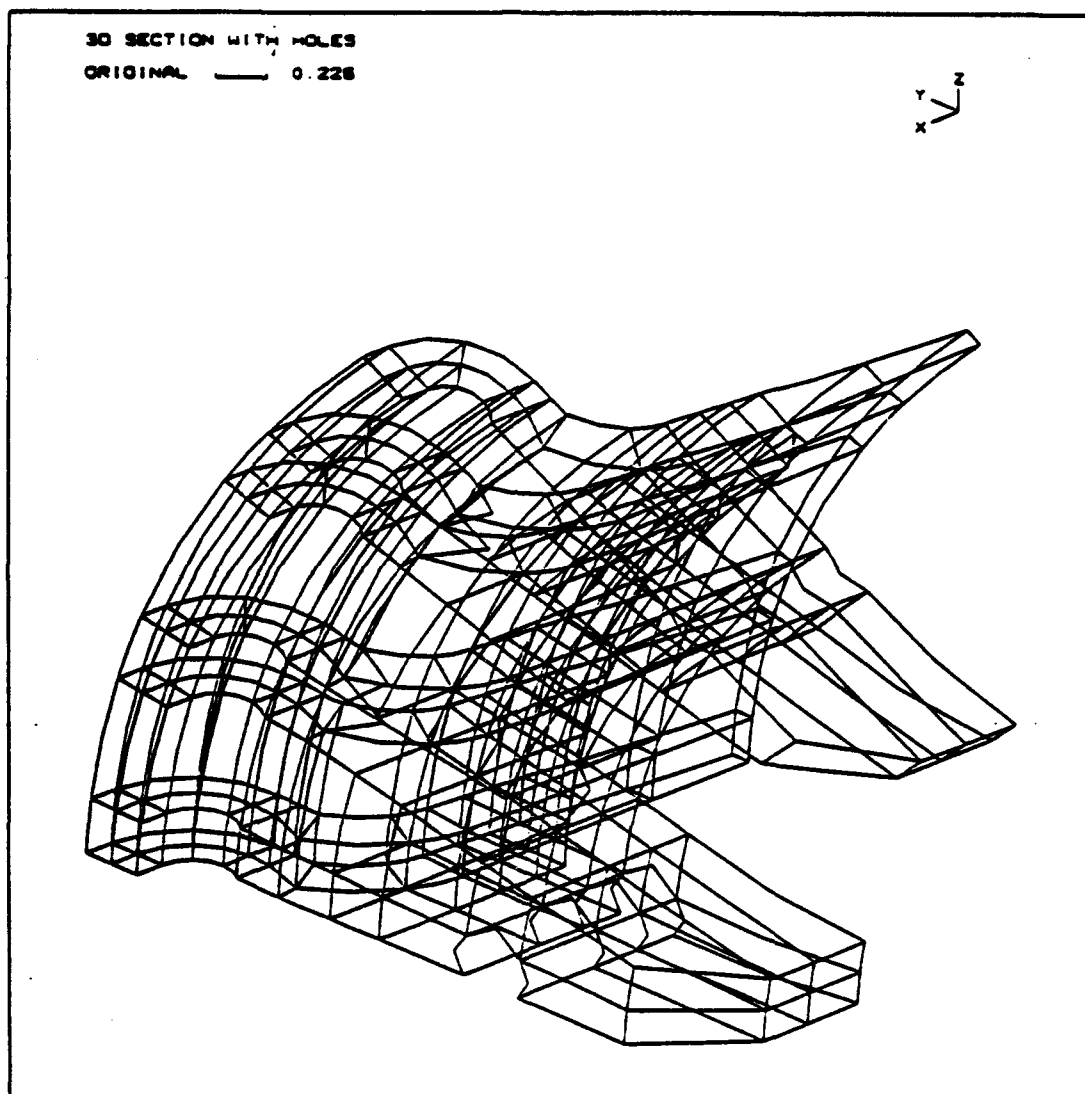


**Figure 4. Typical 3-D Wedge of F-16 Main-Wheel
Outboard-Half Finite-Element Model**

The construction of a finite-element model of the T-38 main wheel was also started. This wheel has also been experimentally investigated using ten strain gages. The T-38 wheel is less complicated to model than the F-16 main wheel due to the absence of lightening holes in the web.

The finite-element code to be used for these analyses is ADINA. The current tire modelling research is also being conducted using the ADINA program. Thus, the tire and wheel finite-element models will be compatible upon the availability of a structural model of the tire.

III.2.B Influence Coefficient Matrix

To determine the flange and beadseat loads, an influence coefficient matrix will be constructed using the finite-element model. Consider a finite-element analysis of the assembled wheel with a single point load P_A at point A as shown in Figure 5. Furthermore, let P_A equal one. The finite-element analysis will calculate the strain distribution throughout the wheel due to this single point load. Only the strains calculated at the nodal points that coincide with the ten experimental strain gage locations are important. These ten calculated strains combine to form the vector which describes how the ten strain gaged points respond to a unit load at point A, i.e.

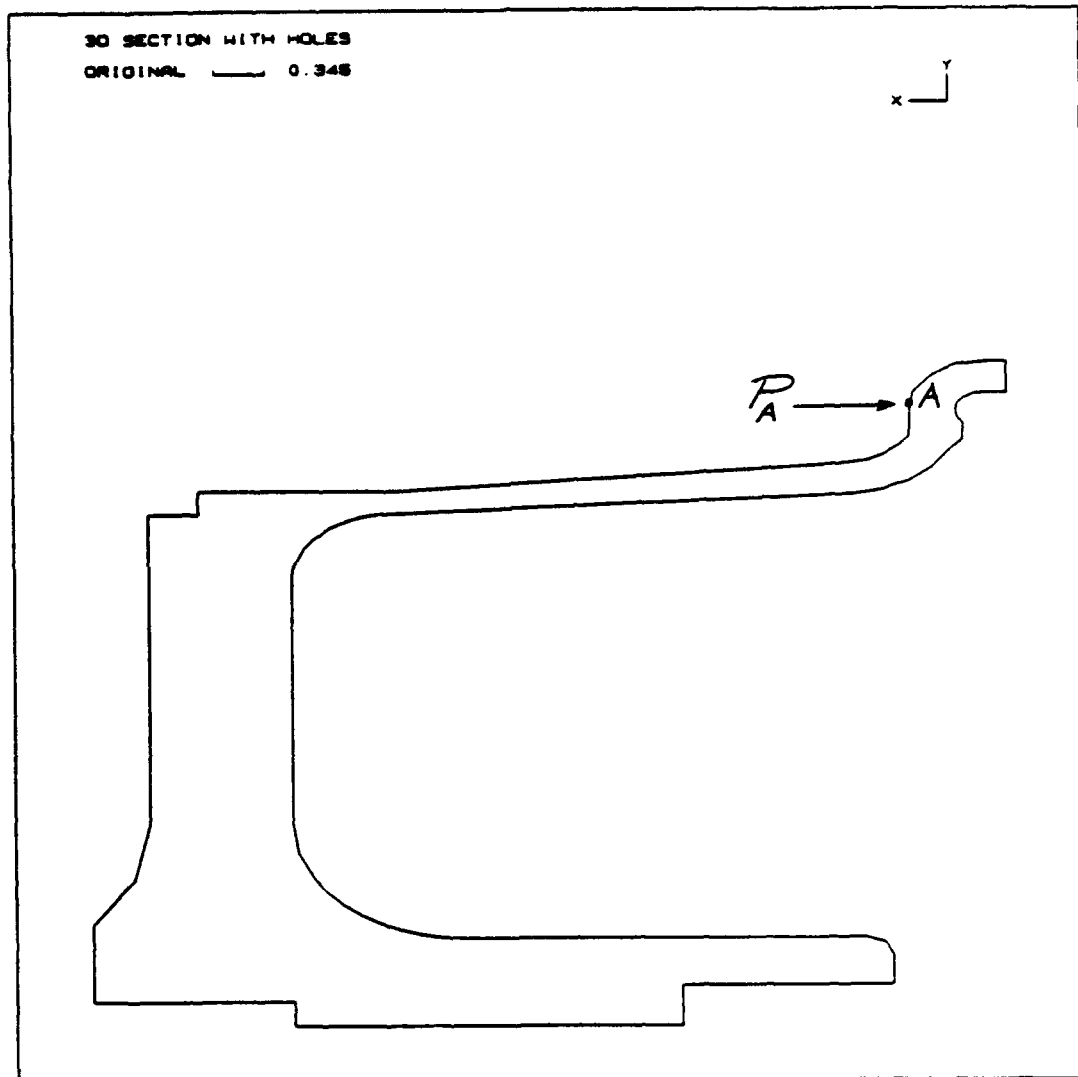


**Figure 5. Typical Unit Force Applied at a Point A
Yielding Strains at points 1 through 10**

$$\epsilon_K = \begin{bmatrix} \epsilon_{1,A} \\ \epsilon_{2,A} \\ \epsilon_{3,A} \\ \epsilon_{4,A} \\ \epsilon_{5,A} \\ \epsilon_{6,A} \\ \epsilon_{7,A} \\ \epsilon_{8,A} \\ \epsilon_{9,A} \\ \epsilon_{10,A} \end{bmatrix} \quad (1)$$

Now consider nine additional unit loads in the flange and beadseat areas, i.e. P_B, P_C, \dots, P_J . Let P_B equal one with all other P_L , $L=A, C, \dots, J$, equal zero—and so on for all P_L . The result is an influence coefficient E_{KL} where $K=1, 2, \dots, 10$ and $L=A, B, \dots, J$. The matrix E_{KL} represents the wheel response as viewed at the ten strain-gage locations, i.e. points 1 through 10, to a set of ten unit loads at the interface points, i.e. points A through J.

$$E_{KL} = \begin{bmatrix} E_{1,A} & E_{1,B} & E_{1,C} & \dots & E_{1,J} \\ E_{2,A} & \cdot & \cdot & \dots & \cdot \\ E_{3,A} & \cdot & \cdot & \dots & \cdot \\ E_{4,A} & \cdot & \cdot & \dots & \cdot \\ E_{5,A} & \cdot & \cdot & \dots & \cdot \\ E_{6,A} & \cdot & \cdot & \dots & \cdot \\ E_{7,A} & \cdot & \cdot & \dots & \cdot \\ E_{8,A} & \cdot & \cdot & \dots & \cdot \\ E_{9,A} & \cdot & \cdot & \dots & \cdot \\ E_{10,A} & \cdot & \cdot & \dots & E_{10,J} \end{bmatrix} \quad (2)$$

Note that the points of load application in the finite-element model do not necessarily correspond with those points where the strains are measured. Thus, the matrix E_{KL} is not necessarily symmetric.

III.2.C Determination of the Tire-Wheel Interface Loads

The tire-wheel interface loads are calculated using the influence coefficient E_{KL} and the measured experimental strain vector ϵ_K for the load under consideration. The load vector required to achieve the experimentally measured strains is the vector P_L which satisfies the set of simultaneous linear equations as given by

$$\epsilon_K = E_{KL} P_L \quad (3)$$

The determination of the tire-wheel interface loads using Equation 3 assumes the finite-element model strains are calculated accurately and the experimental strains are measured correctly. Hence, a "bad" mesh and/or experimental error will be reflected in the tire-wheel interface load distribution. Thus, the vector P_L must be scrutinized to ascertain whether or not it is physically reasonable. If it is not, then the experimental data and the finite-element model should be evaluated for credibility.

IV. SUMMARY

A definitive work on the understanding of the boundary conditions at the tire-wheel interface has been initiated through the completion of several major tasks. A finite-element model of the F-16 main wheel has been built, and the construction of a T-38 main wheel finite-element model is well underway. The experimental program for the T-38 main wheel has been completed with a bias-ply tire. The experimental program for the F-16 wheel has been completed for the bias-ply tire and is proceeding for the radial-tire configuration. A technique for extracting the tire-wheel interface loads from the experimental data has been devised.

V. RECOMMENDATIONS

The feasibility of developing a definitive understanding of the tire-wheel interface loads has been demonstrated through the success of the tools developed during the Summer Faculty and Graduate Student Research Programs. A systematic evaluation of the tools' capabilities in capturing the interface boundary conditions should be undertaken using the F-16 main-wheel finite-element model. During this evaluation process, refinement of the finite-element mesh may be necessary, and some strain-gage data reduction will be required.

V.1 Future Work - Phase I

The first load distribution to be investigated should be static inflation pressure. The axisymmetry of this load condition makes it the least complex of all the loading conditions, and hence, the obvious starting point of the investigation. If the currently proposed technique cannot successfully determine the interface loads for this condition, then the technique will most likely be inapplicable to dynamic loading conditions.

Upon achieving a physically reasonable inflation-pressure load distribution, the model should next be used to calculate the boundary conditions for a static vertical load and then a combined vertical/side load.

Because strain-gage measurements on experimental wheels have exhibited significant strain differences between radial and bias-ply tires [6], the capability of the proposed methodology in attaining the desired goal of describing the interface boundary loads should be investigated for both types of tires. The variation in the boundary conditions as a function of ply-rating should also be studied upon the future availability of strain-gage data.

To expand the available data base of knowledge, the construction of the T-38 main wheel finite-element model should be completed. The proposed methodology should then be used to define the interface boundary conditions for the available static test data associated with this wheel.

V.2 Future Work - Phase II

Upon demonstrating the capability of the proposed methodology in defining the interface boundary conditions for static loads, the approach should be applied to dynamic conditions. These dynamic conditions would include straight roll, yawed roll and cambered roll. With well defined loads for these dynamic conditions used in conjunction with fracture mechanics, accelerated roll test spectra for wheel qualification may be developed. Eventually, the effects of wheel manufacturing processes, such as shot peening and forging induced material anisotropy, on wheel life may be analytically investigated.

One of the most time-consuming tasks of the proposed methodology is the construction of the finite-element model of the wheel. Compounding the problem is the reluctance of the wheel manufacturers to release proprietary forging and machining drawings of their wheel designs. However, the manufacturers are willing to give requested wheel dimensions. To expedite the process of model construction and take advantage of the limited information available from the wheel manufacturers, an automated three-dimensional wheel preprocessor should be developed.

V.3 Improving Experimental and Analytical Capabilities within the Landing Gear Systems Group.

Presently, the number of strain-gage channels available in the Landing Gear Systems Group (LGSG) Lab is limited to ten. To evaluate realistically the structural behavior of a component for a variety of load conditions where the principal strain directions in the component can vary as a function of the load condition, strain-gage rosettes are mandatory. It is recommended that the number of channels be increased to a minimum of forty-eight.

Until recently, the engineers in the LGSG had not used the finite-element technique to investigate tire and wheel behavior. As a consequence, the present computer terminals are not capable of high quality graphics. A state-of-the-art workstation for finite-element

pre- and postprocessing should be acquired. Furthermore, the current preprocessor, i.e. ADINA-IN, is an adequate tool for finite-element mesh generation. However, the ADINA-PLOT program for postprocessing is insufficient. The program is not capable of producing plots of stress, strain or deflection isobands. It is recommended that a more versatile postprocessing program, e.g. PATRAN or IDEAS, be purchased.

REFERENCES

1. Treanor, D.H., and T.J. Carter, "Military Aircraft Wheel Life Improvement Assessment," AFWAL-TM-88-152, Wright-Patterson AFB, OH, 1987.
2. Brockman, R.A., "Design and Analysis of Aircraft Tires," Proposal No. R-6179, University of Dayton, Dayton, OH, 1986.
3. Enneking, T., "A Stochastic Model of Fatigue Crack Growth due to Random Loading for Application to Aircraft Wheels," Proposal No. 760-7MG-124, University of Notre Dame, Notre Dame, IN, 1987.
4. Chen, C.H.S., "Prediction of Bead Area Contact Load at the Tire-Wheel Interface Using NASTRAN," 10th NASTRAN Users' Colloquium, NASA Conference Publication 2249, NASA Scientific and Technical Information Branch, Washington, D.C., p. 133-142, May 13-14, 1982.
5. Treanor, D.H., and D.L. Morris, "F-16 Wheel Test Matrix Description," AFWAL Work Unit 24020150, LGDF Sub Order #88-14, Wright-Patterson AFB, OH, 1988.
6. Wagner, P.M., "Laboratory Evaluation of the Michelin 25.5X8.0R14/18 Ply Rating Aircraft Radial Tire," AFWAL-TM-87-205/FIEM, Wright-Patterson AFB, OH, 1987.

1988 USAF-UES SUMMER FACULTY RESEARCH PROGRAM/
GRADUATE STUDENT RESEARCH PROGRAM

Sponsored by the
AIR FORCE OFFICE OF SCIENTIFIC RESEARCH

Conducted by the
Universal Energy Systems, Inc.

FINAL REPORT

ROBUST EIGENSTRUCTURE ASSIGNMENT FOR FLIGHT CONTROL DESIGN

Prepared by: Kenneth M. Sobel, Ph.D.
Academic Rank: Associate Professor
Department and Electrical Engineering
University: The City College of New York
Research Location: AFWAL/FIGCA
Wright-Patterson AFB
Dayton OHIO 45433
USAF Researcher: Dr. Siva S. Banda
Date: 28 Aug 88
Contract No: F49620-87-R-0004

ROBUST EIGENSTRUCTURE ASSIGNMENT FOR FLIGHT CONTROL DESIGN

by

Kenneth M. Sobel

ABSTRACT

A recent sufficient condition for the stability robustness of linear systems with time varying norm bounded state space uncertainty is extended to include the structure of the uncertainty. Our new result requires that the nominal eigenvalues lie to the left of a vertical line in the complex plane which is determined by a norm involving the structure of the uncertainty and the nominal closed loop eigenvector matrix. Therefore, this robustness result is especially well suited to the design of control systems using eigenstructure assignment. When the uncertainty is time invariant, our norm is also an upper bound on the incremental eigenvalue perturbations. We consider the use of Perron weightings to reduce conservatism and the extension of the results to discrete time systems. An aircraft flight control example is presented which indicates that the new stability condition is less conservative than previous results which do not utilize the structure of the uncertainty.

Acknowledgements

I wish to thank the Air Force Systems Command and the Air Force Office of Scientific Research for sponsorship of this research. Universal Energy Systems must be mentioned for their concern and help to me in all administrative aspects of this program. I would also like to thank all the people at the Flight Dynamics Laboratory who extended their hospitality to me during my summer visit.

The experience of working with my research associate, Dr. Siva S. Banda, was rewarding and enriching. John Bowlus, Group Leader AFWAL/FIGCA, provided me with encouragement and a truly enjoyable work environment. The many valuable technical discussions with Dr. Hsi-Han Yeh contributed to the success of my research. Finally, Lt. Mary Manning and Capt. Michael Dunbar provided assistance with the use of the computer facility.

I. INTRODUCTION:

Eigenstructure assignment is an excellent method for incorporating classical specifications on damping, settling time, and mode decoupling into a modern multivariable control framework. During the period June 1980 to February 1987, I was a research engineer in the Flight Control Research Department at Lockheed California Company. My colleagues and I applied eigenstructure assignment to the design of specialized flight control laws for advanced technology vehicles.

The Flight Control Analysis Group of the Flight Dynamics Laboratory at Wright-Patterson Air Force Base is interested in robust control theory with application to flight control design. The field of robust control theory deals with feedback controllers which guarantee that the closed loop system remains stable even when the parameters of the plant (which is the system to be controlled) are uncertain. This uncertainty may arise due to the approximations involved in obtaining mathematical models of the real physical plant.

Thus, we have a mutual interest in extending the eigenstructure assignment design method such that it yields a robust control law. This will produce a feedback controller which achieves desirable classical specifications for the nominal plant while ensuring stability for all allowable combinations of the uncertain parameters. Research in this area is important for the control of sophisticated statically unstable flight vehicles which have multiple interacting sensors and control effectors.

II. OBJECTIVES OF THE RESEARCH EFFORT:

Robust controller analysis and design for linear systems with time varying state space uncertainty has often been considered by using a Lyapunov approach. Horisberger [1] and Eslami[2] propose iterative algorithms which yield controllers with guaranteed stability robustness. Patel [3] and Yedavalli [4] present bounds on the allowable perturbations under which stability can be ensured. All of these methods require the solution of a Lyapunov matrix equation.

Recently, Chen [5] proposed an approach, based upon the Gronwall lemma, for linear continuous time systems with norm bounded time varying state space uncertainty. Stability robustness is ensured provided that the nominal eigenvalues lie to the left of a vertical line in the complex plane which is determined by norm bounds on the uncertainty and the state transition matrix. If the robustness condition is not satisfied, then Chen [5] suggests moving the nominal eigenvalues farther to the left in the complex plane. Shinkre et. al.[6] extend these results to discrete time systems.

My assignment as a participant in the 1988 Summer Faculty Research Program (SFRP) was to extend the result in Ref.5 to include the structure of the uncertainty. My new result requires that the nominal eigenvalues lie to the left of a vertical line in the complex plane which is determined by a norm involving the structure of the uncertainty and the nominal closed loop eigenvector matrix. Therefore, this robustness result will be especially well suited to the design of control systems using eigenstructure assignment.

III. PROBLEM FORMULATION

Consider a nominal linear time invariant multi-input multi-output system described by

$$\dot{x} = Ax + Bu \quad (1a)$$

$$y = Cx \quad (1b)$$

where $x \in R^n$ is the state vector, $u \in R^m$ is the input vector, $y \in R^r$ is the output vector, and A, B, C are constant matrices.

Suppose the nominal system is subject to linear time varying uncertainties in the entries of A, B described by $\Delta A(t)$ and $\Delta B(t)$, respectively. Then the system with uncertainty is given by

$$\dot{x} = Ax + Bu + \Delta A(t)x + \Delta B(t)u \quad (2a)$$

$$y = Cx \quad (2b)$$

Further, suppose that bounds are available on the absolute values of the maximum variations in the elements of $\Delta A(t)$ and $\Delta B(t)$. That is,

$$|\Delta a_{ij}(t)| \leq (a_{ij})_{\max}; i=1, \dots, n; j=1, \dots, n \quad (3a)$$

$$|\Delta b_{ij}(t)| \leq (b_{ij})_{\max}; i=1, \dots, n; j=1, \dots, m \quad (3b)$$

Define $\Delta A^+(t)$ and $\Delta B^+(t)$ as the matrices obtained by replacing the entries of $\Delta A(t)$ and $\Delta B(t)$ by their absolute values. Also, define A_m and B_m as the matrices with entries $(a_{ij})_{\max}$ and $(b_{ij})_{\max}$, respectively. Then,

$$\{ \Delta A(t): \Delta A^+(t) \leq A_m \} \quad (4a)$$

$$\text{and } \{ \Delta B(t): \Delta B^+(t) \leq B_m \} \quad (4b)$$

where " \leq " is applied element by element to matrices and $A_m \in R_+^{n \times n}$,

$B_m \in R_+^{n \times m}$ where R_+ is the field of non-negative numbers.

Consider the constant gain output feedback control law described by

$$u(t) = Fy(t) \quad (5)$$

Then, the nominal closed loop system is given by

$$\dot{x}(t) = (A + BFC)x(t) \quad (6)$$

and the uncertain closed loop system is given by

$$\dot{x}(t) = (A + BFC)x(t) + [\Delta A(t) + \Delta B(t)FC]x(t) \quad (7)$$

Problem: Given a feedback gain matrix $F \in R^{m \times r}$ such that the nominal closed loop system exhibits desirable dynamic performance, determine if the uncertain closed loop system is asymptotically stable for all $\Delta A(t)$ and $\Delta B(t)$ described by Eq.(4).

IV. STABILITY ROBUSTNESS SUFFICIENT CONDITION

We present a sufficient condition for the robust stability of a linear time invariant system subjected to time varying parametric uncertainty. The proof of the theorem (which is omitted due to space considerations) uses the well known Gronwall lemma[7].

Theorem 1: Suppose F is such that the nominal closed loop system described by Eq.(6) is asymptotically stable with distinct eigenvalues. Then, the uncertain closed loop system given by Eq.(7) is asymptotically stable for all $\Delta A(t)$ and $\Delta B(t)$ described by Eq.(4) if

$$\alpha > || (M^{-1})^+ [A_m + B_m(FC)^+] M^+ ||_2 \quad (8)$$

where $\alpha = -\max_i \operatorname{Re}[\lambda_i(A + BFC)]$

and M is the modal matrix of $(A + BFC)$.

Remark 1: Theorem 1 presents a sufficient condition for the robust stability in terms of the eigenstructure of the nominal closed loop system. Robust stability is ensured provided that the nominal closed loop eigenvalues lie to the left of a vertical line in the complex plane which is determined by a norm involving the structure of the uncertainty and the nominal closed loop modal matrix.

Corollary 1 (Full state feedback): Suppose $u = Fx$ with $F \in \mathbb{R}^{m \times n}$ such that the nominal closed loop system described by Eq.(6), with $C = I$, is asymptotically stable with distinct eigenvalues. Then, the uncertain closed loop system given by Eq.(7), with $C = I$, is asymptotically stable for all $\Delta A(t)$ and $\Delta B(t)$ described by Eq.(4) if

$$\alpha > || (M^{-1})^+ [A_m + B_m [V \Sigma^{-1} U_0^T (M A M^{-1} - A)]^+ M^+ ||_2 \quad (9)$$

$$\text{where } B = [U_0 \ U_1] \begin{bmatrix} \Sigma V^T \\ 0 \end{bmatrix} = U_0 \Sigma V^T \quad (10)$$

is a singular value decomposition of B , $U = [U_0 \ U_1]$ is the matrix of left singular vectors, Σ is a diagonal matrix containing the singular values, V is the matrix of right singular vectors, and A is a diagonal matrix containing the eigenvalues of $A + BF$.

Remark 2: We observe from Corollary 1 that in the case of full state feedback, the norm on the right hand side of the sufficient condition is in terms of the known matrices A_m , B_m , V , Σ , and U_0 and the nominal closed loop modal matrix. Thus, we can try to satisfy the sufficient condition by leaving the nominal eigenvalues at their desired locations and reducing the right hand side by changing the nominal eigenvectors within the allowable subspaces. Alternatively, we could move the nominal eigenvalues farther to the left in the complex plane.

Corollary 2 (Output Feedback): Suppose $u = Fy$ with $F \in \mathbb{R}^{m \times r}$ is such that the nominal closed loop system described by Eq.(6) is asymptotically stable with distinct eigenvalues. Let Λ_r be the $(r \times r)$ diagonal matrix whose entries are the assignable closed loop eigenvalues and let M_r be the $(n \times r)$ matrix whose columns are the corresponding achievable eigenvectors. Let

$$B = [U_0 \ U_1] \begin{bmatrix} \Sigma V^T \\ 0 \end{bmatrix} \quad \text{and} \quad M_r = [U_{r0} \ U_{r1}] \begin{bmatrix} \Sigma_r V_r^T \\ 0 \end{bmatrix} \quad (11)$$

be the singular value decompositions of B and M_r , respectively.

Then, the uncertain closed loop system given by Eq.(7) is asymptotically stable for all $\Delta A(t)$ and $\Delta B(t)$ described by Eq.(4) if

$$\alpha > \left\| (M^{-1})^+ [A_m + B_m [V \Sigma^{-1} U_0^T (M_r \Lambda_r - A M_r) V_r \Sigma_r^{-1} U_{r0}^T]^+ M^+ \right\|_2 \quad (12)$$

Remark 3: We observe from Corollary 2 that in the case of output feedback, the norm on the right hand side of the sufficient condition is in terms of both M and M_r . Recall that M is the nominal closed loop modal matrix while M_r is the matrix whose columns are the r eigenvectors which we can partly assign. For the output feedback problem, we can also minimize the right hand side of the sufficient condition. However, on each iteration we would obtain a new M_r by searching the r allowable eigenvector subspaces for the eigenvectors which we can partly assign. Then, we would compute the eigenvectors of $(A + BFC)$ in order to determine the modal matrix M . Thus, the output feedback control problem requires some additional computation as compared to the full state feedback problem.

V. OPTIMAL DIAGONAL WEIGHTING

The conservatism inherent in the sufficient condition of Theorem 1 can be reduced by the use of diagonal weighting. Let D be a diagonal matrix with real non-negative entries. Then given a nominal closed

loop modal matrix M, another valid modal matrix is MD. This is because the matrix D just serves to scale the nominal closed loop eigenvectors. Therefore, Eq.(8) may be replaced by the sufficient condition given by

$$\alpha > ||D^{-1}(M^{-1})^+[A_m + B_m(FC)^+]M^+D||_2 \quad (13)$$

or equivalently by the D-weighted 2-norm described by

$$\alpha > ||(M^{-1})^+[A_m + B_m(FC)^+]M^+||_{2D} \quad (14)$$

We now state a lemma which gives the infimum of the right hand side of Eq.(14) which has been attributed to Stoer and Witzgall[8].

Lemma [8]: Define the Perron eigenvalue of the non-negative matrix A^+ , denoted by $\pi(A^+)$, to be the real non-negative eigenvalue $\lambda_{\max} \geq 0$ such that $\lambda_{\max} \geq |\lambda_i|$ for all eigenvalues ($i=1, \dots, n$) of A^+ . Then,

$$\inf_D ||A^+||_{2D} = \pi(A^+) \quad (15)$$

We observe that the matrix inside the norm on the right hand side of Eq.(14) is a non-negative matrix. Therefore, our sufficient condition becomes

$$\alpha > \inf_D ||(M^{-1})^+[A_m + B_m(FC)^+]M^+||_{2D} \quad (16)$$

or, by using the lemma

$$\alpha > \pi [(M^{-1})^+[A_m + B_m(FC)^+]M^+] \quad (17)$$

By taking the infimum on the right hand side of Eq.(14), we have placed the vertical line in the complex plane as close to the imaginary axis as possible. Recall that the sufficient condition for robust stability requires that the nominal eigenvalues lie to the left of this vertical line. In this sense, we have reduced the conservatism of the sufficient condition.

VI. NORM BOUNDED UNCERTAINTY

Suppose that instead of using the structural information about the uncertainty, which is available from A_m and B_m , we only use the norm bounds on the uncertainty. Thus, let

$$||\Delta A(t)||_2 \leq \beta_1, \quad ||\Delta B(t)||_2 \leq \beta_2 \quad (18)$$

$$||\Delta A(t)||_1 \leq \beta_3, \quad ||\Delta B(t)||_1 \leq \beta_4 \quad (19)$$

Then, we can obtain a new more conservative sufficient condition described by the next corollary.

Corollary 3 (Norm Bounded Uncertainty): Suppose that $F \in R^{m \times r}$ is such that the nominal closed loop system described by Eq.(6) is asymptotically stable with distinct eigenvalues. Then, the uncertain closed loop system given by Eq.(7) is asymptotically stable for $\Delta A(t)$ and $\Delta B(t)$ described by Eq.(18) if

$$\alpha > \kappa_2(M) [\beta_1 + \beta_2 ||FC||_2] \quad (20)$$

where $\kappa_2(M) = ||M||_2 ||M^{-1}||_2$ is the condition number of the nominal closed loop modal matrix M .

We now compare Eq.(20) with the sufficient condition of Chen and Wong [5] which is given by

$$\alpha > m(\beta_3 + \beta_4 ||FC||_1) \quad (21)$$

where m is chosen such that

$$||\phi(t)||_1 \leq m \exp(-\alpha t) \quad (22)$$

and $\phi(t)$ is the state transition matrix of the nominal closed loop system given by

$$\phi(t) = \exp[(A + BFC)t] \quad (23)$$

We remark that the result of Ref.5 can easily be shown to hold when the 2-norm is used instead of the 1-norm. This will yield the sufficient condition given by

$$\alpha > m_2 (\beta_1 + \beta_2 ||FC||_2) \quad (24)$$

where m_2 is chosen such that

$$||\Phi(t)||_2 \leq m_2 \exp(-\alpha t). \quad (25)$$

We expect that Eq.(24) will usually yield a less conservative condition than the original Eq.(21) which was derived in Ref.5. In any case, when the uncertainty structure is not utilized, our result reduces to Eq.(20) which is seen to be similar to Eq.(24). We remark that Eq.(24) will in general be less conservative than Eq.(20) because $\kappa(M)$ will usually be an upper bound on m_2 . However, calculation of m_2 requires computing $\Phi(t)$ and $\exp(-\alpha t)$ for all $t \geq 0$. We emphasize that our new result which utilizes the uncertainty structure with optimal D weighting, as shown by Eq.(17), will yield less conservative results than either of the sufficient conditions which only utilize norm bounds on the uncertainty.

VII. TIME INVARIANT UNCERTAINTY

Suppose that the uncertainty ΔA and ΔB is time invariant. Then, by an extension of the Bauer-Fike Theorem [9] we have the following:

Theorem: Let $A_c = A + BFC$ and $\Delta A_c = \Delta A + \Delta BFC$. If μ is an eigenvalue of $A_c + \Delta A_c$ and $M^{-1}A_c M = \Lambda = \text{diag}(\lambda_1, \dots, \lambda_n)$, then

$$\min_{\lambda \in \lambda(A_c)} |\lambda - \mu| \leq ||(M^{-1})^+ (\Delta A_c)^+ M^+||_2 \quad (26)$$

Remark 4: The left hand side of Eq.(26) is the magnitude of the perturbation in an eigenvalue λ of the nominal closed loop matrix A_c when the system is subjected to the time invariant perturbation ΔA_c .

The right hand side of Eq.(26) is identical to the right hand side of the robust stability sufficient condition given in Theorem 1. Therefore, when the uncertainty is time invariant, then by reducing the quantity $|| (M^{-1})^+ (\Delta A_c)^+ M^+ ||_2$ in order to satisfy the sufficient condition for robust stability, we also reduce an upper bound on the eigenvalue perturbation caused by the uncertainty.

VIII. DISCRETE TIME SYSTEMS

The robustness results for discrete time systems are omitted due to space considerations. The interested reader is referred to Sobel, Banda, and Yeh [10].

IX. EXAMPLE

Consider the linearized lateral dynamics of an aircraft described by

$$\begin{bmatrix} \dot{\phi} \\ \dot{r} \\ \dot{p} \\ \dot{\beta} \end{bmatrix} = \begin{bmatrix} 0 & 0 & 1 & 0 \\ 0 & N_r & N_p & N_\beta \\ 0 & L_r & L_p & L_\beta \\ g/V & (Y_r/V)-1 & Y_p/V & Y_\beta/V \end{bmatrix} \begin{bmatrix} \phi \\ r \\ p \\ \beta \end{bmatrix} + \begin{bmatrix} 0 & 0 \\ N_{\delta_r} & N_{\delta_a} \\ L_{\delta_r} & L_{\delta_a} \\ Y_{\delta_r}/V & Y_{\delta_a}/V \end{bmatrix} \begin{bmatrix} \delta_r \\ \delta_a \end{bmatrix} \quad (27)$$

We choose the nominal values of the stability and control derivatives from a model of the L-1011 aircraft at a cruise flight condition [11]. The nominal values of the parameters and the maximum absolute values of the uncertainty are shown in Table 1. These maximum absolute values of the uncertainty are the entries in the matrices A_m and B_m which are defined in Eqs.(3) and (4). We use the full state feedback control law which is described in Ref.11 with nominal closed loop eigenvalues given by

$$\lambda_{1,2} = -1.5 \pm j1.5 \quad (\text{dutch roll mode})$$

$$\lambda_{3,4} = -2.0 \pm j1.0 \quad (\text{roll mode})$$

$$\text{Thus, } \alpha = -\max_i \operatorname{Re}[\lambda_i(A + BFC)] = 1.5$$

Sufficient Condition 1 (Chen and Wong [5]): From Eq.(21), the sufficient condition is given by

$$\alpha > m (\beta_3 + \beta_4 \|F\|_1)$$

$$\text{where } \|\Delta A(t)\|_1 \leq \beta_3, \quad \|\Delta B(t)\|_1 \leq \beta_4$$

$$\text{and } \|\Phi(t)\|_1 \leq m \exp(-\alpha t)$$

$$\begin{aligned} \text{For this example, } \beta_3 &= \|A_m\|_1 = 0.3901 \\ \beta_4 &= \|B_m\|_1 = 0.1451 \\ \|F\|_1 &= 9.140 \end{aligned}$$

By computing $\|\Phi(t)\|_1$ and $\exp(-\alpha t)$ for $0 \leq t \leq 5$, we find that $m=4.003$. Thus, for robust stability it is required that

$$\alpha > 6.87$$

which is not satisfied.

Sufficient Condition 2 (Modified Chen and Wong): From Eq.(24), the sufficient condition is given by

$$\alpha > m_2 (\beta_1 + \beta_2 \|F\|_2)$$

$$\text{where } \|\Delta A(t)\|_2 \leq \beta_1, \quad \|\Delta B(t)\|_2 \leq \beta_2$$

$$\text{and } \|\Phi(t)\|_2 \leq m_2 \exp(-\alpha t)$$

$$\text{For this example, } \beta_1 = \|A_m\|_2 = 0.3098$$

$$\beta_2 = \left\| \begin{matrix} B_m \\ F \end{matrix} \right\|_2 = 0.1143$$

$$\left\| F \right\|_2 = 8.391$$

By computing $\|\phi(t)\|_2$ and $\exp(-\alpha t)$ for $0 \leq t \leq 5$, we find that $m_2 = 3.177$. Thus, for robust stability it is required that

$$\alpha > 4.03$$

which is not satisfied.

Sufficient Condition 3 (Structured Uncertainty with Optimal D- Weighting):

From Eq.(17), the sufficient condition is given by

$$\alpha > \pi [(M^{-1})^+ [A_m + B_m F^+] M^+]$$

For this example, the matrix $(M^{-1})^+ [A_m + B_m F^+] M^+$ has eigenvalues given by

$$\lambda_1 = 1.4634, \lambda_2 = 0.6552, \lambda_3 = \lambda_4 = 0$$

Thus, for robust stability we require that

$$\alpha > 1.46$$

which is satisfied.

X. RECOMMENDATIONS

The new sufficient condition for robustness should be combined with eigenstructure assignment to obtain a robust eigenstructure assignment design method. This new design approach should compute a control law with desirable classical specifications for the nominal plant while ensuring closed loop stability for all combinations of the time varying parametric uncertainty.

One approach might be to fix the eigenvalues at their nominal locations and then minimize the right hand side of the robustness condition. This could be accomplished by searching the allowable eigenvector subspaces subject to a constraint on the norm of the difference between the original desired eigenvectors and the new achievable eigenvectors. Recalling that the desired eigenvectors were chosen for mode decoupling, we observe that we will attempt to satisfy the robustness condition by accepting less mode decoupling for the nominal plant. This constrained optimization might be performed by using the Sequential Unconstrained Minimization Technique with a quadratic extended interior penalty function.

Another approach might be to again fix the eigenvalues at their nominal locations and then perform a steepest descent search over the eigenvectors. This could be done by starting at the original achievable eigenvectors which were obtained by projecting the desired eigenvectors onto the achievable subspaces. Then we would move in the direction in which the gradient of the right hand side of the robustness condition with respect to the eigenvectors is decreasing. This gradient might be computed numerically by utilizing the finite difference method. Alternatively, an attempt could be made to obtain an analytical expression for the gradient. Recalling that the right hand side of the robustness condition is a 2-norm, we would need to compute singular value derivatives.

In addition to research on the robust eigenstructure assignment design method, the robustness analysis itself should be extended. The elimination of certain gains in the feedback gain matrix (known as gain suppression) has been shown in some cases to yield a simpler control law with only a small effect on the performance. The effect of gain suppression on the stability robustness should be studied with the goal of obtaining the simplest robust controller which achieves desirable classical specifications for the nominal plant.

However, in some problems it may not be possible to achieve the robustness and performance objectives with a constant gain control law. Therefore, the use of dynamic compensators should be considered, when necessary, for achieving the dual goals of robustness and performance. These dynamic compensators should be designed by using eigenstructure assignment.

The robustness analysis, as it currently exists, only ensures that the eigenvalues remain in the left half of the complex plane for all parameter uncertainty described by Eq.(4). It should be easy to extend the results so that the eigenvalues are guaranteed to lie to the left of some vertical line in the left half of the complex plane for all the uncertainty described by Eq.(4). However, it would be more useful if the eigenvalues were guaranteed to lie in some regions which are related to damping and settling time. Hyperbolic regions, which approximate damping/settling time regions, have been used in connection with the linear quadratic regulator problem. Finally, the conservatism of the robustness condition should be reduced further by the use of state transformations. Such a method has been used in connection with the Lyapunov matrix equation approach to robustness.

REFERENCES

1. H. P. Horisberger and P.R. Belanger, "Regulation for Linear Time Invariant Plants with Uncertain Parameters," IEEE Transactions on Automatic Control, Vol. AC-21, October 1976, 705-707
2. M. Eslami and D. L. Russel, "On Stability with Large Parameter Variations Stemming from the Direct Method of Lyapunov," IEEE Transactions on Automatic Control, Vol. AC-25, December 1980, 1231-1234
3. R. V. Patel and M. Toda, "Quantitative Measures of Robustness for Multivariable Systems," Proceedings of the Joint Automatic Control Conference, San Francisco, California, 1980, TP8-A
4. R. K. Yedavalli, "Perturbation Bounds for Robust Stability in Linear State Space Models," Int. J. Control, 1985, Vol. 42, No. 6, 1507-1517
5. B. S. Chen and C. C. Wong, "Robust Linear Controller Design: Time Domain Approach," IEEE Transactions on Automatic Control, Vol. AC-32, No. 2, February 1987, 161-164
6. R. B. Shinkre, M. T. Tran, and M. E. Sawan, "Robust Controller Design for Discrete Time Systems," Proceedings of the 1988 American Control Conference, Atlanta, Georgia, June 1988, 890-891
7. M. Vidyasagar, Nonlinear System Analysis, Prentice-Hall, Englewood Cliffs, New Jersey, 1978
8. J. Stoer and C. Witzgall, "Transformations by Diagonal Matrices in a Normed Space," Numer. Math, 1964, 4, 458-471
9. G. H. Golub and C. F. Van Loan, Matrix Computations, The Johns Hopkins University Press, Baltimore, Maryland, 1983

10. K. M. Sobel, S. S. Banda, and H. H. Yeh, "Structured State Space Robustness with Connection to Eigenstructure Assignment," submitted to the 1989 American Control Conference, Pittsburgh, PA, June 1989
11. K. M. Sobel and E. Y. Shapiro, "Flight Control Examples of Robust Eigenstructure Assignment," Proceedings of the 26th IEEE Conference on Decision and Control, Los Angeles, California, December 1987

PUBLICATIONS PREPARED DURING 1988 SFRP

K. M. Sobel, S. S. Banda, and E. Y. Shapiro, "Robust Modalized Observer with Flight Control Application," accepted for publication in the Proceedings of the 27th IEEE Conference on Decision and Control, Austin, Texas, December 1988

K. M. Sobel and S. S. Banda, "Design of a Modalized Observer with Eigenvalue Sensitivity Reduction," submitted to the Journal of Guidance, Control, and Dynamics

K. M. Sobel, S. S. Banda, and H. H. Yeh, "Structured State Space Robustness with Connection to Eigenstructure Assignment," submitted to the 1989 American Control Conference, Pittsburgh, Pennsylvania, June 1989

Table 1. Stability and Control Derivatives for L-1011 Aircraft

	Nominal Values	Maximum Absolute Value of Uncertainty	
N_r	-0.154	0.01925	(12.5%)
L_r	0.249	0.031125	(12.5%)
$(Y_r/V)-1$	-0.996	0.0	
N_p	-0.0042	0.0021	(50%)
L_p	-1.00	0.125	(12.5%)
Y_p/V	-0.000295	0.0001475	(50%)
N_β	1.54	0.1155	(7.5%)
L_β	-5.20	0.26	(5%)
Y_β/V	-0.117	0.0146	(12.5%)
g/V	0.0386	0.0	
N_{δ_r}	-0.744	0.093	(12.5%)
N_{δ_a}	-0.032	0.004	(12.5%)
L_{δ_r}	0.337	0.042125	(12.5%)
L_{δ_a}	-1.12	0.084	(7.5%)
Y_{δ_r}/V	0.02	0.01	(50%)
Y_{δ_a}/V	0.0	0.0	

1988 USAF-UES SUMMER FACULTY RESEARCH PROGRAM/

GRADUATE STUDENT RESEARCH PROGRAM

Sponsored by the
AIR FORCE OFFICE OF SCIENTIFIC RESEARCH
Universal Energy Systems, Inc.

FINAL REPORT

A Computer Model for Air-To-Air Combat
(Force on Force) Assessment

Prepared by:	Patrick J. Sweeney, Ph.D. Kathy Bennett, Graduate Student
Academic Rank:	Professor
Department and	Engineering Management and Systems
University:	University of Dayton
Research Location:	AFWAL/FIAA Wright-Patterson AFB Dayton, OH 45433
USAF Researcher	Jack M. Byrnes
Date:	July 22, 1988
Contract No:	F49620-87-R-0004

A Computer Model for Air-To-Air Combat

(Force on Force) Assessment

by

Patrick J. Sweeney, Ph.D.

Kathy Bennett, Grad Student

ABSTRACT

This IBM-PC compatible computer model can be used to assess the affects of changing weapons, aircraft performance, electronic sensors and countermeasures, situational awareness, tactics, observables, and combat support on the force on force air battle. Both enemy and friendly air forces can engage in both BVR and CIC missions. Sortie regeneration is limited by the air losses and by enemy action taken against fixed installations, which is included in the model. The model requires a hard disc for operation and uses menus to direct the user to battle graphics, forces structuring, calculations, and output to the screen and/or printer.

Acknowledgments

I wish to thank the Air Force Wright Aeronautical Laboratories and the Air Force Office of Scientific Research for sponsorship of this research. Universal Energy Systems must be mentioned for their concern and help to me in all administrative and directional aspects of this program.

Mr. Jack M. Byrnes of AFWAL/FIAA was invaluable to the investigators in completing this research program. He provided us with what we needed when we needed it and this included the sharing of his expertise.

I. INTRODUCTION:

Air to Air combat has intrigued fighter pilots and engineers since before World War I and continues to do so today. Both are trying to determine how to improve upon the capabilities of aerial combat. This is particularly true in the STOVL (Short Take Off and Vertical Landing) Office at Wright-Patterson AFB. The ability to assess the affects of varying and new technologies and tactics is a critical need in the STOVL Office, which is often charged with the task of evaluating contractor claims to improved mission effectiveness as a result of new ideas of the contractors.

Our research interests in air to air combat is natural since we flew combat missions in both North and South Vietnam. Prior to this current research project we also designed a tactics testing computer simulation model.

II. OBJECTIVES OF THE RESEARCH EFFORT:

Currently, there are no menu-driven personal computer based models that can easily assess the affects of changing technologies on the force on force air combat scenario. There exists several large main-frame based models that assess the one on one, two on two, and m on n air to air combat scenarios. However, even these large models are not too good with the force on force scenarios.

Our assignment as participants in the 1988 Summer Faculty and Graduate Student Programs was to design an IBM-PC compatible model that could easily be used by personnel in the AFWAL/FIAA Office to assess the affects of new

technologies on the force on force air combat scenario. The model was to be easy to understand in operation and output and address both the BVR and CIC missions associated with air combat.

III. THE MODEL

a. The limitations of the personal computer dictated that this model be structured in many sub-models and that all of these sub-models be linked during operation in the proper sequence. The total model consists of ten sub-models and variations on several of these. The total byte count far exceeds the single floppy disc and therefore, the use of a hard disc is required for running the model.

Since the model was designed for use by the personnel in AFWAL/FIAA it was necessary to select a computer language that was familiar to all of them. Therefore, non-compiled BASIC was selected. This should facilitate easy changes in the model when and if the AFWAL personnel decide to do so.

The different sub-models are explained below in order of general usage during operation of the total model.

b. BEGIN.BAS: The BEGIN program initiates the model and paints the FORCE ON FORCE logo on the screen in multi-colors and depicts the red and blue forces. The size of this program is 6949 bytes. The MENU program is automatically loaded after the screen display is on for several seconds.

c. MENU.BAS: This program permits the user to select the options that are to be run. The options include force file building, graphics, calculations, and quitting. The appropriate programs default to the MENU program during the operation of the model. This program is 3852 bytes in length.

d. GRAF.BAS: This program enables the graphics portion of the model which depicts the "NATO" battle area including three red air bases and one blue air base, the FEBA, and three forward bases for the red forces. Upon actuation the user selects the appropriate red forces to model. The graphics then detail the paths of both the red and blue forces until they meet in air to air combat, which is depicted by an explosion. Up to six red forces can be graphed for each run. The graphics can be terminated by the user and the program returns to MENU automatically. This program is 14,469 bytes long.

e. INBLU1,INBLU2,INBLU3,INBLU4,INBLU5,INBLU6.BAS: These are the programs that enable the user to build the blue forces of six different capabilities. In these programs the user is able to configure four different blue aircraft (B6, B8, BA, AND BT). These are fictitious aircraft that the AFWAL personnel have selected to represent the actual friendly air forces in Europe now and in the near future. The capabilities can be altered to suit any aircraft of choice. The blue force of each program is differentiated by numbers of aircraft, weapons, performance, sensors, countermeasures, situational awareness, tactics, observables, and combat support. The user can alter each of the above capabilities in all of the six input blue

programs. Help information capability is included in the model, but because of time constraints is not included at this time. The model returns to the MENU program upon completion. These six programs consist of 16,067 bytes of information each for a total of 96,402 for the set.

f. INRED1,INRED2,INRED3,INRED4,INRED5,INRED6.BAS: These are the red force input programs and are similar to the INBLU programs described above. The red forces, however, are limited to only three types of aircraft, the R4, the R7, and the R9. Again these are also fictitious aircraft and can be modified to simulated real weapons systems. Each of these programs consists of 88,092 bytes for a total of 14,982 bytes. The MENU program is automatically loaded upon completion.

g. COMPUT.BAS: This program begins the computational sequence by loading TACDTX.

h. TACDTX.BAS: This is the exchange ratio program, the number of blue and red losses as a function of the attack sizes. This is the program that must be altered to change the air to air effectiveness versus various enemy aircraft. Both the BVR and CIC scenarios are included in the data as are every blue versus red aircraft combinations. This program automatically loads the next program in the calculations sequence, RABCX. This program is 5599 bytes in length.

i. RABCX.BAS: The user selects the fighting forces for both the red and the blue and the program computes the totals of each different type of

aircraft at the different bases. This is followed by a graphic presentation of the opposing forces. At this juncture the user determines what blue forces will oppose which of the red forces. This simulates an enemy launch and a friendly or blue force initial response. This program consists of 10,135 bytes of information. Upon completion of this program the SCRNX program is loaded automatically.

j. SCRNX.BAS: This program displays the second selection screen for the user. This screen simulates the enemy action of departing for specific targets and deploying in both high and low altitude attacks. The user must now select the forces from those previously identified for each enemy group and must send his forces to high and/or low enemy bogies. This program is 2903 bytes long. The CALX program automatically loads next.

k. CALX.BAS: This is a set of programs that loads sequentially and automatically to assure that the assigned forces attack the proper enemy bogies. The sequence is RED1 forces with the R9 and part of the R7 in high altitude missions and the R4 and the remainder of the R7 forces in the low altitude missions from enemy Base A being attacked by all of the Blue forces assigned to attack these enemy in high and low missions of BVR and CIC type. All red forces from all red bases are subsequently attacked. There are six different programs in this element and each requires 30,511 bytes of information. At the end of these programs the user can terminate , run another , or return to MENU.

l. POT POURI: All of the results appear on the computer screen and at the

command of the operator can be printed. Modifications to exchange ratios, weapons loads, and other data can be easily made by entering the appropriate program and making normal BASIC program changes. Data files for each force can be created and stored for future usage.

IV. RESULTS:

The results are sketchy but encouraging. This project demonstrated the feasibility of operating a user-friendly personal computer model in the force on force air combat arena. We have been able to show that improved capabilities do in fact improve the kill to losses ratio.

V. RECOMMENDATIONS:

We have merely scratched the surface in this all important area of force on force air combat assessment modeling on the personal computer. As stated above, the results are encouraging and we were limited merely by the length of the ten week program.

We began our preparation soon after notification of of the selection for the Summer Faculty/Graduate Student Program, however, the problem is so complicated and increases exponentially as more and more possibilities are included in the model that we had to terminate well ahead of being satisfied with the model. We are so enamored with the subject that we have agreed to continue to work on the model as time permits. This effort will be accomplished at no expense to the government.

It is our plan to submit for a Mini-Grant to complete this effort and to do so as soon as possible.

1988 USAF-UES SUMMER FACULTY RESEARCH PROGRAM/
GRADUATE STUDENT SUMMER SUPPORT PROGRAM

Sponsored by the
AIR FORCE OFFICE OF SCIENTIFIC RESEARCH
Conducted by the
Universal Energy Systems, Inc.

FINAL REPORT

DAMAGE IN GRAPHITE/EPOXY PLATES SUBJECTED TO LOW VELOCITY IMPACT

Prepared by: William E. Wolfe, Ph.D. and Greg Schoeppner
Academic Rank: Associate Professor , Graduate Student
Department and University: Civil Engineering Department
The Ohio State University
Research Location: AFWAL/FIBCA
Wright Patterson AFB
OH 45433
USAF Researcher: Dr. R. S. Sandhu
Date: 30 Sep 88
Contract No: F49620-87-R-0004

DAMAGE IN GRAPHITE/EPOXY PLATES SUBJECTED TO LOW VELOCITY IMPACT

by_

William E. Wolfe

Gregory Schoeppner

ABSTRACT

A continuation of the experimental program begun during Summer 1987 was conducted. Instrumented impact tests on laminated graphite/epoxy panels. The velocity of the impactor and the load time history were recorded for each specimen tested. In several tests, strains were measured on the back face during the impact event. The depth of surface indentation and the areal extent of internal damage were measured and correlated with the impact energy. Predicted strains in the outermost ply were compared with experimentally obtained values measured both perpendicular to and in the direction of the outermost fiber. The amount of internal damage and the indentation were found to be dependent upon the energy at impact and to a somewhat lesser degree on the velocity of the impactor. The shape of the damaged area in the specimens tested, was largely dependent upon the thickness of the panel and the location of the supports.

ACKNOWLEDGEMENTS

The author wishes to thank the Air Force Systems Command and the Air Force Office of Scientific Research for sponsorship of this research. Universal Energy Systems administered the project and was very helpful during my summer stay.

I want to thank the administration of the Flight Dynamics Laboratory, AFWAL, for allowing me to participate in the Summer Faculty Research Program at their facility and while there to engage in many stimulating conversations with the laboratory staff. These conversations certainly contributed a great deal to my understanding of the behavior of composite structures. The Materials Laboratory performed the C-scan analyses. Their assistance is appreciated. Mr. E. Maddux developed the optical method we used to measure depth of indentation. Without his eager support, this project would not have been possible.

I am particularly grateful to my program monitor, Dr. R. S. Sandhu, and group leader, Mr. G. R. Holderby, who provided the technical background and the work environment that made this summer both educational and enjoyable. I hope the results of this work prove to be useful to them.

I. INTRODUCTION:

The research program described in this report was a continuation of work begun last summer by the author and graduate student Gregory Schoeppner in the Flight Dynamics Laboratory, AFWAL. The experimental studies conducted at that time showed that repeatable low velocity impact tests could be performed on graphite/epoxy laminated composite plates using the instrumented drop tower facility in the Structures Division. Also shown was that a correlation could be made between the impact energy and the extent of internal damage sustained by the composite plate in the form of ply delamination. With the background obtained in the conduct of those tests, the experimental program carried out this year was developed. Target gr/ep plates ranging in thickness from 9 to 96 plies were subjected to different levels of impact energy. The size of the damaged area and a profile of the depth of surface indentation were determined by ultrasonic measurements and Moire methods respectively. The extent of the damage measured in the experiments was compared with the damage zone predicted by a computer program recently received by the Flight Dynamics Laboratory and modified by Mr. Schoeppner.

Last year's tests indicated that the load cell in the instrumented tup tended to vibrate during impact when the target was a graphite/epoxy plate. Because this "ringing" of the load cell makes it difficult to isolate from the total signal, that portion of the load actually being transmitted to the target, a

concern of the investigators during the present testing program was a proper identification of the load time history imparted to the target plate. The necessary measurements were made by positioning strain gages on the back face of the target plate and recording the gage response during the impact event.

II. OBJECTIVES OF THE RESEARCH EFFORT:

The primary objective of this summer research effort was to continue the program begun last summer. That program was designed to determine experimentally, the levels of damage induced in laminated composite plates subjected low velocity impact, and to correlate the damage observed with known properties of the target plate and the impact event. Of particular interest was the identification of the test parameters that would provide us with damage levels consistent with the Air Force and NASA specification for nondetectable damage. That specification states that the limit of nondetectable impact damage is that

damage caused by the impact of a 25 mm (1.0 in) diameter hemispherical impactor with a 135 J (100 ft-lbf) of kinetic energy or that kinetic energy required to cause a dent 2.5 mm (0.10 in) deep, whichever is least. (ASM International, 1987)

Along with the experimental program, the recent literature was reviewed in an expansion of the survey of literature conducted during last summer's effort.

A computer program, only recently received in the Flight Dynamics Laboratory, that predicts the extent of damage in an impacted plate, was investigated. This program allows the user to input the magnitude the impact, the boundary conditions and material properties of the plate, making it possible to simulate our experiments in the computer and thereby to verify the applicability of the model for the material systems currently of greatest interest.

III. REVIEW OF LITERATURE:

The behavior of graphite/epoxy composite systems during impact has been studied extensively over the past twenty years. It has been shown experimentally that interior damage significant enough to reduce overall structural strength by as much as 50% may not be visible on the surface (Cantwell and Morton, 1984 and Ramkumar, 1981). Furthermore, this strength loss may be larger than that resulting from a hole drilled to the same size as the impact and larger than that measured after ballistic tests are performed.

The response of the target has been shown to be a function of specimen thickness. Thin specimens typically fail in flexure, whereas thicker specimens fail in shear. A more thorough review of the existing literature can be found in the author's report of last year's summer program (Wolfe, 1987)

IV. TEST PROGRAM:

Low velocity impact tests were conducted on composite panels from 9 plies to 96 plies thick using the FIBC Dynatup drop test facility. The impact velocity and time history of force were recorded for all tests. Several panels had strain gages attached to the back face allowing time histories of strain to be recorded as well.

The experimental program was divided into two phases. In phase one, the level of impact energy resulting in just detectable surface damage as defined in Reference was determined. Since the level of impact energy required to cause a detectable dent on the impact face resulted in extensive matrix cracking on the backface, reliable strain measurements could only be made during a second phase of tests in which the impact energy was significantly reduced from the phase one levels. Because the impact energy level was low in the phase two tests, the effect of multiple hits on the response of a target plate could be investigated. This was accomplished by subjecting instrumented 26 and 48 ply plates to repeated low impact energy hits.

V. DISCUSSION OF TEST RESULTS:

A listing of the tests performed in the phase 1 portion of the program is given in Table 1. The impact energy was calculated from the measured velocity at impact. The amount of permanent

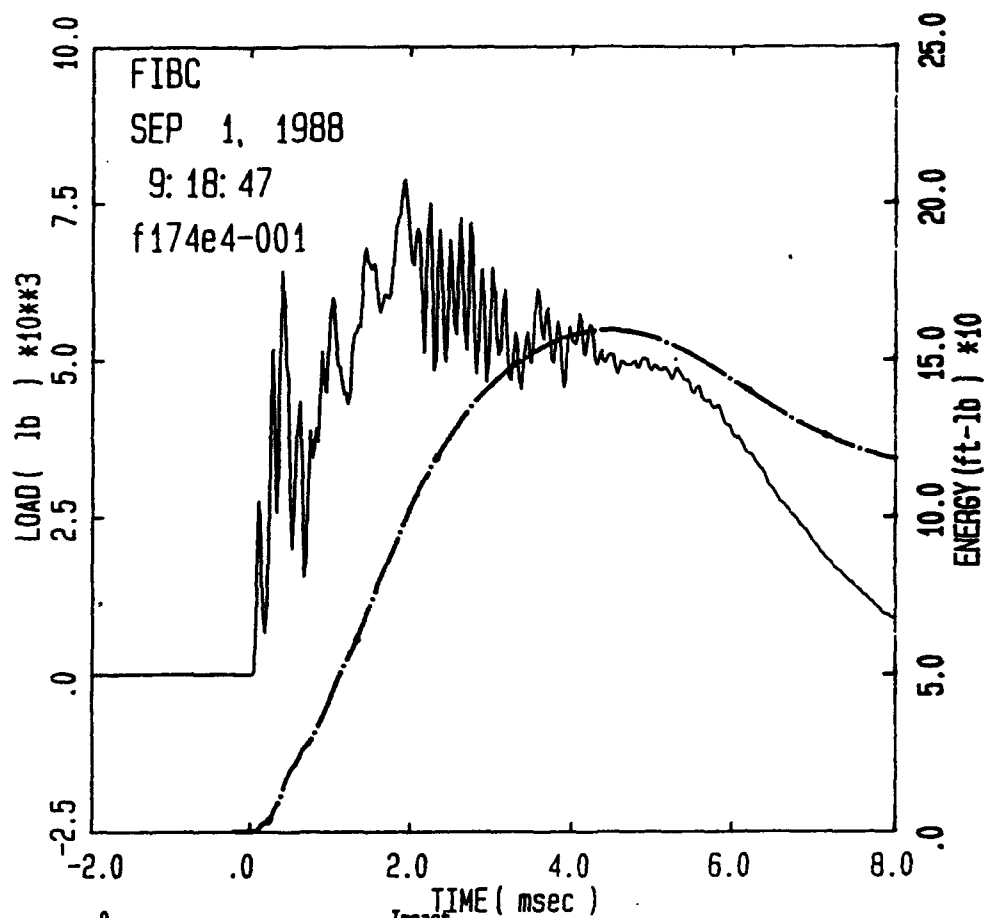
surface indentation was measured for each test using Moire techniques.

An example of typical force and energy time histories (test no. f174e4-001) is shown in Figure 1. Fiber breakage and/or matrix cracking are clearly shown in the figure as a succession of spikes leading up to the maximum load. The maximum load is followed by a series of high frequency spikes which persist for approximately 2 msec. A comparison of the results of the different tests listed in Table 1 is given in Figure 2 in which the ratio of permanent indentation normalized to the thickness of the plate is plotted as a function of impact energy.

An ultrasonic C-scan, was performed on each test panel. The ultrasonic examination showed a significant amount of delamination took place at all phase 1 levels of impact.

TEST NO	THICKNESS in.	DROP HEIGHT in.	HAMMER WEIGHT lbs.	IMPACT ENERGY ft-lbs	SURFACE INDENTATION in.
C3-9E2-001	.0475	6.0	9.315	*	*
C3-9E2-002	.0475	6.0	9.315	4.61	0.008
C3-9E2-003	.0475	9.0	9.315	6.79	0.026
D3-26E3-001	.1365	42.5	9.315	32.72	0.059
D3-26E3-002	.1365	39.0	9.315	30.01	0.051
D3-26E3-003	.1365	36.0	9.315	27.70	0.047
D3-26E4-001	.1365	33.0	9.315	25.44	0.007
D3-26E4-002	.1365	34.0	9.315	26.09	0.022
D3-26E4-003	.1365	35.0	9.315	26.41	0.035
E3-48E4-001	.2520	40.5	30.501	101.80	0.153
E3-48E4-002	.2520	36.0	30.501	90.88	*
E3-48E4-003	.2520	33.0	30.501	82.88	0.060
E3-48E5-001	.2520	34.0	30.501	86.11	0.074
E3-48E5-002	.2520	35.0	30.501	87.80	0.113
E3-48E6-001	.2520	36.0	30.501	90.68	*
E3-48E6-002	.2520	37.0	30.501	92.95	0.118
F2-74E-001	.3885	36.0	53.144	157.46	0.093
F2-74E-002	.3885	38.0	53.144	167.30	0.093
F2-74E-003	.3885	33.0	53.144	144.58	0.084
G2-96E-001	.5046	33.0	77.670	211.40	0.062
G2-96E-002	.5046	38.0	77.670	243.47	0.124
G2-96E-003	.5046	37.0	77.670	237.58	0.091

TABLE 1. SUMMARY OF PHASE 1 TEST RESULTS



Impact								
Specimen Id	Temp (f)	Veloc. (ft/sec)	Energy (ft-lb)	Time (msec)		Load (lb)	Energy (ft-lb)	
				Max	Ld Total	Max	Maxld	Total
f174e4-001	70.	13.82	157.82	1.92	10.00	7879.5	98.309	113.513

Filter No.- 1, No Smoothing.

Comments:

weight 53.144 lbs

drop height 36 inches

FIGURE 1. FORCE AND ENERGY TIME HISTORIES FOR A TYPICAL SAMPLE

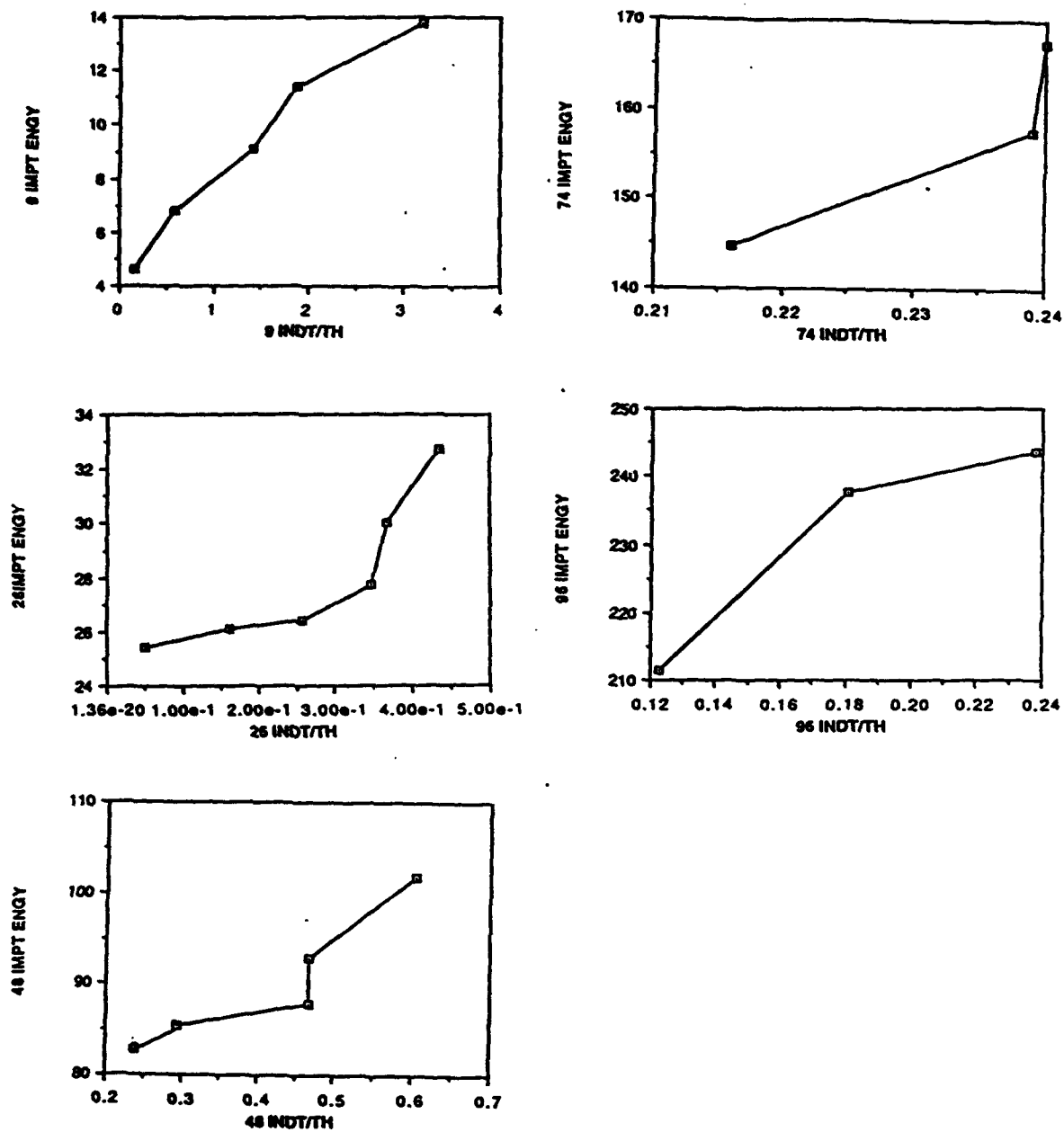


FIGURE 2. PERMANENT INDENTATION VS. IMPACT ENERGY

In order to minimize backface splitting, the magnitude of impact energy was significantly reduced in the phase 2 tests. In addition to measuring the load time history as in phase 1, strain gages were mounted to the backside of the plate and strain time histories were obtained.

TEST NO	THICKNESS in.	DROP HEIGHT in.	HAMMER WEIGHT lbs.	IMPACT ENERGY ft-lbs	INITIAL OR REPEAT HIT
8-10T-001	.1365	9.0	9.315	7.01	initial
8-10T-002	.1365	6.0	9.315		repeat
8-10T-003	.1365	6.0	9.315	6.79	repeat
8-10T-004	.1365	6.0	9.315	4.61	initial
8-10T-005	.1365	6.0	9.315	3.72	repeat
8-10T-006	.1365	6.0	9.315	4.68	repeat
8-10T-007	.1365	6.0	9.315	4.56	repeat
8-10T-008	.1365	6.0	9.315		initial
8-27G-001	.2520	6.0	9.315		initial

TABLE 2. SUMMARY OF PHASE 2 TEST RESULTS

Figure 3 presents the load and two strain time histories for test 8-10T-008. According to Table 2, the target plate used in this test had not been previously impacted. Note that the load time history is very similar in appearance to the load time history presented as Figure 1, i.e. the peak load is followed immediately by a sharp drop in the load. Apparently there is some fiber breakage or matrix cracking even at small energy levels typical of the phase 2 tests. Notice also, that the strains measured on the back face of the panel exhibit the same

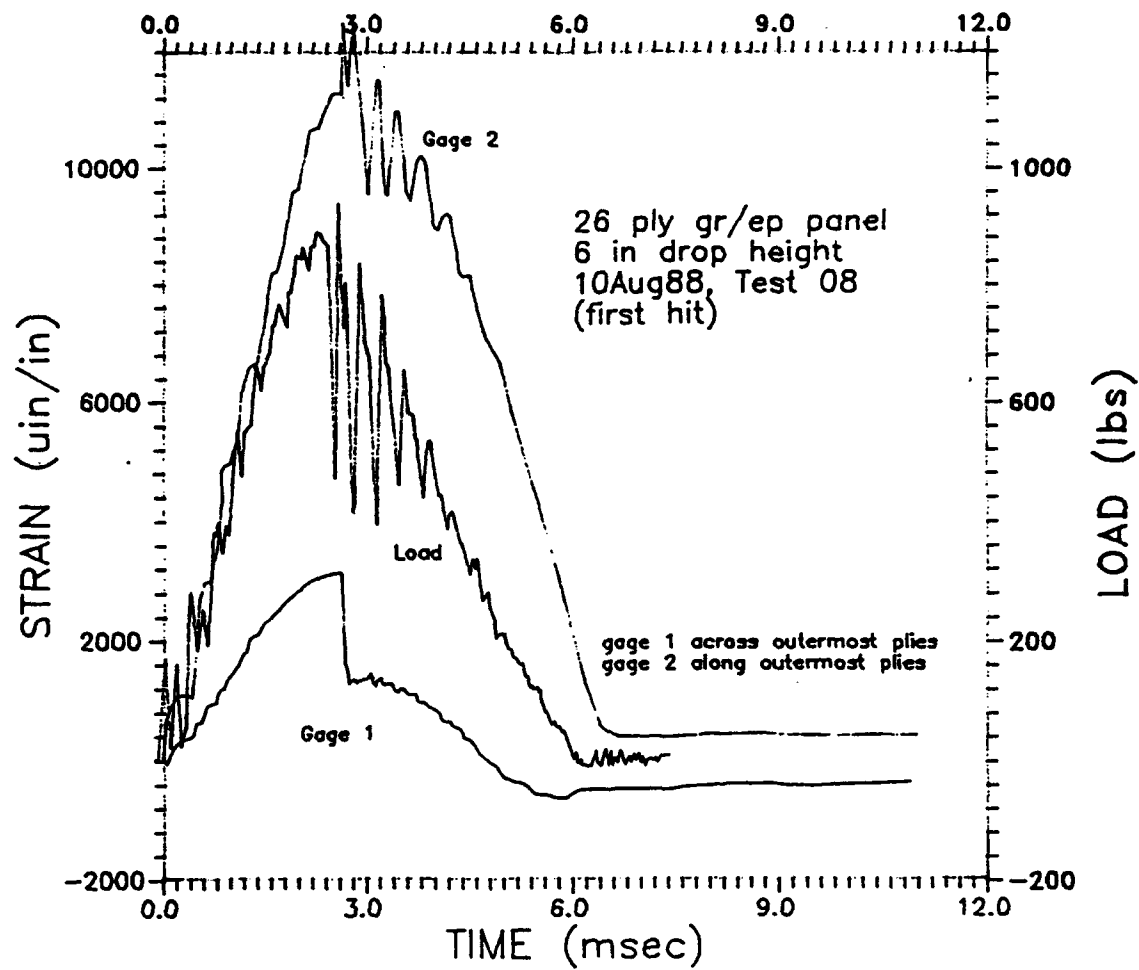


FIGURE 3. PEAK LOAD AND FIBER STRAIN, TEST 8-10T-008

drop that was seen in the load record. Figure 4 presents the load and strain records for a test on a previously impacted panel. Note that there is a significant difference between the behavior observed during an initial impact (Figure 3) and that measured during subsequent tests (Figure 4). These differences in behavior can be clearly seen in the load time history curves presented in Figure 5, which shows three successive impact tests conducted on the same panel. Even at the low load levels employed in this phase, damage occurred during the first test. This damage left the panel less stiff and without the high frequency vibrations which had been typical of the response of the graphite/epoxy composites to impact loads.

Looking again at Figures 3 and 4, it is apparent that the strains measured along the outermost fibers are much larger than those measured across the fiber direction. The program PLATE (Graves and Koontz, 1988) was used to compare the predicted panel strains with these experimentally obtained values. Figure 6 presents a comparison of predicted and observed strains for a 48 ply panel assumed to be simply supported on all four sides. The strains in the direction of the fibers are closely predicted, but present analyses do not adequately predict the strains measured normal to the direction of the fibers.

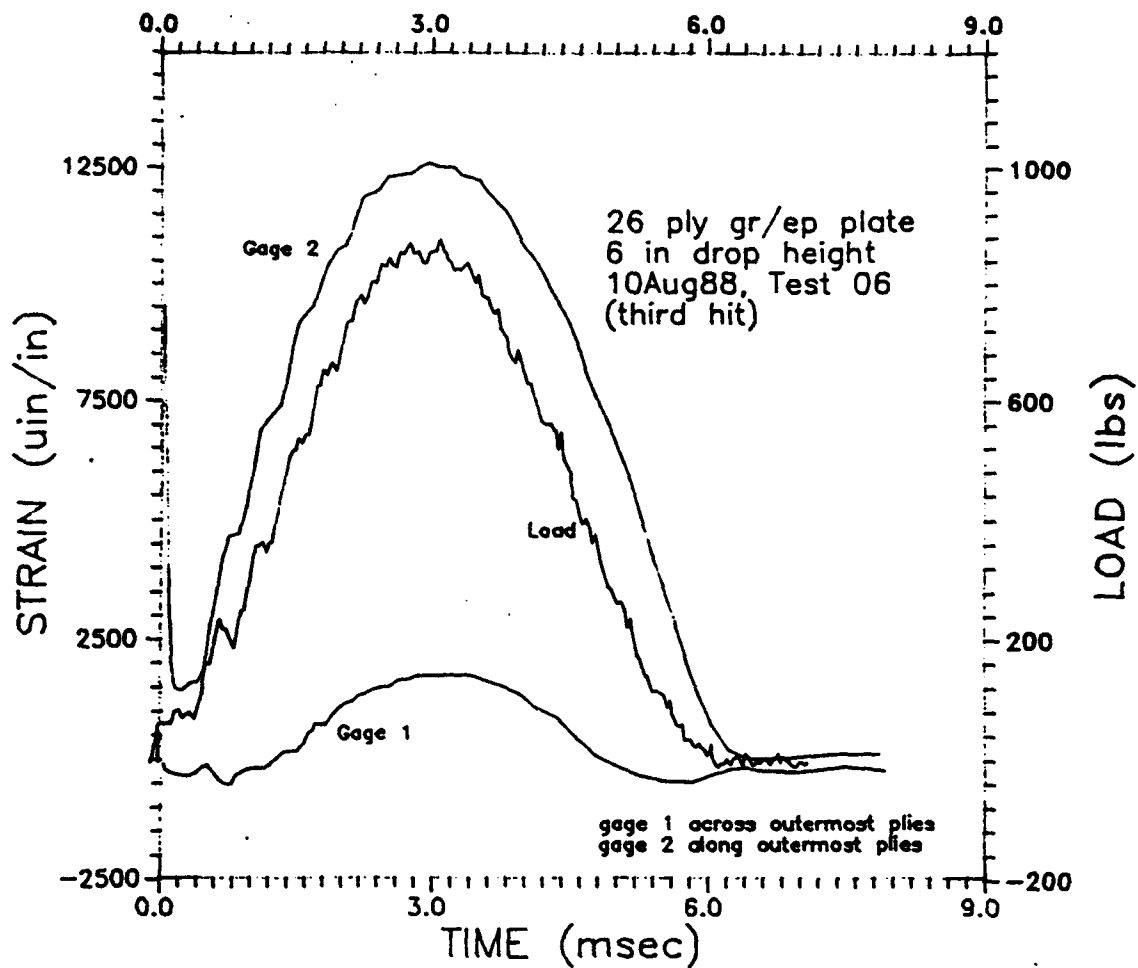
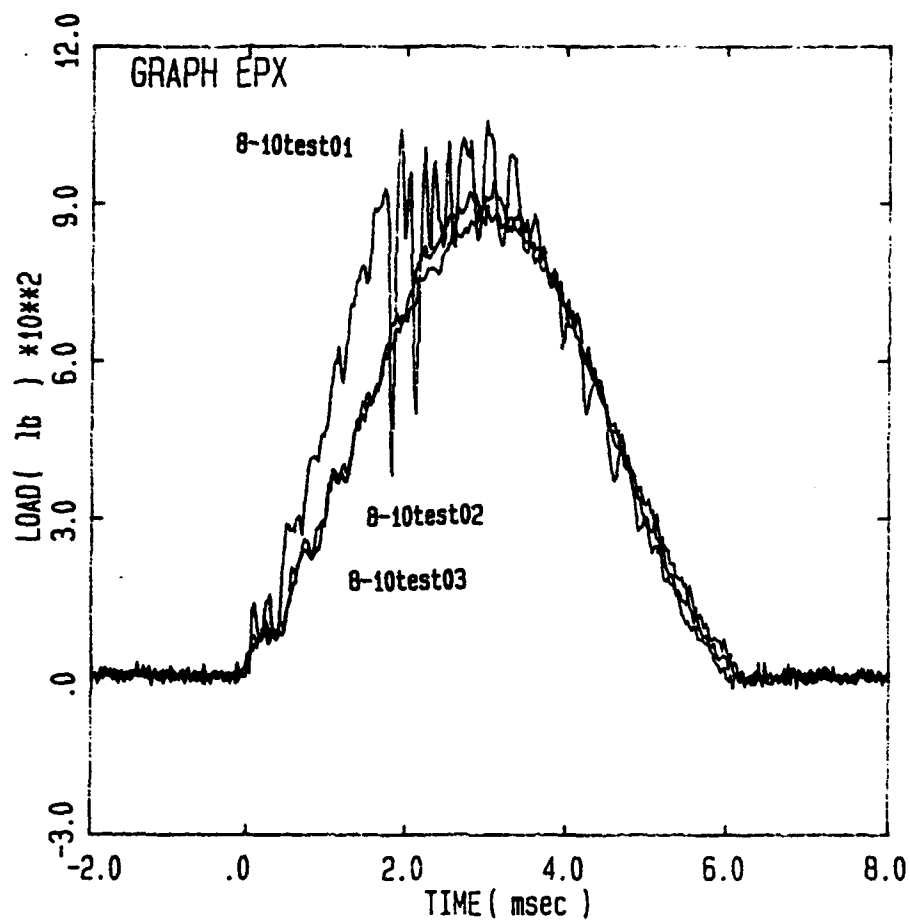


FIGURE 4. PEAK LOAD AND FIBER STRAIN, TEST 8-10T-006



Specimen Id's of Overlaid Curves:

8-10test01 8-10test02 8-10test03

FIGURE 5. COMPARISON OF LOAD VS TIME FOR THREE SUCCESSIVE IMPACTS

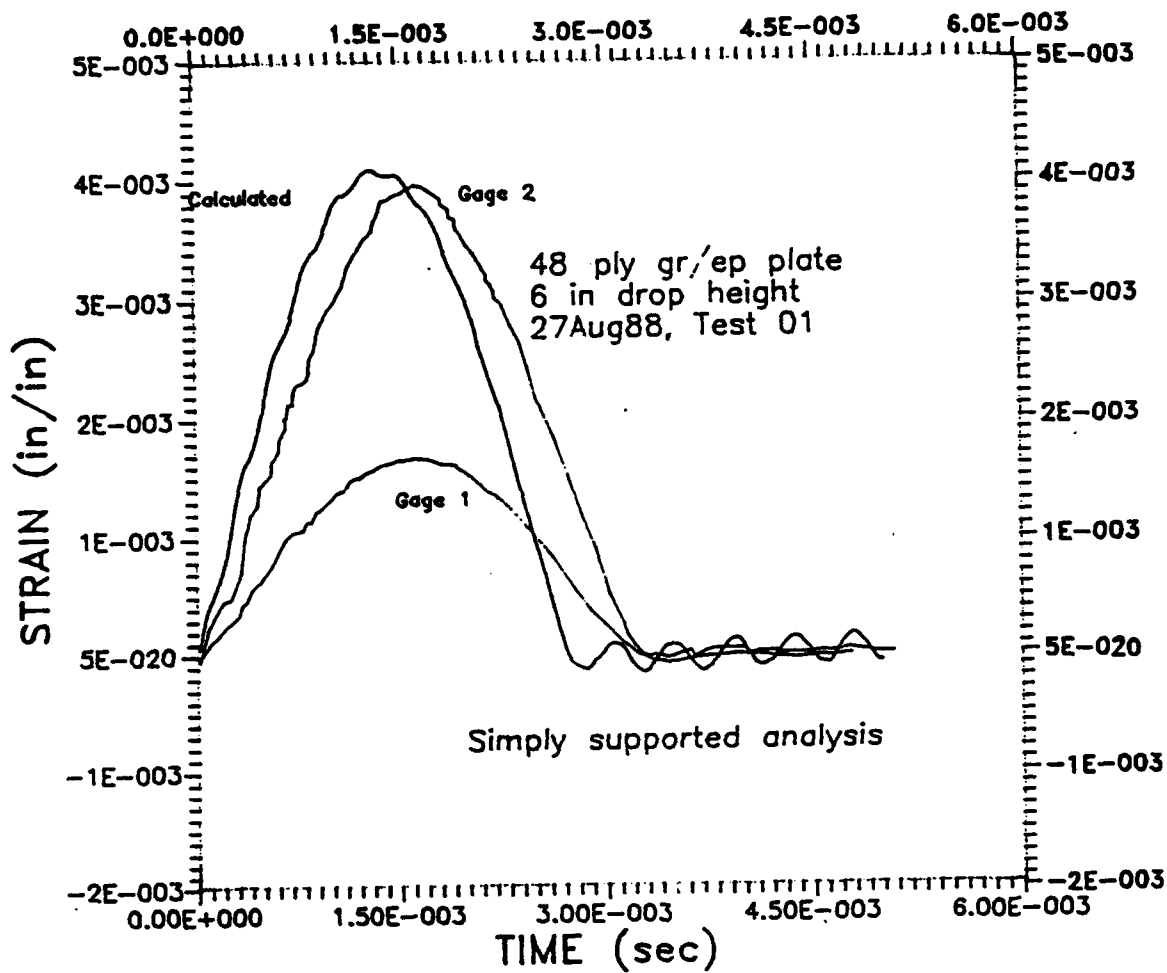


FIGURE 6. COMPARISON OF CALCULATED AND MEASURED STRAIN VS TIME CURVES

VI. RECOMMENDATIONS

The test results presented in the above sections clearly show that the behavior of the test specimen, is dependent on several parameters, impact energy and whether or not the target is subjected to repeated hits. These results combined with compression after impact load tests which still need to be conducted, should form a data base for the development of a method for determining the severity of impact induced damage and the identification of areas requiring repair. Additional tests should be conducted to add to the number of tests in the data base. We propose that additional impact tests be included in a future test program in order to identify the effects of the following on specimen response:

- a) different layup designs maintaining the same energy and velocity
- b) plate thickness on the visible damage on both impact and back faces
- c) support conditions on the levels of damage experienced.

All tests described in this report were performed using the NASA fixture which has a 5in square opening under the impact area. The damage observed in several of our tests extended to the supports and was clearly related to location and fixity of the boundaries. The assumption was made that the NASA fixture provided a fixed condition at the plate boundaries, but our analysis of the response of the test

plate indicates that the boundary conditions are closer to simply supported. The effect of changing boundary fixity needs to be examined.

- d) impactor shape on damage zone. The tests performed to date have all been with hemispherical impactors. The behavior of the composite plate to the hemispherical impactor may be different when the impactor is blunt ended or at the other extreme a sharp corner.

Further tests with the back face of the target plate instrumented need to be conducted. Plates with the same ply orientations studied in this project as well as other orientations need to be studied. Tests in which the deflection of the composite plate is measured without contacting the specimen would complement the strain measurement tests and make it possible to correlate load and strain readings with actual plate deflections.

Tests in which the specimen be impacted is placed under a static load similar to what should be expected to occur in service should be conducted.

REFERENCES

ASM International, Composites, Engineered Materials Handbook, Volume 1, Metals Park, Ohio, 1987

Cantwell, W.J. and Morton, J., "Low Velocity Impact Damage in Carbon Fibre Reinforced Plastic Laminates," Proceedings of the Fifth International Congress in Experimental Mechanics, June, 1984, pp. 241-255. pp. 314-319.

Graves, M.J. and Koontz, J.S., "Initiation and Extent of Impact Damage in Graphite/Epoxy and Graphite/Peek Composites," "AIAA/ASME/ASCE/AHS, 29th Structures, Strucrural Dynamics and Materials Conference, April, 1988, pp. 967-975.

Ramkumar, R.L., "Composite Impact Damage Susceptibility," Final Report, NADC-79068-60, Northrop Corporation, Aircraft Division, Hawthorne CA, January, 1981.

Wolfe, W.E., LOW VELOCITY IMPACT OF GRAPHITE/EPOXY PLATES, Final Report, USAF-UES Summer Faculty Research Program, 1987.

1988 USAF-UES SUMMER FACULTY RESEARCH PROGRAM/
GRADUATE STUDENT RESEARCH PROGRAM

Sponsored by the
AIR FORCE OFFICE OF SCIENTIFIC RESEARCH
Conducted by the
Universal Energy Systems, Inc.

FINAL REPORT

ANALYSIS METHODS FOR NONLINEAR
MECHANICAL BEHAVIOR OF GLASSY POLYMERS

Prepared by:	R. J. Arenz, S.J., Ph.D.
Academic Rank:	Professor
Department and	Mechanical Engineering Department
University:	Gonzaga University
Research Location:	AFWAL/MLBM
	Wright-Patterson AFB, OH 45433
USAF Researcher:	Stephen W. Tsai
Date:	September 10, 1988
Contract No.:	F49620-87-R-0004

Analysis Methods for Nonlinear
Mechanical Behavior of Glassy Polymers

by

R. J. Arenz

ABSTRACT

As thermoplastic polymers become candidates for use as the matrix material of advanced composite structures, one of the aspects needing study is their nonlinear viscoelastic behavior. Even small strains can produce nonlinear effects that are different from thermosetting plastics. This may affect the analysis of the interaction between the matrix and the reinforcing fibers as well as influence the processing conditions to be used during the manufacturing cycle for the composite material. In this investigation recent theories on the nonlinear mechanical response of glassy polymers are examined qualitatively. Several of the more promising formulations involving the free volume of polymer materials are quantitatively compared and related to experimental data by computer techniques to handle the numerical integration and iterative procedures required in solving the associated sets of coupled nonlinear differential equations. Engineering approaches to treating thermoplastic matrix mechanics are suggested. The analysis indicates that more complete viscoelastic characterization of bulk modulus is needed to facilitate the application of the free volume approach.

Acknowledgments

I wish to thank the Air Force Wright Aeronautical Laboratories and the Air Force Office of Scientific Research for sponsorship of this research. Universal Energy Systems provided significant help in administrative and organizational aspects of this program.

The suggestions and encouragement of Dr. Stephen Tsai as my Wright-Patterson research colleague are especially appreciated. The invaluable help of Lt. John Roberts in providing excellent computer system support and programming pointers is gratefully acknowledged. Discussions with Lt. David Curliss contributed greatly in orienting the research results to benefit a broader range of potential applications than originally envisioned.

I. INTRODUCTION:

Many composite (combination) materials in current use consist of an epoxy resin matrix with various kinds of reinforcing fibers. There is considerable interest, especially in the aerospace field, to replace the thermosetting epoxy with thermoplastic glassy polymers to facilitate manufacturing and provide higher toughness (fracture resistance) to the resulting high-strength, low-density composite materials.

Since the glassy polymers can exhibit appreciable strain (beyond the infinitesimal range associated with linear elastic and viscoelastic analysis methods), the interaction of the polymer matrix with the embedded reinforcing fibers during deformation needs to be well understood. In addition, the processes used in manufacture of composites can produce material changes and residual stresses that affect the performance of composites in service. Many of the processes also involve large-scale deformation of the polymeric material; thus, there is a consequent need to assess the material behavior in the nonlinear regime to be able to specify the proper processing conditions (temperature, pressure, etc.) during manufacture.

A necessary preliminary step is the complete characterization of the nonlinear mechanical behavior of the glassy polymers themselves. Ideally it should account for the nonlinearities arising both from viscoelastic response of the long chain molecular structure of the polymer and from finite deformation effects associated with purely elastic analysis.

Previous studies I have made of the nonlinear response of elastomers and knowledge of viscoelastic analysis methods such as time-temperature superposition of stress relaxation phenomena have stimulated my interest in the nonlinear behavior of glassy polymers. Brief qualitative evaluations have been made of several theories proposed in recent years to describe nonlinear viscoelastic behavior. These theories do not lend themselves to direct mathematical solutions in closed form and they generally involve coupled partial differential equations and iterative procedures.

This background of involvement in related viscoelastic analysis areas contributed to my assignment to the Materials Laboratory of the Air Force Wright Aeronautical Laboratories at Wright-Patterson Air Force Base. The

Nonmetallic Materials Division is interested in forwarding the understanding of the design and manufacture of advanced composite structures for aircraft and space vehicles.

II. OBJECTIVES OF THE RESEARCH EFFORT:

Several recent theories (1,2,3) have attempted to describe the nonlinear viscoelastic behavior of glassy (thermoplastic) polymeric materials. The objective of this research is to explore several of these theories, indicating the feasibility of engineering application. Previous investigation by the author has identified the methods of Knauss and Emri (1) and Shay and Caruthers (2) for further quantitative study to assess accuracy, consistency, range of applicability and ease of computation.

A side issue that became an additional goal as the study progressed was to assess the kinds and range of material property data necessary for the adequate engineering treatment of polymer response to stress, strain, and environment.

Where appropriate, comments will be made as to how these considerations relate to the design and manufacturing processing of glassy polymers in advanced composite materials.

III. NATURE OF THE NONLINEAR THEORIES:

Once one leaves the domain of linear mechanical behavior, a variety of theoretical and representational approaches may be taken. Several of the theories (1, 2) of mechanical stress relaxation and creep are based on the concept of fractional free volume below the glass transition temperature (T_g). The free volume is the internal space available for chain movement and relaxation to take place as the material tends toward the equilibrium state of maximum density in which all the volume is occupied. In this case, there is no "hole" or free volume left in the material.

Viscoelastic time dependency is accounted for by suitable time-scale shifting factors. The stress state can in principal be related to free volume since a mechanically induced dilatation tends to increase the free volume.

Qualitative comparisons of the methods have indicated that these theories most closely relate to the physics of the material and goals of

this study; hence, the Knauss-Emri and Shay-Caruthers approaches have been selected for closer examination.

IV. THE KNAUSS-EMRI APPROACH:

Knauss and Emri (1) have used a free volume approach in which they in principle allow it to reflect the effect of not only temperature and stress-induced dilatation but also a swelling due to solvent content. The fractional free volume (with additive contributions from the various factors) is written as

$$f = f_0 + A[\alpha(t) * (dT)] + B[M(t) * (d\tau_{kk})] + C[\gamma(t) * (dc)] \quad (1)$$

where f_0 = fractional free volume at a reference temperature

A, B, C are constants

α = thermal expansion coefficient

T = temperature

M = linear viscoelastic bulk creep compliance

τ_{kk} = first stress invariant = $\tau_{11} + \tau_{22} + \tau_{33}$

γ = solvent-related volume creep function

c = solvent concentration

and the "*" indicates Stieltjes convolution (superposition integral).

Since the tensorial stress and strain components are retained in their formulation, it is valid for very general deformation states. They assume the same stress-induced changes on the scale of relaxation times occur with the change in volume accompanying a uniaxial tensile strain, and convert the general expressions to the case of a uniaxial response to a constant strain rate ($\dot{\epsilon}_0$) input (a readily achieved experimental test condition). Considering further a case for comparison to experimental data where there is no change in solvent content and isothermal conditions for any given test, the following set of corresponding equations for this simpler situation is obtained:

$$\tau_{11}(t) = \dot{\epsilon}_0 \int_0^t E(t' - \xi') d\xi \quad (2)$$

$$t' - \xi' = \int_{\xi}^t \frac{d\xi}{a[\theta(\xi)]} \quad (3)$$

$$\log a(t) = \frac{-b}{2.3f_0} \left[\frac{B \theta(t) + \alpha \Delta T}{f_0 + B \theta(t) + \alpha \Delta T} \right] \quad (4)$$

$$3 \theta(t) = (M_0 + M_1) \tau_{11}(t) - M_1 \int_0^t \left[e^{-\left(\frac{t' - \xi'}{\tau}\right)} \right] \frac{\partial \tau_{11}}{\partial \xi} d\xi \quad (5)$$

where

θ = stress-induced dilatation

$E(t)$ = linear viscoelastic tensile relaxation modulus

b = a material constant

τ_{11} = uniaxial tensile stress

α = linear thermal volume expansion coefficient

ΔT = difference in temperature from some chosen reference temperature

and equation (4) is the Doolittle shift factor equation.

The linear bulk creep compliance $M(t)$ is represented as a standard linear solid, i.e.,

$$M(t) = M_0 + M_1 \left(1 - e^{-\frac{t}{\tau}} \right) \quad (6)$$

with τ representing the bulk retardation time.

The (large-strain) nonlinearity is carried in the time-scale shifting effect, while entirely linear viscoelastic relaxation and creep functions are used in the stress-strain relations. In that sense this method uses a hybrid approach with part-linear, part-nonlinear mechanics involved.

The authors present comparison of several predictions with experiments that appear quite good, including recovery from uniaxial constant strain unloading as well as from the loading portion of the process. The range of situations handled by the method is indicated by the application to simultaneous applied pressure and constant strain rate uniaxial deformation, pressure aging with subsequent superposed straining, thermal volume creep, and volume change following both quenching and sudden increase of temperature. All comparisons with straining experiments are for temperatures close to T_g , so the behavior remote from T_g remains a question.

V. SHAY-CARUTHERS METHOD:

Shay and Caruthers (2) propose a model combining a Boltzmann-type superposition integral involving a linear viscoelastic Poisson's ratio ν to relate lateral to axial strain and a free volume equation of state. Nonlinearity enters in primarily through a volume- and temperature-dependent shifting of the time scale for a relaxing $\nu(t)$. The set of coupled equations to handle the uniaxial extension case is

$$\lambda_{\ell}(t) = 1 + \int_{-\infty}^t [\nu(t^* - \xi^*)] \frac{\partial \lambda_a(\xi)}{\partial \xi} d\xi \quad (7)$$

$$\log a(t) = \frac{B}{2.303} \left[\frac{1}{h(t)} - \frac{1}{h_0} \right] \quad (8)$$

$$\frac{\tilde{P}\tilde{V}}{\tilde{T}} = [1 - 2^{-1/6} y(y\tilde{V})^{-1/3}]^{-1} + \frac{2y}{\tilde{T}} (y\tilde{V})^{-2} [1.011(y\tilde{V})^{-2} - 1.2045] \quad (9)$$

where y = fraction of occupied sites

λ_{ℓ} = lateral extension ratio

λ_a = axial extension ratio

$a(t)$ = generalized shift factor

$h=1-y$ = hole fraction (h_0 is for reference state)

B = material constant

P^*, V^*, T^* = reducing pressure, volume, and temperature parameters
(constants of the given material)

$\tilde{P} = P/P^*, \tilde{V}=V/V^*, \tilde{T}=T/T^*$, reduced pressure, volume and temperature.

Reduced times t^* and ξ^* are as given by equation (3). Equation (8) is essentially the Doolittle equation for fractional free volume and equation (9) is the Simha-Somcynsky statistical thermodynamic equilibrium equation of state for the fraction of occupied sites. The set of equations (7)-(9) must be solved numerically and iteratively for each discrete increment of time over the strain history.

Another Boltzmann superposition then gives the uniaxial tensile stress history

$$\sigma(t) = \int_{-\infty}^t E(t^* - \xi^*) \frac{\partial \lambda_a(\xi)}{\partial \xi} d\xi \quad (10)$$

where $E(t)$ is the linear viscoelastic uniaxial tensile relaxation modulus.

Since the strain relation is basically a three-dimensional one, Shay and Caruthers have also extended this method to the general nonlinear viscoelastic strain state (the parameter ν in essence along with E determines bulk behavior). A feature to be remarked about these equations is that the shift factor is the same in equations (7) and (10) for both ν and E .

The results for uniaxial constant strain rate elongation for PMMA material with some simplified representations of linear material relaxation spectra showed a yield stress that increased with strain rate in qualitative agreement with data obtained experimentally.

VI. ANALYSIS RESULTS FOR KNAUSS-EMRI THEORY:

Since most of the presentations in the literature are theoretical equations that do not have closed form solutions, it has been necessary to develop the mathematics to solve for numerical results in order to evaluate and compare different methods. The theories in general involve coupled nonlinear partial differential equations which require solutions by step-wise time increments and numerical integration. Moreover, iteration is needed to determine the "reduced" (material) time associated with each step.

Attention has been focused so far on the stress response to uniaxial constant strain (relaxation) and constant strain rate processes. Fortran computer programs have been written and run on a VAX11/785 mainframe computer to achieve solutions.

To enable realistic material property representation, Prony series of decaying exponential terms were used throughout to evaluate linear relaxation moduli. We consider first the Knauss-Emri formulation. The authors were unable to furnish computer programs for the results

indicated in reference 1, so it was necessary to develop the software independently. Information from uniaxial relaxation tests on poly (vinyl acetate) material at strain levels of 1%, 3%, and 5% were shown as master relaxation curves (1); these are duplicated in Figure 1. (Unfortunately, no indication of the reference temperature was given in the original paper.)

The nonlinear theory should provide a mathematical technique to predict the finite-strain relaxation behavior knowing the stress relaxation for infinitesimal strain. Similarly, it might be expected that actual experimental results at finite strains would predict the linear infinitesimal-strain results by application of the theory.

To set up the computer program, equations (1) to (4) are recast in numerical integration form as summations for the xth time-step as follows for the determination of nonlinear modulus:

$$M(x) = M_0 + M_1(1 - e^{-t(x)/\tau}) \quad (11)$$

$$\theta(x) = \theta_0 + \frac{1}{3} \sum_{n=1}^x M[t'(x) - t'(n)] \frac{\partial \tau_{11}(n)}{\partial t} \Delta t(n) \quad (12)$$

$$\log \phi(x) = \sum_{m=1}^x \frac{-b}{2.303 f_0} \left[\frac{\alpha \Delta T + B\theta(x)}{f_0 + \alpha \Delta T + B\theta(x)} \right] \quad (13)$$

$$t'(x) = \sum_{m=1}^x \frac{\Delta t(m)}{\phi[\theta(m)]} \quad (14)$$

$$t'(x) - t'(n) = \sum_{m=n}^x \frac{\Delta t(m)}{\phi[\theta(m)]} \quad (15)$$

$$E_{lin}(x) = E_e + \sum_{i=1}^N E_i e^{-\frac{t(x)}{\tau_i}} \quad (16)$$

$$\tau_{11}(x) = \epsilon_0 E_{lin}[t'(x)] \quad (17)$$

$$E_{nonlinear}(x) = \tau_{11}(x)/\epsilon_0 = E_{lin}[t'(x)] \quad (18)$$

For each x , an initial trial value of $t'(x)$ is chosen (based on the previous step) and the calculations are iterated until suitable convergence is obtained for t' . The criterion of convergence used was 10^{-15} min, which proved to be fully adequate and achievable without requiring excessive computer time. Checkout of the program showed it was accepting inputs and solving the set of equations correctly. Since the time range of data and results covered up to eight or nine decades of logarithmic time, the time increment from one solution point to the next was chosen on a logarithmic basis at 0.05 decade; trial solutions using 0.02 decade showed the same result, so 0.05 decade was considered to be sufficiently close spacing.

Material parameters were given for PVAc by the authors (4) as $b=0.16$, $f_0=0.01$, $\alpha = 5.98 \times 10^{-4}/^{\circ}\text{C}$, $B=1$. Bulk time-dependent behavior was less satisfactorily defined. Although at least one measurement of dynamic bulk creep compliance exists for one PVAc material example (5), the proposed method makes determination of bulk behavior a part of the solution technique. That is, in attempting to establish the linear (infinitesimal strain) uniaxial relaxation modulus curve, they try various bulk compliance values and time dependency to arrive at a "best fit." This is the origin of the standard linear solid representation of bulk compliance (or modulus) as a suitable evaluation. Unfortunately, references 1 and 4 give contradictory listings for the bulk modulus so the actual value used by the authors cannot be determined.

In our analysis of reducing to the linear reference state, the best fit bulk modulus for all strains is given by $M_0 = 6.0 \times 10^{-5} \text{ bar}^{-1}$, $M_1 = 0.3 \times 10^{-5} \text{ bar}^{-1}$, $\tau = 10^6 \text{ min}$. (This corresponds to a reasonable glassy value of Poisson's ratio of 0.32, but displays relatively little change in M as it approaches the equilibrium state.) But even this solution does not provide a completely unified result when applied to the reduction of the $\epsilon_0 = 1\%$, 3% and 5% data curves to a reference condition of zero strain (Figure 2). Nor does this set of results agree well in the mid-transition region with the zero-strain curve of references 1 and 4.

While these differences are not large, how are they accounted for? Probably the first place to look at is equation (12) for $\theta(t)$.

Reference 4 gives it as

$$3\theta = (M_0 + M_1) \tau_{11}(t) - \int_0^t e^{-(t' - \xi')/\tau} \frac{\partial \tau_{11}}{\partial \xi} d\xi$$

It is probable that the missing M_1 before the integral is just a typographical error, but more significantly, for a relaxation process with a step strain input, there will be an initial elastic stress response $\tau_{11}(0)$, so the stress in the first term on the right hand side of the equation must read $\tau_{11}(t) - \tau_{11}(0)$. It is not known if the full term was correctly included in the actual calculations. Finally, the exponent $(t' - \xi')$ was approximated by $(t - \xi)$ in the former work (4) whereas we have included the exact term in the computer integrations. Examination of values at various phases of the integration show that the difference $(t - \xi)$ can be too small compared to $(t' - \xi')$ by a factor as large as 13 for the $\epsilon_0 = 0.01$ case and 33 for the $\epsilon_0 = 0.05$ case. Consequently, the approximation could contribute considerable error to the solution.

If one steps outside the theory for the moment and considers the original relaxation data from the standpoint of physical reasoning, a cross-plot of $\log t$ vs. ϵ_0 from Figure 1 for a series of constant E values shows that a reasonable extrapolation of the curves can be made back to $\epsilon_0 = 0$. This resulting linearly viscoelastic relaxation modulus does nearly match with the curve chosen in the previous work (1,4). Taking this zero-strain result to be reasonable and starting from only the $\epsilon_0 = 0.01$ curve, a best fit analysis to match the $\epsilon_0 = 0$ curve of Figure 1 produced a bulk compliance standard linear solid representation with $M_0 = 4.5 \times 10^{-5} \text{ bar}^{-1}$, $M_1 = 1.35 \times 10^{-6} \text{ bar}^{-1}$, $\tau = 10^6 \text{ ,min.}$

Both curves (from Figures 1 and 2) for the infinitesimal strain modulus were then tried as separate linear bases to calculate the variable-strain results. In neither case did the computerized theory using the same bulk characterization for all strains reproduce a satisfactory fit for anything more than the $\epsilon_0 = 0.01$ curve; the 0.03 and 0.05 strain curves were significantly far from fitting the experimental data. The implication from this is that there may be a

nonlinearity required as well in the bulk modulus behavior for different strain levels. The extent of this variation remains to be investigated. (McKinney and Belcher (5) indicate the possibility of nonlinear dependence of bulk compliance on pressure in compressibility tests on PVAc.)

The next test condition examined in relation to the Knauss-Emri theory was a uniaxial constant strain rate input. The equations make use of the relaxation modulus, but the case covered in reference 1 was limited to a total strain of 2.8%, which at a strain rate of 0.01/min produced a total loading time of 2.8 min. The constant strain rate results shown in reference 1 indicated a deviation from linear viscoelastic results starting at about 0.5 minutes ($\log t = -0.3$). The associated uniaxial relaxation modulus curves would show the total test time to be within the glassy behavior region; consequently no viscoelasticity should be expected if the relaxation data were at the same temperature as the chosen test temperature of 26.5°C. Since no reference temperature was given for the relaxation data, it had to be considered that the appropriate temperatures for the two sets of experiments were in fact different. Some other data in the literature on time-temperature shifting of PVAc permitted an estimate of -13°C to be made for the reference temperature of the relaxation curves. (This is quite far removed from the 28°C listed as T_g for the material.) With the change of temperature (ΔT) incorporated in the shift factor (eq. (13)), stress results were obtained for the referenced constant strain rate (Figure 3). Also shown in the figure are lines representing linear elastic behavior, linear viscoelastic response, and the solution of reference 1. Closest agreement with the Knauss-Emri curve was obtained by use of a $\Delta T = +20^\circ\text{C}$ applied to the data of Figure 1. (This is considerably different from the $\Delta T = 26.5 - (-13) = 39.5^\circ$ that would be suggested by the $T_{ref} = -13^\circ\text{C}$ indicated earlier for the data of Figure 1.) Examination of the theory with the time-temperature $\log a_T$ shift of about 6.5 decades removed from the iterative calculation and applied to give a shifted set of relaxation modulus curves prior to the calculation resulted in the curve labeled

" a_T for $\Delta T = 39.5^\circ\text{C}$." The fact that this result shows a similar level of response to the curve with an internal ΔT shift of 20°C suggests that a coefficient originally applied to the $\alpha\Delta T$ term in equation (13) may not in fact be unity, i.e., the change in free volume may not equal the macroscopic thermal volume change.

As the constant strain rate analysis involves only relatively short times, the bulk modulus is not so important a factor and with good reason can be approximated as a constant with the glossy value as was done in the original work (4). Another feature of the constant strain rate problem is that in addition to short times, a further truncation of modulus-curve use is that only $E(t' - \xi')$, not $E(t')$, is involved; thus, the constant strain rate application is in principle a much less stringent test of the overall nonlinear theory than is the relaxation case. Thus, a method may work fairly well for constant strain rate situations but may fail to represent the longer-term relaxation process as well.

Finally, it appears here (and was reinforced by the later treatment of the Shay-Caruthers theory) that the choice of realistic and accurate material properties to put in the analysis may have a strong effect on the results -- so much so as to obscure the physical phenomena the theory is attempting to account for.

An overall question that was first raised by the authors of the theory (4) is whether time-temperature shifting of relaxation data can be done independent of the strain at which measurements are made; further study is needed to determine any nonlinear effect on the shifting procedure.

VII. ANALYSIS RESULTS FOR SHAY-CARUTHERS THEORY:

Computer coding of the the set of equations (7) to (9) was accomplished in a manner similar to that for the Knauss-Emri theory, with numerical summations replacing the integrals. In their approach Shay and Caruthers presented stress results for only the constant strain rate process (2). We analyze the uniaxial tensile case.

The first observation to be made is that the Simha-Somcynsky equation of state (eq. (9)) is derived on the basis of equilibrium

conditions. The time dependent processes that occur in a polymer below T_g will be nonequilibrium in nature. Hence, a certain caution is required in evaluating the results of this method.

Another feature of this formulation is that the value of B in the Doolittle equation (8) must be obtained from experimental equilibrium free volume and temperature measurements. This means usually that the evaluation is made at temperatures near or above T_g and thus has a limited range of temperature applicability. Thus, the strictest interpretation of B is that it is $B(T)$ and not a specific material constant only. (A similar limitation would apply to the Knauss-Emri method discussed previously.)

The method is called "quasi-linear" by Shay and Caruthers because it involves linear elasticity and employs linear viscoelastic material functions, introducing nonlinearity with the deformation-dependent timescale t^* (in parallel with the Knauss-Emri approach). (Shay and Caruthers present also a fully nonlinear formulation where a finite elastic strain tensor is used; we limit our attention here to the quasi-linear approach as it illustrates the principle features of the method.)

Computer coding enables an engineering type of solution but the choice of material property representation turns out to be crucial in determining the nature of the analytical results. Shay-Caruthers choose poly(methyl methacrylate), PMMA, as an example material and show some calculated variations of stress response with different strain rates and temperatures. No experimental comparisons are shown so that the conclusions drawn are all of a qualitative character. This focuses attention on the material representation.

After using standard linear solid representations of E and ν for preliminary results, the authors attempt to be more realistic with what is termed a "box" distribution of relaxation times with $E_g = 2660$ MPa, $E_r = 3.78$ MPa, $\nu_g = 0.33$, $\nu_r = 0.50$. For a reference temperature of 115°C they place the center of the spectrum of relaxation times at 100 seconds. Their box distribution involves the same value for every one of the Prony series relaxation components E_i (of, for example, equation (16)) and thus in no way approximates the spectrum used by McLoughlin and Tobolsky (6), one of their sources for data on PMMA relaxation

behavior. Indeed, almost the entire transition curve with this representation occurs at about 6 decades of logarithmic time longer than a realistic representation of PMMA data.

A comparison of the Shay-Caruthers result at a constant strain rate of 10^{-2} sec^{-1} and a temperature of 70°C with the solution of equations (7) to (10) using the realistic linear relaxation modulus (data from reference 6) is shown in Figure 4; the stress given by the better material representation is less than 10% of the amplified model representation. Thus, the results as shown in reference 2 are purely qualitative in character and may be compared to one another but have very much less relevance to real viscoelastic material behavior. This is another case where idealized model solutions for viscoelastic behavior need to be treated with caution in evaluating their engineering significance.

This analysis suggests that the results of application of the Shay-Caruthers approach shown in reference 2 may be influenced more by the material representation than by the nonlinear analysis itself. Since no comparison with experimental data is given in reference 2, more study of this method is needed before application.

Another aspect investigated was the use of the Simha-Somcynsky equation to evaluate the time-temperature shift factor a_T alone (no specific volume change involved). Comparison of the shift from equations (8) and (9) with the data of reference 6 show values of 4.76 from the former and 7.0 from the latter for $\log a_T$ between 115° and 70°C . (It should be noted that the lower temperature, however, is considerably below T_g (which is in the vicinity of 110°C) where shift data generally show some scatter for materials of very little constitutive difference). It has already been noted that the PV/T equation is an equilibrium equation and its validity below T_g has to be questioned. The value of B itself in equation (9) also has been noted above to be possibly dependent on temperature. Thus, the temperature range of applicability of the theory above and below T_g is not well established.

Shay-Caruthers have taken note of the application of equation (8) to the nonequilibrium condition below T_g and are proposing an alternate

theory based on the use of thermodynamic entropy as a means of dealing with the questions raised above; results from this development have not yet appeared in the literature.

Nonlinear viscoelastic behavior can occur in general at lower strain levels than does nonlinear elastic behavior, but Shay-Caruthers have formulated an alternate theory incorporating a finite strain elasticity tensor which produces a change in volume with pure shear; this consequently predicts a yield condition in shear such as is observed experimentally and represents an improved theory. As with the quasi-linear theory this approach needs verification as to accuracy by experimental data.

VIII. RECOMMENDATIONS:

The free volume approaches in theory offer promise of applicability to the thermoplastic matrix-reinforcement interaction, but several aspects remain to be developed. Since the methods respond strongly to the linear material characterization, further definitive determinations of bulk relaxation modulus are needed for the various materials under study. A correlative property is the Poisson ratio variation with time. These are among the most difficult properties to obtain, but are desirable to fully verify the theories. Further examination of the possible nonlinear behavior in bulk appears called for.

Since the constant strain rate check of results is a less rigorous test of a theory, comparisons should be made using stress relaxation behavior into the nonlinear strain regime.

Most of the published comparisons with experimental data to date have been with conditions not far from T_g . Thus, further analysis and testing is needed to verify the range of temperatures for which the theories are applicable. This is important if a rational approach is to be taken toward understanding the thermal and deformation processing of thermoplastic matrix materials in the manufacture of composites. Deformation beyond the yield point is common in such processes.

The theories examined in detail do not exhaust the range of methods proposed. From a more general outlook, the theories need to be examined for the light they may throw on the fracture process. The three-dimensional possibilities in these theories may suggest when tension or shear may be the predominant factor for failure.

REFERENCES

1. Knauss, W. G., and I. Emri, "Volume Change and the Nonlinearly Thermo-Viscoelastic Constitution of Polymers," Polymer Engineering and Science, 27, 86 (1987).
2. Shay, R., M., and J. M. Caruthers, "A New Nonlinear Viscoelastic Constitutive Equation for Predicting Yield in Amorphous Solid Polymers," Journal of Rheology, 30, 781 (1986).
3. Rendell, R. W., K. L. Ngai, G. R. Fong, A. F. Yee, and R. J. Bankert, "Nonlinear Viscoelasticity and Yield: Application of a Coupling Model," Polymer Engineering and Science, 27, 2 (1987).
4. Knauss, W. G., and I. Emri, "Non-Linear Viscoelasticity Based on Free Volume Consideration," Computers and Structures, 13, 123 (1981)
5. McKinney, J. E., and H. V. Belcher, "Dynamic Compressibility of Poly (Vinyl Acetate) and Its Relation to Free Volume," Journal of Research of the National Bureau of Standards, 67A, 43 (1963).
6. McLoughlin, J. R., and A. V. Tobolsky, "The Viscoelastic Behavior of Polymethyl Methacrylate," Journal of Colloid Science, 7, 555 (1952).

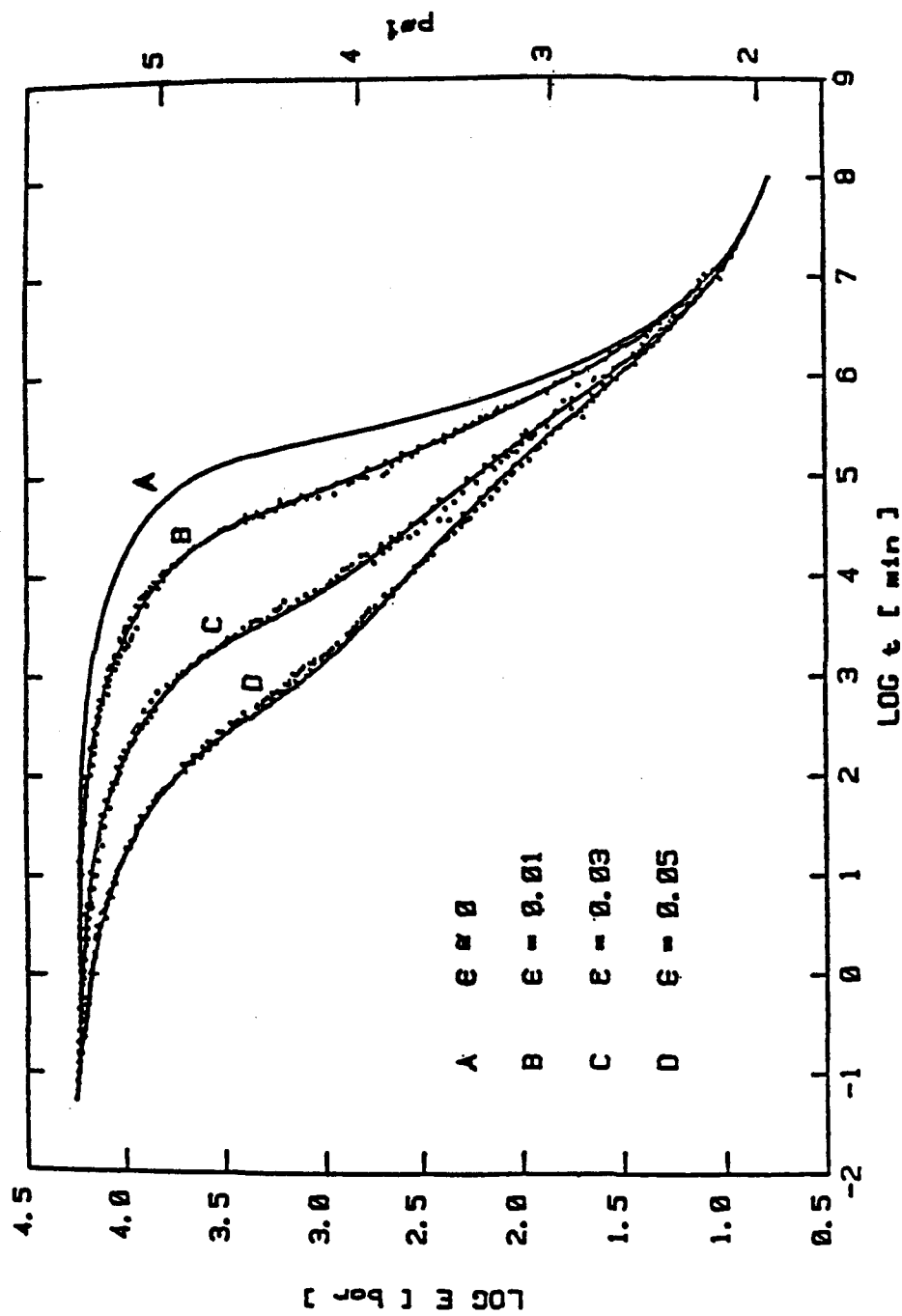


Figure 1. Comparison between experiment and computations for relaxation in PVAc at different levels of strain (from reference 1).

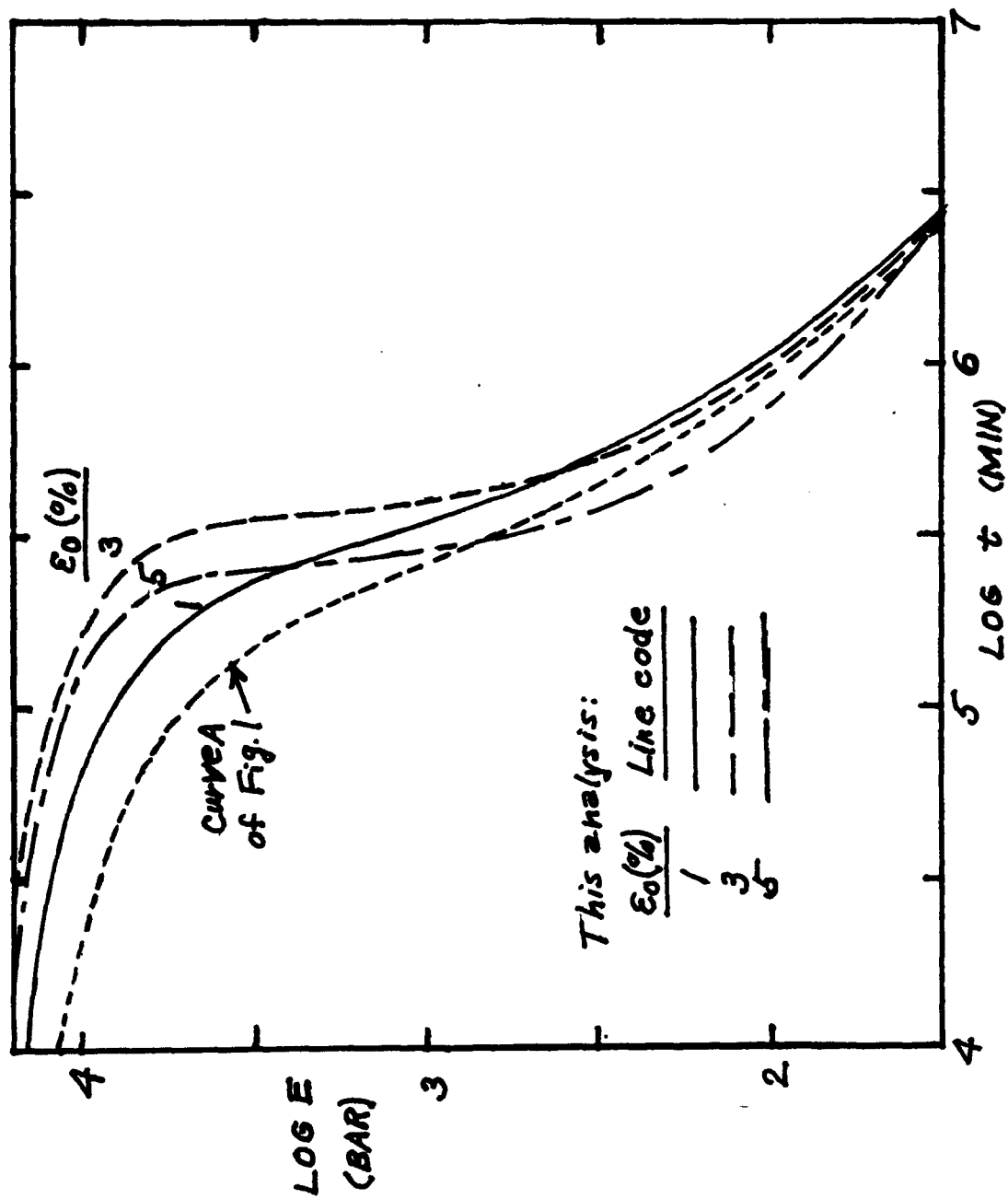


Figure 2. Best fit linear reduced relaxation modulus curves for PVAc from data at 1, 3, and 5% strain by use of Knauss-Emri theory.

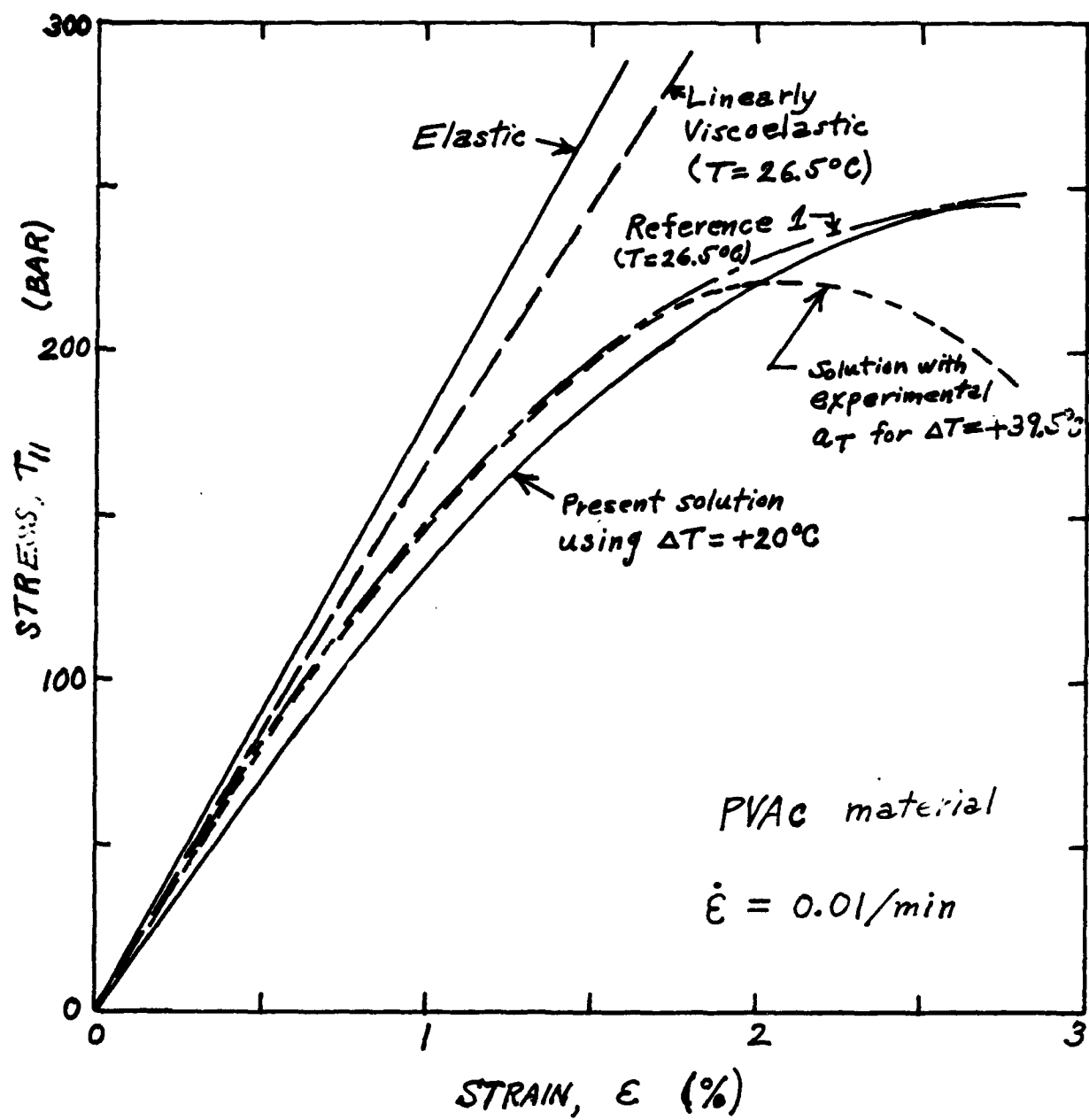


Figure 3. Comparison of stress results for constant strain rate. Closest agreement with reference 1 obtained by using $\Delta T = +20^{\circ}\text{C}$ applied to Figure 1. Also shown is the solution using experimental a_T temperature shift of data of Figure 1 prior to iterative procedure for strain dependence.

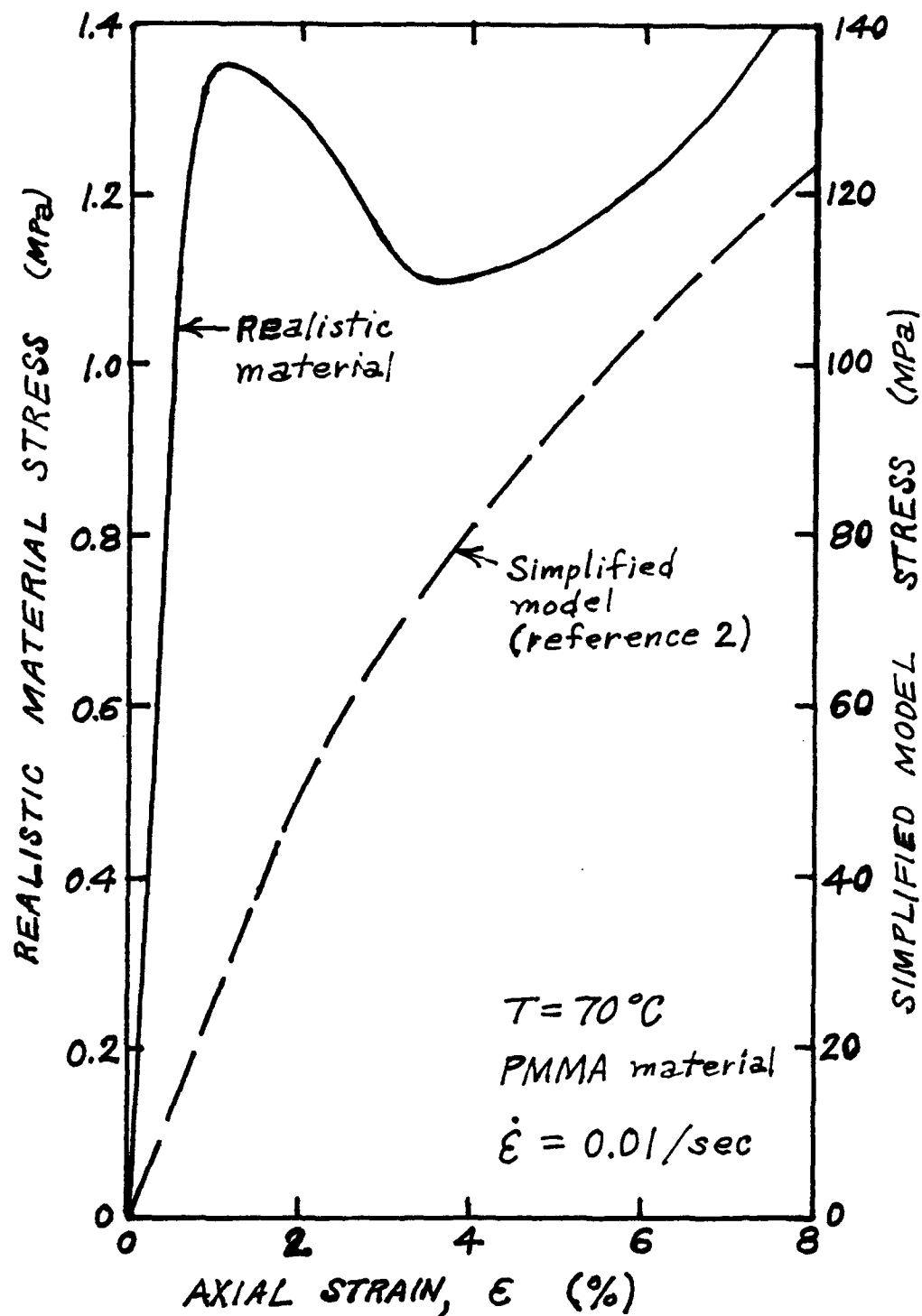


Figure 4. Comparison of stress results for constant strain rate with Shay-Caruthers solution.

1988 USAF-UES SUMMER FACULTY RESEARCH PROGRAM/
GRADUATE STUDENT RESEARCH PROGRAM

Sponsored by the
AIR FORCE OFFICE OF SCIENTIFIC RESEARCH
Conducted by the
Universal Energy Systems, Inc.

FINAL REPORT

LASER HARDENED MATERIALS VIA MAGNETICALLY
ALIGNED POLYPEPTIDE-PHTHALOCYANINES

Prepared by: Gene O. Carlisle, Ph.D.
Academic Rank: Professor
Department and Chemistry Department
University: West Texas State University
Research Location: AFWAL/MLPJ
Wright-Patterson AFB
Dayton, OH 45433
USAF Researcher: Raymond J. Linville
Date: September 21, 1988
Contract No: F49620-87-R-0004

LASER HARDENED MATERIALS VIA MAGNETICALLY
ALIGNED POLYPEPTIDE-PHTHALOCYANINES

by

Gene O. Carlisle

ABSTRACT

The problem of selecting a new nonlinear optical (NLO) material is reviewed, and the rationale for the selection given. The new material selected is a guest-host type of system in which the biomolecule, poly- γ -benzyl-L-glutamate (PBLG) is the host for a guest phthalocyanine (Pc) molecule. Solubility and spectral measurements were taken on three copper phthalocyanine compounds in order to determine compatible solvent-PBLG-Pc systems. The tetrasodium salt of copper phthalocyanine-3,4',4'',4'''-tetrasulfonic acid was determined to be suitable for PBLG in the solvent DMF; however, the combination of PBLG-MgPc-CH₂Cl₂ is recommended as the best system for magnetic alignment. Plans are outlined for the continuation of this research.

I. INTRODUCTION:

The preparation of nonlinear optical (NLO) materials for the purpose of absorption of laser light energy may be effectively accomplished by the use of biomolecules. Biomolecules such as the α -helix forming polypeptides which also form cholesteric liquid crystals may be used as a matrix material to aid in the preparation of highly oriented guest molecules having very large NLO properties. With the application of a magnetic field these cholesterics may be transformed into nematic guest-host systems, which after evaporation of solvent leads to stable and highly ordered laser hardened materials. Fabrication flexibility, especially in thin film processing, tailoring of optical properties via material engineering, and ultrafast with subpicosecond response times are some of the advantages of these materials.

The preparation of such materials is a multidisciplinary effort where a knowledge of chemistry and physics is highly desirable. My background in chemistry (Ph.D.) and physics (M.S.) and research experience in compound preparation, magnetic susceptibility, and electron paramagnetic resonance were contributing factors in my selection as a participant in this research program of the Laser Hardened Materials Branch of the Materials Laboratory.

II. OBJECTIVES OF THE RESEARCH EFFORT:

My assignments as a participant in the 1988 Summer Faculty Research Program (SFRP) were to select a new material which would be effective in the absorption of laser light energy and to begin the experimental studies of the new material.

III. THE RESEARCH PROBLEM:

One effective means of absorption of laser light energy is by the use of materials with large nonlinear optical responses. These responses are caused by the induced polarization of electronic charges in molecules as the electromagnetic field interacts with the material. In a molecule the polarization induced by an applied electric field is

$$P_i = \alpha_{ij}E_j + \beta_{ijk}E_jE_k + \gamma_{ijkl}E_jE_kE_l + \dots \quad (1)$$

where the subscripts i, j, k, l refer to the molecular coordinate system and E_j, E_k , etc. denote the components of the field [1]. α, β, γ , etc. are tensor quantities relating components P_i to the appropriate field components. On a macroscopic basis the polarization induced in a solid medium is

$$P_I = \chi_{IJ}^{(1)}E_J + \chi_{IJK}^{(2)}E_JE_K + \chi_{IJKL}^{(3)}E_JE_K E_L + \dots \quad (2)$$

where $\chi^{(n)}$ have similar meanings to their molecular counterparts. For example $\chi^{(3)}$ is

$$\chi^{(3)} = N\gamma F(\omega_1)F(\omega_2)F(\omega_3)F(\omega_4) \quad (3)$$

where N is the number of molecules per unit volume and F is a local field factor at frequency ω which determines the value of the electric field at the site of the molecule. The first terms of (1) and (2) refer to the familiar linear polarization while the higher-order terms are associated with nonlinear optical effects. Williams [2] has summarized some of these effects along with their applications. For important examples, second harmonic generation (SHG) is represented by $\chi^{(2)}(-2\omega; \omega, \omega)$ which results in frequency doubling and third harmonic generation (THG) is represented by $\chi^{(3)}(-3\omega; \omega, \omega, \omega)$ which results in frequency tripling. The above equations clearly show the importance of the number factor as well as the need for large electric susceptibilities, $\chi^{(2)}$ or $\chi^{(3)}$, in order to produce large nonlinear optical responses in materials.

It is now recognized that organic polymeric materials with highly delocalized π electron systems have extremely large nonlinear susceptibilities which exceed the best values of inorganic dielectrics and semiconductors [2]. Also, because of increased transparency and resistance to laser damage, the organics are generally more useful. Ultrafast with subpicosecond response times, fabrication flexibility, especially in thin film processing, and tailoring of optical properties via material engineering are some of the advantages of using organic polymers with highly conjugated π electron systems. However, most organic

polymers are not well ordered systems as is the case of the crystalline inorganics. Since nonlinear responses are dependent upon orientational order, liquid crystalline polymers offer a very attractive set of properties for NLO materials. NLO properties of liquid crystals and liquid crystal devices for laser systems have been discussed by Jacobs [3].

Biomolecules such as polypeptides, since they possess the aforementioned properties of the organics, have tremendous potential for use in laser hardened materials. The highly-ordered structures [4] of polypeptides are well known...the basic unit of protein in hair, wool, claws, and skin is the famous α -helix. As an example, the synthetic polypeptide, poly- γ -benzyl-L-glutamate (PBLG), has been studied extensively [5-10]. The hyperpolarizability of PBLG has been measured [11]. It possesses both second and third order nonlinear hyperpolarizabilities which are $\beta = +5 \times 10^{-28}$ esu and $\gamma = +1.5 \times 10^{-29}$ esu. The values are quite high because of the large number ($n = 2500$) of peptide monomer units which are bonded together in the α -helix formation. PBLG will form the α -helix in most common organic solvents. Above a critical concentration of about 15% (w/w) in solvents such as dibromomethane and dichloromethane, PBLG forms lyotropic liquid crystals of the cholesteric structure [12]. The cholesteric structure can be transformed in an aligned nematic structure by

mechanical shear [13] and by electric [12,14] and magnetic [14-19] fields. Samulski [19] and coworkers have prepared solid highly oriented films of PBLG by evaporating the solvent dichloromethane from solutions placed in a 2-T magnetic field for about 24 h. Their X-ray studies showed that the rod-shaped molecules align themselves parallel with the field in a hexagonal lattice.

IV. THE SELECTED MATERIAL:

PBLG was chosen as a matrix material for our research because of the desirable properties given above and the fact that stable good quality films can be easily prepared. Our plan however was to prepare a material with NLO properties much superior to those of PBLG alone by utilizing a guest-host system [1] in which PBLG would be the host for a guest substance having one of the highest nonlinear susceptibilities known.

Phthalocyanines [20] were chosen as the class of compounds from which guests would be selected. The structure of copper(II) phthalocyanine is shown in Fig. 1. As was the case with PBLG, phthalocyanines (Pc) have been well characterized. Pc has a two-dimensional π -electron system and has been used as a photosensitive material. These compounds have attracted much attention because of their unusually high thermal, chemical, and photochemical stability. Many will sublime unchanged at $400^{\circ}\text{C}/10^{-6}$ torr.

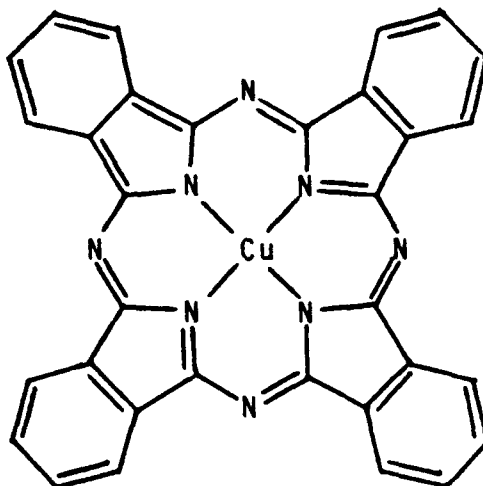


FIG. 1. Structure of copper(II) phthalocyanine.

CuPc is stable up to 900°C in vacuo. THG experiments [21] were performed on AlPc-F and GaPc-Cl, and lower-limit data estimate $\chi^{(3)}$ values of 5×10^{-11} and 2.5×10^{-11} esu, respectively. From these experiments it was concluded that the two-dimensional π -electronic conjugated system can exhibit large optical nonlinearities through resonant enhancements. For comparison, the $\chi^{(3)}$ value of trans- β -carotene glass is 10^{-12} esu and that for polydiacetylene thin films is 1.1×10^{-11} esu if measured parallel to the π -conjugated polymer chain and $<10^{-12}$ esu if measured perpendicular to the chain. Hetherington and coworkers also report that since Pc is transparent at the 1064-nm fundamental, the damage threshold is high.

V. EXPERIMENTAL RESULTS AND DISCUSSION:

After noting from the X-ray studies of the Pc molecule [20] and PBLG films [7] that the Pc molecule should be able to fit within the hexagonal lattice of PBLG, our experimental work was planned as outlined below.

- 1) Solubility measurements on choice Pc compounds to determine compatible solvent-PBLG-Pc systems.
- 2) Prepare films and perform film characteristic work with aid of a polarizing microscope to be done at West Texas State University.
- 3) Orientation of Pc molecules to be determined by electron paramagnetic resonance (EPR) spectroscopy at WTSU. See ref. 22 for method.
- 4) Orientation of PBLG by IR spectral measurements to be done at WTSU.
- 5) X-ray diffraction work to be done at the Materials Laboratory.

The solubilities of copper phthalocyanine (CuPc), copper 4,4',4'',4'''-tetraazaphthalocyanine (CuAPc), and the tetra-sodium salt of phthalocyanine-3,4',4'',4'''-tetrasulfonic acid (CuSPc) were measured in α -helix forming solvents for PBLG. CuPc and CuAPc were not soluble in any suitable solvent for our purposes; however, CuSPc is very soluble in water (>4%) and 0.32% soluble in DMF. DMF is an α -helix forming solvent for PBLG, and although 0.32% solubility may not seem very high, it is quite soluble enough as the molar absorbtivity

for Pc is very high with values around 3×10^5 l/mole·cm. The electronic spectrum for a 7.5×10^{-6} M solution of CuSPc in DMF was measured and is shown in Fig. 2. The Q band at 600-800 nm and the B band at 300-400 nm arise from transitions to $\pi\pi^*$ states of E_u symmetry. The relevant molecular states and their relationships to the photons in the THG process are discussed by Hetherington [21].

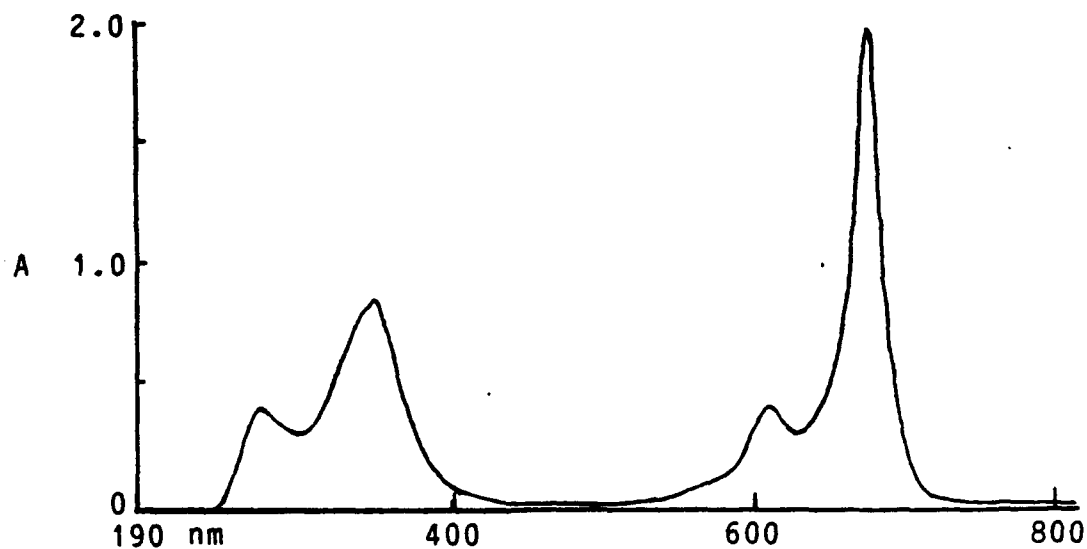


FIG. 2. Absorption spectrum of CuSPc in DMF.

VI. RECOMMENDATIONS:

The PBLG-Pc system has very high potential for laser hardened materials; therefore, the recommendation is that the research be continued as outlined above. Since Stillman [23] and coworkers report that MgPc is highly soluble in CH_2Cl_2 , an α -helix forming solvent for PBLG and the solvent used by Samulski and coworkers [19] to acquire highly oriented PBLG films by use of magnetic fields, it is recommended that the PBLG-MgPc- CH_2Cl_2 combination be given first priority in continuing this research.

PBLG is not the only polypeptide with the properties suitable for the guest-host system; others with different R groups may be more feasible depending on the specific Pc molecule. Also, the pleated-sheet conformations may be well worth considering for aligning host molecules.

ACKNOWLEDGMENTS

I thank Dr. Robert L. Crane and Mr. Raymond J. Linville for the opportunity to do research in their laboratory. The enjoyable working atmosphere they provided and their continued interest in my progress are very much appreciated. I also thank Professor Herbert E. Klei and Mr. Zbigniew Tokarski for their many helpful discussions which gave me much greater insight into the problem.

The sponsorship of the Air Force Systems Command, Air Force Office of Scientific Research, and the Materials Laboratory of the Air Force Wright Aeronautical Laboratory is gratefully acknowledged. The administrative support of Universal Energy Systems, Inc. is much appreciated.

REFERENCES

1. Williams, D. J., "Nonlinear Optical Properties of Guest-Host Polymer Structures," Nonlinear Optical Properties of Organic Molecules and Crystals, Vol. 1, 1987, pp. 405-435.
2. Williams, D. J., "Organic Polymeric and Non-Polymeric Materials with Large Optical Nonlinearities," Angew. Chem. Int. Ed. Engl., Vol. 23, 1984, pp. 690-703.
3. Jacobs, S. D., "Liquid Crystal Devices for Laser Systems," Journal of Fusion Energy, Vol. 5, 1986, pp. 65-75.
4. Dickerson, R. E. and I. Geis, The Structure and Action of Proteins, Menlo Park, California, W. A. Benjamin, Inc., 1969.
5. Robinson, C., "The Cholesteric Phase in Polypeptide Solutions and Biological Structures," Molecular Crystals, Vol. 1, 1966, pp. 467-494.
6. Miller, W. G., P. S. Russo, and S. Chakrabarti, "Composition, Phase Behavior, and Morphology in Poly(amino acid)s forming Lyotropic Liquid Crystals," Journal of Applied Polymer Symposium, Vol. 41, 1985, pp. 49-63.
7. Watanabe, J., K. Imai, R. Gehani, and I. Uematsu, "Structural Differences Between Two Crystal Modifications of Poly(γ -benzyl-L-glutamate)," Journal of Polymer Science: Polymer Physics Edition, Vol. 19, 1981, pp. 653-665.

8. Watanabe, J. and I. Uematsu, "Anomalous Properties of Poly(γ -benzyl-L-glutamate) Film Composed of Unusual 7/2 Helices," Polymer, Vol. 25, 1984, pp. 1711-1717.
9. Samulski, E. and A. Tobolsky, "Cholesteric and Nematic Structures of Poly- γ -benzyl-L-glutamate," Liquid Crystals and Ordered Fluids, edited by J. Johnson and R. Porter, Plenum, 1970.
10. Robinson, C., J. Ward, and R. Beevers, "Liquid Crystalline Structure in Polypeptide Solutions, Part 2," Discussions Faraday Society, Vol. 25, 1958, pp. 29-42.
11. Levine, B. F., and C. G. Bethea, "Second Order Hyperpolarizability of a Polypeptide α -Helix: Poly- γ -benzyl-L-glutamate," The Journal of Chemical Physics, Vol. 65, 1976, pp. 1989-1993.
12. Iizuka, E., "Electric Orientation of Liquid Crystals of Poly- γ -benzyl-L-glutamate," Biochimica et Biophysica Acta, Vol. 243, 1971, pp. 1-10.
13. Horio, M., S. Ishikawa, and K. Oda, "Fine Structures of Fibers and Films Made from Lyotropic Liquid Crystals of Polymers," Journal of Applied Polymer Science: Applied Polymer Symposium, Vol. 41, 1985, pp. 269-292.
14. Iizuka, E., "Electric and Magnetic Orientation of Macromolecules," Journal of Applied Polymer Science: Applied Polymer Symposium, Vol. 41, 1985, pp. 131-147.

15. Orwoll, R. D., and R. L. Vold, "Molecular Order in Liquid Crystalline Solutions of Poly(γ -benzyl-L-glutamate) in Dichloromethane," Journal of the American Chemical Society, Vol. 93, 1971, pp. 5335-5338.
16. Go, Y., S. Ejiri, and E. Fukada, "Magnetic Orientation of Poly- γ -benzyl-L-glutamate," Biochim. Biophys. Acta, Vol. 175, 1969, pp. 454-456.
17. Samulski, E. T., and A. V. Tobolsky, "Some Unusual Properties of Poly(γ -benzyl-L-glutamate) Films Cast in Strong Magnetic Fields," Macromolecules, Vol. 1, 1968, pp. 555-557.
18. Samulski, E. T., "Magnetically Oriented Solutions," Science, Vol. 234, 1986, p. 1424.
19. Murthy, N. S., E. T. Samulski, and J. R. Knox, "Three-Dimensional Order in Magnetically Oriented Poly(γ -benzyl-L-glutamate) Films," Macromolecules, Vol. 19, 1986, pp. 941-942.
20. Lever, A. B. P., "The Phthalocyanines," Advances in Inorganic and Radiochemistry, Vol. 7, 1965, pp. 27-114.
21. Ho, Z. Z., C. Y. Ju, and W. M. Hetherington III, "Third Harmonic Generation in Phthalocyanines," Journal of Applied Physics, Vol. 62, 1987, pp. 716-718.

22. Cook, M. J., A. J. Dunn, A. A. Gold, A. J. Thomson, and M. F. Daniel, "Association and Orientation of Copper(II) Tetra-t-butylphthalocyaninate in Multilayer Langmuir-Blodgett Films as Determined by Electron Paramagnetic Resonance Spectroscopy," Journal of the Chemical Society, Dalton Transactions, 1988, pp. 1583-1589.
23. Ough, E., T. Nyokong, K. A. M. Creber, and M. J. Stillman, "Electrochemistry and Spectroscopy of Magnesium Phthalocyanine. Analysis of the Absorption and Magnetic Circular Dichroism Spectra," Inorganic Chemistry, Vol. 27, 1988, pp. 2724-2732.

1988 USAF-UES SUMMER FACULTY RESEARCH PROGRAM

GRADUATE STUDENT RESEARCH PROGRAM

Sponsored by the

AIR FORCE OFFICE OF SCIENTIFIC RESEARCH

Conducted by the

Universal Energy Systems, Inc.

FINAL REPORT

JOINING OF CARBON-CARBON COMPOSITE MATERIALS

Prepared by:	Parviz Dadras
Academic Rank:	Professor
Department and	Mechanical Systems Engineering
University:	Wright State University
Research Locations:	AFWAL/MLBC, Wright-Patterson AFB Ohio, 45433
USAF Researcher:	Steve L. Szaruga
Date:	August 30, 1988
Contract No:	F49620-87-R-0004

Joining of Carbon-Carbon Composites

by

Parviz Dadras

ABSTRACT

Joining of carbon-carbon composites by diffusion welding and diffusion brazing is proposed in this project. The objective is to produce joints that can retain sufficient strength at service temperatures up to 2000°C (3632°F). Joining of carbon-carbon composites to two refractory metals, tungsten, and tantalum, and to a structural alloy Ti-6Al-4V is also suggested for consideration.

Six different interlayers, a commercial brazing alloy Ti-15Cu-15Ni, an experimental alloy Ti-21V-25Cr, and two brazing compounds MoSi₂ and SiC have been proposed. These materials have appropriate wetting and flow characteristics for joining graphite. In each case, the process variables (time, temperature, and pressure) will be optimized so that the maximum strength and the highest service temperatures can be obtained.

In this project lap joints and squared-edge butt joints will be investigated. The strength of the joints will be evaluated under in-plane tensile and across-ply shear and tensile modes of loadings at the expected service temperatures. Also, the joints will be examined by light and scanning microscopy.

ACKNOWLEDGMENT

I wish to thank Mr. L. Scott Theibert and Mr. Steve L. Szaruga for their support and encouragement throughout my research effort. Also, I would like to thank the Air Force Systems Command, AFWAL/MLBC, and the Air Force Office of Scientific Research for sponsorship of this research program.

I. INTRODUCTION

Joining of carbon-carbon components to each other and to other materials is becoming increasingly important as new applications for larger and more complex carbon-carbon composite structures are encountered. New developments in the science and technology of carbon-carbon composite joining are needed so that reliable joints can be produced which will retain their strength at elevated temperatures and will withstand thermal cyclings and other service conditions expected for carbon-carbon composite materials. At present, only some information on joining graphite can be found in the open literature [1-10]. Selected published works on joining of ceramic materials also have some relevance to joining of graphite [8-16]. In most of these works, however, the strength of the joint under different modes of loading and high-temperature conditions have not been evaluated.

In this project joining of carbon-carbon composites will be investigated. The suggested processes and procedures are based on the available knowledge on joining graphite and ceramic materials. Therefore, some preliminary steps such as new brazing alloy development and wettability and flow characterizations will not be attempted in this project. To cover a wide range of applications, joining for service temperatures up to 2000°C (3632°F) have been considered. Also, joining of carbon-carbon composites to itself, to two refractory metals, and to a structural alloy have been included in this project. Only uncoated carbon-carbon composites have been considered, as it is assumed that the coating process will follow the

joining operation in each case. Two refractory metals, tantalum and tungsten, have been selected for joining to carbon-carbon composites. These metals are likely candidates for components in heat shield and thermal barrier constructions, and they both retain some strength at 1000°C. The selected alloy Ti-6Al-4V is a common alloy in aerospace applications and contains carbide forming elements that have the potential of bond formation with graphite, with or without the use of a diffusion brazing agent.

The surface roughness and near-surface macroporosity of the carbon-carbon materials will be determined by light and scanning electron microscopy. Similarly, the joint characteristics such as phase distributions, brazing alloy penetrations, and diffusion gradients will be examined. Also, the strength of the joints at the expected service temperatures and under different loading conditions will be determined by mechanical testing of the joints in vacuum or in an inert atmosphere.

II. OBJECTIVES OF THE RESEARCH EFFORT

Joining of carbon-carbon composite material to itself, to refractory metals, and to a structural alloy is the objective of this project. The joints are required to retain sufficient strength at the expected service temperatures up to 2000°C and to withstand thermal cycling without cracking and loss of strength. The joints will be produced and tested in vacuum or in an inert atmosphere. It is also planned that the joints will be evaluated by optical and scanning electron

microscopy, and by mechanical testing under different loading conditions. Only uncoated carbon-carbon composites will be used and coating processes are assumed to follow the joining operation.

III. PROCEDURES AND DISCUSSIONS

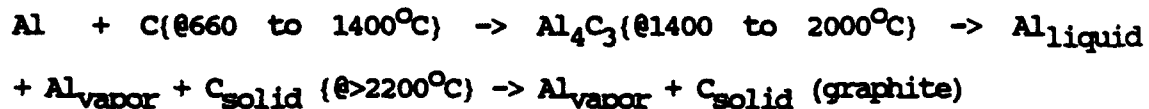
Graphite is not weldable by the fusion welding process because it vaporizes before it can melt. Also, diffusion welding of graphite to itself without a diffusion aid is not possible [10]. By using refractory and reactive metal interlayer foils between two graphite blocks diffusion welds can be produced [10]. In the diffusion welding process joining is by solid-state diffusion and carbide formation which are promoted by the appropriate application of heat and pressure to the interfaces. If the interlayer temperature is raised beyond its melting point, or the melting point of a possible eutectic composition which may form initially by solid state diffusion, then conditions for diffusion brazing will prevail and enhanced diffusion from the liquid-phase will ensue. In this case for low contact angles and good wetting characteristics of the melt, filling of cracks and cavities in a carbon-carbon composite material near the interfaces will occur which may result in an improved joint strength.

For diffusion brazing the interlayer may consist of a pure metal such as titanium or molybdenum foils [10], a clad metal foil such as nickel-clad titanium [8], or a coated foil such as copper-coated titanium [10]. In selecting a metal or a coating for the interlayers the eutectic temperature for the combination of melting has to be taken

into account. For example, copper-coated titanium foils have been used [10] to join graphite to different refractory metals at 885°C (1625°F) which is close to the Ti-Cu eutectic temperature (870°C [17]), and under a low pressure of 100 psi. Without the coating, melting will occur at the Ti-C eutectic temperature of 1645°C [17] which is only slightly lower than the melting point of Ti (1667°C). It is noticed that a substantial drop in the diffusion brazing temperature is produced as a result of the coating. Obviously, variations in other properties such as coefficient of thermal expansion, strength, and wetting characteristics will also result due to the existence of the coating layer. The wetting characteristics can be improved by using appropriate coatings and clads. For example, of the 130 metals and alloys examined by Takamori et. al. [2] for joining pyrolytic graphite, the seven compositions which produced the lowest angles of contact in wettability tests consisted of reactive-noble metal combinations such as Ti-Cu and Ti-Ag. Therefore, it is expected that the Cu-coated Ti and the commercially available Ni-clad Ti will have better flow and wetting characteristic than pure titanium. The choice between pure or coated interlayer foils is also decided, in part, by the expected service temperature, joint strength requirements, and the maximum temperature capabilities of the existing furnaces.

Another concern in the selection of an interlayer material is the nature of the interactions that can occur at the joint as a result of the brazing operation or during a post-brazing heat-treatment schedule. For a pure metal interlayer, in general, a distribution of

a metallic phase and a metal-carbide phase will be present at the joint. The carbide/metal phase ratio and the penetration depth of these phases into the carbon-carbon composite will increase for higher brazing temperatures and longer hold-times at the brazing temperature. Obviously, different joint characteristics will result because of different phase ratios and penetration depths. Additional changes can be initiated by heat-treatment of joints at still higher temperatures. Depending on the phase diagram for the system and the physical nature of the metal and its carbide, free carbon may form at the joint due to thermal dissociation of carbon-bearing melts [4], or due to thermal dissociation of carbide-carbon eutectics [3]. As an example of the former process the following reaction for brazing with an aluminum interlayer [4] can be considered:



It has been shown [4] that creep-resisting joints consisting of only graphite with a strength of 2300 psi at 2500°C can thus be produced. Similar results have been obtained for brazing with iron and nickel interlayers, and for brazing with a molybdenum interlayer which forms a thermally dissociating carbide-carbon eutectic [3]. For very high temperature applications ($T > 2000^{\circ}$), possibly in reentry vehicles and cone heads, joining by graphite formation is an option which requires further investigations. It is likely that by controlling the thermal treatment cycle and pressure application to the interface a denser, more oriented graphite of higher strength can

be produced.

In this project six different interlayers will be used (Table 1). The tungsten interlayer is chosen because of its desirable high temperature strength and thermal expansion properties, as well as those of its carbides. For the tungsten interlayer only diffusion welding, and for the Ti and Mo interlayers both diffusion welding and brazing will be investigated. Full conversion to graphite produced by thermal dissociation of Al_4C_3 and of molybdenum carbide-carbon eutectic will be investigated. In the case of the aluminum interlayer, it is essential that all the Al_4C_3 is converted, as this carbide hydrolyzes readily and cannot be used as a structural material. To prevent excessive evaporation of the furnace graphite elements in vacuum, the high temperature ($T > 2000^\circ C$) heat-treatment operations will be performed in an inert gas atmosphere. The interlayers given in Table 1 will all be used in foil form of 0.05 to 0.1 mm (0.002 to 0.004 inch) thickness. Deposition of copper on titanium will be accomplished by electroplating from an aqueous solution [18].

TABLE 1

Interlayer	Diffusion Welding		(1) Diffusion Brazing		(2) Max. Expected Service Temp., C
	Temp., C	Press, psi	Temp., C	Press, psi	
Cu-Coated Ti			885	100	1400
Ni-Clad Ti			1100	100	1400
Aluminum			700	7	2400
Titanium	1550	100	1760	100	1400
Molybdenum	2000	700	2400	700	2000
Tungsten	2400	700			1800

- (1) Reported diffusion brazing conditions for graphite.
 (2) Maximum temperatures after brazing and heat-treatment.

A number of brazing alloys have been developed for brazing graphite to itself and to refractory metals. Two commercially available brazing alloys which wet graphite and some metals are Ag-26.7%Cu-4.5%Ti and Ti-15%Cu-15%Ni [1]. These alloys are for relatively low temperature applications because their solidus temperatures are 830°C (1526°F) and 910°C (1670°F), respectively. Only the latter of these two alloys will be evaluated in the project for joining carbon-carbon composite materials to each other and to Ti-6Al-4V alloy. For higher temperature applications a number of experimental brazing alloys have been developed at the Oak Ridge National Laboratories [6-9]. In Table 2 some of these alloys have been given.

TABLE 2

Brazing Alloy	Brazing Temp., C	Graphite	Refractory Metals	Al ₂ O ₃	UO	BeO
Ti-49Cu-2Be	1000	G		G	G	G
Ti-28Ag-4Be	1100	G		G	F	F
Ti-48Zr-4Be	1050	G		P	P	P
Ti-46Pd-6Al-2Be	1150	G		F	P	P
Zr-23Cu-2Be	1150	G		F	P	F
Zr-5Be	1050	G		F	G	F
Ti-21V-25Cr	1650	G	G	G		
Ti-Zr-Ta	2100	G	G	G		
Ti-Zr-Ge	1600	G	G	G		
Ti-47.5Zr-5Nb	1700	G	G			

G: Good continuous wetting; F: Fair, intermittent wetting;

P: poor, no flow condition.

Only one of these alloys Ti-21V-25Cr for the expected service temperatures of up to 1300°C will be investigated in this project. This alloy has been successfully used to join graphite, refractory metals and Al₂O₃. Room-temperature ductility of this alloy has not been reported. Therefore, in case of limited ductility the alloy in powder or chunk form will be used.

A number of brazing compounds such as AlB_{12} , TiSi_2 , and MoSi_2 have been used for joining SiC [16] and graphite [10]. The feasibility of the use of molybdenum disilicide and silicon carbide for joining carbon-carbon composites will be investigated in this project. In each case an ethanol slurry of MoSi_2 or SiC powder will be brushed on the faying surface of the carbon-carbon sample and heating ($T = 1950^\circ$) and pressure ($P = 13.8 \text{ MPa}$) will be applied [16].

The joint properties are expected to depend on brazing time and temperature conditions as well as post-joining heat treatments. The effect of processing variables on the strength of the joints will be studied by microscopic examination of joint sections and by mechanical testing. In each case, the optimum process conditions for maximum strength and highest service temperature will be determined.

In selecting alloy systems for the proposed joints thermal expansion compatibility between the alloys, the carbides, and the carbon-carbon composite material must be taken into consideration. Ideally, a good brazing alloy should have a low coefficient of thermal expansion (less than $8 \times 10^{-6}/^\circ\text{C}$), high strength at the expected service temperatures, as well as good ductility and acceptable wetting and flow characteristics. In view of the inherent macroporosity of carbon-carbon composites [19], it is expected that some degree of thermal expansion mismatch can be tolerated. The graded-joint technique, used for joining refractory metal carbides, borides, and nitrides to each other and to refractory metals [13], can be employed

for joining carbon-carbon composites to materials of vastly different coefficient of thermal expansion such as some iron and nickel alloys. In this approach an interlayer consisting of a powder mixture of graphite and the elemental constituents of the metallic alloy will be applied in the form of an ethanol slurry to the faying surfaces. Another approach for joining materials with greatly different thermal expansion coefficients is by using a transition piece. For example, to join graphite to Hastalloy N a transition piece of variable composition has been used [5]. The coefficient of thermal expansion for the piece varied between values close to that of graphite at one end and near Hastalloy N at the opposite end. It is anticipated that the use of the graded-joint method or the transition piece approach will not become necessary in the conduct of this project.

In regard to thermal expansion characteristics, the anisotropic properties of carbon-carbon composites have to be taken into account. The coefficient of linear thermal expansion for carbon-carbon composites in the fill or warp directions is smaller than in the across-ply orientation. For example, for Vought ACC-4 at 1000°C these are $2.5 \times 10^{-6}/^{\circ}\text{C}$ and $7.2 \times 10^{-6}/^{\circ}\text{C}$, respectively. Also, the variations of thermal expansion with temperature in the across-ply direction are different from those in the warp and fill directions. As a result, some differences in the behavior of flat-wise joints (lap joints) and edge-wise joints (square-edge joints) is to be expected. In service, flat-wise joints will be subjected to the same type of loading that would cause the interlaminar shear (ILS) or interlaminar tensile (ILT) stresses in the composite. Since the ILS and ILT

strengths for carbon-carbon composites are commonly limited to two to three ksi, lap joints are expected to be less critically loaded.

In this project three types of specimens will be employed. The first (Fig. 1) is for determining the tensile strength of the butt joints. The shear strength of the lap joints will be determined by using double-notch shear specimens (Fig. 2) loaded in compression. For tensile strength determination of lap joints a special specimen geometry shown in Fig. 3 will be used. This geometry has been proposed and evaluated by the author [20] and the IIT strength of carbon-carbon composites at high temperatures up to 2000°C have been determined [21]. All the specimens will be fabricated from 0.2 to 0.25 inch thick carbon-carbon plates by using a special silicon carbide grinding operation employed by Micro Mech Inc. of Ipsurich, Ma. The mechanical tests will be conducted at temperatures up to 2000°C depending on the joining method and the brazing alloy used. Only uncoated carbon-carbon composites will be used in the project with intention of the coating process to follow the joining operation. The joining process and the mechanical tests will be performed in an existing graphite vacuum furnace mounted on a model 1123 Instron. The effect of thermal cycling on the joints will be investigated by repeated rapid heating and cooling in an inert gas medium followed by either mechanical testing or microscopic examinations.

The joints will be examined by light and scanning electron microscopy at various stages before and after the mechanical testing. This will consist of examination of various sections and fracture surfaces at

the joints. A selected number of specimens will be examined by an ARL electron probe microanalyzer for determining the concentration gradients of various metals in the diffusion zones of the joints.

IV. EXISTING FACILITIES FOR THE IMPLEMENTATION OF THE PROJECT

- a. Front-loaded graphite furnace mounted on a model 1123 Instron. This furnace is capable of operating at 4000°F (2204°C) in vacuum and at 4352°F (2400°C) in an inert atmosphere. The furnace is equipped with the necessary toolings to conduct mechanical testing at the elevated temperatures. For temperatures less than 1600°C, a tantalum sheathed high-temperature thermocouple made of tungsten 5% Rh/tungsten 26% Rh is used. At higher temperatures, a dual wave length Incon optical pyrometer is employed. A two-channel Honeywell Digital Controller Programmer DCP-700 is used for temperature control and programming. A Varian digital auto ranging ionization gauge controller is used to control and monitor the vacuum throughout the operation. A digital data acquisition system is used to record and process data from the load cell and from the temperature measuring instruments.

The graphite vacuum furnace and the accessories, obtained through DOD-URIP AFOSR-86-0224, are the vital components for the implementation of this project. The availability of these items will provide for the prompt execution of this project economically and efficiently.

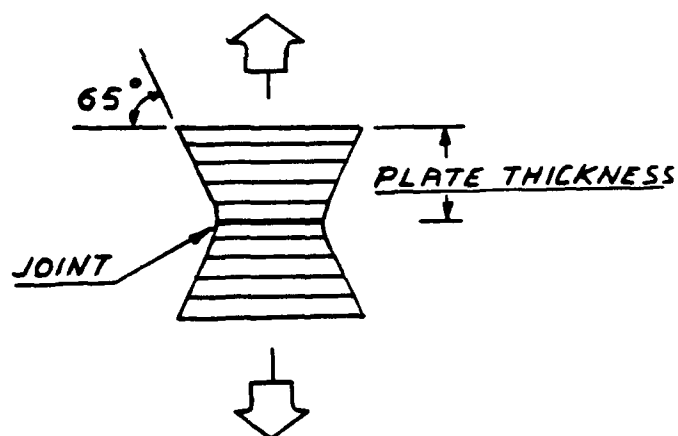
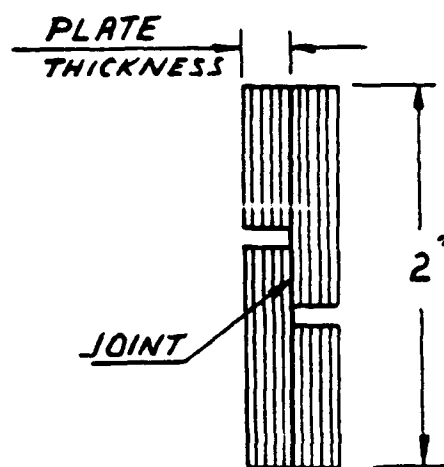
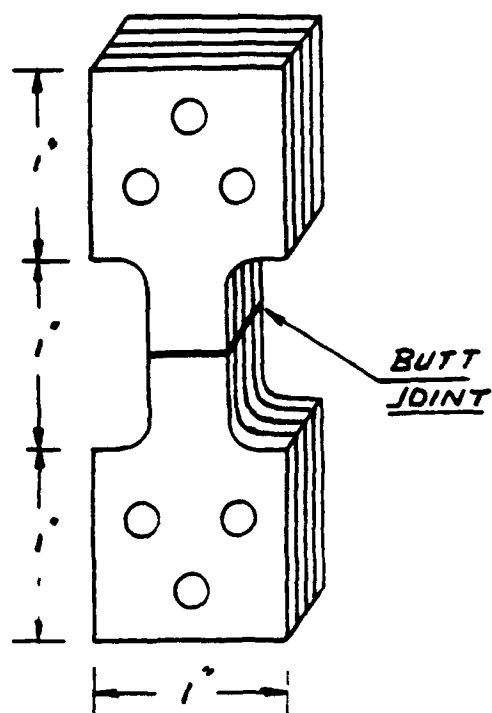
- b. Complete metallography laboratory with an ISI scanning electron microscope, ARL electron microanalyzer, various light microscopes, and specimen preparation facilities.
- c. Processing and heat treatment laboratory. Equipment for swaging, forging, and rolling are available as well as various heat treatment furnaces and machining facilities.

V. RECOMMENDATIONS

Joining of carbon-carbon composites is proposed for investigation. Diffusion welding and diffusion brazing are the recommended processes. Different interlayer materials consisting of pure metal foils or brazing alloys are suggested. Also, it is recommended that the use of interlayer compounds such as MoSi_2 and SiC to be investigated.

It is recommended that the microstructure and the mechanical properties of the joints to be investigated. Light and scanning electron microscopy are the proposed methods for microstructural characterizations. Tension testing of butt joints as well as shear and tension testing of lap joints are the recommended procedures for joint strength determination. It is also suggested that the strength properties to be determined at the expected service temperatures.

It is also recommended that the above investigations to be performed at an institution where the necessary equipment and facilities are already available. In this manner, economical and timely execution of this project will become possible.



FIGURES 1 - 3. GEOMETRY OF SPECIMENS FOR (1) BUTT JOINT IN TENSION, (2) LAP JOINT IN SHEAR, AND (3) LAP JOINT IN TENSION

REFERENCES

1. Moorhead, A.J., and C.R. Kennedy, Metals Handbook, ninth edition, Vol. 6, 1984, pp. 1061-1063.
2. Takamori, T., and M. Akanuma, "Possible Braze Compositions of Pyrolytic Graphite", Am. Ceramic Soc., Bulletin, Vol. 48, No. 7, 1969, pp. 734-736.
3. Anikin, L. T., et al., "The High Temperature Brazing of Graphite", Welding Production, Vol. 24, No. 1, 1977, pp. 39-41.
4. Anikin, L.T., G.A. Kravetskii, and V.S. Dergunova, "The High Temperature Brazing of Graphite Using an Aluminum Brazing Alloy", Welding Production, Vol. 24, No. 7, 1977, pp. 23-25.
5. Amato, I., P.G. Cappeli and P.C. Martinengo, "Brazing of Special Grade Graphite to Metal Substrates", Welding Journal, Vol. 53, No. 10, 1974, pp. 623-628.
6. Werner, W.J., and G.M. Slaughter, "Brazing Graphite to Hastelloy N for Nuclear Reaction", Welding Engineer, March 1968, p. 65.
7. Hammond, J.P., and G.M. Slaughter, "Bonding Graphite to Metals with Transition Pieces", Welding Journal, Vol. 50, No. 1, 1971, pp. 33-40.
8. Fox, C.W., and G.M. Slaughter, "Brazing of Ceramics", Welding Journal, Vol. 43, No. 7, 1964, pp. 591-597.
9. Carmonico, D.A., N.C. Cole, and G.M. Slaughter, "Direct Brazing of Ceramics, Graphite, and Refractory Metals", Welding Journal, Vol. 56, No. 8, 1977, pp. 31-38.
10. Pattee, H.E., R.M. Evans, and R.E. Monroe, Joining Ceramics and Graphite to Other Materials, NASA SP-5052, NASA, Washington, D.C., 1968.
11. Iseki, T., K. Arakawa, and H. Suguki, "Joining of Dense Silicon Carbide by Hot-Pressing", J. Mat. Sci., Letters, Vol. 15, 1980, pp. 1049-1050.
12. Rice, R.W., "Joining of Ceramics", Advances in Joining Technology, Proceedings of the 4th Army Materials Technology Conference, Edited by Burke, J.J., A.E. Gorum, and A. Tarpinian, Boston, MA, 1975, pp. 69-111.
13. Kelley, J.E., D.H. Sumner, and H.J. Kelly, "Systems for Uniting Refractory Materials", Advances in Joining Technology, Proceedings of the 4th Army Materials Technology Conference, Edited by Burke, J.J., A.E. Gorum, and A. Tarpinian, Boston, MA, 1975, pp. 155-183.
14. De Bruin, H.J., A.F. Moodie, and C.E. Warble, "Ceramic-Metal Reaction Welding", J. Mat. Sci., Vol. 7, 1972, pp. 909-918.

15. Burykina, A.L., and O.V. Evtushenko, "Vacuum Diffusion Welding of Metalline Carbides to High-Melting Metals", Soviet Powder Metallurgy and Metal Ceramics, Vol. 25, No. 1, 1965, pp. 66-87.
16. Moore, T.J., "Feasibility Study of the Welding of SiC", J. Am. Ceram. Soc., Vol. 68, No. 6, 1985, pp. C-151-C-153.
17. Elliot, R.P., Constitution of Binary Alloys, First Supplement, McGraw-Hill, New York, 1965, p. 387.
18. Beach, J.G., and C.L. Faust, "Plating on Less Common Metals", Modern Electroplating, F.A. Lowenheim, ed., 3rd edition, John Wiley & Sons, New York, 1974, pp. 627-629.
19. Jortner, J., "Macroporosity and Interface Cracking in Multi-Directional Carbon-Carbons", Carbon, Vol. 24, No. 5, 1986, pp. 603-613.
20. Dadras, P., "Determination of Across-Ply Strength of Carbon-Carbon Composites at High Temperatures", final report submitted to AFWL/MLBC, WPAFB, Ohio, Contract No. F33615-86-C-5131.
21. Dadras, P., "High Temperature Interlaminar Tensile Strength of Carbon Carbon Composite Materials", to appear in the Proceedings of the Co Oca Beach Conference on Carbon-Carbon Composites, January, 1988.

1988 USAF-UES SUMMER FACULTY RESEARCH PROGRAM

GRADUATE STUDENT RESEARCH PROGRAM

Sponsored by the

AIR FORCE OFFICE OF SCIENTIFIC RESEARCH

Conducted by the

Universal Energy Systems, Inc.

FINAL REPORT

Prepared by:	Suren N. Dwivedi, Ph.D.
Academic Rank:	Professor
Department and	Mechanical Engineering
University:	University of North Carolina at Charlotte
Research Location:	ASWAL/MLLM Wright Patterson AFB, 45433
USAF Researcher:	William O'Hara
Date:	September 28, 1988
Contract No.:	F49620-87-R-0004

Rapid Simulation for Experimental Validation of H Section

Forging using Finisher Punch

by

Suren N. Dwivedi

ABSTRACT

Analytical modeling of deformation processes requires material data bases which can adequately describe the dynamic behavior of the material. Dynamic material modeling techniques were applied to determine the constitutive equations. A rigid viscoplastic finite element method based code called ALPID (Analysis of Large Plastic Incremental Deformation) was used to simulate the closed die, flashless, isothermal precision forging of H sections. The H section was simulated to study the metal flow characteristics and the distribution of effective strain, effective strain rate and effective stress were determined. The load requirements were predicted and the behavior of the process was completely analyzed. The H section analytical simulation was experimentally validated.

ACKNOWLEDGEMENTS

I wish to thank the Air Force Systems Command and the Air Force Office of Scientific Research for sponsorship of this research. Universal Energy Systems provided excellent support and help in all administrative and directional aspects of this program.

I would like to thank William O'Hara, Materials Lab, Wright Patterson AFB, for providing me with all the support, encouragement and a truly enjoyable working atmosphere.

I also take this opportunity to express my sincere thanks to Dr. Harold L. Gegel, Director of Processing Science Division, Universal Energy Systems, Dublin, Ohio for generously allowing me to use their computing and testing facilities. I am greatly indebted to Dr. Sokka Doraivelu of Universal Energy Systems, Dublin, Ohio for his full fledged support, involvement and suggestions throughout his research work.

INTRODUCTION

The primary objective in manufacturing research and development is to determine the most efficient and optimum means of producing defect free products with minimum material waste at increased production rate and with reduced lead time. Proper design and control of the manufacturing process require a clear understanding of all the parameters and their effects which control the metal flow characteristics. Computer simulations of manufacturing processes such as forging, for example, predict the behavior of the process under consideration and thus helps to design and control the process more effectively without going through the costly and time consuming process of actually performing the forging operation. The finite element method based code ALPID (Analysis of Large Plastic Incremental Deformation) developed at Battelle is a powerful analytical tool to simulate the metal working processes.

My research interests coincided with some of the research work undertaken by the group at Materials Lab, Wright Patterson AFB. This program provided an opportunity for me to know about the current research work in this above area of dynamic material processing.

OBJECTIVES OF THE RESEARCH EFFORT:

Extensive literature search in the area of the dynamic material behavior of over the entire range of processing conditions illustrated by using dynamic material modeling techniques will be done.

The importance of determining the interface friction factor and its effects will be studied. The development of friction Calibration curves using ALPID simulations of ring compression tests, will also be studied. ALPID analytical simulations will be carried out for precision forgings

of H section. The metal flow characteristics will closely be watched and the load requirements for these processes will be established. The distribution of effective strain, effective strain rate and effective stress will be predicted. The H section analytical simulation will experimentally be validated by conducting actual forging. The simulation results and the actual experimental results will be compared

OVERVIEW OF ALPID:

ALPID is a rigid viscoplastic finite element formulation. Simulation of metal working processes using ALPID can be functionally classified into four major tasks. They are listed as follows

1. Preprocessing or input preparation using a mesh generator package such as PATRAN, SUPERTAB, etc.
2. The finite element analysis code ALPID.
3. Postprocessing of results using the build in program FEMGRA.
4. Remeshing and Interpolation of field variables using the built in program FEMRMS.

Input preparation is done by generating finite element meshes using any commercially available mesh generator packages. The meshes generated should adequately represent the workpiece geometry. In addition to this, die data information such as die geometry, the friction at die-workpiece interface, the velocity and direction of movement of the die should be specified. Boundary conditions should be correctly implemented and the flow stresses of the workpiece material as a function of strain, strain rate and temperature should also be provided. For non-isothermal forging simulations, thermal properties of the die and workpiece as a function of temperature should be provided.

The finite element analysis code ALPID is applicable to both rigid-plastic and rigid-viscoplastic materials under either isothermal or non-isothermal processing conditions. The results of isothermal forging analysis provide information on the material flow during deformation, and it can predict the required deformation load. Besides, the ALPID analysis can predict the distribution of stresses, effective strain and effective strain rate.

The post processing of results is done by using an interactive, menu driven program called FEMGRA. FEMGRA extracts the results of the simulation and it can either display the plots interactively on a Tektronix CRT graphics terminal or can make hard copies of the plot on a HP plotter. Using FEMGRA, one can generate load-displacement curves, grid distortion plots, nodal velocity plots and contour plots of stresses, effective strain and effective strain rate. This facility makes the task of interpretation of the analysis and simulation very simple and straight-forward.

Large deformations are common in the forming process and it might cause the workpiece to deform to such a degree that the workpiece mesh geometry is unacceptable which in turn causes numerical problems. In such cases, the deformed workpiece mesh should be

reconstructed. This is done by extracting the boundary information of the deformed workpiece and the new mesh is constructed by using the same procedure as followed in the construction of the initial workpiece mesh. The field variables such as strain and temperature (in the case of non-isothermal forging simulation only) should be interpolated such that the distribution of field variables at the old and new meshes are the same.

Formulation of ALPID

The workpiece is divided into small finite regions called " elements " and these elements are connected by a discrete number of nodal points located on their boundaries. The workpiece is an assemblage of all the elements connected together appropriately on their boundaries. In ALPID the formulation of element equations in terms of their corresponding nodal point values is achieved by using a variational principle.

While applying finite element method using the variational approach, the foremost requirement is the formulation of proper functionals depending upon specific constitutive relationship. The constitutive equation of a material can be represented [1] as

$$\sigma'_{ij} = \frac{2}{3} \frac{\bar{\sigma}}{\bar{\epsilon}} \dot{\epsilon}_{ij} \quad (1)$$

where

- σ'_{ij} = Deviatoric stress component
- $\dot{\epsilon}_{ij}$ = Strain rate component
- $\bar{\sigma}$ = Effective stress
- $\dot{\bar{\epsilon}}$ = Effective strain rate

For the case of rigid-plastic formulation [2], the effective stress is expressed as

$$\bar{\sigma} = \frac{2}{3} Y(\bar{\epsilon}) \left[1 + \left(\frac{\dot{\bar{\epsilon}}}{\gamma} \right)^m \right] \quad (2)$$

where $Y(\bar{\epsilon})$ is the static yield stress which is a function of total effective strain. m is the strain rate sensitivity parameter and γ is the viscosity constant of the material.

The variational principle functional for a rigid-viscoplastic material as implemented in ALPID [26] is based on an extremum principle which states that, for a plastically deforming body of volume V , under the traction F , prescribed on a part of surface S_F and the Velocity U prescribed on the remainder of the surface S_U is given by

$$\Phi = \int_V \bar{\sigma} \bar{\epsilon} dv + \int_V \frac{1}{2} K (\dot{\epsilon}_v)^2 dv - \int_{S_F} F \cdot U ds \quad (3)$$

where K is a large positive constant which penalizes the dilational strain rate component. A set of non-linear algebraic equations in velocity components U_i is obtained from equation 3 and is solved iteratively by using either Newton-Raphson method or Direct method. Detailed ALPID formulation and theory is discussed elaborately in [1, 2, 3, 4, 5, 6].

Simulation of a Forging process:

Application of the finite element method and the computer simulation of the forging process

using ALPID helps to understand both the behavior of the material and the process. The results derived out of the ALPID simulation such as grid distortion plots, load-stroke relationships, prediction of effective strain, effective stress and effective strain rate distribution in the form of contour plots help to design the process and determine the formability of the material.

In order to conserve materials and reduce machining costs, net or near net shape forgings are widely preferred. Closed die, flashless, isothermal forging is considered to be one of the most efficient means to form high precision components. In a closed die forging, the material is formed by bringing the dies together so that the workpiece will be enclosed on all the sides. The impression for the forging can be either in one of the dies or can be divided between the dies. Complex shapes can be forged within very close dimensional tolerances. Some forgings need to be controlled within a very narrow range of temperatures so as to develop certain desirable microstructures and properties. In the conventional non-isothermal forging one of the major problems is die chilling where the workpiece is cooled by the colder tooling. Die chilling severely limits permissible reductions and shape complexity as the strength of the workpiece increases because of die chilling. In isothermal forgings, both the workpiece and the dies are at the same temperature and the forging is done at low strain rates in order to minimize temperature changes.

ALPID simulation of H section forging

In the isothermal forging simulation of an H section using the finisher punch, the interest lies in the prediction of the deformation requirements and the distribution of process variables during the deformation process. The same set of processing conditions selected in the L section forging was chosen. Because of the symmetry of the H section, only half of the H section was

simulated. The following is the list of process parameters and other related details that are used in simulating the H section using the finisher punch.

Deformation temperature	=	425° C
Average Strain rate	=	0.1 Sec ⁻¹
Top Die Velocity	=	0.05 inch/sec
Bottom Die velocity	=	0.0 (Stationary)
Billet Dimension	=	0.625" width X 0.85" height
Billet Material	=	Aluminum 2024
Interface Friction Factor	=	0.35

The finisher punch geometry for the H section forging is given in Figure 1. The final forged geometry and the workpiece dimensions for the H section forging is shown in Figure 2. The length of the H section to be formed was 4.469 inches which is relatively large when compared with the other dimensions of the H section. Hence the deformation mode was assumed to be plane strain.

The incremental time step used for this simulation was 0.15 second which corresponds to 0.0075 inch stroke. Figure 3 shows the workpiece mesh and the initial position of the dies. It was expected that the material would flow from the web portion of the H section to the legs of the H section. Finer and smaller elements were constructed around the fillet radius of the rib as the local deformation was expected to be large in this area close to the inner legs of the rib portion of the H section. This was done to avoid reaching the negative Jacobian as far as possible in the earlier stages of the deformation. From the grid distortion plots, one could visualize the flow pattern and Figure 4 shows the stage at which a negative Jacobian occurred. Severe distortions of the elements around the rib radius made it impossible to continue the

simulation unless the workpiece was remeshed. After the remesh, the progress in the deformation process is illustrated in Figures 5 (a) and (b). A slight change in the flow pattern is noticed in the web portion, as the material close to the symmetric line tends to flow to the other side of the web. The final grid distortion plot of the H section forging is displayed in Figure 6.

From the grid distortion plots, it is noted that the material flow is more in the upper half of the H section leg (rib portion) than that found in the lower half of the H section leg. This is attributed to the fact that the bottom die was stationary whereas the top die was moving with a velocity of 0.05 inch/sec. This causes a backward extrusion type of material flow in the upper half of the H section. Thus the material fills the top die completely first and the bottom die gets a complete fill only towards the end of the process.

Figure 7 presents the load requirement for the process. The maximum load for forging half of the H section for a unit length was 22000 lbs and this corresponds to a stroke of 0.5975 inch where complete die filling is achieved. The sudden rise in the load requirement occurs when the material fills the bottom die corners. The actual load required to forge a full H section of length 4.469 inches will be 196.5 kips. The load requirements are found to be satisfactory in the sense that there was no sudden increase in the load as the simulation progressed.

The strain rate contours are displayed in Figures 8 (a) and (b). The average strain rate variation for the whole process ranges from 0.09 to 0.13. The strain rates are higher close to the die corners and the distribution is more predominant close to the entrance of the rib regions from the web portion of the H section. These plots reveal that this particular forging of the H section is a fine example of a controlled steady process as the strain rate variation does not show any major drastic changes. Very high strain rates can be noticed at the die corners, when

they get filled by the material and this is not uncommon in any forging process, particularly the rib-web forgings.

Figures 9 (a) and (b) shows the distribution of effective strain. The maximum strain for the whole process is found to be 1.88 and higher strains occur near the inside portion of the legs of the H section. The strain values increase in the web portion as the deformation progresses implying an increased rate of deformation in that region. The effective stress contours are displayed in Figures 10 (a) and (b). During the forging of the H section, the average effective stress was found to be in the range of 6.5 ksi to 8.0 ksi.

Physical Modeling:

The accuracy of the analytical modeling using ALPID can be checked only by conducting the physical modeling. No analytical model including ALPID is 100% accurate and there is a lot of scope for the development and refinement of the analytical model, which in an ideal case should be the exact replica of the actual process under consideration. Obviously building such a 100% perfect analytical tool is an impossible task as there are too many variables involved in the actual process whose interdependence is so complex that they cannot be dynamically implemented as a mathematical model leading to the formulation of an analytical model. In such a situation, the best approach is to use the analytical modeling technique which will closely match the characteristics of the actual process and the analytical results are expected to be in good agreement with that of the actual process.

In this particular thesis work, physical modeling for validating the analytical simulation of H section forging was done to determine how closely the experimental results match with those predicted by the ALPID simulation. The approach followed here was to design the forging process on a laboratory scale basis, which reflected the processing conditions used in the

analytical model. In the validation part, the predicted analytical load requirements were compared with the experimental results.

Experimental Arrangement:

The forging of the H section was done at Wright Patterson Air Force Base, Dayton, Ohio using a 150 ton hydraulic press. This machine is controlled by a MTS controller. Four load and four stroke ranges are available on this machine. It has a 25 gpm servo-valve to actuate the upper ram. The lower ram is fixed even though it can be moved up or down to accommodate different specimen heights. The furnace was controlled by a Wizard temperature controller. The top die, bottom die and the workpiece was heated to 425°C and was maintained at that temperature before the forging was conducted. The machine stroke was calibrated so that it could be controlled precisely. Output voltage for different ram displacements were obtained. Table 5.1 presents a comparison of analytical (ALPID) and experimental load-stroke results for the H section forging.

The predicted ALPID load requirements was found to be higher than the experimental values. This is reasonable as the ALPID formulation is basically an upper bound method implementation. The results compare very well in the earlier stages and towards the end of the process the experimental results were found to be on the low side when compared with the experimental results. The reasons for this difference could be attributed to the following factors.

1. Elastic compensation was not done for the experimental verification of the H section forging. Even though the elastic deformation is very small when compared with that of plastic deformation, it can be observed that the load-stroke curve will shift to the left. Once

the elastic compensation is done, the actual experimental load values will be at least 4 to 12% higher in the later stages of the experiment.

2. The analytical results depend greatly on the material properties. If the flow stress values are not precise then the analytical results will reflect those errors.
3. In the analytical simulation, the friction factor at the die-workpiece interface is considered to be a constant throughout the process. This is not true in the actual conditions.
4. Some unavoidable experimental errors are always possible.
5. A number of assumptions were made in the formulation of ALPID and this might slightly affect the degree of accuracy of the predicted results.

Based on the present study on the physical modeling of the H section, the following conclusions can be drawn.

1. The experimental validation of the H section forging shows a good agreement with the ALPID analytical simulation results.
2. The differences between the results, particularly in the later stages can be attributed to the reasons as mentioned earlier. The differences in the results are therefore considered as insignificant.
3. The use of the ALPID analytical simulation is thus justified and the results derived therein, can be used as a very good indicator of the actual process.

RECOMMENDATIONS:

The dynamic material model can be built processing maps for any material that can be developed. Friction calibration curves using ALPID simulation can also be developed for many commonly used tool-workpiece interfaces. Obviously one of the major requirements for such analytical simulation tasks is to generate dependable material databases. Constitutive equations can be formulated and optimum processing conditions can be identified for various materials. As an extension of this project, preforms for other rib-web sections (such as T) can be designed and analytically simulated using ALPID. The analytical simulation of the other sections can be done and also can be experimentally validated. In a nut shell, the flexibility and excellent features of ALPID to analytically simulate any metal forming process can be full exploited.

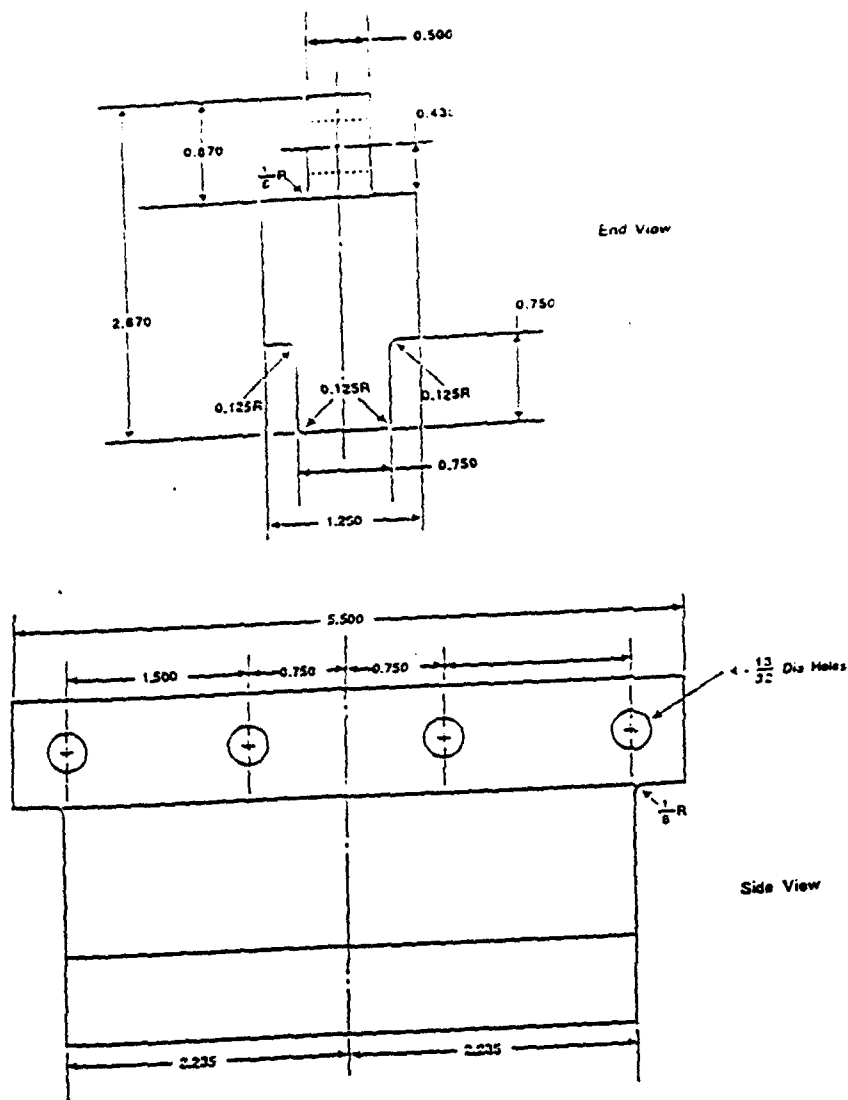


Figure 1 Finisher punch geometry for H section forging.

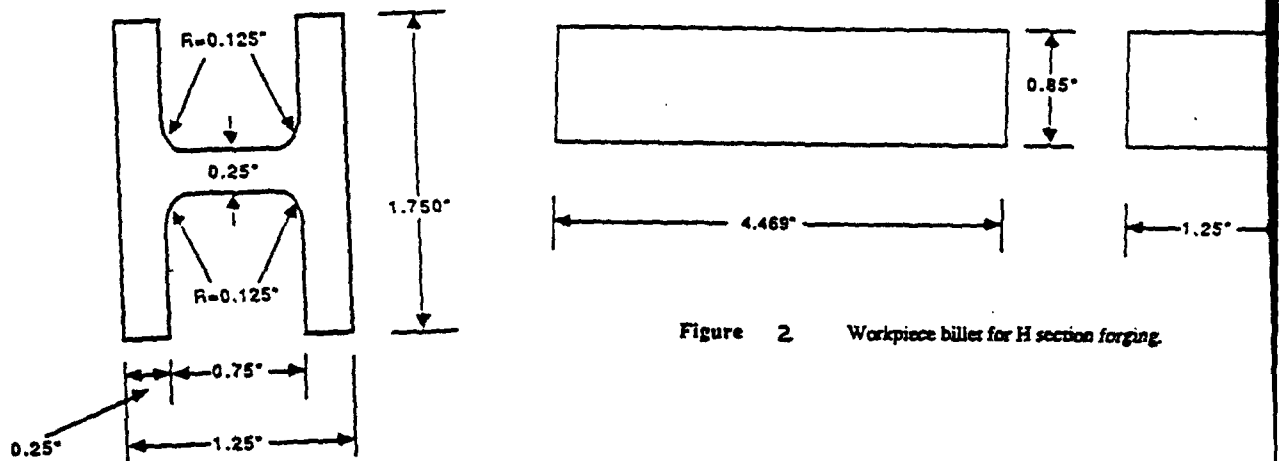


Figure 2 Workpiece billet for H section forging.

Figure 5.11(a). The H section to be formed.

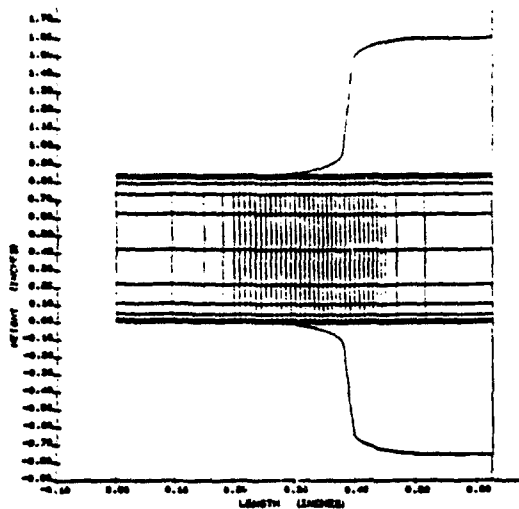


Figure 3 Workpiece and initial position of die in H section forging.
(Due to symmetry only half of the H section is simulated)

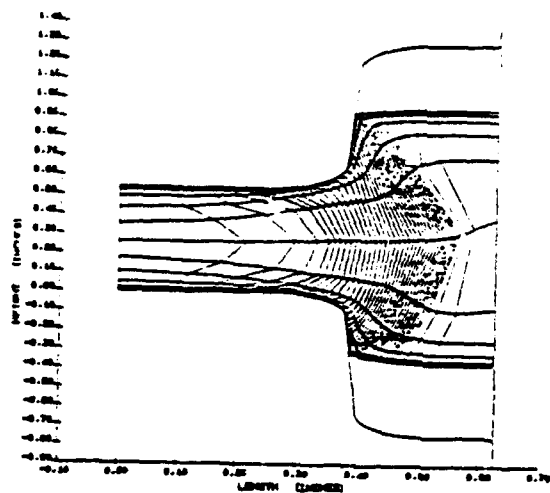


Figure 4 An intermediate stage at which negative Jacobian occurred due to severe grid distortions.

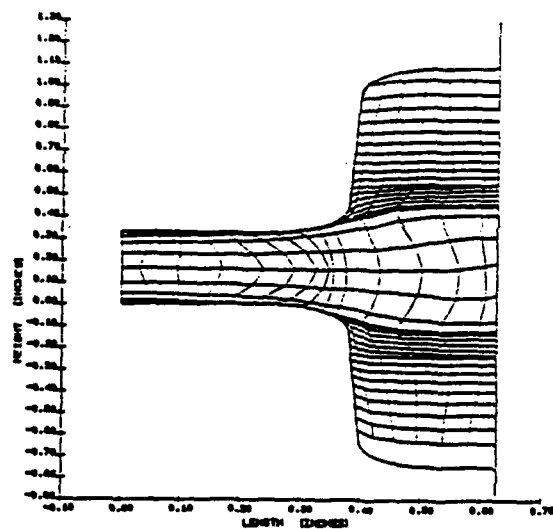
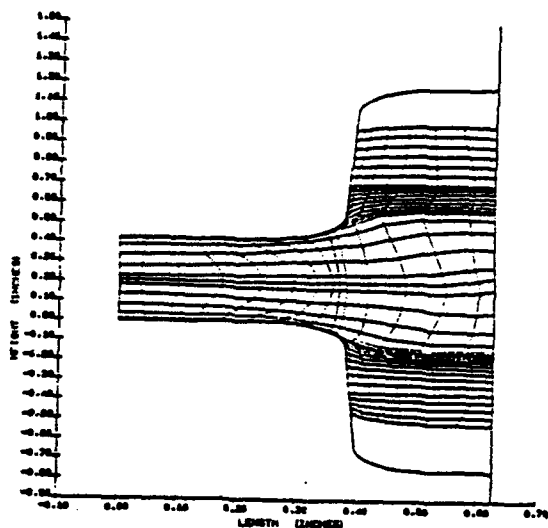


Figure 5 (a) (b) Two intermediate stages of H section forging.

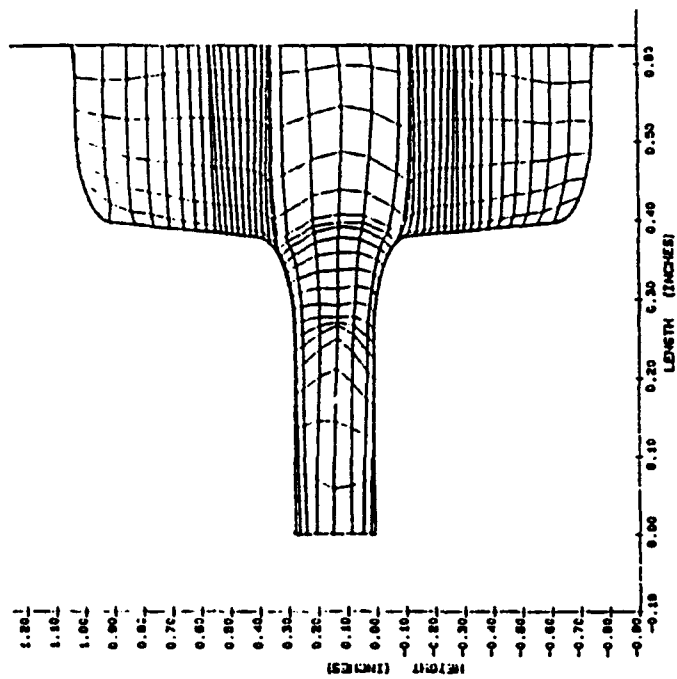


Figure 6 Final grid distortions plot of the H section forging.

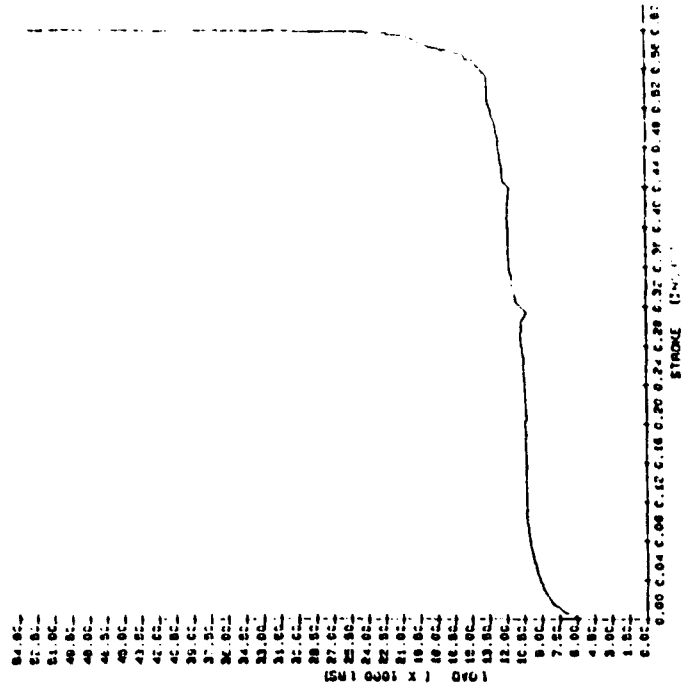
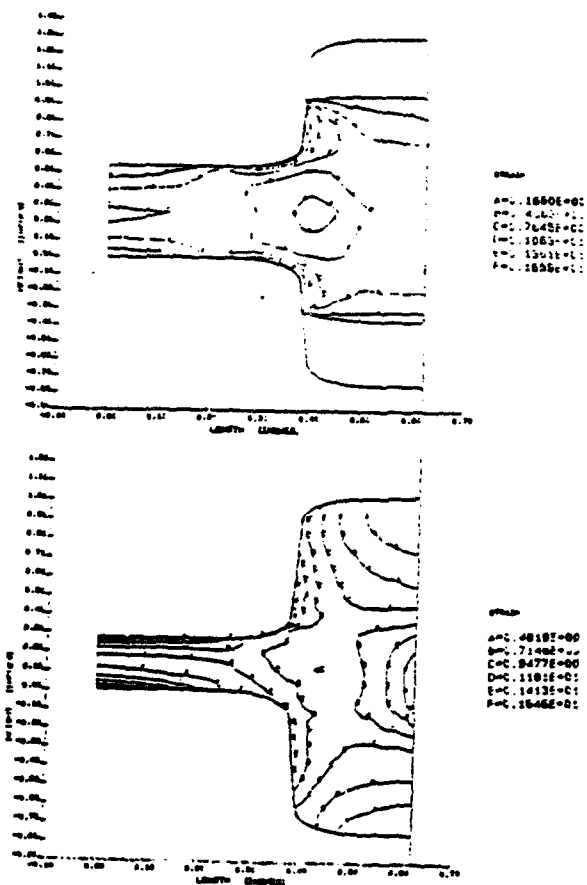
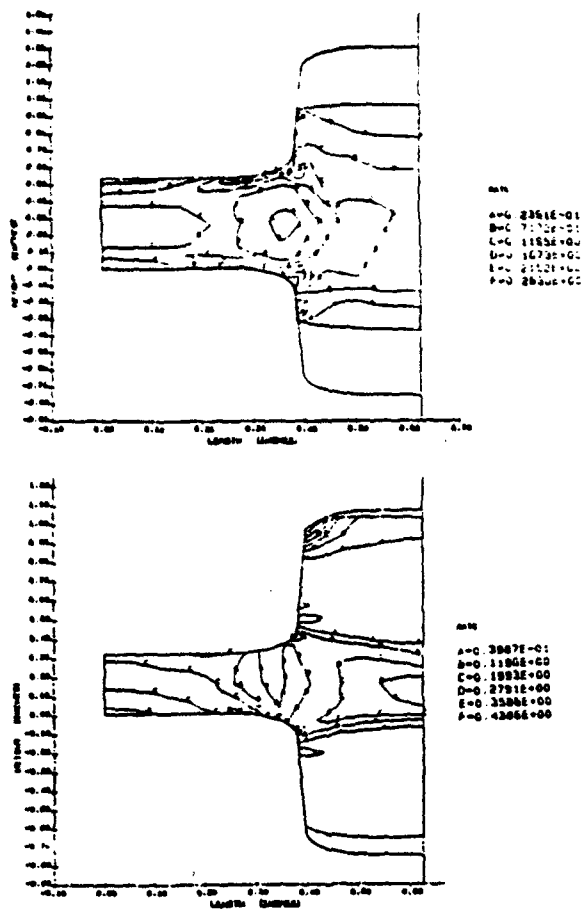


Figure 7 Load requirements for the H section forging.



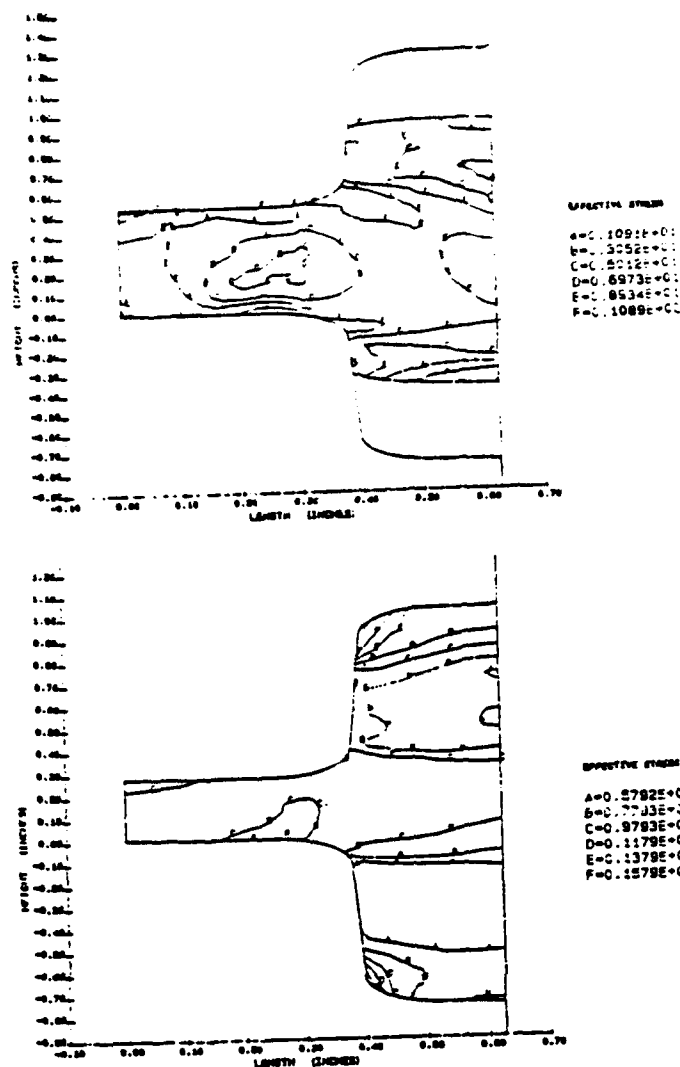


Figure 10 (a) (b) Effective stress contours at two intermediate stages of H section forging

Table 1 Comparison of ALPID and Experimental Load values of 'H' section forging.

Stroke inches	ALPID simulation Load values in kips	Experimental Load values in kips
0.15	93.0	80.0
0.30	96.0	90.0
0.45	111.0	102.0
0.49	114.0	105.0
0.57	117.0	108.0
0.58	143.0	126.0
0.595	170.0	142.0

REFERENCES

- 1) S.I. OH, G.D. Lahoti and T. Altan, "ALPID - A general purpose FEM program for metal forming", Battelle's Columbus Laboratories, Columbus, OH 43201
- 2) S.I. OH, Rebelo, Kobayashi, "Finite element formulation for the analysis of plastic deformation of rate sensitive materials in metal forming", IUTAM Symp., Tutzing, Germany, 1978, pp 273-291
- 3) Shiro Kobayashi, "A review on the finite element method and metal forming process modeling" J. Applied Metal Working, Vol2. No. 3 July 1982 pp 163-169
- 4) W.T. Wu, S.I. Oh, "ALPID T: A general purpose FEM code for simulation of nonisothermal forming processes", NAMRC XIII Conference Berkeley, 1985
- 5) S.I. Oh, G.D. Lahoti and T. Altan, "Application of a rigid-plastic finite element method to some metal forming operations" J. of Mech. Working Tech., 1982 pp 277-290
- 6) Rebelo and Wertheimer, "General purpose procedures for elastic-plastic analysis of metal forming processes", MARC Analysis Research Corporation, Palo Alto, CA
- 7) T. Altan, S.I. Oh and H.L. Gegel "Metal Forming - Fundamentals and Applications", ASM 1983
- 8) S.I. Oh, N. Rebelo and S. Kobayashi "Finite Element Formulation for the analysis of Plastic Deformation of Rate-Sensitive Materials for Metal Forming", Metal Forming Plasticity, IUTAM Symposium, Tutzing, Germany, 1978, pp 273
- 9) S. Kobayashi, "Rigid- Plastic finite element Analysis of Metal forming processes", ASME special publication, PVB-PB-025, 1977, pp 49
- 10) T. Altan and F.W. Boulger, "Flow Stress of metals and its application in metal forming analysis", J. of Engr. for Ind., Vol. 95, 1973, pp 100

1988 USAF-UES SUMMER FACULTY RESEARCH PROGRAM/
GRADUATE STUDENT RESEARCH PROGRAM

Sponsored by the
AIR FORCE OFFICE OF SCIENTIFIC RESEARCH

Conducted by the
Universal Energy Systems, Inc.

FINAL REPORT

QPA Control of the End Milling Process

Prepared by:	Barry Fussell, Ph.D (Doug Gagne)
Academic Rank:	Assistant Professor (Graduate Student)
Department and University:	Department of Mechanical Engineering University of New Hampshire
Research Location:	AFWAL/MLTC
USAF Researcher:	Major Steve LeClair Mr. Tom Lagnese
Date:	28 September, 1988
Contract No:	F49620-87-R-0004

QPA Control of the End Milling Process

by

Dr. B.K. Fussell

Abstract

Qualitative Process Automation (QPA) control was applied to the end milling machining process to maximize feed rates while avoiding unwanted cutting events such as excessive tool deflection, tooth overload and cutter shank overload. QPA controlled the process actively by achieving desired events and preventing undesired events. QPA is a real-time controller with its control output based on process events and not on temporal relationships as are classical control systems. Various procedures for detecting machining events with sensor data were investigated and used with an existing QPA computer structure to develop a controller for the end milling process. The QPA controller used cutting force, spindle speed and feed rate data to predict and avoid excessive tool and tooth loads and to maintain part tolerance with the highest feed rate. Simulation cutting results, using an experimentally validated end milling model, showed the QPA system to be successful in controlling end milling cuts. Successful simulation runs were demonstrated for step changes in the radial and axial depths of cut on aluminum workpieces.

Acknowledgments

I would like to thank the Air Force Systems Command, the Air Force Office of Scientific Research, and the Materials Lab (AFVAL/MLTC) for making this research effort possible. Thanks, also go to Universal Energy System for their concern and thoughtful guidance throughout the summer.

This research would not have been possible without the input and expertise of Major Steve LeClair and Tim Lagnese of MLTC, and I gratefully acknowledge their contributions. I would also like to thank Rick Matejka for his help in understanding the structure of QPA. My experience at the Air Force labs in Dayton was made enjoyable by the many personable individuals I worked with or was associated with. Thanks to all of you.

I. Introduction

One of the major thrusts in Computer Integrated Manufacturing (CIM) is precise control of material processing operations. Through such control, the material quality is enhanced and the fabrication time is reduced, leading to a higher production rate and fewer part rejects. Part of the AFOSR sponsored research in this area is the application of Qualitative Process Automation (QPA) to control an autoclave during curing of epoxy-graphite composites. The Materials Lab (MLTC) at Wright-Patterson Air Force Base has shown that an event driven controller such as QPA can drastically reduce the composite curing time while maintaining the desired part quality [1].

This first success of QPA has encouraged MLTC to apply the technique to a very different type of process, one where the speed of response of the control system is much more demanding. One such process is the cutting of metals on a machining center. Metal cutting is a very fast process that is time-varying and nonlinear in nature. As a result, it is very difficult to control by classical methods and therefore lends itself to QPA control. QPA enables one to control by events rather than by temporal relationships. Thus, nonlinear and time-varying systems are more easily handled, as long as the process can be broken into events.

A particular area of research interest to the author is the adaptive control of machining processes. In specific, he has been studying adaptive force control of end milling. So far, the end milling process has been very difficult to model and even more difficult to control. Research experience has shown that classical, empirical and adaptive methods meet with some success, but have many shortcomings. With this in mind, the author proposed to combine his knowledge of the cutting process with the QPA system developed at MLTC to see if significant gain in part quality and machining time could be obtained.

II. Objectives of the Research Effort

The goal of this project is to apply QPA to a machining operation to determine the feasibility of QPA control of processes very different from the autoclave curing of epoxy-graphite composites. In particular,

QPA is applied to the end milling machining operation to see if improvements in part quality and a reduction in machining time can be obtained. Successful demonstration of this control system should prove the robustness of the QPA structure as opposed to classical systems, and provide a path for more diverse applications.

QPA is earmarked for the machining process because of the significant gains possible in Flexible Manufacturing Systems (FMS). This higher level control system provides a method to replace some of the operator's duties in maintaining part quality and insuring safe machine operation. A perfect example of qualitative control use is where the machining center is unmanned and must depend on sensor input to determine part quality and machine diagnostics.

As mentioned, the goal of the project is to develop a QPA control system for the end milling process. This high level controller will vary the feed drive speed and possibly the spindle speed to maintain the part surface finish and tolerance while avoiding chatter and catastrophic tool failure. In order to develop this system the milling process has to be translated into the existing QPA structure. This requires defining the schedule of the cut as well as the episodes, processes, and influences of the milling operations. While determining the various processes, particular attention must be paid to developing a list of achieve and prevent events and methods to detect them. Examples here would be chatter and tooth breakage. For purposes of this study a literature review is undertaken to determine the various methods of detection and is discussed in Section VI.

Validation of the QPA controller is to be performed by simulation using the Advanced Continuous Simulation Language (ACSL) for the end milling simulation and the Forth language for the QPA controller. The ACSL simulation model has been verified by experiment [2] and is enhanced here to include tooth breakage and tool shank failure. The simulation model accepts feed drive and spindle speed inputs and determines the resulting cutting forces and deflections. The QPA controller has been developed for the autoclave using the Forth language [3] and will be kept in that form for this application. As a result of the two languages, two personal computers are required to allow the Forth and the ACSL programs

to run simultaneously while passing data between themselves. Several difficulties arise because of the input-output (I/O) requirements for passing data, and this will be addressed in Section VII. Simulation results sought here are fairly simple and are intended as a proof of concept as opposed to a rigorous evaluation of QPA. For instance, if tooth fracture and tool failure can be controlled by the QPA system then it is likely that chatter can also be handled.

This report first reviews the existing QPA structure and end milling process simulation model. Next, changes to the end milling model are discussed and implemented. Then, a QPA system for this particular machining operation is developed incorporating the defined episodes, processes, events and influences. A literature search of available sensors and event detection methods is presented along with the issues of computer simulation. Finally, the results of very simple cases of the end milling processes being controlled by QPA is presented and evaluated.

III. QPA Review

In this section, a very short background review of QPA for the autoclave system is given along with the new QPA computer structure. Also, issues of applying QPA to a machining process are addressed by comparing the machining process to the autoclave process.

QPA was developed for control of the composite curing process at Wright Patterson AFB [1] and was based on Qualitative Process Theory developed by Kenneth Forbes [4]. The basis of QPA is that the process is controlled by the onset and ending of events as opposed to temporal relationships. By using events, the set points for the inner loop control of the autoclave process can be adjusted to insure that particular events necessary for part quality are achieved and those causing failure are prevented.

The autoclave process has inner-loop control of pressure and temperature and an outer-loop control used to set a temperature profile such that the part is cured properly. Typical achieve events are cure and compaction while typical prevent events are voids and accelerated reaction. These events are structured within episodes that are sequentially carried out to complete the history of the curing cycle.

Detection of the system state and event occurrence is handled by software and sensors embedded in the process. A sampling time of 30 seconds is used. The detection of events is highly critical to the success of QPA and hence sensor information is of utmost importance. This is true of the autoclave process as well as any other process that is to be controlled by QPA. When conflicts arise between achieve and prevent goals an expert's knowledge is utilized to rank the goals. Goals are then carried out by the system controllers. In this case, the heating system is turned up or down such that a good composite is produced significantly faster than that from a fixed schedule temperature control.

A new QPA computer structure [5] has been developed in hopes of providing a generic format for application to other processes. Figure 1 shows a schematic of the structure. The process instance is utilized to determine when an event occurs, while the process library determines how to respond to that event. The controllers and sensors are the interface between the QPA structure and the process.

The desire of this research is to apply QPA to the end milling process to prove the feasibility of such an approach. To do this, one must first compare and contrast end milling to composite curing to see where difficulties may occur for the existing QPA structure.

There are two main differences between machining and curing; the first being the speed requirements placed on the QPA and the second being the available in-situ sensors for determining events and state of the process. Sampling time for the curing process is thirty seconds while milliseconds are required for machining. This presents some interesting demands on the QPA I/O system. The machining process could benefit from asynchronous sensor sampling rates. Sensor availability, reliability and accuracy is also a critical issue. The machining environment makes it nearly impossible to directly measure the state of the cut, i.e., surface finish, tolerance, tool wear, tool breakage, and chatter. As a result, indirect sensor data has to be utilized to determine the above conditions, not altogether an accurate or speedy process. The ability to detect events and how to execute control is discussed later.

Another difference between the two processes is the outer loop control architecture. The autoclave process has a completely open outer loop with easy access to the temperature control set points. Unfortunately, typical machining centers have a very closed control system that only allows feedrate and spindle speed override signals. This limits the amount of outer-loop control that is possible, and also limits the flow of information.

IV. End Milling Model

The end milling system model is described here along with the computer simulation capabilities. Also, the machining process is described in terms of achieve and prevent events.

A block diagram of the end milling system is shown in Figure 2 [6], and this corresponds to the various elements of the machining center shown in Figure 3. There are three major components in a machining process. The first is the feed and spindle dynamics. Here, a reference signal is used to generate a slide velocity in the x and y directions, and a spindle speed. The second component is the cutting process, which includes geometry of the cut and the force required to remove the material. The geometry of the cut is a combination of the slide and spindle speed, workpiece geometry, tool geometry, and the deflection of cutter from the workpiece. The deflection results from the cutter force acting on the workpiece, tool and machine, and is indicated in Figure 3 as the structure compliance. The resulting deflection causes two feedback paths that affect the cut geometry. The instantaneous feedback causes a reduction in the chip thickness that has to be removed by the next tooth. This effect is shown in the delayed feedback loop, better known as the regenerative loop. Since this is a positive feedback, it can lead to an instability known as chatter. All of the above blocks form the end milling system model.

A computer program previously written [6] uses the mathematical relationships associated with each of the blocks to calculate the resulting force for a given slide and spindle speed, and cutting geometry. From the force, the cutter deflection and resulting cut geometry changes are determined. Additional features that are being

added to the model are cutter tooth fracture and failure of the tool shank under high loads. All of these simulation capabilities are necessary if the QPA concept is to be validated by simulation.

Application of QPA to end milling requires a set of achieve and prevent events. The desire here is to cut a part as quickly as possible with good surface finish and tolerance, while avoiding chatter and tooth breakage. As a result, the achieve events are speed of cut, surface finish and part tolerance while prevent events are system chatter, tooth breakage, excessive tool wear and tool shank failure. The ability to detect these events with sensors will be discussed in a later section. The various cutting errors of the workpiece are shown in Figure 4. e_d is the tolerance error and results from the maximum deflection of the tool. Both e_p and e_s , the profile and surface errors, are related to the surface finish. An example of the effect of profile error during a cornering cut is also shown in the figure. Note that 0° to 90° relates the angle of the right hand corner.

V. QPA Control of End Milling

In order to use QPA to control the end milling process, the structure of the QPA shell as shown in Figure 1 has to be applied to end milling. This proposed structure is explained in detail below along with the influence diagram of the end milling process. Recall that the influence diagram shows how the various parameters, controllers and events, influence each other in a positive or negative fashion.

Figure 5 shows the proposed QPA structure for a general machining operation. The history of the part is the complete cutting routine, while the various episodes are composed of the different tools used to make the cutting history. Examples here would be end milling, face milling, boring and drilling operations. Under each episode are the events that are desired (achieve) and those avoided (prevent). Since end milling is the operation that is being evaluated, only one episode is considered along with its associated events of maximum feedrate, shank failure, tooth failure, tool wear failure, tool deflection and chatter.

Utilization of these events in the QPA structure requires event detection and influences. As mentioned, the event detection is not

straightforward because of indirect sensing and lack of sensor availability. The influences of the end milling process are shown in Figure 6. All of the controller variables are encapsulated by rectangular boxes. Cutter runout, i.e., tool eccentricity, is typically unwanted, but can only be minimized during set-up of the cutter in its tool holder. The achieve events are parallelograms and the prevent events are double ellipses. All other parameters influence these goals in a positive or negative manner. For instance, if the feed per tooth is increased, then the surface finish is degraded and the cutting force is increased. This chart tells the QPA system the effect of changing a control parameter. The QPA control structure wants to achieve or prevent events during machining, thus it uses the influence diagram to trace from an event to a controller that can influence that particular event in the desired positive or negative fashion. When conflicts arise, it is up to the expert to rank the events in order of importance. For end milling, the following rank of importance is used:

1. Shank failure
2. Tooth failure
3. Tool wear failure
4. Chatter
5. Tool deflection (tolerance)
6. Maximum feed rate

Surface finish is not included in this list because at this time it cannot be ascertained from the sensor data during a cut.

VI. Sensor Literature Review

The ability to detect events and to determine the state of the process is critical in any application of QPA. In reality, QPA can only be as effective as the sensors are in giving accurate, reliable data that is informative of the process and events. Unfortunately, in machining operations the environment is very "dirty" as a result of cutting fluids, chips, machine vibration and noise, thus making direct reliable measurements nearly impossible. If direct measurements were possible there would be in-situ sensors for surface finish, tolerance, tool wear, position of tool in cut, etc. Since this is not the case, indirect

sensor data has to be used to infer the events. Even so, sensor reliability and accuracy is still an issue because of their close proximity to the cutting action. A review of the current literature on sensor availability (direct sensing) and event detection (indirect sensing) is now discussed.

Direct sensors are now discussed in very general terms for machining operations:

A. Part and Tool Dimensions

This must be performed before or after a cutting operation. Usually, the check is done with a spindle-mounted Reinshaw touch probe which must replace the tool in the spindle before gauging. Additional methods of obtaining part dimensions include triangulation and interferometry. Interferometry is not as robust as triangulation but can be used inside the machine to give a precise location of the machine axes. In a clean environment vision systems may also be useful [8].

B. Preload in a Roller Type Bearing

A strain gage in the bearing housing gives the cyclic loading and unloading as the rollers pass by, enabling a measurement of bearing preload increase due to thermal expansion, and a determination of the external cutting forces. Monitoring preload is important in maintaining safe machine operation.

C. Cutting Force

The cutting force during machining operations can be measured by a variety of configurations using piezo-electric dynanometers, strain gage load cells, or indirect methods. A list is given below [7].

1. Tool holder dynanometer or load cell on lathes.
2. Table top dynanometer or load cell on machining centers.
3. Spindle bearing load cell.
4. Calculate force from spindle motor current, voltage and speed.
5. Cutting insert dynamometer [8].

All methods are adequate to give average values, but the bandwidths are somewhat limited. The dynamometer has a bandwidth of 1000 to 2000 Hz depending on the workpiece weight, while the load cell is less than a 1000 Hz. The spindle bearing load cell bandwidth is 200 Hz and the spindle force calculation has a bandwidth of 20 Hz. The cutting insert force transducer has a much higher frequency range, 100 Hz to 500 kHz, but can only be utilized in tooling that requires inserts, an example being turning.

D. Machining Center Parameters

Direct measurements also include the spindle motor current, voltage and speed. Also, the x,y and z slide position and velocity can be obtained. The slide position is obtained from an incremental encoder and the velocities are obtained from tachometers.

E. Acoustic Emission

Acoustic emission (AE) waves result from high frequency stress waves occurring as the metal is deformed or fractured during cutting. The stress waves are caused by the release of strain energy as the micro-structure of the material is being rearranged [7]. The acoustic emissions can be picked up with a piezoelectric acoustic transducer that has a bandwidth of 100 KHz to 1 MHz.

A near-complete listing of the available sensors and the various tasks they can perform is indicated in reference [7]. Note that the events are not directly determined from a particular sensor, but are inferred by either empirical means or mathematical modeling.

Since this study is intended for control of the end milling process, the rest of this section will concentrate on indirect event detection in end milling using force, speed, spindle motor current, and acoustic emission. The event detections methods presented here do not address all of the known techniques, only the ones thought by the authors to be most promising.

Tooth and Tool Breakage

Lan and Naerheim [9] propose a discrete autoregressive model (AR) of order 15 to detect tooth and tool breakage in end milling. Tool and tooth fracture are determined by looking for substantial changes in the prediction error,

$$\epsilon = Y(K + 1) - \hat{\theta}^T(K) \phi(K) \quad (1)$$

where $\hat{\theta}$ are the estimated process parameters, found by a fixed gain MRAS least squares estimation algorithm, and ϕ are the past values of the measured feed force Y . Complete shank failure is fairly easy to determine, but tooth chipping often times is difficult, especially when there are changes in the axial depth and radial depth of cut. For all of the tests run here the spindle speed was held constant, so the effect of varying spindle speed on their algorithm is unknown.

Another method of in-process detection of tooth breakage was developed by Attanis et al. [10] and Attanis and Yellowley [11]. They use the first and second differences of the resultant cutting force, averaged over 1 tooth period, to predict breakage.

$$\Delta_1 F(i) = F(i) - F(i-1) \quad (2)$$

$$\Delta_2 F(i) = \Delta_1 F(i) - \Delta_1 F(i-1) \quad (3)$$

To utilize the first and second difference equations, a threshold relationship is derived to eliminate the disturbance effects of radial immersion and runout. The radial immersion is predicted, if not known in the cut, and used in the threshold relationship.

$$\Delta'F = [F(i) - F(i-1)]/F(i-1) \quad (4)$$

By comparing the value of this relationship during a cut to that predicted by a simulation model, a triggering of the second difference is initiated. If the second difference of the average force is found to be larger than the first difference, then tooth damage is assumed.

Other methods of tool breakage detection are performed after the cut and involve the Renishaw touch probe, proximity switches and possibly vision systems. In addition, there are several acoustic emission (AE) methods in detecting tool breakage in turning, but unfortunately most have not been applied to end milling [12,13].

Tool Deflection

Tool deflection is associated with the part tolerance and as such, must be held below a certain limit. Typically, the deflection is inferred from the cutting force that is perpendicular to the feed direction [14]. The perpendicular force is obtained from a three axis dynamometer that is mounted below the workpiece. If this force exceeds a predetermined limit, then the feed rate is decreased or the spindle speed is increased.

Chatter

Chatter is a complicated self-excited vibration that is very difficult to predict a priori. While it can be detected in-situ, it's not easy to determine what course of action to take to eliminate chatter and still maintain an aggressive cut. Smith and Tlustý [15] provide a method for determining the necessary system changes. Their algorithm is discussed below.

A force dynamometer or an acoustic emission sensor can be used to detect the presence of chatter. However, the best detection is afforded by using both sensors; the dynamometer to give indication of force oscillations and the AE sensor to give the frequency content. Chatter detection is made by checking the following criteria,

$$F_R > F_R(\text{set point}) \quad (5)$$

$$\omega(\phi_p) \neq \omega(\phi_r) \quad (6)$$

$$|\phi_p| > |\phi_t| \quad (7)$$

Equation (5) states that the force oscillation amplitude is higher than a predetermined set point. Equation (6) indicates that the frequency of the power spectral density (PSD) peak is not equal to the tooth frequency. Finally, Equation (7) requires that the PSD peak away from the tooth frequency is greater than PSD at the tooth frequency. If all 3 equations are satisfied, then chatter exists and some action must be taken. That action is now described.

The first step is to decrease feedrate. This reduces oscillation amplitudes as a result of chatter. Second, the spindle speed is increased if the frequency of the PSD peak point is greater than the tooth frequency, and decreased if the PSD peak point is less than the

tooth frequency. If chatter still exists, then the axial depth of cut is decreased. Finally, the feedrate is increased. The purpose behind the spindle speed changes is to run the end miller at the system natural frequency, which gives a very high axial depth limit on stability.

The methods to detect and prevent many of the events described above is very limited in scope at this time, and much more work needs to be completed in order to formulate algorithms that are adequate for a large variety of cuts. Also, more research is needed on sensing surface finish, tool wear and part tolerance.

VII. Simulations

QPA control of the end milling process is tested here by simulation, using an experimentally validated end milling model that is capable of simulating workpiece geometry changes, cutter deflection, and tooth and shank failure. In the simulations, the X feedrate input command signal is determined by the QPA controller, based on the X and Y cutting force, the feedrates, and the spindle speed. The QPA uses this "sensed" information to determine if any prevent events are occurring. If these events are occurring, then the QPA takes action to prevent them by adjusting the feedrates. Once prevented, the QPA will increase the feedrate or hold it constant, depending on the band limit around the particular event in question.

Three simulation trial results are presented here. Table 1 lists the trials and the various geometry changes associated with them. For trials 2 and 3, the QPA controller is trying to achieve maximum feedrate while preventing tool shank failure, tooth failure and part out-of-tolerance. The tool shank failure is associated with the total force on the end of the cutter. If this force exceeds a certain limit, then the cutter is in imminent danger of failure. The QPA response is to reduce the feedrate when the total force reaches a set limit. The tooth failure occurs as a result of overloading an individual tooth edge on the end mill. This can be detected by measuring the feedrate and the spindle speed and calculating the feed per tooth in inches. If this value is

above a set limit, then the QPA reduces the feedrate so damage will not occur. Tolerance conditions are determined from the cutting force perpendicular to the path of the end mill. For all of the simulation runs the cutter is moving in the x direction, so the tolerance is determined solely by the Y force. The limit for the Y force is determined by the length and material of the cutter and the accepted deflection.

All of these prevent events have two process instances associated with them. The maximum level indicates to the QPA that the feedrate needs to be reduced, while the region between the minimum level and maximum level indicates that the feedrate should be held. The hold region is necessary to keep the feedrate command signal from oscillating from the on/off nature of the controller.

The results of trial 1 are shown in Figure 7. Plot (a) shows the total force on the cutter while (b) shows the Y force. The axial depth is doubled, 0.25 to 0.5 inches, around one second into the run, and this causes a large increase in the force. Plot (b) has the maximum and minimum values associated with part tolerance. After the AD change the feedrate is reduced until the Y force is inside the band. Once inside the band, the feedrate is held constant until the Y force goes below the lower band. When this happens the feedrate is again increased until the force is inside the acceptable band. The only prevent event being considered here is part tolerance, and it is very effective in maintaining a constant force despite an axial depth change.

The results of trial 2 are shown in Figure 8. In this run the axial depth is doubled from 0.25 to 0.5 inches at approximately one second, and the radial depth of cut is held constant at 0.25 inches. All three prevent events are considered in this run. Before the axial depth change, the tooth failure prevent mode is in effect (plot (d)). This limits the feed per tooth and reduces the possibility of tooth failure. After the axial depth change, both the total force FF, plot (b), and the perpendicular force FFY, plot (c), are above their limits. This results in a lowering of the feedrate until FFY is inside the force band. The feedrate is now held constant until the force FFY is below the minimum value. Once this occurs, none of the prevent events are active and the

feedrate is increased until FFY is once again within the given limits. Plot (c) shows the commanded feedrate from the QPA to the end milling system.

Trial 3 results are shown in Figure 9. For this trial the axial depth is held constant at 0.25 inches and the radial depth is increased slowly from 0.25 to 0.5 inches and then back to 0.25 inches. Plot (a) shows the total force. The large oscillations at the beginning and end of the run are the result of a radial depth smaller than the cutter diameter. Plot (b) shows that the shank failure event was never active. Plot (c) indicates that the middle of the run is governed by FFY, the part tolerance event. The role of the tooth failure event is shown in plot (d). Both the beginning and end feedrate of the run are limited by the feed per tooth. This makes sense because the total force for a half-immersion cut may be small while the feed per tooth may be extremely high. The results of the various prevent events is shown in plot (e), the command feedrate input.

VIII. Conclusions and Recommendations

The conclusion of this simulation work is that QPA is effective in adaptively controlling the feedrate of the end milling process to produce the fastest possible cut while preventing shank and tooth overloads, and maintaining part tolerance. Proof of the feasibility of QPA was demonstrated by the three simulation runs incorporating step changes in the axial and radial depth of cut. For these runs, shank failure was detected by the total cutting force, tooth overload by the feed per tooth, and past out-of-tolerance by the cutting force perpendicular to the tool path. QPA maintained the highest feedrate possible while preventing the undesired events mentioned above. When a prevent event such as past out-of-tolerance was detected in the simulation run, the QPA system reduced the feedrate to keep the part within the desired values. If more than one prevent event occurred at the same time then a priority established by the expert was followed such that the highest priority event was handled first.

A literature review of critical events in end milling, and how to detect them, produced a significant amount of material on tool breakage,

tooth breakage, chatter and deflection. This information was useful in developing algorithms for event detection, but only under very limited cutting conditions. For cuts such as contouring or radial depth changes the available algorithms are insufficient for accurate event detection. Obviously, more research is needed in this area.

There are several areas of QPA control of end milling that need to be addressed in future work. This includes sensor performance and availability, event detection, and QPA evaluation. The success of QPA is very dependent on the ability to detect events such as chatter, surface finish, etc., and to react to them in the correct manner. Sensors and sensor fusion methods that clearly indicate when events such as chatter are occurring must be investigated and evaluated through simulation and experimentation. Likewise, various QPA strategies to eliminate the undesired event must be evaluated through simulation. These simulation models would include new sensor strategies and events in the QPA system and a more complex end milling model that is capable of modeling chatter. Obviously, more complex models enables one to evaluate more sophisticated QPA systems. Finally, the QPA system should be evaluated through experimentation so some of the practical issues of implementation can be addressed, and so the real world feasibility can be proved.

References

- [1] Abrams, F., P. Garrett, T. Lagnese, S. LeClair, C.W. Lee and J. Park, "qualitative Process Automation for Autoclave Curing of Composites", AFWAL/MLTC Interim Report for the Period 15 October 1985-15 May 1987, AFWAL-TR-87-4083.
- [2] Fussell, B.K. and K. Srinivasan, "An Investigation of the End Milling Process Under Varying Machining Conditions", Submitted for publication to ASME Journal of Engineering for Industry, 1986.
- [3] Matejka, R.F., A Programming Environment for Qualitative Process Control, M.Sc. Thesis, Department of Electrical and Computer Engineering, University of Cincinnati, Cincinnati, Ohio, 1988.
- [4] Forbus, K., "qualitative Process Theory", in Qualitative Reasoning About Physical Systems, edited by D.G. Bobrow, MIT Press, pp. 85-168, 1982.
- [5] Matejka, R.F. and T.J. Lagnese, "A Representational Language for Qualitative Process Control", 1988.
- [6] Fussell, B.K., Modeling and Adaptive Force Control of End Milling Operations, Ph.D. Thesis, Dept. of Mechanical Engineering, The Ohio State University, Columbus, Ohio, 1987.
- [7] Andrews, G.C. and J. Tlusty, "A Critical Review of Sensors for Unmanned Machining", Annals of CIRP, Vol. 32, 2, 1983, pp. 563-572.
- [8] Barkman, W.E., E.F. Babelay, and T.L. Hebble, "A Review of the Advanced Technology Features Available for the Enhanced T-Base Project", Report on Oak Ridge Y-12 Plant, June 27, 1988.
- [9] Lan, Ming-Shang and Y. Naerkeim, "In-Process Detection of Tool Breakage in Milling", ASME Journal of Engineering for Industry, August 1986, Vol. 108, pp. 191-197.
- [10] Attanis, Y., I. Yellowley and J. Tlusty, "the Detection of Tool Breakage in Milling", ASME Winter Annual Meeting, Miami, Florida, 1985, pp. 41-48.

- [11] Attanis, Y. and I. Yellowley, "In-Process Detection of Tool Failure in Milling Using Cutting Force Models", ASME Winter Annual Meeting, Boston, MA, 1987, PED-Vol. 26, pp. 1-16.
- [12] Dornfeld, D.A., "The Role of Acoustic Emission in Manufacturing Process Monitoring", 13th NAMRC, May 1985, pp. 69-74.
- [13] Emel, E. and E. Kannatey-Asibu Jr., "Tool Failure Monitoring in Turning By Pattern Recognition Analysis of AE Signals", ASME Winter Annual Meeting, Boston, MA, PED-Vol. 26, 1987, pp. 39-57.
- [14] Smith, S. and J. Tlusty, "NC Programming for Quality in End Milling", 16th NAMRC, May 1988, SME, pp. 279-286.
- [15] Smith, S. and J. Tlusty, "Update on High-Speed Milling Dynamics", ASME Winter Annual Meeting, Boston, MA, PED-Vol. 25, 1987, pp. 153-165.

Tr.	Type of Transfer:	Controller:
1	Slot Cut with AD increase AD: 0.25 to 0.5 inches RD: 0.5 inches	Tool Detection
2	Radial Cut with AD increase AD: 0.25 to 0.5 inches RD: 0.25 inches	All Modes
3	Corner Cut AD: 0.25 inches RD: 0.25 to 0.5 to 0.25 inches	All Modes
Cutter Data		
4 Flute, HSS, 0.5 inch Dia., 1.75 inch Length, Dry Cutting		
Workpiece Data		
2024-T6 Aluminum		

Table 1. Geometry, Cutter, and Workpiece Details.



Figure 3. End Mill Machining Center.

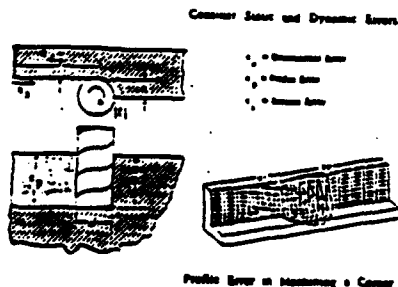


Figure 4. End Milling Cutting Errors.

Figure 1. QPA Structure.

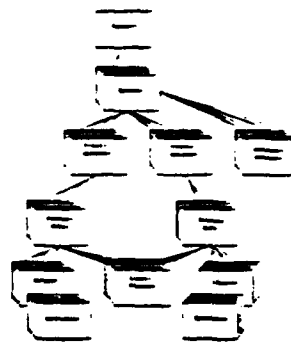


Figure 1. QPA Structure.

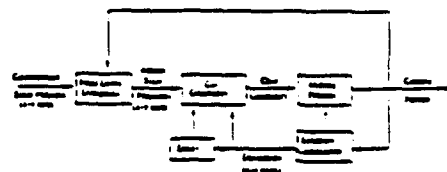


Figure 2. End Milling Block Diagram.

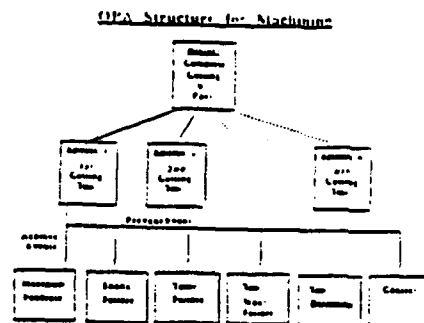


Figure 5. QPA Control Structure for End Milling.

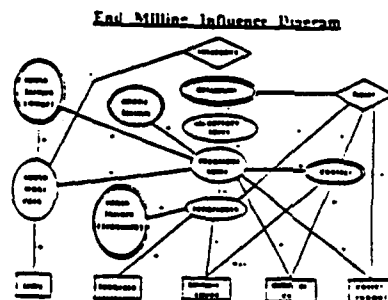


Figure 6. End Milling Influence Diagram.

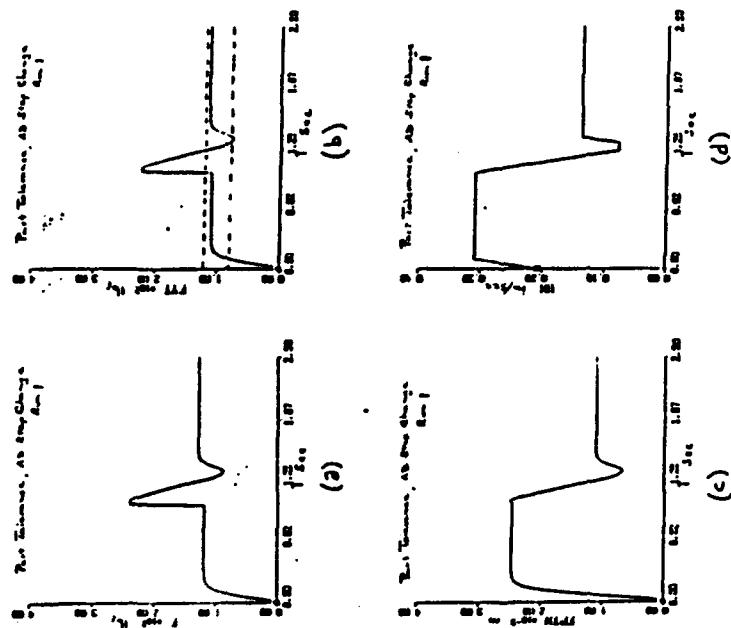


Figure 7. Results for Simulation Trial 1.

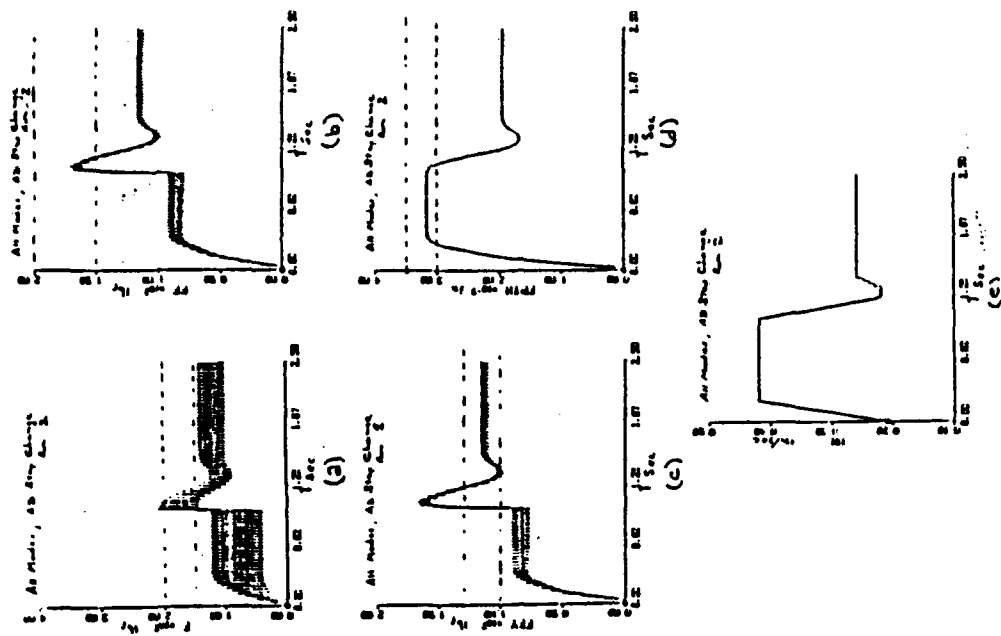


Figure 8. Results for Simulation Trial 2.

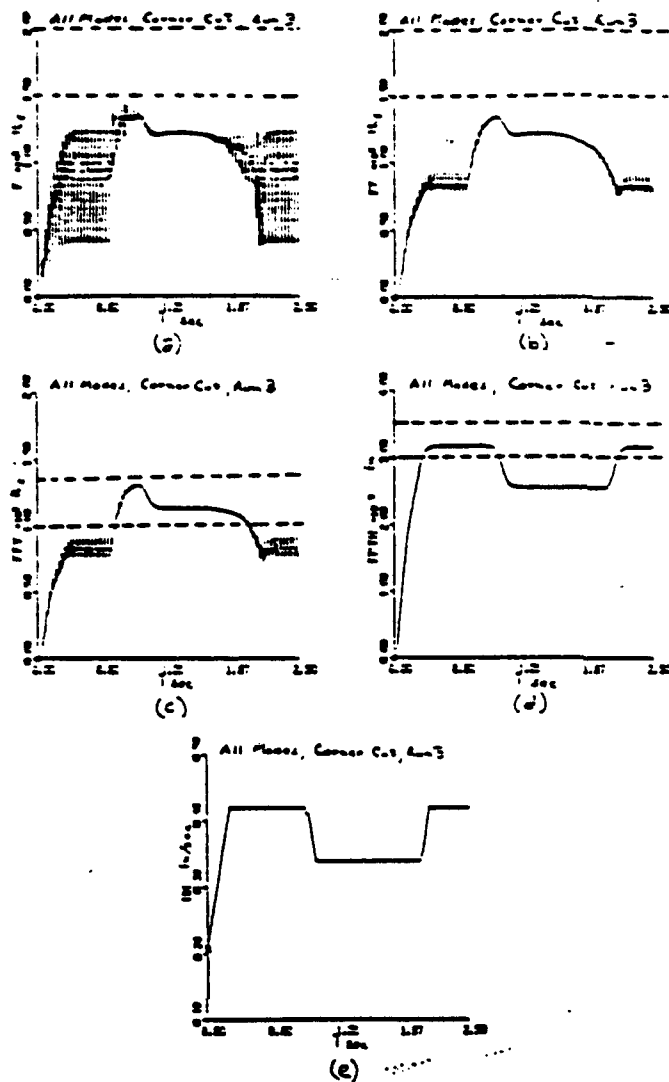


Figure 9. Results for Simulation Trial 3.

1988 USAF-UES SUMMER FACULTY RESEARCH PROGRAM/
GRADUATE STUDENT RESEARCH PROGRAM

Sponsored by the
AIR FORCE OFFICE OF SCIENTIFIC RESEARCH

Conducted by the
Universal Energy Systems, Inc.

FINAL REPORT

SINGLE-CRYSTAL DIFFRACTION ANALYSIS OF COMPOUNDS WITH
POTENTIAL NONLINEAR OPTICAL PROPERTIES

Prepared by:	David A. Grossie, Ph.D.
Academic Rank:	Assistant Professor
Department and	Department of Chemistry
University:	Wright State University
Research Location:	AFWAL/MLBP Wright-Patterson AFB Dayton, OH 45433
USAF Researcher:	W. W. Adams
Date:	8 Sep 88
Contract No:	F49620-87-R-0004

SINGLE-CRYSTAL DIFFRACTION ANALYSIS OF COMPOUNDS WITH
POTENTIAL NONLINEAR OPTICAL PROPERTIES

by

David A. Grossie, Ph.D.

ABSTRACT

Single-crystal x-ray diffraction data was collected on two compounds having potential nonlinear optical (NLO) properties, $C_{13}H_{18}N_2O_2Si$ and $C_{22}H_{17}N_5O_5$. The former compound is a derivative of 2-methyl-4-nitroaniline, a molecule with known NLO properties. It crystallizes in a monoclinic crystal lattice with cell constants of $a=20.258(6)$, $b=10.444(4)$, $c=7.129(2)$ Å, and $\beta=93.05^\circ$. The observed space group is $P2_1/c$, a centric space group. The structure was solved and refined, yielding a R-factor of 0.085. $C_{13}H_{18}N_2O_2Si$ is planar with little distortion in the internal bond distances and angles.

$C_{22}H_{17}N_5O_5$ crystallizes in a triclinic crystal lattice having cell constants of $a=8.179(4)$, $b=16.915(4)$, $c=8.190(2)$ Å, $\alpha=94.98(2)$, $\beta=116.54(3)$, and $\gamma=83.99(3)^\circ$. The space group was determined to be $P\bar{1}$. This compound has defied structure solution, in spite of application of the most recent and capable direct methods programs.

ACKNOWLEDGEMENTS

I would like acknowledge the Air Force Systems Command and the Air Force Office of Scientific Research for sponsorship of this research. Additionally, acknowledgement of Universal Energy Systems must be given for their assistance in the administrative aspects of the program.

I wish to thank the personnel of the Polymer Branch of the Materials Laboratory and University of Dayton Research Institute for their assistance during the execution of this research project. I especially would like to thank Drs. Wade Adams and Al Fratini for their many discussions of single-crystal methodology.

I. INTRODUCTION:

The Polymer Branch of the Materials Laboratory at the Wright Aeronautical Laboratory, Wright-Patterson Air Force Base is interested in the synthesis and characterization of polymeric materials. Basic research is also conducted in the structure of polymeric materials and the correlation of the structure and physical properties. The emphasis of this area is to predict the properties of a polymer prior to its synthesis. In this way, the synthesis problem can have greater direction and produce new and better materials with more efficiency. One of the techniques used in determining the structure of polymers is to examine by single-crystal x-ray diffraction methods compounds that may be used to form the backbone, pendants, or cross-links of the polymer. By knowing the structure of a small, repeating portion of the polymer, the polymer itself may be mathematically modeled, yielding the physical properties.

My research interests are in the structural analysis of small organic and inorganic molecules by single-crystal x-ray diffraction. My experience in the structural determinations of organic molecules with similar features to those of interest and my considerable familiarity with the available diffraction hardware and software contributed to my assignment to the Morphology Section of the Polymer Branch.

II. OBJECTIVES OF THE RESEARCH EFFORT:

A study of model compounds of polymeric materials that have potential nonlinear optical properties will be conducted. This study will involve the structural analysis of several compounds by single-crystal x-ray diffraction techniques, with the intent to amass data which may be used to correlate the observed structure and the magnitude of the nonlinear optical response. The primary structural information that is needed by the currently accepted theories is the centrality of the crystal lattice in which the compound of interest crystallizes and the extent of π -orbital conjugation. To this end, the study will examine derivatives of 2-methyl-4-nitroaniline, a compound with known nonlinear optical properties, and other conjugated systems with separated electron donor and acceptor groups.

III.

a. Crystalline samples of a series of compounds were examined using an optical microscope to determine the size and quality of the individual crystals. Two of the compounds examined showed promise of containing suitable crystals for diffraction analysis, whereas the remainder were of insufficient size to be analyzed. Single crystals of $C_{13}H_{13}N_2O_2Si$ and $C_{22}H_{17}N_5O_3$ were prepared for analysis by attaching them

to a thin glass fiber and placing them at the center of an Enraf-Nonius CAD-4 automated diffractometer.

Preliminary x-ray analysis of each of the selected crystals was made. These results are summarized in Table 1, along with the parameters of the subsequent data collection.

b. Data collected on each of the crystalline samples was examined for the presence of space-group-determining systematic absences using the program LOOK (Chapuis, 1984). For each sample, an appropriate space group was determined-- $P2_1/a$ for $C_{13}H_{18}N_2O_2Si$, and $P\bar{1}$ for $C_{22}H_{17}N_5O_5$. Since the space group $P2_1/a$ is considered a non-standard space group, the data for $C_{13}H_{18}N_2O_2Si$ was transformed into the equivalent standard space group $P2_1/c$.

c. Using the program MULTAN-11/82 (Main, 1982), a program for the direct solution of crystal structures from diffraction data, the structure of $C_{13}H_{18}N_2O_2Si$ was determined. The initial structure of $C_{13}H_{18}N_2O_2Si$ was refined using the full-matrix least-squares refinement program contained in SDP/VAX (Frenz, 1978). The structure of $C_{22}H_{17}N_5O_5$, however, defied solution, in spite of the application of several of the most recent and capable direct methods programs available in the laboratory.

d. Figure 1 shows an ORTEP (Johnson, 1971) drawing of the refined structure of $C_{13}H_{13}N_2O_2Si$, and a summary of the interatomic distances and angles is presented in Table 2. The molecule is essentially planar, with a maximum deviation from planarity of 0.244 Å. The degree of planarity of the central benzene ring, 0.022 Å, is much better. This would indicate that the substituents on the benzene ring do not fit into a common plane as well as the ring itself. The nitro group at the 4-position of the ring is found to be coplanar with the ring, whereas the dimethylamine and trimethylsilylethynyl groups noticeably deviate. The dimethylamine appears to be twisted with respect to the ring, moving C11 and C12, the methyl carbon atoms, 0.138 Å below and 0.655 Å above the plane, respectively. The almost linear trimethylsilylethynyl group is found to extend slightly below the plane of the benzene ring, with deviations of 0.213, 0.446, and 0.892 Å for C21, C22 and Si, respectively. Additionally, this group has distortions in the bond angles at C21 and C22. Normally a carbon-carbon triple bond is linear, with bond angles of 180° at each end, but in the trimethylsilylethynyl group, the bond angles found are 175° and 173°, at C21 and C22, respectively. The bond distances and angles within the benzene ring are reasonable in their regularity, with only one distance, C1-C2, differing greatly from any of the others (1.426 Å vs. 1.371-1.396 Å).

IV.

From the completed analysis of $C_{13}H_{18}N_2O_2Si$ and partial analysis of $C_{22}H_{17}N_5O_5$, certain conclusions can be made regarding to the nonlinear optical properties of these compounds. Since both crystallize in lattices that are centrosymmetric, the second-order term of the polarizability equation must be zero. The response due to the third-order term for these compounds is less certain. The third-order term is thought to correlate with the extent of conjugation within the molecule, so in $C_{13}H_{18}N_2O_2Si$ the predicted response from the third-order term would be minimal. $C_{22}H_{17}N_5O_5$ would be expected to have a higher response, though a completed analysis will indicate the exact extent of conjugation upon which any accurate prediction will depend.

V. RECOMMENDATIONS:

There is a need to improve the synthesis of nonlinear optical materials, with one of the improvements being in the selection of potential compounds for synthesis. A second area where improvement is needed is in the quantification of the molecular parameters that produce a nonlinear optical response. This second area can potentially provide the information needed to make the improvement in the selection of synthesis candidates.

Currently, there are three factors that are assumed to produce the desired NLO response, with one factor being quantitative and a second based on a relative scale. These two factors are the centricity of the crystal lattice and the electron-donating and withdrawing effects of the commonly used functional groups. The third factor, the extent of conjugation within the molecule, is currently unquantified. Molecular planarity is normally taken as the first clue that a non-fused, π -bonded ring system is conjugated. Since this information, like the centricity, is directly obtainable from the structural analysis of a crystalline compound, the extent of conjugation can be quantified by this process.

As a final step, the same compounds examined by x-ray diffraction need to be tested for a nonlinear optical response and the magnitude of that response. With the above pieces of data obtained and analyzed, the synthesis of nonlinear optical materials can be by rational design. This will allow the physical properties of the material to be optimized without compromising the desired nonlinear optical properties.

REFERENCES

Chapius, G., "LOOK. A FORTRAN Program for Generating Simulated Precession Photographs from Diffractometer Data," University of Lausanne, Switzerland, 1984.

Frenz, B.A., "The Enraf-Nonius CAD-4/SDP--A Real-Time System for Concurrent X-Ray Data Collection and Crystal Structure Determination," Computing in Crystallography, H. Schenk, R. Olthof-Hazelkamp, H. van Konigsveld, and G. C. Bassi, Eds, Delft University Press, Delft, Holland, 1978, pp. 64-71.

Johnson, C.K., ORTEP II. Report ORNL-3794, revised. Oak Ridge National Laboratory, Tennessee, 1971.

Main, P., "MULTAN 11/82. A System of Computer Programs for the Automatic Solution of Crystal Structures from X-Ray Diffraction Data," University of York, England, 1982.

Table 1. Experimental Details

	<u>Compound 1</u>	<u>Compound 2</u>
Formula:	$C_{13}H_{18}N_2O_2Si$	$C_{22}H_{17}N_3O_5$
Formula weight:	262.39	431.4
F(000):	560	448
Crystal dim.:	0.30 x 0.50 x 0.60 mm	
Radiation:	Mo K α	Mo K α
Wavelength:	0.71073 Å	0.71073 Å
Temperature:	23°	23°
Crystal form:	monoclinic	triclinic
Space group:	$P2_1/c$	$P\bar{1}$
Cell constants:	$a = 20.258(6)$ Å $b = 10.444(4)$ Å $c = 7.129(2)$ Å $\beta = 93.05(2)^\circ$	$a = 8.179(4)$ Å $b = 16.915(4)$ Å $c = 8.190(2)$ Å $\alpha = 94.98(2)^\circ$ $\beta = 116.54(3)^\circ$ $\gamma = 83.99(3)^\circ$
Volume:	1505.9 Å ³	1008.3 Å ³
Z:	4	2
Density:	1.16 g/cm ³	1.42 g/cm ³
Absorption coeff.:	1.5 cm ⁻¹	0.97 cm ⁻¹
Scan type:	$\omega/2\theta$	$\omega/2\theta$
Scan rate:	0.57 - 2.79°/min	0.29 - 2.79°/min
Scan width:	1.2 + 0.344 tan θ	0.85 + 0.344 tan θ
Maximum 2 θ :	64.0°	60.0°
Refl. measured:	5592 total 5266 unique	4581 total 4470
Corrections:	Lorentz-polarization Reflection averaging (agreement on I = 4.4%) Numerical absorption (from 93.29 to 96.06 on I) Extinction (coefficient = 1.21×10^7)	Lorentz-polarization Reflection averaging (agreement on I = 3.3%)
Observations:	1536 with $F_o^2 > 3\sigma(F_o^2)$	1567 with $F_o^2 > 3\sigma(F_o^2)$
Parameters:	164	
R:	0.085	
wR:	0.108	
Goodness-of-fit:	2.98	
Max. shift/error:	0.01	
Residual density		
maximum:	0.30(7) e/Å ³	
minimum:	0.27(7) e/Å ³	

Table 2. Interatomic Bond Distances (Å) and Angles (°) for C₁₃H₁₈N₂O₂Si

<u>Atom 1</u>	<u>Atom 2</u>	<u>Distance</u>	<u>Atom 1</u>	<u>Atom 2</u>	<u>Atom 3</u>	<u>Angle</u>
Si	C22	1.819(6)	C22	Si	C23	109.4(4)
Si	C23	1.832(8)	C22	Si	C24	110.4(4)
Si	C24	1.72(2)	C22	Si	C25	110.1(4)
Si	C25	1.77(1)	C23	Si	C24	107.5(5)
O1	N4	1.227(6)	C23	Si	C25	105.2(5)
O2	N4	1.215(6)	C24	Si	C25	114.1(5)
N1	C1	1.368(7)	C1	N1	C11	119.6(4)
N1	C11	1.471(7)	C1	N1	C12	123.8(4)
N1	C12	1.447(7)	C11	N1	C12	113.8(4)
N4	C4	1.455(7)	O1	N4	O2	123.4(5)
C1	C2	1.426(7)	O1	N4	C4	118.0(4)
C1	C6	1.396(8)	O2	N4	C4	118.6(4)
C2	C3	1.387(7)	N1	C1	C2	122.1(4)
C2	C21	1.425(7)	N1	C1	C6	119.7(5)
C3	C4	1.373(7)	C2	C1	C6	118.1(5)
C4	C5	1.385(7)	C1	C2	C3	118.9(4)
C5	C6	1.371(8)	C1	C2	C21	124.2(4)
C21	C22	1.195(7)	C3	C2	C21	116.5(4)
			C2	C3	C4	121.0(4)
			N4	C4	C3	119.7(4)
			N4	C4	C5	119.4(4)
			C3	C4	C5	120.8(5)
			C4	C5	C6	119.1(5)
			C1	C6	C5	122.0(5)
			C2	C21	C22	175.0(5)
			Si	C22	C21	173.0(6)

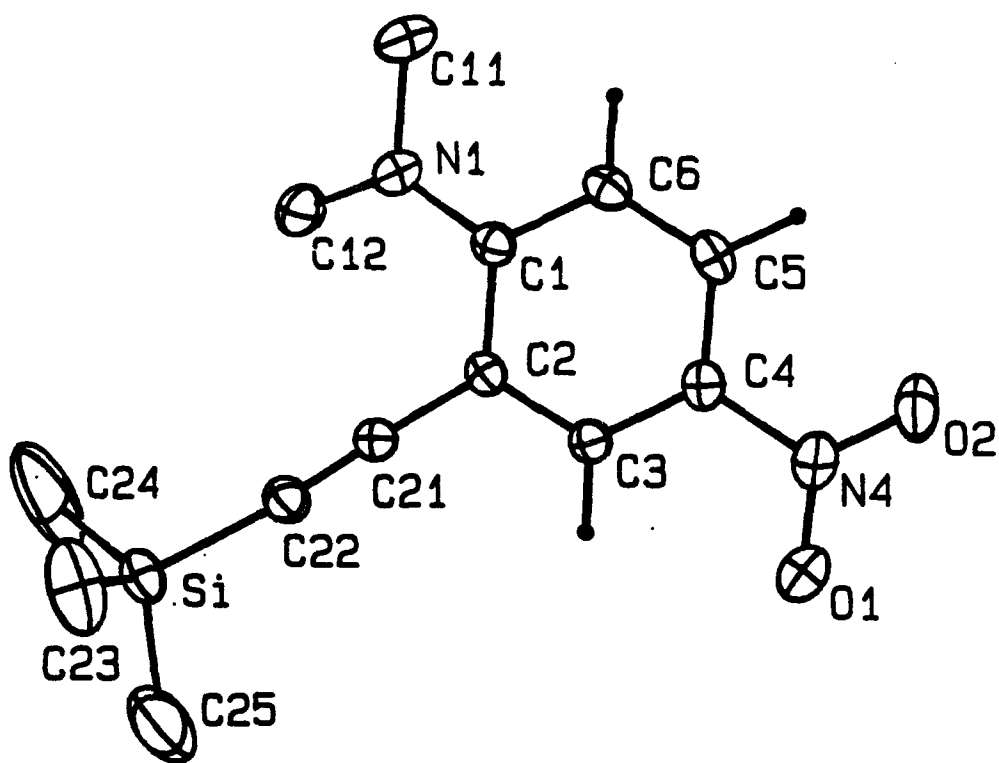


Figure 1. ORTEP drawing of the refined structure of $C_{13}H_{18}N_2O_2Si$. Methyl hydrogen atoms have been omitted for clarity.

1717s

1988 USAF-JES SUMMER FACULTY RESEARCH PROGRAM

GRADUATE STUDENT SUMMER SUPPORT PROGRAM

Sponsored by the

AIR FORCE OFFICE OF SCIENTIFIC RESEARCH

Conducted by the

Universal Energy Systems, Inc.

FINAL REPORT

EFFECT OF VARIOUS METALS ON THE THERMAL DEGRADATION OF

A CHLOROTRIFLUORETHYLENE BASED FLUID

Prepared by:	Vijay K. Gupta	and	Oden L. Warren
Academic Rank:	Professor of Chemistry		Graduate Student
Department and	Chemistry Department		Chemistry Department
University:	Central State University		Iowa State University
	Wilberforce, Ohio 45384		Ames, Iowa 50010
Research Location:	Materials Laboratory (AFWAL/MLBT)		
	Wright Patterson Air Force Base		
	Ohio 45433		
USAF Researcher:	Dr. Kent J. Eisentraut		
Date:	August 31, 1988		
Contract No.:	F49620-87-R-0004		

Effect of Various Metals on The Thermal Degradation of
A Chlorotrifluoroethylene Based Fluid

by

Vijay K. Gupta and Oden L. Warren

ABSTRACT

Thermal stability characteristics of a chlorotrifluoroethylene (CTFE) basestock candidate nonflammable hydraulic fluid, MLC 86-7, have been investigated as a function of time and temperature via micro-thermal stability tests in the presence of various metal powders and alloys. It has been found that this fluid is a complex mixture of chlorofluorocarbon compounds. The fluid was found to be thermally stable when stressed for 22 hours at 232°C or below, but when stressed at temperatures above 232°C, degradation was observed, and the extent of degradation increased with increasing stress temperature. The fluid degraded severely when stressed at 302°C for 66 hours. When the fluid was also stressed at 177°C for time periods ranging up to 40 days in the presence of alloys or metal powders, some degradation of the fluid was observed. At 177°C, the presence of Cu in the fluid caused more degradation as compared to other metals and alloys, and the degradation was further accelerated by the presence of water. At 302°C, the elements Cu, Fe, Sn, and Ti seem to have accelerated the degradation of the CTFE fluid whereas elements like Al, Co, Cr, Mn, Ni, W, and Zn do not seem to have any significant impact on the degradation of the CTFE fluid. The increase in acidity of the fluid caused by thermal degradation processes at temperatures much higher than 175°C (anticipated maximum use temperature) in the presence of metals and moisture produces corrosive products.

ACKNOWLEDGEMENTS

The authors would like to thank the Air Force Systems Command and Universal Energy Systems Inc. for providing an opportunity to work as Summer Research Participants at the Materials Laboratory, Wright-Patterson Air Force Base, Ohio 45433-6533. Thanks are also due to the personnel of the Nonstructural Materials Branch of the Materials Laboratory for their hospitality and excellent working conditions. The authors are thankful to Mr. Lee D. Smithson of the Materials Integrity Branch, and Dr. Jeff Workman and Dr. Chi Yu of Technical Services Inc. for providing gas chromatographic/mass spectrometric (GC/MS) analysis. The authors are also thankful to Mr. Rick Bacon and Dr. Albert Jackson of Systems Research Labs. Inc. of the Characterization Facility of AFWAL Materials Laboratory for providing surface analysis of the alloy samples. Thanks to all the members of University of Dayton Research Institute lubricants group for their technical assistance. The authors are thankful to Mr. Carl E. Snyder Jr. and Ms. Lois J. Gschwender for their helpful suggestions. Finally, the authors would like to thank Dr. Kent J. Eisentraut for suggesting this area of research and for his collaboration and helpful suggestions.

Effect of Various Metals on The Thermal Degradation of A Chlorotrifluoroethylene Based Fluid

INTRODUCTION

The hazards associated with the flammability of MIL-H-5606, an aerospace hydraulic fluid, are well known. MIL-H-5606 hydraulic fluid is a naphthenic mineral oil basestock product with a Cleveland Open Cup flash point of 93°C to 107°C. The hazard generated by the flammability of the fluid is greatly increased by the high pressure (2.07×10^7 pascals) required for hydraulic system operation and also by the vulnerability of the hydraulic lines widely distributed throughout the aircraft. As a result, a need was identified by the Air Force for a fire-resistant direct replacement for MIL-H-5606. A synthetic hydrocarbon-based fluid, MIL-H-83282, was developed and was found to be completely compatible with MIL-H-5606 hydraulic fluid systems and associated materials (1). All physical properties were equivalent or superior to those of MIL-H-5606 except low temperature viscosity: MIL-H-83282 had a kinematic viscosity of 3000 centistokes (cSt) at -46°C compared to an equivalent value for MIL-H-5606 at -54°C. All fire-resistance properties of MIL-H-83282 were superior to those of MIL-H-5606 with the exception of hot manifold ignition temperature which was found to be somewhat lower than that of MIL-H-5606. These two deficiencies resulted in an Air Force decision not to adopt MIL-H-83282 as a total fleet replacement fluid for MIL-H-5606 until 1980.

In 1975, the Air Force Materials Laboratory at Wright Patterson Air Force Base began a program to develop a -54°C to 175°C nonflammable hydraulic fluid without the constraints of compatibility with existing systems (2-6). In the initial stages of the program (4) many fluid classes such as: phosphate esters; alkyl aromatics and alpha-olefin-based synthetic hydrocarbons; silicones; chlorophenyl substituted silicones (Nadraul MS-5 and MS-6); cyclic ethers; alkyl amines; fluorinated phosphonates; fluoroalkylethers, chlorofluorocarbon polymers; perfluoropolyalkylethers; and perfluoroalkylether triazines, were considered as nonflammable candidates. Only those fluids were considered which were known as fire resistant or were identified from an industry survey to companies known to have experience in fire resistant fluids. The essential properties for a candidate fluid to be considered

seriously as a nonflammable candidate were: heat of combustion less than 5,000 BTU/lb.; auto ignition temperature greater than 1300°F; hot manifold ignition temperature, (both stream and spray in excess of 3000°F); and atomized spray open flame (no ignition). Of all the above fluid classes, four fluid chemical classes that had acceptable flammability and physical property characteristics were: chlorofluorocarbon (CTFE), fluoroalkylether (FAE), linear perfluoroalkylether, and perfluoroalkylether triazine. Later, CTFE was selected as the preferred approach. In an earlier work on CTFE (7), it was found that the metal surface of the bomb had some deleterious effect on the degradation of the fluid. Thus thermal stability characteristics of a commercially available chlorotrifluoroethylene oligomer (CTFE base stock fluid MLO 86-7) were investigated as a function of time and temperature and in the presence of various metal powders and alloys.

OBJECTIVES

The objectives of this program were to understand the thermal stability characteristics of the nonflammable CTFE basestock fluid (MLO 86-7) as a function of time and temperature and in the presence of various metal powders and alloys. The results from this program were expected to develop suitable experimental conditions for conducting accelerated thermal stability studies on CTFE based pure and well-defined model compounds.

RESULTS AND DISCUSSION

The composition of the fluid MLO 86-7 was determined by gas chromatography coupled with mass spectrometry (GC/MS) analysis, and the results are given in Table 1. Specific gas chromatographic (GC) conditions used are given in Table 2. The chromatogram of the fluid sample is given in Figure 1(A). From the data in Table 1, it appears that this fluid is a mixture of several components. The concentrations in Table 1 represent the amount of a specific component determined by GC analysis using area percentage of the peak as percent concentration. Other components present in small amounts which were not identified account for about 3% of the total. Four major components $C_6F_9Cl_5$, $C_7F_{11}Cl_5$, $C_7F_{10}Cl_6$, and $C_8F_{12}Cl_6$ and their corresponding isomers constitute about 94.5% of the fluid. CTFE fluid was stressed at 260°C for 22 hours in micro bombs using the procedure described

earlier (7), and the chromatogram is given in Figure 1(B). When the same fluid was stressed in a glass lined bomb, the chromatogram given in Figure 1(D) was obtained. From the two chromatograms, it appears that the contact of the metal surface of the bomb with the fluid accelerated fluid degradation resulting in a higher % degradation, lower viscosity, and higher acid number (see Table 5). A similar effect of accelerated fluid degradation due to the fluid and bomb metal surface contact was reported earlier (7), when the fluid was stressed at 288°C for 22 hours. Thus it was decided to conduct further thermal stability studies in glass lined bombs so that any potential interferences due to the metal surface of the bomb are eliminated. The results of these studies are given below:

A. Effect of Metals. The effect of the presence of various metal powders on the degradation of CTFE fluid was investigated. The various metal powders used for this study are described in Table 3. Thermal stability data of CTFE basestock fluid stressed at 302°C for 22 hours in the presence of metal powders is reported in Table 4. The % degradation values in Table 4 represent the total concentration of all new components formed during the degradation process. The viscosities were determined at 37.8°C and acid numbers were determined using the ASTM D664 method. A sample chromatogram of the fluid stressed under the above conditions in the presence of elemental Cu is given in Figure 2(B). The data from Table 4 has been plotted in Figure 3 in the form of a bar graph. In Figure 3, the bar for CTFE indicates unstressed fluid and the bar for the blank indicates fluid stressed without metal added to the fluid. Based on % degradation data in Figure 3, it appears that the presence of the elements Cu, Fe, and Sn caused greater degradation of the fluid as compared to the blank. The presence of the elements Cr, Ti, and Zn caused no additional degradation over the blank, and the presence of the elements Al, Co, Mn, Ni, and W appeared to lower the level of degradation as compared to the blank. The viscosity values did not show any significant differences. From the acid number data, it appears that the presence of the elements Cu, Fe, Mn, Sn, Ti, and Zn resulted in higher acid numbers as compared to the blank. It is to be noted that the presence of the element Mo in the fluid could not be investigated as the glass liner in the bomb was broken into pieces, the fluid turned black and pungent vapors were noticed on opening the bombs when the CTFE fluid was stressed at 302°C for 22 hours.

Thermal stability data for CTFE fluid stressed for 22 hours in the presence of the elements Cu, Fe, and Zn as a function of temperature is given in Table 5 and plotted in Figures 5, 6 and 7. From the data in Table 5, it appears that increasing the stress temperature causes increased degradation of the fluid. From Table 5 and Figures 4 to 6, it appears that at a lower temperature, 232°C, the degradation of the CTFE fluid in the presence of elemental Cu results in a higher acid number of the fluid than when the fluid was degraded in the presence of the elements Fe and Zn. At a stress temperature of 302°C, the fluid when degraded in the presence of elemental Fe resulted in higher % degradation, lower viscosity, and higher acid number than when the fluid was degraded in the presence of elemental Cu and Zn.

Thermal stability data for CTFE fluid stressed at 302°C in the presence of the elements Cu, Fe, and Zn as a function of time is given in Table 6 and % degradation data is plotted in Figure 7. A sample chromatogram of the fluid stressed at 302°C for 48 hours in the presence of elemental Cu is given in Figure 2(D). From the data in Table 5 it appears that the fluid experienced severe degradation when stressed at 302°C for 66 hours especially in the presence of metals. From the graph in Figure 7, it appears that the presence of the elements Fe and Cu caused increased levels of degradation as compared to the blank. The stressed samples after filtering through 0.2 micron Millipore filters were examined for any soluble metals via inductively coupled plasma (ICP) atomic emission spectroscopy, and the analysis did not indicate the presence of any metals in the degraded fluid. The change in the appearance of the metal powders and the formation of fine suspended particles in the fluid did indicate reaction between the fluid and the metals. Hence any metal compounds formed with the fluid were either formed on the surface of the metal or were insoluble in CTFE and were removed by filtration.

The experiments to investigate the effect of metals on thermal decomposition of CTFE fluid at 177°C were carried out in sealed Pyrex glass tubes. Thermal stability data for CTFE fluid stressed at 177°C in the presence of various metal powders for 12 days is given in Table 7. A sample chromatogram of the stressed fluid containing elemental Cu is given in Figure 2(A). From the data, it appears that the presence of element Cu in the fluid causes a higher % degradation of the fluid than the blank, and the presence of the elements Cu, Fe and Sn in the fluid increased the acid number of the fluid

more than the blank. The presence of other elements in the fluid such as Al, Co, Cr, Mn, Mo, Ni, Ti, W, and Zn, had no observable effect on the degradation of CTFE fluid when stressed under the above conditions. The stressed sample for Cu after filtering through a 0.5 micron Millipore filter was examined for its metal content by ICP analysis, and no Cu was detected. However, when 0.5% water by volume was added to the CTFE fluid, the presence of Cu caused twice the % degradation in three days as compared to a similar experiment for 12 days containing Cu but no water. A sample chromatogram of the stressed fluid containing both Cu and water is given in Figure 2(C). The stressed sample containing Cu and water after filtering through a 0.5 micron Millipore filter was also examined for its metal content by ICP analysis and 87 ppm of Cu as found. It appears that the presence of water helped to form copper compounds that were more soluble in CTFE fluid. The CTFE stressed samples containing copper with or without water when filtered through a 0.5 micron filter experienced a lowering of acid number indicating that some acidic compounds were insoluble in CTFE and were retained on the filter.

B. Effect of Alloys. The alloys: 304 stainless steel, 440C stainless steel, M-50 steel, 52100 steel, and 674 bronze were investigated for their impact on thermal decomposition of CTFE fluid at 176.7°C as a function of time. The alloys were polished with sandpaper (500SIC) and then soaked in the solvent naphtha to remove any dust from the sandpaper and dried with Kimwipes. These alloys were in the form of washers having 18.75 mm. outside diameter and 6.25 mm. inside diameter which yielded approximately 5 cm² surface area. Five alloy samples were placed in 5 ml. of CTFE fluid in Pyrex glass tubes and the tubes were sealed. The samples were placed in an oven maintained at 177°C and were withdrawn at time intervals of 11, 20, 31, and 40 days. The stressed samples of the fluid, when examined via GC analysis, viscosity measurements, and acid number measurements did not show any change in values when compared with unstressed CTFE fluid. However, visual examination of the samples indicated formation of fine suspended particles in the fluid and changes in the appearance of the surface of the alloy washers. ICP analysis of 40 days stressed samples of the fluid containing the above alloys provided the following results:

Sample	Elemental Analysis
304-40D	0

440C-40D	1 ppm Fe
M-50-40D	3 ppm Fe
52100-40D	2 ppm Fe
674-40D	7 ppm Cu and 4 ppm Zn
674-40D*	0

* The sample was filtered through 0.5 micron Millipore filter.

The stressed samples of the fluid containing alloys removed after 20 days were also examined for their metal content by ICP analysis, but no metals were detected. From the above analyses, it appears that the degradation of the fluid at 177°C is a very slow process and the degradation products combined with the metal surface of the alloys. Scanning electron microscope pictures were taken for the clean samples of the five alloys and labelled as control while the five alloy samples exposed to CTFE fluid at 177°C for 40 days were labelled as 40 D are given in Figure 8 and 9. It appears that bronze 674-40D surface had the most deposition, and M-50-40D and 52100-40D have lesser deposition than 674-40D, and 440C-40D and 304-40D have very little or no deposition as the surface was shiny even after 40 days exposure to CTFE fluid at 177°C. In order to determine the nature of deposits on the surface of the alloys, Energy Dispersive X-Ray (EDX) Spectroscopy was performed, and the data is given in Table 8. From the data in Table 8, it appears that the metal surfaces of the above alloys have reacted to form compounds with chlorine and fluorine from the CTFE fluid, and some of those compounds have adhered to the alloy surface. It should be understood that elements with atomic number less than 12 cannot be detected. Therefore, the fluorine analysis was obtained by Wavelength Dispersive Spectroscopy (WDS). The elemental analysis by EDS is very sensitive to the spot on the surface of the alloy, different spots provided significant variation in the analysis (see the data for bronze 674-40D). It is observed that the fluorine concentrations on the surface of the alloys are generally lower as compared to chlorine concentrations. The accurate determination by WDS analysis requires that the surface be very smooth, so the rough surface of the alloys may have resulted in lower values for fluorine.

Using gas chromatography coupled with mass spectrometry, the degradation components present in the gas and liquid phase of CTFE fluid MLO 86-7 stressed at 288°C for 22 hours were identified and the data is reported in Table 9.

Carbon dioxide and low molecular weight chlorofluorocarbon compounds were found as the degradation products along with the chlorofluorocarbon compounds originally present in the basestock fluid.

CONCLUSIONS.

Based upon the results presented in the previous section, the following conclusions are derived.

1. The CTFE basestock fluid MLO 86-7 is a complex mixture of chlorofluorocarbon compounds.
2. The experimental fluid was found thermally stable when stressed at 232°C or below for 22 hours, and the extent of degradation increased as the stress temperature was raised above 232°C, the degradation was severe when the fluid was stressed at 302°C for 66 hours specially in the presence of some metals.
3. The active metal surface of the bomb was found to have an effect on the degradation of the fluid indicated by the increased degradation of the fluid in the presence of metals and alloys at temperatures much higher than 175°C (anticipated maximum use temperature).
4. When the fluid was stressed at 177°C for time periods up to 40 days, in case of metal powders, some degradation was observed as indicated by an increase in the acid number and % degradation, and in case of alloys, the degradation was indicated by the elemental analysis of the fluid and surface analysis.
5. The elements Cu, Fe, Mo, Sn, and Ti need special attention as these elements caused severe degradation of the CTFE fluid at 302°C for 22 hours.
6. The presence of water can accelerate the degradation of the CTFE fluid.
7. The increase in acidity of the fluid during thermal degradation may result in the formation of undesirable corrosive products.

RECOMMENDATIONS

In order to gain a good understanding of the structure-property relationships in CTFE basestock fluids, the experiments should be performed on pure well defined chlorofluorocarbon model compounds. The catalytic effect of the active metal surface on thermal degradation of chlorofluorocarbon compounds needs further investigation. Pure metal coupons should be used instead of metal powders as the metal coupons can easily be investigated for fluid reaction on the metal surface. The techniques such as ion chromatography, differential scanning calorimetry and thermogravimetric analysis along with thermal stability studies may also be helpful.

REFERENCES

1. Snyder, C.E. Jr., Krawetz, A.A., and Tovrog, T., "Determination of the Flammability Characteristics of Aerospace Hydraulic Fluids", Lubr. Eng., 37, 705-714, 1981.
2. Snyder, C.E. Jr., and Gschwender, L.J., "Development of Nonflammable Hydraulic Fluid for Aerospace Applications Over a -54°C to 135°C Temperature Range", Lubr. Eng., 36, 458-465, 1980.
3. Snyder, C.E. Jr., Gschwender, L.J., and Campbell, W.B., "Development and Mechanical Evaluation of Nonflammable Aerospace -54°C to 135°C Hydraulic Fluids", Lubr. Eng., 38, 41-51, 1982.
4. Snyder, C.E. Jr., Gandee, G.W., Gschwender, L.J., Graham, T.L. Jr., Berner, W.E., and Campbell, W.B., "Nonflammable Aircraft Hydraulic Fluid Systems Development", SAE Technical Paper Series #821566, 1982.
5. Snyder, C.E. Jr., and Gschwender, L.J., "Nonflammable Hydraulic Fluid Systems Development for Aerospace", J. Syn. Lubr., 188-200, 1984.
6. Snyder, C.E. Jr., and Gschwender, L.J., "Fluoropolymers in Fluid and Lubricant Applications", Ind. Eng. Chem. Prod. Res. Dev., 22, 383-386, 1983.
7. Gupta, V.K., and Prazak, M., "Thermal Stability Characteristics of a Non-flammable Chlorotrifluoroethylene CTFE Base Stock Fluid", USAF-UES Summer Faculty Research Program/Graduate Student Support Program 1988, Technical Reports, Contract No. F49620-85-C-0013, Vol.2, 61-1 to 61-22, 1988.

Table 1. Composition of MLO 86-7 (CTFE Basestock Fluid) Determined by GC/MS Analysis.

Component	Concentration (%)	Retention Time (min.)
$C_5F_7Cl_5$	0.363	2.45
$C_6F_9Cl_5$	39.068	3.00-3.35
$C_7F_{11}Cl_5$	13.489	3.95-4.10
$C_8F_{12}Cl_4$	1.064	4.80-5.00
$C_7F_{10}Cl_6$	11.102	6.80-7.00
$C_8F_{12}Cl_6$	31.065	7.60-8.00
Unidentified	0.932	8.45-8.65
Total* =	97.083	

* There were other components present in small amounts which were not identified.

Table 2. Gas Chromatographic Conditions.

Model: Hewlett-Packard 5710A
 Detector: FID
 Column: Fused Silica Capillary Column
 Length: 12 meters
 Diameter: 0.22 mm
 Liquid Phase: Methyl Silicone Carbowax Deactivated
 Carrier Gas: 1 ml/min He
 Auxiliary Gas: 40 ml/min He
 Chart Speed: 10 cm/hr.
 Attenuation: 10 x 32
 Temperatures:
 Injector: 300°C
 Detector: 350°C
 Column: 70°C to 270°C
 Program Rate: 8°C/min
 Initial Hold: 2 min
 Final Hold: 32 min
 Sample Size: 1 Microliter

Table 3. Various Metal Powders Used in Experimental Studies.

Element	Particle Size	Supplier
Aluminum	40-325 mesh	Alpha Inorganics Ventron
Cobalt	50 mesh	Alpha Inorganics Ventron
Chromium	100 mesh	Matheson Coleman & Bell
Copper	10-15 micron	Research Organic/Inorganic Chemicals
Iron	10-15 micron	Research Organic/Inorganic Chemicals
Manganese	60 mesh	Alpha Inorganics Ventron
Molybdenum	200 mesh	Research Organic/Inorganic Chemicals
Nickel	100 mesh	Alpha Inorganics Ventron
Tin	325 mesh	Research Organic/Inorganic Chemicals
Titanium	100 mesh	Alpha Inorganics Ventron
Tungsten	100 mesh	Alpha Inorganics Ventron
Zinc	20 mesh	Malinkrodt Chemical Works

Table 4. Thermal Stability Characteristics of CTFE Basestock Fluid Stressed at 302°C for 22 Hours in Presence of Metal Powders.

Element	% Degradation	Viscosity (cSt)	Acid # mg.KOH/g.
CTFE Unstressed	0.00	2.95	0.05
CTFE Stressed	8.74	2.40	0.32
Al	6.94	2.49	0.32
Co	7.34	2.47	0.39
Cr	8.65	2.42	0.30
Cu	10.01	2.37	0.84
Fe	10.29	2.32	0.96
Mn	4.29	2.48	0.55
Mo*			
Ni	7.69	2.47	0.35
Sn	10.20	2.47	1.06
Ti	8.65	2.42	1.10
W	6.52	2.47	0.42
Zn	8.79	2.40	0.64

* Fluid was severely degraded as indicated by the broken small pieces of glass in the bomb, black color of the fluid, and pungent smell of vapors.

Table 5. Thermal Stability Characteristics of CTFE Basestock Fluid Stressed for 22 Hours in Presence of Metal Powders at Different Temperatures.

Element	% Degradation	Viscosity (cSt)	Acid # mg.KOH/g.
CTFE Unstressed	0.00	2.95	0.051
Stress Temperature 232° C			
Cu	0.12	2.96	0.22
Fe	0.12	2.94	0.17
Zn	0.05	2.94	0.04
Stress Temperature 260° C			
CTFE Blank	0.21	2.92	0.21
CTFE(in bomb)	0.49	2.83	0.47
Cu	0.75	2.92	0.12
Fe	0.67	2.89	0.12
Zn	0.69	2.90	0.05
Stress Temperature 288° C			
CTFE Blank	2.41	2.79	0.44
Cu	4.38	2.66	0.71
Fe	5.46	2.66	0.69
Zn	3.64	2.66	0.51
Stress Temperature 302° C			
CTFE Blank	8.71	2.40	0.32
Cu	10.01	2.37	0.84
Fe	10.29	2.32	0.96
Zn	8.79	2.40	0.64

Table 6. Thermal Stability Characteristics of CTFE Basestock Fluid Stressed at 302°C in Presence of Metal Powders as a Function of Time.

Element	22			Time (Hours)			66
	% Degradation	Viscosity (cSt)	Acid # mg.KOH/g.	% Degradation	Viscosity (cSt)	Acid # mg.KOH/g.	
CTFE Blank	9.74	2.40	0.32	7.35	2.37	0.50	14.68
Cu	10.01	2.37	0.84	17.88	2.33	1.82	19.41
Fe	10.29	2.32	0.96	13.09	2.23	1.73	38.52
Zn	8.79	2.40	0.64	9.80	2.36	0.75	ND

ND Element Zn was not investigated for 66 hours time.

Table 7. Thermal Stability Characteristics of CTFE Basestock Fluid Stressed at 177°C for 12 Days in Presence of Metal Powders.

Element	% Degradation	Viscosity (cSt)	Acid # mg.KOH/g.
CTFE Unstressed	0.00	2.95	0.05
CTFE Stressed	0.00	2.94	0.02
CTFE Stressed#	0.00	2.94	0.02
Al	0.00	2.95	0.05
Co	0.00	2.95	0.05
Cr	0.00	2.95	0.05
Cu**	0.82	3.21	2.60(1.98*)
Cu#^	1.53	2.94	1.37(0.69*)
Fe	0.00	2.95	0.083
Fe#^	0.04	2.95	0.24
Mn	0.00	2.95	0.05
Mo	0.06	2.95	0.05
Ni	0.00	2.95	0.05
Sn	0.06	2.95	0.39
Ti	0.00	2.95	0.04
W	0.00	2.95	0.05
Zn	0.00	2.96	0.02
Zn#	0.00	2.95	0.01

* After the sample was filtered through 0.2 micron filter paper.

** Sample was of yellow color.

These samples were stressed in CTFE fluid containing 0.5% water by volume for 3 days.

^ The color of the Fe sample was light brown and Cu sample was blue.

Table 8. Surface Analysis of Some Alloys Exposed to CTFE Basestock Fluid at 177°C for 40 Days.

Alloy	% Concentration of the Element												
	Al	Cl	Cr	Cu	F ⁺	Fe	Mn	Ni	Pb	S	Si	V	Zn
304 Control*	0.37	-	19.20	-	-	71.43	-	8.35	-	-	0.64	-	-
304 ppt**	0.61	9.10	16.27	-	0.38	65.94	-	7.02	-	0.69	0.37	-	-
440C Control	0.23	-	23.63	-	-	75.43	-	-	-	0.26	0.44	-	-
440C ppt.	0.85	2.30	3.81	-	0.38	92.71	-	-	-	0.04	0.28	-	-
M-50 Control	0.30	-	4.01	-	-	91.33	-	-	-	1.84	1.63	0.90	-
M-50 ppt.	1.30	4.5	0.53	-	0.50	93.48	-	-	-	-	0.19	-	-
52100 Control	1.54	-	1.48	-	-	95.12	-	-	-	0.19	1.67	-	-
52100 ppt.	3.51	7.07	0.07	-	0.69	89.17	-	-	-	-	0.18	-	-
674 Control	1.75	-	-	57.17	-	-	3.22	-	-	-	1.50	-	36.35
674 ppt.	0.52	13.16	-	49.90	1.61	-	2.12	-	12.19	-	0.63	-	21.48
674 Overall	0.70	3.94	-	42.13	1.61	-	3.51	-	3.19	-	1.79	-	44.74
674 ppt. glob#	1.21	11.67	-	10.57	1.61	-	6.71	-	1.25	-	0.75	-	67.85

^a Fluorine analysis was obtained by wavelength Dispersive Spectroscopy.

* Control means alloy samples polished with sandpaper but not treated with CTFE.

** ppt. means white precipitate region of the alloy sample exposed to CTFE.

means wh. the globular precipitate region of the sample.

Table 9. GC/MS Analysis of MLO 86-7 (CTFE Basestock Fluid) Stressed at 288°C for 22 Hours.

Component	Concentration (%)		Retention Time (min.)
	Unstressed	Stressed	
CO ₂		g	
CFC1 ₃		g	
C ₂ F ₃ Cl		g	
C ₂ F ₃ Cl ₃		g	
C ₃ F ₅ Cl		g	
C ₂ F ₃ Cl ₃		1.316	0.48-0.50
C ₄ F ₆ Cl ₂			
C ₃ F ₄ Cl ₄			
C ₄ F ₆ Cl ₂		0.986	0.60-0.70
C ₇ F ₁₀ Cl ₂			
C ₄ F ₆ Cl ₄		1.074	0.80
C ₅ F ₇ Cl ₅	0.363	0.676	2.45
C ₆ F ₉ Cl ₅	39.068	37.593	3.00-3.45
C ₇ F ₁₁ Cl ₅	13.489	13.511	3.95-4.10
C ₈ F ₁₂ Cl ₄	1.058	1.064	4.80-5.00
C ₇ F ₁₀ Cl ₆	11.102	9.918	6.80-7.00
C ₈ F ₁₂ Cl ₆	31.065	29.086	7.60-8.00
Unidentified	0.932	0.922	8.45-8.65

g Found in the gas phase of the stressed fluid.

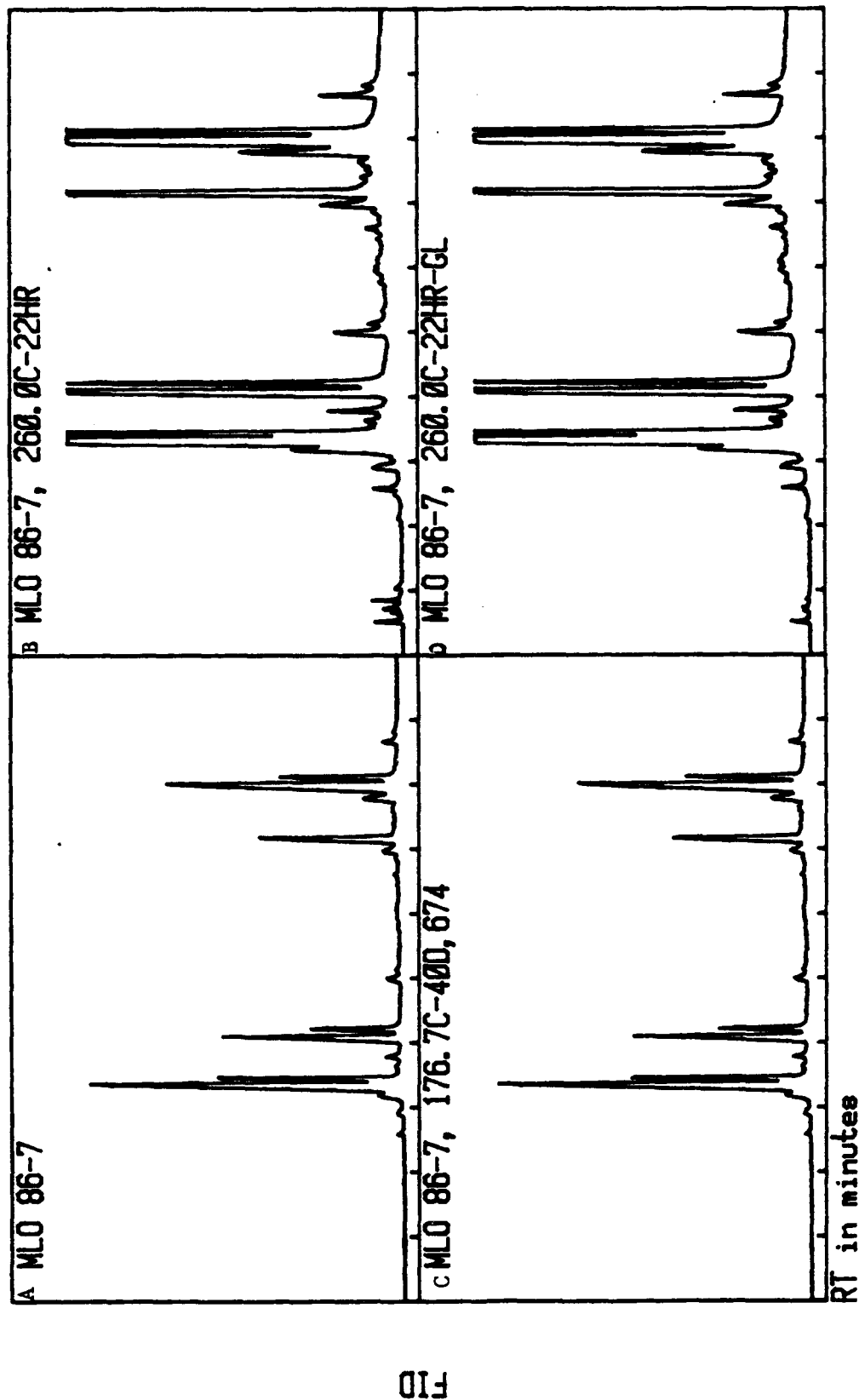


Fig. 1. SAMPLE CHROMATOGRAMS FOR FLUID MLO 86-7

- A. CTFE Unstressed
- B. CTFE Stressed at 260°C for 22 Hours in a Micro-Bomb
- C. CTFE Stressed at 177°C for 40 Days in the Presence of Bronze 674.
- D. CTFE Stressed at 260°C for 22 Hours in a Glass-lined Bomb.

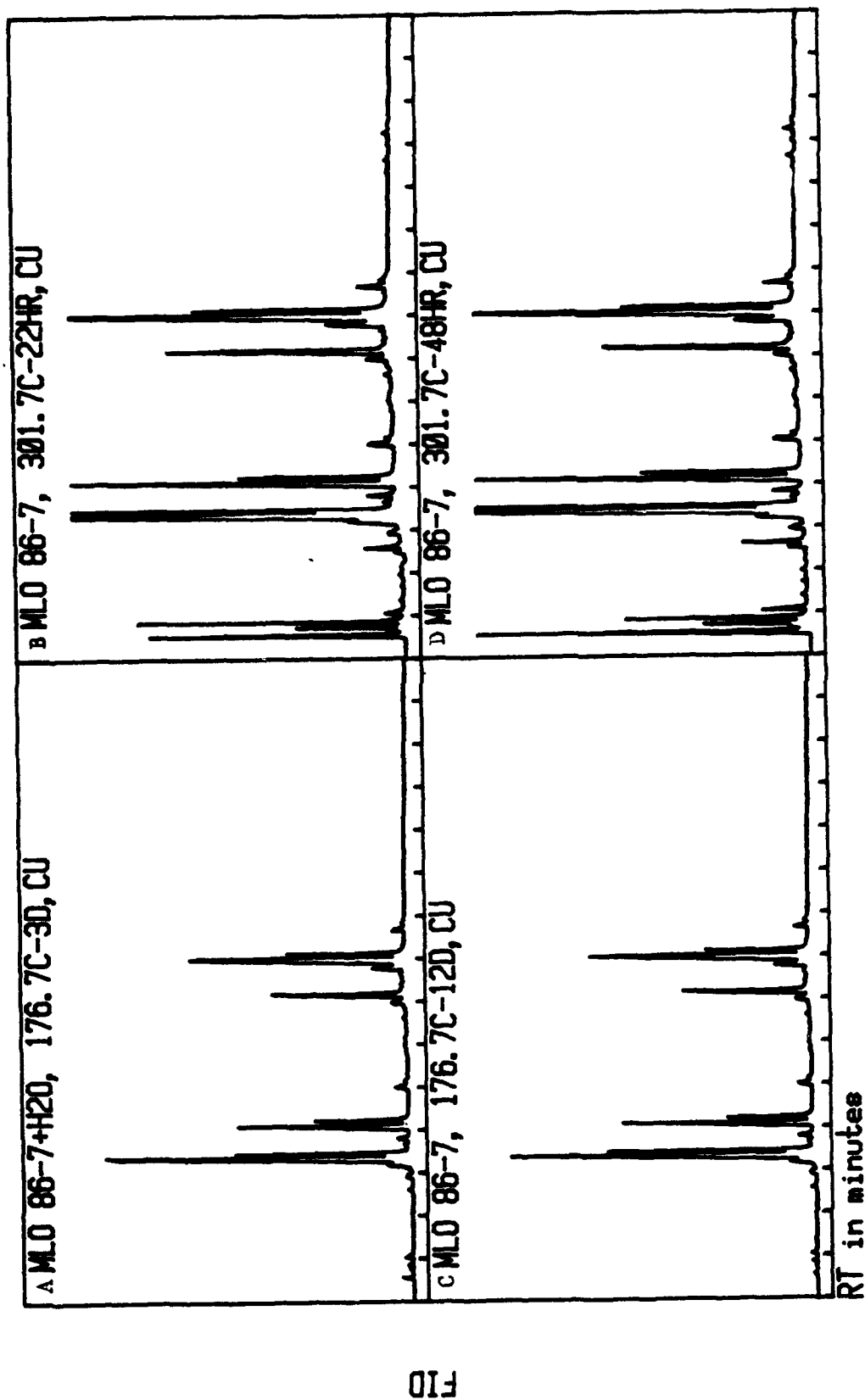


Fig. 2. SAMPLE CHROMATOGRAMS FOR FLUID MLO 86-7

- A. CTFE containing 0.5% H₂O stressed at 177°C for 3 days in the presence of Cu.
- B. CTFE stressed at 302°C for 22 Hours in the presence of Cu.
- C. CTFE stressed at 177°C for 12 days in the presence of Cu.
- D. CTFE stressed at 302°C for 48 hours in the presence of Cu.

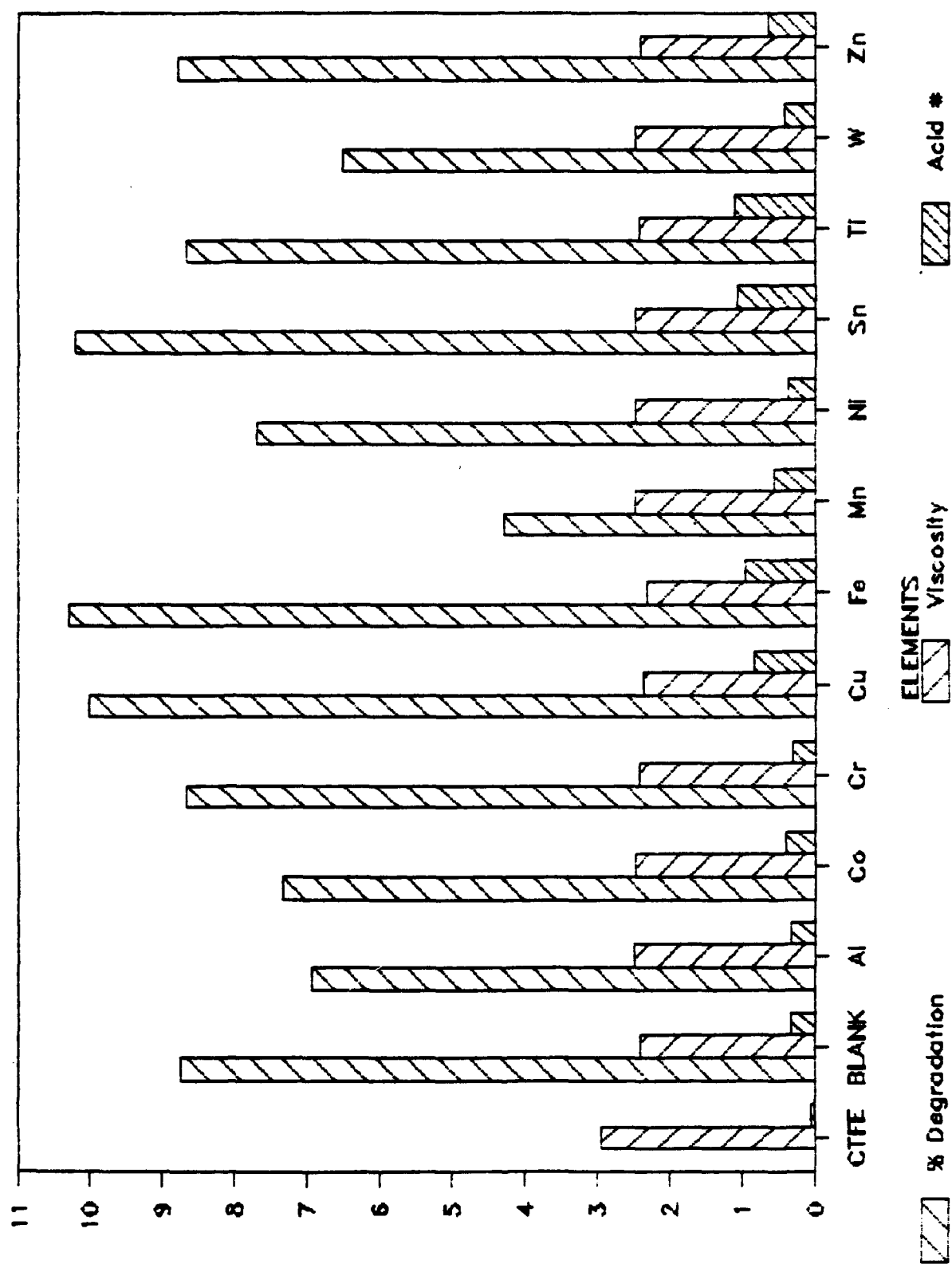


Fig. 3. Thermal degradation data of CTFE stressed at 302°C for 22 hours in presence of metal powders.

THERMAL STABILITY DATA

O BLANK
 Δ Cu
 + Fe
 X Zn

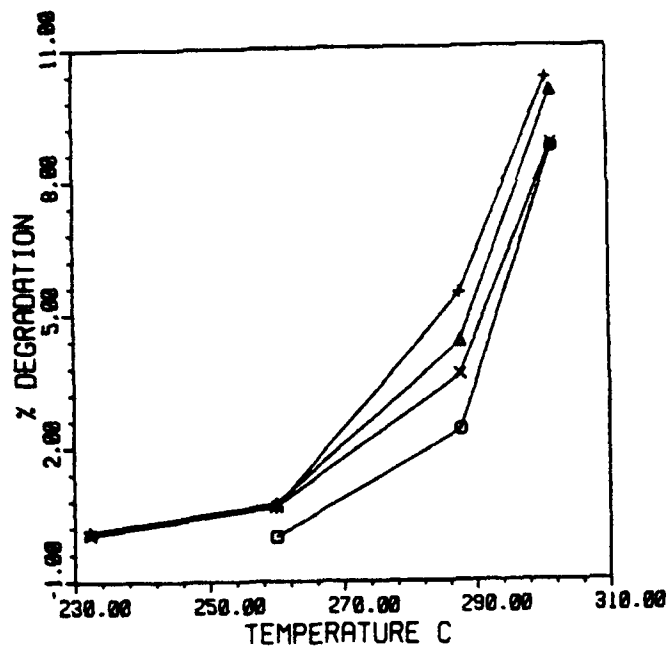


Fig. 4. % Degradation Data for CTFE as a Function of Temperature.

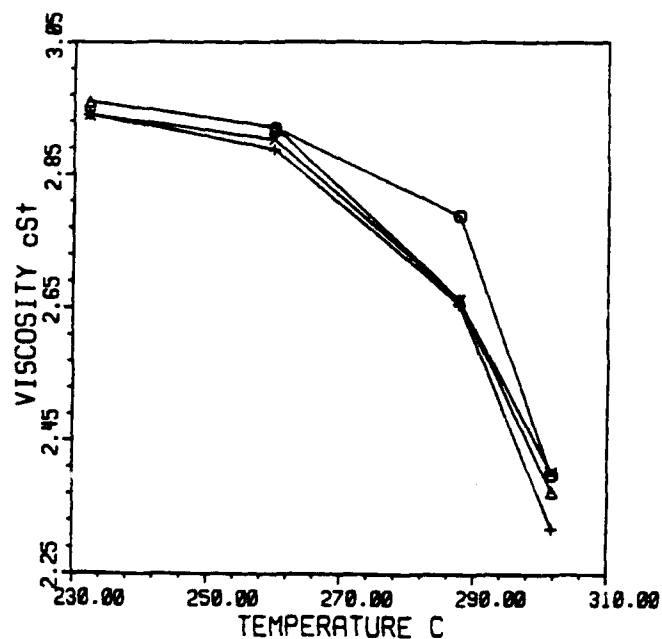


Fig. 5. Viscosities of CTFE as a Function of Temperature.

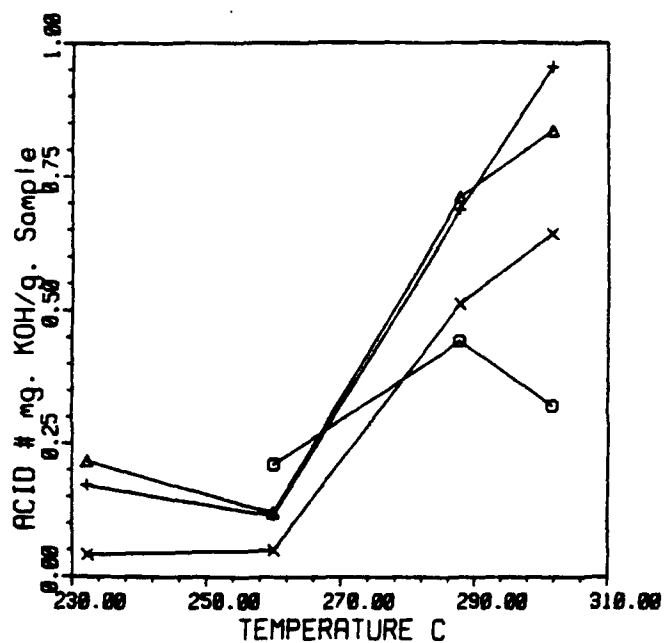


Fig. 6. Acid # Data for CTFE as a Function of Temperature.

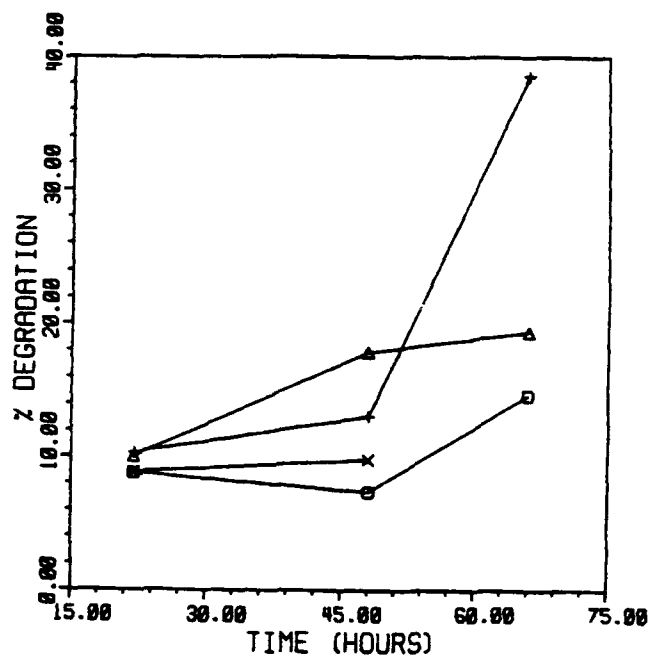
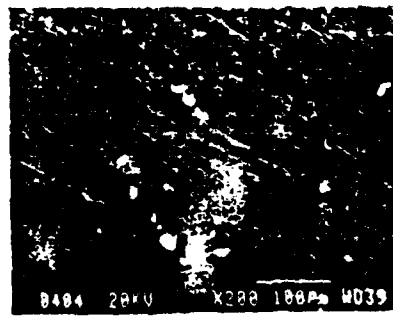


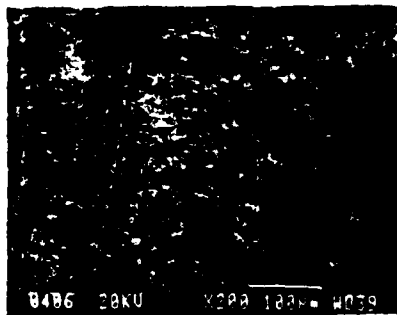
Fig. 7. % Degradation Data for CTFE Stressed at 302°C as a Function of Time.



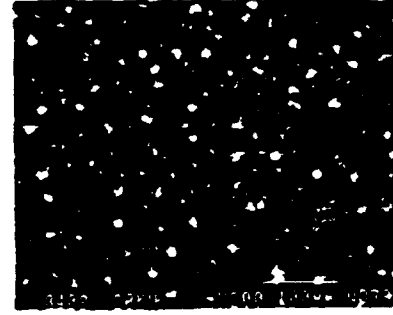
304 CONTROL



304-40D



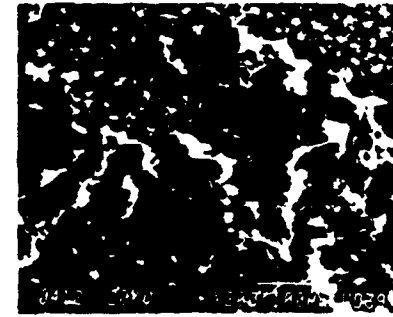
440C CONTROL



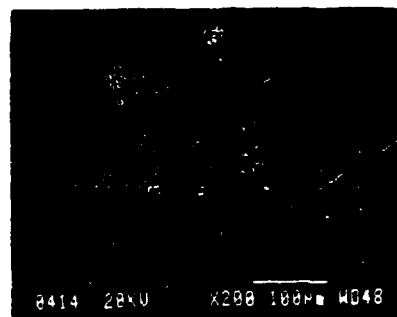
440C-40D



M-30 CONTROL



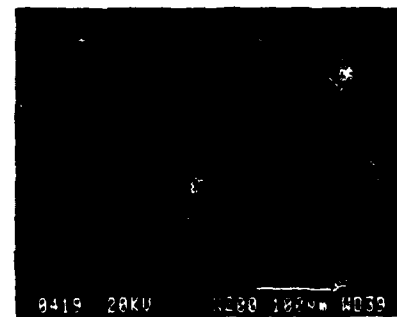
M-30-40D



52100 CONTROL



52100-40D

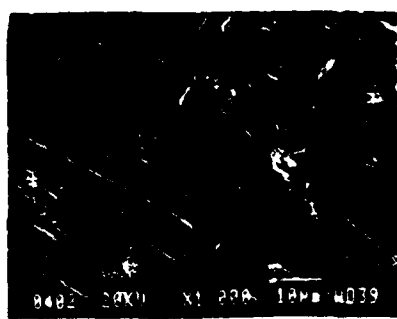


674 CONTROL

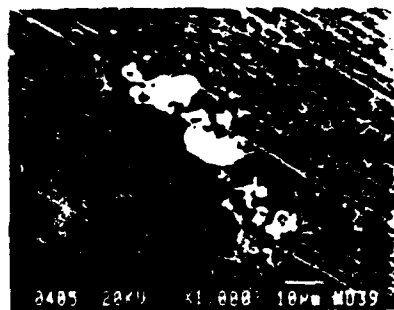


674-40D

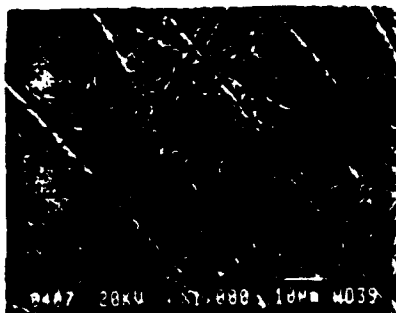
Fig. 8. Surface Analysis of Alloy Samples Stressed at 177°C for 40 Days in CTFE (200 X)



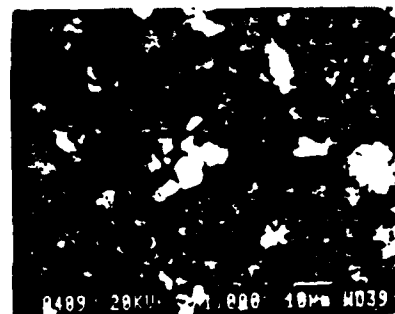
304 CONTROL



304-40D



440C CONTROL



440C-40D



M-50 CONTROL



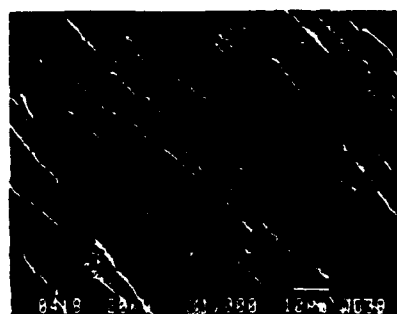
M-50-40D



52100 CONTROL



52100-40D



674 CONTROL



674-40D

Fig. 9. Surface Analysis of Alloy Samples Stressed at 177°C for 40 Days in CTFE (1000 X).

**1988 USAF-UES SUMMER FACULTY RESEARCH PROGRAM/
GRADUATE STUDENT RESEARCH PROGRAM**

**Sponsored by the
AIR FORCE OFFICE OF SCIENTIFIC RESEARCH
conducted by the
UNIVERSAL ENERGY SYSTEMS, INC.**

FINAL REPORT

Prepared by:	L. James Lee, Ph.D.
Academic Rank:	Associate Professor
Department and	Chemical Engineering
University:	The Ohio State University
Research Location:	AFWAL/MLBC
	Wright-Patterson AFB
	Dayton, OH 45433-6533
USAF Researcher:	Frances L. Abrams
Date:	September 7, 1988
Contract No.	F49620-87-R-0004

Characterization of Heat Transfer and Reaction in the
Autoclave Curing of Graphite/Epoxy Composites by Scaling Analysis

by

L. James Lee

ABSTRACT

The temperature distribution and the degree of cure of the resin in the autoclave curing of graphite/epoxy composites are governed by heat transfer through bagging materials and laminates, and the exothermic reaction of epoxy resins. Determination of the major heat transfer and reaction characteristics was carried out by a scaling analysis. Heat transfer can be described by a time constant for overall thermal response. Its value can be determined by on-line temperature measurements. Exothermic reaction is best described by a lumped parameter, Damkohler number (Da), which is a function of reaction activation energy (E) and heat of reaction (ΔH). The value and/or the change of Da can be used to establish rules for the control of autoclave heating/cooling in order to prevent any thermal run-away problem. The change of Da at any given spot in the laminate can be estimated by three temperature sensors or two heat flux sensors located near that spot.

Acknowledgements

I wish to acknowledge the Air Force Systems Command and the Air Force Office of Scientific Research for sponsorship of this research. Further acknowledgements go to Universal Energy Systems for their administrative assistance and for providing the opportunity for me to participate in this program.

My experience at the Materials Laboratory was rewarding. Dr. Bill Lee provided me with a great deal of assistance. The help of Frances Abrams was greatly appreciated. Many stimulating discussions with Bill, Frances and Dr. Charles Lee were invaluable in understanding the QPA system and autoclave curing. I also wish to thank Dr. Charles Lee for his arrangement and interest in this project.

I. INTRODUCTION

Graphite/epoxy composite materials are often cured by the autoclave process where resin impregnated fiber laminates are stacked and covered by various bagging materials. The entire assembly is placed in the autoclave and the laminates are cured by applying heat and pressure. The pressure-temperature vs. time cycles are generally established by modification of cycles which have been successfully used for similar parts and materials based on trial and error (1). This means of developing process cycles has been improved somewhat by the incorporation of analytical models which serve to simulate the autoclave process (2). Use of analytical models as simulators, however, has the limitations that it cannot handle the unexpected variations of resin properties and autoclave responses when the simulator developed from one case is to be applied for other cases.

Most recently, several researchers in the Materials Laboratory at Wright-Patterson Air Force Base have developed an expert system based automation method, Qualitative Process Automation (QPA), capable of monitoring and controlling the autoclave curing process (3). The system contains a knowledge base consisting of rules which have been established through experimentation and analysis of the curing process. These rules use several on-line sensors (i.e., thermocouples and micro-dielectric sensor) to monitor the progress of the curing. Commands are then sent to the autoclave controller to maintain a desirable cure by varying the autoclave temperature. This system has been successfully applied for the autoclave cure of thin and thick laminates. In order to further extend the application of QPA to the cure of laminates composed of a diverse range of thicknesses, shapes and prepreg materials, and other manufacturing processes for advanced polymeric

composites, it is necessary to refine and improve the current knowledge base to make the system more rigorous.

II. OBJECTIVES

Since the autoclave curing is governed by heat transfer between the autoclave and the composite assembly (i.e., bagging materials and laminates), and the exothermic reaction of polymeric resins, this work seeks to determine the major heat transfer and reaction characteristics by a scaling analysis. The goal is to develop rules which can better control the accelerated reaction and thermal runaway in autoclave curing. Both on-line sensor measurements and simple off-line measurements are considered in the analysis.

III. SCALING ANALYSIS OF ACCELERATED REACTION AND THERMAL RUNAWAY

In autoclave curing, thermal runaway is most easily identified by monitoring the temperature at the middle laminate during cure. Depending upon process conditions such as autoclave temperature, laminate thickness, the competing effects of heat removal by conduction and heat generation by reaction may or may not result in thermal runaway. The thermal and kinetic properties of the laminate material and the heat transfer characteristics of the bagging materials are key factors in the achievement of thermal runaway as well.

The relative contributions of heat conduction and generation can be expressed in a dimensionless quantity known as the Damkohler number (Da). This number can be derived from the one-dimensional heat transfer equation

describing the system, assumed to be essentially infinite in the other two dimensions:

$$\rho C_p \frac{\partial T}{\partial t} = k \frac{\partial^2 T}{\partial x^2} + \Delta H R \quad (1)$$

(heat (heat
conduction) generation)

where ρ is density, C_p heat capacity, k thermal conductivity, ΔH heat of reaction and R reaction rate (i.e., $\frac{d\alpha}{dt}$, α is conversion).

Defining dimensionless variables $\bar{T} = T/T_{ref}$, $\bar{x} = x/L$ and $\bar{R} = R/R_{ref}$ where ref represents a location of interest (e.g. middle laminate), then Equation (1) becomes

$$\frac{\partial \bar{T}}{\partial t} = \left(\frac{k}{\rho C_p L^2} \right) \frac{\partial^2 \bar{T}}{\partial \bar{x}^2} + \left(\frac{\Delta H R_{ref}}{\rho C_p T_{ref}} \right) \bar{R} \quad (2)$$

where $\frac{\rho C_p L^2}{k} = \frac{L^2}{\nu} = \lambda_C$ characteristic time for heat conduction

$\frac{\rho C_p T_{ref}}{\Delta H R_{ref}} = \lambda_G$ characteristic time for heat generation

and L is the characteristic thickness of the laminate, ν thermal diffusivity.

If we define a dimensionless time $\bar{t} = t/\lambda_C$, then Equation (2) becomes

$$\frac{\partial \bar{T}}{\partial \bar{t}} = \frac{\partial^2 \bar{T}}{\partial \bar{x}^2} + Da \bar{R} \quad (3)$$

where $Da = \lambda_C / \lambda_G = \frac{\Delta H L^2 R_{ref}}{k T_{ref}} = \frac{\text{heat generation rate}}{\text{heat conduction rate}} \quad (4)$

The Damkohler number Da is the ratio of the heat generation rate to the heat conduction rate. For a fixed system, i.e. ΔH , L and k unchanged, Da reflects the reaction rate and laminate temperature (i.e. $Da \sim R_{ref}/T_{ref}$).

If Da , for some point in the laminate, is evaluated using the prevailing conditions of temperature and concentration of reactive species, for a transient system such as autoclave curing, Da will change with time because R_{ref} and T_{ref} are functions of time. Figure 1 shows a typical middle laminate temperature and transient Da curves as a function of time during cure (4). Three noticeable changes of Da can be identified in Figure 1a. When Da becomes non-zero, it indicates the on-set of cure reaction (point a). When Da becomes larger than one, it indicates the heat generation rate is higher than the heat conduction rate, i.e. on-set of accelerated reaction (point b). When Da reaches the peak, it indicates the highest reaction exotherm during cure (point c). The peak of the Da curve occurs at the steepest portion of the temperature rise curve and can have a value much larger than one. Many researchers (4,5) have defined that an inflection in the temperature versus time trace obtained during cure (i.e. $dT/dt > 0$ and $d^2T/dt^2 > 0$) is the on-set of thermal runaway. Since this inflection occurs at the steepest portion of the temperature rise, point c indicates the on-set of thermal runaway. There are, however, cases where Da is always less than one (e.g. Figure 1b), which implies that the heat generation rate is always lower than the heat conduction rate. In these cases, accelerated reaction and thermal runaway will not occur and there will not be an inflection point in the temperature rise curve (i.e. d^2T/dt^2 is always negative).

Based on the change of Da during cure, several rules can be established and can be used to control the cure process. They are explained as follows for a simple n -th order reaction. For more complicated reactions, similar rules can be obtained following the same approach.

For an n -th order reaction, the reaction rate can be expressed as

$$R = \frac{d\alpha}{dt} = KC_0^n (1 - \alpha)^n = AC_0^n \exp(-E/RT) (1 - \alpha)^n \quad (5)$$

and Damkohler number can be expressed as

$$Da = \frac{\Delta H L^2 AC_0^n}{k} \cdot \frac{\exp(-E/RT) (1 - \alpha)^n}{T} = \frac{\bar{K} \exp(-E/RT) (1 - \alpha)^n}{T} \quad (6)$$

where K is rate constant, C_0 initial concentration of reactive species, n reaction order, A pre-exponential coefficient and E activation energy. For a fixed system (i.e. \bar{K} is constant), the maximum possible Da is when temperature equals to the maximum allowable temperature (e.g. degradation temperature) and conversion equals to zero. If $Da (T = T_{\max}, \alpha = 0) \leq 1$, the system will not have accelerated reaction and thermal runaway problem. On the other hand, if the initial $Da (T = T_{\text{initial}}, \alpha = 0)$ is larger than one, then accelerated reaction starts in the beginning of the cure. And if T_{initial} equals to the minimum obtainable temperature in the system, then thermal runaway is inevitable and cannot be controlled. A rule can be set as

"If $Da (T = T_{\max}, \alpha = 0) \leq 1$, then no accelerated reaction and thermal runaway" and,

"If $Da (T = T_{\min}, \alpha = 0) \geq 1$, then uncontrollable thermal runaway."

From equations (4) and (6), one can easily see that thicker laminates, a higher reaction rate and a larger reaction exotherm lead to a larger Da , while a higher thermal conductivity leads to a smaller Da . For a chosen graphite/epoxy prepreg material cured at a pre-specified maximum and minimum allowable temperatures, there are two critical laminate thicknesses, L_{low} and L_{high} . Below L_{low} , there will be no thermal runaway problem and the autoclave temperature can be maintained at the highest allowable level through the entire cure. Above L_{high} , the thermal runaway problem is inevitable and the system is uncontrollable. L_{low} and L_{high} are defined as

$$L_{low} = \left[\frac{kT_{max}}{\Delta H A C_0^n \exp(-E/RT_{max})} \right]^{1/2} \quad (7)$$

$$L_{high} = \left[\frac{kT_{min}}{\Delta H A C_0^n \exp(-E/RT_{min})} \right]^{1/2} \quad (8)$$

For a typical graphite/epoxy composite (i.e. 3501-6/AS4 prepreg), AC_0^n is about $1.22 \times 10^{12} \text{ sec}^{-1}$, E is 29 kcal/mole and $n = 1$ (6). If we choose $k = 0.002 \text{ cal/cm-sec-}^\circ\text{k}$ and $\rho = 2 \text{ gm/cm}^3$ (7), the relationship between L_{low} and ΔH is shown in Figure 2 for $T_{max} = 375^\circ\text{F}$ and 350°F . For 3501-6/AS4 prepreg, ΔH is 118 cal/gm for the neat resin or 47 cal/gm for a prepreg with 40% resin (8). Any laminate thinner than 0.6 inch at $T_{max} = 375^\circ\text{F}$ or 1 inch at $T_{max} = 350^\circ\text{F}$ will not have any accelerated reaction. For this epoxy resin, the reaction rate is very low at low temperatures, therefore L_{high} is no need to be considered.

For controllable laminates (i.e. $L_{low} < L < L_{high}$), several process instances can be set based on the change of Da . Examples are:

(I) FRAME = CURE

preconditions = current episode is PRECURE - EPISODE and $Da \neq 0$ or current episode is CURE - EPISODE

effects = increase degree-of-cure

(II) FRAME = ACCELERATED - RXN

preconditions = lam - mid - temp is increasing and;

lam - mid - $Da \geq 1$ or a certain value

effects = decreasing heating.

Here, the value of Da at the middle laminate instead of the positive second derivative of the temperature rise curve, is chosen as the precondition of accelerated reaction because the latter is an indication of thermal runaway, i.e. the maximum acceleration instead of the on-set of acceleration.

In order to apply these rules or process instances, Da has to be determined experimentally or numerically. One approach is to rely on off-line measurements and models. Equation (6) shows that the value of Da depends on reaction parameters such as ΔH , AC_0^n , E, n and α , and heat conduction parameters such as k and L. For each laminate, the heat conduction parameters k and L can be measured off-line. These values, however, may vary during cure because of the pressure and temperature induced resin flow when pressure is applied to the laminate. It would be desirable that these parameters can be estimated based on the on-line sensor data. Such an approach will be presented later.

The reaction parameters can be determined by a scanning DSC run (9, 10). With the availability of computerized DSC, this is a relatively easy task. The limitations here are that α has to be estimated from a kinetic model such as Equation (5). Models sometimes may not be accurate enough and some of reaction parameters may be path dependent, which cannot be easily handled by any simple models.

For the current QPA system, the knowledge base is obtained from on-line sensor measurements and the rules are established based on qualitative changes, instead of quantitative changes, of sensor signals. This kind of systems is less affected by minor variations of material properties and process variables, and are more adoptable for scale-up applications and other manufacturing processes. In the following paragraphs, I shall discuss a method of using on-line sensors to determine the change of Damkohler number during cure.

As shown in Equation (4), Da is a combination of three terms: k/L^2 , the heat conduction characteristic of the laminate; T, the laminate temperature at the targeted location, say middle laminate temperature; and ΔHR , the

heat generation rate. T can be easily measured by a thermocouple or other temperature sensors. ΔHR can be expressed as dQ_R/dt or $\Delta Q_R/\Delta t$ for a small sampling time interval, where ΔQ_R (or dQ_R) is the reaction heat generated in a time interval Δt (or dt). Therefore,

$$Da = \frac{\Delta H R L^2}{k T} = \frac{L^2}{k} \cdot \frac{1}{T} \cdot \frac{\Delta Q_R}{\Delta t} \quad (9)$$

If ΔQ_R can be measured by on-line sensors, Da can be determined either quantitatively (i.e. Equation (9)) or qualitatively (i.e. Equation (10)).

$$Da = \Delta Q_R / T \quad (10)$$

Equation (1) can be rewritten as

$$\rho C_p \frac{dT}{dt} = \frac{-dq}{dx} + \frac{dQ_R}{dt} \quad (11)$$

where q is heat flux. For a short time interval (e.g. sampling time interval Δt) and a small control volume (i.e. temperature, T , is uniform in this small volume characterized by a length scale δx), the differential equation can be expressed as a difference equation, i.e.

$$\rho C_p \frac{\Delta T}{\Delta t} = \frac{-\delta q}{\delta x} + \frac{\Delta Q_R}{\Delta t} \quad (12)$$

$$\text{and } \Delta Q_R = \rho C_p \Delta T + \left(\frac{\Delta t}{\delta x} \right) \delta q$$

$$\text{or} \quad (13)$$

$$\Delta Q_R = \rho C_p \Delta T + \left(\frac{\Delta t}{\rho C_p / \delta x} \right) \delta q$$

δq can be measured by three thermocouples (or two heat flux sensors) located in and near the control volume as shown in Figure 3, where

$$\delta q = q_{in} - q_{out} = -k \left[\frac{dT}{dx} \Big|_{in} - \frac{dT}{dx} \Big|_{out} \right] \quad (14)$$

$$= -k \left[\frac{T_1 - T}{\delta x_1} - \frac{T - T_0}{\delta x_0} \right] = \frac{-k}{\delta x} [T_1 + T_0 - 2T] \text{ if } \delta x_1 = \delta x_0 = \delta x$$

Substituting Equation (14) into Equation (13), one gets

$$\frac{\Delta Q_R}{\rho C_p} = \Delta T - \left(\frac{\nu \Delta t}{\delta x^2} \right) (T_i + T_o - 2T) \quad (15)$$

where $\nu \Delta t / \delta x^2$ is a dimensionless time, often called as the Fourier number, Fo. Fo can be estimated by temperature profiles measured by the three thermocouples before the start of cure reaction (i.e. $\Delta Q_R = 0$) since

$$Fo = \frac{\Delta T}{T_i + T_o - 2T} = \bar{T} \quad (16)$$

After the on-set of cure reaction (i.e. $\Delta Q_R > 0$), $\bar{T} > Fo$. Therefore, a simple criterion $\Delta \bar{T} = \bar{T}_j - \bar{T}_{j-1} > 0$ can be used as an indication of the on-set of cure reaction where j and j-1 represents the current and the previous time steps. For better accuracy, T_i , T_o and T should be taken as average values before and after a sampling time.

Since the on-set of accelerated reaction is defined as $Da > 1$, from Equations (9) and (15), one gets $\frac{\Delta T}{T_i + T_o - T} > Fo$

The thermal runaway condition can also be detected by the three thermocouples because the peak of the Da curve is equivalent to the peak of the $\Delta Q_R / T$ curve and ΔQ_R is proportional to $\Delta T - Fo (T_i - T_o + 2T)$.

In principle, all three major reaction characteristics: the on-set of cure reaction, the accelerated reaction and the thermal runaway, can be estimated by three thermocouples (or two heat flux sensors) located in the vicinity of the targeted area in the laminate. There are, however, several possible difficulties in the temperature measurement and parameter estimation. First, the entire estimation is based on the measurements of temperature differences in a time interval Δt and a spatial interval δx . Δt and δx need to be small enough to ensure a near linear relationship among temperatures such that Equation (11) can be converted into Equation (15),

and large enough to result in measurable temperature differences with acceptable accuracy. This also means that the thermocouple signal noises need to be low. Second, the value of the Fourier number, Fo , depends on the thermal diffusivity of the laminate, ν , and the distance between each two thermocouples, δx . These values may change during evacuation, consolidation (e.g. resin flow and viscosity change) and curing (e.g. gelation, vitrification, thermal expansion and polymerization shrinkage). For example, Fo may change substantially when vacuum and pressure are applied to the bag, which needs to be differentiated from the change resulted from cure reaction. Other preconditions may need to be added to the frames in order to resolve these interactions.

IV. SCALING ANALYSIS OF HEAT TRANSFER

The cure process knowledge developed in the previous section can be used by the Parser to determine the process state and the desired effects. For the Thinker to make control decisions, information regarding the thermal response of the system is needed. For the autoclave curing of graphite/epoxy composites, the cure cycle is controlled by varying the autoclave temperature, which then affects the cure reaction and temperature change in the laminate by heat conduction through the bagging materials and the laminate. A quantitative optimization of such a distributed parameter system (i.e. spatial dependent) by boundary control is not an easy task. Although some optimization theories have been developed in the last two decades, they are often limited to relatively simple applications and are highly model dependent (11). For QPA applications, our goal is to achieve a qualitative process automation, instead of a quantitative process optimization. In other words, we are seeking a better or an acceptable solution for a given manufacturing process, instead of the optimal solution. Based on

this concept, the detailed heat transfer phenomenon (i.e. micro-scale changes) can be largely simplified as long as the major thermal response of the system (i.e. macro-scale changes) can be measured by on-line sensors and sufficient information can be generated for the Thinker to make appropriate control decisions.

For autoclave curing, heat transfer from the autoclave air through the bagging materials to the laminate is often much slower when compared with heat conduction in the laminate as long as the laminate is not too thick (3). This allows us to use an integral energy equation (i.e. a zero-dimension unsteady heat conduction) by assuming that heat transfer is mainly determined by an overall heat transfer coefficient, h , which represents the thermal conductivities of the laminate and bagging materials, and the local heat transfer coefficient of the autoclave air. Equation (11) can be written in the integral form as

$$\int_0^L \left[\rho C_p \frac{dT}{dt} = \frac{-dq}{dx} + \frac{dQ_R}{dt} \right] dx \quad (17)$$

$$\text{or} \quad L \rho C_p \frac{dT}{dt} = -\tilde{q} + \frac{d\tilde{Q}_R}{dt} \quad (18)$$

where $\frac{dT}{dt}$, \bar{q} and $\frac{d\bar{Q}_R}{dt}$ represent average values in the laminates, and

$$\bar{q} = h(T - T_A) \quad (19)$$

Here, T is the laminate temperature and T_A is the autoclave air temperature. Equation (18) can be rewritten as

$$\frac{dT}{dt} = \frac{T_A - T}{\tau} + \frac{\Delta\bar{Q}_R}{\rho C_p} \quad (20)$$

where $\tau = \frac{L\rho C_p}{h}$ is the thermal response time constant of the system.

Before the on-set of cure reaction, τ can be estimated by the temperature profiles of T and T_A . This was described by Norfleet (12) using a piece-wise linear path for the temperature profiles. The equation he used is

$$T_j = T_{Aj} - \beta_j \tau + (T_{j-1} - T_{Aj-1} + \beta_j \tau) \exp(-t/\tau) \quad (21)$$

where the autoclave temperature is expressed as $T_{Aj} = T_{Aj-1} + \beta_j \Delta t$ and β_j the rate of temperature change for the time interval.

From equation (15), $\Delta\bar{Q}_R/\rho C_p$ can be measured by on-line temperature sensors assuming $\Delta\bar{Q}_R = \Delta Q_R$ and from Equation (20)

$$\frac{dT}{dt} = \frac{T_A - T}{\tau} + \frac{\Delta T - F_0 (T_i + T_0 - 2T)}{\Delta t} \quad (22)$$

T_A can be adjusted according to the values of T_i , T_0 and T to control the rate of change of the laminate temperature.

If the objective of the control is to keep the value of Da less than a certain number (e.g. 1) at the targeted location in order to avoid accelerated reaction or thermal runaway, then the control action can be set as to lower the autoclave temperature to a level such that $\frac{dT}{dt} = 0$ according to equation (22) when Da approaches 1 or a certain value. After this goal is reached, T_A should be gradually increased to provide a small positive $\frac{dT}{dt}$ because ΔQ_R is a decreasing function if temperature is unchanged. For systems with a large τ (e.g. an autoclave with a poor thermal response, thick bagging materials, or thick laminate), T_A may have to be lowered to an unobtainable value when a control action is needed. In such cases, a smaller Da should be chosen as the critical point and the cooling action should start earlier.

V. RECOMMENDATIONS

1. The analysis presented in this report provides a more rigorous knowledge base for the process automation of autoclave curing. The advantages of this method compared with the current method and the methods based on off-line measurements and models should be investigated.

2. The major drawbacks of the lumped energy analysis presented in this report is that the local temperature distribution in the laminate is not considered. The effect of this simplification on the control action needs to be studied using both simulator and autoclave experiments.

3. The analysis presented in this report considers only the cure reaction and heat transfer by manipulating the autoclave temperature. Other process instances such as resin flow, void formation and residual stresses, and other manipulated variables such as autoclave pressure have not been

investigated. To develop a complete on-line automation strategy for autoclave curing, these instances and variables should be included in the study. This requires more on-line sensors. In addition to the temperature sensors and micro-dielectric sensors, ultrasonic devices and strain gauges may also be useful.

4. This report emphasizes the knowledge and rule development based on on-line sensor measurements. For many applications, sensors cannot present in some critical locations, or variables needed to be controlled are not measurable. In such cases, one has to rely on indirect control or predictive control methods. These methods depend heavily on off-line measurements and process models. Because the models may not be always accurate and there may be disturbances which are not considered in the process models, on-line sensor measurements are still necessary. They provide a means to continuously adjust the process parameters (i.e. adaptive function) and to compensate the limitations of process models. An ideal case would be the one shown in Figure 4 where the QPA is connected to both the on-line sensors and a simulator. The former provides direct control and updated information of the process, while the latter provides indirect and/or predictive control, and can serve as a back-up system in the case of sensor failure.

5. QPA has been demonstrated by the WPAFB researchers as a very useful tool for the automation of autoclave curing. Similar applications for other composite manufacturing processes should also be feasible. One example is resin transfer molding (RTM), which is considered as a more efficient way of fabricating continuous fiber reinforced polymeric composites than autoclave curing. Since this investigator has currently an ongoing research project in this area, a proposal will be written for the RIP program aimed at the qualitative process automation (QPA) of RTM.

6. The concept of using three thermocouples (or two heat flux sensors) to measure the heat generation rate at a local area can also be applied to the compression molding of thermoplastic composites, where the formation of crystalline structure will generate heat (i.e. equivalent to heat generation in epoxy resins), while the melting of crystalline structure will absorb heat (i.e. a negative heat generation). Therefore, a parameter similar to Damkohler number can be defined as an index of crystalline formation or melting.

REFERENCES

1. Servais, R.A., Lee, C.W., and Browing, C.E., "Intelligent Processing of Composite Materials," SAMPE Journal, September/October 1986, pp. 14-18.
2. Loos, A.C. and Spring, G.S., "Curing of Epoxy Matrix Composites," Journal of Composite Materials, vol. 17, No. 2, March 1983, pp. 135-160.
3. Abrams, F., Carrett, P., Lagnese, T., LeClair, S., Lee, C.W., and Park, J., "Qualitative Process Automation for Autoclave Curing of Composites-," AFWAL-TR-87-4083, November 1987.
4. Osinski, J.S., Manzione, L.T., and Chan, C., "Thermal Runaway in Fast Polymerization Reactions," Polymer Process Engineering, Vol. 3, No. 1 & 2, 1985, pp. 97-112.
5. Biesenberger, J.A. and Sebastian, D.H., Principles of Polymerization Engineering, Wiley-Interscience Publication, 1983, pp. 403-472.
6. Campbell, F.C., Mallow, A.R., Muncoster, F.R., Boman, B.L. and Blase, G.A., "Computer-Aided Curing of Composites," AFWAL-TR-86-4060, July 1986, pp. 2-9.

7. Brandrup, J. and Immergut, E.H., Polymer Handbook, Wiley-Interscience Publication, 1967, pp. II-381.
8. Campbell, F.C., Mallow, A.R., Muncaster F.R., Boman, B.L. and Blase, G.A., "Computer-Aided Curing of Composites," AFWAL-TR-86-4060, July 1986, pp. 2-3.
9. Kamal, M.R., Slurour, S. and Ryan, M. "Integrated Thermo-Rheological Analysis of the Cure of Thermoset," SPE ANTEC Technical Papers, Vol. 19, 1973, pp. 187-197.
10. Lee, L.J., "Curing of Compression Molded Sheet Molding Compound," Polymer Engineering and Science, Vol. 21, No. 8, Mid-June 1981, pp. 483-492.
11. Huang, Y.J. and Lee, L.J., "Optimization of Diffusion-Controlled Free Radical Polymerizations in a Distributed Parameter System," Chemical Engineering Science, in press.
12. Norfleet, C.W., "Determination of Lumped-Mass Thermal Properties Associated with Autoclave Curing of Graphite/Epoxy Composites," Final Report to USAF-UES Graduate Student Summer Support Program, F49620-85-C-0013, September 1987.

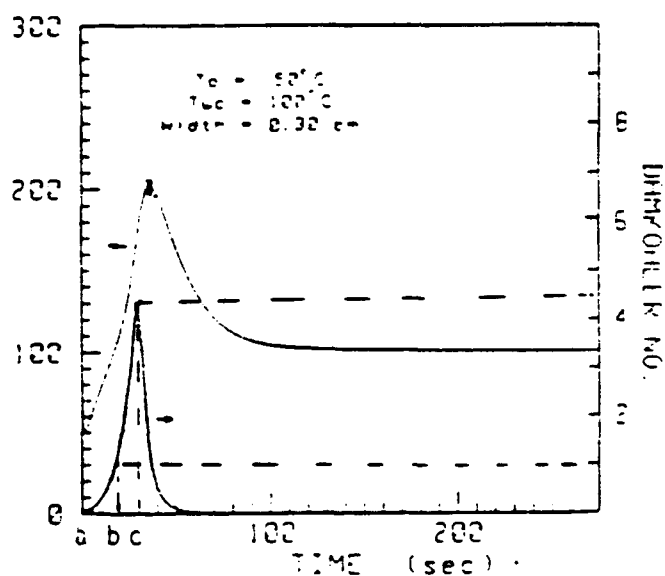


Figure 1_a

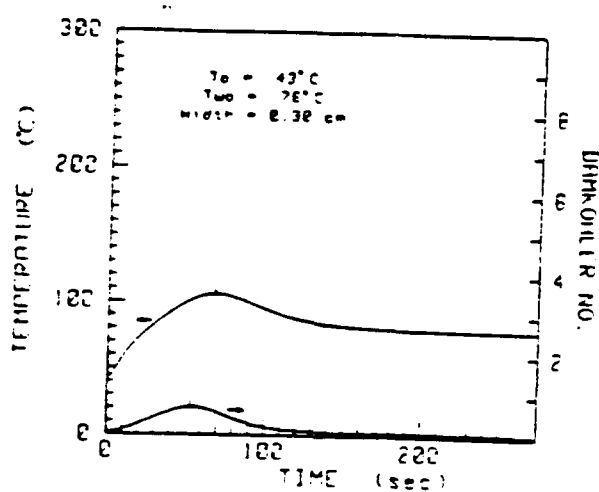


Figure 1_b

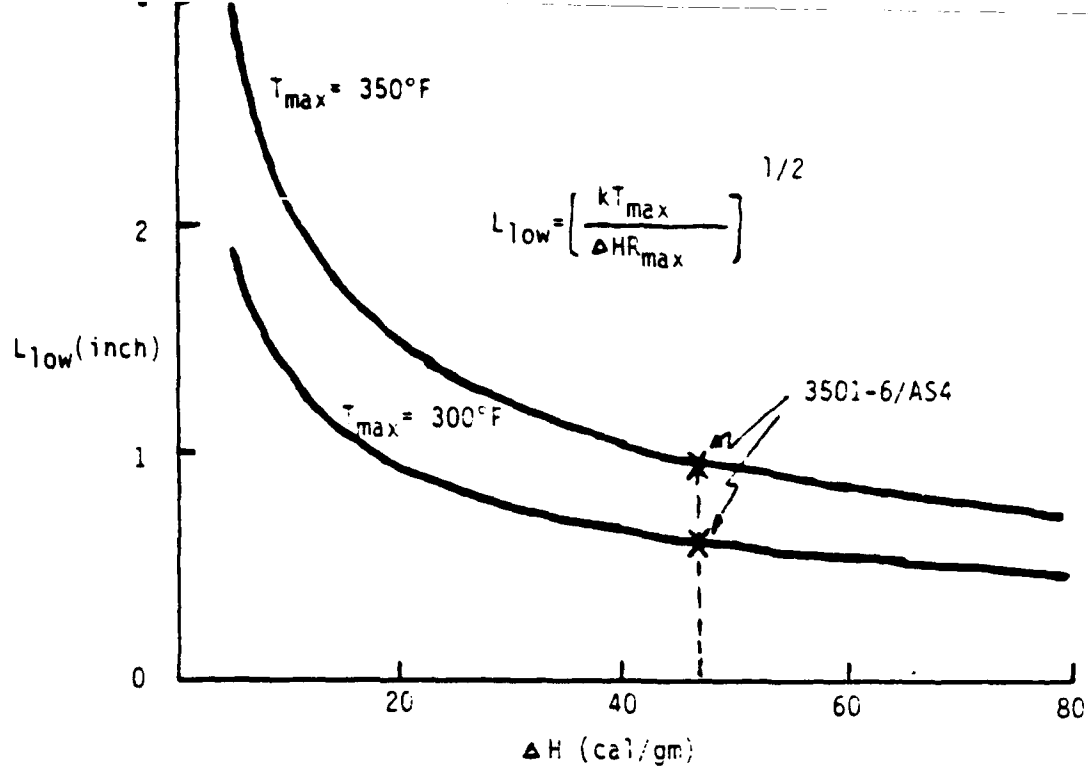


Figure 2.

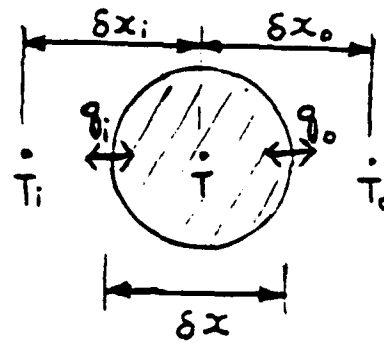


Figure 3.

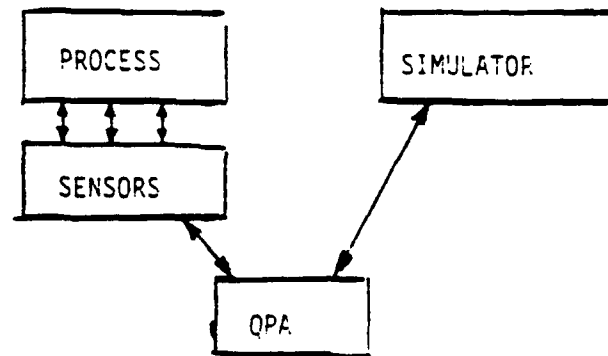


Figure 4.

1988 USAF - UES Summer Faculty Research Program

**Sponsored by the
AIR FORCE OFFICE OF SCIENTIFIC RESEARCH**

**Conducted by the
Universal Energy Systems, Inc.**

Final Report

A Study of the Melting of the Plagioclase Feldspars in a Microwave Field

Prepared by:	Thomas T. Meek, Ph.D.
Academic Rank:	Associate Professor
Department and	Materials Science and Engineering
University:	The University of Tennessee
Research Location:	AFWAL/MLLM Wright Patterson AFB Dayton, Ohio
USAF Researcher:	Paul Jero, Ph.D.
Date:	12 August 1988
Contract No.:	F49620-87-R-0004

A Study of the Melting of the Plagioclase Feldspars in a Microwave Field

by

Thomas T. Meek

ABSTRACT

Thermal processing of dielectric materials using microwave radiation has recently become of interest to the scientific community. Work in this area spans over four decades; however, only recently have results indicated potential economic and technical benefits from this thermal processing technique.

This work investigates melting phenomena which occur in the albite-anorthite system ($\text{NaAlSi}_3\text{O}_8$ - $\text{CaAl}_2\text{Si}_2\text{O}_8$) when heated using 2.45 GHz electromagnetic radiation. Compositions of 90, 81, and 72 weight percent albite were synthesized from alkoxides. Five or ten gram quantities were heated in alumina crucibles to 1200°C and held for 1, 2, and 4, hours before cooling to 800°C in a nine minute period. Heating was done in a conventional electric furnace and in a 2.45 GHz microwave furnace. Sample microstructure was then determined and compared to see if the 2.45 GHz electromagnetic radiation had any affect on equilibrium phase compositions.

Acknowledgements

I thank the Materials Laboratory of the Wright-Patterson Air Force Base and the Office of Scientific Research for sponsorship of this research. I also thank Universal Energy Systems for their concern and help in all administrative and directional aspects of this program.

This experience was very rewarding and enriching for me, especially my interaction with personnel in the MLLM branch of the Materials Laboratory. Dr. Ron Kerans provided me a stimulating work environment and Drs. Paul Jero and T. A. Parthasarathy were enjoyable to work with. Mr. Joe Dorsey, and Mr. Bob Sweeney provided help in overcoming problems with obtaining equipment and having samples prepared. I thank Mr. Glenn Myers for the design and fabrication of a microwave cavity capable of either single mode or multi-mode operation.

I. Introduction

Microwave processing of ceramic and composite materials has been carried out over the past four decades by various researchers. A short bibliography is included at the end of this report covering much of this work (1-34).

Potential advantages of this thermal processing technique are: rapid sintering, less labor required to process the material, generally less energy required to process material, possibly different microstructures, uniform heating of the material of interest, and possible control over reaction kinetics, and nucleation kinetics.

This report addresses work of a fundamental nature which investigated equilibrium phase compositions in the albite-anorthite system. This system is shown in Figure 1. The primary interest here was to better understand how electromagnetic radiation may affect the final phase compositions of an oxide system heated in a 2.45 GHz field. Compositions within the albite-anorthite system were heated to a given temperature in the two phase liquid-solid region. Specimens were held at the annealing temperature for different times and then cooled rapidly to room temperature. Similar samples were made by heating in a conventional furnace. The microstructures of the two groups will be determined using SEM and TEM techniques to see if any differences exist. Microprobe analysis will be used to determine the compositions of any phases present.

Another side issue of this work dealt with the accurate measurement of temperature in a microwave field. A section of this report will be devoted to this subject.

II. Objectives of the Research Effort

Researchers as yet have not studied equilibrium phase compositions in an oxide system that has been heated using 2.45 GHz electromagnetic radiation. If the presence of an electromagnetic field affects the composition of phases in a dielectric material, then the possibility exists for modifying the properties of existing materials. It is the objective of this summer research effort to study an oxide system which has been extensively studied using conventional heating techniques. The system chosen for this study is the albite-anorthite ($\text{Na}_2\text{O} \cdot \text{Al}_2\text{O}_3 \cdot 6\text{SiO}_2 - \text{CaO} \cdot \text{Al}_2\text{O}_3 \cdot 2\text{SiO}_2$) system. Before a detailed experiment could be performed, confidence had to be gained in a method for temperature measurement. As the volume of technical literature on this subject indicates this is not an easy problem.

III. Temperature Measurement in a Microwave Field

Many researchers have investigated this problem and to date there is no adequate method in use. Many researchers use shielded thermocouples to acquire temperature data; however, the shield will perturb the field in the region around the thermocouple. This field perturbation will also affect the field distribution in and around the dielectric sample being heated if the thermocouple is placed either in, or close to, the sample. The question becomes how does the altered field affect the sample temperature. Much effort was placed into a study of whether or not a thermocouple may be used to measure average local temperature in a microwave field. Experiments

were carried out with a thermocouple next to a porous block of NaCl (table salt) and next to a single crystal of NaCl. This material was heated using 2.45 GHz radiation and the thermocouple output was compared with the output of an IR meter focused directly on the sample. Further experiments were conducted with the thermocouple placed in a hole drilled into the salt sample. Again these samples were heated and the thermocouple output compared with the output of an IR meter focused directly on the salt sample. Data for these experiments are shown in Figures 2-5. The thermocouple data indicates a much lower melting temperature for NaCl while the IR meter consistently records a higher melting temperature. The lower thermocouple temperature and its delay in reaching temperature may be due to a back emf generated in the thermocouple due to inductive coupling with its shield. The consistently higher temperature measured by the IR meter may be due to the effect of the electromagnetic field on the surface emissivity of the salt. A further problem also caused difficulty in making the IR temperature measurements. When the salt began to melt, the resulting liquid almost instantaneously vaporized creating a cloud in the reaction cavity which obstructed the IR meters view of the sample. The surface the IR meter focused on was partly liquid, partly solid and partly vapor. Under these conditions, it is easy to understand the inability to obtain accurate IR temperature readings. In all of these experiments the thermocouple shield is grounded. The great differences in the two temperatures may be a result of a back emf being setup in the thermocouple due to inductive coupling between the TC and the shield. An ungrounded, shielded TC was also used, and temperature measured in this manner more closely matched the output

of the IR meter; however, the agreement was not close enough to use the TC. Manual control based on the IR meter output was used during all of the runs for which useful data were obtained. All samples were placed in the same position in the cavity and the thermocouple position remained unchanged throughout the experiments.

IV. The Albite-Anorthite System

Sample material was synthesized from alkoxides and compositions of 90wt%, 81wt% and 72wt% albite were prepared and characterized by x-ray diffraction and DTA techniques. Five or ten gram quantities were heated in a 2.45 GHz microwave field (model SF6 Cober multimode 2.45 GHz resonant cavity) for varying lengths of time. Table 1 shows the design of the experiment.

This particular material system was chosen because it exhibits complete solid solution between end components at relatively low temperatures and the system is relatively insensitive to rapid changes in temperature. This system has also been extensively studied for over 80 years and any deviation from the norm would be quickly recognized. The basis upon which we believe that heating compositions within the albite - anorthite system in a 2.45 GHz electromagnetic field may result in a change in equilibrium phase compositions is detailed below. First consider a boundary between two dielectric phases. Assume that phase A is dispersed uniformly throughout phase B and that Phase A has a dielectric constant k_A and phase B has dielectric constant k_B . Let the density of phase A be greater than the density of phase B and the dielectric constant of phase A be less than that of phase B.

Before proceeding with the development, the following definitions are introduced.

E = vector electric field

V = applied electric potential

d = dielectric thickness

$E = V/d$

k = dielectric constant

D = vector electric flux density

$D = kE$

We shall start the development of a heating model using an expression developed in (30) which describes how the vector electric field intensity E_A in one portion of the dielectric media (phase A) depends on a vector electric field intensity E_B in a second portion of the dielectric media (phase B). Again it is assumed that k_B is greater than k_A . Then expression (1) is:

$$E_B = E_A (\cos^2 \alpha_A + (k_A / k_B)^2 \sin^2 \alpha_A)^{1/2} \quad (1)$$

Here α_A is the angle the electric field vector makes with the dielectric boundary. It is clear that only in the case where $\alpha_A = 0^\circ$ is $E_B = E_A$. For all other cases the value of E_A is greater than E_B . Thus expression (1) shows that the intensity of the electric field is greater in the lower dielectric constant phase (phase A) and less in the higher dielectric constant phase (phase B). This fact has great significance because it indicates where an electromagnetic field will deposit its energy in a two phase region and how the location of this energy will vary as the two phase region is heated.

To continue with the development of the model, we now introduce three expressions obtained from texts such as (30) which will serve to

characterize how a two phase region will heat in an electromagnetic field.

Expression two gives the power deposited per unit volume into a single phase by an applied electromagnetic field.

$$P = K f E^2 k \tan \delta \quad (2)$$

where P = power per unit volume

K = constant

f = frequency of incident radiation

E = vector electric field intensity

k = relative dielectric constant

$\tan \delta$ = loss tangent

The next expression permits us to determine the depth into a single phase where the power is half of its value at the surface. This is called the half power depth of penetration, H , and is defined as follows:

$$H = 3 \lambda_0 / (8.686 \pi (k)^{1/2} \tan \delta) \quad (3)$$

where H = half power depth

λ_0 = characteristic wavelength of the incident radiation

k = relative dielectric constant

$\tan \delta$ = loss tangent

The last expression used in the model gives an approximate rate of temperature increase in a single phase within a dielectric region. This expression is only approximate because it does not include heat losses due to conduction, convection, radiation, or change of state.

$$\dot{T} = 8 \times 10^{-12} f E^2 k \tan \delta / (\rho C_p) \quad (4)$$

where \dot{T} = the heating rate in degrees celcius per minute

f , E , k , and $\tan \delta$ are as defined above

ρ = material density

C_p = heat capacity of material

Let us now consider a two phase region which comprizes a dielectric media that is to be heated in a 2.45 GHz electromagnetic field. Initially phase A is uniformly dispersed in phase B and the electromagnetic field sees a uniform media dielectric constant. This media dielectric constant is a function of the respective phase A and B dielectric constants and the volume fraction of the dispersed phase and matrix phase. Expression (5) is Maxwell's expression for mixtures and from it is obtained an average dielectric constant.

$$k_c = \frac{V_B k_B (.667 + k_A / 3 k_B) + V_A k_A}{V_B (.667 + k_A / 3 k_B) + V_A} \quad (5)$$

where k_c = the composite dielectric constant

V_B = the volume fraction of the matrix phase

V_A = the volume fraction of the dispersed phase

k_A = the dielectric constant of the dispersed phase

k_B = the dielectric constant of the matrix phase

There are then three dielectric constants of importance here, the composite dielectric constant and the dielectric constants of phase A and B. As the dielectric media begins to heat, local regions within the media may change in density (i.e., the volume fraction of phase B may change relative to phase A). Namely local regions of phase A may increase in density relative to phase B. If phase A is a crystalline phase and phase B is a liquid then as phase A grows relative to phase B its perturbation of the electromagnetic field will change relative to phase B's perturbation of the field. How these perturbations occur will affect the relative amounts of energy the electromagnetic field will

deposit in the growing phase A and the shrinking phase B or vice-versa.

Using the general assumption made above and one more, that being that $\tan \delta_A = \tan \delta_B$, let us calculate power density, half power depth of penetration, and heating rates in the two phases which comprise the dielectric media being heated.

$$\frac{P_A}{P_B} = \frac{k_B}{k_A} \quad (6)$$

Since $k_B > k_A$ more power will be deposited into phase A than phase B.

$$\frac{H_A}{H_B} = \left(\frac{k_B}{k_A} \right)^{\frac{1}{2}} \quad (7)$$

Since $k_B > k_A$ the half power depth of penetration will be greater in phase A than phase B.

$$\frac{\dot{T}_A}{\dot{T}_B} = \frac{E_A^2 k_A \rho_B C_{PB}}{E_B^2 k_B \rho_A C_{PA}} \quad (8)$$

Since k_A is less than k_B , and $\rho_B C_{PB}$ is larger than $\rho_A C_{PA}$, then depending on the exact values of k_A , k_B , ρ_A , C_{PA} , ρ_B and C_{PB} , \dot{T}_A could be either less than or greater than \dot{T}_B . Table 2 summaries a variety of scenarios for some assumed values of k_A , k_B , ρ_A , ρ_B , C_{PA} and C_{PB} . For table 2 the value of the ratio $\rho_B C_{PB} / \rho_A C_{PA}$ is either 0.81 or its inverse 1.24. The value .81 is for the case where $\rho_B = .9\rho_A$ and $C_{PB} = .9C_{PA}$ and the value 1.24 is for the case where $\rho_A = .9\rho_B$ and $C_{PA} = .9C_{PB}$. These values are arbitrary values chosen for the purpose of illustration.

It is clear from table 2 that depending on the intensive properties of phase A and phase B the relative heating rates of the two phases may vary over 12 orders of magnitude. Table 2 covers only a small range over which

the intensive properties may vary and thus only gives a clue as to how a generalized two phase media might heat in a 2.45 GHz electromagnetic field.

Further work on the albite-anorthite system will serve to classify which area of table 2 we are working in and thus enable a more exact model of the heating of this system in a 2.45 GHz electromagnetic field.

V. Recommendations

- a. It is recommended that since initial results indicate that equilibrium conditions were not satisfied, the albite-anorthite system be studied more extensively. Compositions should be heated to the same temperature as in the initial study for longer periods of time.**
- b. It is further recommended that upon the conclusion of part a of the recommendations, that if it is shown that an electromagnetic field does alter the microstructure of oxide materials, a suitable system of technical importance to the United States Air Force should be studied to see if microstructures in that system can be altered beneficially.**

VI. References

1. White, J. R., "Why Materials Heat," Proceedings of IMPI, Short Course on Theory and Application of Microwave Power in Industry, May 1970, p. 7.
2. Whitehead, S., and Nethercot, W., "The Breakdown of Dielectric Under High Voltage, with Particular Reference to Thermal Instability," Proc. Phys. Soc., London, 1935, Vol. 47, pp. 974-997.
3. Von Hippel, A. R., Dielectrics and Waves, J. Wiley and Sons, Inc., 1954.
4. Von Hippel, A. R., Dielectric Materials and Applications, John Wiley and Sons, New York, 1954.
5. Tinga, W. R., "Interactions of Microwaves with Materials," Proceedings of IMPI, Short Course for Users of Microwave Power, Nov. 1970, pp. 19-29.
6. Tinga, W. R., and Nelson, S. O., "Dielectric Properties of Materials for Microwave Processing-Tabulated," Journal of Microwave Power, March 1973, Vol. 8 (73), No. 1, pp. 23-66 3.
7. Tinga, W. R., and Voss, W.A.G., Microwave Power Engineering, Academic Press, New York, 1968, Vol. 2, pp. 189-194.
8. Tinga, W. R., and Edwards, E. M., "Dielectric Measurement Using Swept Frequency Techniques," Journal of Microwave Power, 1968, Vol. 3 (68), No. 3 pp. 144-175.
9. Tinga, W. R., Multiphase Dielectric Theory - Applied to Cellulose Mixtures, Thesis, Department of Electric Engineering, University of Alberta, 1969, pp. 62-65.
10. Ford, J. D., and Tinga, W. R., "Temperature Dependence of Dielectric Constant of Powdered Metallic Oxides," Unpublished work, July 25, 1968.
11. Haas, P. A., "Heating of Uranium Oxides in a Microwave Oven," American Ceramic Society Bulletin, 1979, Vol. 58, [9] 873.
12. Kemer, E. L., and Johnson, D. L., "Microwave Plasma Sintering of Al_2O_3 ," American Ceramic Society Bulletin, 1985, Vol. 64, pp. 1132-1136, .

13. Microwave Coupler and Method, C. E. Holcombe, Patent No. 4559429.
14. Holcombe, C. E., "New Microwave Coupler Material," Bulletin of the American Ceramic Society, 1983, Vol. 62, No. 12, p. 1388.
15. Meek, T. T., and Blake, R. D., "Ceramic-Ceramic Seals by Microwave Heating," Journal of Materials Science Letter, 1986, 5, 270-274.
16. Meek, T. T., Blake, R. D., Katz, J. D., and Brooks, M. H., "Cation Diffusion in Glass Heated in a Microwave Field," Submitted to Journal of Materials Science Letters.
17. Meek, T. T., et al., "Microwave Processing of Ceramics," Journal of Microwave Power and Electromagnetic Energy, 1986, Vol. 21, Number 3, 193-194.
18. Blake, R. D., and Meek, T. T., "Microwave Processing of Composite Materials," Accepted for publication in Journal of Materials Science Letters.
19. Meek, T. T., Blake, R. D., and Gregory, T. E., "Low Density Inorganic Foams Fabricated Using Microwaves," Ceramic Engineering and Science Proceedings, 1988, 6, 1161-1170.
20. Wright, R. A., Cocks, F. H., Vaniman, D. T., Blake, R. D., and Meek, T. T., "Fusing Lunar Material with Microwave Energy. Part I: Studies of Doping Media," Proceedings of the 17th Lunar and Planetary Science Conference, Johnson Space Center at Houston, TX, March 17-21, 1986.
21. Vaniman, D. T., Meek, T. T., and Blake, R. D., "Fusing Lunar Material with Microwave Energy. Part II: Melting of a Glassy Apollo 11 Soil Simulant," Proceedings of the 17th Lunar and Planetary Science Conference, Johnson Space Center at Houston, TX, March 17-21, 1986.
22. Wright, R. A., Cocks, F. H., Vaniman, D. T., Blake, R. D., and Meek, T. T., "Thermal Processing of Ilmenite and Titania Doped Hematite Using Microwave Energy," Submitted for publication to the Journal of Material Science.
23. Meek, T. T., Cocks, F. H., Vaniman, D. T., and Wright, R. A., "Microwave Processing of Lunar Materials, Potential Applications," Lunar Bases and Space Activities of the 21st Century, 1986, W. Mendell Editor, Lunar Planetary Institute, Publication Office, Houston, TX.

24. Meek, T. T., Vaniman, D. T., Blake, R. D., and Cocks, F. H., "Electromagnetic Energy Applied to and Gained from Lunar Materials," to be published in the Proceedings of Symposium '86, held at Atlantic City, New Jersey, September 22- 24, 1986.
25. Meek, T. T., "A Proposed Model for the Sintering of a Dielectric in a Microwave Field," Submitted to the Journal of Materials Science Letters.
26. Meek, T. T., Vaniman, D. T., Blake, R. D., and Godbole, M. J., "Sintering of Lunar Soil Simulants using 2.45 GHz Microwave Radiation," published in the Proceedings of the 18th Lunar and Planetary Science Conference, March 23- 27, 1987, Houston, TX.
27. Meek, T. T., Vaniman, D. T., Blake, R. D., and Cocks, F. H., "Electromagnetic Energy Applied to and Gained from Lunar Materials," to be published in the Proceedings of Symposium '86, September 22-24, 1986, Atlantic City, NJ.
28. Meek, T. T., Holcombe, C., Dykes, N., "Microwave Processing of Ceramics using Sintering Aides," accepted for publication in the Journal of Materials Science Letters.
29. Meek, T.T., Holcombe, C. E., "Unusual Properties of Microwave-Sintered Yttria-2 wt% Zirconia," submitted to the Journal of Materials Science Letters.
30. Puschner, H., Heating with Microwaves, Fundamentals, Components and Circuit Technique, 1966, Philips Technical Library, Springer-Verlag, New York.
31. Panofsky, W.K.H., and Phillips, M., Classical Electricity and Magnetism, Stanford University Press, 1955.
32. Kingston, W. E., The Physics of Powder Metallurgy, 1951, McGraw-Hill Book Company, Inc., .
33. Berry, K. A., and Harmer, M. P., "Effect of MgO Solute on Microstructure Development in Al_2O_3 ," Journal of the American Ceramic Society, 1986, Vol. 69, 143-149.
34. Ford, J. D., and Pei, D.C.T., "High Temperature Chemical Processing via Microwave Absorption," Journal of Microwave Power, 1967, Vol. 2(2), pp. 61-64, .

Table 1 - Design of the Experiment

Sample	Thermal Processing Technique	Temperature °C	Time (min)
90A-M-1	Microwave	1200	60
90A-M-2	Microwave	1200	120
90A-M-3	Microwave	1200	240
81A-M-1	Microwave	1200	60
81A-M-2	Microwave	1200	120
81A-M-3	Microwave	1200	240
72A-M-1	Microwave	1200	60
72A-M-2	Microwave	1200	120
72A-M-3	Microwave	1200	240
90A-C-1	Conventional	1200	60
90A-C-2	Conventional	1200	120
90A-C-3	Conventional	1200	240
81A-C-1	Conventional	1200	60
81A-C-2	Conventional	1200	120
81A-C-3	Conventional	1200	240
72A-C-1	Conventional	1200	60
72A-C-2	Conventional	1200	120
72A-C-3	Conventional	1200	240

Table 2
Heating of a two phase dielectric media in a 2.45 GHz electromagnetic field

$\tan \delta_A$	$\tan \delta_B$	k_A	k_B	P_A/P_B	H_A/H_B	$\rho_B C_{PB}/\rho_A C_{PA}$	T_A/T_B
10^{-4}	10^{-4}	10	100	10	3.16	.81	8.1
10^{-4}	10^{-4}	10	100	10	3.16	1.24	12.35
10^{-4}	10^{-4}	100	10	0.1	.316	.81	.081
10^{-4}	10^{-4}	100	10	0.1	.316	1.24	.124
10^{-4}	10^{-2}	10	100	0.1	316	.81	8.1×10^{-2}
10^{-4}	1	10	100	10^{-3}	3.16×10^4	.81	8.1×10^{-4}
10^{-4}	10^2	10	100	10^{-5}	3.16×10^6	.81	8.1×10^{-6}
10^{-2}	10^{-4}	10	100	10^3	3.16×10^{-2}	.81	8.1×10^2
1	10^{-4}	10	100	10^5	3.16×10^{-4}	.81	8.1×10^4
10^{-2}	10^{-4}	10	100	10^7	3.16×10^{-6}	.81	8.1×10^6
10^{-4}	10^{-2}	100	10	10^{-3}	31.6	.81	8.1×10^{-4}
10^{-4}	1	100	10	10^{-5}	3.16×10^3	.81	8.1×10^{-6}
10^{-4}	10^2	100	10	10^{-7}	3.16×10^5	.81	8.1×10^{-8}
10^{-2}	10^{-4}	100	10	10	3.16×10^{-3}	.81	8.1
1	10^{-4}	100	10	10^3	3.16×10^{-5}	.81	8.1×10^2
10^2	10^{-4}	100	10	10^5	3.16×10^{-7}	.81	8.1×10^4

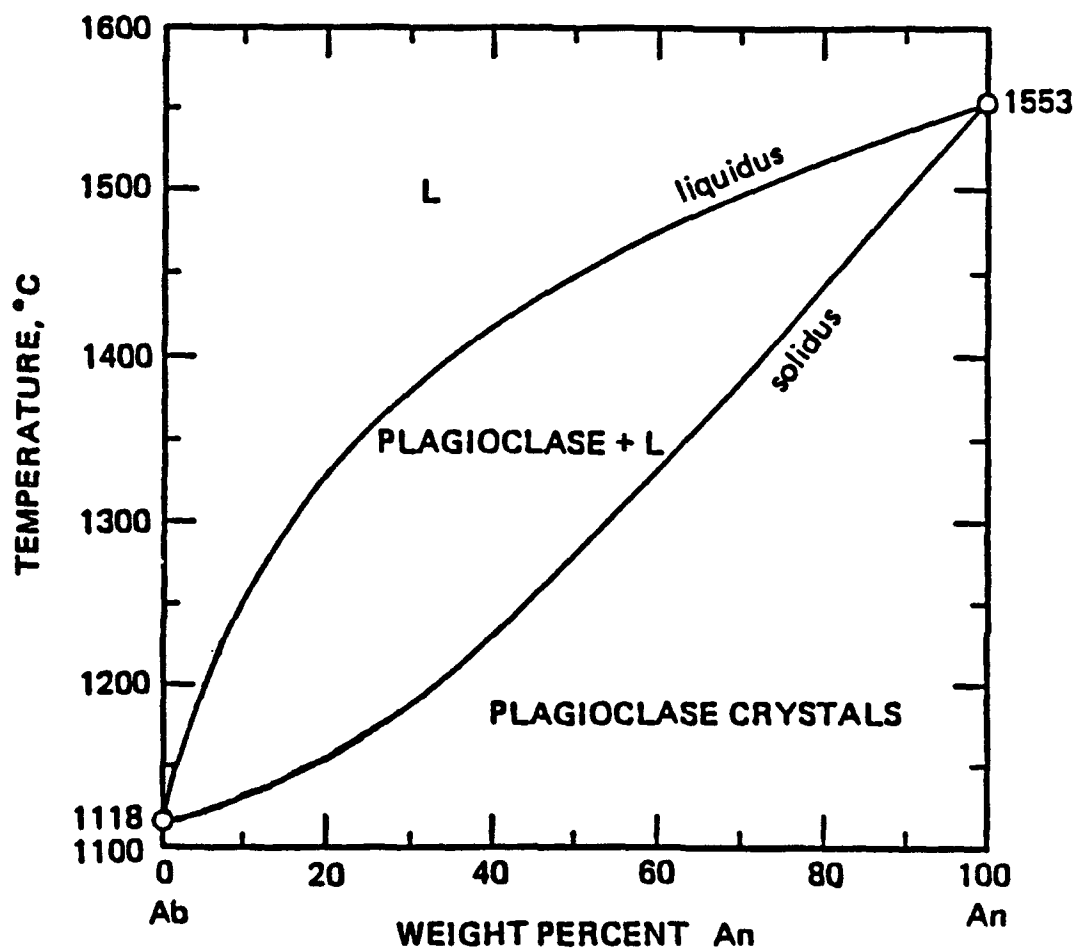


Figure 1. The Albite - Anorthite System

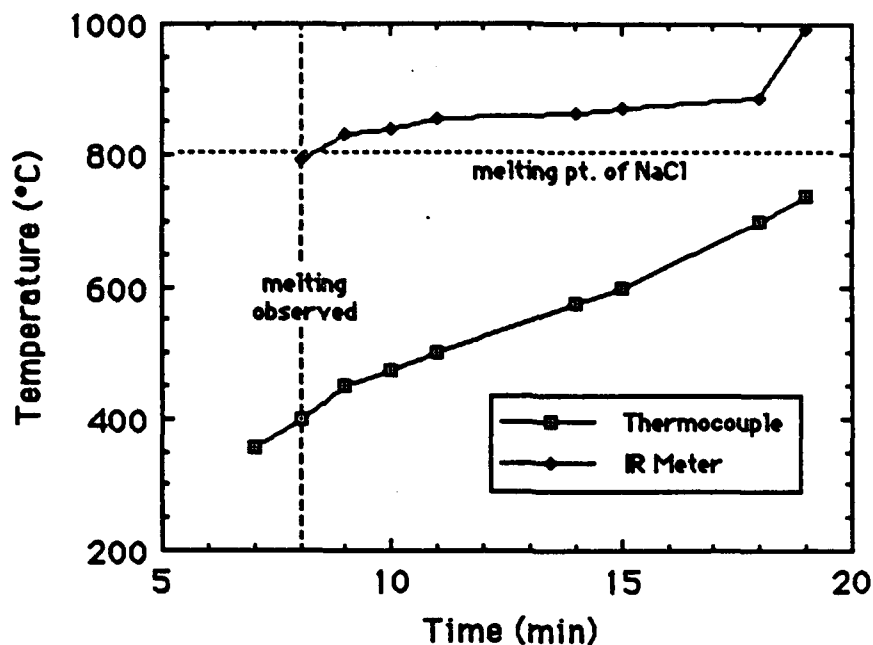


Figure 2. The melting of polycrystalline NaCl in a microwave field. Thermocouple next to sample. Emissivity setting of IR meter = 1.0.

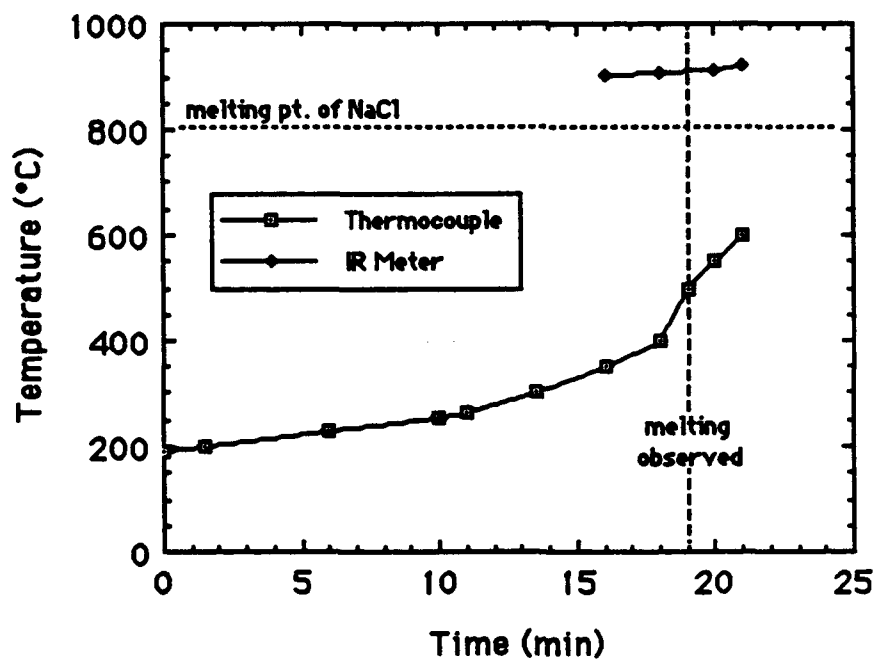


Figure 3. The melting of single crystal NaCl in a microwave field. Thermocouple next to sample. Emissivity setting of IR meter = 1.0.

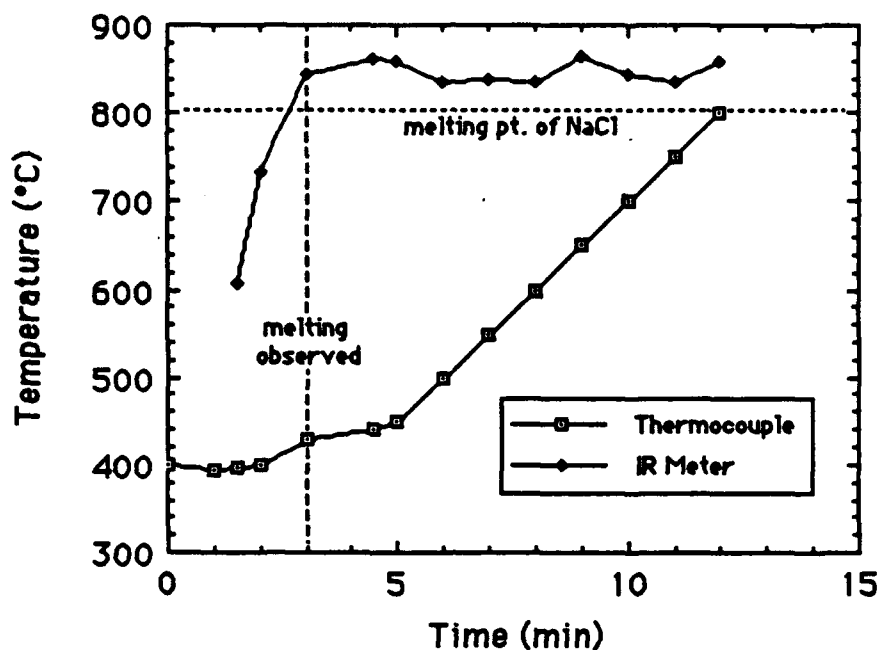


Figure 4. The melting of polycrystalline NaCl in a microwave field. Thermocouple embedded in sample. Emissivity setting of IR meter = 1.0.

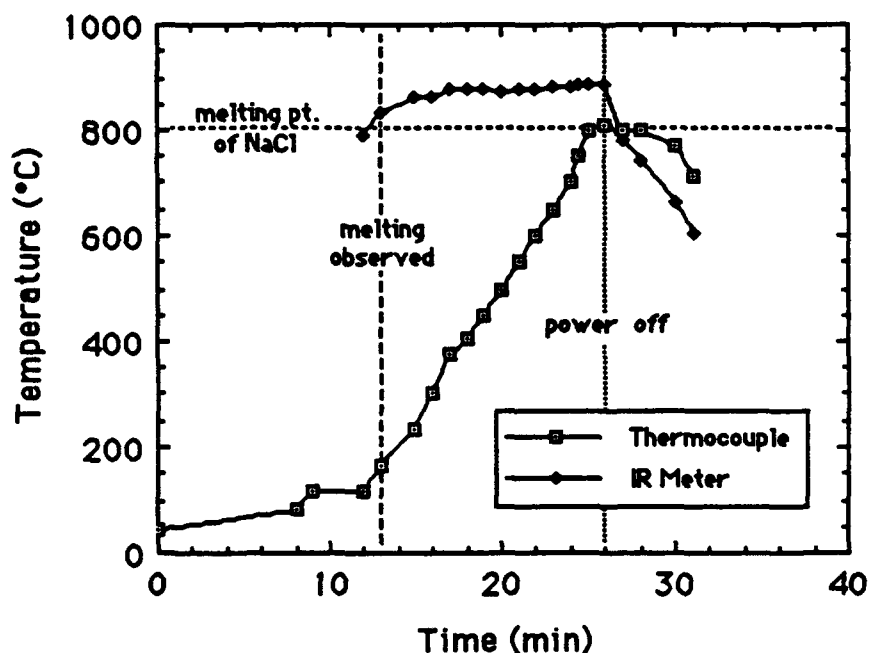


Figure 5. The melting of polycrystalline NaCl in a microwave field. Thermocouple embedded in sample. Emissivity setting of IR meter = 1.0.

**1988 USAF-UES SUMMER FACULTY RESEARCH PROGRAM/
GRADUATE STUDENT RESEARCH PROGRAM**

**Sponsored by the
AIR FORCE OFFICE OF SCIENTIFIC RESEARCH**

**Conducted by the
Universal Energy Systems, Inc.**

FINAL REPORT

Reaction Zone Characteristics of Titanium Aluminide Composites

Prepared by:	Carolyn W. Meyers
Academic Rank:	Assistant Professor
Department and University:	George W. Woodruff School of Mechanical Engineering, Georgia Institute of Technology
Research Location:	Air Force Wright Aeronautical Laboratories, Metals and Ceramics Division, Structural Metals Branch
USAF Researcher:	Dr. Theodore Nicholas
Date:	October 24, 1988
Contract No:	F49620-87-R-0004

**REACTION ZONE CHARACTERISTICS OF TITANIUM
ALUMINIDE COMPOSITES**

by

CAROLYN W. MEYERS

ABSTRACT

To obtain optimum performance of metal matrix composites, the reinforcing agents are coated prior to consolidation. The purpose of this treatment is to reduce the chemical reactions between the fibers and the matrix. However, during the consolidation of the composite, the coating breaks down forming a reaction layer. The extent of this reaction layer as well as its characteristics significantly influence the mechanical behavior of the composite. In this research, the nature and properties of the reaction layer are studied for two titanium matrix alloys, each reinforced with two types of fibers.

ACKNOWLEDGMENTS

The author of this Final Report thanks the Air Force Systems Command and the Air Force Office of Scientific Research for providing this research experience. Gratitude is also extended to Universal Energy Systems, especially Miss Sue Espy and Mr. Danichek, for their helpful administration of the Summer Faculty Research Program.

At the Materials Laboratory, Mrs. Susie Kirchoff's interest in facilitating the proposed research is greatly appreciated as is Dr. Theodore Nicholas' support and encouragement. Capt. Jerry Tarnacki's assistance in providing relevant literature was valuable as were discussions with Mr. Steve Schwenker. And through the efforts and concern of Dr. Simon Shong of Metcut, an enjoyable working atmosphere was provided.

I. INTRODUCTION

The high specific strength, the reasonable ductility and the dimensional stability of titanium and its alloys have contributed to the growth of their usage in aerospace applications. With the development of more advanced aerospace components, the property requirements for the materials are approaching the limits of those of the monolithic titanium alloys. To extend these properties while concurrently minimizing weight, titanium alloys reinforced with strong, stiff fibers have been developed.

The performance of a number of these Ti-based metal matrix composites has been acceptable but not as extraordinary as expected. The degradation in mechanical properties most probably originates in the relationships between the matrix material, the reinforcing agent and the interface between the matrix and the reinforcing agent.

My research interests have been in the area of structure property relationships in metallic materials. Specifically, my work on the diffusion driven reactions during the solution heat treatment of alloys is complementary to the study of the diffusion-based reactions at the interface between the matrix and the reinforcing agent in metal matrix composite materials. The study of these reactions and their effects on the deformation response of metal matrix composites was the basis of my desire to be assigned to the Structural Metals Branch of the Materials Laboratory.

II. OBJECTIVES OF THE RESEARCH EFFORT

As previously stated, the level of the performance of Ti metal matrix composites is strongly influenced by the nature and the characteristics of the interface between the matrix and the reinforcing fibers.

To improve wettability and to impede chemical reactions between the fibers and the matrix, the fibers are coated prior to composite consolidation. However, during this latter process, a reaction product forms. The effect of this reaction product between the fiber and the matrix is to degrade mechanical properties.

The objective of this research effort is to study the influence of different vacuum hot pressing conditions on the nature of the reaction zone. These objectives are to be accomplished by the characterization of the reinforcements and the microstructures, in general, after consolidation of two titanium matrix alloys each with two different types of reinforcing fibers. Two sets of vacuum hot pressing conditions are to be used for each metal matrix composite. Scanning electron microscopy, microprobe analysis, and microhardness tests are to be employed in the characterization work.

IV. RECOMMENDATIONS

As the researcher is interested in structure-property relationships in metal matrix composites, it is desirable to proceed with the proposed reaction zone studies. It would be extremely beneficial to perform mechanical property tests (e.g., tensile, short rod fracture toughness, and low cycle fatigue) on specimens subjected to the same processing conditions. Through interrupted tests, completed tests and microstructural analyses on unreinforced as well as reinforced material, insights into operative deformation and fracture mechanisms could be gained. These types of studies are natural follow-on to the reaction zone studies.

III. TWO TITANIUM ALLOYS WERE PROVIDED BY ALCOA:

AF1: Ti-6.4 Al-3Zr - .25 Sn - 2.5 Hf - 1 Nb - 0.3Mo - 0.2Si

- 3 Er

(in weight percent) and

Ti - 10V - 2Fe - 3Al

Each alloy was reinforced with Ti_3Si_3 and TiB_2 . For AF1 the vacuum hot press conditions were 2012°F/4 ksi/2hr and 1800°F/15 ksi/2hr. Similarly for the Ti-10-2-3, the conditions were 1652°F/4 ksi/2 hr and 1625°F/15 ksi/2 hr.

The intended purpose of these conditions was to study the effects of variable hot pressing conditions on the reaction zone characteristics. Additionally, both alloys, unreinforced, were to be vacuum hot pressed under the same conditions. These microstructures were to be characterized and contrasted with those of the reinforced alloys. Prior to leaving the Materials Lab, the vacuum hot pressing was completed. However, sample preparation for microscopy was not. The researcher requested that the samples be forwarded to her home institution to continue the work. This request has not been granted to date.

1988 USAF-UES FACULTY RESEARCH PROGRAM/
GRADUATE STUDENT RESEARCH PROGRAM

Sponsored by the
AIR FORCE OFFICE OF SCIENTIFIC RESEARCH

Conducted by the
Universal Energy Systems, Inc.

FINAL REPORT

PHOTOREFLECTANCE MEASUREMENTS OF UNINTENTIONAL IMPURITIES
IN UNDOPED GALIUM ARSINIDE

Prepared by:	Micheal Sydor
Academic Rank:	Professor
Department and	Physics Dept.
University:	Univ. of Mn. Duluth
Research Location:	AFWAL/MLPO Wright-Patterson AFB Dayton Ohio 45433
USAF Researcher:	William Mitchel
Date:	26 Aug 88
Contract No:	F49620-88-C-0053

PHOTOREFLECTANCE MEASUREMENTS OF UNINTENTIONAL IMPURITIES
IN UNDOPED GALIUM ARSINIDE

ABSTRACT

Photoreflectance (PR) is used to measure the unintentional impurity and defect concentrations in undoped epitaxial GaAs. The PR signature above the band gap spreads with defects and shows well defined Franz-Keldysh peaks whose separation provide a good measure of the unintentional impurity concentration as compared with Hall data. The PR signal at and below the band edge has a large excitonic component, and contains surface effects which preclude analysis by the usual three point functional fits for low electric fields.

Bulk semi-insulating materials generally provide a wide, single PR structure whose breadth depends on traps and bound excitons. Analysis of PR shows that a three point functional fit with excitonic function alone provides a reasonable fit to semi-insulating bulk data.

ACKNOWLEDGEMENTS

I wish to thank the Air Force Systems Command and the Air Force Office of Scientific Research for sponsorship of this research. I would also like to thank the Materials Laboratory for allowing me to use their facilities for my research. Universal Energy Systems also deserves mention for their help with the administrative aspects of the program.

I would like to thank Dr. P.M. Hemenger for opening the right doors for us and being a friend. We had a lot of equipment to put together. My thanks to Dr. William Mitchel for the use of his lab, for the samples and participation in the experiment. I would like to thank my colleague Dr. Ming-Yuan Yen for collaboration on the research, and the enthusiasm for the experiment. My special thanks to Dr. Tim Peterson, Dr Dave Zelmon, and Dr. Chris Mudare who helped out with equipment loan. My thanks to Ron Perrin, Tom Kensky, and Laura Rae for indispensable help with computer and electronic work. I am especially grateful to Paul Von Richter, for his help in construction of the apparatus. Last but not least my thanks to Jim Angelo, my student, for the support, the questions, the enthusiasm and friendship as well as hard and devoted work well beyond the ordinary requirements of students.

I. INTRODUCTION:

There is a great deal of interest in the scientific and technological community in epitaxial structures of GaAs and AlGaAs. Material quality is essential in good device performance.

The Materials Laboratory of the Air Force Wright Aeronautical Laboratory at Wright-Patterson Air Force Base is particularly interested in characterizing both GaAs and GaAs/AlGaAs structures grown by Molecular Beam Epitaxy (MBE) for use in detectors and electronic devices.

My research interests are in Optics, and Solid State Physics, with special interest in excitons and their properties at interfaces. My interest in the field dates to 1965.

II. OBJECTIVES OF THE RESEARCH EFFORT:

Photoreflectance (PR) has become a versatile tool for rapid assessment of sample properties from Molecular Beam Epitaxy (MBE) and Chemical Vapor Phase Epitaxy (CVPE). Our purpose was to build the apparatus and perform tests on MBE samples to assess their quality, in terms of unintentional defect concentrations, and their composition. Besides demonstrating the utility of PR we wanted to do some basic research on the properties of undoped GaAs.

III.

Photoreflectance (PR) has been established as an accurate, and quick method for measurement of band edge energies, alloy composition, and doping levels of GaAs and AlGaAs¹⁻⁵. As a result the technique is a prime candidate for use in bulk material quality control, and quick assessment of sample quality from MBE and chemical vapor phase epitaxy.

Shay⁴ (1970) has pointed out the applicability of PR technique to monitoring of doping levels in GaAs. Peters² et al (1987) use the shift in PR band edge to determine doping concentrations in the 3×10^{15} – 8×10^{17} cm⁻³ range. Bottka⁷ et al (1988) utilize the energy period of Franz-Keldysh Oscillations (FKO), prominent in doped material, for the same purpose.

We examine here the potential of using PR in the measurements of unintentional impurity and defect concentrations in undoped GaAs. The results may be applicable to optical testing of quality in device material where unintentional defects in undoped layers play a significant role in device performance. We also investigate the physical nature of PR in undoped MBE material and in semi-insulating bulk material to examine the limits on use of PR, and the validity of interpretation of PR, in measurements of carrier concentrations under low field conditions.

There are questions whether the theory based on free carrier-electric field interaction really does account for most of the PR signal, at the band edge, for low field conditions. This has been often taken for granted in analysis of PR data.

A usual arrangement of photorefectance apparatus^{1,3,4} was set up using a 5 mW HeNe laser with sample illumination intensity ranging from 10-100 mW/cm². The laser beam was chopped at 400 Hertz. The probe beam was due to a 100 W Tungsten Halogen lamp coupled to a .25m monochromator. A narrow band pass filter in front of the detector was used to check for room temperature photoluminescence⁶.

To examine the PR from undoped GaAs, a series of samples ranging from .2-6 μm were grown by MBE. Some samples were grown on substrates taken from pieces of the same bulk wafer. Some were grown as duplicates. Often, two pieces of the same sample were examined as a check on the experimental results. This was usually done for the thin samples, when substrate effects were apparent in the PR below the band edge. Fig. 1 shows a range of PR signals from various samples of undoped epitaxial GaAs.

Since the samples were grown under the same conditions, questions arose regarding the origin of the spread in PR. The PR signal generally had the same shape in all undoped samples thicker than 3 μm . All samples displayed a distinct second FKO at higher energies¹. Since the two FKO peaks could be identified clearly in all cases, we used their energy separation to estimate the unintentional carrier concentrations in our samples. we calibrated our method against samples with known carrier concentrations ranging from 5×10^{14} - $1 \times 10^{15} \text{ cm}^{-3}$ n-type material. Fig. 2 shows the calibration curve and our measured defect concentrations. Table 1 lists some samples and shows a trend which indicates that higher defect concentrations occur for thin samples but get progressively better in the thicker growths. In all 26 samples, including 5 duplicates were examined.

Samples grown on substrates cut 2 degrees off the (100) axis also showed greater defect concentrations as did samples grown on AlGaAs.

The width of PR peak at and below the band edge, showed a superposition of effects. Samples which had few defects but were less than $3\text{ }\mu\text{m}$ thick, consistently showed a secondary structure some 20 meV below the band edge as shown in curve 1, fig. 1. This structure comes from the substrate-epilayer interface, and will be treated in detail elsewhere. Here, it demonstrates the fact that PR at the band edge changes with transparency of the sample just below the band edge. Thus, for thin high optical quality layers, PR is sensitive to the interfaces. However our determination of defect concentrations in such samples was unaffected by the interface properties, since at energies above the band edge where FKO are measured, the samples are optically thick. Hall measurements shown in Table 1 vary, and are less consistent than the PR measurements, but they generally confirm the range of carrier concentrations measured by the PR. Hall measurements also provided an indication that the spread in PR at the band edge was largely due to nonelectrical defects which appeared to provide traps for the excitons. Thus analysis of the shape of PR at the band edge, could provide a false measurement of carrier concentrations at these low values (10^{14} - $5 \times 10^{15}\text{ cm}^{-3}$).

Bulk semi-insulating material produced a weak PR at the band edge, but showed no FKO. Its comparison with an undoped $4\text{ }\mu\text{m}$ GaAs sample grown on the same material, is shown in fig.3. Notice the broad Cu impurity structure in both samples at $\sim 1.36\text{ eV}$. It can be seen that subtraction of flat-band behavior represented by the bulk sample would leave the FKO in the epitaxial sample relatively unchanged. Thus our method of basing our analysis on the FKO seems well justified.4.

The results indicate that PR can be used to probe unintentional defect concentration in undoped GaAs by using the spread in FKO above the band gap energies. PR signal at and below the band edge is sensitive to interface and substrate effects. Furthermore the PR at the band edge appears to have a component which is associated with nonelectrical defects. The defects trap excitons⁷ and provide a general broadening of the PR to the low energy side. This broadening may be inherent to all samples under low electric field conditions.

Functional fits for PR using sums of critical point forms, including excitonic contributions, provide reasonable carrier concentrations and effective band gap energies in the doped bulk sample, but perhaps does so fortuitously. Further work on the excitonic contributions to PR is needed before semi-insulating materials can be investigated reliably by using this technique.

Sample	Hall Value (cm ⁻³)	PR Value (cm ⁻³)	Thickness (μm)
Yen12	2.1x10 ¹⁴	1.5x10 ¹⁴	3.8
Yen13	1.5x10 ¹⁴	2.7x10 ¹⁴	2.4
Yen14	2.1x10 ¹⁴	1.6x10 ¹⁴	3.9
Yen16	4.2x10 ¹⁴	2.2x10 ¹⁴	4.0
Mo5-128	1.8x10 ¹⁵	1.8x10 ¹⁵	7.0

Table 1: Hall and PR determined values
of carrier concentration for 5 samples

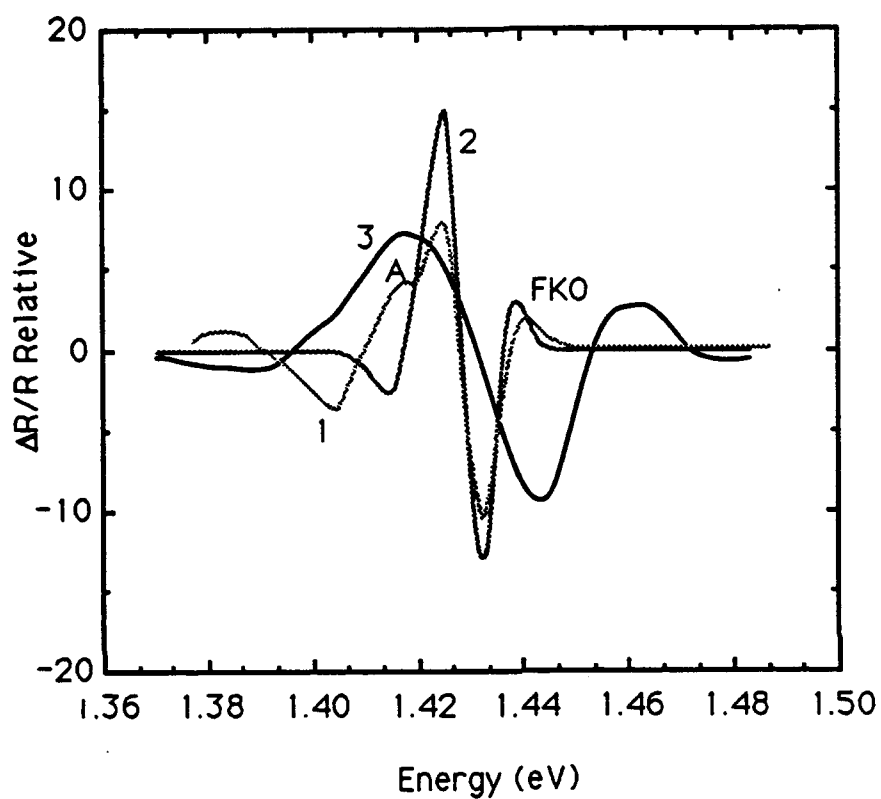


Figure 1. Curve 1 shows 2.4 μm , low defect sample. Structure A is due to the epilayer-substrate interface. Curve 2, shows a typical 4 μm , low defect undoped sample. Curve 3, shows a .05 μm sample grown on $\text{Al}_{.25}\text{Ga}_{.75}\text{As}$ layer.

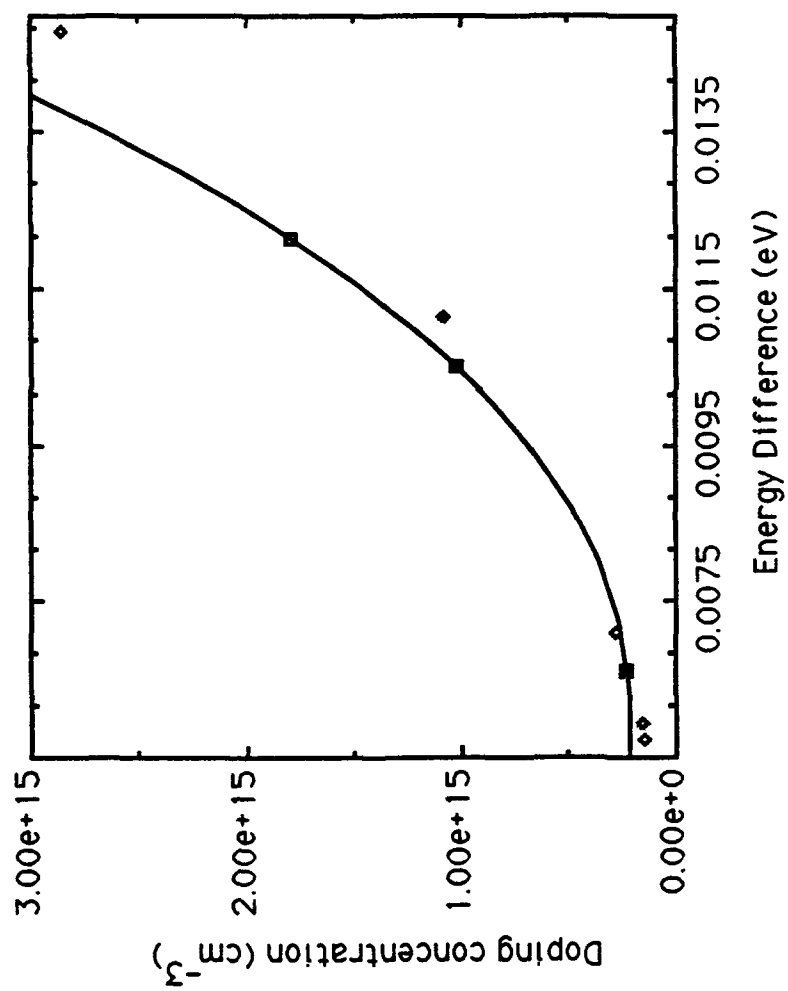


Figure 2 Franz-Keldysh peak separation vs. carrier concentration. As the concentration of defects increases the undoped GaAs samples depart from the calibration curve.

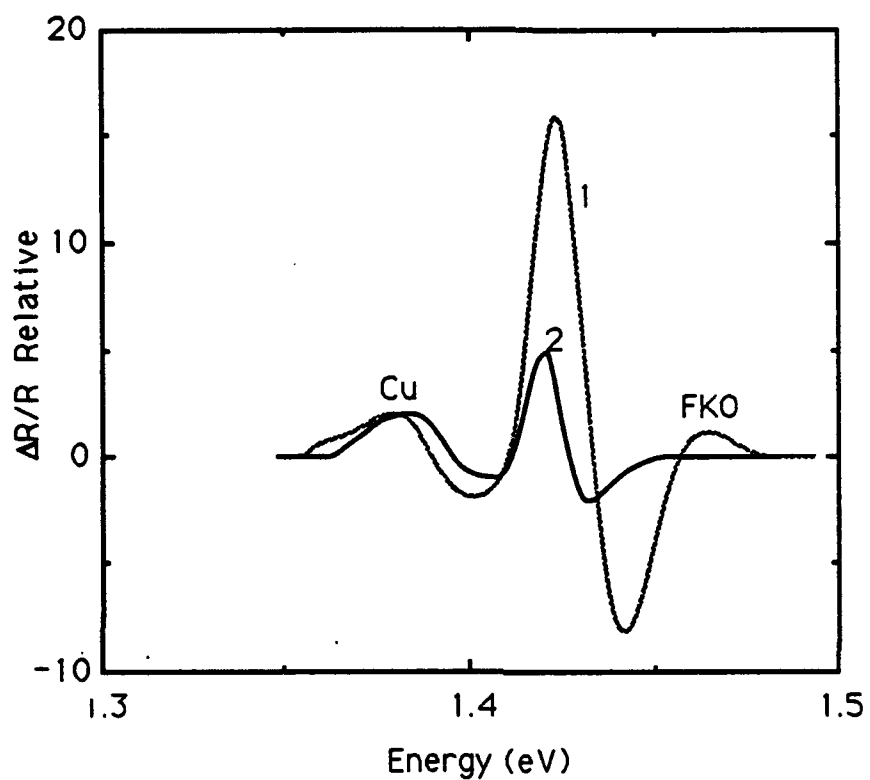


Figure 3 Comparison of undoped 4 μm sample with $6.5 \times 10^{15} \text{ cm}^{-3}$ defect concentration, curve 1, with semi-insulating bulk sample, curve 2. The sample was grown the same bulk material.

REFERENCES:

1. Bottka, N., D.K. Gaskill, R.S. Sillmon, R. Henry, R. Glosser 1988 J. Electron. Materials 17, 161
2. Peters, L., L. Phaneuf, L.W. Kapitan, and W.M. Theis 1987 J. Appl. Phys. 62(11), 4558
3. Glembocki, O.J., B.V. Shanabrook, N. Bottka, W.T. Beard, and J. Comas 1985 Appl. Phys. Letters 46, 970
4. Shay, J.L. 1970 Phys. Rev. B 2, 803
5. Pollak, Fred.H., C.E. Okeke, P.E. Vanier, and P.M. Racciah 1979 J. App. Phys. 50, 5375
6. Theis, W.M., G.D. Sanders, C.E. Leak, K.K. Bajaj, and H. Markoc Phys. Rev. B 37, 3042
7. Shay, J.L. and R.E. Nahory 1969 Solid State Commun. 7, 945
8. Zheng, X.L., D. Heiman, B. Lax, F.A. Chambers, and K.A. Stair 1988 Appl. Phys. Letters 52(12), 984
9. Aspnes, D.E. 1973 Surf. Sci. 37, 418

10. Raccah, P.M., J.W. Garland, S.E. Buttrill, L. Francke, and J. Jackson 1988
Appl. Phys. Letters 52(9), 1584

IV. RECOMMENDATIONS:

- a. The apparatus we have constructed has been taken over by our colleague Dr. Chris Mudare who will pursue the program we have started, and upgrade the apparatus to a routine technique for sample analysis at the Materials Laboratory.
- b. We would hope to continue our contacts with Dr. Yen and the MBE group as well as Dr. Mudare in further pursuit of PR as a Research tool.

1988 USAF-UES SUMMER FACULTY RESEARCH PROGRAM

Sponsored by the
AIR FORCE OFFICE OF SCIENTIFIC RESEARCH

Conducted by
UNIVERSAL ENERGY SYSTEMS, INC.

FINAL REPORT

THE SYNTHESIS OF 2-FORMYL PYRIDOIMIDAZOLES

Prepared by:	Dr. Richard S. Valpey III
Academic Rank:	Assistant Professor of Chemistry
Department and	Natural Science Department
University:	Wilberforce University
Research Location:	Wright Patterson AFB, AFWAL/MLBP, OH
USAF Researcher:	Dr. Robert C. Evers
Date:	July 18, 1988
Contract No.:	F49620-87-R-0004

THE SYNTHESIS OF 2-FORMYL PYRIDOIMIDAZOLES

by

Dr. Richard S. Valpey III

ABSTRACT

The synthesis of a new class of monomers for use in developing heterocyclic rigid-rod polymers with nonlinear optical properties has been developed. A model compound, 2-formyl-1-phenyl pyridoimidazole was prepared in three steps starting with 2-chloro-3-nitropyridine. This new methodology was then applied to the synthesis of 2,6-diformyl-1,7-diphenyl pyridobisimidazole.

ACKNOWLEDGEMENTS

First and foremost, I wish to thank the Air Force Systems Command, the Air Force Office of Scientific Research and Universal Energy Systems, Inc. for sponsorship of this work.

Analytical services; combustion analysis and mass spectra were provided by The University of Dayton Research Institute. A special acknowledgement goes to all my colleagues at MLBP (Make Lots of Bad Polymers), particularly the synthesis groups, headed by Dr. Robert C. Evers, Dr. Fred Arnold and Mr. Bruce Reinhardt whose technical assistance proved invaluable. Also appreciated was the interaction with the polymer morphology and processing groups headed by Dr. Thaddeus Helminiak, Dr. Ivan Goldfarb and Lt. Col. Wade Adams. The computer laboratory implemented by Lt. Scott Wierschke clearly added to the success of this research project.

Finally, a most precious recognition for Robin, Carolyn and Marty who make all of this work worthwhile.

I. INTRODUCTION

The Department of Defense is developing new materials for aircraft structural components. One line of research currently under investigation is the replacement of systems that have traditionally been manufactured from metals with high strength polymers. The Materials Laboratory, a branch of the Air Force Aeronautical Systems Division, AFWAL/MLBP at Wright-Patterson AFB has spearheaded the research and development of polymers to serve this end. Particular attention is currently focused on rigid-rod aromatic heterocycles. When processed properly, these polymers possess extraordinarily high tensile strength-to-weight ratios. For example, this ratio for polybenzimidazole (See figure 1 on the following page), a derivative of which was used in America's Cup sails, is five times greater than that of steel.¹ These materials whose properties can be altered through the manipulation of their atomic structures have the added capabilities of being able to be spun into fibers, plated into films, extruded into shapes and incorporated into molecular composites.

At the focal point of attention is the optical nonlinearity of aromatic rigid-rod polymers. The task to which the project described in this report pertains is ultimately aimed at investigating the atomic structural requirements upon this nonlinearity. The experiments described herein are predicated on the hypothesis that incorporation of additional heteroatoms containing nonbonding electrons into the backbone of the rigid-rod will increase the $n-\pi^*$ transitions leading to enhanced nonlinear optical coefficients. Specifically, we wonder how a string of nitrogen atoms along the backbone (as in figure 2 below) would affect this property.

¹E. Baer 'Advanced Polymers' Scientific American 1986 255, 178.

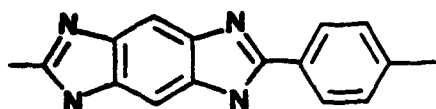


Figure 1: Polybenzimidazole

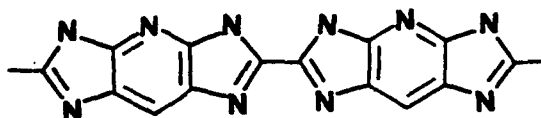


Figure 2: Un-named polymer

High molecular weight polymers possessing 2,2'-imidazole linkages have yet to be prepared. The approach under investigation in this laboratory is based on current technology. Rigid-rod polymers such as 1 are manufactured using polycondensation reactions of tetramines with terephthalic acid. The approach based on known technology substitutes terephthalic acid with the diacid of an arylbisimidazole. However, experiments in this laboratory have shown that these materials decarboxylate. The research described in this report addresses this problem by focusing attention to the corresponding dialdehyde, 3.

II. OBJECTIVES

Since a preparation of this molecule has never appeared in the literature, our first objective addressed the task by synthesizing a model compound comprised of only one imidazole ring, hence only one aldehyde, (compound 4). The second objective applied the same experimental conditions in synthesizing the dialdehyde, 3.

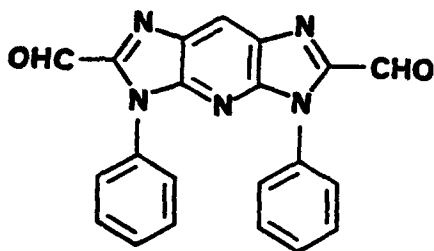


Figure 3: Dialdehyde

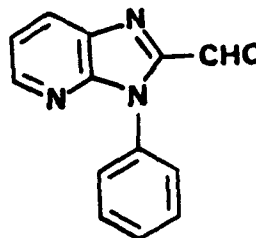
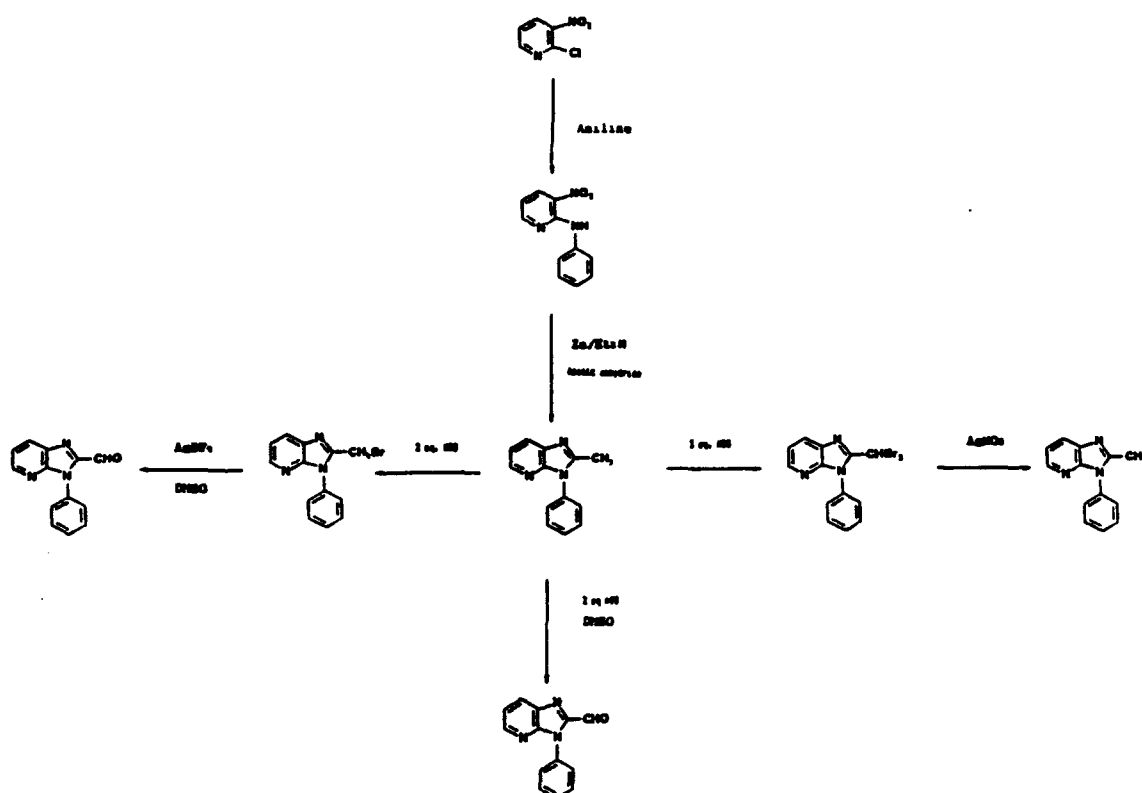


Figure 4: Model Aldehyde

III. RESULTS AND DISCUSSION

A. Model System

The first objective of synthesizing 2-formyl pyridoimidazole was accomplished as depicted in scheme 1.



Scheme 1: Model System chemistry.

Commercially available 2-chloro-3-nitropyridine was treated with aniline at 100°C then reacted with zinc and triethyl amine in refluxing acetic anhydride. Oxidation of the resulting 2-methyl-1-phenyl pyridoimidazole was then studied in great detail.

The classical reagent, selenium dioxide² failed to oxidize the electron rich aromatic methyl group. A number of other oxidizing agents including benzeneselenenic anhydride,³ chromium trioxide in acetic anhydride,⁴ ceric ammonium nitrate,⁵ lead tetra-acetate,⁶ and the Etard reaction⁷ also failed to oxidize 2-methyl-1-phenyl pyridoimidazole. Attention then turned to two step methodologies.

Although 2-bromomethyl-1-phenyl pyridoimidazole was oxidized with silver tetrafluoroborate in anhydrous DMSO, conventional bromination did not proceed in high yield. Treatment of 2-methyl-1-phenyl pyridoimidazole with N-bromosuccinimide or liquid bromine in chlorinated solvents furnished less than 10% yields of 2-bromomethyl-1-phenyl pyridoimidazole. The major product, the salt $C_{12}H_{11}N_2Br_2$,⁸ precipitated out of solution. Switching to a more polar solvent media resulted in increased yields of bromine adducts. An optimum rate of bromination was achieved by using 20% acetic acid in ethyl acetate. However, the dibromo adduct represented the largest component in the product mixture. Quantitative conversion to 2-dibromomethyl-1-phenyl pyridoimidazole was by achieved using three molar equivalents of N-bromosuccinimide. Although this dibromide was inert to conventional hydrolysis with concentrated sulfuric acid at 110°C, conversion to 2-formyl-1-phenyl pyrido-imidazole was achieved using silver nitrate in refluxing 2-methoxyethanol.

²D. Liotta Acc. Chem. Res. **1984** 17, 28.

³D. H. Barton et. al. Tetrahedron Lett. **1979** 3331.

⁴See S. M. Tsang, E. H. Wood and J. R. Johnson Organic Synthesis Col. Vol. III p. 641 and references therein.

⁵W. S. Trahanovsky and L. B. Young J. Org. Chem. **1966** 31, 2033.

⁶G. W. K. Cavill and D. H. Solomon J. Chem. Soc. **1954** 3943.

⁷See W. H. Hartford and M. Darrin Chem. Rev. **1958** 58, 1 and references cited therein.

⁸Examples of bromine complexes of related imidazoles are well known. For a review see P. M. Preston 'Benzimidazoles and Congeneric Tricyclic Compounds' vol. 1, New York: John Wiley & Sons, **1981** 321-31.

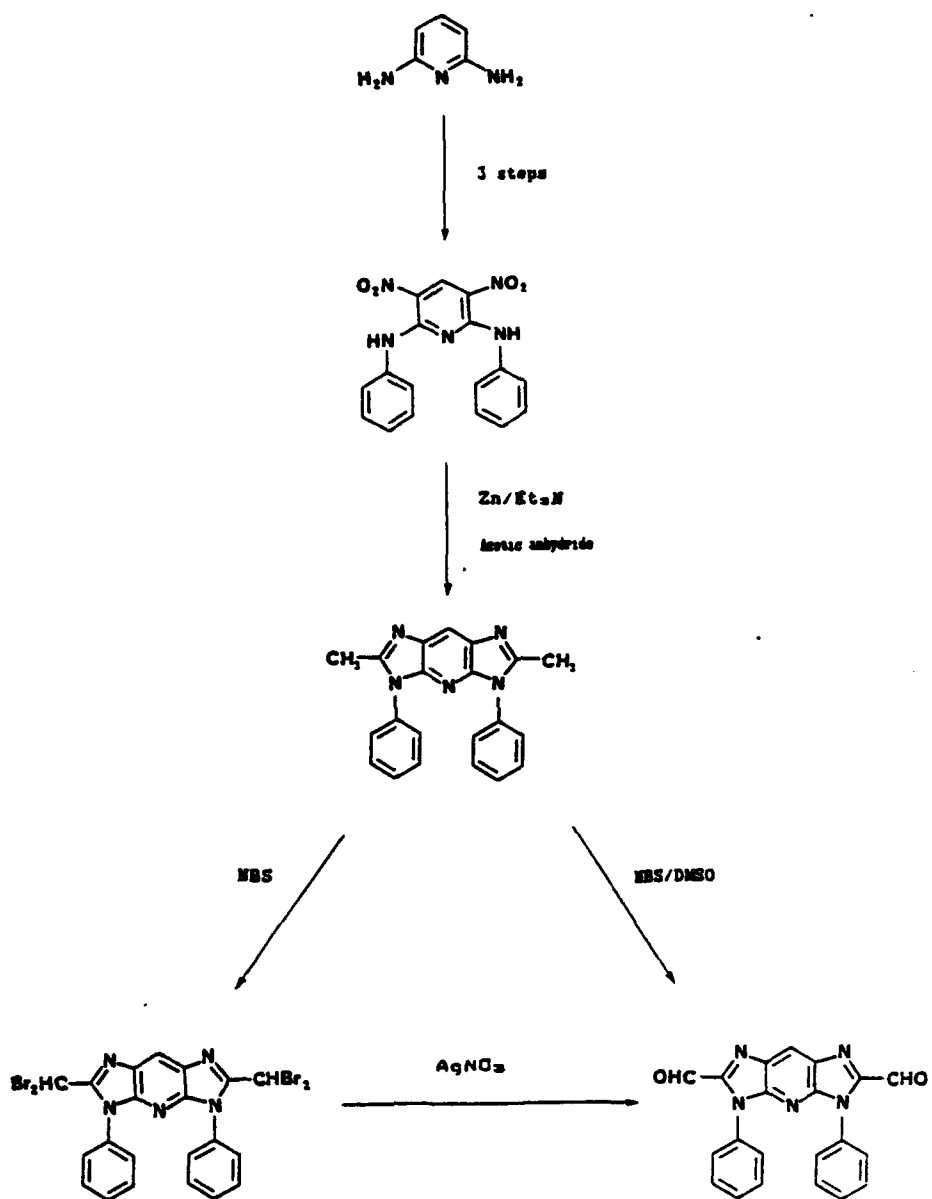
During the course of investigating solvent systems favoring bromination of 2-methyl-1-phenyl pyridoimidazole, a new one step oxidation reaction was discovered. Direct oxidation to 2-formyl-1-phenyl pyridoimidazole was observed using no fewer than two equivalents of N-bromosuccinimide in DMSO at 110°C.

To conclude the first objective, two efficient procedures were found for synthesizing 2-formyl-1-phenyl pyridoimidazole. Both involved oxidations of 2-methyl-1-phenyl pyridoimidazole which was conveniently prepared from commercially available 2-chloro-3-nitropyridine; one, a two step sequence involving silver(II) assisted hydrolysis of an intermediary dibromide and the other a direct N-bromosuccinimide mediated oxidation in DMSO. The ultimate choice between these two routes may depend not on their comparative yields, but rather on the ease of purification. The two step route furnished material contaminated heavily with solvent, which was found to be very difficult to remove. The one step route produced small amounts of several byproducts.

B. Dialdehyde

The penultimate intermediate in the synthesis of the desired dialdehyde, 2,6-dimethyl-1,7-diphenyl pyridoimidazole, was synthesized from 2,6-dianilino-3,5-dinitropyridine^a using zinc and triethyl amine in refluxing acetic anhydride. Bromination of this material did not proceed as smoothly as the model system. Insolubility of the initially formed bromine complex resulted in a poor (25%) yield of the tetrabromine adduct which was transformed into the desired dialdehyde using silver nitrate in refluxing 2-methoxyethanol. A route utilizing the NBS/DMSO oxidation uncovered during our investigation of model system chemistry represented the preferred route to this material (see scheme 2 below).

^aThis known compound was prepared starting with 2,6-diaminopyridine; U.S. patent no. 3,943,125.



Scheme 2: Dialdehyde Synthesis

IV. EXPERIMENTAL SECTION

Preparation of 2-methyl-1-phenyl pyridoimidazole¹⁰

A mixture of 2-anilino-3-nitropyridine (13.15 g, .0611 mole), triethyl amine (the triethyl amine does not require distillation; it should be colorless and stored over hydroxide, 17.2 mL, .122 mole), and acetic anhydride (175 mL) was mechanically stirred very vigorously while purified zinc dust¹¹ was added slowly in small portions. After a brief induction period of approximately fifteen minutes an exothermic reaction commenced. Zinc dust was then added at such a rate as to maintain a gentle reflux. The resulting heterogeneous reaction was refluxed for sixteen hours during which time the color changed from orange to black and then to crimson. After cooling to room temperature glacial acetic acid (35 mL) was added and the yellow slurry was heated at reflux for 24 hours. The slurry was again cooled to room temperature and excess acetic anhydride was quenched with H₂O (40 mL). This addition created an exotherm and the mixture lost its turbidity. After 14 hours at reflux, unreacted zinc was removed by hot filtration. The filtrate was added to a liter of H₂O then neutralized with ammonia. Organic material was extracted with methylene chloride (200 mL) three times. The combined organic layers were washed with brine (200 mL) then dried over anhydrous magnesium sulfate. The concentrated brown oil was purified by bulb-to-bulb distillation at 1 mm Hg. The resulting colorless plates weighed 8.9 g (70% purified yield). The analytical data were as follows:

¹H NMR (CDCl₃) δ 8.4(dd, J_{A-B}=14Hz, 1H), 8.3(dd, J_{A-C}=2Hz, 1H), 7.7(m, 6H), 2.6(s, 3H).

IR (KBr) 3050(w), 3030(w), 2970(w), 1600(m), 1516(m), 1501(m), 1425(s), 1392(m).

¹⁰notebook reference no. 69369-14 and 26.

¹¹The following procedure was used to purify the zinc used in this experiment: Zinc dust (120 g) was slurried for one minute with 2% aqueous HCl (300 mL) two times, deionized H₂O (200 mL) three times, absolute ethanol (200 mL) two times, and finally with anhydrous ether (200 mL) two times. The filtered solid was dried at 100°C and 0.1 mm Hg overnight.

1299(m), 1288(m), 1240(m), 780(m), 700(m) cm^{-1} . Mass spectrum 209(M^+), 208($M-H$, parent), 168($M-CH_2CN$), 140($M-CH_2C_2H_5$), 77(C_6H_5), 51(C_6H_5). Combustion analysis
Calculated for $C_{13}H_{11}N_3$: C, 74.62; H, 5.30; N, 20.08; Found: C, 74.48; H, 5.45; N, 20.35.

Bromination of 2-methyl-1-phenyl pyridoimidazole¹²

A mixture of 2-methyl-1-phenyl pyridoimidazole (4.0 g, 19 m.moles) and N-bromosuccinimide (6.4 g, 59 m.moles) in CCl_4 (purified by filtration through a tube of neutral alumina; 40 mL) was heated at reflux for 16 hours during which time the solid NBS on the bottom of the flask changed to a solid floating on top of the reaction medium. Starting material had disappeared as evidenced by thin layer chromatography (20% ethyl acetate in cyclohexane is a good solvent system for monitoring this reaction by TLC). The resulting slurry was filtered, the filter cake was washed with copious CCl_4 , and the filtrate was concentrated. Brominated pyridoimidazoles were separated by chromatography over silica gel eluting with 20% ethyl acetate in cyclohexane.

2-Dibromomethyl-1-phenyl pyridoimidazole (0.05 g, 1% yield) eluted first. The spectral data of this yellow solid were as follows: ¹HMR (CDCl_3) δ 8.4(dd, $J_{A-B}=12\text{Hz}$, $J_{A-C}=2\text{Hz}$, 1H), 8.3(dd, $J_{A-B}=13\text{Hz}$, $J_{A-C}=2\text{Hz}$, 1H), 7.7(s, 5H), 7.4(ddd, $J_{A-B}=12\text{Hz}$, $J_{A-C}=13\text{Hz}$, $J_{B-C}=2\text{Hz}$, 1H), 6.7(s, 1H).

2-Bromomethyl-1-phenyl pyridoimidazole (0.70 g, 13% yield) followed. The spectral data for this light yellow solid were as follows: ¹HMR (CDCl_3): δ 8.4(dd, $J_{A-B}=7\text{Hz}$, $J_{A-C}=2\text{Hz}$, 1H), 8.2(dd, $J_{A-B}=11\text{Hz}$, $J_{A-C}=2\text{Hz}$, 1H), 7.2-7.8(m, 6H), 4.6(s, 2H). Mass Spectrum: 288(M^+), 207 ($M-HBr$; parent), 77, 51 m/e.

¹²Notebook reference no. 541-41.

Preparation of 2-dibromomethyl-1-phenyl pyridoimidazole¹³

To a mixture of 2-methyl-1-phenyl pyridoimidazole (8.8 g, 0.042 mole) in ethyl acetate (240 mL) and glacial acetic acid (60 mL) was added N-bromosuccinimide (14.0 g, 0.12 mole) in one portion. After heating at reflux for 24 hours another 10 g of NBS was added. After another 24 hour period of reflux 5 g more NBS was added. After heating 24 more hours the solution was cooled and then added to 10% aqueous ammonium hydroxide (500 mL). Organic material was extracted with ethyl acetate (200 mL) three times. The combined organic layers were washed with brine (200 mL) then further dried over anhydrous magnesium sulfate. The concentrated residue weighed 14 g (quantitative). Three crops of material that were recrystallized from absolute ethanol weighed 8.0 g (52% purified yield). An analytical sample was prepared by first dissolving in hot (110°C) sulfuric acid then pouring into ice water. The resulting precipitate was air dried then recrystallized once more from absolute ethanol. The analytical data were as follows:

¹HMR (CDCl₃) δ 8.4(dd, J_{A-B}=12Hz, J_{A-C}=2Hz, 1H), 8.3(dd, J_{A-B}=13Hz, J_{A-C}=2Hz, 1H), 7.7(s, 5H), 7.4(ddd, J_{A-B}=12Hz, J_{A-C}=13Hz, J_{B-C}=2Hz, 1H), 6.7(s, 1H). IR (KBr) 3050(w), 3030(w), 2970(m), 1579(m), 1498(s), 1480(w), 1455(w), 1430(m), 1390(m), 1347(w), 1315(m), 1288(m), 1240(m), 1010(m), 960(w), 810(m), 775(m), 740(w), 725(w), 796(m), 630(m), 615(m) cm⁻¹. Mass Spectrum 365, 367, 369 (three M⁺ isotopes), 386, 388 (M-Br), 207 (M-Br₂, parent), 179 (M-Br₂H₂CH), 152(M-Br₂H₂C₂H₂), 103(C₆H₅CH⁺), 77(Ph⁺) m/e. Combustion analysis Calculated for C₁₃H₈Br₂N₂: C, 42.58; H, 2.47; Br, 43.52; N, 11.45. Found: C, 42.23; H, 2.54; Br, 43.45; N, 11.37.

¹³Notebook reference no. 69369-20.

Preparation of 2-formyl-1-phenyl pyridoimidazole from 2-bromomethyl-1-phenyl pyridoimidazole¹⁴

All glassware used in this experiment was dried at 100°C overnight and flushed with H₂ while cooling. The reaction was carried out under a nitrogen atmosphere.

While working in a H₂ glove bag, silver tetrafluoroborate (140 mg, 0.719 m.moles) was weighed into a 10 mL round bottom flask. Dimethyl sulfoxide (freshly distilled from CaH₂; 1.0 mL) was added followed by 2(bromomethyl)-1-phenyl pyridoimidazole (159 mg, 0.553 m.moles). A tan precipitate gradually formed over 24 hours indicating that a reaction had occurred even though no change in TLC was observed. Triethyl amine (freshly distilled from CaH₂; 0.1 mL) was added and the reaction was stirred at room temperature for 30 minutes. The resulting solution was transferred into 25 mL of H₂O and extracted with ether (30mL) three times. The combined ethereal layers were washed with brine (25 mL) twice the dried over MgSO₄. Concentration of the liquid under reduced pressure followed by chromatography over silica gel eluting with 20% ethyl acetate in cyclohexane afforded a light yellow solid (60 mg, 49% yield) which melted at 122-8°C. The analytical data were as follows:

¹HMR (CDCl₃): δ 10.3(s, 1H), 8.7(dd, J_{A-B}=7Hz, J_{A-C}=2Hz, 1H), 8.4(dd, J_{A-B}=10Hz, J_{A-C}=2Hz), 8.3-7.8(m, 6H). IR (KBr): 3055(m), 3030(w), 2930(m), 2855(w), 1702(s), 1595(m), 1501(m), 1425(m), 1255(w), 775(m), 758(m), 693(m) cm⁻¹. Mass Spectrum: 223(M⁺), 195(M-CO), 194(M-CHO), 169, 140 77, 51 m/e.

¹⁴notebook reference no. 541-42.

Preparation of 2-formyl-1-phenyl pyridoimidazole from 2-dibromomethyl-1-phenyl pyridoimidazole^{1a}

To a refluxing mixture of 2-dibromomethyl-1-phenyl pyridoimidazole (3.2 g, 8.7 mmole) in 40 mL of 2-methoxyethanol was added dropwise a solution of silver nitrate (4.4 g, 26 mmole) in 20 mL of H₂O. A lime colored precipitate formed immediately. The resulting slurry was heated at reflux for an additional 30 minutes to insure completion of reaction. The filtrate resulting from hot filtration was distilled under vacuum. The analytical data were identical to that described in the preceding paragraph.

Preparation of 2,6-dimethyl-1,7-diphenyl pyridobisimidazole^{1a}

A mixture of 2,6-dianilino-3,5-dinitropyridine (5.10 g, 14.5 m.moles), triethyl amine (the triethyl amine does not require distillation; it should be colorless and stored over hydroxide, 4.0 mL, 29 m.moles), and acetic anhydride (40 mL) was mechanically stirred very vigorously while purified zinc dust^{1a} was added slowly in small portions. After a brief induction period of approximately fifteen minutes an exothermic reaction commenced. Zinc dust¹¹ was then added at such a rate as to maintain a gentle reflux. The resulting heterogeneous reaction was refluxed for sixteen hours during which time the color changed from black to yellow. After cooling to room temperature glacial acetic acid (8 mL) was added and the yellow slurry was heated at reflux for 13 hours. The slurry was again cooled to room temperature and excess

^{1a}Notebook reference no. 69369-44.

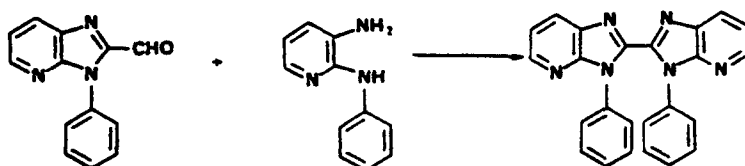
^{1b}Notebook reference no. 541-25.

acetic anhydride was quenched with 8 mL of H₂O. This addition created an exotherm and resulted in an increase in viscosity. The golden yellow solution was heated at reflux for 4 hours then hot filtered to remove unreacted zinc. The filtrate was added to a liter of 10% aqueous ammonium hydroxide. Precipitation was allowed to take place over 30 minutes. The yellow filtrate was collected by filtration. Its color changed to light green during the filtration process. The crude solid weighed 4.16 g. This material was purified by recrystallization from supersaturated absolute ethanol solutions. Five crops totalling 3.20 g were isolated (65% yield). The cleanest crop melted at 311-2°C. The analytical data were as follows:

¹HMR (CDCl₃): 8.4(s, 1H), 7.4-7.8(m, 10H), 6.6(s, 3H). IR (KBr) 3040(w), 3028(w), 2912(m), 2825(w), 1740(w), 1655(m), 1602(m), 1520(w), 1495(m), 1450(s), 750(m), 700(s) cm⁻¹. Mass Spectrum: 339(M⁺; parent), 338, 77 m/e.

V. RECOMMENDATIONS

- A. A synthesis of 2-formyl pyridoimidazoles has been developed. However, before these materials can be incorporated into the manufacture of polymers a better purification procedure needs to be developed.
- B. Once pure aldehydes are obtained, model studies on simple 2,2'-bisimidazoles can begin. The parent 2,2'-bispyridoimidazole can be prepared in the following manner (equation 1).



C. A second family member, one containing two such linkages, can also be prepared (equation 2)



D. Optical properties of this family of molecules can then be measured.¹⁷

E. The ultimate task of using 2,6-diformyl-1,3,5-trisubstituted pyridine in a polymerization reaction and subsequent evaluation of the product's properties will then be addressed.

¹⁷These measurements are planned through joint experiments with Professor Paras M. Prasad at the State University of New York at Buffalo.

VI. REFERENCES

1. Baer, E., 'Advanced Polymers,' Scientific American, 1986, pp. 178-186.
2. Barton, D. H., et. al., 'Preparation of Aldehydes and Ketones by Oxidation of Benzylic Hydrocarbons with Benzeneselenenic anhydride,' Tetrahedron Letters, 1979, pp. 3331-3335.
3. Cavill, G. W. K. and Solomon, D. H., 'The Reaction of Lead Tetra-acetate with Toluene and Related Compounds,' Journal of the Chemical Society, 1954, pp. 3943-3946.
4. Fieser, L. F. and Fieser, M., Reagents for Organic Synthesis, New York, John Wiley and Sons Publishers, 1976.
5. Ganem, B. and Boeckman, R. K., 'Silver Assisted Dimethylsulfoxide Oxidations; An Improved Synthesis of Aldehydes and Ketones,' Tetrahedron Letters, 1974, pp. 917-920.
6. Gilman, H., editor-in-chief, Organic Synthesis, Collective Volumes I-V, New York, John Wiley and Sons Publishers, 1951.
7. Hartford, W. H. and Darrin, M., 'The Chemistry of Chromyl Compounds,' Chemical Reviews, 1958, pp. 1-72.
8. Liotta, D. 'New Organoselenium Methodology,' Accounts of Chemical Research, 1984, pp. 28-34.
9. Preston, P. N., Benzimidazoles and Congeneric Tricyclic Compounds, New York, John Wiley and Sons Publishers, Volume 1, pp. 321-331.

10. Trahanovsky, W. S. and Young, B., "Controlled Oxidation of Organic Compounds with Cerium (IV)," Journal of Organic Chemistry, 1966, Volume 31, pp. 2033-2035.